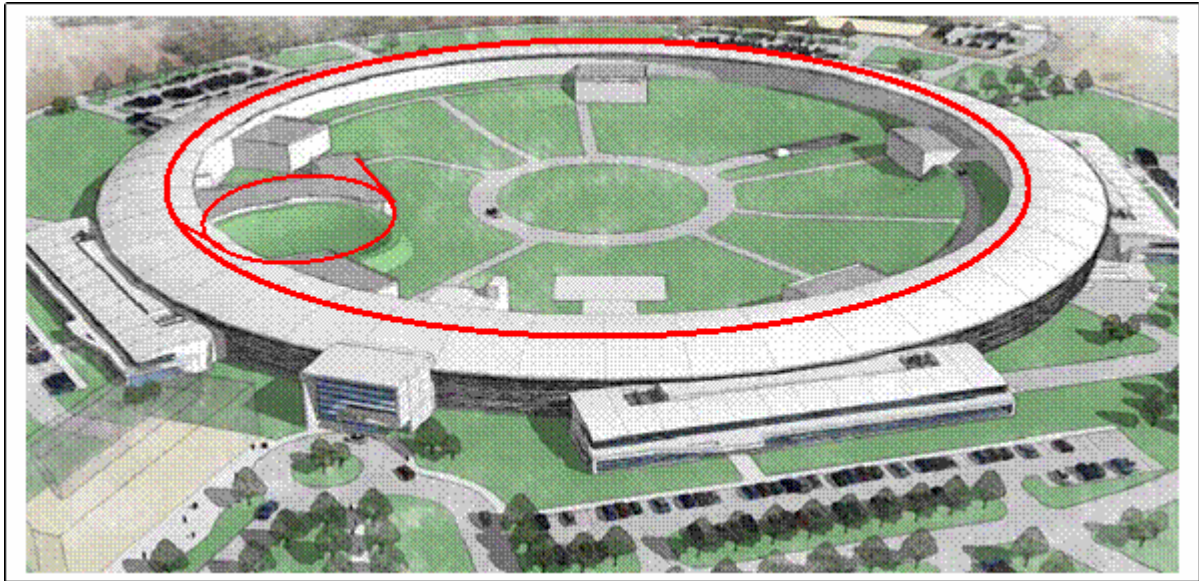


# 1 ACCELERATOR OVERVIEW

This chapter describes the main requirements and features of the NSLS-II accelerator complex, focusing on the philosophy and the approach used to select the NSLS-II ring lattice, injection scheme, and main components. Based on the considerations presented here, we believe we have arrived at an optimal, or near-optimal, design. This description is brief, and important details of the individual systems and subsystems are presented in other chapters of this preliminary design report.



**Figure 1.1.1** Schematic layout of the NSLS-II accelerators: a 200 MeV linac, a 3 GeV booster ring, and the 3 GeV storage ring.

## 1.1 Scope of the Accelerator Complex

NSLS-II is designed to deliver photons with average spectral brightness in the 2 keV to 10 keV energy range exceeding  $10^{21}$  ph/mm<sup>2</sup>/mrad<sup>2</sup>/s/0.1%BW. The spectral flux density should exceed  $10^{15}$  ph/s/0.1%BW in all spectral ranges and with a peak value approaching  $10^{16}$  ph/s/0.1%BW for photon energies around 2 keV. This cutting-edge performance requires the storage ring to support a very high-current electron beam ( $I = 500$  mA) with sub-nm-rad horizontal emittance (down to 0.5 nm-rad) and diffraction-limited vertical emittance at a wavelength of 1 Å (vertical emittance <8 pm-rad). The electron beam will be stable in its position (<10% of its size), angle (<10% of its divergence), dimensions (<10%), and intensity ( $\pm 0.5\%$  variation). The latter requirement provides for constant thermal load on the beamline front ends.

A schematic layout of the NSLS-II accelerators is shown in Figure 1.1.1. Electrons generated in the linac are accelerated to 3 GeV in the booster. The accelerated electrons are periodically added to the electron beam circulating in the storage ring to keep the stored current nearly constant in time, a process known as top-off injection. This chapter presents the main parameters of the accelerator systems and main subsystems for NSLS-II and descriptions of the considerations and process that led to their optimization.

## 1.1.1 Physics Design and Parameters of NSLS-II

### 1.1.1.1 Storage Ring

Everywhere possible, NSLS-II will use known, reliable, and cost-effective solutions for its subsystems. Examples of such subsystems extend from a simple low-energy linac to the ring and booster RF systems, which are commercially available. Subsystems that are not critical to NSLS-II performance will be based on the simplest, most robust, and best-proven technologies. Hence, all magnetic elements of the accelerators have a significant margin in their design, but are not over-designed. Only the few subsystems that are crucial for attaining the ultimate NSLS-II performance require cutting-edge technologies and engineering solutions.

The overall layout of the storage ring and beamlines is shown in Figure 1.1.2 and in more detail in Figure 1.1.3. The chosen lattice meets the challenge to provide record-low electron beam emittance. The choice of large-radius bending magnets enhances the effectiveness of damping wigglers to reduce the emittance. The lattice is optimized to meet the required performance within budget and size constraints.

As described in this chapter, the optimized storage ring lattice consists of 30 DBA cells, with straight sections alternating in length between 6.6 m and 9.3 m. There are thus 15 super-periods for the lattice. The lattice functions of one DBA cell (one half super-period) are shown in Figure 1.1.4. Each straight section is achromatic and has three quadrupoles at each end. These quadrupoles provide for appropriate matching of the optic functions ( $\beta_x$ ,  $\alpha_x$  and  $\beta_y$ ,  $\alpha_y$ ) and tune advances ( $\Delta\nu_{x,y}$ ) in the straights to compensate the strong influence of the IDs on the linear lattice [1.1.1].

In order to accommodate a number of three-pole wigglers as additional sources of hard x-rays, a 0.6-m long straight was inserted at the down stream end of all dispersion sections. In order to maintain the symmetry of these dispersion straights, the same empty spaces were also added at the up stream end of the section. Although insertion of TPWs in these non-achromatic sections will impact the effort of reducing the emittance, the impact is estimated to be about 10% for 15 such insertions around the ring.

The total number of quadrupoles per cell is 10. Each cell also has three chromatic sextupoles and seven geometric sextupoles. All quadrupoles in the SR will have individual power supplies, which will be fully utilized for high-precision, beam-based alignment and for experimental verification and correction of the linear electron optics [1.1.2]. The sextupoles will be powered by family in each pentant. The main parameters of the storage ring are summarized in Table 1.1.1.

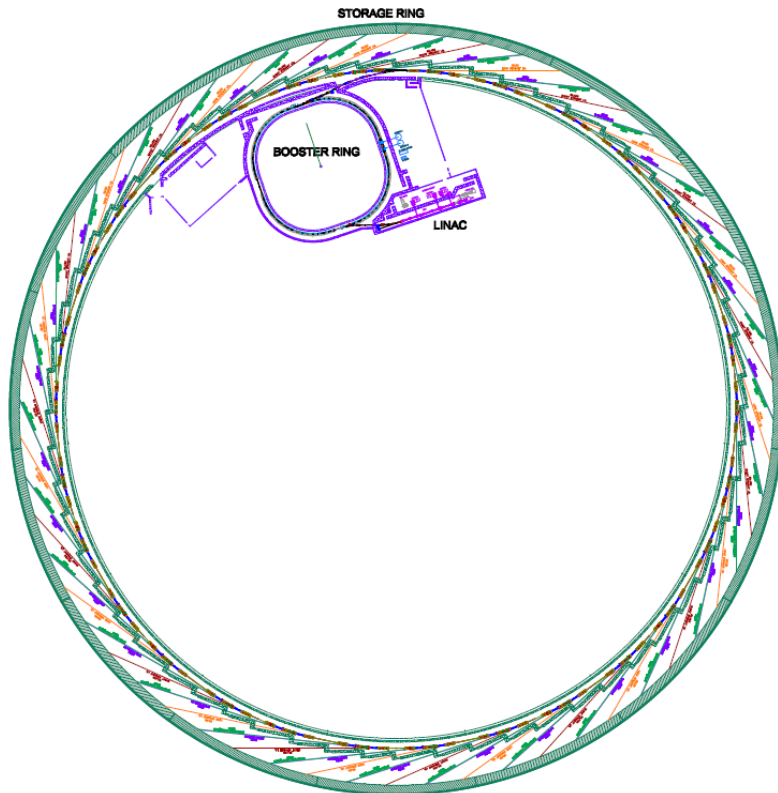


**Figure 1.1.2** Geometry of the NSLS-II light source and its beamlines; green and purple lines indicate beamlines from the Three Pole super-periods) with short (6.6 m) and long (9.3 m) wiggler and dipole, and orange and brown lines indicate those from long (9.3 m) straight sections and short ID straights.

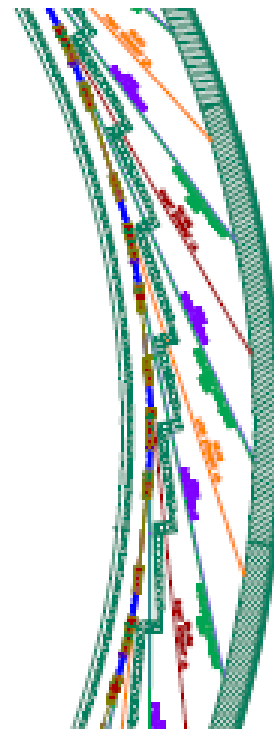


**Figure 1.1.3** Three DBA cells (one and a half super-periods) with short (6.6 m) and long (9.3 m) wiggler and dipole, and orange and brown lines indicate those from long (9.3 m) straight sections and short ID straights.

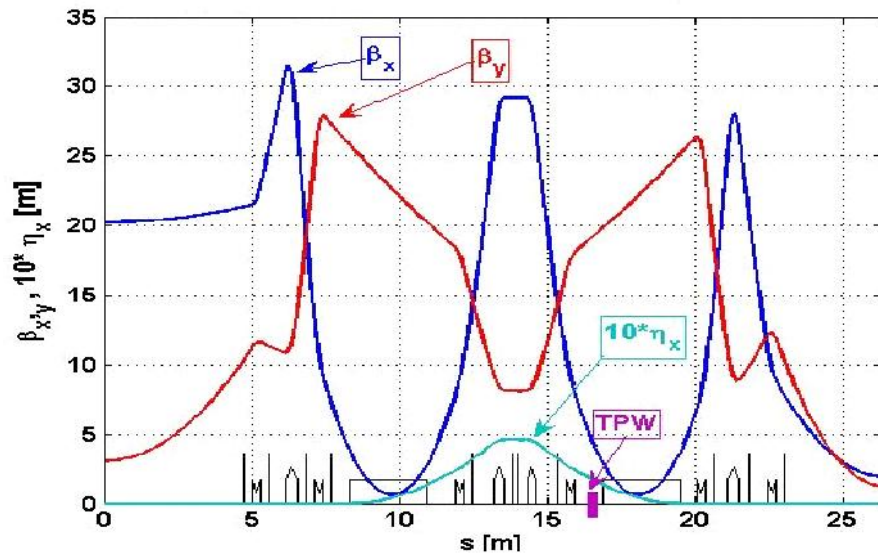


**Figure 1.1.4** Lattice functions of half of an NSLS-II storage ring super-period.

**Table 1.1.1 Basic Parameters of the NSLS-II Storage Ring**

Energy [GeV]	3
Circumference [m]	792
Number of DBA cells	30
Number of 9.3 m straights	15
Beta-functions in the center of the 9.3 m straights: $\beta_x, \beta_y$ [m]	21, 3.0
Number of 6.6 m straights	15
Beta-functions in the center of the 6.6 m straights: $\beta_x, \beta_y$ [m]	2.0, 1.0
Number of dipoles	60
Number of quadrupoles	300
Number of sextupoles	300
Circulating current at 3 GeV, multi-bunch [mA]	500
Radio frequency [MHz]	499.68
Harmonic number	1320
Number of bunches at 80% fill	1040
Nominal bending field at 3 GeV [T]	0.4
Dipole critical energy at 3 GeV [keV]	2.4
Total Bending magnet radiation energy loss [keV]	286.4
Radiation energy loss per damping wiggler [keV]	129.3
Vertical emittance [nm-rad]	0.008
Horizontal emittance of bare lattice [nm-rad]	2.0
Horizontal emittance with three 7 m 1.8 T damping wigglers [nm-rad]	1.0
Horizontal emittance with eight 7 m 1.8 T damping wigglers [nm-rad]	0.6
Momentum compaction factor	$3.7 \times 10^{-4}$
Bunch length, RMS, natural [mm, ps]	2.9, 10
Energy spread, RMS	0.05–0.1%

The 3 GeV storage ring is designed to be a reliable light source of hard and soft x-rays with average spectral brightness and flux in the target energy range from  $\sim 10$  eV to  $\sim 20$  keV, significantly exceeding all synchrotron light sources currently operating or under construction. All of its components are designed with an operational safety margin of  $\sim 10\%$ . The parameters of the magnets and their tolerances are specified in Section 7.1. None of the magnet parameters goes beyond well-established standards. The stability and alignment requirements are challenging but achievable (Section 6.1.2.4), as demonstrated at the Swiss Light Source. To achieve these tolerances, the clusters of quadrupoles and sextupoles will be assembled on individual girders, as shown in Figures 1.1.5 and 1.1.6. Their magnetic centers will be aligned precisely with respect to the girder fiducials using the vibrating wire technique. The pre-aligned girders will then be moved into the ring tunnel and installed. The alignment tolerances between girders ( $\sim 100$  microns) are less critical than between individual elements ( $\sim 30$  microns).



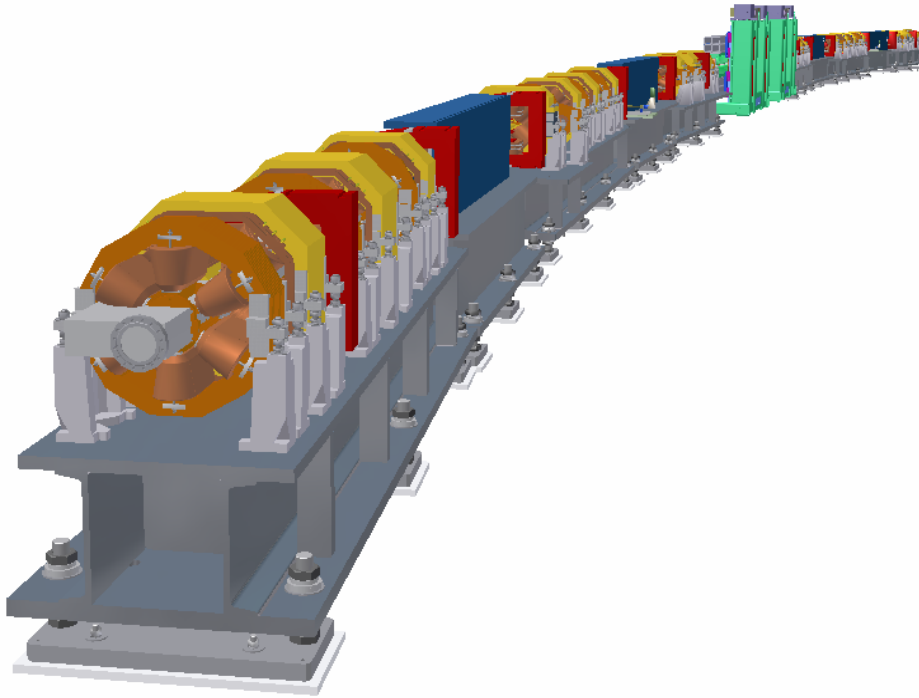


**Figure 1.1.5** 3D-view of the SR super-period comprised of two DBA cells and two straight sections (half of the 9.3 meter straight is shown at each end). The super-period has bilateral symmetry with respect to the center of the long or short straight section.

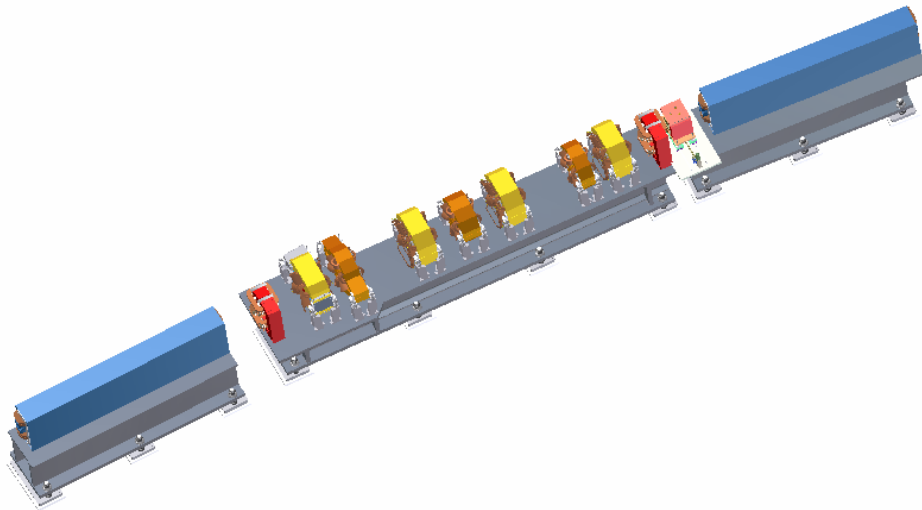


**Figure 1.1.6** 3D view of a standard DBA cell with bilateral symmetry. It consists of two dipoles, four quadrupoles, and five sextupoles. All quadrupoles and sextupoles are located on a single low-height rigid girder.

The girders are designed with natural resonant frequencies  $>50$  Hz to avoid amplification of low-frequency floor vibrations. The orbit feedback system will damp beam motion at frequencies below 100 Hz keeping the orbit motion below 10% of the electron bunch transverse dimensions.

The necessity for relatively long lifetime and large dynamic aperture require the very nonlinear, sextupole-dominated, ultra low emittance SR lattice to be very robust and capable of tolerating manufacturing and installation errors. Furthermore, the presence of high-field and short-period undulators at the relatively low energy of the SR imposes an additional, very strong nonlinear component on the lattice, which changes when users change the undulator gaps. The three quadrupole families per ID provide the capability of minimizing the linear impact of these IDs, maintaining to a high degree the corrected nonlinear dynamics behavior of the beam.

The NSLS-II storage ring will be equipped with a full set of beam diagnostics and feedbacks necessary for prompt commissioning and reliable operation of this cutting-edge facility. The diagnostics will monitor

closed beam orbit position, tunes, beam current and lifetime, filling pattern, beam emittances, bunch length, positions of the photon beam in insertion devices, coherent bunch instabilities, and distribution of beam losses around the ring. It will allow for the measurement and study of parameters for the linear and nonlinear optics (including lattice functions, chromaticities, local and global coupling, momentum compaction, and magnet and RF system parameters [1.1.2]), to measure the beam energy spread as well as impedances of vacuum chambers, and to use beam-based alignment relative to the quadrupoles and sextupoles. Beam diagnostics and feedbacks will include at least the following:

- two high-precision DCCTs and two bunch-to-bunch current monitors
- beam position monitors (six BPMs with sub- $\mu\text{m}$  sensitivity per cell plus two BPMs per each installed ID, with average and single turn capabilities) plus photon BPMs (1-2 per ID) paired with 120 fast orbit correctors with stainless steel chambers and 60 slow orbit correctors with aluminum chambers.
- a set of fast correctors with feedback bandwidth of 100 Hz may be provided for each ID
- monitors of both transverse tunes and synchrotron tunes
- diagnostic undulator equipped to monitor horizontal and vertical emittances of electron beam (not in baseline)
- dual-sweep streak-camera with picosecond resolution for measuring the bunch length
- beam loss monitors

All the diagnostics listed above are non-interceptive. A few interceptive diagnostics (such as flags) will be used for commissioning purposes. (See complete descriptions in Section 7.8.)

NLSLS-II will use CESR-B type superconducting RF (SRF) 500 MHz cavities. In addition, passive cavities operating at the 3rd harmonic (1.5 GHz) will be used to increase the bunch length and improve the beam lifetime. Initially, the RF system will be comprised of two 500 MHz cavities and a single harmonic cavity installed in a 9.3 m straight section. A single 310 kW klystron amplifier will drive each of the main ring cavities through a 350 kW rated circulator and load (see Section 7.5 for further detail on the RF system and its cryogenics). When the facility is fully built out with insertion devices, two additional RF cavities (for a total of four) and one additional harmonic cavity (for a total of two) will be required. These additional devices will occupy one additional 9.3 m straight section.

Of the 1,320 RF buckets, only 80 to 90% will be filled. The remaining buckets will stay empty, providing a clearing gap (or gaps) for ions. Because of nonuniform beam loading in the Landau cavity, the presence of the ion clearing gap (or gaps) impacts the bunch lengths and hence the Touschek beam lifetime (see detailed discussion in Section 6.2.7).

### 1.1.1.2 Injection System

Due to the relatively short lifetime of the electron beam with the goal of  $\sim 3$  hours, full-energy top-off injection is required. Injections will be very brief (milliseconds) and occur about once per minute. In contrast with the previous generation of light sources based on high-energy storage rings, the short lifetime of NLSLS-II means that it cannot perform at its target level if the injector is not readily available. Thus, it is imperative that the injector be a very robust and reliable device. This requirement led to the selection of a full energy booster for the injector and placement of the storage ring septum and kicker magnets in the injection straight which has been carefully designed to minimize deflection of the stored electron beam.

Layout of the injection system is shown in Figure 1.1.7. It consists of a 200 MeV linac in its own shielding enclosure, linac to booster beam transport lines, 3 GeV booster in its own tunnel, booster to storage ring beam transport line, and the injection straight that is part of the storage ring. The main parameters of the injector are given in Table 1.1.2 and a detailed description is given in Chapter 5. A 200 MeV linac with thermionic triode electron gun will serve as the injector for the booster. For straightforward commissioning and reliable operation, the injector will be equipped with a full set of beam diagnostics (DC and fast current transformers, 29 BPMs, 17 fluorescent flags, and streak-camera).

**Figure 1.1.7**  
Schematic  
layout of the full  
energy booster.

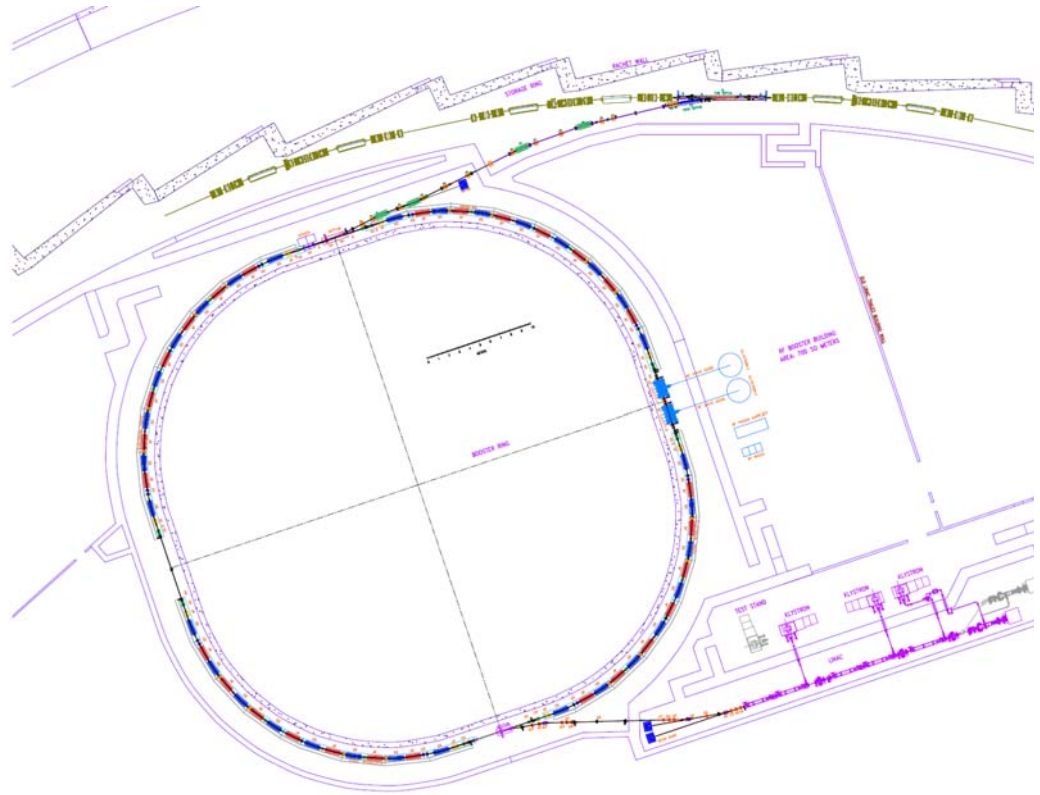


**Table 1.1.2 Main Parameters of the NSLS-II Injector**

Linac	
Nominal linac energy [MeV]	200
Frequency [GHz]	2.998
Pulse repetition rate [pps]	1
Pulse charge [nC]	15
Booster	
Injection energy [MeV]	200
Nominal booster energy [GeV]	3
Circumference [m]	258.4
Ramping repetition rate [Hz]	1
Acceleration time [sec]	~0.4
Radio frequency [MHz]	499.68
Total number of superperiod	4
Total number of bending magnets (combined function)	60
Total number of quadrupoles	24
Energy loss per turn at 3 GeV [MeV]	0.625
Natural emittance at 3 GeV [nm-rad]	26.6

The booster RF system (Section 5.8) will be based on five-cell “PETRA” (room temperature, copper) cavities that will provide 1.2 MV accelerating voltage, which is sufficient for the acceleration and required energy acceptance.

### 1.1.1.3 Photon Sources

The NSLS-II storage ring has 27 straight sections available for insertion devices (one 9.3m straight section will be used for the injection and two for the RF system). A 9.3m straight section can also accommodate two short undulators whose radiation is separated by a local angular bump (so-called canting). NSLS-II will host a variety of different types of undulators and wigglers that will generate high brightness and high flux beams of hard and soft x-rays. A full description of these IDs and their performance, together with that of the bending magnets, is given in Chapter 8. The storage ring lattice is designed to withstand the influence of a complete set of insertion devices set to arbitrary gap (field) values in the fully developed facility (see Section 6.1.2.8).

NSLS-II will use damping wigglers (see Section 1.2) for two purposes [1.1.3]:

1. to reduce horizontal beam emittance to the desired level while minimizing the number of cells of the lattice and thus the circumference (and cost) of the storage ring
2. to serve as broadband sources of very bright and high flux x-rays superior to conventional bend-magnet sources

### 1.1.1.4 Mechanical Design and Magnets

Many of the mechanical designs for NSLS-II are now conventional technology for third-generation light sources. Most of the NSLS-II storage ring uses extruded aluminum vacuum chamber. Short stainless steel bellows (about 15 cm) provide space for fast feedback orbit correctors. This vacuum chamber allows for in-situ bakeout to 130°C using pressurized hot water circulated within the cooling water channel of the Al profile. Synchrotron radiation is either extracted to a user beamline or intercepted by a localized water-cooled copper absorber (see Section 7.4). All bellows in the storage ring vacuum chamber will be RF shielded to provide low impedance and low losses. The most complex are the vacuum chambers for the insertion devices, especially those for in-vacuum undulators with flexible transitions. These devices are described in Section 7.4.3. Vacuum pressure of  $1 \times 10^{-9}$  Torr will be provided by 240 ion vacuum pumps, 180 titanium sublimation pumps, and about 250 NEG pumps distributed around the ring, IDs, and front ends. The ring vacuum system will have 90 gate valves. The pressure and the residual gas content in the storage ring will be monitored by 270 ion gauges and by 104 residual gas analyzers.

The main parameters of the magnets for the booster and storage ring are discussed in detail in Sections 5.6 and 7.1, respectively. A number of pulsed elements (kickers and septa) are also used in NSLS-II, as described in Sections 5.9 and 7.6.2.2.

Among the most challenging requirements are those associated with the precise alignment of magnetic elements in the storage ring. Another challenge is the design of the girder system, which must be as rigid as possible to reduce vibration of the elements that results in low-frequency noise in the position and angle data from the x-ray beams. The solutions for these challenging problems are described in Section 7.2.

## 1.2 Optimization of the NSLS-II Design

The pre-conceptual design of NSLS-II [1.2.1] was based on 24 triple-bend achromatic cells (TBA24) with a circumference of 630 m. Further extensive studies [1.2.2] demonstrated that this lattice, with a horizontal emittance of 1.5 nm-rad, was not robust. The dynamic aperture for this lattice collapsed in the presence of realistic errors. Further studies explored possibilities of various lattices (DBA vs. TBA), radii of curvature, and circumferences, as well as damping wigglers.

The performance goals for the current NSLS-II lattice, including the effects of all realistic errors and of small gap undulators, are listed in Table 1.2.1. They are based on analyzing alternative designs for NSLS-II

and on the experience of the most advanced operational mid-energy light sources (such as the Swiss Light Source [1.2.3]).

**Table 1.2.1 Goals for the NSLS-II Lattice**

Beam lifetime [hours]	~3
2D dynamic aperture [mm-mrad] <sup>2</sup>	~25 x 25
Energy aperture [%]	~±3
Horizontal emittance at 3 GeV with 21 m damping wigglers (baseline) [nm-rad]	~0.9
Horizontal emittance at 3 GeV with 56 m damping wigglers (fully builtout) [nm-rad]	~0.6
Horizontal geometrical aperture for injection [mm]	~±20

Sextupole-dominated lattices of modern low-emittance synchrotron light sources are intrinsically non-linear and do not allow the traditional approach of designing a linear lattice and later retrofitting it with the appropriate number of sextupole families. Instead, nonlinear aspects of the lattice must be addressed from the very beginning of the lattice design through continuous iterations of both linear and nonlinear elements. Furthermore, for convergence of these iterations to a robust (i.e., operational) lattice, the following decisions are vital: the number and locations of beam position monitors (BPMs) and correctors, target BPM accuracy, the scheme for orbit correction, and methods for beam-based alignment. Details on the process of selecting an operational lattice for NSLS-II are in Section 6.1.

This process of proper lattice design is labor intensive and lengthy. As a result, only a very limited number of lattices can be studied in sufficient detail. To streamline the NSLS-II design process and to avoid dead ends such as the “zero-dynamic aperture desert,” the restrictions given in Table 1.2.2 were imposed on the choices for the lattice cell in the presence of realistic errors and IDs.

**Table 1.2.2 Restrictions on the NSLS-II Linear Lattice Design**

Chromaticity per cell, $\xi_x$	$\leq 3$
Maximum $\beta$ -functions [m]	$\leq 30$
Maximum $\eta$ -functions [m]	$> 0.3$
Maximum $\beta$ -beating: $\Delta\beta_x/\beta_x, \Delta\beta_y/\beta_y$ [%]	$\leq 5\%, \leq 1\%$
Maximum tune-spread per cell: $\Delta\nu_x, \Delta\nu_y$	$< 0.05, < 0.002$
Transverse alignment accuracy of quadrupoles, sextupoles and BPMs [ $\mu\text{m}$ ]	$\pm 30$
Roll-off errors for quadrupoles, sextupoles and BPMs [mrad]	$\leq 0.5$

Within the framework above, the following design philosophy was pursued to attain sub-nm horizontal emittance for NSLS-II:

- use a lattice with reasonable natural emittance (~2 nm-rad) and robust dynamic aperture
- keep achromatic conditions in the straight sections so IDs reduce emittance, and also to avoid additional nonlinear 3D driving terms
- use damping wigglers to reduce emittance
- limit total losses of synchrotron radiation to 1 to 2 MeV per turn to limit electrical power consumption
- increase bending radius to maximize impact of damping wigglers while keeping emittance under control
- monitor the cost

Using a larger radius for the bending magnets causes a modest increase in the ring’s circumference and some increase in the maximum dispersion, resulting in reduced sextupole strengths. Our studies showed that it is possible to keep the bare emittance under control while increasing the bending radius of the dipole magnets.

Increasing the bending radius reduces the dipole field ( $B_o = pc/e\rho_o$ ) and (in the case of the same coil cross-section) reduces the power consumption.

The approach of using damping wigglers to achieve low horizontal emittance has been used previously in accelerators designed for high energy physics, but it has not been widely used for light source designs. Usually the use of damping wigglers is associated with large synchrotron radiation losses and large consumption of RF power. This is not the case for NSLS-II – the use of a large bending radius proportionately reduces the radiation losses from both the bending magnets ( $U_{bends}$ ) and the damping wigglers. This is a unique feature of the NSLS-II design. The emittance for a given total loss per turn from synchrotron radiation ( $U_{total}$ ), i.e., for a given RF power, decreases with the increase of the radius of curvature:

$$\begin{aligned} \varepsilon_{nat} &\cong \varepsilon_{bare} \cdot \frac{U_{bends}}{U_{total}}; \quad U_{bends} \cong 88.5 [keV] \cdot \frac{E^4 [GeV]}{\rho_o [m]}, \\ U_{bends} (@3GeV) &\cong \frac{7.17 [MeV]}{\rho_o [m]} \end{aligned} \quad (1.2-1)$$

where  $\varepsilon_{bare}$  is the emittance of the bare lattice (without wigglers) and  $\varepsilon_{nat}$  is the natural emittance in the presence of damping wigglers [1.2.4].

This approach to emittance control is straightforward and has a rather modest effect on the vertical dynamic aperture (see Section 6.1). The fact that the damping wigglers at NSLS-II will be also very bright, high-intensity sources of broadband x-rays makes this approach even more attractive.

Using this design approach, two promising lattices, the TBA24 (bending radius of 18 m) and the DBA32 (bending radius of 15.3 m), emerged in the early stages of the conceptual design development. Both lattices at the time of consideration had circumference  $\sim 750$  meters with bare natural horizontal emittance between 1.8 and 2 nm-rad. Both could go well below 1 nm-rad with the use of damping wigglers and clearly indicated a potential for robustness.

A key advantage of lattices based on a DBA cell compared to a TBA cell is that, for lattices with comparable bare emittance, the DBA cell allows significantly more straight sections for user IDs while having a similar number of magnets and circumference. Lattices based on a DBA cell are thus preferred, and further studies were focused on selecting the optimum number of DBA cells.

Table 1.2.3 shows the key parameters used in selecting the optimum size DBA lattice. All lattices considered had a super-period of two cells, with alternating straight section lengths of  $\geq 8$  m and  $\geq 5$  m, and a bend magnet radius of 25 m (the optimum choice of bend magnet radius is discussed in the next section). A straight section length of  $\geq 8$  m is required in order to inject in a single straight, as well as to accommodate two RF cavities and one harmonic cavity in a single straight. The second straight section length of 5 m was chosen as a compromise between having longer IDs and minimizing the storage ring circumference. Shorter straights are also conducive to having smaller beta functions, and hence smaller beam sizes, as discussed in Chapter 6. Achieving very small beam sizes is especially beneficial in enabling the photon beam to be focused down to a 1 nm spot size, as discussed in Chapter 11. As discussed generally in the next section, and shown in Table 6.1.3 and Figure 6.1.3 for the choice of a DBA30 lattice with 25m bend magnet radius, eight 7m-long damping wigglers are sufficient to achieve nearly the full emittance reduction that can be achieved from damping the beam. Thus, eight of the 8m straights are assumed to be occupied by damping wigglers. Table 1.2.3 shows the resulting expected straight section utilization.

As discussed in Chapter 11, the DBA30 lattice will provide nearly the same number of beamlines, when the possibility of canting multiple independent undulators per straight is included, as exist on the present NSLS x-ray and VUV storage rings. This will enable NSLS-II to accommodate a user community comparable in size to that of the existing NSLS. The DBA30 lattice will also achieve nearly the same performance as the



DBA32. We carried out a parametric estimate of the cost savings from reducing the number of lattice cells from 32 to 24, and found a cost reduction of ~\$16M (including all burdens, escalation, and contingency) per super-period (two cells). Overall, we find that the DBA30 lattice with a circumference of 780 m provides a good compromise between many competing parameters and goals (cost, length and number of user IDs, and performance). Later the circumference was changed to 792 m in order to adjust the harmonic number to 1,320, which is highly factorizable.

**Table 1.2.3 Storage Ring Parameters for Number of DBA Lattice Cells Varying from 32 to 24.**

Lattice	DBA32	DBA30	DBA28	DBA26	DBA24
Circumference [m]	822	780	739	697	656
Bend magnet radius [m]	25	25	25	25	25
Straight sections [n x (m)]	16x(8, 5)	15x(8, 5)	14x(8, 5)	13x(8, 5)	12x(8, 5)
Horizontal emittance, $\varepsilon_x$ (bare) [nm-rad]	1.7	2.1	2.6	3.2	4.1
Horizontal emittance, $\varepsilon_x$ (full set of damping wigglers) [nm-rad]	0.5	0.6	0.7	0.8	1.1
<b>Straight Section Utilization</b>					
8 m straights					
RF and injection	3	3	3	3	3
Damping wigglers	8	8	8	8	8
Undulators	5	4	3	2	1
5 m straights					
Undulators	16	15	14	13	12

### 1.2.1 Large-Radius Bends and Intrabeam Scattering (IBS) Limits

Following the choice of a DBA30 lattice, studies were carried out to determine the optimum bend magnet radius and number of damping wigglers. As the bare emittance is reduced, it ultimately becomes limited by the effects of intra-beam scattering. Therefore, an important part of our studies was related to the issue of the ultimate IBS-limited emittance for the lattice with fixed synchrotron radiation losses per turn. Even though the detailed calculations of the single and multiple intrabeam scattering on the beam lifetime and the beam emittance were performed using appropriate computer codes (see Section 6.2), the conclusions reached are very similar to those that could be derived using analytical formulae for these processes. Furthermore, such an approach allowed rapid parametric studies and avoidance of multiple, labor intensive trial-and-error lattice designs. Well-known synchrotron radiation integrals for radiation damping and quantum excitation [1.2.4] and the IBS formula for flat electron beam [1.2.5] can be used to calculate the equilibrium energy spread  $\sigma_\delta$  and horizontal emittance  $\varepsilon_x$ :

$$\begin{aligned}\sigma_\delta^2 &= \tau_E (D_{\delta \text{ SR}} + D_{\delta \text{ IBS}}); \quad \delta = \frac{E - E_0}{E_0}; \\ \varepsilon_x &= \tau_x \langle H \cdot D_{\delta \text{ SR}} \rangle + \tau_x \langle H \cdot D_{\delta \text{ IBS}} \rangle; \\ H &= \frac{1}{\beta_x} \left[ \eta_x^2 + (\beta_x \eta'_x - \beta'_x \eta_x / 2)^2 \right]\end{aligned}\tag{1.2-2}$$

where  $E_0$  is the energy of the electron beam,  $E$  is the energy of individual electrons, and  $\tau_E$  and  $\tau_x$  are the damping time of energy (synchrotron) oscillations and horizontal betatron oscillations, respectively.  $D_{\delta \text{ SR}}$  and  $D_{\delta \text{ IBS}}$  are relative energy diffusion coefficients caused by quantum fluctuations of synchrotron radiation (i.e., causing so-called natural emittance) and by the intrabeam scattering, respectively. The  $H$ -function is the well-known connection between emittance growth and the energy diffusion coefficients.

The energy diffusion induced by IBS can be expressed in the following terms:

$$D_{\delta \text{ IBS}} = \frac{N_e r_e^2 c}{2^5 \pi \gamma^3 \varepsilon_x \sqrt{\varepsilon_y} \beta_y(s) \sigma_s} f(\chi_m(s)); \quad f(\chi_m) = \int_{\chi_m}^{\infty} \frac{d\chi}{\chi} \ln\left(\frac{\chi}{\chi_m}\right) e^{-\chi}; \quad (1.2-3)$$

$$\chi_m = \frac{r_e m^2 c^4}{b_{\max} \Delta E_{\text{acc}}}; \quad b_{\max} \cong n^{-1/3},$$

where  $\gamma = E_o/mc^2$  is the relativistic factor of the electron ( $\gamma \approx 6,000$  for 3 GeV electrons),  $N_e = I/N_b/e$  is the number of electrons per bunch,  $m$  is the mass and  $r_e$  is the classical radius of an electron,  $c$  is the speed of light, and  $\sigma_s$  is the electron bunch length.  $f(\chi_m)$  is the scattering integral depending on the following parameters:  $\Delta E_{\text{acc}}$  is the energy acceptance (in the location of scattering) and  $n$  is the density of electrons (see [1.2.5] for details of the definition). As shown in Figure 1.2.1, this function depends very slowly (logarithmically) on its parameter  $\chi_m$ . For the case of NSLS-II, variations of horizontal emittance (by an order of magnitude, from 0.2 nm-rad to 2 nm-rad) change the value of  $f(\chi_m)$  by only  $\pm 20\%$ .

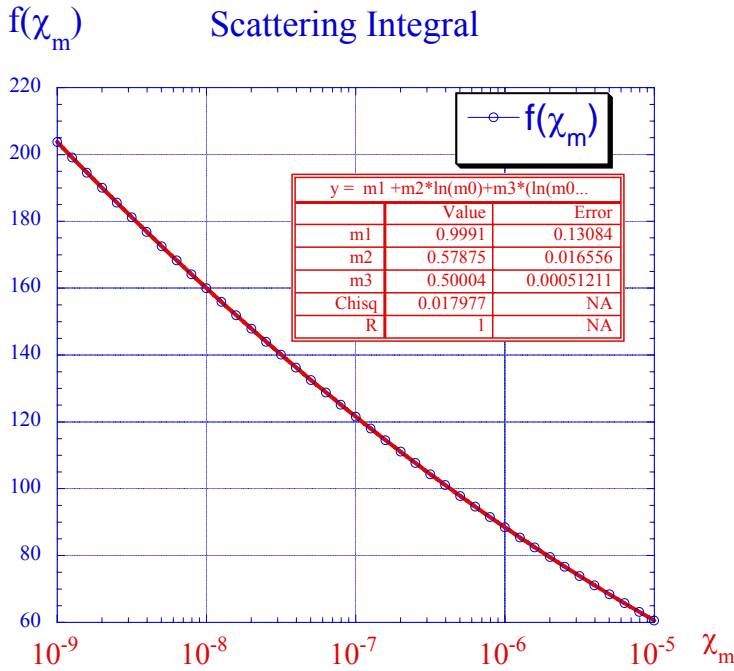


**Figure 1.2.1** Dependence of the scattering integral on the maximum scattering parameter  $\chi_m$ .

The NSLS-II designs have a number of parameters that are either constant or have very small variations. First, vertical emittance will be held at the diffraction level for 1 Å radiation ( $\varepsilon_x \approx 8$  pm-rad). Second, both low emittance and low energy spread are paramount for the attainment of the required spectral brightness at high harmonics and in the hard-x-ray range (see Chapter 8), which led to a natural selection of a separate function lattice (i.e., there is no field gradient in the dipoles) and constant ratio of synchrotron and horizontal damping times:

$$\tau_E \cong \frac{\tau_x}{2} \cong \frac{1}{f_o} \cdot \frac{E_o}{U_{\text{total}}}; \quad (1.2-4)$$

where  $T_o = 1/f_o$  is the revolution time of electrons around the ring. Thus the damping time is simply proportional to the ring circumference and to the ratio between the beam energy and total losses on

synchrotron radiation  $E_o/U_{total}$ . Third, the bunch length in NSLS-II will be kept about constant (between 3 mm and 4.5 mm,) by various means, including its lengthening by harmonics cavity (see Section 6.2.7).

Equations (1.2-2) and (1.2-3) can be solved with respect to the natural emittance ( $\epsilon_{nat} = \tau_x \langle H \cdot D_{\delta SR} \rangle$ ; i.e., the beam emittance in the absence of the IBS) using weak dependence of the scattering integral on the beam emittance:

$$\epsilon_{x total} \cong \frac{\epsilon_{nat}}{2} \left( 1 + \sqrt{1 + \frac{4\epsilon_{IBS}^2}{\epsilon_{nat}^2}} \right), \quad (1.2-5)$$

where  $\epsilon_{IBS}$  is the minimum emittance that can be achieved in a given lattice for a given current per bunch  $I_b = eNf_o$ :

$$\epsilon_{IBS} = \sqrt{\frac{\tau_x N_e r_e^2 c}{2^5 \pi \gamma^3 \sigma_s} \left\langle H(s) \frac{f(\chi_m(s))}{\sqrt{\epsilon_y \beta_y(s)}} \right\rangle}. \quad (1.2-6)$$

The expression for  $\epsilon_{IBS}$  (Eq. 1.2-5) can be easily evaluated for any given lattice and bunch parameters, and it naturally has very weak (square root) dependence on the bunch length, bunch current, and damping time, and even weaker (4<sup>th</sup> power root) dependence on vertical emittance. Overall, this number is a good measure of the ultimate emittance one can approach with realistic beams. For all realistic TBA24 and DBA24 through DBA32 lattices and related beam parameters under consideration (and maximum total losses limited to 1 MeV per turn), the value of  $\epsilon_{IBS}$  was between 0.2 nm-rad and 0.25 nm-rad, thus setting the natural limit for attainable emittance. Naturally, increasing the power losses by a factor of two, to 2 MeV per turn would further reduce  $\epsilon_{IBS}$  by  $\sqrt{2}$ .

The dependence of the beam emittance on the natural emittance also sets a natural scale for the bending magnet radius. As shown in Figure 1.2.2, reduction of the natural emittance below  $\sim(2-3)\epsilon_{IBS}$  is increasingly ineffective at reducing  $\epsilon_{x total}$  and is increasingly expensive as the circumference grows.

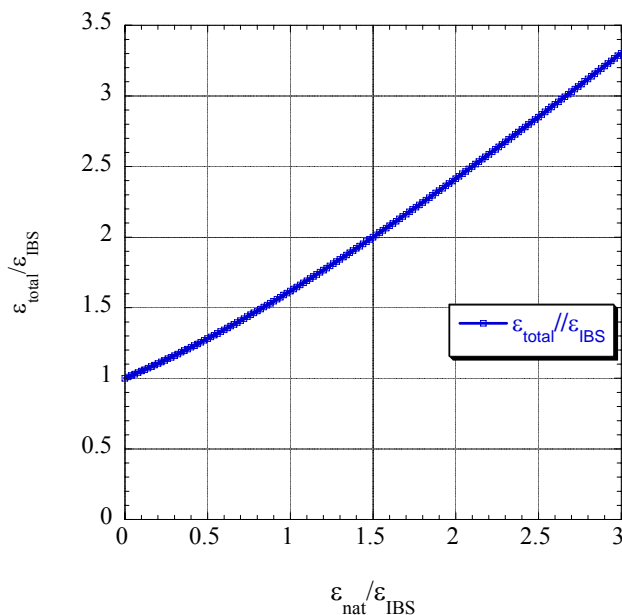


**Figure 1.2.2** Dependence of the horizontal beam emittance (given by Eq. 1.2-6).

Reduction of the natural emittance by a factor of two from  $2\varepsilon_{IBS}$  to  $\varepsilon_{IBS}$  (by roughly a doubling of the bending magnet radius) results in only a 33% reduction in emittance. A further doubling of the bending magnet radius only results in a 23% further emittance reduction. Hence, the optimum choice for the natural emittance is about 2 to 3 times  $\varepsilon_{IBS}$ . When combined with (Eq.) 1.2-1, this yields a simple expression for the optimum power radiated by the bending magnets:

$$U_{bends} = (2 - 3)U_{total} \frac{\varepsilon_{IBS}}{\varepsilon_{bare}} . \quad (1.2-7)$$

For the 3 GeV NSLS-II storage ring, with total synchrotron radiation losses of 1 MeV per turn, this ratio also gives an optimum range for the radius of the bending magnets:

$$\rho_o [m] = (2.4 - 3.6) \frac{\varepsilon_{bare}}{\varepsilon_{IBS}} . \quad (1.2-8)$$

Thus, the present DBA30 lattice with a bare emittance of  $\sim 2.1$  nm-rad and  $\varepsilon_{IBS} \sim 0.25$  nm-rad ( $\varepsilon_{bare}/\varepsilon_{IBS} \sim 8.4$ ) has an optimum bending magnet radius  $\sim 25$  m.

A bend magnet radius of 25 m is rather large compared to that at other synchrotrons. For example, the existing NSLS x-ray ring bend magnet radius is 6.9 m. As a result, the bend magnet critical energy at NSLS-II will be  $\sim 2.4$  keV, compared to a critical energy of 7.1 keV for the bend magnets at the existing NSLS x-ray ring. As discussed in Chapter 8, this makes the NSLS-II bend magnets less attractive as sources of high flux, hard x-rays ( $>4$  to 5 keV). However, they will be excellent sources of VUV and soft x-ray radiation. Furthermore, the damping wigglers will also serve as radiation sources for beamlines, and their brightness and flux will be about 100 times greater than would be provided by bend magnets with a small radius.

Finally, the parameters for the damping wigglers (see Chapter 8) were determined by a combination of the following effects (with the assumption that  $U_{total} \gg U_{bends}$ ):

- The wiggler magnetic field,  $B_w$ , in the damping wigglers should not be very high because it will increase the energy spread according to  $\sigma_\varepsilon \propto \sqrt{B_w(T)}$ , which will reduce the brightness of high harmonic radiation from the undulators.
- The wiggler period should not be too large, in order to serve as a source of very bright broadband x-rays.
- It should not be too small, to keep nonlinear effects under control.
- The wiggling angle and horizontal  $\beta$ -function should be limited to avoid excitation of horizontal emittance in the damping wiggler caused by  $H \cong \beta_x \theta_w^2$ .

As the result of optimization, damping wigglers with 1.8 T peak field and 10 cm period were selected. These damping wigglers provide synchrotron radiation losses of 18.5 keV per meter. The initial baseline configuration of NSLS-II will have three 7m-long permanent magnet wigglers. This will achieve an emittance below 1 nm-rad. All damping wigglers will have fixed gap and field and will also serve as excellent sources of user radiation. The final configuration allows up to eight damping wigglers, with which the horizontal emittance will reach a value below 0.6 nm-rad.

## 1.2.2 Emittance and Lifetime

Electron beam lifetime is an important parameter of the NSLS-II light source. It defines the frequency of top-off injections and, ultimately, defines the radiation environment and necessary shielding. The lifetime has a strong dependence on the energy acceptance of the storage ring. For low-emittance light sources, the energy

acceptance depends not only on the linear compaction factor  $\alpha_1$  (in NSLS-II, higher order compaction factors are not important,  $\alpha_1/\alpha_2 \approx 3.7 \times 10^{-4}/4.1 \times 10^{-4} = 92\%$ ) and the parameters of the RF system (harmonic, voltage, synchronous phase), but also may depend on nonlinear coupling and the vertical gap in IDs.

Here we will focus on two unusual phenomena in the lifetime dependences for the NSLS-II storage ring, and their consequences:

- For a given energy acceptance, the beam lifetime depends very weakly on the value of the horizontal emittance (within the range from 0.2 nm-rad to 2 nm-rad).
- Lifetime dependence on the energy acceptance is approaching the fourth power of the latter.

Conventional wisdom says that lowering the beam emittance in an electron storage ring leads to a proportional reduction of the lifetime. This conclusion can be drawn from the following formula [1.2.5]:

$$\frac{1}{\tau_{Touschek}} = \frac{N_e r_e^2 c}{8\pi \cdot \sigma_x \sigma_y \sigma_s \cdot \gamma^2 \cdot \delta_{acc}^3} D(\xi); \quad \xi = \left( \frac{\delta_{acc}}{\gamma \sigma_\theta} \right)^2; \quad (1.2-9)$$

$$D(\xi) = \sqrt{\xi} \left\{ -\frac{3}{2} e^{-\xi} + \frac{\xi}{2} \int_{\xi}^{\infty} \frac{\ln u \cdot e^{-u}}{u} du + \frac{1}{2} (3\xi - \xi \ln \xi + 2) \int_{\xi}^{\infty} \frac{e^{-u}}{u} du \right\}$$

where  $\delta_{acc} = \Delta E_{acc} / E_o$  is the relative energy acceptance,  $\sigma_\theta$  is the transverse angular spread (dominated by horizontal oscillation for the NSLS-II case),  $\sigma_{x,y} = \sqrt{\beta_{x,y} \epsilon_{x,y}}$  are the transverse RMS beam sizes, and  $D(\xi)$  is the scattering integral causing loss of the electrons.

Nevertheless, direct use of this formula (integrated over the NLSL-II circumference) gives a lifetime dependence (shown in Figure 1.2.3) which shows very weak lifetime variation in a (0.2, 2.0) nm-rad interval, and (exponential!) lifetime growth for emittances below 0.2 nm-rad. This dependence has a very solid physics foundation [1.2.6].

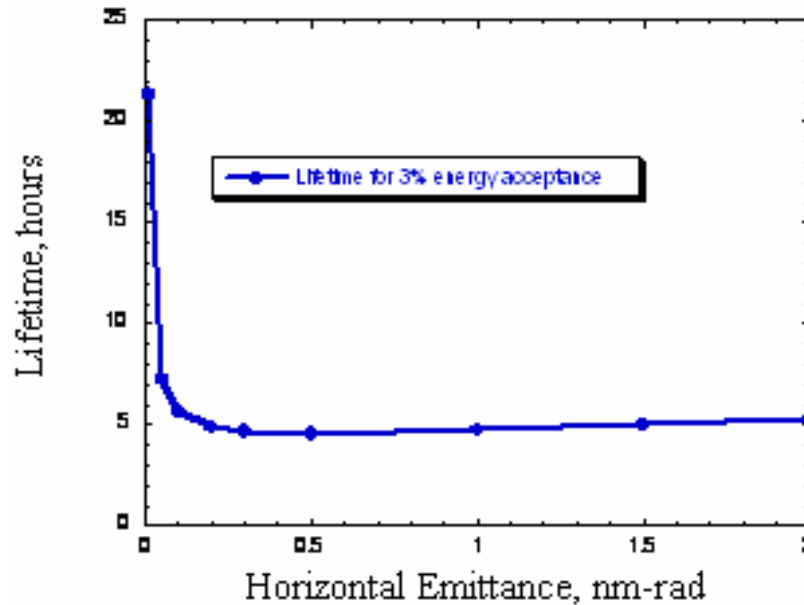


**Figure 1.2.3** Dependence of the beam lifetime in NSLS-II on the horizontal emittance for 0.008 nm-rad vertical emittance and fixed uniform 3% energy acceptance.

The main loss mechanism for ultra relativistic electrons ( $\gamma \gg 1$ ,  $\gamma_{\text{NSLS-II}} \sim 6000$ ) in storage rings comes from the mechanism first described by Touschek. The simple picture can be presented as follows: In the co-

moving frame (i.e., that moving with the electron bunch), two electrons execute betatron oscillations having transverse momenta  $\pm p_t$  (in the case of a flat beam, mostly in the horizontal direction:  $p_x = \pm \gamma m c x'$ ). They then scatter on each other and transfer the momenta ( $p_s = \pm \gamma m c x'$ ) in the direction of motion (s-direction). The Lorentz transformation into the laboratory frame gives a relativistic boost to  $p_s$  momenta by a factor of  $\gamma$  and generates an energy deviation of  $\Delta E \approx \pm \gamma^2 m c x'$ . If the energies of the scattered electrons are outside the energy acceptance ( $\gamma^2 m c x' > \pm \Delta E_{acc}$ ), then the electrons may get lost. For most storage rings, the angular RMS spread of the electrons,

$$\sigma_\theta(s) = \sqrt{\varepsilon_x (1 + \alpha_x^2(s)) / \beta_x(s) + \varepsilon_y (1 + \alpha_y^2(s)) / \beta_y(s) + \eta^2(s) \sigma_\delta^2}, \quad (1.2-10)$$

is sufficient for such a process to occur (note that  $\sigma_\theta$  is a function of azimuth  $s$ ). But for storage rings with extremely low emittances (in the NSLS-II case, sub-angstrom emittances), only the far tails of the electron distribution  $f(\theta) = \exp(-\theta^2 / 2\sigma_\theta^2) / \sqrt{2\pi}\sigma_\theta$  can cause such processes, and the lifetime of such beams increases with the decrease of the emittance. Formally, this dependence can be seen from a formal evaluation of the  $D(\xi)$  function, shown in Figure 1.2.4.

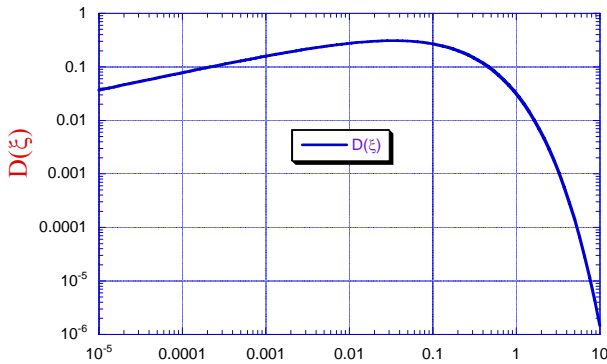


**Figure 1.2.4** Dependence of the loss integral  $D(\xi)$  on the parameter  $\xi$ :  $D(\xi)$  is a rather slow function of  $\xi$  for  $\xi < 0.01$ , flat in the range  $0.01 < \xi < 0.1$ , and falls exponentially for  $\xi > 0.1$ . (nearly a Gaussian dependence).

For NSLS-II,  $\xi$  spans the range from  $2 \times 10^{-3}$  to 2 (the large range is an indication of very strong variation of the  $\beta$ -function with  $s$ ). The explanation of the lifetime dependence shown in Figure 1.2.3 is very straightforward: while reduction of the horizontal emittance increases the electron density  $\propto 1/\sqrt{\varepsilon_x}$ , it also increases  $\xi \propto 1/\varepsilon_x$  and, as a result, increases the portion of the ring where  $\xi > 0.1$  and the losses are exponentially suppressed. Figure 1.2.5 shows that for the range of NSLS-II parameters under consideration, the beam lifetime exhibits an extremely weak dependence on the horizontal emittance, but a very strong dependence on the energy acceptance. As shown by the fit in Figure 1.2.6, the lifetime of NSLS-II is proportional to the fourth power of the energy acceptance. In contrast, storage rings having larger emittances and operating in the regime of  $\xi < 0.01$  typically have a power dependence on the energy acceptance of about 2.7. This strong dependence for NSLS-II, again, comes from the fact that large values of the  $\xi$ -parameter (where losses are suppressed) are important for the reduction of the losses and increase of the lifetime of NSLS-II. This underlines the importance of a large energy acceptance for NSLS-II.



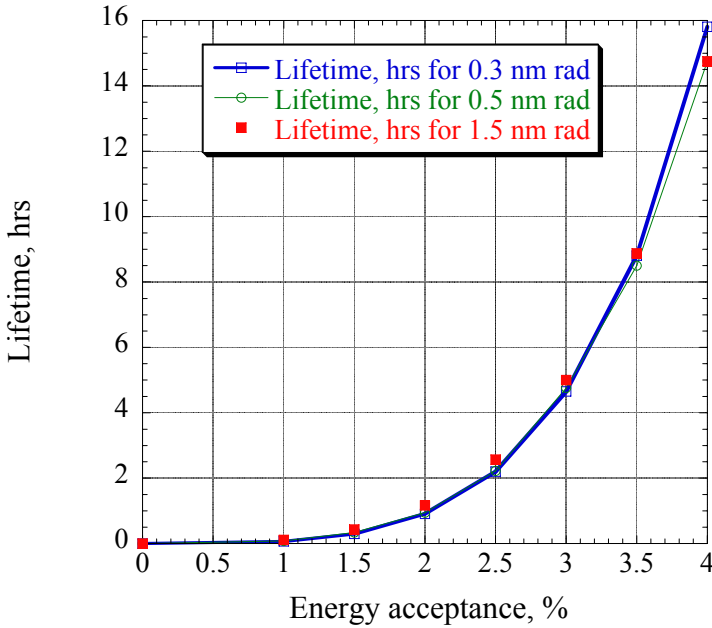


**Figure 1.2.5** Dependencies of the beam lifetime on the energy acceptance for horizontal emittances of 0.3, 0.5, and 1.5 nm-rad and vertical emittance of 0.05 nm-rad. Note: the bunch length is assumed to be constant.

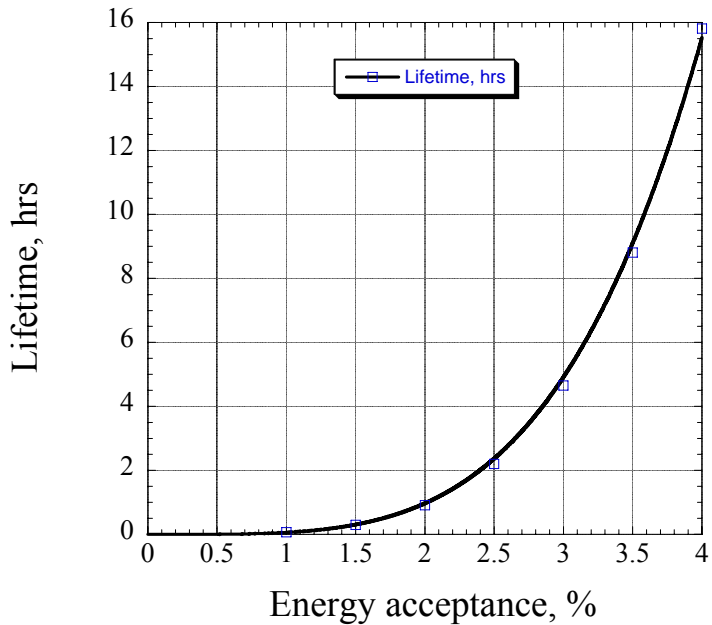


**Figure 1.2.6** Fit of the beam lifetime dependence to the fourth power of the energy acceptance for horizontal emittance of 0.3 nm-rad and vertical emittance of 0.008 nm-rad.

Detailed calculations in Section 6.2.6 show features similar to those discussed in this chapter, supporting the assertion that reduction of the horizontal beam emittance at NSLS-II will not adversely affect the beam lifetime.

At the same time, any reduction of the energy acceptance for NSLS-II would have a substantial impact: a 19% reduction of the energy acceptance reduces the lifetime by a factor of two. Because of this, intense and detailed studies of the effects of the lattice and insertion devices on the beam lifetime were carried out, as reported in Chapter 6.

### 1.2.3 Collective Effects

Collective effects, described in detail in Section 6.2, have two distinct subgroups: instabilities and effect on the beam parameters (IBS and lifetime). We touched on the latter in the previous section. In this section, issues related to beam instabilities will be briefly reviewed.

The studies of beam instabilities were based both on well-established theoretical estimations as well as on detailed calculations of specific impedances using the code GdfidL for the most convoluted structures (such as RF cavities and ID transitions). GdfidL was also used intensively for calculating the impedance budget for the ring with resulting longitudinal impedance values of  $(Z/n)_o \sim 0.4 \Omega$ .

The impedance model was used for estimating instability thresholds or their growth rate for the following: CESR-B SRF cavity, 720 m of Al vacuum chamber with  $\pm 12.5$  mm vertical gap, 60 meters of copper shielding for in-vacuum undulators with gap of  $\pm 2.5$  mm, and transverse ( $1 \text{ M}\Omega/\text{m}$ ;  $Q = 1$ , 30 GHz) and longitudinal ( $R_s = 30 \text{ k}\Omega$ ,  $Q = 1$ ,  $Z/n = 0.4 \Omega$ ) broadband impedances to represent transitions and other imperfections in the vacuum chamber.

The studies of instabilities were performed for the most conservative case of short electron bunches (i.e., without the use of harmonic cavities). These conservative estimates predict that an electron beam with the NSLS-II parameters will be stable, with only one exception: the transverse coupled bunch instability has a threshold  $\sim 15$  mA (with 500 mA required) at zero value of vertical chromaticity (see Section 6.2.3.3 for details). The studies using computer tracking predicted that increasing the chromaticity to at least +4 will stabilize the 500 mA beam. Being prudent, we include a well-known multi-bunch feedback system in the list of instrumentation for the NSLS-II storage ring. This feedback system will guarantee the suppression of this and other multi-bunch instabilities.

### References

- [1.1.1] T. Shaftan, J. Bengtsson and S. Kramer, "Control of Dynamic Aperture with Insertion Devices," <http://accelconf.web.cern.ch/AccelConf/e06/PAPERS/THPLS091.PDF>
- [1.1.2] J. Safranek, "Experimental Determination of Linear Optics Including Quadrupole Rotations," <http://accelconf.web.cern.ch/AccelConf/p95/ARTICLES/FAB/FAB11.PDF>; also, J.A. Safranek, "Beam-Based Accelerator Modeling and Control," Proc. of Beam Instrumentation Workshop 2000, AIP Conf. Proc. 546, pp. 23–34.
- [1.1.3] S. Krinsky, J. Bengtsson, and S. Kramer, "Consideration of a Double Bend Achromatic Lattice for NSLS-II," <http://accelconf.web.cern.ch/AccelConf/e06/PAPERS/THPLS090.PDF>
- [1.2.1] NSLS-II CD-0 proposal, [http://www.bnl.gov/nsls2/docs/PDF/NSLS-II\\_CD-0\\_Proposal.pdf](http://www.bnl.gov/nsls2/docs/PDF/NSLS-II_CD-0_Proposal.pdf)
- [1.2.2] S.L. Kramer, and J. Bengtsson, "Dynamic Aperture Optimization for Low Emittance Light Sources," <http://accelconf.web.cern.ch/AccelConf/p05/PAPERS/RPAE057.PDF>; and J. Bengtsson, "Control of Dynamic Aperture for Synchrotron Light Sources," <http://accelconf.web.cern.ch/AccelConf/p05/PAPERS/MPPE020.PDF>
- [1.2.3] <http://sls.web.psi.ch/view.php/about/index.html>
- [1.2.4] J. Murphy, *Data Book on Synchrotron Light Sources*, ver. 4, May 1996, BNL 42333, Upton, NY.
- [1.2.5] J. LeDuff, "Single and Multiple Touschek Effects," Proc. of CERN Accelerator School, Rhodes, Greece, 20 Sept. – 1 Oct., 1993; Ed.: S. Turner, CERN 95–06, 22 November 1995, Vol. II, p. 573.
- [1.2.6] V.N. Litvinenko, "Review of Ring-Based Light Sources," Proc. of ICFA Future Light Sources Workshop, April 2–5, 1999, APS, Argonne, IL.

## 2 INJECTION SYSTEMS

### 2.1 NSLS-II Injection Requirements

The NSLS-II injection system must meet several user requirements:

- maintain a stable level of the ring current in order to maintain a constant intensity to experiments and heat load on beamline optics
- minimize frequency of interruptions of user experiments, especially for those involving long scans that cannot accommodate interruptions in beam intensity
- minimize the disturbance of the beam during and immediately after injection due to the residual orbit perturbation from an incompletely closed injection bump and/or transients in fast magnets
- minimize bunch-to-bunch variation of current in order to minimize intensity-correlated orbit oscillations due to uneven bunch patterns [1]
- fill the storage ring from zero to full charge in a reasonable amount of time

These requirements must all be accomplished in a way that is as transparent to the users as possible. They are summarized in Table 2.1.1.

**Table 2.1.1 User Requirements.**

Stability of average current	<1%
Time between injections	>1 min
Bunch-to-bunch variation of current	<20%
Time to fill ring from zero to full charge	<5 min

To achieve these requirements, NSLS-II will utilize a full-energy injection system that will operate in top-off mode with minimal disturbance to the circulating beam. The technical specifications for the NSLS-II injection system are summarized in Table 2.1.2. As follows from that table, the NSLS-II injection system must supply approximately 7.3 nC of charge once per minute, assuming a lifetime of 3 hours. For single-bunch injection mode and a moderate repetition rate of a few Hz, replenishing this amount of charge would take a few seconds, occupying a significant fraction of the overall beam time. Therefore, multi-bunch injection has been adopted, leading to minimal disturbance for user experiments and lower power consumption by the injection system.

The main ring contains 1,320 RF buckets at 500 MHz. To alleviate the problems of ion trapping in the stored electron beam, approximately one-fifth of the buckets must be left empty. The exact number of buckets to fill is difficult to predict and will be determined empirically during commissioning. Feedback systems and the ultimate vacuum conditions in the ring will determine what requirements will be imposed on the bunch structure. In any case, to keep the current constant with high accuracy, considerable flexibility and accuracy must be built in to the bunch transfer timing system, the single-bunch capability, and the current and bunch structure measurement system of the main ring.

**Table 2.1.2 Storage Ring Parameters Related to the NSLS-II Injector.**

Parameter	Value
Energy [GeV]	3.0
Circulating current [A]	0.5
Circumference [m]	791.96
Revolution period [ $\mu$ s]	2.64
RF frequency [MHz]	499.68
Circulating charge [ $\mu$ C]	1.32
Total number of buckets	1320
Number of filled buckets at 80% filling	1080
Charge per bucket [nC]	1.22
Current per bucket [mA]	0.46
Lifetime [min]	180
Interval between top-off cycles [min]	1
Current variation between top-off cycles [%]	0.55
Current variation between top-off cycles [mA]	2.77
Charge variation between top-off cycles [nC]	7.31

### 2.1.1 Future Upgrades of the Bunch Pattern Formats

As described above, the NSLS-II injector must support uniform filling pattern in the storage ring starting with the beginning of operations. Two basic patterns were considered (Figure 2.1.1, two upper plots): uniform fill with the ion-clearing gap of about 20% and multiple uniform bunch trains with mini-gaps between them. Both of these bunch patterns are in the baseline design of the NSLS-II project.

Also, in response to NSLS user requests, consideration is being given to specialized bunch patterns that are not a part of the baseline design; these will be developed during later stages of the project. In addition to the nominal uniform fill, users require a single high-current bunch (“camshaft” bunch, two lower plots in Figure 2.1.1) located in the middle of the ion-clearing gap, as well as multiple camshaft bunches whose repetition rate is matched to the pulse format of modern pump lasers.

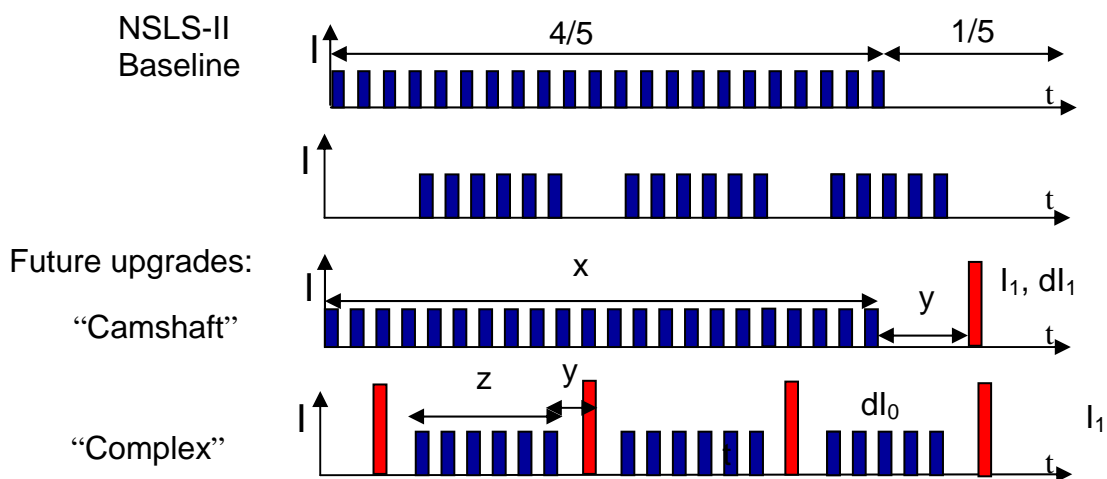


**Figure 2.1.1** User requirements on the storage ring bunch patterns.

User experiments set the following conditions for the time intervals and current stability of these complex bunch patterns:

- time interval separating regular pattern from the camshaft bunch ( $\gamma$ ) more than 20ns
- number of camshaft bunches (N) is about 5
- current stability in the regular bunch pattern ( $dI_0$ ) is less than 1%
- current stability in camshaft bunch(es) is less than a few percent

The maximum current of the camshaft bunch(es) will be determined by calculating thresholds of single-bunch instabilities.

For simplification of filling and maintaining current in the camshaft bunches, as well as for enhancing capabilities of the “hunt-and-peck” mode of operation, we have considered including a second gun that would operate exclusively in the single-bunch mode. Electron beam from the second gun would enter into and be accelerated in the same linac using a dog-leg merging system. This is not included in the baseline design and is slated as a possible future upgrade of the injector.

The baseline scope for the NSLS-II project includes developing an injector that will enable initial fill and maintaining of 500 mA of the circulating current in the top-off mode. Support of the complex bunch patterns is foreseen as a future upgrade.

### 2.1.2 Injection Sequence

The initial fill occurs at the rate of 1 Hz, and 40 bunches are transferred to the main ring, nominally, at each injection (this number can be increased to 150 bunches) to fill consecutively 1,080 of the 1,320 RF buckets available. The number of bunches in the injected train is constrained to about 40 minimum (based on beam loading physics) and a maximum of 150 (limited by the booster circumference).

Bunch trains from the injector enter the ring in sequence, starting with the front of the ring train and stepping sequentially back in time along the ring train until the end is reached, then skipping over the empty section and starting again at the head of the train, until the required current has been established.

Assuming the same amount of charge per injection (7.3 nC per bunch train) as for top-off mode, the duration of the initial fill will be about 3 minutes with the injection system running at a 1 Hz repetition rate.

Top-off operation to keep the current within 0.55% of the nominal value will be the standard operating mode of NSLS-II. The frequency of operation to keep the current within these boundaries depends on the beam lifetime and is expected to take place about once per minute. The injected bunch trains from the booster are stepped sequentially around the ring bunch structure. Users expect bunches to stay relatively constant in charge relative to each other (a difference of  $\pm 10\%$  has been adopted). We are considering several possible techniques for providing a filling pattern with sufficient uniformity.

NSLS-II users have provided feedback regarding possible top-off formats, which is summarized in Figure 2.1.2.

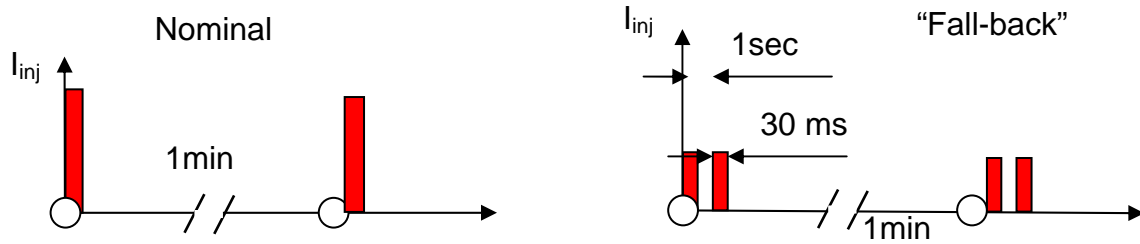


**Figure 2.1.2** Format of top-off injections: Dependence of the injected beam current vs time in minutes. 30 msec corresponds to the value of the damping time, during which the stored beam will be disturbed by the injection process.

The first scenario corresponds to the nominal case, when charge increments of 7.3 nC are injected once a minute. The second scenario allows reducing the amount of injected charge in half; however, the time interval between top-off cycles (1 second given by the injector repetition rate) is unusable for the user experiments.

Other scenarios are unacceptable for users. In one scenario involving a few low-charge, consecutive top-off injections, user experiments could be disabled for a substantial fraction of the total time. Another foreseeable scenario would be maintaining the ring current at the stability level of 0.1%. In this case, unperturbed beamtime reduces down to a few seconds, which is unacceptably short for majority of users.

## 2.1.2 Injector scope

There are several possible basic schemes for the injection system that can meet the requirements stated above. One is to use a full-energy linear accelerator, which would require no booster synchrotron at all; another is to use a booster synchrotron fed by a small linac.

A full-energy linac would provide flexible injection operations in a single bunch mode at the repetition rate of about 50 Hz [1]. However, performance and reliability of storage ring kickers and septa at this repetition rate may present a technically challenging problem together with frequent disturbances for the storage ring current, which can lead to a charge loss. On the other hand, operating in multi-bunch mode is difficult, due to significant beam loading in the linac structures at the amount of charge that is specific for the NSLS-II injector. Another disadvantage would be the high cost for the linac and the additional cost of a building to house the linac and transport line. In addition, a full-energy linac is likely to have lower reliability and a higher operations cost than a full-energy booster. A highly reliable injection system is especially important for NSLS-II, given its short beam lifetime.

For these reasons, a full-energy booster was selected as the NSLS-II injector. Two approaches were considered for its design. In the first approach, the booster was located in the storage ring tunnel [2]. This results in a much larger circumference for the booster, but most of this is taken up by small stainless steel vacuum pipe. In the second, a “compact” booster design was evaluated [3]. Comparing both approaches [4] revealed a substantially higher total cost for the compact booster due to the extra costs of constructing and shielding a separate building to house it. However, the concerns, regarding 1) potential cross-talk between the “same-tunnel” booster and storage ring, and 2) potential schedule conflicts from installing, testing, and commissioning of both machines located in the same tunnel as well as future booster troubleshooting have lead to the choice of the compact booster as the NSLS-II injector. Therefore, the NSLS-II design employs a compact booster located in a separate tunnel.

The 200MeV linac is specified for injection into the booster. Higher injection energy is advantageous from the following points of view:

<sup>1</sup> Limited by an interval of few damping times in the storage ring between consecutive bunch injections



- Relatively high value of magnetic field in the booster elements at injection
- Lower losses due to booster vacuum
- Energy redundancy (if one klystron goes down, injection can still be accomplished)
- Higher energy linac produces beam with lower energy spread and emittance, which is easier to inject into the booster

Two transport lines will be constructed: one to connect the linac to the booster and a second to connect the booster to the main ring. A full set of beam diagnostics will be installed for commissioning and routine operations of the injection system.

Strategically, BNL is developing the complete preliminary design of the injector and then procuring the major components of the injector (linac and booster) from vendors. The vendors will install the equipment and jointly commission it with BNL staff. BNL will design, procure, install, and commission the transport lines and injection straight section.

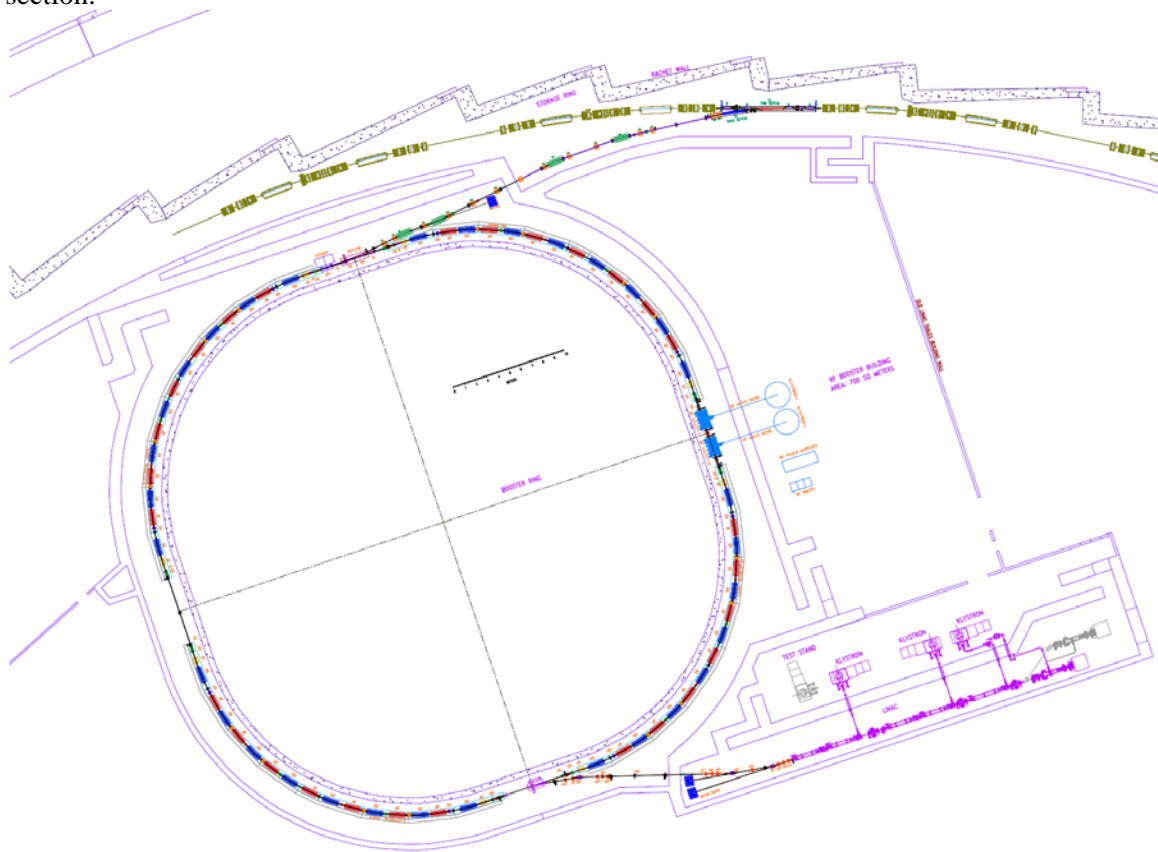


**Figure 2.1.3** Layout of the NSLS-II injector.

Figure 2.1.3 demonstrates the injector layout, where the linac and booster are housed in separate tunnels and the injector service area is adjacent to these accelerators and the ring injection straight section.

In this chapter we describe all the components of the NSLS-II injection system in the following order: linac and electron gun, linac-to-booster transport line, booster with booster-to-storage ring transport line, and injector service area.

## References

---

- 1 <http://accelconf.web.cern.ch/AccelConf/e04/PAPERS/THPLT186.PDF>
- 2 NSLS-II Conceptual Design report, 2006
- 3 T. Shaftan *et al.*, “Design of 3 GeV Booster for NSLS-II,” Proc. of PAC-2005, p. 3473.
- 4 D. Hatton *et al.*, “Considerations of the in-tunnel versus compact booster design”, NSLS-II Tech. note-2007

## 2.2 Linac

### 2.2.1 Linac Scope

The NSLS-II storage ring requires approximately 7 nC of charge to be delivered in top-off mode once every minute to replace charge lost through Touschek scattering. This charge should be delivered in a single booster cycle, so that the storage ring beam is disturbed only for the duration of the ring damping time (tens of milliseconds) each minute. Details of this will be presented later in this section. In addition, future storage ring requirements may include single camshaft bunch or timing bunches for user experiments or machine studies. To meet these requirements, two modes of linac operation are envisioned: single-pulse mode with about 1 nC charge per bunch, and multi-bunch mode, delivering bunches by tens of pC up to more than 100 pC, totaling 15 nC of charge. To inject bunch trains into a booster with a 500 MHz RF system, a 3GHz linac bunch structure must fit into the booster buckets of  $\sim 1$  ns length, separated by 2 ns.

To minimize the booster cost, the aperture of the magnets is kept small. To keep the injection efficiency high given the small magnet aperture, a reasonably small emittance is required. Likewise, a small energy spread is needed to prevent beam loss in the high-dispersion regions of the booster lattice. An additional requirement is that the linac be able to provide sharp edges to the electron bunch train, to avoid injecting electrons into the ion clearing gap.

Thales and ACCEL have produced turn-key linac systems for Soleil and Diamond, respectively. The Soleil linac, using CERN “LIL” 3.5m structures, has a smaller energy spread that meets the NSLS-II design specification. An approach similar to the Soleil linac is used as a baseline and described below (Figure 2.2.1). The Diamond injector uses the DESY 2.2m accelerator structures, resulting in a slightly longer linac. To keep both options open in the preliminary design phase, the linac building has been designed to accommodate either four 5.2m tanks or five CERN 3.5m structures.

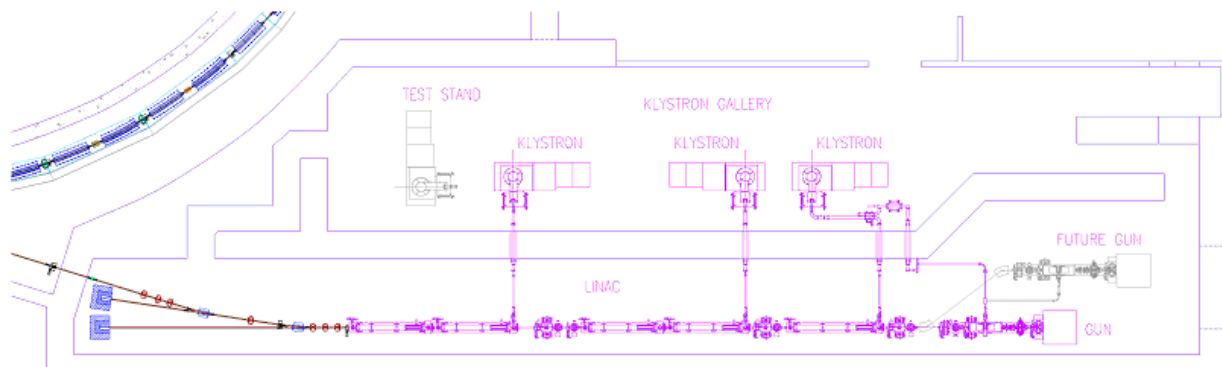


**Figure 2.2.1** Layout of the 200 MeV linear accelerator.

The linear accelerator [1] consists of the following subsystems:

- 100 kV triode gun (e.g., Eimac Y-845) with a 500MHz modulation at the gun grid and a high-voltage deck
- four shielded lenses, situated between the gun and the buncher
- a 500MHz subharmonic pre-bunching cavity with  $\pm 25$  kV modulation
- a 3GHz pre-bunching cavity with  $\pm 10$  kV modulation (100 W power)

- a 3GHz stationary wave buncher surrounded by two shielded coils (1.2 m long, 5.5 MW, energy gain of 15 MeV)
- five traveling wave-accelerating structures at 3 GHz in the  $2\pi/3$  mode and with a length of 3.5 m (flange to flange)
- a Glazer lens between the buncher and the first accelerating structure
- two focusing doublets
- three Klystrons (TH2100, 35 MW) and their modulators
- low-level RF controls

Objects colored in grey in Figure 2.2.1 represent elements of the linac that are considered as a future upgrade. As discussed in the introduction, the injector must possess sufficient flexibility in order to support complex bunch patterns. For filling and maintaining current in these, we considered including a second gun that will work exclusively in the single-bunch mode. Beam after the second gun is prebunched and accelerated in the following gun buncher system and injected in the linac at an energy of about 15 MeV using a dog-leg. Also depicted in grey is a test stand for klystrons testing.

## 2.2.2 Physics Design and Parameters

Although a range of parameters will meet the requirements, we focus here on a specific case of approximately 375 pC per bunch in bunch trains of 40 bunches for a total of 15 nC to provide details on the injector design. Having about a factor of two greater than the charge required in the storage ring top-off allows for faster initial fills and for losses in the injection process. Studies of booster injection and extraction losses will be included at the next design stage.

The energy spread must be controlled throughout the acceleration process. The maximum horizontal size of the beam injected into the booster (Section 2.5) is dominated by the energy spread. For  $\varepsilon = 125$  nm-rad ( $2\sigma$  emittance) and maximum  $\beta_x = 12$  m at the maximum dispersion,  $\eta = 0.35$ , and energy spread,  $\Delta E/E = 0.5\%$ , the maximum RMS beam size is  $\Delta\sigma_x \approx \eta\Delta E/E \approx 1.75$  mm.

Recent experience at SOLEIL [2.3] has shown that industry can produce turn-key linac systems that meet these specifications. Because the approach taken may differ significantly from one machine to the next, only the salient points of a generic linac are presented.

A planar triode electron gun, the EIMAC Y845 [2.4], is used with a fast-pulsed cathode driver. In single-bunch mode, the cathode is pulsed to create  $\sim 1$  ns pulses of  $\sim 0.5$  nC. The DC gun inherently has small energy spread. However, to compress the gun pulse for acceleration in the 2.998 GHz linac and capture it in the 500 MHz booster RF, we need to prevent nonlinearities in the RF from increasing the energy spread beyond the 0.5% (RMS) requirement. This translates into a requirement on the length of the micro-bunches exiting the linac to be less than  $\sim 11$  ps.

To create these short bunches, a bunching system is required. First, a 500MHz subharmonic buncher is used to compress the charge into bunch lengths less than 1 ns to match the 500MHz booster bucket. This is followed by a 2.988GHz pre-buncher that micro-bunches the 1.5ns bunch train to  $\leq 11$  ps bunches within the linac buckets. A final buncher simultaneously accelerates the electrons to 3 MeV to increase capture efficiency. In bunch-train mode, the cathode is pulsed on for the duration of the train, up to 200 ns, and is bunched in the process described above. During the preliminary design phase, system performance will be confirmed by E-Gun [2] and Parmela [3] simulations, and cathode driver experiments at the NSLS electron gun test stand.

The main accelerator is comprised of 3GHz traveling wave structures, with an energy gain of:

$$E[\text{MeV}] = 12.5\sqrt{P[\text{MW}]} \quad (2.2-1)$$

The accelerating structures being considered obtain 52 MeV per tank for an input power of 17.5 MW. Using readily available 35MW klystrons, the first klystron is power split, with about 5.5 MW feeding the 3GHz pre-buncher and buncher. The latter has an energy gain of more than 15 MeV. The remaining power feeds the first linac structure. Individual waveguide phase shifters and attenuators are used for adjusting amplitude and phase between elements.

The remaining four tanks are powered by two klystrons for an energy gain of an additional 52 MeV each. Thus, a total of 255 MeV energy gain is possible. For redundancy, two waveguide switches can connect the second klystron to power the two bunchers and first tank. In this scheme, an energy of 170 MeV can be achieved if one klystron fails. This will be explored in the next design phase.

The bunch charge and train current—although not beyond that which has been achieved in other applications [4, 5]—is sufficient to warrant close attention to beam-loading issues. For traveling wave tanks, the voltage induced along the bunch train on short time scales (compared to the fill time of the cavity) is given by:

$$V_b = -ir_0L[(1 - \tau^{-1})(1 - e^{-x\tau}) + xe^{-x\tau}] \quad (2.2-2)$$

where  $r_0$  is the shunt impedance,  $\tau$  the attenuation constant in nepers,  $L$  the length of the tank, and  $x$  the ratio  $t/t_f$ , where  $t$  is the time duration of the macro-pulse and  $t_f$  the fill time of the structure.

For forty 375 pC bunches separated by 2 ns (187.5 mA), this corresponds to about 1.6% in the correlated energy spread along the bunch train. There are several methods of reducing this beam loading. For a given beam current, the beam loading compensation can be achieved by sending the beam during the filling time of the second structure. This approach has been successfully implemented at SOLEIL [4] for a 300ns-long train current of 9 nC. Alternatively, the effect of beam loading can be diminished by lengthening the macro-pulse, either by simply lengthening the pulse and proportionally reducing the charge per bunch, or by pulsing the gun once every fourth, sixth, or eighth 500MHz bucket with constant charge per bunch to reduce the effect by the corresponding factor. For example, by filling 150 bunches of 100 pC each, the average current falls to 50 mA and the energy spread due to beam loading drops to 0.5%.

### 2.2.3 Klystron Modulators and Power Supplies

Pulsed 3GHz high-power klystrons are a mature technology and several manufacturers can meet or exceed the 35MW power requirement. The klystrons are powered by pulsed modulators. The traditional approach is to use Pulse Forming Networks with hard-tube (thyatron) switches to produce RF pulses between 2 and 4 microseconds long. NSLS has recently designed and built such a modulator for the 45MW tube installed at its DUVFEL facility. Our own experience and studies of reliability at SLAC/PEP-II and Pohang Light Source have shown that the mean time between failure (MTBF) and mean time to repair (MTTR) of the PFN/hard tube modulator dominate the linac downtime, with rates three times those of the klystron tube and its filament/core bias power supplies [6, 7]. For this reason, solid-state modulators are being explored for NSLS-II. Several competing designs have been developed for both medical linacs and the X-band International Linear Collider. One such example is the design by Scandi-nova [8], which uses a multi-turn primary pulse transformer, reducing the modulator voltage from about 40 kV to 3 kV, further increasing reliability by limiting the high voltage to only the pulse transformer and klystron cathode assembly in the oil tank [9]. These systems are also between one-half and one-third the size of similar PFN-type modulators. The decision to use a solid state or a PFN-hard tube modulator will be made during the preliminary design phase.

The 500MHz subharmonic pre-buncher requires about 6 kW (for a shunt impedance of 250 k $\Omega$ ) to reach 36 kV. This is well within the range of solid-state RF amplifiers.

The 3GHz pre-buncher is a single cell with  $\pm 10$  kV modulation, requiring only 100 W of RF power.

The 3GHz final buncher is a standing wave structure, requiring 5.5 MW of RF power, and delivering an energy gain of 15 MeV.

The low-level RF can be a duplicate of the DUVFEL RF system [10], with a master clock in common with the booster and storage rings driving a 2.988GHz DRO-based synthesizer whose output is split and feeds direct I/Q modulators for the amplitude and phase control of the individual klystrons. The 500 MHz will be derived from the booster RF that is synthesized in a similar way. Complimentary I/Q demodulators can be used to down-convert to baseband and close amplitude and phase loops around the cavity fields.

## 2.2.4 Diagnostics/Instrumentation for Linac

Table 2.4.1 shows beam diagnostics for the electron source and linac.

**Table 2.4.1 Linac Diagnostics.**

System	Quantity	Monitor Type	Measured beam parameter
Electron source	3	Wall current monitor	intensity, longitudinal beam characteristics
Linac	3	Fluorescent screens	position, profile
	2	Current transformers	intensity

The gun diagnostics consist of three resistive wall current monitors (WCM) to observe the longitudinal profile of the electron bunches after the gun, pre-buncher, and buncher. The WCM is formed by equally spaced broadband ceramic resistors mounted on a flexible circuit board, wrapped around a short ceramic break [11].

The bunch charge, produced by the gun and accelerated by the linac, is monitored by five fast current transformers [12]. The current transformers will monitor beam losses in the linac. Three fluorescent screens installed between the linac tanks will be used to observe the transverse profile and the position of the electron beam [13].



## References

- 1 <http://cern.ch/AccelConf/p07/PAPERS/TUPMS081.PDF>
- 2 W. B. Herrmannsfeldt, “EGUN – An Electron Optics and Gun Design Program,” SLAC 331, 1988.
- 3 Parmela, Ver. 3, by Lloyd M. Young, Documentation by James H. Billen, Los Alamos Nat. Lab.
- 4 A. Setty, et al., “Commissioning of the 100 MeV Preinjector HELIOS for the SOLEIL Synchrotron,” EPAC06.
- 5 C. Christou, et al., “Commissioning of the Diamond Pre-Injector Linac,” EPAC06.
- 6 C.W. Allen et al., “PEP-II Hardware Reliability,” SLAC-PUB-10835.
- 7 S.S. Park et al., “Reliability Analysis of the PLS Klystron-Modulator System,” Proc. of the Second APAC, Beijing, 2001.
- 8 <http://www.sc-nova.com/>
- 9 W. Crewson, “A new solid-state high-power pulsed modulator,” 5th Modulator-Klystron Workshop for Future Linear Colliders MDK-2001 Geneva, 25-27 April 2001.
- 10 J. Rose, et al., “Radio-Frequency Control System for the DUVFEL,” PAC03.  
<http://epaper.kek.jp/p03/PAPERS/TPAB006.PDF>
- 11 B. Fellenz, and J. Crisp, “An Improved Resistive Wall Monitor,” Proc. of Beam Instrumentation Workshop 1998, AIP Conf. Proc. 451, pp. 446–453.
- 12 <http://www.bergoz.com>
- 13 E. Johnson, W.S. Graves, and K.E. Robinson, “Periscope Pop-In Monitor,” Proc. of Beam Instrumentation Workshop 1998, AIP Conf. Proc. 451, pp. 479–484.



## 2.3 Booster

### 2.3.1 Booster Scope

The NSLS-II booster is required to produce a 3 GeV bunch train with an extracted charge of about 7.5 nC at a repetition rate of 1 Hz and a geometric emittance around 30 nm-rad. Injection in the booster ring takes place at an energy of 200 MeV. The booster magnetic field and RF voltage are ramped for 400 ms to accelerate the electron beam from the injection energy to the nominal energy of 3 GeV. At the maximum field of the ramp, the electron beam is extracted from the booster and injected into the main ring. As mentioned in section 5.2.1 we allow for a maximum beam loss of 30% during injection, a 20% maximum loss during acceleration and extraction, and 10% maximum loss for injection into the storage ring. Thus the charge to be accelerated in the booster is 10 nC which corresponds to an average beam current of 19 mA.

Since the storage ring Dynamic Aperture is limited, the injected beam quality has received serious consideration. In particular, the booster emittance may impact on the injection efficiency, which is a concern, in particular, because of frequent top-off cycles (see Chapter 4) carrying a high charge.

During the last 10 years many 3<sup>rd</sup> generation synchrotron light facilities have been put into operation. Nearly all of these facilities have chosen a full energy booster synchrotron as an injector together with a low energy linac as preinjector. The main parameters of several modern booster synchrotrons are listed in Table 2.3.1.

**Table 2.3.1 Modern Boosters.**

	ASP	DIAMOND	SOLEIL	SLS	ALBA	BINP
Energy, GeV	3	3	2.75	2.4	3	2.5
Tunnel	separate	Separate	separate	same	same	separate
Circumference, m	130.2	157	157	270	249.6	132
Lattice	4-fold	2-fold	2-fold	3-fold	4-fold	2-fold
Rep rate, Hz	1	5	3	3	3	1
Emittance, nm	34	144	150	9	9	50
Tunes, X/Y	9.2/3.3	6.8/4.6	6.4/4.4	12.4/8.4	12.4/7.4	9.1/9.1
Chromaticity, X/Y	-8.8/-11.5	-8.4/-6.2		-15/-12	-17/-10	-11.6/-11.4
RF freq., MHz	500	500	352	500	500	181
Damping times, X/Y/E	2.7/3.5/2.0	5.4/5.5/2.7	6.3/5.7/2.7	11/19/14	4.5/8.0/1.8	4.4/4.2/2.1
Current, mA	7	20	15	1	5	50
Source of info	[ASP]	[DIA]	[SOL]	[SLS1]	[ALB]	[BINP]

Modern boosters with energies around 3 GeV have natural horizontal emittances of the extracted beam in the 10–150 nm range. For example DIAMOND and SOLEIL boosters (located in separate buildings) have emittance of 140 nm; SLS and ALBA boosters (located in the ring tunnel) have emittances of 9 nm. The recently commissioned booster for the Australian light source (ASP) with a circumference of 130.2 m has emittance of 33 nm. The relatively low ASP booster emittance in combination with rather small circumference and conventional choice of a combined-function FODO lattice, looks attractive from the point of view of the design optimization level. A series of injection tracking simulations for the storage ring convincingly demonstrated the adequacy of the booster emittance in the range of 30-50 nm to the low-loss injection with sufficient margins for injection errors. Thus we have chosen the ASP booster model to serve as a basis for the NSLS-II booster development. To minimize the cost of the booster turn-key procurement, we are working to keep the NSLS-II booster design as close to that of the ASP booster. However, there are a few major differences between the NSLS-II and the ASP design:

- The NSLS-II booster injection energy is 200 MeV (in contrast with 100 MeV at ASP)
- The maximum dipole field is chosen to be 1 T (in contrast to 1.25 T at ASP)
- The NSLS-II booster circumference is 158.4 m (one-fifth of the storage ring circumference)
- Straight section length is 7.05 m, compared with 5.8 m at ASP
- The NSLS-II booster current is expected to be 20 mA (in contrast to 5 mA at ASP)

The booster revolution period of 528 ns restricts the length of the injected bunch train to be shorter than about 300 ns because of finite rise- and fall-time of the injection and extraction kickers. Therefore the longest bunch train generated by the linac will consist of 150 bunches.

One of the important requirements for the NSLS-II booster is in high efficiency of the charge transport through the booster. Therefore careful job must be done for optimization of the booster injection and extraction, expansion of booster magnet tolerances, design of robust orbit correction system and adequacy of Dynamic Aperture. In the next chapter we discuss the NSLS-II booster model in detail.

### 2.3.2 Booster lattice

The four-fold symmetry lattice is designed with five identical cells together with two modified cells containing dispersion suppressors. This results in a sufficiently low horizontal emittance of 26.5 nm-rad at the nominal energy of 3.0 GeV. The booster lattice is presented in Figure 2.3.1.

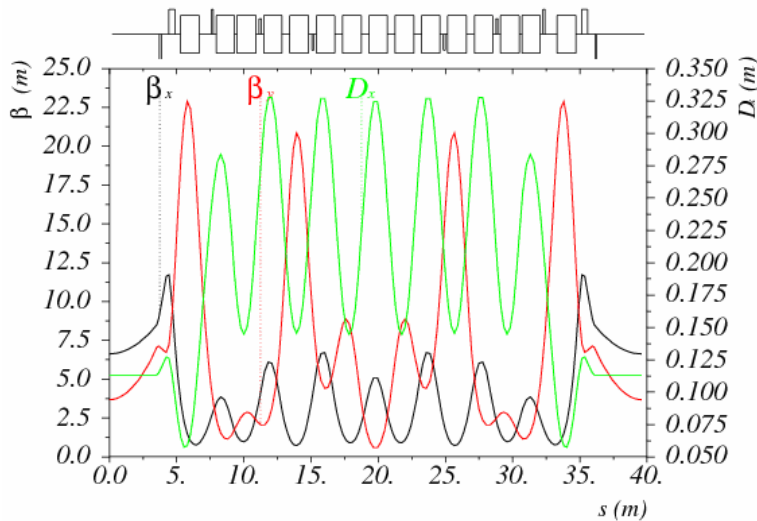


**Figure 2.3.1** : One-quarter of NSLS-II booster lattice.

The lattice consists of four long (7.05 m) straight sections with low dispersion (less than 12 cm) suitable for the installation of RF cavity, injection, and extraction systems. Low lattice emittance results in the low level of dispersion and stronger focusing, which increases natural chromaticity (horizontal: -13.8, vertical -18.9), and thus sextupolar gradients integrated in the combined function dipoles. Beta-functions are limited to 25 m, which corresponds to the maximum injected beam size of about 1.7 mm RMS in the vertical plane.

The lattice is composed of two families of combined-function dipoles, together with three families of quadrupoles: QF, QD and QG (Figure 2.3.2). Three separate power supplies for the booster quadrupoles provide freedom in optimizing the lattice and controlling tunes, dispersion, and chromaticity.

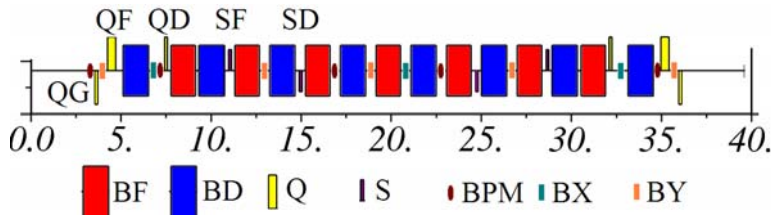


**Figure 2.3.2** Elements in one-quarter of the NSLS-II booster lattice.

Chromaticity correction is implemented by introducing sextupolar gradients into the dipole pole tips. In addition, four discrete sextupoles are introduced in every booster quadrant, shown as SSF and SSD in Figure 2.3.2. Separate power supplies for both sextupole families enable independent adjustments of horizontal and vertical chromaticity.

**Table 2.3.2** Part count/Magnetic Element Parameters.

Parameter	ASP Booster	NSLS-II Booster
<b>Dipole parameters</b>		
Number, BF/BD	28/32	28/32
Length, BF/BD	1.35/1.15 m	1.35/1.4 m
Angle, BF/BD	3.43/8.25°	3.43/8.25°
Injection energy	100 MeV	200 MeV
Field, BF/BD (inj)	0.015/0.042 T	0.030/0.069 T
Field, BF/BD (ext)	0.443/1.25 T	0.443/1.00 T
Quadrupole K1, BF/BD (ext)	0.82595/-0.66977 m <sup>-2</sup>	0.82800/-0.63831 m <sup>-2</sup>
Sextupole K2, BF/BD (ext)	3.54/-4.925 m <sup>-3</sup>	4.10/-5.65 m <sup>-3</sup>
<b>Quadrupole parameters</b>		
Number, QF/QD/QG	8/8	8/8/8
Length, QF/QD/QG	0.25/0.15 m	0.45/0.15/0.15 m
Quadrupole K1, QF/QD/QG (inj)	-0.0784/0.0133 m <sup>-2</sup>	0.1229/0.0581/-0.0869 m <sup>-2</sup>
Quadrupole K1, QF/QD/QG (ext)	-2.351/0.400 m <sup>-2</sup>	1.8442/0.87119/-1.3028 m <sup>-2</sup>
<b>Sextupole parameters</b>		
Number, SF/SD	8/8	8/8
Length, SF/SD	0.2/0.2 m	0.15/0.15 m
Sextupole K2, SF/SD (ext)	50/-30 m <sup>-3</sup>	40/-40 m <sup>-3</sup>

Table 2.3.2 illustrates the main parameters of the booster elements in comparison with them in the ASP booster lattice [ASP]. Reducing the booster cost we kept parameters of the focusing dipoles to be close to the original design (see Figure 2.3.3). Defocusing dipoles are similar to the ASP ones but longer (1.4 meters versus 1.15 meters), which shall require reworking hardware for the lamination stacking. Increasing the injection energy from 100 to 200 MeV significantly increased the magnet fields at injection, which simplifies achieving required field quality of the combine-function dipoles.

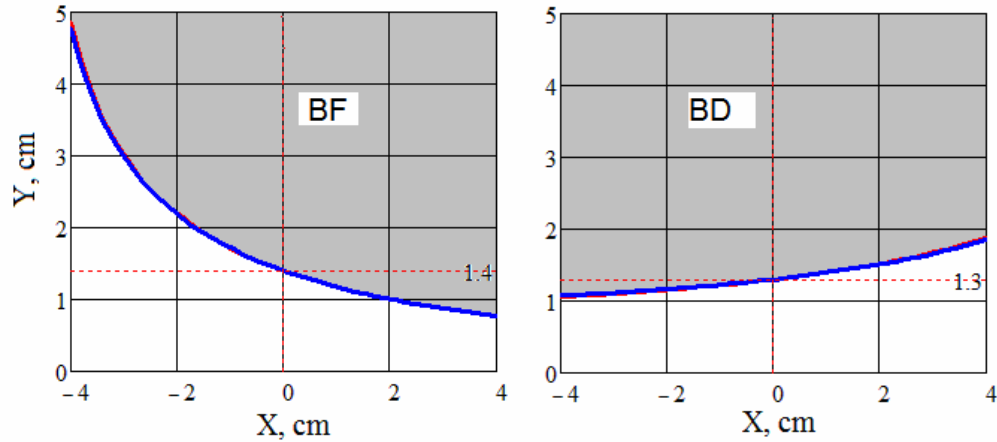


**Figure 2.3.3** Magnet pole tip profiles<sup>1</sup>, red – original ASP, blue – NSLS-II. Left plot corresponds to the focusing dipole; right plot corresponds to the defocusing dipole.

The main parameters of the chosen booster lattice are summarized in Table 2.3.3. The parameters of the ASP booster are also listed, for comparison.

**Table 2.3.3** Booster Parameters.

Parameter	ASP Booster	NSLS-II Booster
Emittance, nm	34.4	26.6
Circumference, m	130.2	158.4
Booster current, mA	<5	<28
Revolution time, ns	434	528
RF frequency, MHz	499.654	499.68
RF voltage, MV	1.2	1.5
Harmonic number	217	264
X/Y tune	9.2/3.25	10.91/6.69
X/Y chromaticity	-8.83/-11.5	-13.8/-18.9
Expected X/Y coupling	5%	10%
Corrected chromaticities	+0.83/+0.87	+1.7/+1.7
Momentum Compaction	0.0098	0.0072
Energy loss per turn, keV	743	625
X/Y/E damping time, ms	2.7/3.5/2.0	5.4/5.1/2.5
Damped energy spread, %	0.094	0.078
Damped bunch length, mm	19	13.9

The developed lattice is close to the original ASP one; however all of the requirements listed in previous introductory section are fulfilled.

In particular, attention has been paid to increase tunability of the booster lattice in the tune space. In particular, this is important for the tune adjustment at injection and tune correction during energy ramp. Including the third quadrupole family provided with large footprint in the tune space (Figure 2.3.4). While developing this footprint we constrained maximum beta-functions to stay below 20 meters for horizontal and 30 meters for

<sup>1</sup> Thanks to S. Mikhailov (Duke University) for his magnet design program.

vertical. This, in turn, has constrained the booster emittance to be below 50 nm for the whole upper half of the tune footprint (right plot on Figure 2.3.5). As follows from Figure 2.3.4, two defocusing quadrupole families are redundant with respect to each other, in the sense that there exist solutions (not necessarily optimal), which may be accomplished by only a single defocusing family.

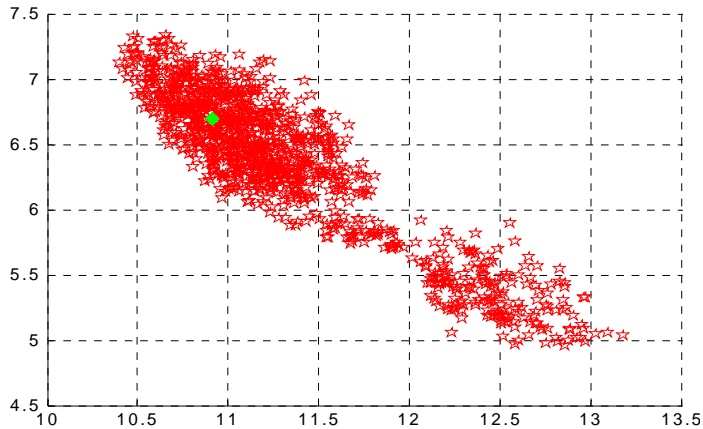


**Figure 2.3.4** Tunability of the booster lattice. The plot shows a footprint of the existing lattice solutions under constraints imposed on beta-functions. Green point points the working tune location.

Large tuning range of the booster optics is also beneficial from the Dynamic Aperture optimization. The left plot on Figure 2.3.5 exhibits tune scan for DA optimization. In the peak the booster DA reaches  $\pm 10$  mm in both planes, which should be sufficient for low-loss injection. We will continue optimizing the DA on the next stage of the design.

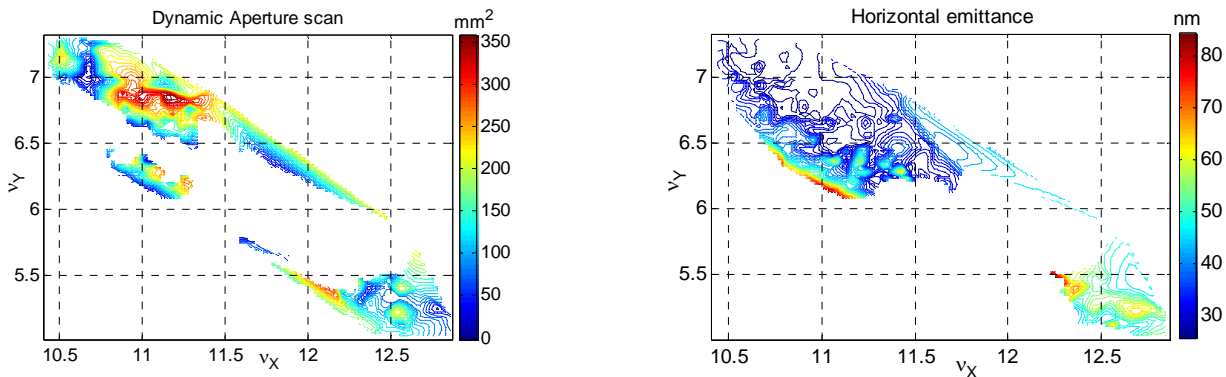


**Figure 2.3.5** Tune scan for Dynamic Aperture in  $\text{mm}^2$ .

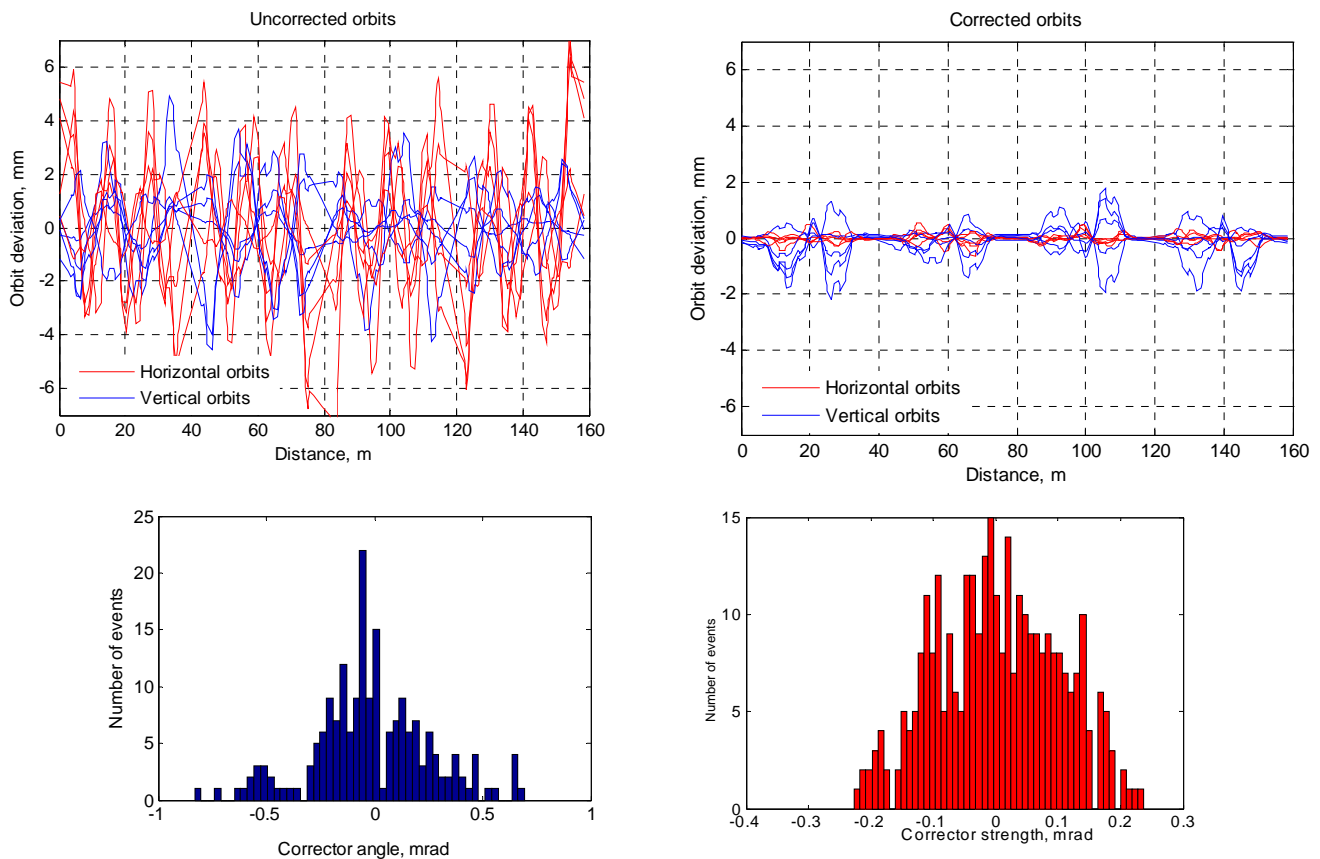
**Left:** abscissa – horizontal tune, ordinate – vertical tune. **Right:** corresponding emittance scan in nm-rad (right plot).

Preliminary consideration has been given to evaluation of the magnet tolerances and orbit correction system. The following tolerances for the magnet alignment and fields were assumed (Table 2.3.4). Tolerances on the magnet parameters were developed using analytical estimates that assumed normally distributed random errors in all magnets.

**Table 2.3.4 Magnet Tolerances.**

Source of error	Tolerance
Dipole length (relative)	0.1%
Dipole field (relative)	0.1%
Dipole long. displacement	1mm
Dipole transverse misalignment	0.1mm
Quad transverse misalignment	0.1mm
Quad gradient (relative)	0.2%

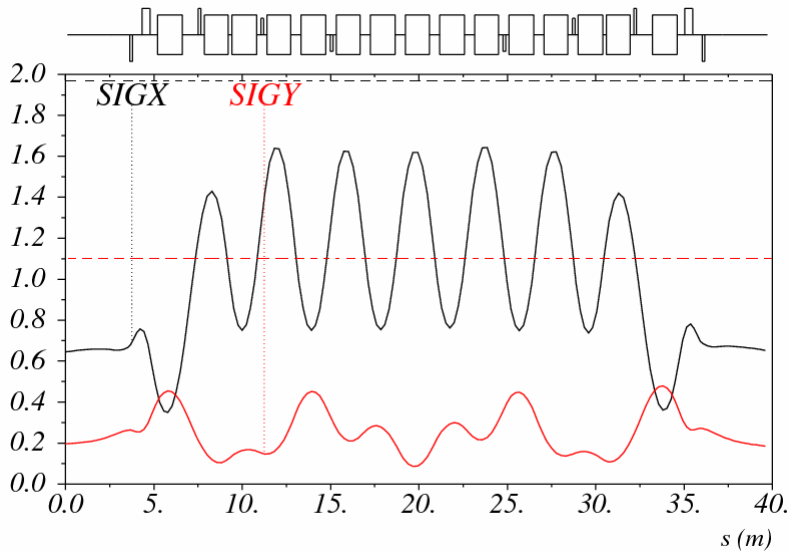
Orbit correction is implemented using 20 beam position monitors and 20 horizontal and 12 vertical trim magnets. The trim fields will follow the energy ramp, enabling orbit correction at all energies. The developed trim-BPM arrangement allows correcting the booster orbit down to a mm maximum deviation in each plane (Figure 2.3.6). This requires below 0.75 mrad (maximum value) in the corrector strength, making its design simple, with low magnet weight and size. This orbit correction system results in alignment tolerances for the dipoles and quadrupoles summarized in Table 2.3.4. These tolerances can be relaxed further by further optimizing the trim arrangement and adding one more vertical trim per quadrant.



**Figure 2.3.6** Uncorrected (left upper plot) and corrected (right upper plot) booster orbits. The two lower plots correspond to the statistics of the corrector angles. Red and blue traces and histograms correspond to horizontal and vertical orbits and correctors, respectively.

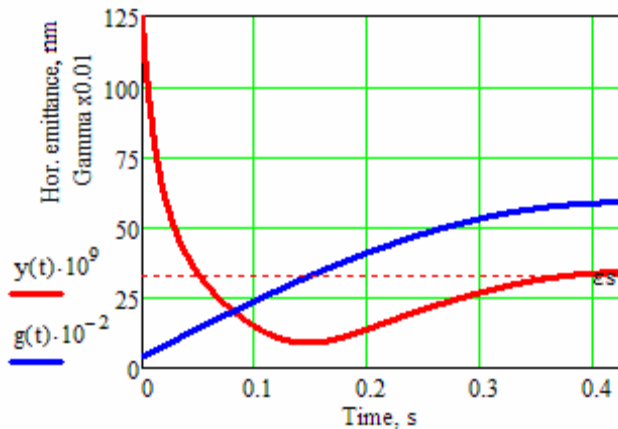


Figure 2.3.7 shows envelopes of the beam injected from the linac. Linac beam parameters were chosen according to values in chapter 2.2. Electron beam phase space ellipse was matched to that of the circulating beam at the booster injection point.



**Figure 2.3.7** RMS injected beam envelopes in mm (solid curves). Dashed lines show approximate location of the dipole vacuum chamber (magnified ten times).

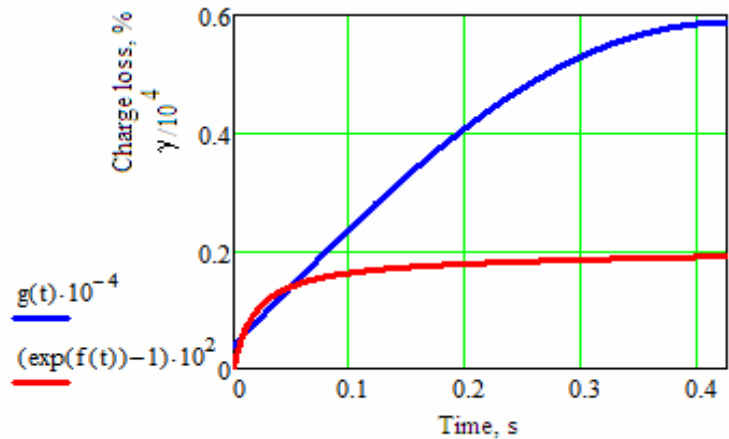
Short damping time at the maximum booster energy leads to the fully damped beam at the end of the ramp (Fig. 2.3.8). Here we assumed a sinusoidal ramp profile with the injection point “on the fly”, i.e. on the rising slope of the energy ramp.



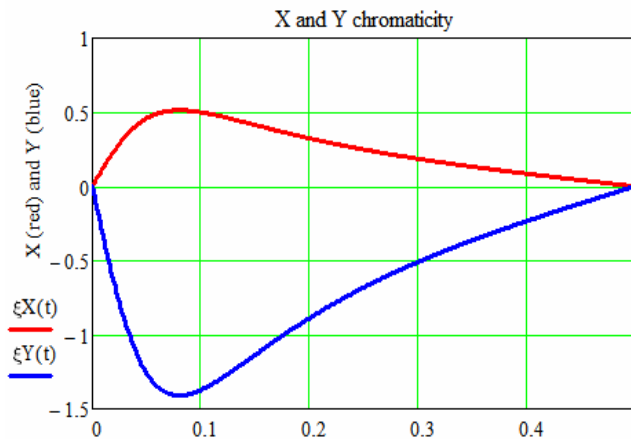
**Figure 2.3.8** Booster energy ramp (in units of  $\gamma/100$ , blue curve) and dependence of the horizontal booster emittance versus ramp time (in nm·rad, red curve). Dashed line shows damped value of the booster emittance at 3 GeV.

Figure 2.3.9 shows the estimated beam loss throughout the energy ramp due to residual gas (mainly elastic scattering on the gas nuclei). Total relative charge loss is expected to be about 0.2% at the average value of the booster vacuum of  $10^{-7}$  torr. We estimate the beam lifetime at the injection energy of 200 MeV to be around 10 seconds.

**Figure 2.3.9** Relative gas-scattering losses in % of the charge throughout energy ramp.



For an estimate of the chromaticity driven by eddy currents (Figure 2.3.10), we used a formalism developed in [Edd]. For the given lattice parameters, the estimated maximum value of the sextupolar moment is  $0.085 \text{ m}^{-3}$  at 1 Hz of repetition rate. Corresponding calculated values of chromaticity are  $+0.5$  horizontally and  $-1.4$  vertically, which is much smaller than the natural chromaticity and can be compensated by local modification of the sextupole ramp.



**Figure 2.3.10** Eddy-currents induced chromaticity during the energy ramp

Concluding this section, we note that the developed booster design is close to the existing ASP booster except for a few important differences between the two designs that are specific for the NSLS-II and were discussed in the introduction. These were realized in the current booster layout and the overall design appears to be feasible and cost-effective.

In the line of future work, we will pay close attention to the optimization of the Dynamic Aperture and perform modeling of the ring at injection and particle tracking, for evaluating and mitigating potential injection losses. In addition we will explore high average current effects that may be of interest at the maximum value of the booster current.

### 2.3.3 RF Acceleration System

The booster RF acceleration system must capture the bunch train injected from the 3 GHz linac, accelerate a beam charge of 10 nC (19 mA average current) to 3 GeV, and transfer the bunch train to the storage ring 500 MHz RF buckets (Table 2.3.5). At maximum energy a bucket height of 0.85% is necessary (see Figure 2.3.12) which translates into a necessary accelerating voltage of 1.5 MV. At injection energy this rf voltage can provide a much larger bucket height so that the energy spread of the accepted beam is limited by the physical aperture and/or the transverse off energy dynamic aperture of the lattice and not by the rf system.

**Table 2.3.5 RF and Beam Parameters for the Booster.**

RF frequency [MHz]	499.68
Loss per turn (3 GeV) [keV]	625
Overvoltage	2
Accelerating voltage [MV]	1.5
Momentum compaction	0.0072
Bunch charge [pC]	1375
RF acceptance %	0.85
Number of bunches	40-150
Nominal beam current [mA]	
Nominal beam power at 3 GeV [kW]	12

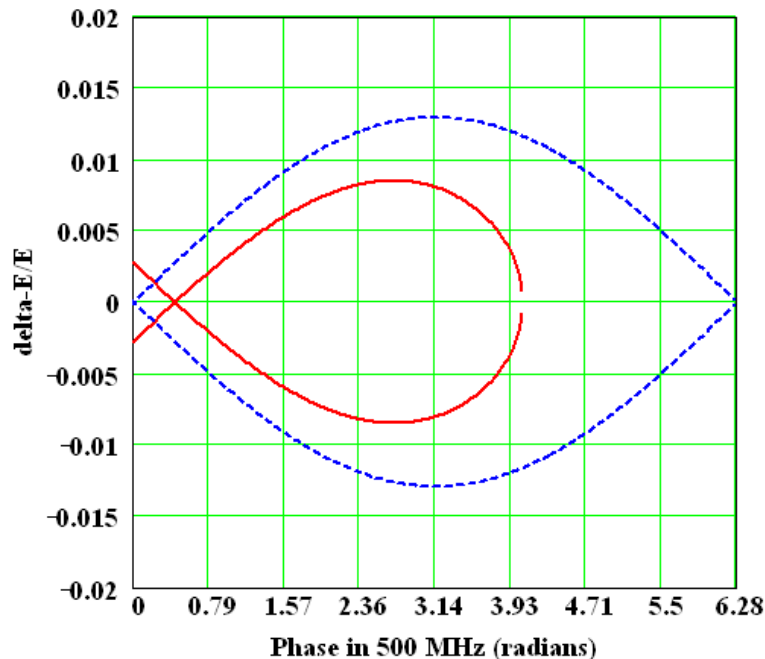


**Figure 2.3.11:** RF separatrix for 1.5 MV RF field at 3 GeV, with radiation losses (red curve) and the stationary bucket without losses (blue curve). The separatrix provides an energy acceptance of 0.85% at 3 GeV.

As the rf voltage requirement of 1.5 MV is significantly more demanding compared with the beam power requirement of 12 kW a multicell cavity is the appropriate choice, e.g. the PETRA type 5-cell cavity with a shunt impedance of 15 MOhm. With a single PETRA type cavity the total necessary rf power (cavity wall losses, beam power, 10% transmission losses and safety margin) is in excess of 100 kW. For this reason two PETRA 5-cell cavities will be used. The geometry of this cavity is shown schematically in Figure 5.3.11

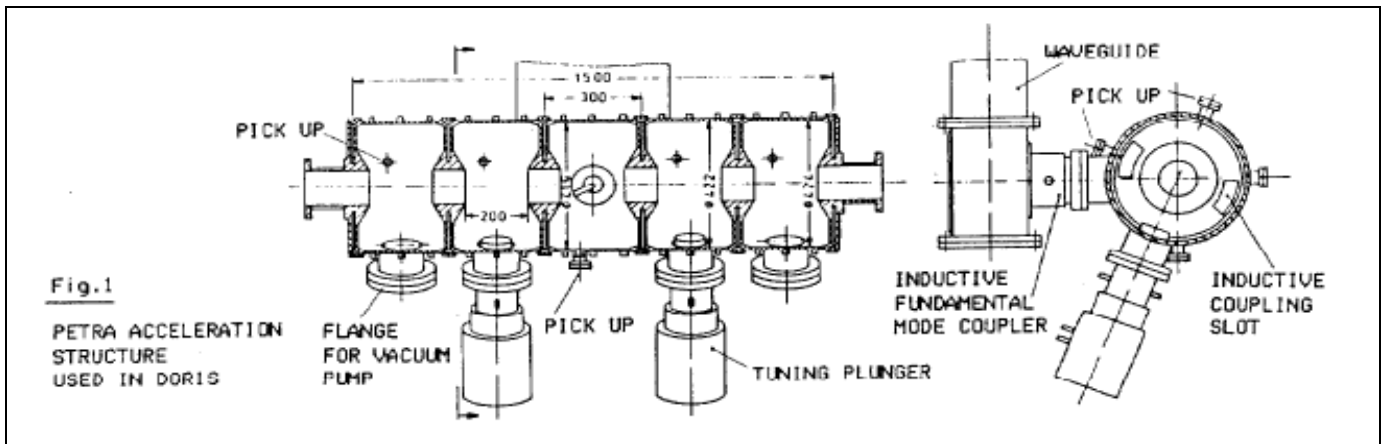


Figure 2.3.12 The five-cell PETRA cavity.

Klystrons and inductive output tubes (IOT) are available as rf power sources at 500 MHz to generate the necessary rf power. In the power range from several ten kW to 80 kW the klystron market became rather small in recent years as these tubes have been replaced by IOTs for TV applications with the consequence of significant increase in cost. IOTs have a higher efficiency (typically 65%) than klystrons and tube cost are about 30% lower as compared to klystrons. For these reasons the baseline power source will be a modified broadcast IOT transmitter capable of 80 kW output power at 499.68 MHz. Since a few years such transmitters are in use at several synchrotron light source facilities. Similar as klystrons IOTs can operate safely only under matched load conditions. Therefore a circulator is necessary between the transmitter and the cavities. Figure 2.3.13 shows a footprint of the cavity section and the IOT transmitter system including the rf power feeding line and the circulator.

The IOT transmitter utilizes a broadcast IOT tube. Several tubes are available to provide 80 kW at 500 MHz, including the THALES TH793, E2V e2v2130, and Communication and Power Industries K5H90W. Tube parameters for the TH793 are given in Table 2.3.7.

Table 2.3.7 Tube Parameters for TH793 IOT.

Beam voltage [kV]	36
Beam current [A]	3.2
Maximum output power [kW]	90
Maximum collector dissipation [kW]	70

For the HV power supply of the transmitter two technical options are in use to provide the DC power to the IOT transmitter: a standard broadcast transformer-rectifier or a Pulse-Step-Modulated switching power supply. The PSM supply has lower ripple, which results in lower residual modulation of the beam and a lower stored energy. These attributes, combined with the fast turn-off capability, eliminate the need for a hard-tube crowbar circuit.

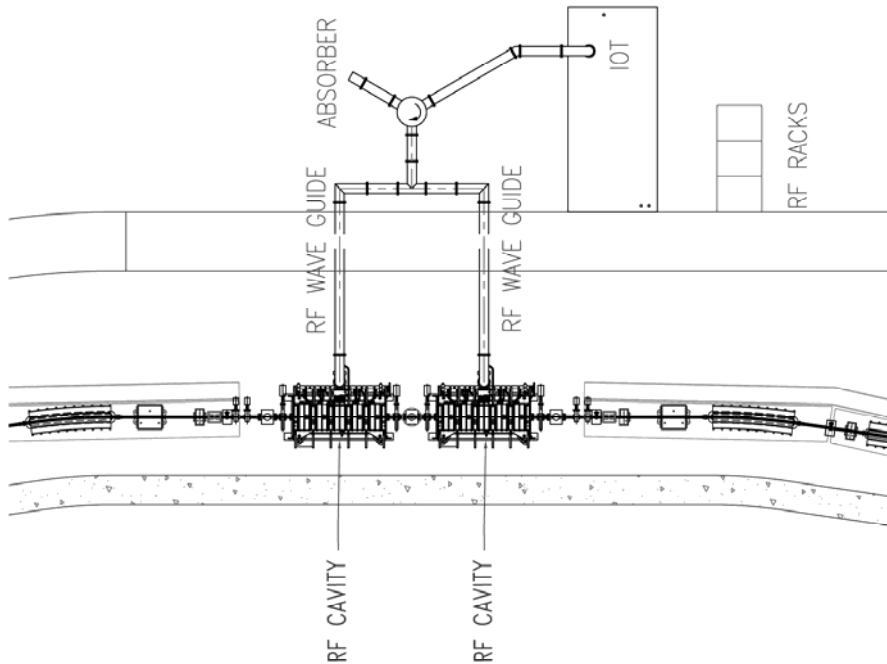


**Figure 2.3.13:** Footprint of the cavity section and the IOT transmitter system including the rf power feeding line

### 2.3.4 Booster Injection System

The booster injection system consists of the pulsed septum and kicker with their power supplies (Figure 2.3.14). It is a simple single turn on-orbit injection, allowing a maximum of about 150 consecutive bunches to be injected into the booster RF buckets. The bend angle of the septum is 140 mrad and that of the kicker is 10 mrad, making the total bend angle the same as that of the other LtB TL dipoles. This solution is viable and gives very reasonable field values for the pulsed magnets.

Separation of the trajectory of the injected beam orbit at the end of the septum and the closed orbit of the booster is 20 mm, placing the inside edge of the injection septum at 16 mm from the nominal booster orbit.

Thought is also being given to making the kicker angle larger, thus allowing the septum to be placed further away from the circulating beam in the booster and possibly replacing the pulsed septum with a well-shielded DC magnet.

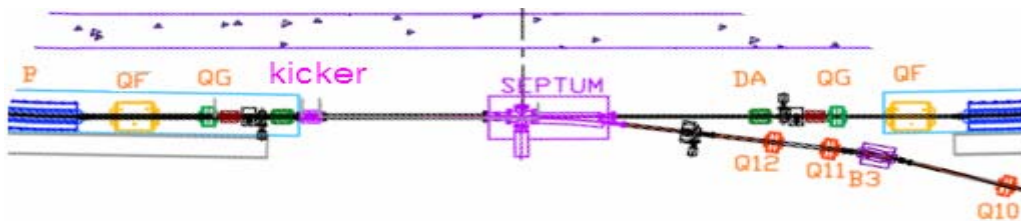


**Figure 2.3.14** Booster injection system layout.

The basic magnet parameters are shown in Table 2.3.8.

**Table 2.3.8 Booster Injection System Pulsed Magnet Parameters.**

Injection Energy 200 MeV	Booster Injection Septum	Booster Injection Kicker
Magnetic Field (T)	0.0933	0.02
Magnetic Field (T)	0.0933	0.02
Length (m)	1.0	0.3
H x V (mm x mm)	20 x 15	50 x 25
Bend angle (mR)	140	10.0
Inductance ( $\mu$ H)	1.676	0.754
Peak Current (A)	1200	450
Drive Capacitor ( $\mu$ F)	340	70 m transmission line
Voltage (kV)	0.08	5.4
Pulse Shape	75 $\mu$ sec half sine	100 nsec risetime, 300 nsec flat-top
100 nsec fall time Magnetic Material	¼ mm Si steel	CMD5005
Ceramic chamber Coat	N/A	2 – 3 $\Omega$ /l Ti

The capacitor banks or transmission line PFN's are charged with voltage regulated DC power supplies with up to, at least for the extraction system and ring injection system, 16-bit resolution voltage regulation. The transmission line for the injection kicker is terminated with a de-Q'ing circuit to pull the current/field down before the head of the injected bunch train re-enters the kicker after completing a booster orbit. The system impedances need to be matched carefully to prevent excessive ringing, although the requirements for the booster injection system are not very stringent. Damping during the ramp will erase all memory of injection abnormalities; these will not be translated into extraction orbit displacements.

While searching for ways of reducing charge requirements on the NSLS-II linac we are considering the possibility of the booster injection system to allow stacking of the low-energy beam at the maximum linac repetition rate of 10 Hz. Tracking calculations are in progress for attempting to stack two consecutive bunch trains (separated by 0.1 seconds or more) transversely in the booster by injecting them with  $\sim 1/2$  of the nominal kicker strength. Recharging the capacitor banks/transmission line for 10Hz operational capability may require high current supplies and will most likely run more cost effectively at a slower rate to allow the power supplies to settle at the required voltage. As mentioned above, a larger angle for the kicker may allow replacement of the pulsed septum and its large capacitor bank with a DC magnet, eliminating this problem. Further optimization is in progress.

### 2.3.5 Booster Extraction System

The booster extraction system consists of four slow orbit bumpers, pulsed septum and kicker (Fig. 2.3.15). The orbit of the circulating bunch train is moved out toward the extraction septum over several hundred turns by the slow orbit bumpers and is kicked into the extraction septum by the extraction kicker. The arrangement is shown in the plan view below, and the pulsed magnet specifications are outlined in Table 2.3.9.

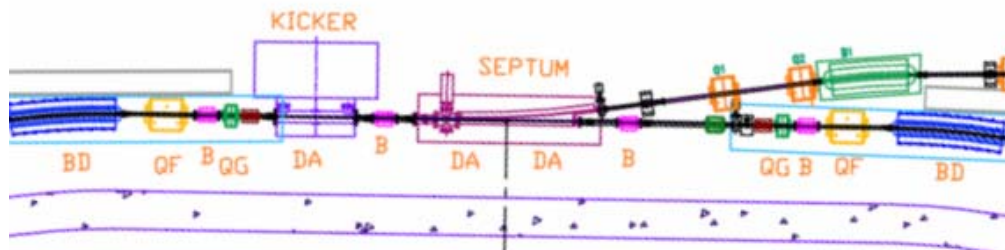


**Figure 2.3.15** Booster extraction system layout. B -- orbit bumps.**Table 2.3.9** Booster Extraction System Pulsed Magnet Parameters (at the Extraction Energy of 3 GeV).

	Extraction Septum	Slow Bumps	Extraction Kicker
Magnetic Field [T]	0.8	0.4	0.05
Magnetic Field [T]	0.8	0.4	0.05
Length (m)	1.75	0.2	1.0
H x V [mm x mm]	20 x 15	50 x 25	50 x 25
Bend angle [mR]	140	7.5	5.0
Inductance [ $\mu$ H]	2.932	201	2.513
Peak Current [A]	10,000	400 in 20 turns	1.0
Drive Capacitor [ $\mu$ ]	125	505	65 m transmission line
Voltage [kV]	1.465	0.3	19.75
Pulse Shape	60 $\mu$ sec half sine	1000 $\mu$ sec half sine	<200 nsec risetime, 300 nsec flat-top
Magnetic Material	$\frac{1}{4}$ mm Si steel	$\frac{1}{4}$ mm Si steel laminate	CMD5005
Ceramic chamber Coat	N/A	N/A	0.5 $\Omega$ /l

The slow orbit bumps use 20 turns of conductor carrying a current of up to 400 A. Consideration to power these in series is under discussion at the moment. The steel laminations will be made of grain oriented heat-treated Si transformer steel with thin insulating coating on one side to reduce eddy currents. A 1.1 T septum with a 75 $\mu$ sec half-sine wave excitation has been running at NSLS for many years.

The extraction septum entrance is 16 mm outside of the central closed orbit of the booster; during extraction the displaced orbit is pushed to coast as close to the extraction septum as possible without incurring beam loss.

The kicker is a full-aperture device producing a field of 500 Gauss, and will be driven by a circuit similar to the one shown below (Figure 2.3.16). It turns on and reaches full flat-top field during the gap in the booster bunch train.

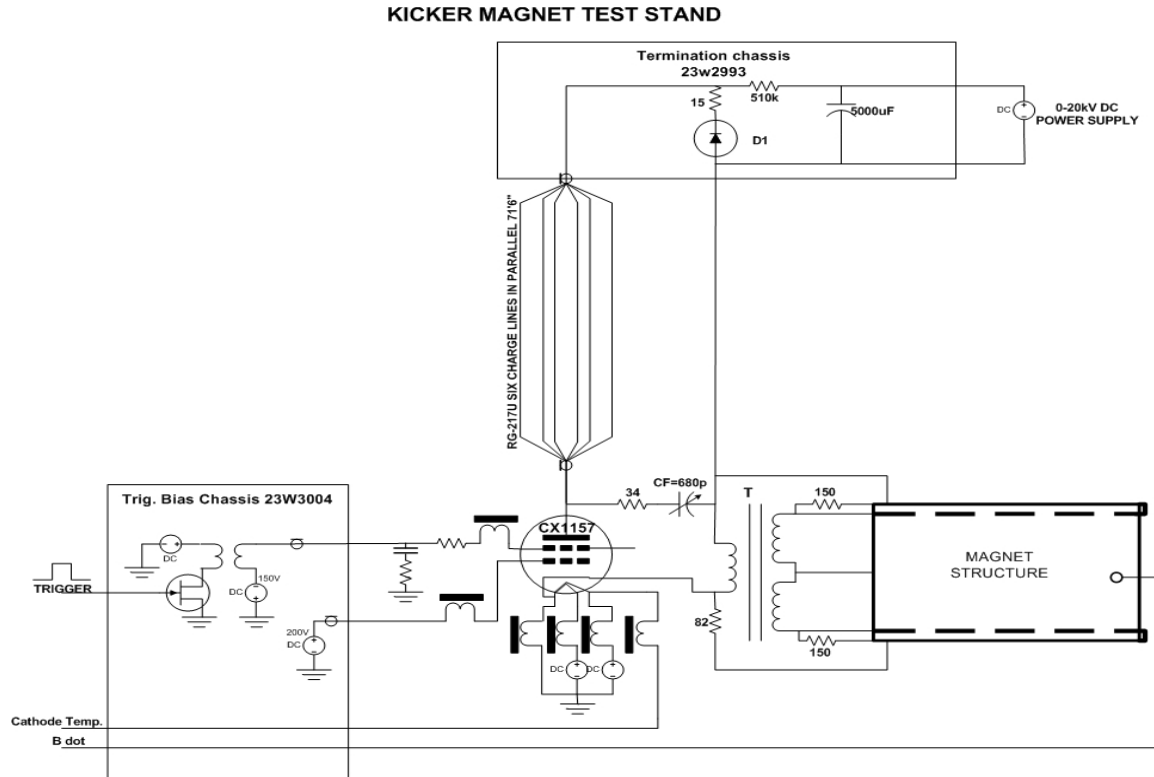


Figure 1

Figure 2.3.16 Booster extraction system layout.

### 2.3.6 Booster Diagnostics and Instrumentation

This section describes diagnostics and instrumentation for the booster ring. The following parameters will be monitored:

- orbit
- working point (tunes in both planes)
- circulating current and filling pattern
- emittances
- bunch length

Booster diagnostics are summarized in Table 2.3.10.



**Table 2.3.10 Beam Diagnostics for the Booster Ring.**

Monitor	Quantity	Beam parameter
DC current transformer	1	Beam current
4-button pick-ups	20	Beam position
Fluorescent screens	6	Injection position, profile
Stripline set and amplifier	2	Betatron tune and bunch cleaning system
Fast current transformer	1	Filling pattern
Optical beamline with streak-camera	1	Bunch length
Firewire camera	1	Beam position, profile

Six fluorescent screens will be used to observe shape and position of the injected electron beam during the first turn. The screen material will be YAG:Ce. This was chosen because it results in an excellent resolution of the beam image and exhibits high sensitivity and high radiation hardness.

The booster orbit will be monitored with 20 pick-up electrodes instrumented with Libera receivers. The receivers are the same as used for the storage ring and have the specifications shown in Table 2.3.11 [ite]:

**Table 2.3.11 RF BPM Specifications.**

Beam intensity range [dB]	>70
Input signals	0 dBm -70 dBm, 50 $\Omega$
Operating frequency [MHz]	500 MHz
Noise RMS for k=10 mm [ $\mu$ m]	<3 (1.15 MHz BW) @ -20 dBm <15 (1.15 MHz BW) @ -44 dBm
Beam current dependence 0...-50 dBm [ $\mu$ m]	1
Fill pattern dependence 100%-20% [ $\mu$ m]	1

The booster current will be measured with a parametric current transformer, such as the one manufactured by Bergoz [ber1]. Its radiation-hardened sensor head is equipped with 30 m cable and its inner diameter of 115 mm is sufficient to fit over the flange. The parametric current transformer has the following specifications:

**Table 2.3.12 Booster Current Monitor Specifications.**

Full scale ranges	$\pm 20$ mA, $\pm 200$ mA, $\pm 2$ A, $\pm 20$ A
Range control	2 TTL lines
Output [V]	$\pm 10$
Output bandwidth (-3 dB)	8 kHz in 20 mA range, 10 kHz other ranges
Response time (at 90%) [ $\mu$ s]	<50
Resolution [ $\mu$ A/Hz <sup>1/2</sup> ]	<5
Output accuracy [%]	$\pm 0.1$
Linearity error [%]	<0.1
Output impedance [ $\Omega$ ]	100

The filling pattern will be monitored with a fast current transformer. For example, the Bergoz FCT has the following specifications [ber2]:

**Table 2.3.13 Fast Current Transformer specifications for measurements of the filling pattern.**

Turns ratio	20:1
Nominal sensitivity [V/A]	1.25
Rise time (typ.) [ps]	200
Droop [%/ $\mu$ s]	<6
Upper cutoff frequency (-3 dB typical) [MHz]	1750
Lower cutoff frequency (-3 dB) [kHz]	<9.5
Position sensitivity [%/mm]	<0.2
Minimal L/R time constant [ $\mu$ s]	17
Maximum charge per pulse (pulses<1 ns) [ $\mu$ C]	0.4

We will evaluate a design of an in-flange version of FCT from the vacuum point of view and perform analysis of the wake-fields. If the design will be found unsatisfactory then the FCT will be placed over ceramic break equipped with RF shield.

The synchrotron radiation from one of the bends will be used for bunch-length measurements with the help of a streak camera [stca].

The fractional tune measurement system will be based on real-time spectral analysis of the signal induced on the strip-lines by the electron beam. Electron beam motion will be excited by broadband noise generator with fixed cutoff frequencies. The real-time spectrum analyzer will be used to observe tune evolution along the ramp. Tune measurement system based on the PLL will also be considered.

The synchrotron radiation from the bending magnet will be used for beam observation with CCD cameras. The beam image will be analyzed for the emittance measurements and also will provide information on the beam position and stability during the ramp.

## 2.3.7 Beam Chambers and Vacuum System

### 2.3.7.1 Vacuum System Scope

The booster ring vacuum system includes all vacuum chambers, vacuum pumps, vacuum instrumentation and diagnostics, vacuum controllers, and connecting wiring. The vacuum chamber design, materials, and processes are described in Section 2.3.7.2. The estimated gas load, pumping scheme, and expected pressure distribution in the booster are given in Section 2.3.7.3. The vacuum monitoring and control are explained in Section 2.3.7.4.

An average pressure below  $1 \times 10^{-7}$  Torr (see Section 2.3.2) is needed within the booster to minimize the beam loss and bremsstrahlung radiation due to beam-residual gas scattering. The booster vacuum system will be designed with sufficient pumping capability to achieve vacuum pressures in the  $10^{-8}$  Torr range. Most booster vacuum chambers will be constructed from seamless stainless steel tubing and will utilize Conflat flanges.

### 2.3.7.2 Vacuum System Design

The booster vacuum will be divided into eight sections isolatable with radiation-resistant EPDM-sealed gate valves. The four (4) arc sectors will be  $\sim 33$  m each and the four (4) straight sections of  $\sim 6$  m each. Each arc sections will have 15 bending chambers of  $\sim 1.5$  m long for BF and BD magnets, and short straight pipes for multipole magnets, bellows and side ports for appendage components such as gauges, valves, ion pumps, etc. The four straight sections will house injection, extraction, RF cavities and beam diagnostics. Conventional ultra high vacuum technology will be implemented. High vacuum will be achieved with small sputter ion pumps distributed around the booster ring.

The booster will accelerate the 200MeV bunch train from the linac to the full energy of 3 GeV at 1 Hz repetition rate. To minimize the eddy currents during the fast ramping fields (and the associated sextupole effect), the vacuum chambers will be made of thin-wall stainless steel. A wall thickness of about 0.7 mm is sufficiently strong for a bending chamber with an elliptical cross section of 24 mm (V)  $\times$  40 mm (H), while having sufficiently low eddy currents. The 60 bending chambers will be about 1.5 m long with bending radii of 10 m and 23m for defocusing and focusing chambers, respectively. They will be made from seamless stainless tubing, drawn and pressed into elliptical shape, then roll-curved to give the required bend angles. The ends of the bending chambers will be tapered from elliptical to round cross-section and welded to Conflat flanges. The maximum stress and deflection of the bending chamber under the external atmospheric pressure occurs at the top and bottom of the chambers. Using finite element analysis, the stress and deflection are found to be 11000 psi and 0.2 mm, respectively (Figure 2.3.17), which is well within acceptable ranges with large safety margins.

The straight drift pipes between bending chambers will have an inner radius of 20mm and made of thin wall stainless steel. Each drift pipe is approximately 0.8m long consisting a section for multipole magnets, a precision machined block for mounting of the four BPM buttons, a cross for vacuum pumps and gauges, and a short bellows. Conflat flanges (size DN38) will be used throughout the booster ring.

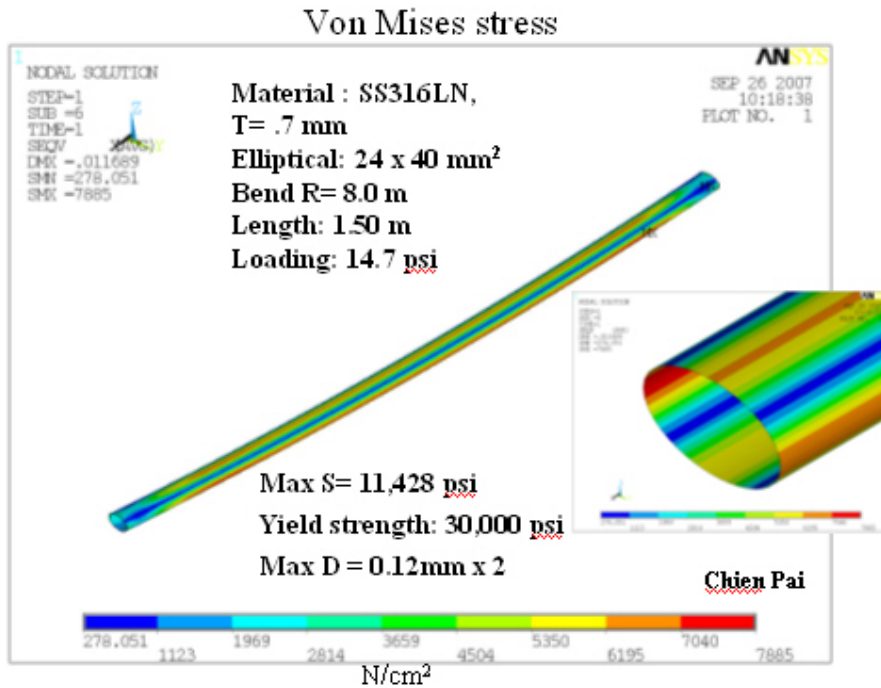


**Figure 2.3.17** Calculated stress of the thin-wall bending chamber under vacuum load. The high stress is at the side of the tube along the horizontal plane with maximum stress of less than 11kpsi. The calculated deflection is ~0.2 mm.

After proper chemical cleaning, the completed chambers and drift pipes will be vacuum degassed at 450°C in a vacuum furnace for several days to remove any trace of surface contaminants and to reduce outgassing, eliminating the need for in-situ baking. The chambers and the pipes are then assembled into the magnets, welded with end flanges, and tested prior to installation in the tunnel. Once they are installed and connected to other beam pipes, two gate valves will be mounted at the end of arc sections, so each section can be pumped down to high vacuum.

### 2.3.7.3 Vacuum Pumping and Pressure Distribution

The thermal outgassing of the clean stainless chamber surface will be less than  $1 \times 10^{-10}$  Torr-l/s/cm<sup>2</sup>, 24 hours after pumping down. This is equivalent to a total thermal gas load of  $\sim 2 \times 10^{-5}$  Torr-l/s for the whole booster ring, excluding the contributions from RF, injection, extraction, and diagnostics. The pressure in the booster will be

dominated by the synchrotron radiation-induced desorption during the filling of the storage ring. This effect will be much less pronounced during the tophoff injection mode due to low duty factor. Assuming a 25 mA multi-bunch beam accelerated to 3.0 GeV in the booster during the 0.4 sec acceleration cycle, the average synchrotron radiation power on the vacuum chamber wall will be less than 2000 W for the whole ring, concentrated at the downstream end of the dipole chambers, with a linear power density less than 40 W/m. No observable temperature rise at the chamber wall is expected.

The average photon flux during acceleration is approximately  $1 \times 10^{19}$  photons/sec. Assuming a PSD yield of  $\eta = 2 \times 10^{-4}$  molecules/photon, the total photon-desorbed gas load will be about  $1 \times 10^{-4}$  Torr-l/s, which is much higher than the thermal desorption gas load. Desorption yield of  $\eta = 2 \times 10^{-4}$  mol/ph can be achieved with an integrated dosage of  $10^{19}$  ph/meter, reached in a few hours of continuous booster operation. Both the thermal- and photon-desorbed gas load will be handled with the 30 l/s ion pumps at the downstream end of each bending chamber. The pressure distribution in booster arc section can be estimated using standard linear conductance formulae and super imposing photon stimulated desorption over the thermal desorption. The pressure distributions of a 10 m long arc section for three different pumping schemes are plotted in Figure 2.3.18, with one 30 l/s ion pump downstream of each bending chambers ( $\sim 2.2$ m pump spacing); with one 100 l/s ion pumps downstream of each bending chamber; and with one 30 l/s ion pump at every other bending chambers ( $\sim 4.4$ m pump spacing). The average pressure for 1<sup>st</sup> case is about  $1.2 \times 10^{-7}$  Torr and 25% lower with 100 l/s ion pumps. Due to the limited conductivity of the small-diameter beam pipes, the average pressure will improve with shorter pump spacing, rather than with larger ion pumps, as illustrated in the 3<sup>rd</sup> case, where pressure increases by factor of 3 when number of pumps is halved. The average pressure will improve rapidly to mid  $10^{-8}$  Torr within a week, since  $\eta$  decreases with integrated beam dose and thermal outgassing decreases with time.

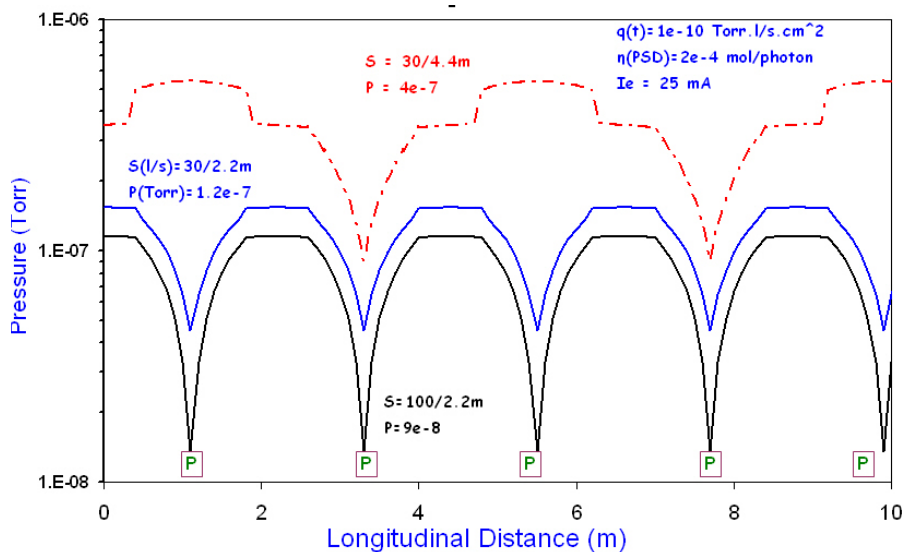


**Figure 2.3.18** Pressure distribution in booster arc sections from both thermal desorption and photon-stimulated desorption. Each arc section will have fifteen (15) 30 l/s ion pumps, at downstream end of each bending chamber. Due to the limited linear conductance of the small diameter beam pipes, the average pressure only decreases by 25% if 100 l/s ion pumps are used in place of the 30 l/s pumps. The average pressure will increase three folds if only one ion pump is installed for every two bending chambers.

The booster ring vacuum sectors will be roughed down from atmospheric pressure with portable turbo-pumps (TMP) backed with dry mechanical pumps before transferring to the sputter ion pumps. Two right-angle, all-metal valves will be mounted at each vacuum sector for roughing, bleed-up, and for other vacuum diagnostics. The TMP stations will have their own vacuum gauges and an electro-pneumatic valve to isolate the TMP from the vacuum section in the event of pump or power failures. The TMPs will be manually isolated with valves, once each booster ring sector is at high vacuum. Large ion pumps of about 200 l/s, identical to those deployed in the storage ring, will provide sufficient UHV pumping speed at the straight sections for RF cavities, injection, extraction, and diagnostics.

### 2.3.7.4 Vacuum Monitoring and Controls

Power supplies and controllers for linac and booster vacuum systems will be located in the satellite electrical racks in the Injector service area. Commercial dual ion pump controllers and vacuum gauge controllers with local and remote capabilities will power, monitor, and control the ion pumps and vacuum gauges, and interface with the PLC and control computers. Ion pump currents and the vacuum gauges will provide information on the pressure distribution in the booster ring.

#### 2.3.7.4.1 Vacuum Monitoring

The booster vacuum will be monitored and interlocked with the ion pump current and the vacuum gauge readings. Each arc vacuum section will have a convection-enhanced Pirani gauge (TCG), two inverted-magnetron cold cathode gauges as the primary gauges, and 15 30 l/s ion pumps. One set of vacuum gauges and two large ion pumps will be installed at the short straight sections to handle the extra outgassing from RF cavities, kickers, septums and diagnostics. Residual gas analyzer heads will also be installed at short straight sections for diagnostics during operation and maintenance periods. A residual gas analyzer head may be mounted on the portable TMP stations to assist the pumpdown and troubleshooting of arc vacuum sections. Table 2.3.14 presents a list of booster vacuum devices, together with those for linac and beam transport lines.

**Table 2.3.14 List of Vacuum Components for the Linac and Booster Vacuum Systems.**

	IP (30 l/s)	IP (200 l/s)	TCG	CCG	TMP	RGA	GV
E-gun	2	2	2	2	1	1	2
GtL		2	1	2	1		2
Linac		8	4	8	1	1	2
LtB	4		2	4	1		2
Booster	60	8	8	12	4	3	8
BtSR	6		1	2	1	1	2
Total	72	20	18	30	10	6	18

#### 2.3.7.4.2 Vacuum Controls

The vacuum control system will interface with vacuum devices while being part of the machine control. Due to the high radiation levels in the tunnel, all the vacuum devices will be located at the satellite control racks. These vacuum devices (such as gauge controllers, ion pump controllers, RGA, etc.), with local and remote capabilities, will communicate with the machine control system through RS232 or Ethernet links for remote monitoring, operation, and control. The low-level vacuum control will consist of dedicated vacuum programmable logic controllers. Each PLC has both digital and analog I/O modules with inputs from various vacuum devices, and provides the logic for the operation of the sector gate valves, the interlocks for other subsystem devices, and generation of the beam permits. For the gate valve control, a voting scheme with inputs from the setpoint contacts of several ion pumps will be used to initiate the interlock functions, therefore minimizing false triggering due to the failure of a single pump.

### 2.3.8 Booster PS

Since the booster system is foreseen as a turn-key procurement, power supplies will be design to match our requirements on the booster magnet lattice. Given that our magnet design is close to that at the existing ASP booster we expect that the dipole and quadrupole power supplies specifications will be close to that at the ASP (Table 2.3.15).

**Table 2.3.15 Preliminary specifications for the booster power supplies.**

Name	Number	Io, A	Vo, V
Dipole BF	1	900	220
Dipole BD	2	900	400
Quadrupole QD	1	100	50
Quadrupole QF	1	200	50
Quadrupole QG	1	100	50
Sextupole SXV	8	21	73
Sextupole SXH	8	18	45
Corrector	32	12	25

### 2.6.8.1 Power Supply Interlocks

All power supplies will have sufficient interlocks to prevent the power supply from damage due to changes in cooling conditions, AC power disturbances, and out-of-range setpoints. All magnet coils will have an over-temperature interlock if damage can occur due to a change in cooling or operating conditions. All power supplies will have an electrical safety interlock that will prevent the power system from turning on if the machine safety system requirements so warrant.

### 2.6.8.2 Electrical Safety

All power supplies will conform to the latest BNL safety requirements, especially concerning arc flash protection. Whenever possible, NRTL-listed equipment will be used.

### 2.6.8.3 Cable Tray

The cable tray for the magnet circuits will be located inside the main tunnel, on the ceiling. All cables will be tray-rated. Power cables will be arranged to minimize pickup from other circuits. All power cables will be separated from signal cables. All cables and trays will meet NEC requirements.

### 2.6.8.4 Power Supply Instrumentation

Redundant DCCTs or shunts will be used to confirm the power supply current reproducibility. High-precision DMMs and scanners will be used to monitor the power system current, the redundant current sensor, and the analog current setpoint. This equipment will ensure long-term stability and reproducibility. Temperature monitoring of the magnet coils and power system environment will be accomplished using low-cost digital temperature sensors. With such system, a problem can be identified before it becomes an emergency, making it possible for repairs to be scheduled more conveniently and economically.

### 2.6.8.5 Power Supply Controls

Each booster power supply circuit will require a Waveform Function Generator. These VME device cards will be located in a control system's VME chassis, mounted in one of the power supply system racks. The WFGs will generate the reference current profiles, input analog data, and perform digital state control and status readbacks. A timing system will be needed to synchronize all the WFGs. The output of the WFGs is connected via fiber optics to a Power Supply Interface. The PSI has a precision digital-to-analog converter for generating the reference current, and a multi-channel analog-to-digital converter for inputting power system signals. The PSI also has digital IO for state control and status readbacks of the power supply.

The other controls will include the operation of the high-precision DMM and scanner, and readout of the digital temperature sensors.

### 2.3.9 Injection System Service Building

In the following we briefly describe the injector service building layout (Figure 2.3.19). The service area will contain all injector equipment including that for the linac, transport lines, booster and the SR injection straight section. It will also include rooms for utility distribution system, workbenches and local control room.

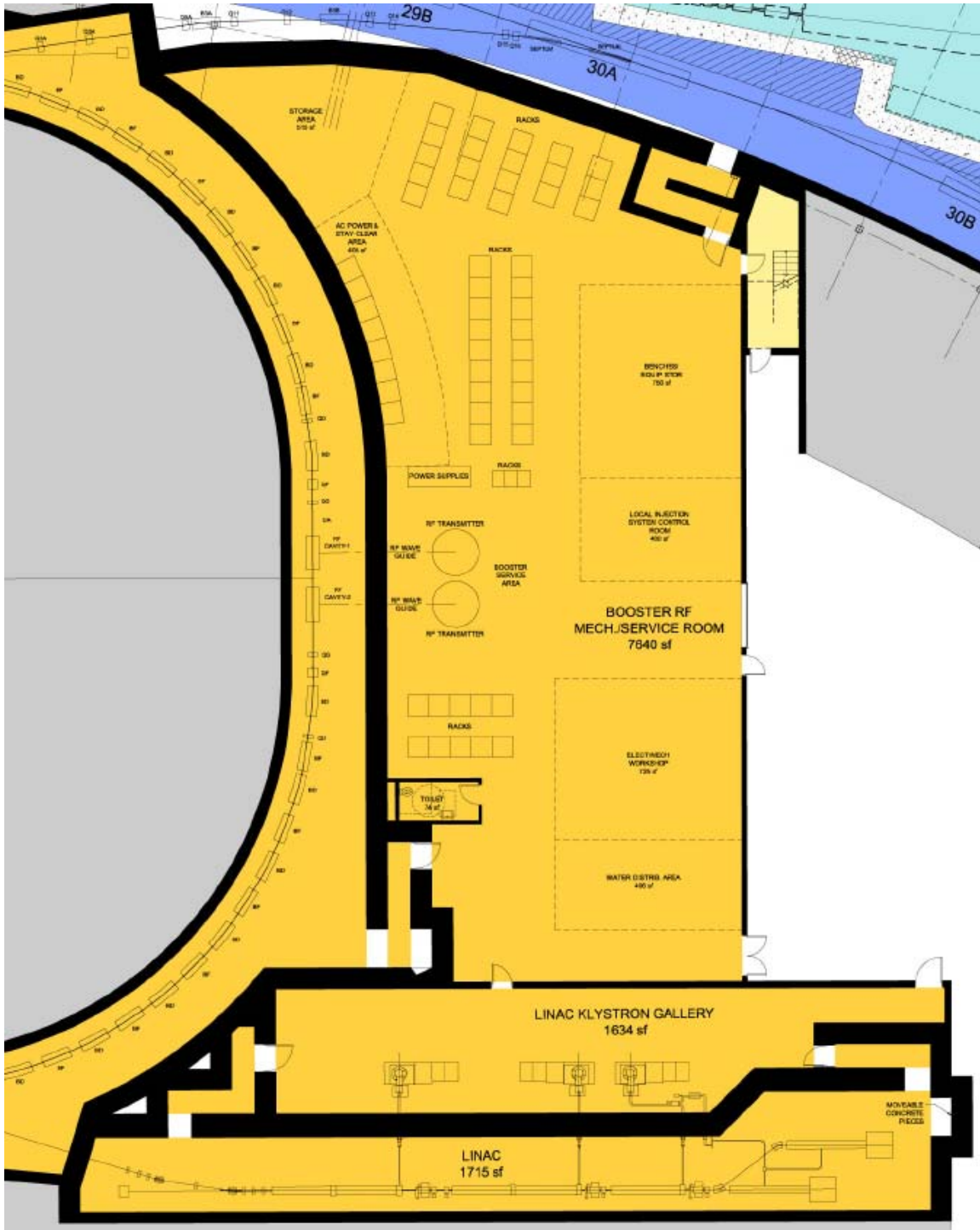


Figure 2.3.19 Layout of the injector service area

Service areas in the injector service building are listed below.

1. Booster service area

- three dipole power supplies
- three quadrupole power supplies
- two sextupole power supplies
- 40 corrector power supplies
- vacuum power supplies
- Injection Pulsed Magnets
- Extraction Pulsed Magnets (bumps, kicker and septum)
- Diagnostics: two racks

2. LbTL Service Area

Nine racks altogether

3. B-SR TL Service Area (all areas with power supplies, vacuum equipment and diagnostics)

- Storage ring injection system Area
- Timing System
- B-SR: ten racks altogether
- SRIS: four racks (bumps), three racks (septa)
- TS: two racks

4. AC power disconnects/ switch gear + stay-clear area  
eight panels + stay-clear area during switch operation

5. two entry labyrinths

7. bathroom

8. local Injection System Control Room

10. equipment storage area (spare parts and test instruments)

11. electronic/mechanical workshop

12. water and air distribution area (linac)

13. booster RF area

**Total for building**

**610m<sup>2</sup>**



### 2.3.10 Linac and Booster Utilities System

The cooling water for both the linac and booster ring will be provided from one of the Mechanical Equipment Rooms (MERs), whose process water system will be sized such that it will supply the necessary capacity for the linac and booster, as well as the MERs' respective copper and aluminum systems. The total heat load for this MER will be ~1.2 MW, with the linac requiring cooling for ~100 KW and the booster needing ~400 KW cooling capacity.

Both a supply and return pipe will originate from the MER and travel to both the linac and booster, at which point the necessary connection points will be supplied so as to allow their respective components to be connected to the process water. The process water will have the following thermal hydraulic parameters:

- supply (inlet) pressure ~ 120 psig
- supply (inlet) temperature ~80 F
- supply (inlet) temperature stability  $\pm 1^\circ\text{F}$
- The booster piping will be sized for ~212 gpm and the linac piping will be sized for ~53 gpm; this results from a temperature differential across the components of ~13°F.
- The water will be clean with a resistivity of ~ 1 MOhm-cm.

Compressed air is expected to serve only for a few applications, such as, powering the phosphor screens and will be discussed in details during the next stage of the design.

## References

- [asp] <http://ieeexplore.ieee.org/iel5/10603/33511/01591747.pdf?arnumber=1591747> asp
- [dia] <http://accelconf.web.cern.ch/AccelConf/e02/PAPERS/TUPRI097.pdf>
- [sol] <http://ieeexplore.ieee.org/iel5/10603/33511/01591041.pdf?arnumber=1591041>
- [sls] The SLS booster synchrotron, W. Joho, M. Muñoz and A. Streun, Nucl. Instrum. and Meth. A, Vol. 562-1, pp. 1-11
- [alb] <http://epaper.kek.jp/e06/PAPERS/THPLS057.PDF>
- [binp] <http://ieeexplore.ieee.org/iel5/10603/33511/01590651.pdf?arnumber=1590651>
- [Edd] M. Munoz and V. Joho, Eddy current effects in the SLS booster:  
<http://slsbd.psi.ch/pub/slsnotes/tmeta9810/eddy.html>
- [ite] <http://www.i-tech.si/products.php>
- [ber1] <http://www.bergoz.com/products/NPCT/PCT-downloads/files/NPCTflyer.pdf>
- [ber2] <http://www.bergoz.com/products/FCT/d-fct.html>
- [stca] <http://www.optronis.com/>

## 2.4 Transport Lines

### 2.4.1 Linac-to-Booster Transport Line

#### 2.4.1.1 Scope

The main function of the linac-to-booster (LtB) transfer line is to transport the 200MeV electron beam from the linac to the booster. A schematic diagram of the transport line in relation to the booster is shown in Figure 2.4.1.

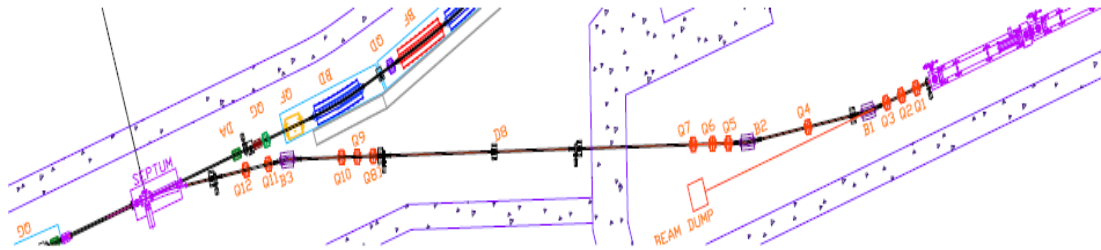


**Figure 2.4.1** Schematic diagram of the LtB beam transport line. The beamline starts at the exit of the linac (30 cm upstream of Q1 shown in the figure) and ends at the exit of the injection septum which is part of the booster synchrotron. A section of the booster is shown at the left side of the figure.

The LtB line is defined between the exit point of the 200MeV linac, located 30 cm upstream of Q1, as shown in Figure 2.4.1, and the “booster injection point,” located at the exit of the injection septum, shown also in same figure. The beamline has been partitioned into three sections, which are briefly discussed below.

- *The linac to achromatic section:* This section of the beamline transports the beam from the exit of the linac to the beginning of the “achromatic section.” It consists of four quadrupoles and two dipoles, which each bend the beam to the right by 150 mrad. The beam is achromatic at the exit of this section.
- *The achromatic section:* The transported beam in this section is achromatic, and consists of six quadrupoles.
- *The Injection-matching section:* This is the last section of the line, and matches the transported beam to the circulating beam of the booster at the injection point, which is located at the exit point of the septum (Figure 2.4.1). This section of the line consists of a “bend to the left” dipole of 150 mrad, the injection septum, which also is a 150mrad “bend to the left” dipole, and two quadrupoles.

#### 2.4.1.2 Beam Constraints along the LtB Line

The main beam constraints of the LtB line is to transport the extracted beam from the exit of the linac to the booster injection point, and match the beam parameters of the beam at the booster injection point to those of the circulating beam in the booster. The beam parameters [SOLL] at the linac’s exit and booster injection point are shown in Table 2.4.1. The values of vertical dispersion and angular dispersion functions at these two points are zero.

**Table 2.4.1** Beam Parameters at the Linac Exit Point and Booster Injection Point.

	$\alpha_x$	$\beta_x, \text{m}$	$\eta_x, \text{m}$	$\eta'_x$	$\alpha_y$	$\beta_y, \text{m}$
Linac exit point	-1.7	40.0	0.0	0.0	-1.7	40.0
Booster Injection point	7.212	8.027	-0.128	0.0	-0.523	3.043

The following additional constraints are also imposed on the LtB transport line.

- The maximum values of the horizontal and vertical beta function along the line should be less than 100 m ( $\beta_{x,y} < 100$  m). Similarly, the absolute values of the horizontal dispersion should be below 0.5 m ( $|\eta_x| < 0.5$  m) at any point along the line. This will make the size of the beam along the line compatible with the physical aperture of the line. The geometrical projected beam emittance is  $50\pi$  mm·mrad in both the horizontal and vertical directions.
- The “achromatic section” of the line is designed to provide an achromatic beam in both the horizontal and vertical directions. This section of the line will be used to characterize the transported beam by measuring its projected emittance and the beam parameters at any point upstream of this section. The beam characterization can be performed by utilizing the “nominal” settings of the quadrupoles that are used to transport the beam or by altering the settings of the quadrupoles.

### 2.4.1.3 Beam Optics of the LtB Beam Transport Line

The beam optics of the LtB line must satisfy the constraints mentioned earlier. The beam optics were calculated with the MAD computer code, Version 8b.

The calculated values of the beta functions ( $\beta_{x,y}$ ), and dispersion function ( $\eta_x$ ) are plotted in Figure 2.4.2. The horizontal and vertical beam envelopes that correspond to geometrical projected beam emittances  $\epsilon_x = 50\pi$  mm·mrad and  $\epsilon_y = 50\pi$  mm·mrad are plotted in Figure 2.4.3. The projected beam emittances  $\epsilon_x$  and  $\epsilon_y$  correspond to two standard deviation of the beam intensity.

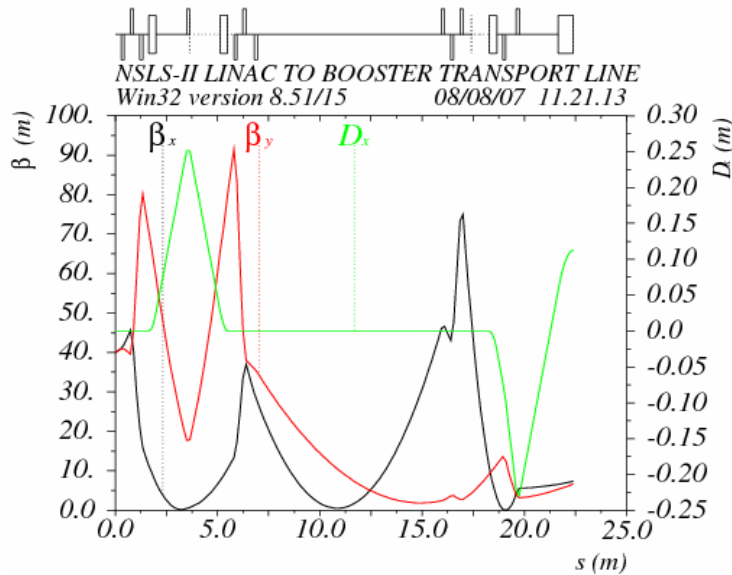


**Figure 2.4.2** The  $\beta_{x,y}$  (black and red lines) and  $\eta_x$  function (green line) at the beginning and the end of each magnetic element. The large black rectangles shown on the top of the figure represent the dipoles, and the thin black rectangles represent the quadrupoles.

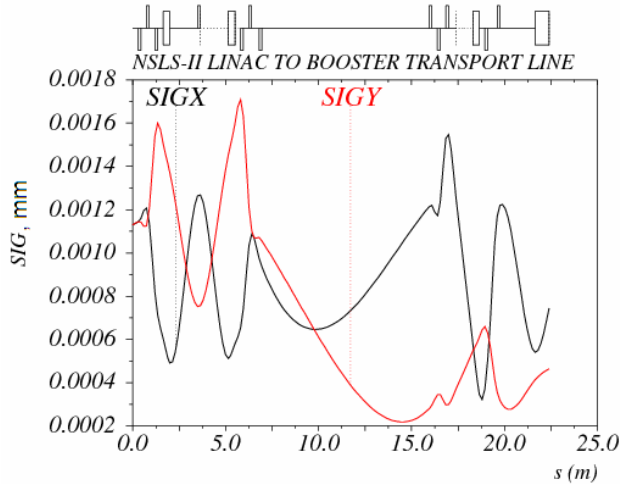


**Figure 2.4.3** Half of the horizontal and vertical beam envelopes (black and red lines) that correspond to  $2\sigma_{x,y}$  beam emittance. The black rectangles at the top of the figure represent the dipoles and the quadrupoles magnets.

#### 2.4.1.4 Magnetic elements of the LtB beam transport line

In this section we provide a table with the geometry (length, aperture) and the strength of the dipoles and quadrupoles of the LtB line. Table 2.4.2 shows all the main magnetic elements of the LtB line that are used to generate the line's first-order optics, discussed in the previous section. Each magnetic element has its own power supply.

**Table 2.4.2 Length, Aperture and Strength of the Main Magnetic Elements of the LtB Line.**

Element Name	Type	L [m]	Gap/Rad[cm]	Strength [rad] or [m <sup>-1</sup> ]	Power Supply
Q1	Quadrupole	0.150	2.0	-0.09548	P Q1
Q2	Quadrupole	0.150	2.0	1.02667	P Q2
Q3	Quadrupole	0.150	2.0	0.90802	P Q3
B1	Dipole	0.350	3.0	0.150	P B1
Q4	Quadrupole	0.150	2.0	1.17679	P Q5
B2	Dipole	0.350	3.0	0.150	P B2
Q5	Quadrupole	0.15	2.0	-1.04264	P Q5
Q6	Quadrupole	0.150	2.0	1.15803	P Q6
Q7	Quadrupole	0.150	2.0	-0.04559	P Q7
Q8	Quadrupole	0.150	2.0	0.32202	P Q8
Q9	Quadrupole	0.150	2.0	-0.95966	P Q9
Q10	Quadrupole	0.150	2.0	1.10812	P Q10
B3	Dipole	0.350	3.0	-0.150	P B3
Q11	Quadrupole	0.150	2.0	-1.09038	P Q11
Q12	Quadrupole	0.150	2.0	1.70708	P Q12
BUMP	Dipole	0.350	3.0	-0.150	P BUMP

#### 2.4.1.5 Linac-to-Booster Power Supplies

The LtB power supplies are connected to dipoles, quadrupoles, and vertical/horizontal correctors. The supplies will stay at the nominal setpoint only during the ring fill. For energy savings, it is anticipated that the supplies' output will be lowered during the dwell time in top-off mode and brought back to the operating point slightly before the fill cycle.

### 2.4.1.5.1 Power Supply Control

Each transfer line power supply will be set by its analog programming interface. Either a micro-controller or PLC could be used to control the supply. Analog output voltages from the control system will be used to control the current setpoint of the supply, and the digital-to-analog converter will have a resolution of at least 16 bits. Both supply output voltage and current will be read back by medium-speed analog-to-digital converters with a resolution of 16 bits. Monitoring of the supply outputs should be able to detect transients as short as 1 ms. Long-term monitoring of drift will be done by an independent external shunt connected to a high-precision analog channel.

### 2.4.1.5.2 Interlock

An external power distribution unit will be installed in each power supply rack and will contain a primary contactor that can be controlled remotely and independently. This contactor will be controlled by the Personnel Safety System and will be independent of the power supply controller. Each power supply will have its own circuit breaker and power receptacle. The breaker will be sized to withstand turn-on in-rush power and to limit steady-state current to the line cord rating.

### 2.4.1.6 Allowed Misalignment Error of the Magnetic Elements of the LtB Transport Line

The placement of the magnets along the LtB line is subject to misalignment errors: the transverse and longitudinal placement errors DX, DY, and DS; the angular placement errors about the transverse axes DPHI and DTHETA; and angular error about the longitudinal axes, DPSI.

The results of a study to determine the maximum allowed error of each geometrical misalignment appear in Table 2.4.3. In the study we assumed that any misalignment error should not generate transverse beam displacement larger than  $\pm 1.5$  mm nor measurable beam coupling effects.

Table 2.4.3 shows the upper limits of the allowed errors in the placement of the magnetic elements of the LtB line. The first three quantities DX, DY, and DS, correspond to the lateral and longitudinal position error. The last three quantities, DPHI, DTHETA, and DPSI, correspond to the rotation error about the transverse axes.

**Table 2.4.3 Upper Limits of the Allowed Error in the Placement of the Magnets.**

	DX [mm]	DY [mm]	DS [mm]	DPHI [mrad]	DTHETA [mrad]	DPSI [mrad]
Dipoles	$\pm 1.0$	$\pm 1.0$	$\pm 1.0$	$\pm 2.0$	$\pm 2.0$	$\pm 0.5$
Quadrupoles	$\pm 0.5$	$\pm 0.5$	$\pm 2.0$	$\pm 2.0$	$\pm 2.0$	$\pm 5.0$

### 2.4.1.7 LtB Transport Line Instrumentation and Diagnostics

The beam instrumentation that will be used for the commissioning and normal operation of the LtB line are the horizontal and vertical corrector dipole magnets (HC, VC), the beam position monitors (HBPM, VBPM), the Fluorescent screens (FS), the current transformer (CXF). The relative location of these devices along the LtB line is presented in Table 2.4.4. The first column contains the location of the beam instrumentation, which is identified in the second column.

**Table 2.4.4 Beam Instrumentation (Column 2) at Various Locations (Column 1) along the LtB Line.**

Location	Instrumentation	Comment
UpStrm of Q1 line	FS1, HC1, VC1, HBPM1, VBPM1	Fluor. Screen Retractable

DownStrm of Q4	FS2, HC2, VC2,	Fluor. Screen Retractable
DownStrm of Q7	FS3, HC3, VC3, HBPM2, VBPM2	Fluor. Screen Retractable
UpStrm Q8	FS4	Fluor. Screen Retractable
UpStrm B3	HC4, VC4	
DownStrm B3	HC5, VC5	
UpStrm BUMP	FS5, HC6, VC6, CXF, HBPM3, VBPM3	Fluor. Screen Retractable

Any deviations of the actual beam trajectory from the ideal trajectory due to magnet misalignment errors will be corrected with the six horizontal and six vertical dipole correctors.

The first dipole in the LtB achromatic bend is used to steer the beam either to the booster or emittance measurement setup and also serves as an energy spectrometer. Two fluorescent screens provide for coarse and fine (with switched-off achromatic quadrupole) measurements of energy spread. The beam dumps can include Faraday cups for charge measurement. With the first dipole switched off, the electron beam is directed to the emittance measurement system.

Two additional fluorescent screens after the second dipole of the achromatic bend will be used to measure electron beam size and position. The beam trajectory during normal operations is monitored by three pick-up electrodes equipped with Libera beam position monitors (BPM) [ber3, itc]. An integrating current transformer will measure the amount of charge passing through the transport line.

#### 2.4.1.8 Shielding

The radiological study of the NSLS-II building complex is documented in [shie]. In this study, three radiological enclosures separate the linac, the booster and the storage ring. The radiological enclosure that separates the linac from the booster partitions the LtB line into two sections. The partition of the LtB line by the radiological enclosure occurs at the straight section between quadrupoles Q7 and Q8, as shown in Figure 2.4.1. The wall thickness of the enclosure that separates the linac from the booster is sufficient to attenuate any radiation levels that can be produced by a fault condition in the linac enclosure, to radiation levels less than 2.5  $\mu\text{Sv/h}$  at the area of the booster enclosure.

It is therefore possible for personnel to occupy the booster area while the linac is operating, under the condition that the safety devices of the LtB line (see next section) are fully functioning and the critical devices of the LtB line have been LOTO'ed (Lock-out Tag-out).

#### 2.4.1.9 Linac-to-Booster Critical Devices

The linac-to-booster radiation transport will have two critical devices to stop the electron beam from entering the booster, to protect personnel from prompt radiation hazard in the booster area. This redundant pair of stops will consist of a shutter mechanism and a bending magnet.

The stop will be constructed of a block of material engineered to effectively stop all the radiation produced by the linac when the block is placed in the beam path. The stop will be redundantly monitored by the interlock system using two switches. The switches monitor the closed position of the shutter: one switch for chain A, and one for chain B. When in the closed position, the stop will block all radiation from entering the booster ring.

The bending magnet upstream of the stop will provide another safety function: when it is not powered, it allows the beam to follow a straight path into a beam dump area. This will prevent the electron beam from entering the booster tunnel area. When it is safe to allow beam in the booster area, the magnet will be powered and will bend the beam into the booster ring. The magnet will be redundantly monitored by the interlock system: for current by chain A, and voltage by chain B. In the event of the stop or bending magnet failing to reach a safe state when required to do so, the interlock system will reach back and shut off the linac and gun.

## 5.4.2 Booster-to-Storage Ring Transport Line

### 2.4.2.1 Scope

The main function of the booster-to-storage ring (BtS) transport line is to transport the 3GeV electron bunches from the booster to the storage ring (SR). A schematic diagram of the transport line, in relation to the booster and storage ring, is shown in Figure 2.4.4. The BtS line is defined between the “booster extraction point,” which is located at the entrance point of the “BR1” local beam-bump-dipole, and the “storage ring injection point,” which is located at the exit of the injection kicker “IS.” Both magnets, BR1 and S1, are shown in Figure 2.4.4.

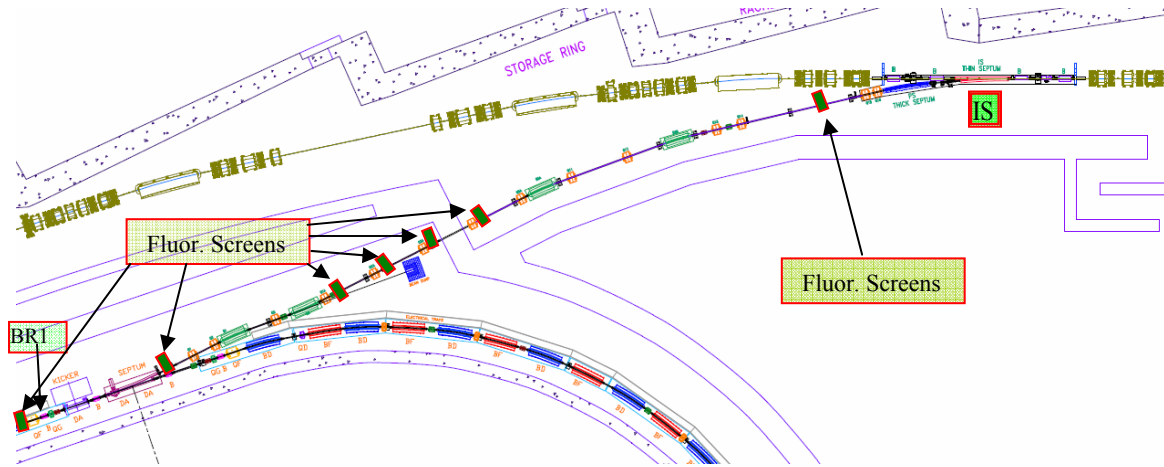


**Figure 2.4.4** Schematic diagram of the BtS beam transport line. The arc at the bottom of the figure is a section of the booster, and at the top of the picture the green elements are part of the storage ring. The dark green rectangles on the BtS line are the fluorescent screens/ visual flags (VF).

For reasons, of easing the optical design, the beamline has been partitioned into three sections, which are briefly discussed below.

- *The extraction section:* This section of the beamline contains, the extraction devices, (extraction bumps, and extraction kicker, and extraction septum), two dipoles of 120 mrad bend each, that both form a horizontal “dogleg”, and three quadrupoles. The two 120 mrad dipoles which form the horizontal “dogleg” and the three quadrupoles serve to generate an achromatic beam and also adjust the beam parameters, at the end of the extraction section.
- *The achromatic section:* This section of the beamline follows the extraction section, and consists of five quadrupoles. The transported beam in this section is achromatic. The secondary function of this section is to be used for measuring the projected beam emittance and the beam parameters, with the help of four visual flags installed along this section.
- *The injection section:* This is the last section of the line, and matches the transported beam to the circulating beam of the storage ring at the injection point which is located at the exit point of the Injection kicker SI. This section of the line consists of two “bend to the right” dipoles of 120 mrad each, the injection septum and the injection kicker, both bending to the right. It also includes six quadrupoles for the required beam matching at the injection point.

### 2.4.2.2 Beam Constraints along the BtS Line

The main beam constraints of the BtS line is to transport the extracted beam from the Booster to the Storage ring and match the beam parameters of the beam at the Injection point to those of the circulating beam. The beam parameters at the extraction and injection point are shown in Table 2.4.5. The values of vertical dispersion and angular dispersion functions of booster and storage ring lattices at these two points are zero therefore do not appear on the Table 2.4.5.

**Table 2.4.5 Beam Parameters at the Booster Extraction Point, and Storage Ring Injection Point.** The values of the vertical dispersion and angular dispersion functions of the booster and storage ring lattices at these two points are zero.

	$\alpha_x$	$\beta_x, \text{m}$	$\eta_x, \text{m}$	$\eta'_x$	$\alpha_y$	$\beta_y, \text{m}$
Booster extraction point	0.0	5.0	0.1	0.0	0.0	3.0
Storage ring injection point	0.0	5.0	0.0	0.0	0.0	3.0

The following additional constraints are also imposed on the BtS transport line.

- The maximum values of the horizontal and vertical beta function along the line should be less than 100 m ( $\beta_{x,y} < 100$  m). Similarly the absolute value of the horizontal dispersion function should be below 2 m ( $|\eta_x| < 2$  m) at any point along the line. This will make the size of the beam along the line compatible with the physical aperture of the line. The geometric projected beam emittance is  $27\pi$  nm-rad and  $3\pi$  nm-rad in the horizontal and vertical directions respectively.
- The “achromatic section” of the line is designed to provide an achromatic beam in both the horizontal and vertical directions. This section of the line will be used to characterize the transported beam by measuring its projected emittance and the beam parameters at any point upstream of this section. The beam characterization can be performed by utilizing the “Nominal” settings of the quadrupoles that are used to transport the beam or by altering the settings of the quadrupoles.

### 2.4.2.3 Beam Optics of the BtS Beam Transport Line

The beam optics of the BtS line must satisfy the constraints mentioned earlier. The beam optics was calculated with the MAD computer code, version 8b.

The calculated values of the beta functions ( $\beta_{x,y}$ ), and dispersion function ( $\eta_x$ ) are plotted in Figure 2.4.5. The horizontal and vertical beam envelopes that correspond to the geometric projected beam emittances  $\epsilon_x = 50\pi$  nm-rad and  $\epsilon_y = 3\pi$  nm-rad are plotted in Figure 2.4.6. The projected beam sizes correspond to one standard deviation of the beam intensity.



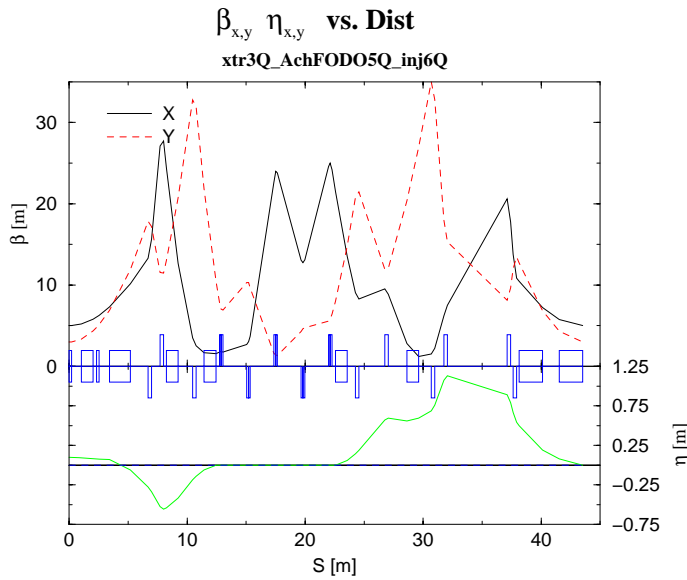


**Figure 2.4.5** The  $\beta_{x,y}$  (black and red lines) and  $\eta_x$  function (green line) at the beginning and the end of each magnetic element. The large blue rectangles represent the dipoles and the thin blue rectangles indicate the quadrupoles.

**X and Y 1 $\sigma$  Beam Envelope vs. Dist.**

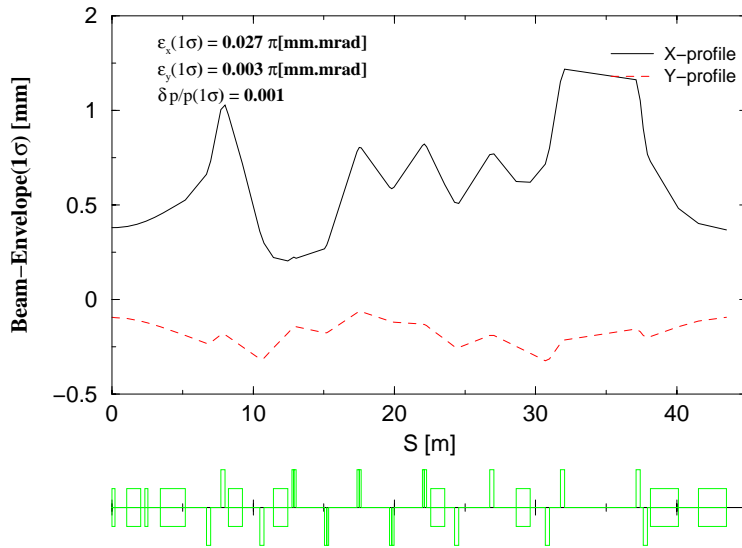


**Figure 2.4.6** Half of the horizontal and vertical beam envelopes (black and red lines) that corresponds to  $1\sigma_{x,y}$  beam emittance. The green rectangles at the bottom of the figure represent the dipoles and the quadrupoles.

**2.4.2.4 Magnetic Elements of the BtS Transport Line**

In this section we provide a table with the geometry (length, aperture) and the strength of the dipoles and quadrupoles of the BtS line. Table 2.4.6 shows all the main magnetic elements of the BtS line that are used to generate the line’s first order optics which is discussed in the previous section. Each magnetic element has its own power supply except the B3I and B4I dipoles which are connected in series with a single power supply.

**Table 2.4.6 Length, Aperture and Strength of the Main Magnetic Elements of BtS Line.**

Element Name	Type	L [m]	Gap/Rad[cm]	Strength [rad] or [m <sup>-1</sup> ]	Power Supply
BR1X	Dipole	0.200	3.0	-0.080	P BR1X

KIX	Dipole	1.000	3.0	-0.005	P KIX
BR2X	Dipole	0.200	3.0	0.080	P BR2X
ESX	Dipole	1.750	3.0	-0.140	P ESX
Q1X	Quadrupole	0.300	2.0	-0.372582	P Q1X
Q2X	Quadrupole	0.300	2.0	0.5835372	P Q2X
B1X	Dipole	1.000	3.0	0.120	P B1X
Q3X	Quadrupole	0.300	2.0	-0.4201152	P Q3X
B2X	Dipole	1.000	3.0	-0.120	P B2X
Q1A	Quadrupole	0.300	2.0	0.6153693	P Q1A
Q2A	Quadrupole	0.300	2.0	-0.4201239	P Q2A
Q3A	Quadrupole	0.300	2.0	0.4269711	P Q3A
Q4A	Quadrupole	0.300	2.0	-0.350637	P Q4A
Q5A	Quadrupole	0.300	2.0	0.3244197	P Q5A
B3I	Dipole	1.000	3.0	0.120	P BI
Q1I	Quadrupole	0.300	2.0	-0.3434886	P Q1X
Q2I	Quadrupole	0.300	2.0	0.3373026	P Q2X
B4I	Dipole	1.000	3.0	0.120	P BI
Q3I	Quadrupole	0.300	2.0	-0.4447095	P Q3X
Q4I	Quadrupole	0.300	2.0	0.4081164	P Q4X
Q5I	Quadrupole	0.300	2.0	0.6599952	P Q5X
Q6I	Quadrupole	0.300	2.0	-0.6455421	P Q6X
PSI	Dipole	2.0	3.0	0.150	P PSI
ISI	Dipole	2.0	3.0	0.080	P ISI

### 2.4.2.5 Booster-to-Storage Ring Transport Line Power Supplies

The BtSR power supplies are connected to dipoles, quadrupoles, and vertical/horizontal correctors. The supplies will be operated around a static operating point, eliminating the need for significant voltage head room. For energy savings, we anticipate that the supply's output will be lowered during the dwell time in top-off mode and brought back to the operating point slightly before the top-off cycle. Unmodified commercial power supplies are currently used at NSLS in its transfer lines and are analog programmed by 14-bit digital-to-analog converters. The supplies are operated in current mode with shunt feedbacks.

#### 2.4.2.5.1 Power Supply Control

Each transfer line power supply will be set by its analog programming interface. Either a micro-controller or PLC could be used to control the supply. Analog output voltages from the control system will be used to control the current setpoint of the supply, and the digital-to-analog converter will have a resolution of at least 16 bits. Both supply output voltage and current will be read back by medium-speed analog-to-digital converters with a resolution of 16 bits. Monitoring of the supply outputs should be able to detect transients as short as 1 ms. Long-term monitoring of drift will be done by an independent external shunt connected to a high-precision analog channel.

#### 2.4.2.5.2 Interlock

An external power distribution unit will be installed in each power supply rack and will contain a primary contactor that can be controlled remotely and independently. This contactor will be controlled by the personal safety system and will be independent of the power supply controller. Each power supply will have its own circuit

breaker and power receptacle. The breaker will be sized to withstand turn-on in-rush power and to limit steady-state current to the line cord rating.

#### 2.4.2.6 Misalignment Error of the Magnetic Elements of the BtS Transport Line

The placement of the magnets along the BtS line is subject to misalignment errors, which are the transverse and longitudinal placement errors  $DX$ ,  $DY$ , and  $DS$ ; the angular placement errors about the transverse axes,  $DPHI$  and  $DTHETA$ ; and angular error about the longitudinal axes,  $DPSI$ .

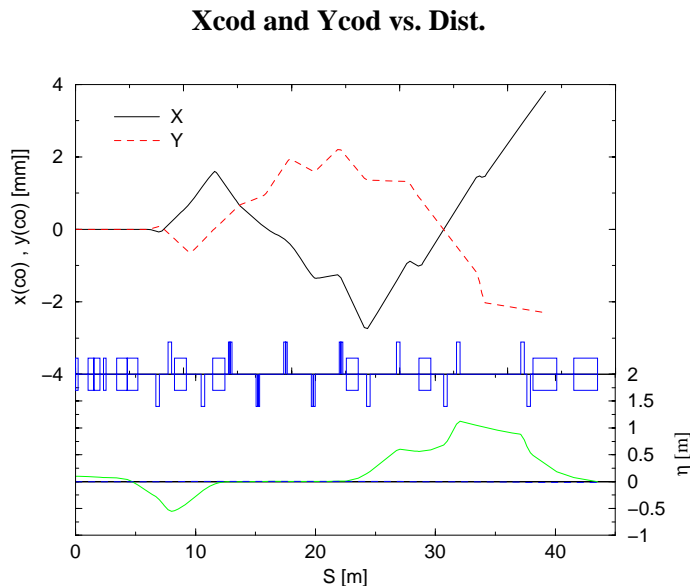
The results of a study to determine the maximum allowed error of each geometrical misalignment appear in Table 2.4.7. In the study we assumed that any misalignment error should not generate transverse beam displacement larger than  $\pm 1.5$  mm.

Table 2.4.7 shows the upper limits of the allowed errors in the placement of the magnetic elements of the BtS line. The first three quantities  $DX$ ,  $DY$ , and  $DS$ , correspond to the lateral and longitudinal position error, and the last three quantities,  $DPHI$ ,  $DTHETA$ , and  $DPSI$ , to the rotation error about the transverse axes (columns 5 and 6) and the longitudinal axis, (column 7).

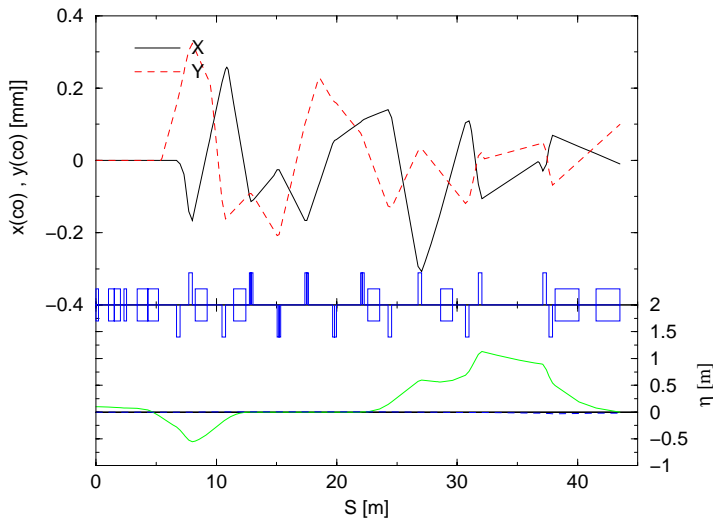
**Table 2.4.7 The Upper Limits of the Allowed Error in the Placement of the Magnets.**

	$DX$ [mm]	$DY$ [mm]	$DS$ [mm]	$DPHI$ [mrad]	$DTHETA$ [mrad]	$DPSI$ [mrad]
Dipoles	$\pm 1.0$	$\pm 1.0$	$\pm 1.0$	$\pm 2.0$	$\pm 2.0$	$\pm 1.0$
Quadrupoles	$\pm 0.5$	$\pm 0.5$	$\pm 2.0$	$\pm 2.0$	$\pm 2.0$	$\pm 5.0$

Next, we give an example of how the corrector dipoles can be used to minimize the transverse beam displacement caused by random misalignments of the quadrupoles. Figure 2.4.7 shows the horizontal (black line) and vertical (red dashed line) displacements of the beam due to random misalignments of the quadrupoles. The possible misalignments of the quadrupoles are shown in Table 2.4.7 (columns 2 to 7), and the maximum value of each random misalignment is taken from the third row of Table 2.4.7. Figure 2.4.8 is similar to Figure 2.4.7, but with the corrector magnets excited, to minimize the horizontal and vertical displacements of the beam along the BtS line.



**Figure 2.4.7** The X (black line) and Y (red dashed line) beam displacements along the BtS line caused by random misalignments of the quadrupoles. The possible misalignments are shown in Table 2.4.8 (columns 2 to 7) and the maximum value of a particular random misalignment is shown in the third row of Table 2.4.8.

**Xcod and Ycod vs. Dist.**

**Figure 2.4.8** Same as Figure 2.4.7 but the X (black line) and Y (red dashed line) beam displacements along the BtS line are minimized by the use of the horizontal and vertical correctors.

#### 2.4.2.7 BtS Transport Line Instrumentation and Diagnostics

The beam instrumentation that will be used for the commissioning and normal operation of the BtS line includes the horizontal and vertical corrector dipole magnets (HC, VC), the beam position monitors (HBPM, VBPM), the visual flags (VF), and the current transformer (CXF). The relative locations of these devices along the BtS line are presented in Table 2.4.8. The first column contains the location of the beam instrumentation, which is identified in the second column.

**Table 2.4.8 Beam Instrumentation (Column 2) at Various Locations (Column 1) along the BtS Line.**

Location	Instrumentation	Comments
Downstream of Extraction Septum	VF2, VC1, HBPM1, VBPM1	Visual Flag Retractable
Downstream of Q1X	HC1	
Downstream of B1X dipole	VC2, HBPM2, VBPM2	
Downstream of Q3X	HC2	
Downstream of Q1A	VF3, HC3, HBPM3, VBPM3	Visual Flag Retractable
Downstream of Q2A	VF4	Visual Flag Retractable
Downstream of Q3A	VF5, VC3	Visual Flag Retractable
Downstream of Q4A	VF6	Visual Flag Retractable
Downstream of Q5A	HBPM4, VBPM4	
Downstream of Q2I	HC4, HBPM5, VBPM5	
Downstream of Q3I	HC5, HBPM5, VBPM5	
Downstream of Q4I	VC5	
Upstream of Q5I	VF7, HC6, VC6, HBPM6, VBPM6, CXF	Visual Flag Retractable

Six fluorescent screens (VF), accompanied by six RF beam position monitors, will be used to measure the beam position and size. We plan to use Libera BPM receivers, which have up to 1 micrometer resolution in the single-shot mode, for processing signals from the pick-up electrodes. An integrating current transformer will be used for monitoring the injected bunch charge and injection efficiency. We are considering the possibility of installing two gated cameras with external triggers for observing the electron beam with radiation from the bending magnet.

#### 2.4.2.8 Shielding

The radiological study of the NSLS-II building complex is documented in [shie]. In this study, three radiological enclosures separate the linac, the booster, and the storage ring. The radiological enclosure that separates the booster from the storage ring partitions the StR line into two sections. The partition of the BtS line by the radiological enclosure occurs at the straight section between quadrupoles Q3A and Q4A, as shown in Figure 2.4.1. The wall thickness of the enclosure that separates the booster from the storage ring is sufficient to attenuate any radiation levels that can be produced by a fault condition in the booster enclosure, to radiation levels less than 2.5  $\mu\text{Sv/h}$  at the storage ring enclosure.

It is therefore possible for personnel to occupy the storage ring area while the booster is operating, under the condition that the safety devices of the BtS line (see next section) are fully functioning and the critical devices of the BtS line have been LOTO'ed.

#### 2.4.2.9 Booster-to-Storage Ring Critical Devices

The BtSR radiation transport will have two critical devices to stop the electron beam from entering the storage ring. These two devices will protect personnel from prompt radiation hazard in the storage ring area. This redundant pair of stops will consist of a shutter mechanism and a bending magnet.

The stop will be constructed of a block of material engineered to effectively block all the radiation produced by the booster when the block is placed in the beam path. The stop will be redundantly monitored by the interlock system using two switches that monitor the closed position of the shutter: one switch for chain A and one for chain B. When in the closed position, the stop will block all radiation from entering the storage ring.

The bending magnet upstream of the stop will provide another safety function: when it is not powered, the beam will follow a straight path to a beam dump area. This will prevent the electron beam from entering the storage ring tunnel area. When it is safe to allow beam in the storage ring area the magnet will be powered and will bend the beam into the storage ring. The magnet will be redundantly monitored by the interlock system—for current by chain A, and voltage by chain B. In the event of the stop or bending magnet failing to reach a safe state when required to do so, the interlock system will reach back and shut off the booster RF, linac, and gun.

## References

- [SOLL] <http://ieeexplore.ieee.org/Xplore/login.jsp?url=/iel5/10603/33511/01590552.pdf?arnumber=1590552>  
[ber3] [http://www.gmw.com/beam\\_diagnostics/Bergoz/bpm/pdf/GMW-DS-BPM-UHV-50\\_B.pdf](http://www.gmw.com/beam_diagnostics/Bergoz/bpm/pdf/GMW-DS-BPM-UHV-50_B.pdf)  
[shie] Technical Note “Preliminary Radiological Considerations for the Design and Operation of NSLS II Accelerator Enclosures” by P.K. Job and W.R. Casey  
[sls2] <http://slsbd.psi.ch/pub/slsnotes/sls1697>

## 2.5 Storage Ring Injection Straight Section

### 2.5.1 Scope

The injection straight is situated in one of the “long” straight sections of the storage ring. The total straight section length is 9.3 m long from steel to steel from the adjacent magnetic elements. The injection scheme is to displace the circulating orbit a distance of 15 mm toward the septum magnet (which at its closest approach to the beam is 17 mm away from the normal closed orbit), using two pulsed orbit bump magnets, followed by two identical bumps to place the circulating beam plus the injected bunches back on the normal orbit. Ideally, if all the bumps are identical, if the current pulses are all alike, if the pulse timing is perfect and if the survey to place the magnets is perfect, this procedure should be invisible to the users except for the halo of injected electrons (horizontally) which damps down with a time constant of a few tens of milliseconds. A slightly less than ideal but still acceptable condition is when the residual orbit disturbance is below the resolution capability of the user optics and experimental apparatus. An estimate of the required precision in alignment and operation of the injection magnets was done for the SLS by C.H. Gough and A. Streun [sls2].

Some methods that may be able to compensate for the errors in alignment, variation of magnetic fields of the kickers due to magnetic material differences, excessive stray field of the injection septum are under consideration.

### 2.5.2 Ring injection straight section layout

At present there are commercially available pulsed magnets with their power supplies that could be procured as a turn-key system. Outsourcing of pulsed magnets is a viable option, which, together with designing and building pulsed systems in-house, received careful consideration during preliminary design. Below we discuss parameters and performance of feasible injection straight components that can be developed using either option. Their feasibility is confirmed by comparison with kickers and septa of other light sources.

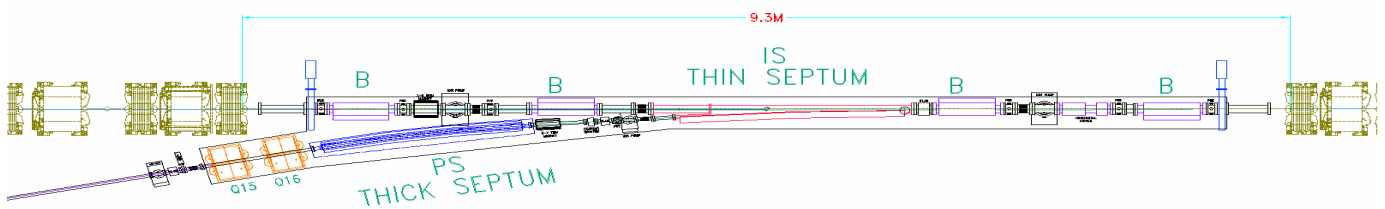


Figure 2.5.1 Injection straight layout.

The pulsed magnets contained in the injection straight are outlined in Table 2.5.1 below. These are the basic specifications required. The revolution time of the electrons in NSLS-II is 5.2  $\mu\text{sec}$ , so with this configuration, the injection takes place in one turn. It is planned to inject no more than 150 bunches at one time, a train 300 nsec long. This is easily done with a 5  $\mu\text{sec}$  long half sine wave pulse. However since the fractional tune for the ring is  $\sim 0.3$ , longer bump pulses (in units of ring revolution period) may be used, lessening the voltage requirements for the magnets and reducing the stringent timing requirements, one of the more important causes of residual beam motion caused by the injection transient. However, in this case, the beam will make several passes through the possibly not quite closed injection bump system. This may cancel some errors and lead to lower beam disturbance or it may aggravate the errors. Further studies are necessary; at this point a 5  $\mu\text{sec}$ -long orbit bump is the baseline.

**Table 2.5.1 Ring Injection System pulsed magnet parameters.**

	Injection Septum	Thick Septum	Injection Bump
Magnetic field [T]	0.4	0.833	0.165
Length [m]	2.0	1.8	0.5
H x V [mm x mm]	20 x 15	20 x 15	60 x 23
Bend angle [mR]	80	150	8.25
Inductance [ $\mu$ H]	3.5	3.02	1.64
Peak current [A]	5,000	10,000	3.15
Drive capacitor [ $\mu$ F]	18.9	84.1	1.55
Voltage [kV]	2.1	1.9	3.1
Pulse shape	50 $\mu$ sec full sine	100 $\mu$ sec full sine	5 $\mu$ sec half sine
Magnetic material	CMD5005 or $\frac{1}{4}$ mm Si steel	$\frac{1}{4}$ mm Si steel laminate	CMD5005
Ceramic chamber coat	N/A	N/A	0.5 $\Omega$ / $\square$

### 2.5.3 Residual Orbit Jitter

The stringent performance and alignment and positioning parameters of the injection components of the NSLS-II synchrotron were alluded to above. Preliminary analysis of the required parameters showed very tight tolerances in placement of the orbit bumps not only in pitch and yaw and especially in roll (which produces vertical orbit distortions) but also in transverse placement and even longitudinal position. Inhomogeneities in the magnetic material used for the orbit bumps contribute magnetic field errors. Temperature changes alter the permeability of the ferrite in unpredictable ways.

Correcting coils, orbit measurement-based feed-forward of voltages on the charge capacitors and stringent control of bump timing will be imperative. Correction trims and auxiliary windings on beam bumps will most likely be necessary and extreme care must be taken in mechanical manufacturing of bump magnetic structures, ceramic chamber coating and support structures. High resolution survey during installation and accurate placement of components will be required.

To be able to attack the residual beam oscillation problem, several capabilities should be built into the injection straight section. Provisions should be made for four dedicated correction trim bumps, up to six places for precision orbit position monitors in the straight section itself and especially at the downstream end where the orbit disturbance both in position and angle must be reduced to zero, and for winding small correction coils on the bumps to possibly compensate for unwanted field components.

The correction kickers or correction coils should be driven with current pulses that exactly mimic the drive pulses of the main bumps, possibly using operational current amplifiers controlled by signals derived from the current pulses in the main magnets. Response matrices for the correctors have to be determined and algorithms to reduce the orbit errors of the circulating beam to zero at the output of the injection straight need to be developed.

The important part is that as much of this work as possible should be done on the assembled girder before installation; For these reasons, a laboratory and electronics shop dedicated to the pulsed magnets is needed to not only verify the performance of any manufactured pulsed magnets, but also to ascertain the optimum design of these devices.

The following activities regarding pulsed magnets of the NSLS-II need to be performed so that the injection system component design and specifications can be determined and verified and further to ultimately determine performance parameters and acceptance testing of delivered components, no matter where they are manufactured:

1. Prototyping of kickers and septa for verification of pulsed magnet current, voltage, pulse length to achieve required parameters.
2. Determination of optimum (lowest inductance) pulsed magnet driver configuration.
3. Evaluation and testing of ferrite magnetic properties (permeability, loss factor, electrical conductivity).
4. Risetime, pulse shape/flat-top design verification of booster injection and extraction kicker magnets.
5. Elimination of causes of timing jitter and other noise in magnet current and field pulses.
6. Testing and evaluation of uniformity of conductive coating on inside of ceramic chambers for kicker magnets.
7. Measurement and acceptance testing of pulsed magnets received from vendor before installation in accelerators.
8. Tuning of the main ring injection straight section as a unit and setting up corrector bumps pulse shapes for minimum disturbance of circulating beam.
9. Measurements and compensation of fringing fields from pulsed components placed closely to the main ring circulating beam.
10. Training of technical staff for future upgrades and servicing of pulsed magnet systems.
11. Test bed for novel ideas in pulsed magnet technology.

The final adjustments would occur during commissioning with the actual beam, and time stability for feed-forward systems will be established.

Proposed possible correction kicker configurations are shown in Table 2.5.2 below. It is possible to wind horizontal and vertical correction windings on the same ferrite yoke, necessitating only two additional ceramic chambers in the injection straight.

**Table 2.5.2 Kicker parameters for proposed correction scheme.**

	Horizontal Correction Kicker	Vertical Correction Kicker
Magnetic Field [T]	0.04	0.04
Length [m]	0.2	0.2
H x V [mm x mm]	60 x 23	30 x 60
Bend angle [mR]	1	1
Inductance [ $\mu$ H]	0.656	0.126
Peak Current [A]	<750	1900
Drive Capacitor [ $\mu$ F]	3.86	20
Voltage [kV]	0.31	0.15
Pulse Shape	5 $\mu$ sec half sine	5 $\mu$ sec half sine
Magnetic Material	CMD5005	CMD5005
Ceramic chamber Coat	0.5 $\Omega$ /Ti	0.5 $\Omega$ /Ti



The capacitor banks for all magnets in the ring injection straight should have at least 16-bit voltage resolution and if it is feasible to use longer excitation pulses, all kickers could be driven in series due to lower voltage requirements and the pulse transmission time through the kicker string becomes a negligible fraction of the kicker system pulse length.

## References

[s1s2] <http://s1sbd.psi.ch/pub/s1snotes/s1s1697>.

## 3 LATTICE AND ACCELERATOR PHYSICS

### 3.1 Lattice and Beam Dynamics

The storage ring lattice is designed to provide a stable, closed orbit on which the electron beam can circulate with long lifetime and efficient injection of beam from the booster. This injection will be capable of filling the ring from zero beam current to the operating values ( $\leq 500$  mA) in a short time, as well as to provide top-off injection to maintain a constant level of beam current ( $< \pm 0.5\%$  variations) and thus provide a constant radiated beam power on the users' beamline components, with low thermal distortions.

The electron beam will be damped by the synchrotron radiation to a small beam emittance lower than that of any storage ring light source currently operating or under construction. The photon beams radiated from undulators will, therefore, have lower emittance and higher brilliance, surpassing any existing light sources in the 2 to 10 keV range in focused beam flux on small specimens.

#### 3.1.1 Physics and Design Goals for the Storage Ring Lattice

The design of the NSLS-II storage ring is driven by goals required to achieve the baseline performance as well as challenge goals that will provide the potential for future upgrades of beam performance. The challenge goals will keep NSLS-II at the frontier of the field for an extended time. Table 3.1.1 lists the required and challenge goals.

**Table 3.1.1 Goals for the NSLS-II Design.**

Beam Property	Required Goal	Challenge Goal
Ultra low horizontal emittance [nm-rad]	$\leq 1.5$ (achromatic)	$\leq 0.5$
Vertical emittance [nm-rad]	0.010	0.008
Stored currents [mA]	500	750
Straights for insertion devices	$\geq 21$	27
Low dispersion space for Three Pole Wigglers	$\geq 15$	$\geq 15$
Electron beam stability [ % of beam size]	10	$< 5$
Top-off injection current stability ( $\Delta t \geq 2$ min) [%]	$< 1$	$< 1$

Several lattices have been studied over the past few years. As work progressed, it became clear that the Double Bend Achromatic lattice could meet the emittance goals while providing an increased number of insertion device straight sections. To achieve our low emittance goals, we maintain achromatic arcs and install damping wigglers in the extra ID straight sections to enhance the SR power without significantly increasing the quantum excitation of the electron beam [3.1.1]. This process yields a net reduction of the beam emittance proportionally related to the ratio of dipole-radiated power to the DW-radiated power, reducing the beam emittance up to five-fold without significantly impacting the dynamic aperture performance of the ring.

The minimum emittance for a DBA lattice with 2M dipole magnets and electron energy  $E_0 = \gamma mc^2$  is given by

$$\varepsilon_0^{\min} = (7.7 \times 10^{-4} \text{ nm-rad}) \gamma^2 / M^3. \quad (3.1-1)$$

The achievable emittance for a realistic lattice design is about twice this minimum value. The momentum compaction is

$$\alpha = \frac{\pi^2}{6M^2} \frac{2\pi \rho_0}{C}, \quad (3.1-2)$$

where  $\rho_0$  is the dipole magnet bending radius and  $C$  is the ring circumference. Note that the momentum compaction increases linearly with bend radius.

The emittance  $\varepsilon_w$  with damping wigglers is related to that without damping wigglers,  $\varepsilon_0$ , by  $\varepsilon_w \approx \varepsilon_0 / (1 + U_w / U_0)$ , where  $U_w / U_0$  is the ratio of the energy lost per turn in the wigglers to that lost in the dipoles. For NSLS-II, we chose to have a large dipole bending radius. This reduces the energy radiated in the dipoles, which means we need to radiate less energy in the wigglers to reduce the emittance by a given factor.

To be more precise, consider a wiggler of length  $L_w$  having bending radius  $\rho_w$  and period  $\lambda_w$  centered in the insertion section. The ratio of the fractional energy spread with the wiggler to that without is

$$\frac{\delta_w}{\delta_0} = \sqrt{\left[ 1 + \frac{L_w}{2\pi \rho_0} \frac{4}{3\pi} \left( \frac{\rho_0}{\rho_w} \right)^3 \right] \left[ 1 + \frac{L_w}{4\pi \rho_0} \left( \frac{\rho_0}{\rho_w} \right)^2 \right]^{-1}}, \quad (3.1-3)$$

and the ratio of the emittance with the wiggler to that without is

$$\frac{\varepsilon_w}{\varepsilon_0} = \frac{1 + f}{1 + \frac{L_w}{4\pi \rho_0} \left( \frac{\rho_0}{\rho_w} \right)^2}. \quad (3.1-4)$$

The fluctuation factor,  $f$ , is given by

$$f = \frac{2C_q \gamma^2}{3\pi^2 \varepsilon_0} \frac{L_w \rho_0}{\rho_w^3} \left[ \frac{K_w^2}{5\gamma^2} \langle \beta_x \rangle + \frac{\eta_0^2}{\beta_{x0}} + \beta_{x0} \eta_1^2 \right], \quad (3.1-5)$$

where  $C_q = 3.84 \times 10^{-13} m$ , and strength parameter  $K_w = \lambda_w \gamma / 2\pi \rho_w$ . The horizontal beta function is given by  $\beta_x(s) = \beta_{x0} + s^2 / \beta_{x0}$ , where  $s = 0$  is the center of the wiggler and insertion, and  $\langle \beta_x \rangle$  denotes the average value of  $\beta_x$  in the wiggler. We express the dispersion function in the wiggler in the form  $\eta(s) = \eta_w(s) + \eta_0 + \eta_1 s$ , where  $\eta_w(s)$  is the sinusoidal dispersion generated by the wiggler itself, and  $\eta_0 + \eta_1 s$  is the dispersion generated by errors elsewhere in the ring. Eq. (3.1-5) can be used to determine a tolerance on the dispersion in the insertions arising from errors.

As at ESRF, the NSLS-II lattice has alternating high and low horizontal beta function straight sections for insertion devices. A large value of  $\beta_x$  is desired at the injection septum. Small  $\beta_x$  is desired in undulators for beamlines designed to focus the radiation down to a small spot. The vertical beta function should be small in undulators to optimize brightness. In fact, it is essential that  $\beta_y$  not be large in any of the insertion devices. The linear tune shift produced by an undulator or wiggler is

$$\Delta \nu_y = \frac{\langle \beta_y \rangle L_w}{8\pi\rho_w^2}. \quad (3.1-6)$$

Small  $\beta_y$  keeps the tune shift within acceptable limits. We have bounded the straight sections with quadrupole triplets in order to provide a local correction for the modification of the betatron functions and phases due to undulator or wiggler focusing.

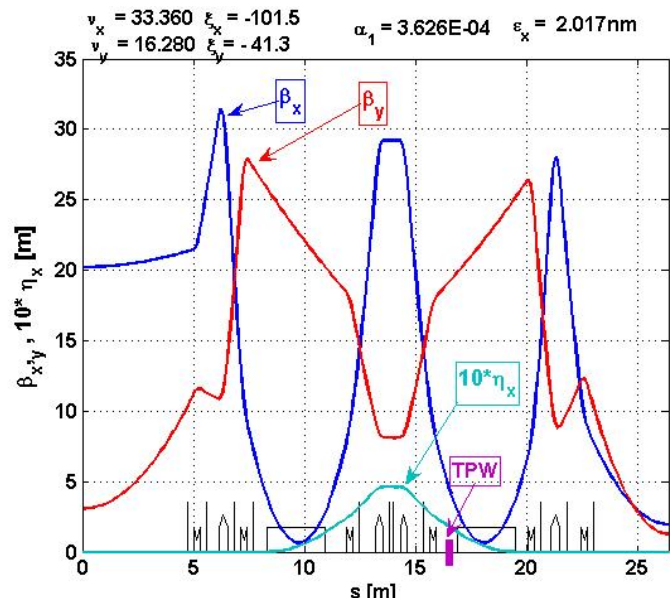
The tune shift with amplitude due to nonlinear undulator or wiggler focusing is

$$\frac{d\nu_y}{dJ} = \frac{\pi \langle \beta_y^2 \rangle L_w}{4\lambda_w^2 \rho_w^2}. \quad (3.1-7)$$

To minimize the effect of the nonlinear focusing on dynamic aperture, it is essential to have small  $\beta_y$  in the insertion devices.

This is the approach taken for NSLS-II [3.1.2]. A DBA with 30 cells was chosen as the lattice structure, with a natural emittance of 2.0 nm. One cell of the lattice, shown in Figure 3.1.1, comprises half a super-period with reflection symmetry about the right or left hand end of the cell. The lattice functions have been optimized to achieve achromatic arcs, low emittance and modest chromatic sextupole strengths, small Closed Orbit Amplification Factors, and desired betatron functions in the long and short straight sections, which are required for small impact on the DA of the IDs, as given by Eq. (3.1-6 and 3.1-7). The working point tune was selected for optimization of the sextupole correction of the nonlinear driving terms that limit the DA, as well as reduced COAF and instability sensitivity. The dipole magnets have been optimized (bend radius  $\rho_0 = 25$  m,  $B_0 = 0.399$  T at 3 GeV) to enhance the reduction of the beam emittance with the DWs. Although the bare lattice doesn't quite meet the required emittance goal (2.0 nm instead of 1.5 nm), this goal is exceeded with only one 7 m DW installed and operated at a peak field of 1.8 T.

**Figure 3.1.1** The lattice functions for one-half of a DBA period. A super-period consists of this cell reflected about either ID center: 9.3 m on the left-hand side or 6.6 m on the right.



The impact of DWs on the emittance and the energy spread, given by Eq. (3.1-3 and 3.1-4), is shown in Figure 3.1.2 for the designed  $\rho_0 = 25$  m and a stronger dipole with 1.5 times the field ( $2/3$  the bend radius). This calculation also assumes no significant spurious dispersion in the straight section, since the individual quadrupole powering in this lattice should allow the dispersion to be corrected cell-by-cell for any dipole variations. The gain in undulator brightness resulting from the smaller emittance provided by more damping

wigglers is somewhat reduced by the increased energy spread of the beam, especially at x-ray energies corresponding to higher harmonics of the undulator. Increasing the bend radius from 16.68 m to 25 m reduces both the emittance as well as the energy spread. Continuing to increase the bend radius to larger values is increasingly less effective at reducing the emittance as it approaches the IBS limit, and at the same time increasingly expensive, as it increases the circumference of the ring. As discussed in Chapter 5, a bend radius of 25 m is about optimal for NSLS-II. The installed RF power also provides a practical limit to the gain from more damping wigglers, since the beam lifetime will be reduced if the radiated power exceeds the installed power necessary for sufficient RF bucket height.

**Figure 3.1.2** The fractional reduction of the ring emittance and the increase in energy spread for dipole magnets of bend radii:  $\rho_0 = 25$  m (proposed for NSLS-II) and  $\rho_0 = 13.7$  m dipole that could yield a shorter circumference lattice.

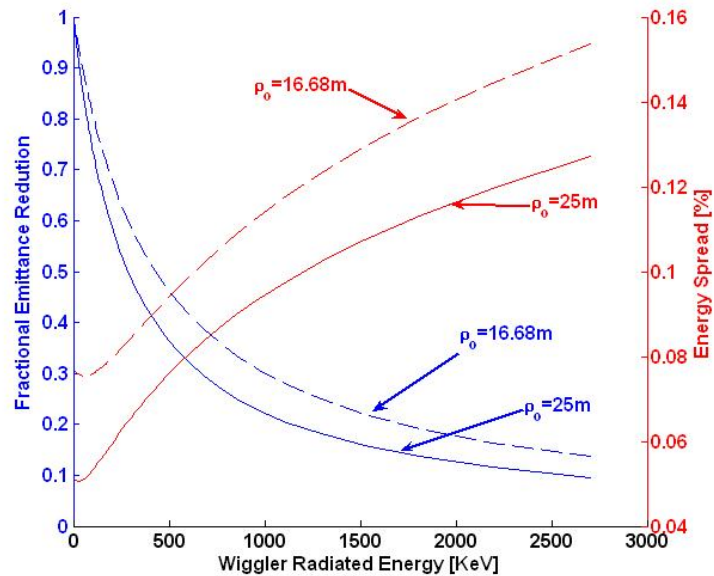
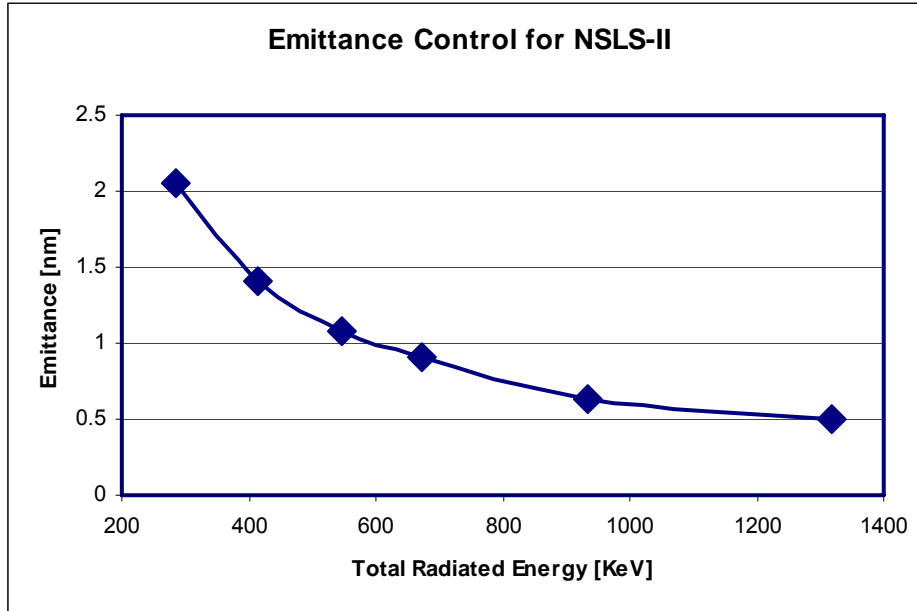


Table 3.1.2 lists the design parameters for this 15 super-period DBA ( $15 \times 2$ ) lattice. The choice of low dipole field restricts the photon beam energies radiated by the dipoles to 2.4 keV critical energy at 3 GeV. The dipole radiation will provide very bright VUV and soft-x-ray beams. Hard x-rays will be available from the installed DWs (10.8 keV critical energy) with high brilliance and flux.

**Table 3.1.2 Storage Ring Parameters.**

Energy [GeV]	3
Circumference [m]	791.96
DBA cells	30 (15 x 2)
Bending radius [m]	25.019
RF frequency [MHz]	499.68
Harmonic Number	1320
Momentum compaction	0.000368
Ring Tune: $\nu_x, \nu_y$	32.35, 16.28
Natural chromaticity: $\zeta_x, \zeta_y$	-103, -44.8
Maximum dispersion [m]	0.46
High-beta 9.3-m straights: $\beta_x, \beta_y$ [m]	20.85, 2.94
Low-beta 6.6-m straights: $\beta_x, \beta_y$ [m]	2.02, 1.06
Dipole radiated energy loss [keV]	286.5
Dipole critical energy [keV]	2.394

Figure 3.1.3 shows the expected reduction of the emittance as one to eight 7 m DWs are added to the ring.



**Figure 3.1.3**  
Emittance reduction for NSLS-II as 0, 1, 2, 3, 5, and 8 DW (7 m each) are installed and operated at 1.8 T peak field.

Table 3.1.3 compares the basic lattice properties with those obtained with 21 or 56 m of DWs installed in the ring. All of these DWs will have a fixed gap and will be available to drive user beamlines.

**Table 3.1.3 Effect of Three and Eight 7 m Damping Wigglers on Beam Properties at 3 GeV.**

	Zero DWs	Three 7 m DWs (21 m)	Eight 7 m DWs (56 m)
Energy loss [keV]	287	674	1320
RF voltage (3% bucket) [MV]	2.5	3.1	3.9
Synchrotron tune	0.0079	0.00876	0.0096
Natural emittance: $\epsilon_x, \epsilon_y$ [nm-rad]	2.0, 0.01	0.9, 0.008	0.50, 0.008
Damping time: $\tau_x, \tau_s$ [ms]	54, 27	23, 11.5	12, 6
Energy spread [%]	0.05	0.089	0.099
Bunch duration [ps]	10	15.4	15.5

The lattice shown in Figure 3.1.1, like that at ESRF, has low and high beta function straight sections. However, we have increased the length of the high- $\beta_x$  straight section to provide for injection, space for RF cavities, and space for longer DWs and user IDs. The drift space between quadrupole magnets is 9.3 m. The space available for insertion devices is 7 m. The magnet layout for the Long ID straight section, with field free drift space of 9.3 m between sextupoles, is shown in Figure 3.1.4. Half the long ID is shown with reflective symmetry about the centerline (left-hand side). There are a total of six quadrupoles [(QH1, QH2, QH3) $\times$ 2] and eight sextupoles [(SH1,... SH4) $\times$ 2] in this ID straight section. Although they are considered as families of focusing strengths, each will be independently powered to account for magnet-to-magnet differences and for the possibility of shifting the symmetry condition for improved photon beam focusing. The three quadrupole families provide sufficient variables for correcting the local distortions of the linear lattice when IDs are installed or when the gaps are changed by the users [3.1.4, 3.1.5]. The center quadrupole (QH2) is 40cm long, while the other two are 25 cm long, in order to satisfy the maximum gradient of <22 T/m design criteria. The four families of sextupoles in this ID are required in order to correct the nonlinearity of

the lattice arising from the strong chromatic sextupoles located in the dispersive regions. For certain tunes, some sextupoles have small strengths. These might be dropped from a future optimized design.

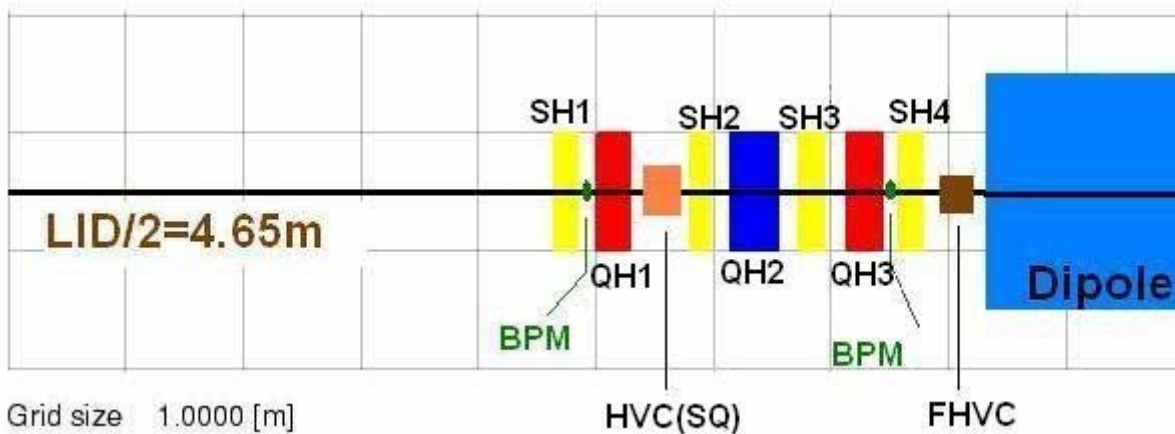


**Figure 3.1.4** Layout for half of a long (high beta function-H) ID straight section, with reflection symmetry on left side.

The short ID straight section layout is shown in Figure 3.1.5. The short ID has a 6.6 m drift between the inner sextupoles and is similar to the long ID in layout of the quadrupoles and sextupole families. Differences include additional drift between quadrupoles to reduce the chromaticity, while providing the increased focusing needed for the lower beta functions. The quadrupoles are 25 cm long except for the center quadrupole (QL2) is 40 cm as in the long ID straight section. The QL2 quadrupole has the maximum gradient of the lattice quadrupoles, this magnet has a 10% safety margin of its maximum gradient to allow for tuning range for reducing the horizontal beta function in the short ID, for increase brightness of the ID source.

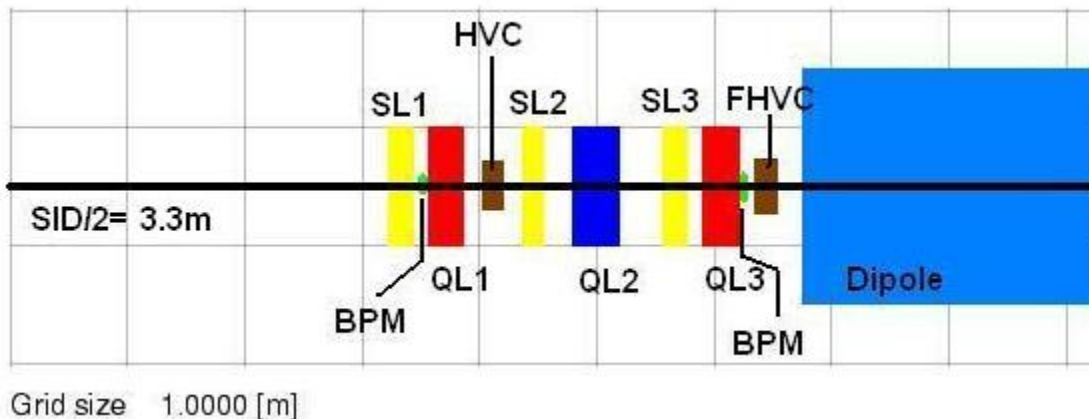


**Figure 3.1.5** Layout for half of a short (low high beta function-L) ID straight section, with reflection symmetry on left side.

Two slow horizontal and vertical closed-orbit correction magnets are included in each ID straight section (some also include a skew quadrupole winding). For the purposes of this design, we assume independent corrector magnets, as shown in Figures 3.1.4 and 3.1.5. Also shown are two beam position monitors to be used for closed-orbit correction. When a user ID is installed in the ring, it is assumed that two pairs of fast horizontal and vertical correctors and a pair of user BPMs may also be installed. These will be optimized for the aperture of the ID vacuum chamber to yield increased sensitivity to orbit motion and the increased frequency of correction for fast orbit motion required for the ID beamline. To accomplish this will require

some advanced engineering, but there is adequate drift space provided. The FHVCs and UBPMs will be used as part of a global feedback system to provide submicron photon beam stability up to 100 Hz. Since the four FHVCs will provide a closed bump, the possibility of adding a photon beam position signal to the feedback system will also be available, without that signal impacting the beam for other users. Also shown in Figure 3.1.4 is a skew quadrupole in one of the HVC corrector magnets. This is one of two families of skew quadrupoles (see Figure 3.1.6 for the second family) and is used to correct the vertical coupling of the horizontal and vertical betatron phase space resulting from alignment of the dipoles and quadrupoles in the ring.

Figure 3.1.6 shows the magnet layout for the dispersion region of the lattice with the dipoles included. This region has four quadrupoles in two families and three chromatic sextupoles in two families. These magnets give some flexibility for optimizing the dispersion function for reduced chromatic sextupole strength. The two chromatic sextupoles allow the linear chromaticity to be tuned, while also reducing the 2<sup>nd</sup> order chromaticity. Space has been provided between the dipole and the vertically focusing quadrupole in order to accommodate a Three Pole Wiggler. Although the drift for the TPW is provided symmetrically around the dispersive section, only the location closest to the dipole could have a TPW installed. These TPW ( $\leq 15$ ) will provide source points for hard X-ray beams, for support of migrated NSLS user beamlines. As in the ID straight sections, two BPMs are included close to the quadrupoles near the ends of the girder. This is to provide improved alignment of the magnets on the girder using a beam based alignment of the BPM to the quadrupoles magnetic center. A third BPM (electrodes only) is included near the QF1 quadrupole (near the maximum dispersion point). This BPM will be used for accelerator physics measurements of the dispersion and beta functions, when needed, and could improve the orbit correction for large alignment or settlement errors. Also included are two discrete correctors (FHVC) that will be used for static and fast global orbit correction. These correctors are not symmetric about the dispersion section, in order to allow extraction of the damping wiggler beams and space for insertion of a three pole wiggler (TPW). These locations in the lattice for the TPW's will provide up to 15 possible beam sources for hard X-ray beam lines that can be migrated from the existing NSLS-Xray ring. Also show in one of the FHVC correctors is the location of one family of skew quadrupoles for coupling correction and vertical emittance control, see Section 3.1.2.?

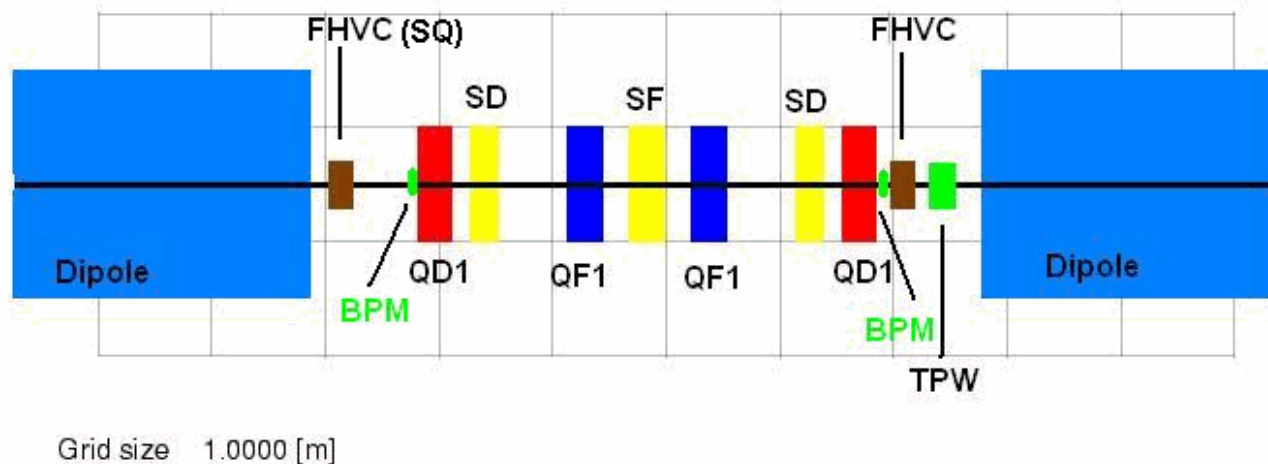


**Figure 3.1.6** Layout for the dispersion section, including the two dipole magnets.

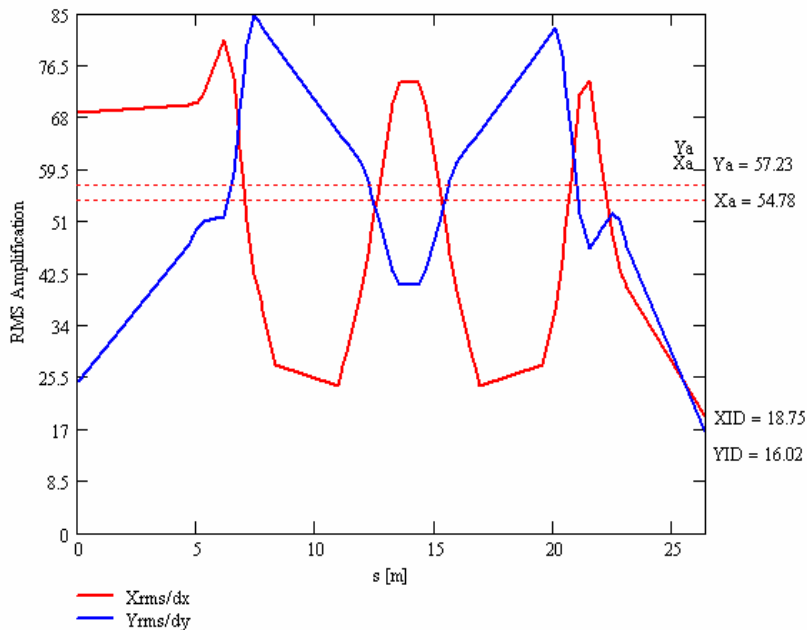
Table 3.1.4 lists a summary of the basic storage ring magnets and BPMs in the lattice design and for closed-orbit control. Also included are alignment tolerances for these magnets.



**Table 3.1.4 List of Magnets, tolerances and BPMs for the NSLS-II Storage Ring.**

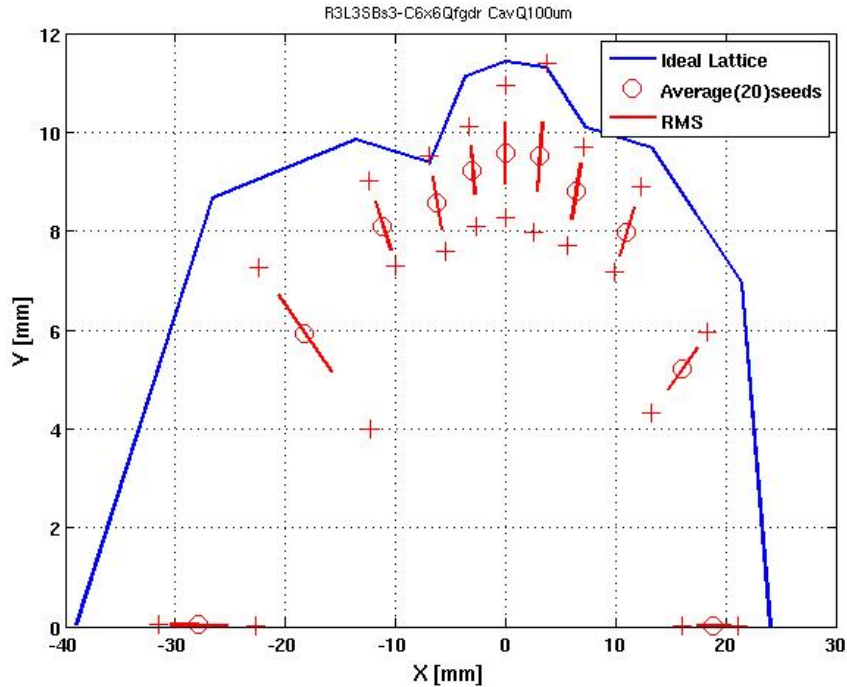
Qty.	Magnet Type	Length [m]	B, B', B" [T,T/m,T/m <sup>2</sup> ]	Alignment Tol.
60	Dipole	2.62	0.4, 0, 0	0.1 mm, 0.5 mrad
270	Quadrupole (S)	0.25	0, 22, 0	0.03 mm, 0.2 mrad
30	Quadrupole (L)	0.40	0, 22, 0	0.03 mm, 0.2 mrad
30	Sextupole (L)	0.25	0, 0, 500	0.03 mm, 0.2 mrad
270	Sextupole (S)	0.20	0, 0, 500	0.03 mm, 0.2 mrad
180( 210)	BPM readouts (positions)	0.05		0.1 mm, 0.2 mrad
120	H&V Fast Correctors(SS)	0.30	0.027, 0	0.1 mm, 0.2 mrad
60	H & V Slow Correctors	0.20	0.04, 0	0.1 mm, 0.2 mrad
150	Magnet girders			0.1 mm, 0.5 mrad

The alignment and field tolerance errors are still being studied further. However, initial testing of the lattice with tolerance that has been achieved at other light sources has shown the DA is robust for individual errors. As with most synchrotrons light sources, the closed-orbit amplification factors contribute the most significant tolerance to be handled. COAFs give the RMS closed-orbit distortion around the ring per unit of RMS alignment error (assumed to be a random Normal distribution) for all the quadrupoles in the ring. The COAF for this lattice is shown in Figure 3.1.7 for one cell and has an average value in each plane of greater than 50. This means a 100  $\mu\text{m}$  RMS alignment error in the quadrupoles will yield an average closed-orbit distortion of  $>5$  mm. This closed orbit error in the sextupoles contributes to a nonlinear focusing error in the lattice, which breaks the sextupole strength settings that yield the large DA.



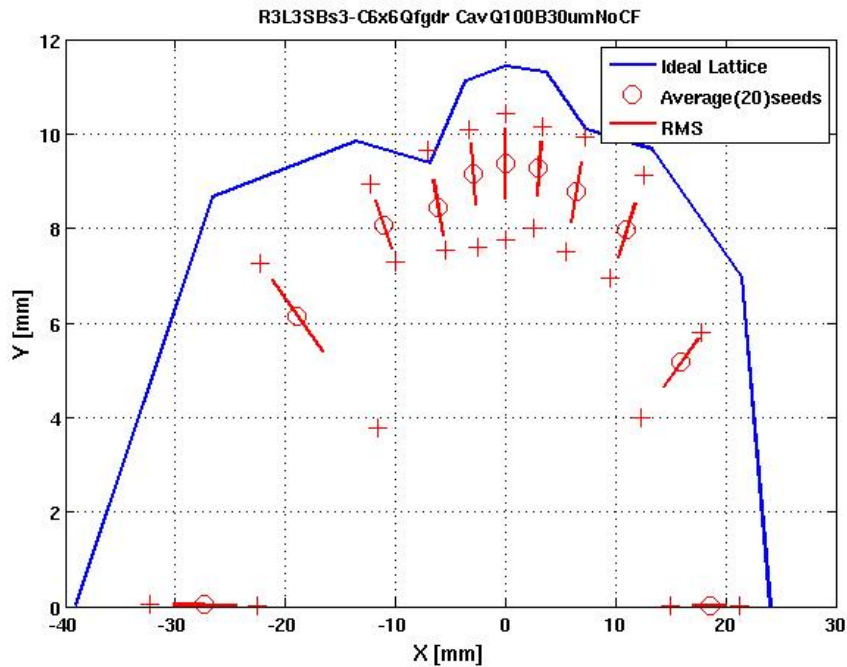
**Figure 3.1.7** RMS expected closed-orbit amplification factors for random alignment errors in the quadrupoles of the lattice. Listed are the average amplification factors ( $X_a, Y_a$ ) and values at the short ID ( $X_{ID}, Y_{ID}$ ).

Figure 3.1.8 shows the impact of random quadrupole alignment errors of 100  $\mu\text{m}$  that are corrected using the 6 BPMs and the 6 correction magnets per cell. We have corrected the orbit to the BPMs with an assumed no BPM noise or offset from the reference orbit. The corrected orbit DA for 20 different starting seeds (lattice layout errors) is shown with the average and RMS spread of the DA, together with the extreme values. The DA remains adequately large and is more than sufficient for injection and lifetime.



**Figure 3.1.8** The DA (average, RMS and extremes values) for the lattice with 100  $\mu\text{m}$  quadrupole alignment errors corrected to ideal BPMs located at the quadrupoles. It includes synchrotron oscillations, and the DA is tracked for 1 K turns around the lattice. The bare DA is also shown.

Adding a 30  $\mu\text{m}$  random alignment tolerance of the BPM-to-quadrupole magnetic center yields little additional reduction of the DA, as shown in Figure 7.1.3, and is more than adequate. This random offset of the BPMs is equivalent to a BBA resolution of the BPM center relative to the quadrupole magnetic center, which could be much better than the 30  $\mu\text{m}$  assumed in Figure 3.1.9, as described below.



**Figure 3.1.9** DA with 100  $\mu\text{m}$  quadrupole alignment tolerances corrected with 30  $\mu\text{m}$  BBA tolerance for BPMs (20 random seeds shown, with synchrotron oscillations).

We have assumed that the BPMs are close to the quadrupoles, since they are the source of the closed-orbit distortions in the sextupole magnets that cause the reduction of the DA. The two BPMs on a girder are aligned to the centers of the neighboring quadrupole magnetic center using the BBA procedure, which has become

common at many synchrotrons. This method uses a beam bump to vary the beam position ( $x, y$ ) in the quadrupole and its neighboring BPM. If that quadrupole has its strength modulated ( $\Delta K_2$ ), then the magnitude of the closed-orbit distortion measured by the BPMs is ( $X_m, Y_m$ ). The BPM reading that yields a null in ( $X_m, Y_m$ ) is then the magnetic center of this quadrupole, as measured by the BPM. With two BPMs on a girder, the beam can be magnetically centered to all elements on the girder using the magnetic alignment instruments: pulsed wire, vibrating wire, and/or rotating coils. Therefore we specify the alignment tolerances for the magnetic elements in terms of: 1) an alignment tolerance of centers one to another, 2) alignment of girder ends one to another and a common roll error of the girder, and 3) a BBA alignment tolerance of the BPMs to their neighboring quadrupole. The sensitivity of the closed-orbit distortion amplitude to the quadrupole modulation ( $\Delta K_2 L$ ) and beam offset relative to the quadrupole center position, ( $x_c, y_c$ ), is given by:

$$X_m(s) = \frac{\sqrt{\beta_x(s) \beta_x(\text{quad})}}{2 \sin(\pi Q_x)} (\Delta K_2 L) x \geq 5.2 (\Delta K_2 L) x \quad (3.1.1-8)$$

and

$$Y_m(s) = \frac{\sqrt{\beta_y(s) \beta_y(\text{quad})}}{2 \sin(\pi Q_y)} (\Delta K_2 L) y \geq 7.2 (\Delta K_2 L) y \quad (3.1.1-9)$$

where we assume the smallest beta function at a quadrupole and the average beta function at the BPMs. We assume that the closed-orbit amplitude is measurable to the resolution of the BPMs,  $\sim 1 \mu\text{m}$ , and the modulation is 3% of the quadrupole strength; the magnetic center should be measured in the neighboring BPM with an accuracy of better than

$$\sigma_{x_c} \leq 8 \text{ to } 10 \mu\text{m} \quad \text{and} \quad \sigma_{y_c} \leq 15 \mu\text{m}. \quad (3.1.1-10)$$

Consequently, the random tolerances on the magnet-to-magnet alignment in Table 3.1.1 will be greater than the BBA resolution. However, we have assumed the BBA resolution of  $30 \mu\text{m}$  in Figure 3.1.9, which is two to three times greater than achievable.

The impact of the larger values for the girder alignment tolerances were evaluated assuming that either end of the girder is aligned to an RMS level (random Normal distribution  $\Delta x, \Delta y$ ). This misalignment of the girders contributes a correlated misalignment error in all magnets and BPMs on the girder. The sensitivity to this type of error is shown in Figure 3.1.10, where the Girder Amplification Factor is shown. The GAF is defined as the RMS closed-orbit distortion per unit of RMS girder misalignment. This shows a reduction in the averaged COAF (Figure 3.1.7) by a factor of 2X (H) and 3X (V). The GAF values at the center of the short straight section are 9.4 in the horizontal and 4.3 in the vertical plane, compared to 18.8 and 16.0 for the COAF, respectively. However, correcting for the assumed  $100 \mu\text{m}$  girder alignment tolerances yields almost complete restoration of the DA (without BPM errors), since the correlations of the quadrupole misalignments are easier to remove by BBA alignment to the quadrupoles on the misaligned girders.

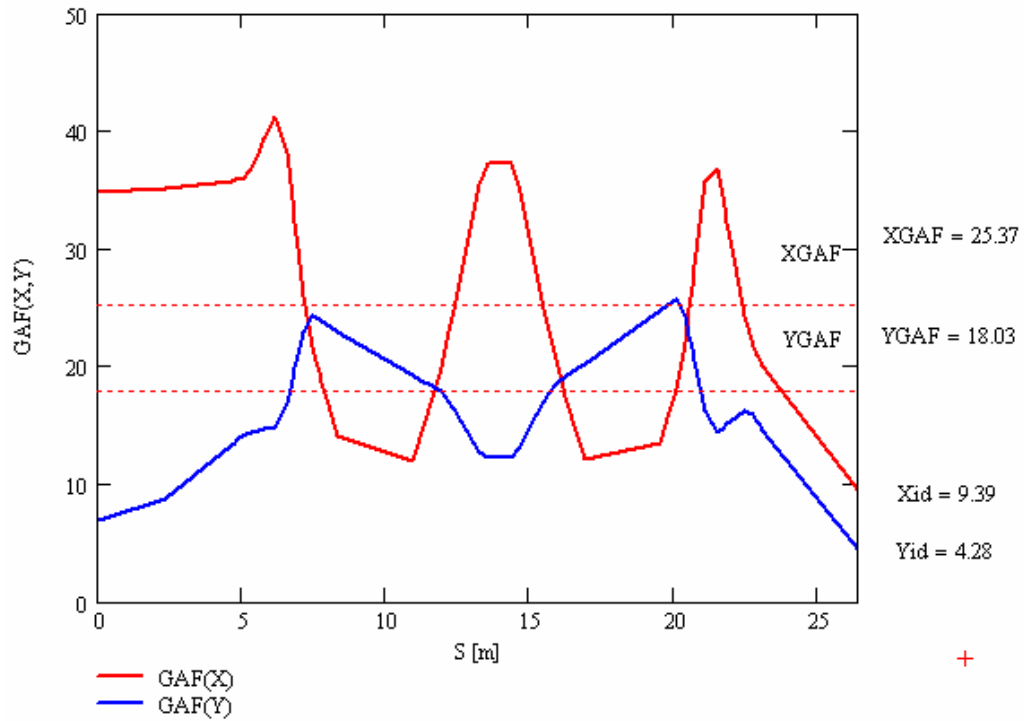


**Figure 3.1.10** Girder Amplification Factors for one period of the storage ring. The average GAF values are 25 (H) and 18 (V) with values for the short ID of 9.4(H) and 4.3(V).

The corrected DA is shown in Figure 3.1.11 for 100  $\mu\text{m}$  RMS random girder alignment tolerances, where no other errors are assumed in the BBA resolution for the BPMs, nor any quadrupole misalignment errors on the girder.

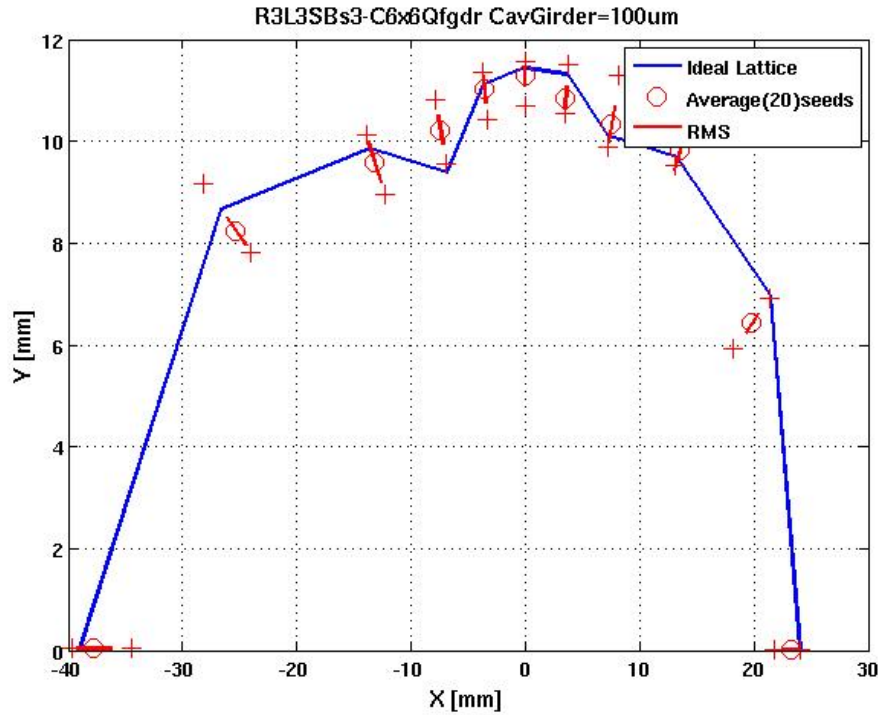


**Figure 3.1.11** DA for 20 seeds (lattices) with 100  $\mu\text{m}$  RMS girder alignment tolerances corrected using the BPMs with zero error in the BBA resolution.

The impact on the DA of all the misalignment tolerance, listed in Table 3.1.4 and including a 10  $\mu\text{m}$  BBA resolution, as given by Eq. 3.1.1-10, is shown in Figure 3.1.12. Although there is significant reduction of the DA for this level of tolerance errors, it is well outside the physical aperture of the ring. Relaxing the alignment tolerances is still acceptable but will make the field and multipole tolerances on the magnets even tighter and will have a significant cost impact. The complete analysis of the DA with all alignment and field tolerances is presented in Section 3.1.2. The COAF and GAF presented here will also be used to estimate the orbit stability resulting from magnet vibrations in Section 7.2.2.

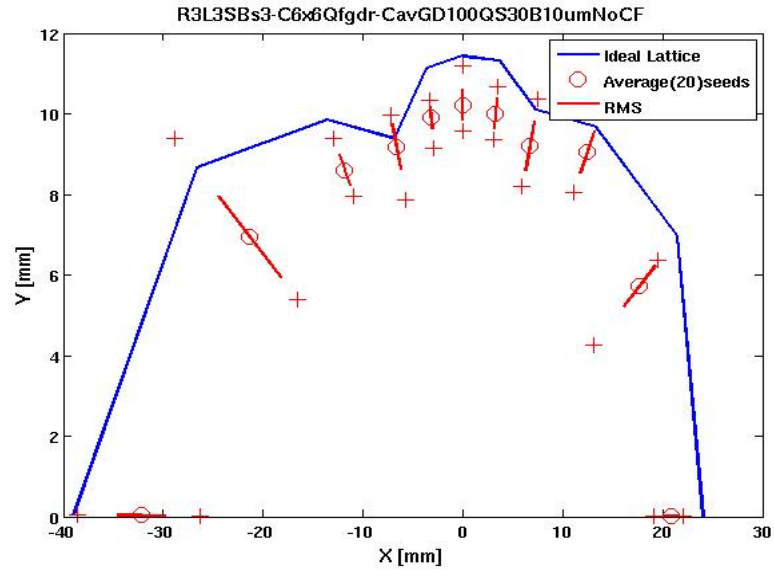


**Figure 3.1.12** DA for 20 seeds (lattices) with all alignment tolerances included and using a 30  $\mu\text{m}$  BBA resolution for BPMs. No quadrupole rotations are included.



## 3.1.2 Nonlinear Dynamics

### 3.1.2.1 Guidelines

One of the main design challenges for a strongly focusing lattice is to obtain adequate dynamic aperture for injection and Touschek lifetime<sup>1</sup>. As the required strength of the chromatic sextupoles increases, the DA can be improved by introducing extra families of geometric and chromatic sextupoles. However, once the sextupoles become too strong, this is no longer feasible. Eventually, cross terms generate higher-order terms, and when more families are introduced, the lattice will become pathological [3.1.5]. To avoid this, the following guideline has been provided for the linear optics design:

- horizontal chromaticity per cell,  $\xi_x \leq 3$ ,
- peak dispersion,  $\eta_x \geq 0.3$  m.

Similarly, we have adopted the guidelines for the DA summarized in Table 3.1.5. This is a conservative approach<sup>2</sup> to satisfy the requirements for the injection aperture for efficient top-off, as well as to ensure sufficient Touschek lifetime.

**Table 3.1.5 Dynamic Aperture Guidelines.**

	Horizontal and Vertical Dynamic Acceptance [mm-mrad]	Horizontal Dynamic Aperture [mm]	Momentum Acceptance [%]
Bare lattice (2.5 degrees of freedom <sup>3</sup> )	~25	±20	±3
"Real" lattice (3 degrees of freedom <sup>4</sup> )	~20	±15	±3

This also provides some leeway for magnetic alignment and field tolerances, and nonlinearities due to insertion devices, which, when included, the former perturb the symmetry of the linear optics and diminish the cancellation of the nonlinear effects whereas the latter contribute directly, reducing the DA.

### 3.1.2.2 Sextupole Scheme

The linear lattice has a chromaticity of  $\xi_{x,y}^{(1)} \sim (-100, -37)$  and a natural momentum spread of  $\sim 0.1\%$  leading to a tune spread of  $\Delta\nu_{x,y} \sim (0.1, 0.04)$ , which must be corrected<sup>5</sup>. The linear chromaticity is given by

$$\xi_{x,y}^{(1)} = \mp \frac{1}{4\pi} \sum_{k=1}^N [(b_2L)_k - 2(b_3L)_k \eta_{x,k}] \beta_{(x,y),k}, \quad (3.1-8)$$

<sup>1</sup> For medium energy rings:  $\sim 3$  GeV.

<sup>2</sup> Based on the experience from the Swiss Light Source conceptual design, i.e., a highly nonlinear lattice [3.1.6] with straightforward commissioning [3.1.7], excellent top-off injection efficiency [3.1.8], and stability [3.1.9].

<sup>3</sup> With  $\delta$  (momentum deviation) treated as a parameter, i.e., the adiabatic approximation.

<sup>4</sup> In particular, with synchrotron oscillations.

<sup>5</sup> Moreover, a positive linear chromaticity in the range 0–5 is required to stabilize the head-tail instability.



where  $(b_2L)$ ,  $(b_3L)$  are the integrated quadrupole and sextupole strengths, and  $\beta$  and  $\eta$  are the beta function and dispersion, respectively at the quadrupoles and sextupoles,  $k$ . The driving terms for linear chromaticity from sextupoles are shown in Figure 3.1.7. Two mirror symmetric chromatic families are introduced inside the dispersion section and 3+4 geometric families in the short and long straight sections, i.e., a total of 9 sextupole families. While one of the families in the latter tends to be weak, it has been left as place holders until a more comprehensive optimization has been completed. Individual power supplies for all the quadrupoles are provided, whereas the sextupole families are powered in groups of five; to allow for local optics correction [3.1.10–3.1.16] and control of residual nonlinear resonances. The latter by analyzing the betatron sidebands from turn-by-turn BPM data and controlling them with the inverted “sextupole response matrix” [3.1.17-3.1.19].

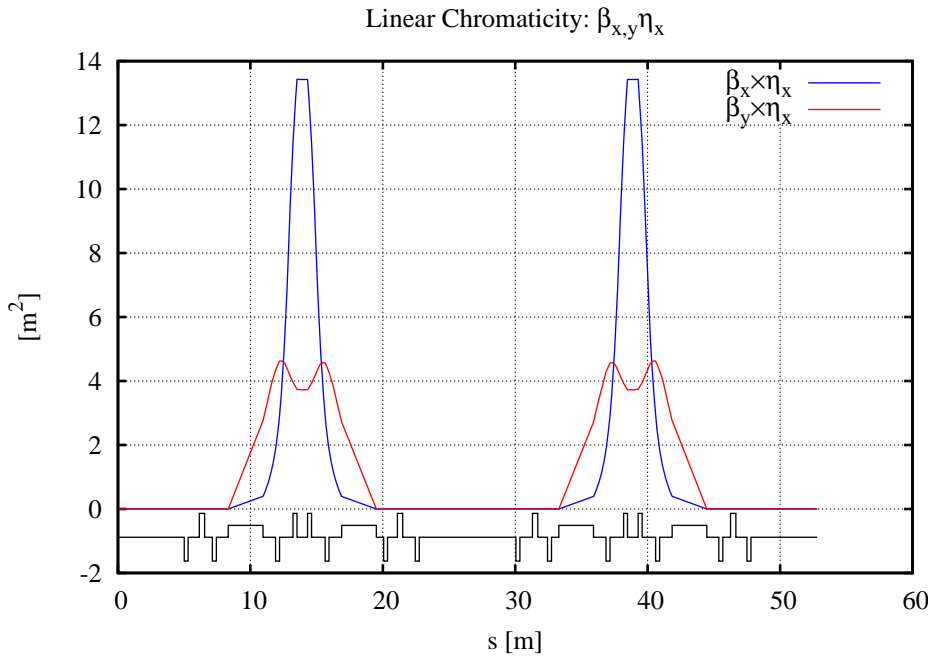


**Figure 3.1.7** Driving terms for zeroing linear chromaticity with sextupoles,  $\beta_{x,y} \eta_x$ .

After linear chromaticity has been zeroed, the residual (nonlinear) chromaticity is one of the limiting factors. The second-order chromaticity is given by [3.1.17]:

$$\xi_{x,y}^{(2)} = -\frac{1}{2}\xi_{x,y}^{(1)} \pm \frac{1}{8\pi} \sum_{k=1}^N \left\{ 2(b_3L)_k \frac{\partial \eta_{x,k}}{\partial \delta} \beta_{(x,y),k} \mp [(b_2L)_k - 2(b_3L)_k \eta_{x,k}] \frac{\partial \beta_{(x,y),k}}{\partial \delta} \right\} \quad (3.1-9)$$

where

$$\frac{\partial \eta_{x,j}}{\partial \delta} = -\eta_{x,j} + \frac{\sqrt{\beta_{x,j}}}{2 \sin(\pi \nu_x)} \sum_{k=1}^N [(b_2L)_k - (b_3L)_k \eta_{x,k}] \eta_{x,k} \sqrt{\beta_{x,k}} \cos(\mu_{j \rightarrow k, x} - \pi \nu_x)$$

and

$$\frac{\partial \beta_{(x,y),k}}{\partial \delta} = \pm \frac{\beta_{(x,y),j}}{2 \sin(2\pi\nu_x)} \sum_{k=1}^N [(b_2 L)_k - 2(b_3 L)_k \eta_{x,k}] \beta_{(x,y),k} \cos(2\mu_{j \rightarrow k, (x,y)} - 2\pi\nu_x)$$

The driving terms are shown in Figures 3.1.8 and 3.1.9. Clearly, small variations of the sextupole locations may lead to large changes of the nonlinear chromaticity<sup>6</sup>. In particular, the quite large momentum dependence of the optics functions  $\eta_x(\delta)$  and  $\beta_{x,y}(\delta)$  leads to considerable residual second and cubic terms in the horizontal chromaticity [3.1.19]. Therefore, all the sextupole families are chromatic, i.e., part of the reduction of the nonlinear chromaticity originates from the reduction of the latter with the “geometric” sextupoles, see Figures 3.1.10 and 3.1.11. The former is not reduced, because there are only two chromatic families.

---

<sup>6</sup> As noted from numerical simulations for the DIAMOND conceptual design [3.1.18].

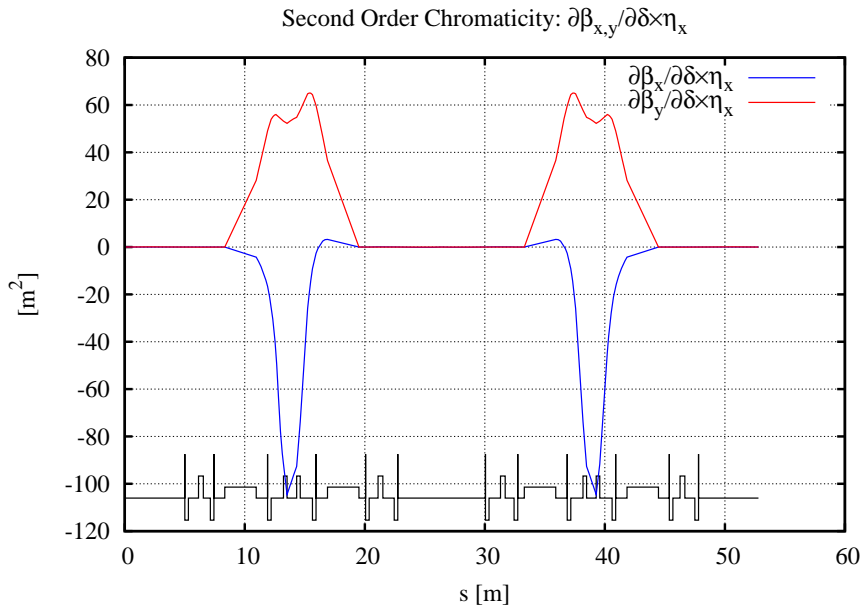


**Figure 3.1.8** Driving terms for second-order chromaticity,  $\partial\beta_{x,y}/\partial\delta \times \eta_x$  (no sextupoles).

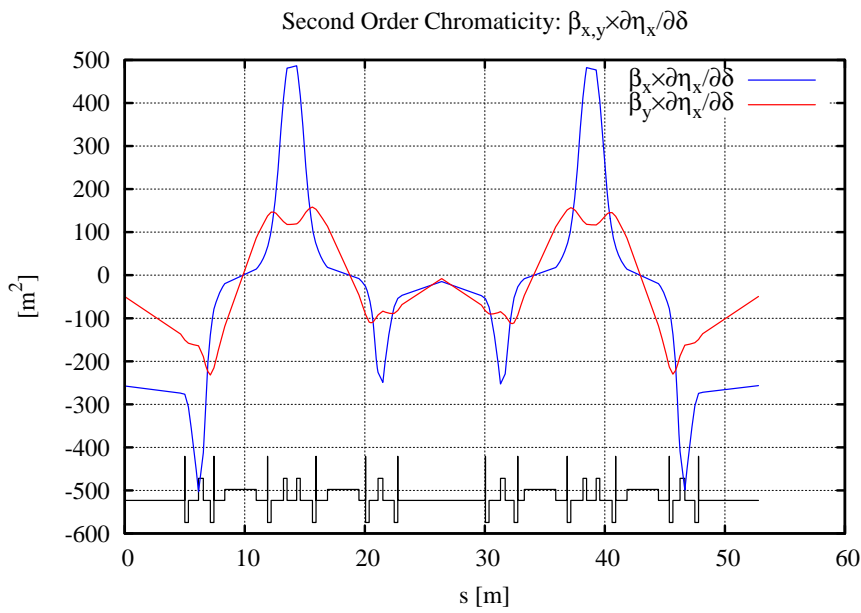


**Figure 3.1.9** Driving terms for second-order chromaticity,  $\beta_{x,y} \partial\eta_x/\partial\delta$  (no sextupoles).

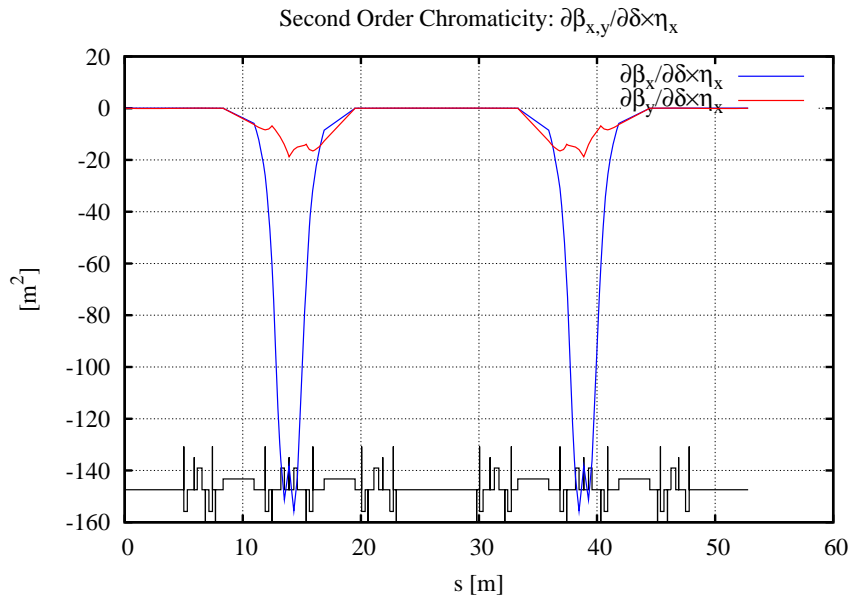


**Figure 3.1.10** Driving terms for second-order chromaticity,  $\partial\beta_{x,y}/\partial\delta \times \eta_x$  (with sextupoles).

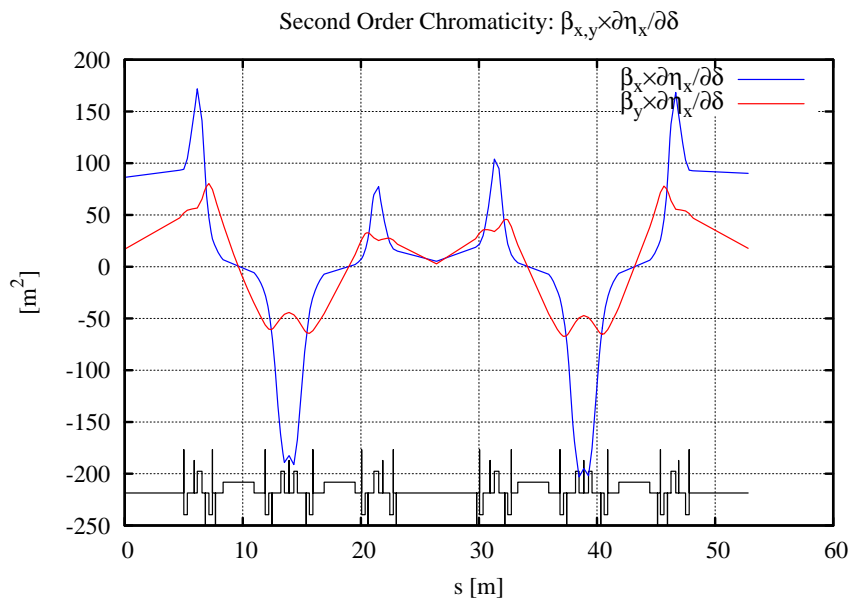


**Figure 3.1.11** Driving terms for second-order chromaticity,  $\beta_{x,y} \partial\eta_x/\partial\delta$  (with sextupoles).

### 3.1.2.3 Dynamic Aperture Optimization

The Poincaré map has the formal Lie series representation [3.1.17]:

$$\mathcal{M} = e^{:h:} \mathcal{M}_{\text{linear}} \quad (3.1-10)$$

where  $\mathcal{M}_{\text{linear}}$  is the linear one-turn map, and the Lie generator  $h$  represents the nonlinear kicks parallel transported to the lattice entrance. It can be written in the normal form<sup>7</sup> [3.1.22]

$$\mathcal{M} = \mathcal{A}^{-1} \dots e^{g(\bar{J}, \bar{\phi})} e^{k(\bar{J})} e^{-g(\bar{J}, \bar{\phi})} \mathcal{A},$$

where  $[\bar{J}, \bar{\phi}]$  are the action-angle variables,  $\mathcal{A}$  is a linear transformation to Floquet space<sup>8</sup>,  $g(\bar{J}, \bar{\phi})$  a canonical transformation, and  $k(\bar{J})$  a nonlinear rotation. A nonlinear pseudo-invariant is obtained from

$$\mathcal{K}(\bar{J}, \bar{\phi}) = e^{g(\bar{J}, \bar{\phi})} k(\bar{J}) = \text{cst.} \mathcal{A}.$$

In particular, the terms are of the form:

$$\mathcal{K}_i \propto \frac{J_x^{a_x} J_y^{a_y}}{\sin(\pi(n_x \nu_x + n_y \nu_y))} \quad (3.1-11)$$

where  $[n_x, n_y]$  are integers,  $[a_x, a_y]$ , and  $[\nu_x, \nu_y]$  the cell tune; note the resonance denominator. For a validation of the goodness of the pseudo-invariant as a description of the nonlinear dynamics see [3.1.23].

In contrast to the linear case, the long-term stability now depends on:  $\mathcal{K}(\bar{J}, \bar{\phi})$ , the cell tune, and the initial conditions. In other words, for a systematic approach, the pseudo-invariant and the working point have to be optimized simultaneously. We have implemented a generalized (partial) third-order achromat by introducing 9 sextupole families to the super-period, and minimized the coefficients of  $\mathcal{K}(\bar{J}, \bar{\phi})$  over two super-periods, i.e., four DBA cells, for a range of cell tunes. At each working point with optimized sextupole strengths, we evaluated the DA by tracking. To the second order in the sextupole strengths, there are:

- 2+3+2 chromatic terms
- 5+8 geometric terms (modes)
- 3+3 tune shift with amplitude and momentum

This is a total of 26 terms<sup>9</sup> (see Table 3.1.6 for an inventory). These are minimized by varying the sextupole strengths using the following automated method<sup>10</sup> [3.1.5]:

1. For a given cell tune, the pseudo-invariant  $\mathcal{K}(\bar{J}, \bar{\phi})$  and its parametric dependence on the sextupole strengths (i.e., the Jacobian) are calculated for  $J_{x,y}$  and  $\delta$  at the anticipated DA.
2. The norm of  $\|\mathcal{K}(\bar{J}, \bar{\phi})\|$  is minimized<sup>11</sup> and the DA is evaluated by tracking.
3. The cell tune is changed by using a grid of working points<sup>12</sup> from the optics optimizations, and steps 1–3 are repeated.

<sup>7</sup> Recursively, i.e., to arbitrary order, by Lie series and Truncated Power Series Algebra (TPSA).

<sup>8</sup> Normalized phase space.

<sup>9</sup> The corresponding overconstrained system of nonlinear equations for the sextupole strengths can be minimized because of symmetry and the fact that the higher order terms are due to cross terms of the lower order.

<sup>10</sup> Feasible only because of the use of symmetry and the fact that the higher order terms appear due to cross terms of the lower order.

<sup>11</sup> In particular, a least-square of the individual terms.

<sup>12</sup> Each working point meets all the optics requirements.

The off-momentum aperture is included by using a weighted average for the DA at  $\delta = 0, \pm 3\%$ . A robust solution is obtained by establishing a broad local maximum for the DA see Figure 3.1.12<sup>13</sup>. The tune scan is then redone with engineering tolerances included in the tracking, see Figure 3.1.13<sup>14</sup>, which has a broad maximum centered near  $\nu_{x,y} \approx [32.87, 15.67]$ . The resulting DA is shown in Figure 3.1.14, for  $\delta = 0, \pm 3\%$ . The linear chromaticity is set to  $\xi_{x,y}^{(1)} \approx [2.0, 2.0]$ , and the residual nonlinear chromaticity is shown in Figure 3.1.15.

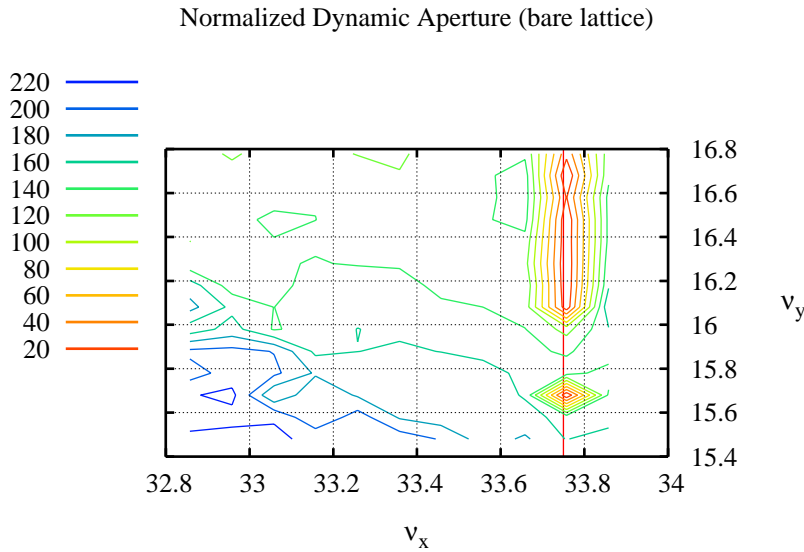


**Figure 3.1.12** Normalized DA ( $\text{Area}/\sqrt{\beta_x\beta_y}$ ) versus tune per super-period (bare lattice).

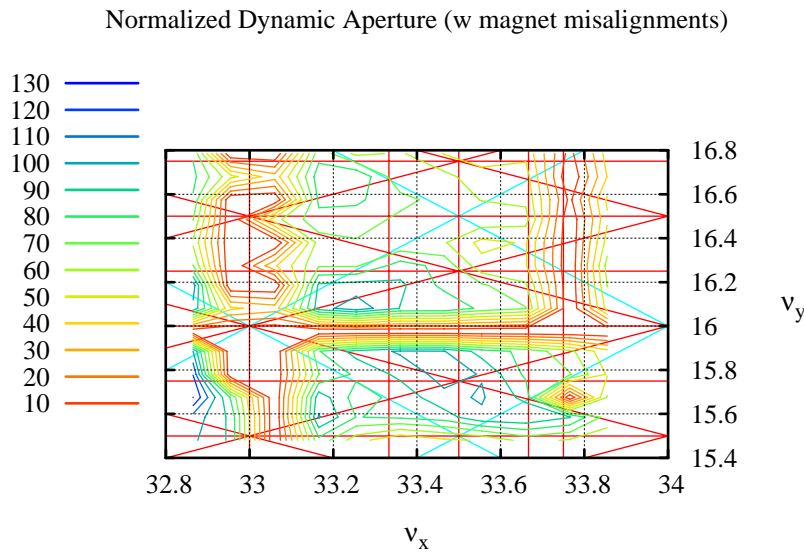


**Figure 3.1.13** Normalized DA ( $\text{Area}/\sqrt{\beta_x\beta_y}$ ) versus tune per super-period (with errors).

<sup>13</sup> The red line shows the (systematic)  $4\nu_y = 135$  resonance.

<sup>14</sup> The red lines shows the resonances up to first order in the sextupole strength.

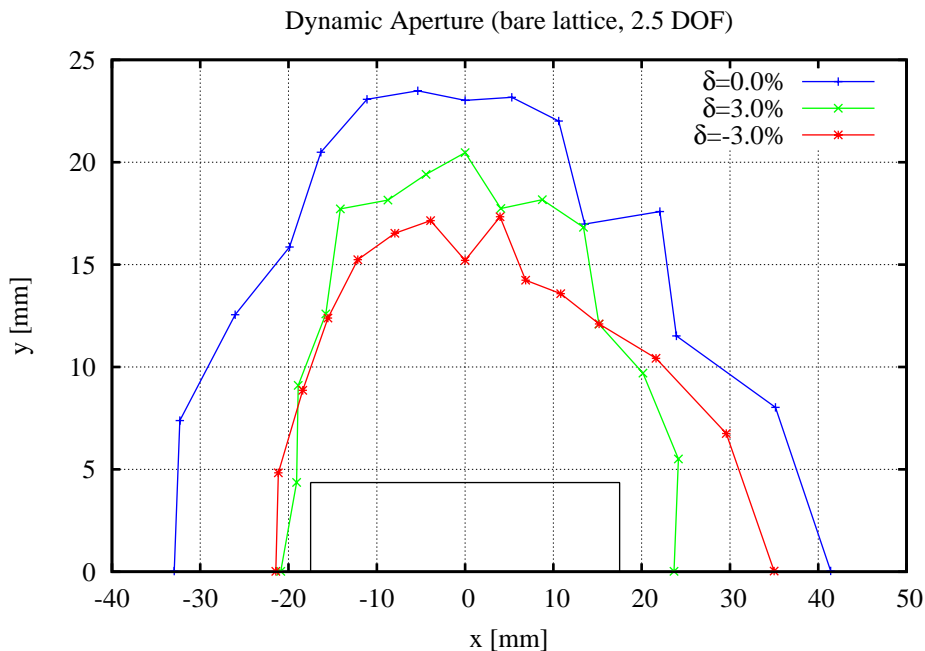


**Figure 3.1.14** DA for  $\delta = 0, \pm 3\%$  for the optimized tune and sextupoles at the center of the long straight section (i.e., at injection),  $\beta_{x,y} = [20.8, 3.4]$  m for  $\nu_{x,y} \approx [32.833, 15.616]$ .

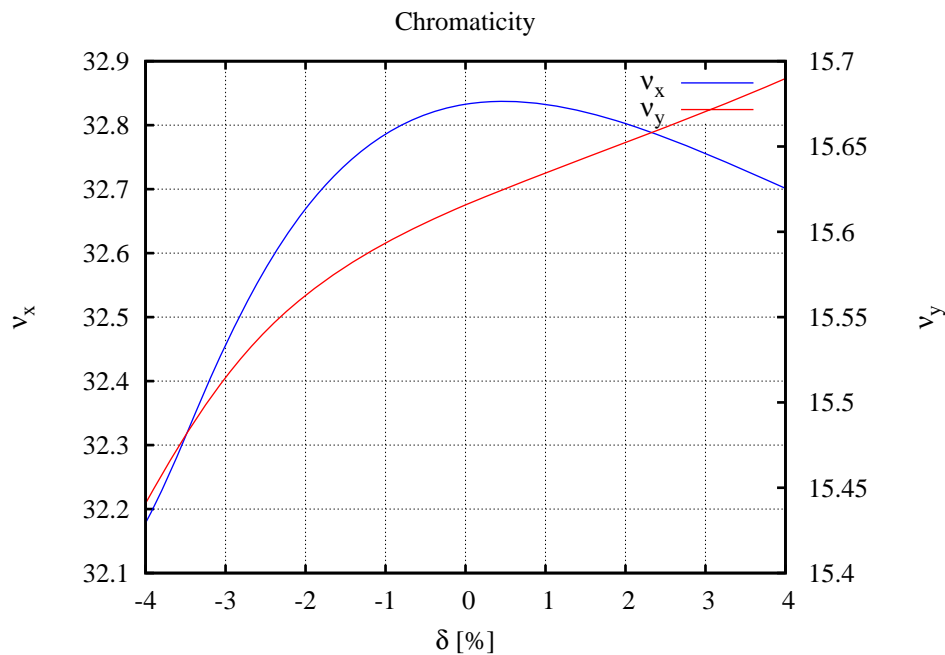


**Figure 3.1.15** Residual nonlinear chromaticity for the optimized tune and sextupoles for  $\xi_{x,y}^{(1)} \approx [2.0, 2.0]$ .

As mentioned earlier, the horizontal chromaticity has a substantial quadratic and cubic term originating from  $h_{10002}, h_{20001}, h_{00201}$ , which generate momentum dependence of the optics function. The amplitude-dependent tune shifts are shown in Figures 3.1.16 and 3.1.17, and the balancing of the pseudo-invariant terms

is summarized by Table 3.1.3. Moreover, the crossing of the linear coupling resonances during synchrotron oscillations should be avoided (Figure 3.1.18); otherwise, the Touschek lifetime is likely to be affected.

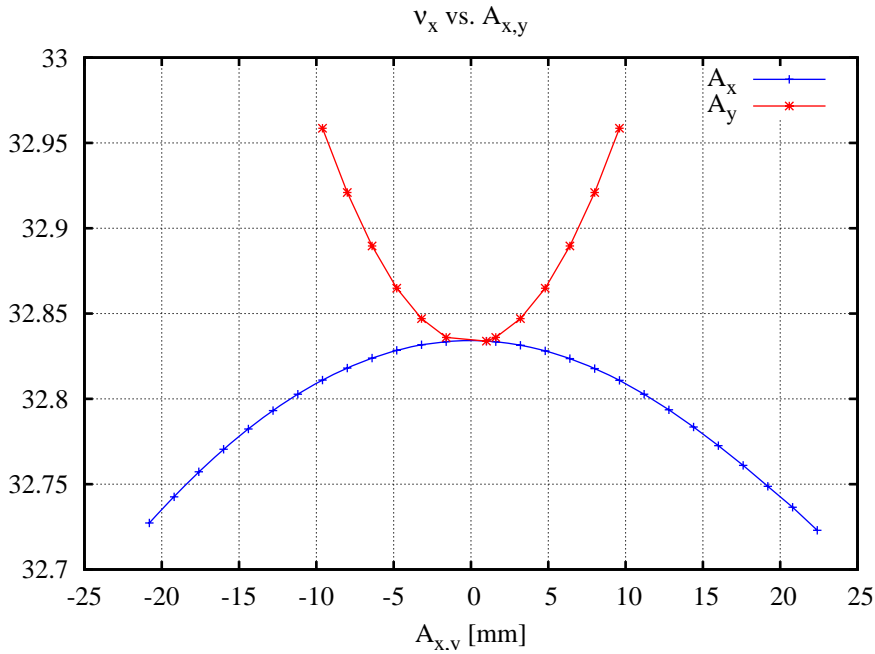


**Figure 3.1.6** Horizontal tune,  $v_x$ , vs. transverse amplitude  $(x_0, y_0)$  at the long straight section for  $A_x = (x_0, y_0 \sim 0)$  and  $A_y = (x_0 \sim 0, y_0)$ .

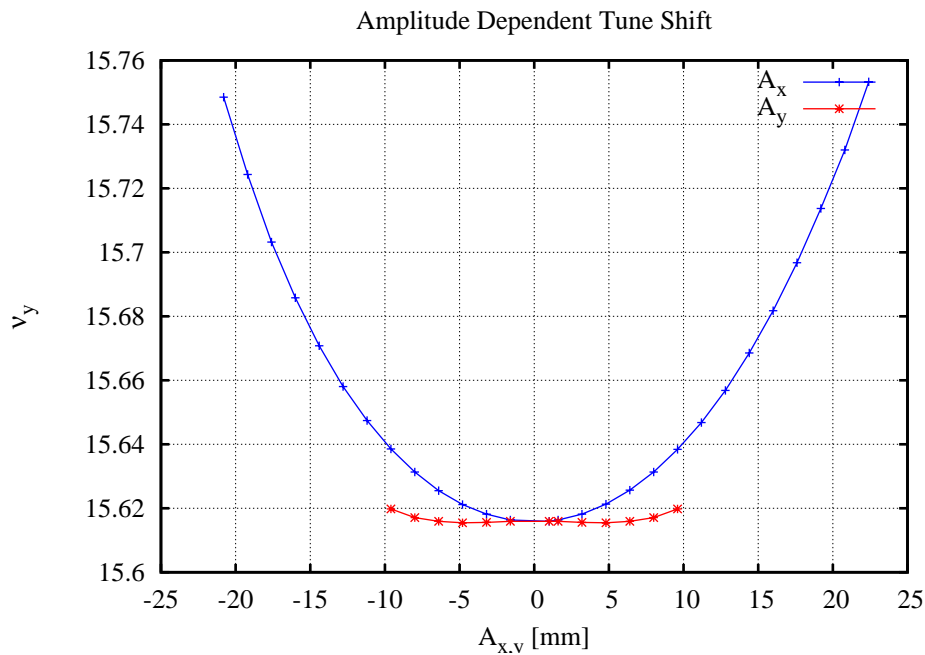


**Figure 3.1.17** Vertical tune,  $v_y$ , vs. transverse amplitude  $(x_0, y_0)$  at the long straight section for:  $A_x = (x_0, y_0 \sim 0)$  and  $A_y = (x_0 \sim 0, y_0)$ .



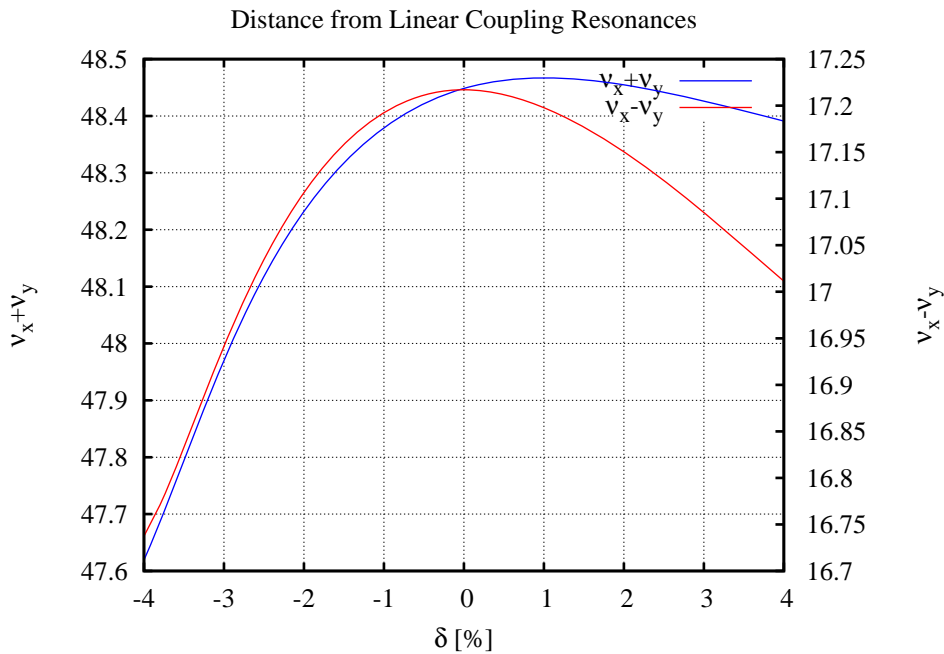


**Figure 3.1.18** Distance to the linear coupling resonances.

A frequency map [3.1.15] shows diffusion rate as a function of amplitude or tunes. The diffusion rate, as defined by

$$D(v_x, v_y) = \log_{10} \left( \sqrt{(\Delta v_x)^2 + (\Delta v_y)^2} \right), \quad (3.1-12)$$

is an indicator of chaotic behavior, where  $\Delta v$  is the tune change between the first and second half of the particle tracking with initial amplitude  $J_{x,y}$ . The frequency map for the optimized working point and sextupole settings for the selected linear chromaticity is shown in Figure 3.1.19, with the diffusion parameter plotted as a color-weighted value. Similarly, a frequency map for  $x$  vs.  $\delta$  is shown in Figure 3.1.20; since crossing of leading order resonances for the Touschek/synchrotron oscillation/radiation damping process must be avoided.

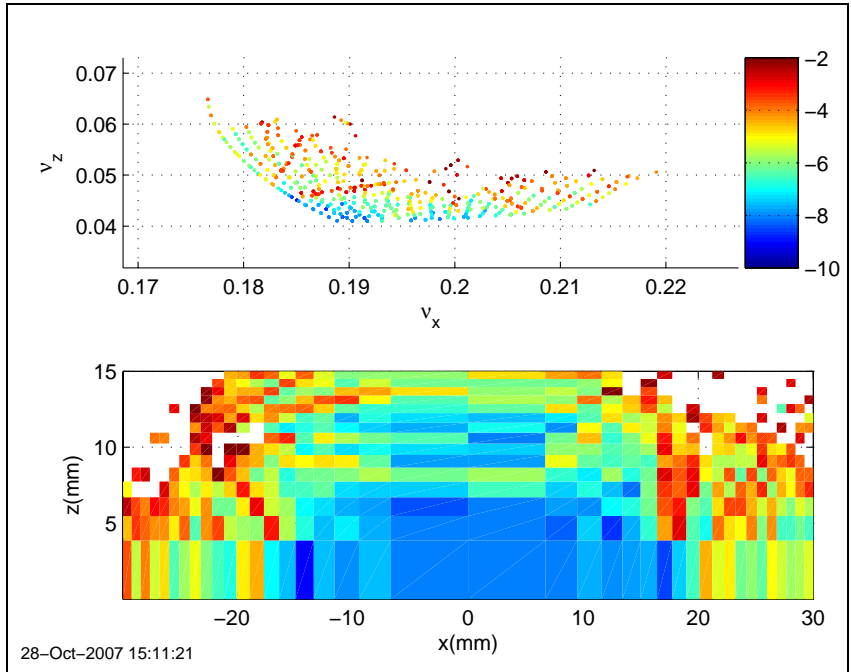


**Figure 31.19** Frequency map vs. transverse amplitudes at the Long Straight Section,  $\beta_{x,y} = (20.8, 3.4)$  m.

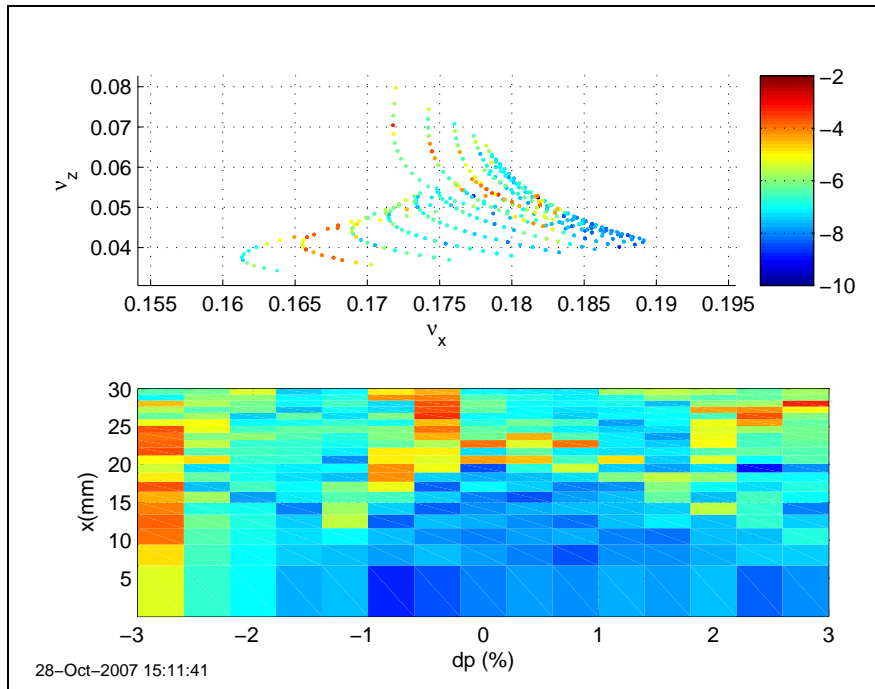


**Figure 3.1.20** Frequency map vs. momentum and horizontal amplitude at the Long Straight Section,  $\beta_{x,y} = (20.8, 3.4)$  m.

**Table 3.1.6 Residual Normalized Lie Generators.**

<b>Lie Generator</b>	<b>Effect</b>	<b>Normalized Value</b>
$ h_{11001} $	$\partial v_x / \partial \delta$	$5.4 \times 10^{-7}$
$ h_{00111} $	$\partial v_y / \partial \delta$	$1.5 \times 10^{-6}$
$ h_{10002} $	$\partial \eta_x / \partial \delta$	$2.0 \times 10^{-6}$
$ h_{20001} $	$\partial \beta_x / \partial \delta$	$2.4 \times 10^{-6}$
$ h_{00201} $	$\partial \beta_y / \partial \delta$	$1.7 \times 10^{-6}$
$ h_{21000} $	$v_x$	$8.6 \times 10^{-7}$
$ h_{10110} $	$v_x$	$9.2 \times 10^{-7}$
$ h_{30000} $	$3v_x$	$7.0 \times 10^{-7}$
$ h_{10020} $	$v_x - 2v_y$	$3.7 \times 10^{-6}$
$ h_{10200} $	$v_x + 2v_y$	$9.8 \times 10^{-7}$
$ h_{20110} $	$2v_x$	$3.1 \times 10^{-7}$
$ h_{31000} $	$2v_x$	$5.0 \times 10^{-8}$
$ h_{40000} $	$4v_x$	$7.3 \times 10^{-7}$
$ h_{20020} $	$2v_x - 2v_y$	$1.5 \times 10^{-6}$
$ h_{20200} $	$2v_x + 2v_y$	$5.1 \times 10^{-8}$
$ h_{11200} $	$2v_y$	$6.0 \times 10^{-7}$
$ h_{00310} $	$2v_y$	$3.9 \times 10^{-7}$
$ h_{00400} $	$4v_y$	$1.7 \times 10^{-7}$
$ h_{22000} $	$\partial v_x / \partial J_x$	$9.0 \times 10^{-7}$
$ h_{11110} $	$\partial v_{x,y} / \partial J_{y,x}$	$3.8 \times 10^{-6}$
$ h_{00220} $	$\partial v_y / \partial J_y$	$7.3 \times 10^{-7}$
$ h_{22001} $	$\partial^2 v_x / \partial J_x \partial \delta$	$3.2 \times 10^{-7}$
$ h_{11111} $	$\partial^2 v_{x,y} / \partial J_{y,x} \partial \delta$	$8.1 \times 10^{-7}$
$ h_{00221} $	$\partial^2 v_y / \partial J_y \partial \delta$	$4.5 \times 10^{-7}$
$ h_{11002} $	$\partial^2 v_x / \partial \delta^2$	$9.7 \times 10^{-7}$
$ h_{00112} $	$\partial^2 v_y / \partial \delta^2$	$1.9 \times 10^{-7}$
$ h_{11003} $	$\partial^3 v_x / \partial \delta^3$	$1.8 \times 10^{-7}$
$ h_{00113} $	$\partial^3 v_y / \partial \delta^3$	$1.4 \times 10^{-7}$

### 3.1.2.4 Impact of Alignment and Field Tolerances on Dynamic Aperture

Systematic and random magnetic field errors further reduce the DA, and their impact has been evaluated by simulations. Figure 3.1.21 shows the impact on the DA as the random quadrupole gradient errors are increased for all the quadrupoles of the lattice. At a relative RMS error of  $\Delta b_2/b_2 \approx 5 \times 10^{-4}$ , they reduce the DA by  $\sim 20\%$ , which is taken as the tolerance level for the quadrupole powering errors.

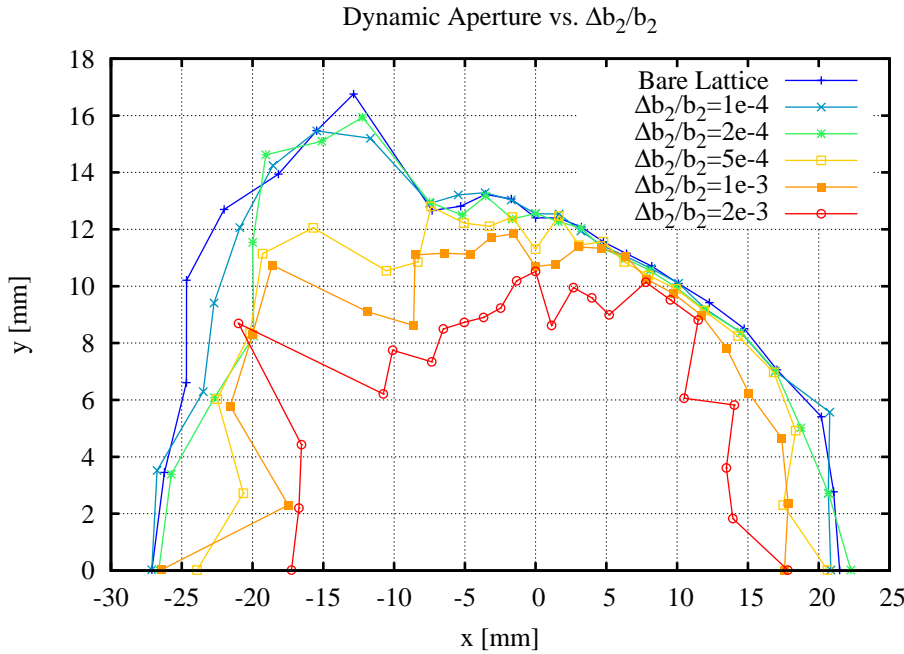


**Figure 3.1.21** DA sensitivity versus the fractional gradient errors in the quadrupoles.

This reduction in DA originates from distortions of the linear optics at the sextupole magnets that perturb the influence of the carefully balanced sextupole strengths that were chosen to minimize the nonlinear driving terms. The resulting RMS beta and phase advance beats at the sextupoles can therefore be used as a tolerance level, regardless of their source [3.1.24]. These latter tolerance levels, as well as the gradient tolerance level, are listed in Table 3.1.7.

**Table 3.1.7** Optics Tolerances for Robust DA of the NSLS-II Lattice.

Location	At the Quadrupoles	At the Sextupoles	
Parameter	$\left(\frac{\Delta b_2 L}{b_2 L}\right)_{\text{rms}}$	$\left(\frac{\Delta \beta_{x,y}}{\beta_{x,y}}\right)_{\text{rms}}$	$(\Delta v_{x,y})_{\text{rms}}$ $(\Delta x_{\text{cod}}, \Delta y_{\text{cod}})_{\text{rms}}$
Tolerance	$\sim 5 \times 10^{-4}$	$\sim (0.02, 0.03)$	$\sim (0.003, 0.01)$ $\sim (50, 50) \mu\text{m}$

Similarly, a tolerance level can be specified for the residual Closed-Orbit Distortions at the sextupoles, which introduce beta and phase advance beats proportional to the sextupole gradients times the COD offset. This impact on the DA was simulated by introducing random transverse alignment errors to all the sextupoles and is shown in Figure 3.1.22 vs. the RMS error. At a level of  $\sigma_x = \sigma_y \sim 50 \mu\text{m}$ , the DA area is reduced by about 20%. These RMS values can be taken as the tolerance level for the misalignments and residual COD at the sextupoles that must be maintained by the global orbit correction system (see Table 3.1.7).

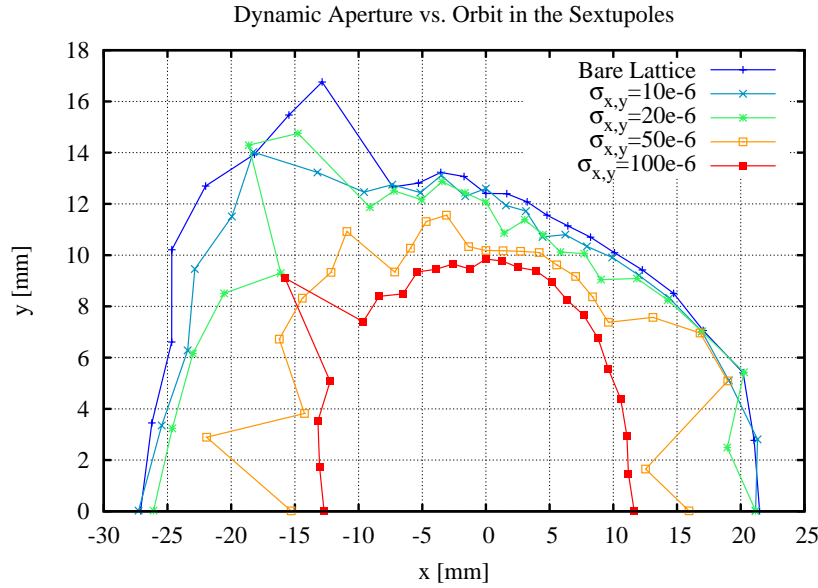


**Figure 3.1.22** DA sensitivity to transverse alignment errors of the sextupoles.

Correspondingly, the required transverse magnet alignment tolerances are summarized in Table 3.1.8, assuming the COD errors are corrected using the seven BPMs and seven correctors of the lattice. Details on the global orbit correction scheme are given in Section 3.1.2.5.

**Table 3.1.8** Transverse Magnet Alignment Tolerances.

	$\Delta x$ RMS [ $\mu\text{m}$ ]	$\Delta y$ RMS [ $\mu\text{m}$ ]	Roll RMS [m-rad]
Dipole	~100	~100	-0.5
Girder	~100	~100	-0.5
Quadrupoles	~30	~30	-0.2
Sextupoles	~30	~30	-0.2

The magnetic field error tolerances are specified in terms of the normal and skew multipole coefficients ( $b_n, a_n$ ), defined by the normalized transverse magnetic field expansion:

$$\frac{1}{(B\rho)} [B_x(x, y) + i B_y(x, y)] \equiv \sum_n (b_n + i a_n) (x + i y)^{n-1} = \sum_n (b_n + i a_n) e^{i(n-1)\phi} \quad (3.1-13)$$

where  $n=1,2,3,\dots$  are the dipole, quadrupole, sextupole, ... components, respectively.

In particular, the multipole errors,  $\Delta B_n^{(N)}$ , relative to the desired field component,  $b_N$ , are normalized at a reference radius  $R$  and defined by<sup>15</sup>

$$\Delta B_n^{(N)}(R) \equiv R^{n-N} \frac{\Delta b_n}{b_N} \quad \text{or} \quad \Delta A_n^{(N)}(R) \equiv R^{n-N} \frac{\Delta a_n}{b_N} \quad (3.1-14)$$

<sup>15</sup> Using the peak B-field for insertion devices.

where  $(\Delta b_n, \Delta a_n)$  are the multipole field errors.

The tolerances for the multipole errors are given in Table 3.1.9 using values achieved at the SLS facility [3.1.25, 3.1.26]. The impact is an additional  $\sim 20\%$  DA reduction for the lattice with the previously defined alignment tolerances. Future work will include parametric studies for a more precise specification.

**Table 3.1.9 Tolerance Levels for RMS Normalized Multipole Errors.**

Magnet Type	Normalized Field Error ( $R = 28$ mm)						
Quadrupoles	$\Delta B_2^{(2)}$	$\Delta B_3^{(2)}$	$\Delta A_3^{(2)}$	$\Delta B_4^{(2)}$	$\Delta A_4^{(2)}$	$\Delta B_6^{(2)}$	$\Delta B_{10}^{(2)}$
	$2.5 \times 10^{-4}$	$2.8 \times 10^{-4}$	$2.9 \times 10^{-4}$	$1.9 \times 10^{-4}$	$1.4 \times 10^{-4}$	$1.3 \times 10^{-4}$	$0.3 \times 10^{-4}$
Sextupoles	$\Delta B_3^{(3)}$	$\Delta B_4^{(3)}$	$\Delta A_4^{(3)}$	$\Delta B_5^{(3)}$	$\Delta B_9^{(3)}$	$\Delta B_{15}^{(3)}$	
	$5.0 \times 10^{-4}$	$5.2 \times 10^{-4}$	$4.9 \times 10^{-4}$	$3.5 \times 10^{-4}$	$0.8 \times 10^{-4}$	$0.5 \times 10^{-4}$	

Similarly challenging is the impact of the linear optics distortions from the insertion devices listed in Table 3.1.10. In particular, the proposed superconducting undulators will substantially affect the nonlinear dynamics in the vertical plane due to their short period (see Section 3.1.2.8). The effect of elliptically polarized undulators on the DA remains to be studied. Table 3.1.11 lists the allowed multipole field tolerances for these undulators [3.1.27]. The potential configuration includes the following IDs:

- CPMUs in the 6 m straights
- CPMUs in the 9 m straights
- DWs in the 9 m straights
- EPUs in the 6 m straights<sup>16</sup>

Details on the impact of these insertion devices and the control of their nonlinear terms are presented in Section 3.1.2.8.

**Table 3.1.10 Insertion Device Parameters and Their Impact on the Vertical Tune.**

ID	$\lambda_u$ [mm]	B [T]	$K_u$	$L_u$ [m]	Gap [mm]	$\Delta v_y$
SCU (2+1)	14	1.7	2.2	2	-5	0.002
CPMU (3)	19	1.24	2.2	3	5	0.002
DW	100	1.8	16.8	7	-11	0.028
EPU	$\sim 40$	0.88	(3.3, 3.3)	$\sim 4$	$\sim 6.5$	TBD

<sup>16</sup> Presumably as  $2 \times 1$  m canted devices.

**Table 3.1.11 RMS Normalized Field Errors for Insertion Devices (CPMU,  $R = 20$  mm).**

Multipole	$\Delta B_3^{(1)}$	$\Delta A_3^{(1)}$	$\Delta B_4^{(1)}$	$\Delta A_4^{(1)}$
Random	$6.6 \times 10^{-7}$	$6.6 \times 10^{-7}$	$2.2 \times 10^{-8}$	$2.2 \times 10^{-8}$

Note: Based on tolerances from the Swiss Light Source.

### 3.1.2.5 Control of Closed-Orbit Distortions (“Golden Orbit” philosophy)

While essentially a linear problem, effective orbit control is crucial for robust DA<sup>17</sup> and orbit stability. From a DA point of view, the main objective for the global orbit correction system is to establish and maintain an orbit at the magnetic centers of the sextupoles (to avoid breaking the symmetry of the linear optics), to within  $\sim 50 \mu\text{m}$  (Table 3.1.7). As a rough guideline, the BPMs should be spaced by  $\sim 90^\circ$  in phase advance and placed close to the sextupoles. With a horizontal DBA cell tune of  $\sim 1.1$ , about six BPMs per cell should provide good coverage. In order to center the orbit in all the BPMs, one corrector for each BPM is needed. In theory, the DA can be restored if the BPM is at the sextupole magnetic center [3.1.6]. The number of correctors can be reduced in the vertical plane, since the cell tune is only  $\sim 0.5$ . From the horizontal phase advance (Figure 3.1.23), it is clear that at least one BPM is required in each of the dispersive and straight sections.

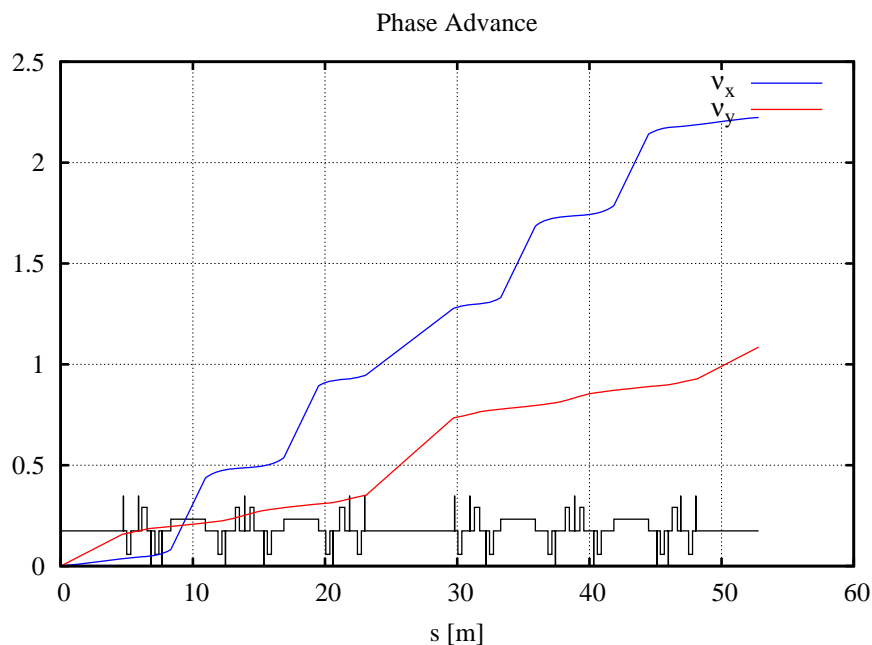


**Figure 3.1.23** Normalized Phase Advance for one super-period.

Figures 3.1.24 a and b show the corrected horizontal and vertical RMS closed-orbit distortions (for 1,000 seeds) due to  $100 \mu\text{m}$  RMS random horizontal and vertical quadrupole misalignment errors, with the (H-BPM $\times$ H-Corrector, V-BPM $\times$ V-Corrector) = (6 $\times$ 6, 6 $\times$ 6) baseline configuration. Clearly, the resulting orbit is well within the guidelines of Table 3.1.7. BPM buttons are included at the center of each DBA for optics checks during commissioning. Beam-based alignment [3.1.29, 3.1.30] with BPMs at the end of the girders

<sup>17</sup> To avoid the collapse of DA observed in the ALS CDR [3.1.26], eventually addressed by “Global Matching of the Normalized Ring” [7.1.10–7.1.15].

will make it possible to reduce orbit errors below the survey and alignment tolerances for the girders, particularly since the alignment tolerances for the magnetic centers on the girders are tighter than the girder alignment in the tunnel.

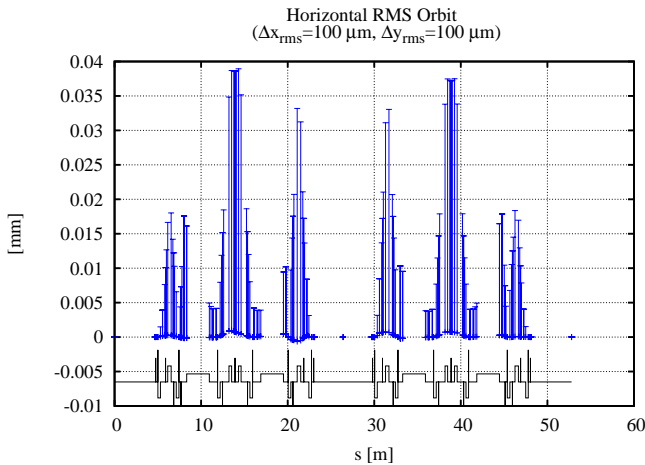


**Figure 3.1.24 a** Corrected horizontal RMS COD (over 1,000 seeds) for one super-period.

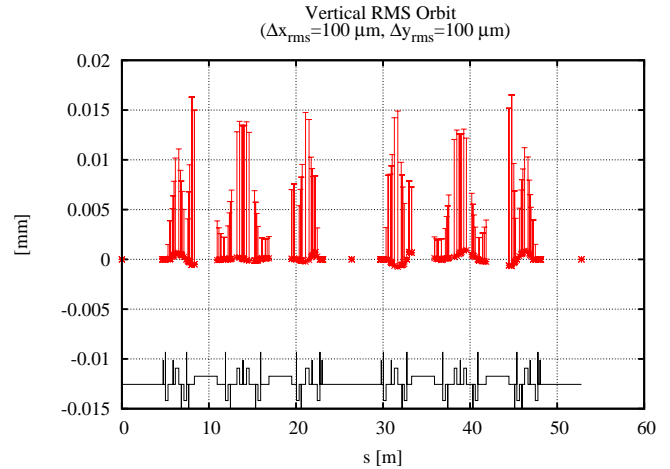


**Figure 3.1.24 b** Corrected vertical RMS COD (over 1,000 seeds) for one super-period.

Although placing the BPMs close to the sextupoles reduces the residual COD at the sextupoles, the BBA resolution is better for quadrupole centering ( $<10 \mu\text{m}$  both H and V) by at least a factor of three [3.1.27, 3.1.28]. This allows for orbit centering beyond the magnet alignment tolerance on the girder. Therefore, we have adopted the  $(6 \times 6, 6 \times 6)$  correction scheme, with the BPMs close to the quadrupoles for BBA with a resolution of  $10 \mu\text{m}$ . The impact on the DA of the corrected COD resulting from the alignment tolerances<sup>18</sup> listed in Table 3.1.8 is shown in Figure 3.1.25 (for 20 random seeds). Clearly the  $(6 \times 6, 6 \times 6)$  orbit correction system provides adequate DA, and provides margin for error.

<sup>18</sup> Except for roll errors, to be treated later.



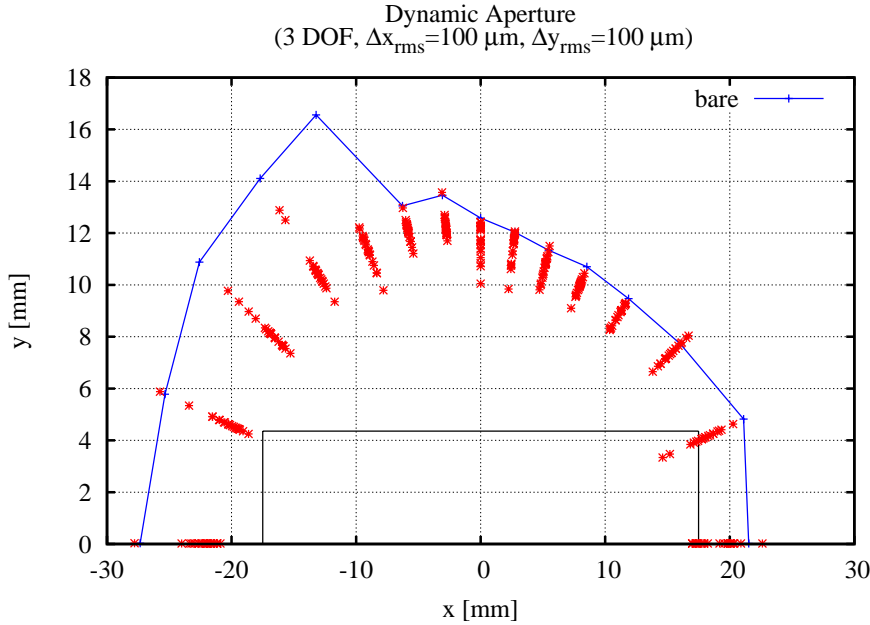


**Figure 3.1.25** DA for lattice with transverse misalignment errors (20 seeds), according to Table 3.1.8. These CODs are corrected with the baseline (6×6, 6×6) system.

### 3.1.2.6 Control of Vertical Beamsize

The vertical beamsize is given by

$$\sigma_y = \sqrt{\beta_y \varepsilon_y + (\eta_y \sigma_\delta)^2} \quad (3.1-15)$$

where  $\beta_y$  and  $\eta_y$  are the vertical beta function and dispersion,  $\varepsilon_y$  is the vertical emittance, and  $\sigma_\delta$  is the momentum spread. The design goal is  $\varepsilon_y \sim 0.01$  nm-rad, corresponding to  $\sigma_y \sim 5 \mu\text{m}$  in the short straights.

The non-vanishing vertical emittance originates from:

- linear coupling of the horizontal emittance due to roll errors of the quadrupoles and vertical orbit displacement in the sextupoles,
- and vertical dispersion due to roll errors of the dipoles and linear coupling of the horizontal dispersion.

Local control of the vertical beamsize is straightforward. In particular, by controlling the off-diagonal beam response matrix elements given by [3.1.29]:

$$\frac{\partial y_k}{\partial p_{x,i}} = -\frac{(\Delta a_2 L)_j \sqrt{\beta_{x,i} \beta_{x,j} \beta_{x,k}} \cos(\mu_{x,i \rightarrow j} - \pi \nu_x) \cos(\mu_{y,j \rightarrow k} - \pi \nu_y)}{4 \sin(\pi \nu_x) \sin(\pi \nu_y)} + O(\Delta a_2 L)^2, \quad (3.1-16)$$

$$\frac{\partial x_k}{\partial p_{y,i}} = -\frac{(\Delta a_2 L)_j \sqrt{\beta_{y,i} \beta_{y,j} \beta_{y,k}} \cos(\mu_{y,i \rightarrow j} - \pi \nu_y) \cos(\mu_{x,j \rightarrow k} - \pi \nu_x)}{4 \sin(\pi \nu_x) \sin(\pi \nu_y)} + O(\Delta a_2 L)^2$$

for a dipole kick,  $p_{(x,y),i}$  at  $i$ , due to a skew quadrupole ( $a_2 L$ ) at  $j$  produces an orbit change ( $\Delta x_k, \Delta y_k$ ) at a BPM located at  $k$ . Similarly, the local control of the vertical dispersion is done by:

$$\Delta\eta_{y,k} = -\frac{(\Delta a_2 L)_j \eta_{x,j} \sqrt{\beta_{y,j} \beta_{x,k}} \cos\left(\mu_{x,j \rightarrow k} - \pi\nu_x\right)}{2 \sin(\pi\nu_y)} + O(\Delta a_2 L)^2. \quad (3.1-17)$$

The driving term for the linear coupling is shown in Figure 3.1.26, whereas the driving term for vertical dispersion is similar to the one for vertical linear chromaticity, (Figure 3.1.7). Adequate control is obtained by introducing one skew quadrupole:

- in each long matching section
- in one of the dispersion cells for each super-period

for a total of  $15 + 15 = 30$  skew quadrupoles for the full lattice. The corresponding (linear) system of equations

$$\left[ \frac{\partial \bar{x}}{\partial \bar{p}_y}, \frac{\partial \bar{y}}{\partial \bar{p}_x}, \Delta \bar{\eta}_y \right]^T = S \cdot (\Delta a_2 L) \quad (3.1-18)$$

was solved in a least-square sense by the Singular Value Decomposition method. The vertical dispersion after correction for the coupling introduced by the roll errors in Table 3.1.8, is shown in Figure 3.1.27. It turns out that the vertical emittance can be corrected significantly below  $\varepsilon_y \sim 0.01$  nm-rad. To optimize the Touschek lifetime, a vertical dispersion wave<sup>19</sup> is introduced to obtain the desired vertical beamsizes, e.g.,  $\eta_y = 5$  mm  $\Rightarrow \sigma_y \sim \eta_y \sigma_\delta = 5$   $\mu$ m (Figure 3.1.28). Similarly, the vertical beam size and the transverse coupling angle is shown in Figures 3.1.29 and 3.1.30, respectively. Since it is straightforward to measure the beam response matrix and vertical dispersion on the real storage ring, the correction algorithm implemented for this simulation will eventually be used for commissioning as well.

---

<sup>19</sup> To avoid affecting the dynamics 0.

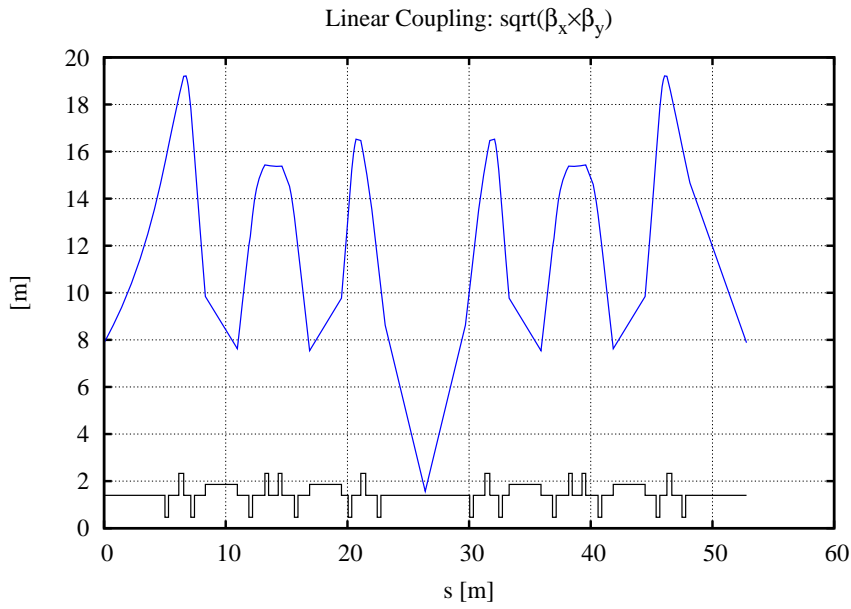


**Figure 3.1.26** Driving term for linear coupling, for one super-period.

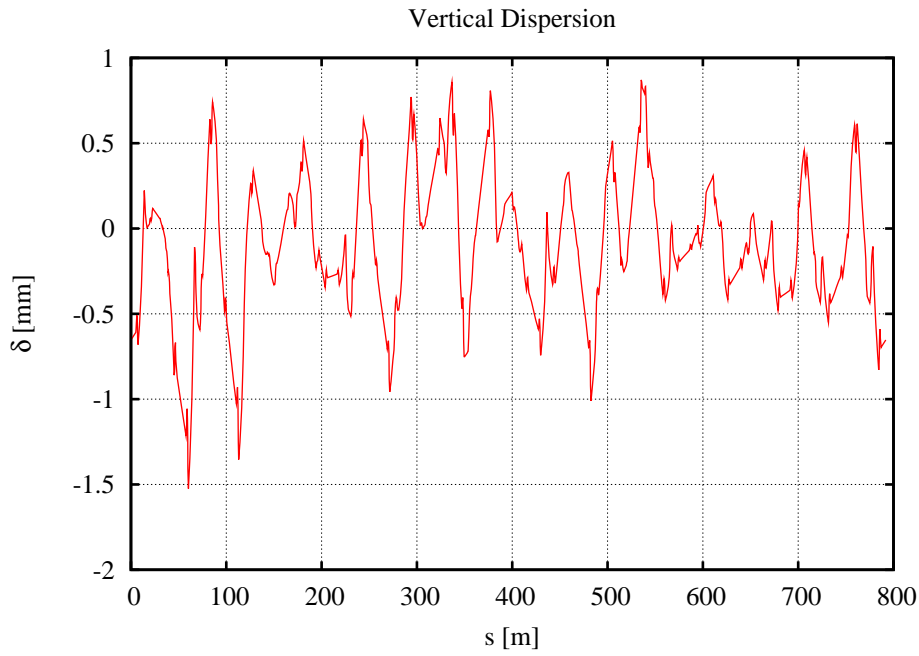


**Figure 3.1.27** Corrected vertical dispersion for the quadrupole and dipole roll tolerances.

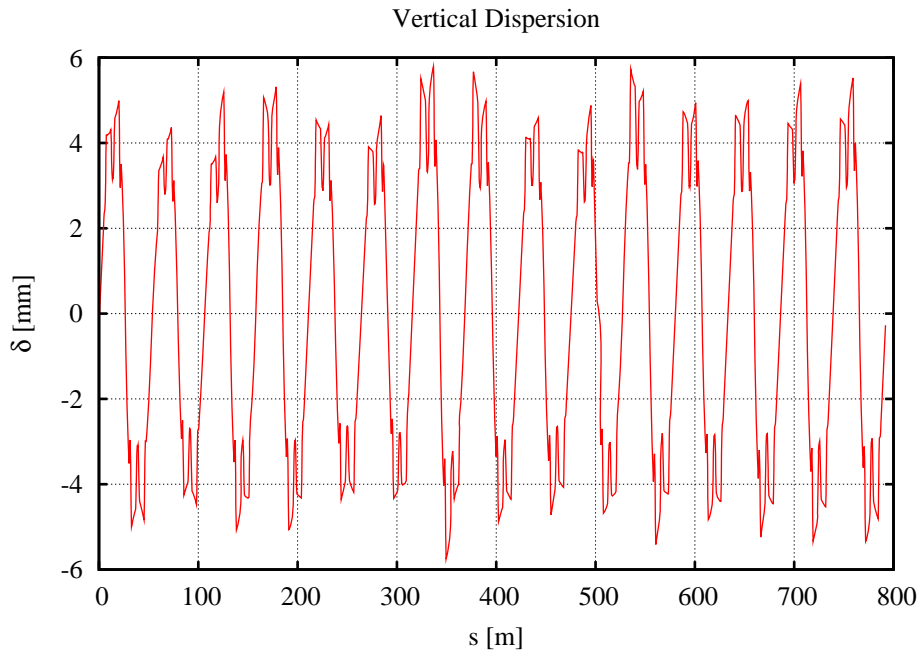


**Figure 3.1.28** Corrected vertical dispersion with a residual 5 mm dispersion wave for vertical beamsize control.

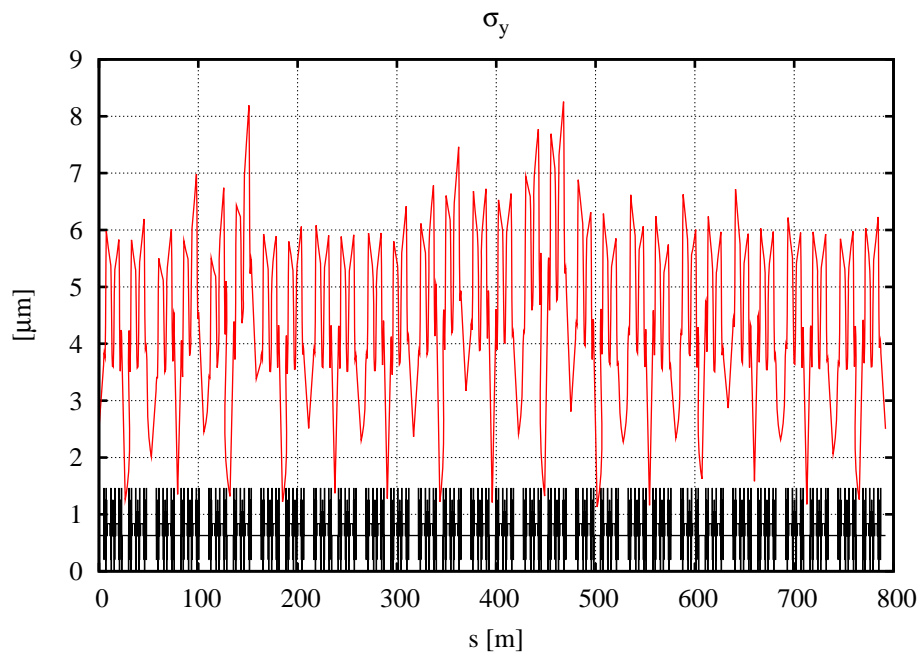


**Figure 3.1.29** Vertical beam size with a residual 5 mm dispersion wave.

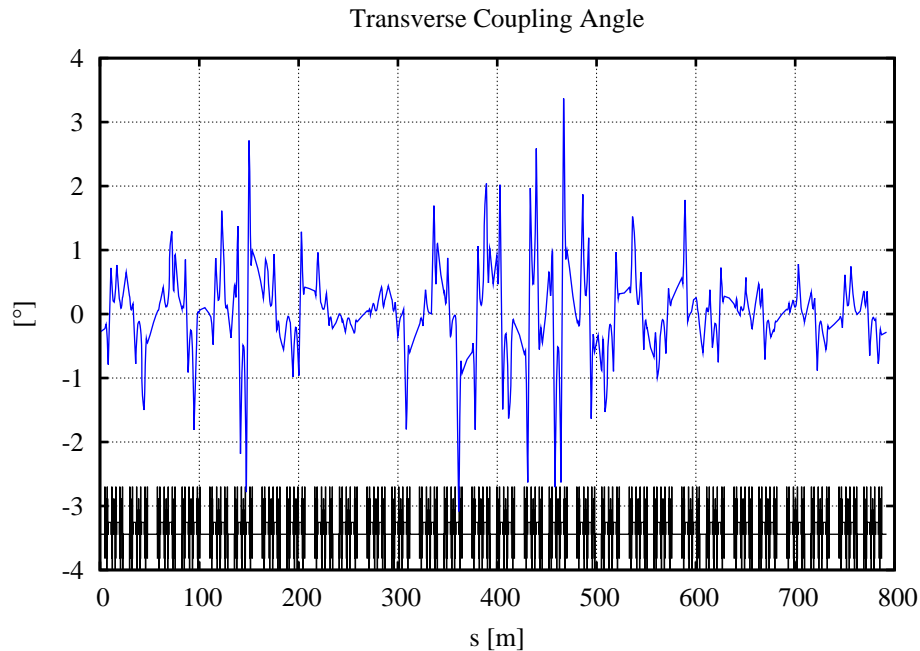


**Figure 3.1.30** Transverse coupling angle around the ring with a residual 5 mm dispersion wave.

### 3.1.2.7 Robustness of DA

The introduction of alignment errors in the lattice leads to orbit distortions, which generate magnetic field errors due to feed-down in the multipoles. These errors are summarized in Table 3.1.12. A robust DA requires that the global orbit correction system maintains the orbit centered in the sextupoles, since feed-down leads to gradient errors. To correctly evaluate this impact, correlations between magnet-magnet alignment errors, e.g., from girder misalignments, need to be included. Also, real magnets are not pure dipoles, quadrupoles, or sextupoles, requiring systematic and random multipole errors to be included. A detailed study of the individual maximum tolerance levels of these multipole errors remains to be done, but the realistic values listed in Table 3.1.9 have been used to evaluate the impact on the DA.

**Table 3.1.12** Effect of Mechanical Tolerances on the Magnetic Field Quality.

	Dipole	Quadrupole	Sextupole
Horizontal orbit		horizontal dipole error	gradient error
Vertical orbit		vertical dipole error	skew quadrupole error
Roll error	vertical dipole error	skew quadrupole error	skew sextupole error

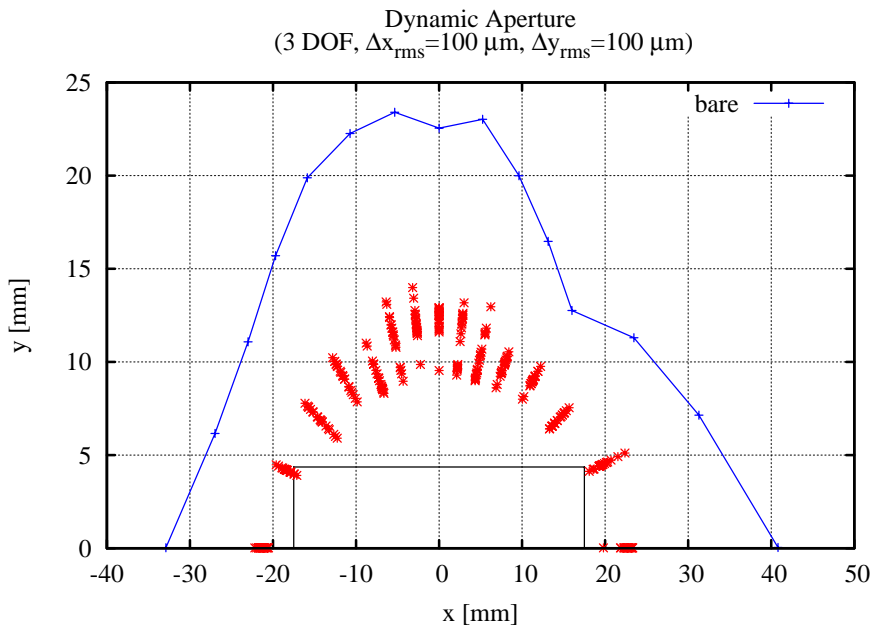
Also, due to the nonlinear chromaticity, tracking for at least one synchrotron oscillation period is required to obtain realistic estimates of the DA, since the off-momentum particle will be slowly crossing betatron resonances, which may limit the stability to smaller amplitudes. The design goal for the RF acceptance is  $\pm 3\%$ . To obtain a conservative estimate of the momentum aperture, an RF voltage sufficient to produce a 4% bucket height was used to evaluate the DA. The impact on the DA and momentum aperture is shown in Figures 3.1.31 – 3.1.33, where the black-outlined rectangle (Figure 3.1.31) represents the physical aperture of the lattice, propagated to the center of the long straight section. The 20 seeds shown represent 20 lattices generated with randomly distributed alignment and multipole errors having RMS values given by the tolerance values and corrected for COD, as described above. The tracked particles undergo synchrotron oscillations, but do not radiate. Since the radiation damping will also lead to the crossing of resonances, it should also be included in refined studies.

Low-emittance lattices tend to have a small linear momentum compaction,  $\alpha_1$ , requiring the second-order term,  $\alpha_2$ , to be included for a proper evaluation of the RF bucket, which becomes distorted and reduces the momentum acceptance [3.1.31]. The source of this distortion is a second stable fixed point, which has an energy offset given by the ratio:

$$\alpha_1/\alpha_2 \approx 3.7 \times 10^{-4} / 4.1 \times 10^{-4} = 92\%. \quad (3.1-19)$$

Since it only becomes important for ratios  $<20\%$ , it will not pose a problem for this lattice<sup>20</sup>. This is further demonstrated by the phase space for the longitudinal Hamiltonian (shown in Figure 3.1.34), including terms to  $\alpha_3$ , as well as the radiation loss of 35 m of damping wigglers.

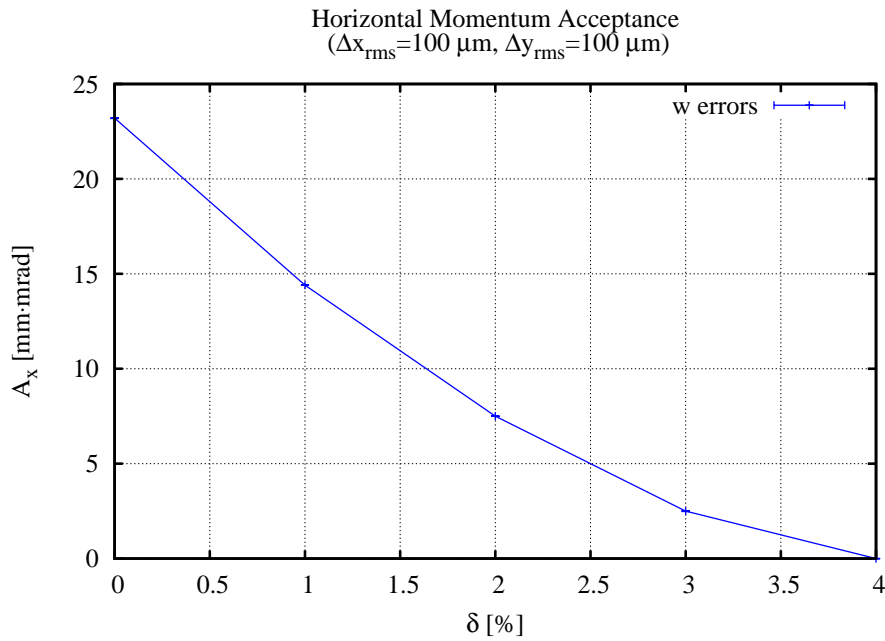
To summarize, the DA guidelines from Table 3.1.5 are easily met for the bare lattice, as well as when the impact of realistic alignment and field tolerances, listed in Tables 3.1.8 and 3.1.9, are included in the lattice model using the correction schemes described above.



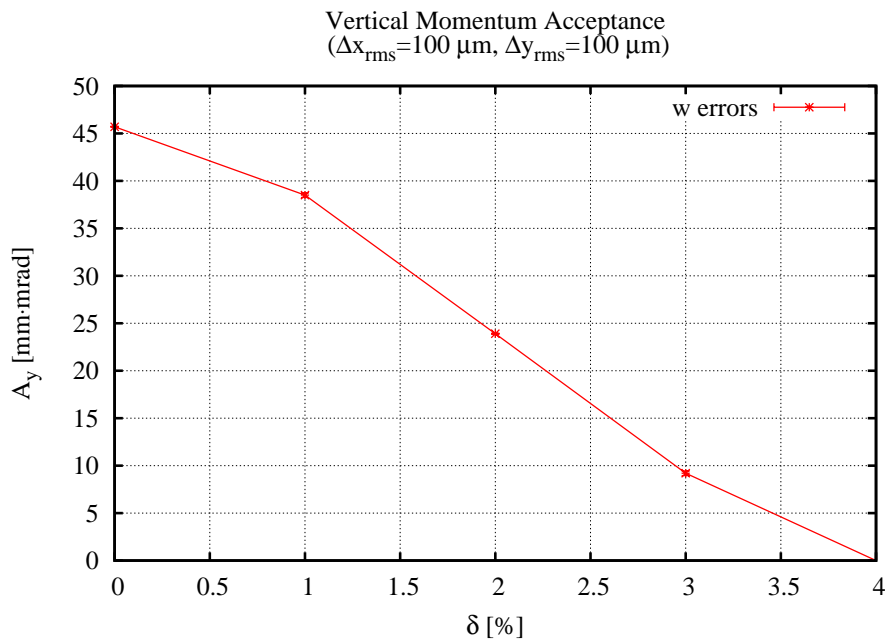
**Figure 3.1.31**  $DA^{21}$  for a “realistic” lattice (20 seeds) with engineering tolerances and corrections. The black outline indicates the physical aperture.

<sup>20</sup> An advantage of the achromatic straights for the DBA lattice.

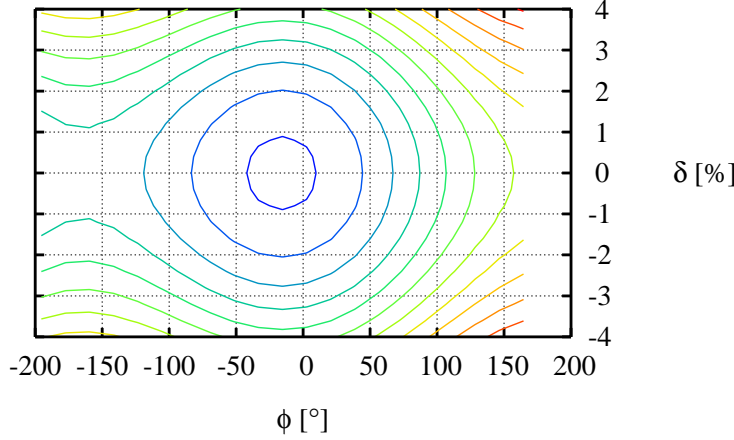
<sup>21</sup> The relatively large drop to  $x, y \approx [22, 12]$  mm is due to the crossing of  $\nu_x = 33, 4\nu_y = 63$  at these amplitudes, see Figures 6.1.6 and 6.1.7.



**Figure 3.1.32** Average and RMS horizontal momentum acceptance for a “realistic” lattice (20 seeds) with engineering tolerances and corrections.



**Figure 3.1.33** Average and RMS vertical momentum acceptance for a “realistic” lattice (20 seeds) with engineering tolerances and corrections.

Longitudinal Phase Space to  $O(\alpha_4)$ 

**Figure 3.1.34** Longitudinal phase-space, including the radiation loss from damping wigglers.

### 3.1.2.8 Control of Impact from Insertion Devices

The Hamiltonian for an ID averaged over one undulator period,  $\lambda_u$ , is given by [3.1.36, 3.1.37]:

$$\langle H \rangle_{\lambda_u} \approx \frac{p_x^2 + p_y^2}{2(1 + \delta)} - \frac{B_u^2 y^2}{4(B\rho)^2(1 + \delta)} + \frac{\pi^2 B_u^2 y^4}{3(B\rho)^2 \lambda_u^2 (1 + \delta)} - \delta + O(p_{x,y}^4) \quad (3.1-20)$$

with phase-space coordinates  $\bar{x} = [x, p_x, y, p_y, \delta, c\Delta t]$ , peak field  $B_u$ , and magnetic rigidity  $(B\rho)^{22}$ . Note that both the leading-order linear and nonlinear effect scales with  $1/(B\rho)^2$ , i.e., the effect is reduced with the energy squared for a given undulator field,  $B_u$ . The term quadratic in  $y$  introduces a vertically focusing term with the integrated gradient

$$(b_2 L) \approx -\frac{B_u^2 L_u}{2(B\rho)^2} \quad (3.1-21)$$

i.e., quadratic in  $B_u$ . The beta-beat at location  $i$  due to integrated quadrupole kicks,  $(\Delta b_2 L)_j$ , is given by:

$$\frac{\Delta \beta_{(x,y),i}}{\beta_{(x,y),i}} = \sum_{j=1}^N \frac{(\Delta b_2 L)_j \beta_{(x,y),j} \cos\left(2\mu_{(x,y),i \rightarrow j} - 2\pi\nu_{(x,y)}\right)}{2 \sin(2\pi\nu_{(x,y)})} + O(\Delta b_2 L)^2 \quad (3.1-22)$$

where  $\beta, \mu, \nu$  are the beta functions, phase advance, and tune. Similarly, the phase-beat is given by:

<sup>22</sup>  $(B\rho) \approx 10.007$  T-m at 3 GeV.



$$\Delta\mu_{(x,y),i} = -\sum_{j=1}^N \frac{\text{sgn}(\mu_{(x,y),i \rightarrow j}) (\Delta b_2 L)_j \beta_{(x,y),j} \left( \sin(2\pi\nu_{(x,y)}) + \sin\left(2\mu_{(x,y),i \rightarrow j} - 2\pi\nu_{(x,y)}\right) \right)}{4\sin(2\pi\nu_{(x,y)})} + O(\Delta b_2 L)^2, \quad (3.1-23)$$

and the total tune shift is given by

$$\Delta\nu_{(x,y)} = \pm \frac{1}{4\pi} \sum_{j=1}^N (\Delta b_2 L)_j \beta_{(x,y),j} + O(\Delta b_2 L)^2. \quad (3.1-24)$$

The parameters for the proposed insertion devices are summarized in Table 3.1.10, and the impact of three DWs on the linear optics is shown in Figure 3.1.35, where the beta-beat is rather obvious.

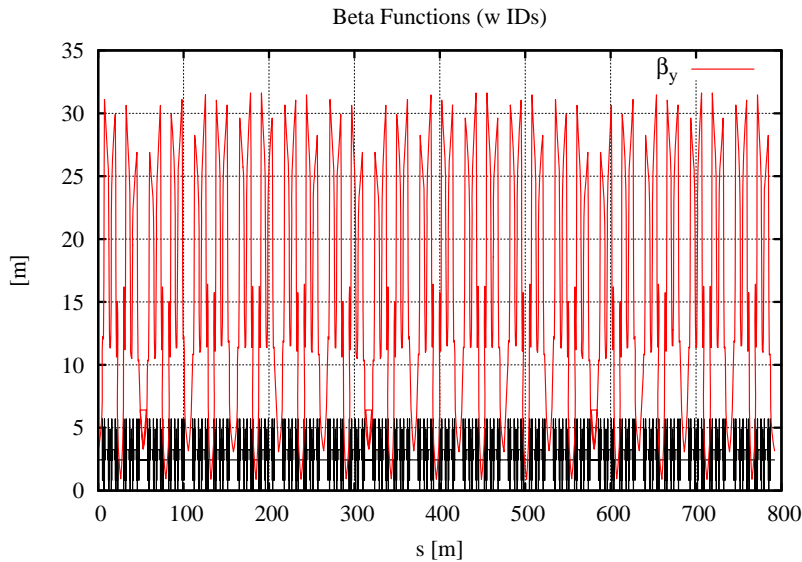


**Figure 3.1.35** Perturbed beta functions of the lattice with three DWs installed.

The perturbation of the optics is corrected by adjusting the quadrupole quadruplets in the matching sections. With four quadrupole strengths as parameters, it is expected<sup>23</sup> that the beta- and phase advance beat can be removed in both planes. In particular, the optics deviations at all of the lattice sextupoles,  $i$ , are represented in a linearized system of equations that includes the focusing impact of all installed IDs  $(\Delta b_2 L)_j$ . These equations are given in matrix form by

$$\left[ \begin{array}{c} \left( \frac{\Delta\beta_{(x,y)}}{\beta_{(x,y)}} \right)_i \\ \Delta\mu_{(x,y),i}, \Delta\nu_{x,y} \end{array} \right]^T = A \cdot [\Delta\bar{b}_2 L] \quad (3.1-22)$$

which was solved using an iterated SVD algorithm[3.1.34, 3.1.35], see Figure 3.1.36. The corrected beta and phase advance beats satisfy the optics tolerances specified in Table 3.1.7.

<sup>23</sup> If the parameters are independent.

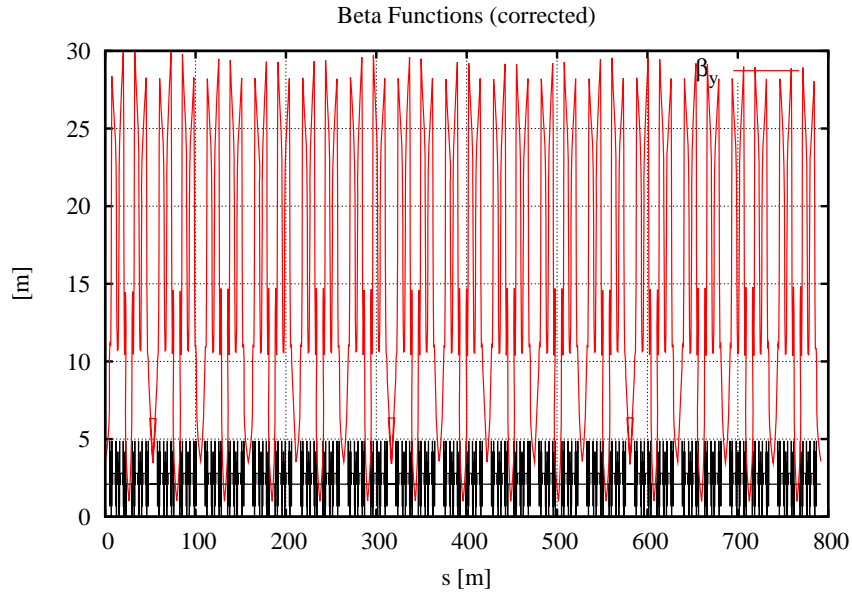


**Figure 3.1.36** Corrected beta functions for the lattice with three DWs installed.

The leading order nonlinear part of the ID focusing contains an octupole-like term in the vertical plane which drives amplitude dependent vertical tune shift and  $2\nu_y$  and  $4\nu_y$  resonances. Table 3.1.13 presents a comparison of the magnitude of the main driving terms from the IDs with those from sextupoles in the lattice. The choice of the length for the CPMUs have been validated by tracking, see Figure 3.1.37.

**Table 3.1.13** Lie Generators from the Sextupole Scheme and a Single ID.

Lie Generator	Effect	Sextupole Scheme	DW (Long Straight)	CPMU (Short Straight)	CPMU (Long Straight)	SCU (Short Straight)	SCW (Short Straight)
$ h_{00220} $	$\partial \nu_y / \partial J_y$	363	609	570	1,982	641	492
$ h_{00310} $	$2\nu_y$	22	72	22	976	163	251
$ h_{00400} $	$4\nu_y$	1	18	57	79	43	16

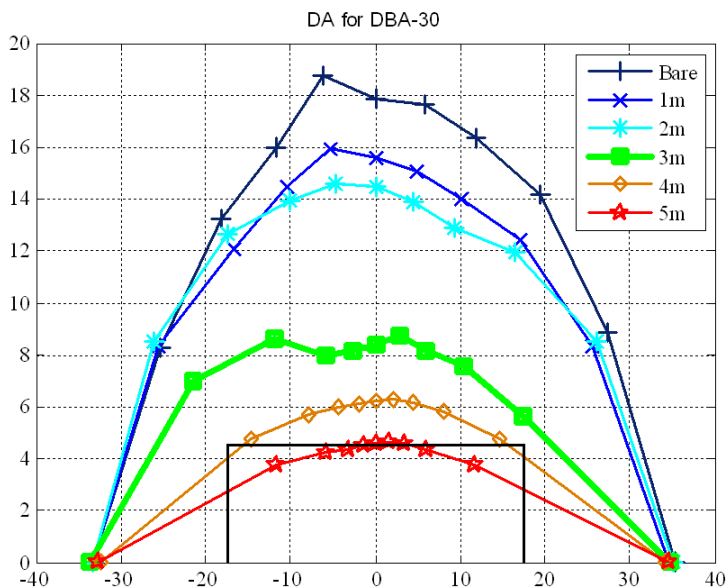


**Figure 3.1.37** Impact of the length of one CPMU on the DA.

The effects on the DA and momentum aperture of a lattice with errors and 3 DWs are shown in Figures 3.1.38 and 3.1.39, respectively. The DA is reduced in the vertical to the limited physical aperture. However, there is now considerable diffusion in the interior, which will require further study. Similarly, Figures 3.1.40 and 3.1.41 show the impact of three DWs and 15 CPMUs. Again, the DA is reduced in the vertical due to the reduced vertical aperture. Also, the impact of one APPLE-II EPU is shown in Figures 3.1.42 and 3.1.43. It is well known that the latter are strongly nonlinear devices, and while the dynamic aperture is maintained, control of the impact of these devices may require further work. However, we have now established a realistic (numeric approach) ID model, based on RADIA kick maps [3.1.40], from which it is straightforward to extract the driving terms (analytic approach). Moreover, pioneering work to control the dynamic terms with L-shims has been developed at the ESRF [3.1.41] and BESSY-2 [3.1.42]; guided by fitted generating function techniques.

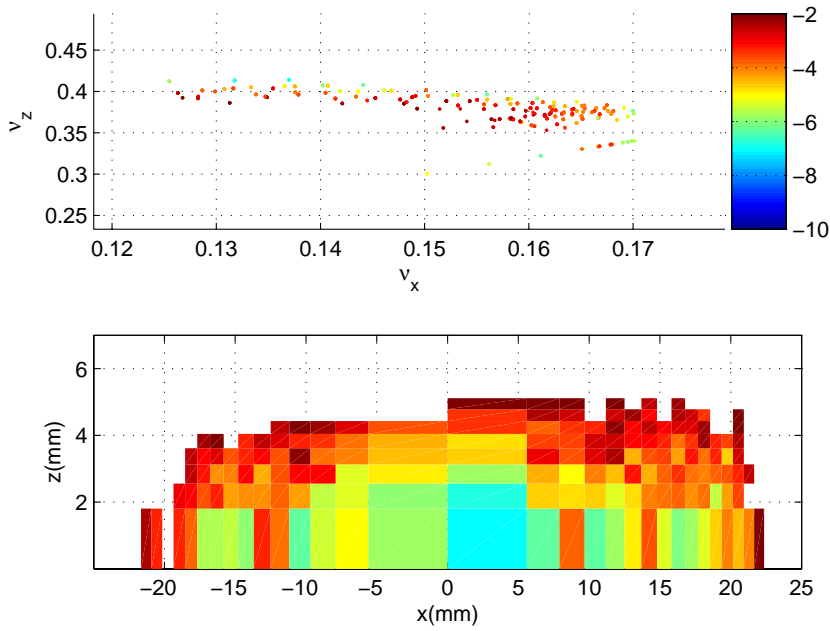


**Figure 3.1.38** Frequency map vs. transverse amplitudes for a lattice with three DWs and engineering tolerances.

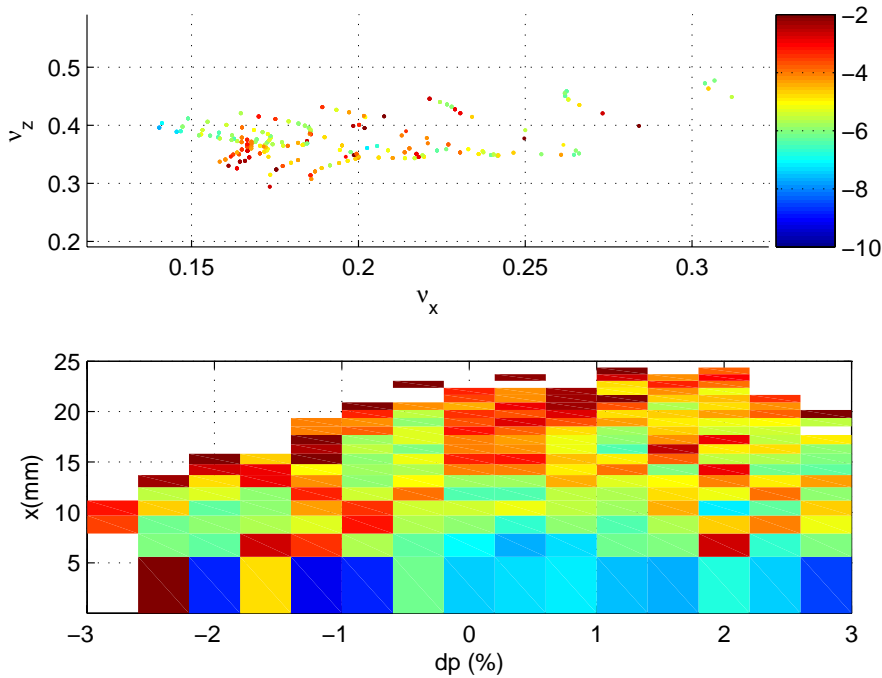


**Figure 3.1.39** Frequency map vs. momentum and horizontal amplitude for a lattice with three DWs, 15 CPMUs, and engineering tolerances.

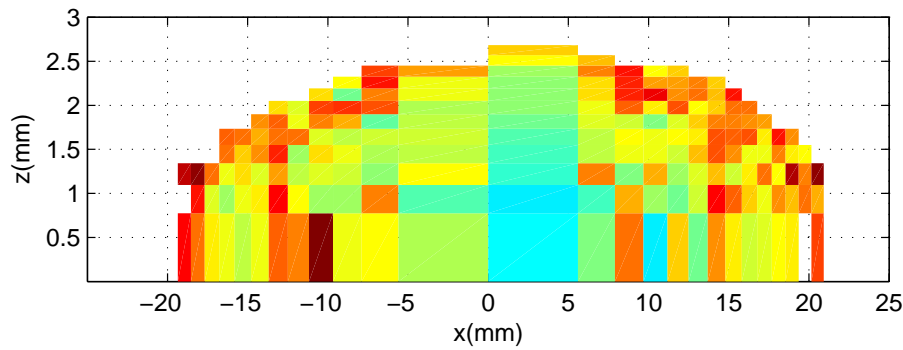
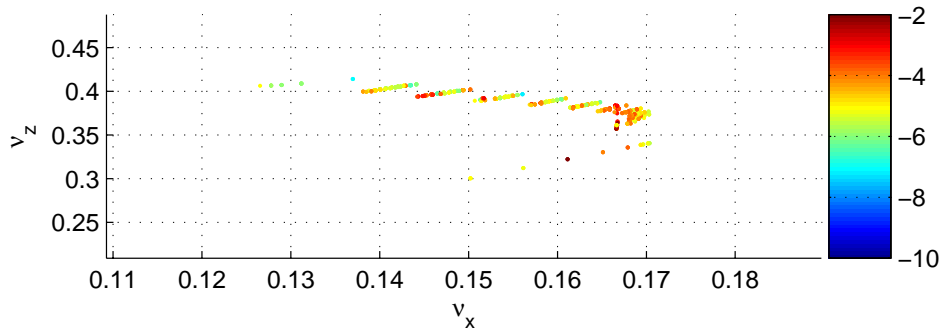


**Figure 3.1.40**  
Frequency map vs. momentum and horizontal amplitude for a lattice with three DWs, 15 CPMUs, and engineering tolerances.

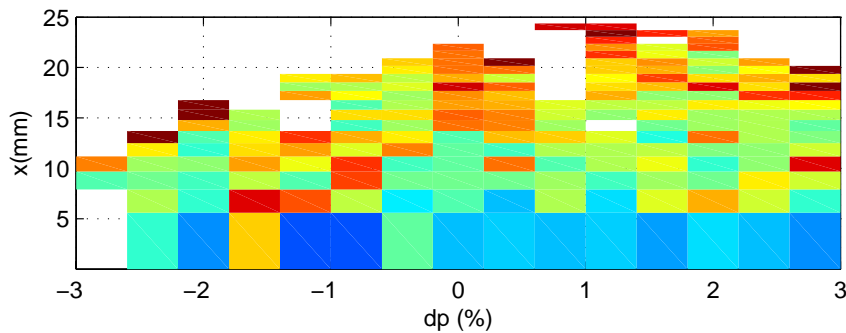
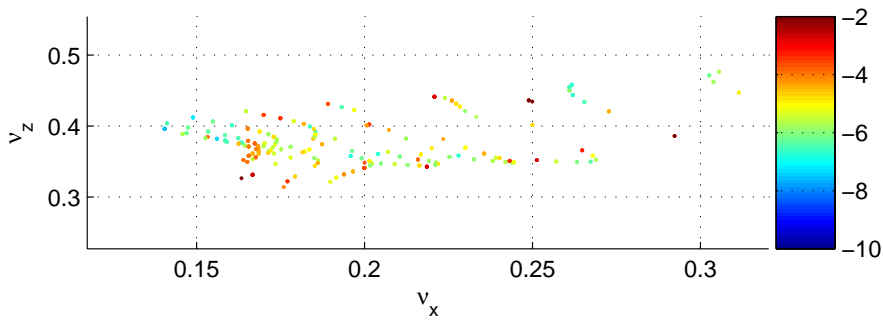


**Figure 3.1.41**  
Frequency map vs. momentum and horizontal amplitude for a lattice with three DWs, 15 CPMUs, and engineering tolerances.

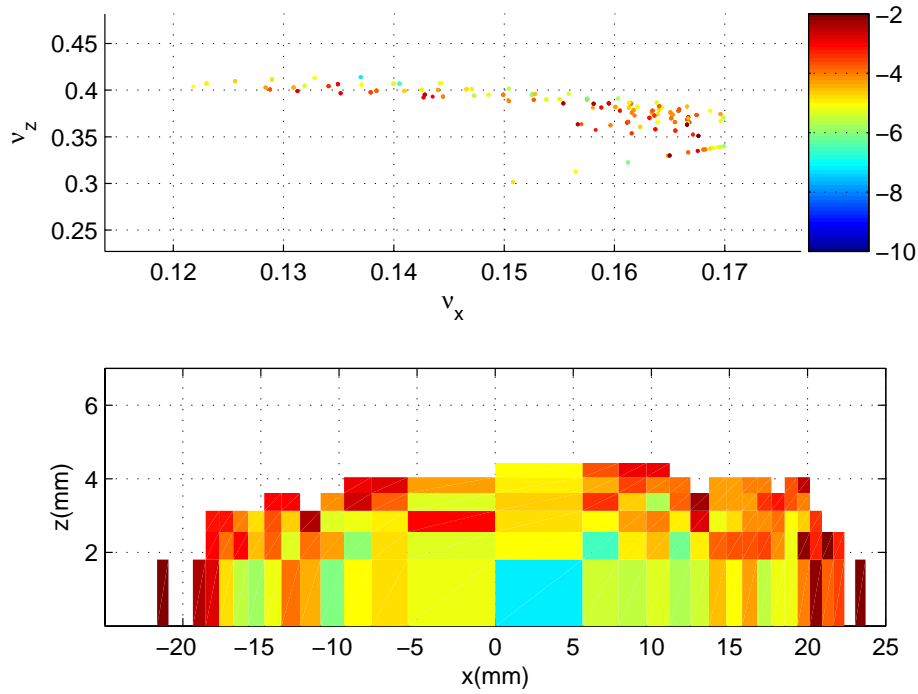


**Figure 3.1.42**  
 Frequency map vs. transverse amplitudes for a lattice w 1 EPU of APPLE-II type and engineering tolerances.

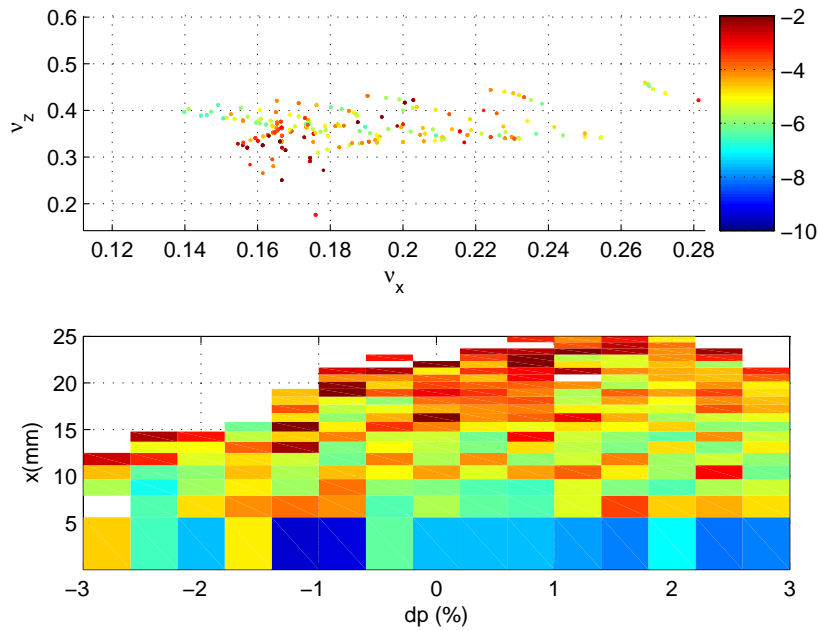


**Figure 3.1.43**  
 Frequency map vs. momentum and horizontal amplitude for a lattice w 1 EPU of APPLE-II type and engineering tolerances.

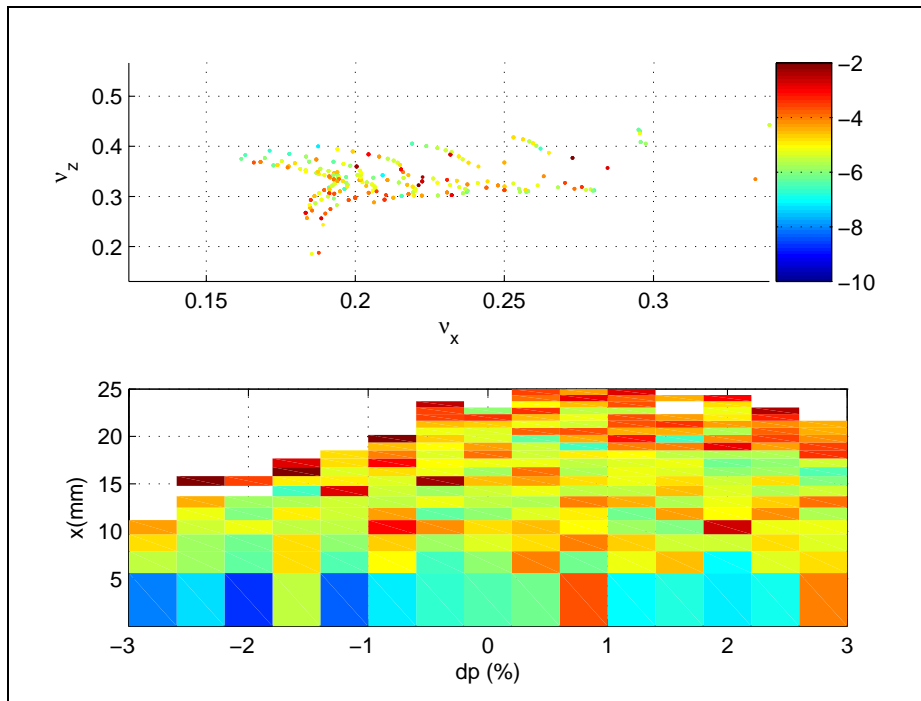


**Figure 3.1.43** Frequency map vs. momentum and horizontal amplitude for a lattice w 1 EPU of APPLE-II type and engineering tolerances.

### 3.1.2.9 Future Work in Lattice and Beam Dynamics Issues

The work presented here shows that the lattice is robust for the errors and realistic magnets. Moreover, that the main impact from the damping wigglers is the perturbation of the optics, which can be restored, and that the dynamic aperture remains outside the physical when 3 DWs and 15 CPMUs are included. However, fine tuning of the working point is required to reduce the considerable amount of tune shift, i.e., resonances, that are observed in the interior of the DA for a realistic lattice. And, to validate the performance with a full set of IDs.

### References

- [3.1.1] H. Weidemann, NIM **A266**, p. 24 (1988).
- [3.1.2] S. Krinsky, et. al., EPAC06, p.3487 (2006).
- [3.1.3] G. Decker, and O. Singh, *Phys. Rev. STAB* **2**, p. 112801 (1999).
- [3.1.4] S. Krinsky, J. Bengtsson, and S. Kramer, "Consideration of a Double Bend Achromatic Lattice for NSLS-II," pp. 3487–3489, EPAC06.
- [3.1.5] J. Bengtsson, "A Control Theory Approach for Dynamic Aperture," pp. 3478–3480, EPAC06.
- [3.1.6] J. Bengtsson, W. Joho, P. Marchand, G. Mülhaupt, L. Rivkin, and A. Streun, "Increasing the Energy Acceptance of High Brightness Synchrotron Light Storage Rings," *Nucl. Instr. Meth. A* **404**, 237–247 (1998).
- [3.1.7] A. Wrulich, et al., "Commissioning of the Swiss Light Source," pp. 224–226, PAC01.
- [3.1.8] A. Wrulich, et al., "Achievements of the SLS Commissioning," PSI. Scientific Report 2001 Vol. VII, 2002.
- [3.1.9] M. Böge, "Achieving Sub-Micron Stability in Light Sources," pp. 211–213, EPAC04.
- [3.1.10] J. Bengtsson, and E. Forest, "Global Matching of the Normalized Ring" Workshop on Effects of Errors in Accelerators, their Diagnosis and Corrections," Corpus Christi, TX, Oct. 3–8, 1991.
- [3.1.11] J. Bengtsson, and M. Meddahi, "Modeling of Beam Dynamics and Comparison with Measurements for the Advanced Light Source (ALS)," pp. 1022–1024, EPAC94.

- [3.1.12] D. Robin, G. Portmann, H. Nishimura, and J. Safranek, "Model Calibration and Symmetry Restoration of the Advanced Light Source," pp. 971–973, EPAC96.
- [3.1.13] J. Safranek, "Experimental Determination of Storage Ring Optics Using Orbit Response Measurements," *Nucl. Instr. and Meth. A* **388**, 27-36 (1997).
- [3.1.14] D. Robin, C. Steier, J. Safranek, and W. Decking, "Enhanced Performance of the Advanced Light Source through Periodicity Restoration of the Linear Lattice," pp. 136–138, EPAC00.
- [3.1.15] J. Laskar, L. Nadolski, D. Robin, and C. Steier, "Global Dynamics of the Advanced Light Source Revealed through Experimental Frequency Map Analysis," *Phys. Rev. Lett.* **85**, 558–561 (2000).
- [3.1.16] J. Bengtsson, "X-Ray Ring Optics: the Inverse Problem," NSLS Tech Note 540 (2005).
- [3.1.17] J. Bengtsson, "The Sextupole Scheme for the Swiss Light Source (SLS): An Analytic Approach," SLS Note 9/97 (1997).
- [3.1.18] A. Streun, J. Bengtsson, beam studies collaboration at the SLS, May 14-25, 2007.
- [3.1.19] Y. Luo, M. Bai, R. Calaga, J. Bengtsson, W. Fischer, N. Malitsky, F. Pilat, T. Satogata "Measurement and Correction of Third Resonance Driving Term in the RHIC.
- [3.1.20] Diamond Synchrotron Light Source: Report of the Design Specification," CCLRC (2002).
- [3.1.21] S.L. Kramer, S. Krinsky, and J. Bengtsson, "Comparison of Double Bend and Triple Bend Achromatic Lattice Structures for NSLS-II" pp. 384–386, EPAC06.
- [3.1.22] E. Forest "A Hamiltonian-Free Description of Single Particle Dynamics for Hopelessly Complex Systems" *J. Math. Phys.* **31**, pp. 1133-1144 (1990).
- [3.1.23] J. Bengtsson "The Poincaré Map, Lie Generator, Nonlinear Invariant, Parameter Dependence, and Dynamic Aperture for Rings" pp. 4315-4317, PAC07
- [3.1.24] J. Bengtsson, "On the NSLS-II Dynamic Aperture: Robustness," NSLS-II Tech Note 8 (2005).
- [3.1.25] A. Streun, "SLS Dynamic Acceptance Degradation due to Magnet Multipole Errors," SLS-TME-TA-1998-0002 (1998).
- [3.1.26] E.I. Antokhin, et al., "Multipoles of the SLS Storage Ring: Manufacturing and Magnetic Measurements," *IEEE Trans. of Appl. Super.* vol. 12, no. 1, 51–54 (2002).
- [3.1.27] J. Safranek, C. Limborg, A. Terebilo, K.I. Blomqvist, P. Elleaume, and Y. Nosochkov, "Nonlinear Dynamics in a SPEAR Wiggler," *Phys. Rev. ST* **5**, 010701 (2002).
- [3.1.28] C. Steier, G. Portmann, and A. Young, "Commissioning of the First Elliptically Polarizing Undulator at the ALS," pp. 2343–2345, EPAC00.
- [3.1.29] B. Singh, and A. Streun, "Limits for Normal and Skew Sextupole and Octupole Field Errors in the First ( $I_1$ ) and Second ( $I_2$ ) Field-Integrals of Insertion Devices planned for SLS," SLS-TME-TA-2001-0170 (2001).
- [3.1.30] "1-2 GeV Synchrotron Radiation Source Conceptual Design Report," LBNL PUB-5172 (1986).
- [3.1.31] G. Portmann, D. Robin, and L. Schachinger, "Automated Beam Based Alignment of the ALS Quadrupoles," pp. 2693–2695, EPAC96.
- [3.1.32] S.L. Kramer, "Beam Based Alignment," NSLS-II Tech Note (2006).
- [3.1.33] J. Bengtsson, and I. Pinayev, "NSLS-II: Control of Vertical Emittance," NSLS-II Tech Note (2006).
- [3.1.34] C. Steier, D. Robin, A. Wolski, G. Portmann, and J. Safranek, "Coupling Correction and Beam Dynamics at Ultralow Vertical Emittance in the ALS," pp. 3213–3215, PAC03.
- [3.1.35] D. Robin, E. Forest, C. Pellegrini, and A. Amiry, "Quasi-Isochronous Storage Rings," *Phys. Rev. E* **48**, 2149–2156 (1993).
- [3.1.36] L. Smith, "Effect of Wigglers and Undulators on Beam Dynamics" LBL-21391 (1986).
- [3.1.37] Y. Wu, V.N. Litvinenko, and J.M.J. Madey, "Lattice and Dynamic Aperture of the Duke FEL Storage Ring," pp. 218–220, PAC93.
- [3.1.38] T. Shaftan and J. Bengtsson, "Impact of Insertion Devices on the NSLS-II lattice," NSLS-II Tech. Note (2006).
- [3.1.39] T. Shaftan, J. Bengtsson, and S. Kramer, "Control of Dynamic Aperture with Insertion Devices" pp. 3490–3492, EPAC06.



- [3.1.40] P. Elleaume “A New Approach to the Electron Beam Dynamics in Undulators and Wigglers” pp. 661-663, EPAC92.
- [3.1.41] J. Chavanne, P. Van Vaerenbergh, P. Elleaume, T. Günzel, “Recent Achievements and Future Prospect of ID Activities at the ESRF” pp. 2346–2348, EPAC00.
- [3.1.42] J. Bahrtdt, W. Frentrup, A. Gaupp, M. Scheer, G. Wüstefeld “Dynamics Multipole Shimming of the APPLE Undulator UE112” pp. 941–943, PAC07.

## 3.2 Collective Effects

### 3.2.1 Introduction

In this section, we discuss the effect of multi-particle interactions [3.2.1] on the electron beam in the NSLS-II storage ring. The storage ring has 500 MHz RF and a revolution period of 2.6  $\mu$ s. The baseline design configuration corresponds to filling 80% (or 90%) of the RF buckets and leaving one or more gaps to allow for ion clearing. In this case we have  $M = 1040$  bunches, each containing  $N_e = 7.8 \times 10^9$  electrons ( $N_e e = 1.25$  nC) corresponding to a total average current  $I_{av} = MN_e e / T_0 = 500$  mA and a single-bunch current  $I_0 = N_e e / T_0 = 0.5$  mA. For an RMS bunch duration  $\sigma_t = 15$  ps, the peak bunch current is  $I_p = N_e e / \sqrt{2\pi}\sigma_t = 33$  A.

Limitations on the single bunch current result from the short-range wakefield (broadband impedance). The longitudinal microwave instability depends primarily on the impedance of the vacuum vessel. The transverse mode coupling instability depends on the resistive wall impedance and the geometric impedance due to changes in the vacuum chamber cross-section.

Limitations on the total average current arise from the long-range wakefield (narrowband impedance). The longitudinal coupled-bunch instability is predominantly driven by the longitudinal higher-order modes in the RF cavity. The transverse coupled-bunch instability is primarily due to the resistive wall and the transverse higher-order modes in the RF cavity.

The most accurate approach to estimating the instability thresholds for NSLS-II is to carry out computer simulation tracking studies using the wakefields determined by numerical calculations of the wakefield for each component comprising the storage ring. This is a large effort that is now underway. Here, we shall provide estimates of the instability thresholds using a simplified model of the ring impedance, which has been developed based on impedance calculations performed to-date and on the experience at existing storage rings [3.2.2], especially APS and ESRF. We also present results of impedance calculations obtained thus far using the electromagnetic simulation code GdfidL [3.2.3].

In addition to the wakefield effects mentioned above, we also discuss intrabeam scattering. We report estimates of the Touschek lifetime resulting from single scattering, and of the increase in emittance due to multiple scattering.

We plan to use third-harmonic Landau cavities to increase the bunch length and synchrotron tune spread. Lengthening the bunch will be useful in raising the longitudinal microwave instability threshold, increasing the Touschek lifetime and reducing the effect of intrabeam scattering on the emittance. Increasing the bunch length and synchrotron tune spread improves the effectiveness of positive chromaticity in raising the single and coupled bunch transverse instability thresholds. The beam dynamics issues involved in the operation of the Landau cavities will be addressed.

### 3.2.2 Wakefields and Impedance

We provide a short overview of wakefields and impedance [3.2.4, 3.2.5] to clarify the approach we plan to adopt. Consider a point charge  $q$  (the drive particle) traveling very close to the speed of light in the  $z$ -direction through a vacuum enclosure displaced from the design trajectory by  $\vec{r}_d$ . A unit test charge travels at a distance  $s$  behind the first (Figure 3.2.1) on a trajectory parallel to the  $z$ -axis but displaced by  $\vec{r}_t = (x, y)$ .

The change of momentum  $\Delta \vec{p}$  of the second particle, caused by the electromagnetic field of the first, is given by

$$\Delta \vec{p} = \int_{-\infty}^{\infty} dt \left[ \vec{E}(\vec{r}_t, z, t) + c \hat{z} \times \vec{B}(\vec{r}_t, z, t) \right]_{z=ct-s}. \quad (3.2-1)$$

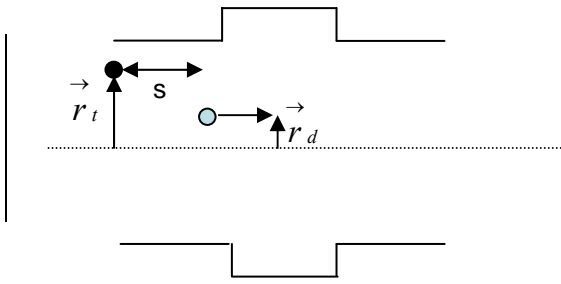


**Figure 3.2.1.** A drive particle  $d$  leading a test particle  $t$  through a vacuum structure.

For  $\vec{r}_t = \vec{r}_d = 0$ , we define the longitudinal wakefield  $w_{\parallel}(s)$  [volt/coul] by

$$w_{\parallel}(s) = -\frac{c}{q} \Delta p_z = -\frac{1}{q} \int_{-\infty}^{\infty} dz E_z \left( z, t = \frac{z+s}{c} \right), \quad (3.2-2)$$

and the longitudinal impedance  $Z_{\parallel}(k)$  [ohms] is determined by the Fourier transform,

$$Z_{\parallel}(k) = \int_{-\infty}^{\infty} \frac{ds}{c} w_{\parallel}(s) e^{iks}. \quad (3.2-3)$$

For a Gaussian bunch containing  $N_e$  electrons, the energy loss is  $\Delta E = \kappa_{\parallel} (eN_e)^2$  and the power loss is  $P = \kappa_{\parallel} I_0^2 T_0$ , where the energy loss factor  $\kappa_{\parallel}$  [V/C] is given by

$$\kappa_{\parallel} = \int_{-\infty}^{\infty} \frac{cdk}{2\pi} \text{Re} Z_{\parallel}(k) e^{-k^2 \sigma_s^2}. \quad (3.2-4)$$

The transverse wakefield [V/C-m] is

$$\vec{w}_{\perp} \left( s, \vec{r}_t, \vec{r}_d \right) = \frac{c}{q} \Delta \vec{p}_{\perp} = \frac{1}{q} \int_{-\infty}^{\infty} dz \left[ \vec{E}(\vec{r}, z, t) + c \hat{z} \times \vec{B}(\vec{r}, z, t) \right]_{t=\frac{z+s}{c}}. \quad (3.2-5)$$

The transverse impedance  $\vec{Z}_{\perp}$  [ $\Omega/m$ ] is determined by the Fourier transform,

$$\vec{Z}_{\perp}(\vec{r}_t, \vec{r}_d, k) = \frac{-i}{c} \int_0^{\infty} ds w_{\perp}(\vec{r}_t, \vec{r}_d, s) e^{iks}. \quad (3.2-6)$$

When the vacuum enclosure has reflection symmetry about the xz and yz planes, the transverse wakefield vanishes for  $\vec{r}_t = \vec{r}_d = 0$  and the first terms in a Taylor expansion yield [3.2.6],

$$w_x(s, x_t, x_d) \cong w_{Dx}(s) x_d + w_{Qx}(s) x_t \quad (3.2-7)$$

$$w_y(s, y_t, y_d) \cong w_{Dy}(s) y_d - w_{Qy}(s) y_t \quad (3.2-8)$$

where  $w_D$  is the dipole wakefield and  $w_Q$  is the quadrupolar wake. The dipole and quadrupolar impedances are determined by the Fourier transforms

$$Z_x(x_t, x_d, k) \cong Z_{Dx}(k) x_d + Z_{Qx}(k) x_t \quad (3.2-9)$$

$$Z_y(y_t, y_d, k) \cong Z_{Dy}(k) y_d - Z_{Qy}(k) y_t \quad (3.2-10)$$

The coherent betatron tune shift in a Gaussian bunch of  $N_e$  electrons produced by the transverse dipole impedance is approximately given by

$$\Delta \nu_{x,y} = \frac{e^2 N_e}{4 \pi E} \sum_j \beta_{x,y,j} \kappa_{x,y,j}, \quad (3.2-11)$$

where E is the electron energy and  $\beta_{x,y,j}$  is the average value of the betatron function at the  $j^{\text{th}}$  impedance element and  $\kappa_{x,y,j}$  [V/C-m] is the kick factor of the  $j^{\text{th}}$  element defined by

$$\kappa_{x,y,j} = \frac{c}{\pi} \int_0^{\infty} dk \text{Im} Z_{Dx,y,j}(k) e^{-k^2 \sigma_s^2}. \quad (3.2-12)$$

In a similar manner the quadrupolar impedance contributes to an incoherent tune spread. Some authors employ the effective impedance  $(Z_{x,y})_{\text{eff}}$  defined by

$$(Z_{x,y})_{\text{eff}} = \frac{\int_0^{\infty} dk Z_{Dx,y}(k) e^{-k^2 \sigma_s^2}}{\int_{-\infty}^{\infty} dk e^{-k^2 \sigma_s^2}} \quad (3.2-13)$$

The kick factor is related to the effective impedance by

$$\kappa_{x,y} = \frac{c}{2\sqrt{\pi}\sigma_s} \text{Im}(Z_{Dx,y})_{\text{eff}}. \quad (3.2-14)$$

To estimate instability thresholds, we use a model in which the impedance is comprised of a broadband resonator plus the resistive wall. The analytic forms for the wakefield and impedance of these elements are summarized in Table 3.2.1.

**Table 3.2.1 Analytic Expressions for Impedance and Wakefield.**

Resonator	
$Q' = \sqrt{Q^2 - 1/4} \quad k_r' = k_r Q' / Q$	
$w_{\parallel}(s) = \frac{ck_r R_s}{Q_s} \exp\left(-\frac{k_r s}{2Q_s}\right) \left[ \cos k_r' s - \frac{1}{2Q_s'} \sin k_r' s \right]$	$w_{\perp}(s) = \frac{ck_r R_{\perp}}{Q_{\perp}'} \exp\left(-\frac{k_r s}{2Q_{\perp}'}\right) \sin k_r' s$
$Z_{\parallel}(k) = \frac{R_s}{1 - iQ_s(k/k_r - k_r/k)}$	$Z_{\perp}(k) = \frac{k_r}{k} \frac{R_{\perp}}{1 - iQ_{\perp}(k/k_r - k_r/k)}$
$\kappa_{\parallel} = \frac{\omega_r R_s}{2Q_s} \quad (k_r \sigma_s \ll 1)$	$\kappa_{\perp} \cong \frac{1}{\sqrt{\pi}} \frac{c R_{\perp}}{Q_{\perp}} (k_r^2 \sigma_s) \quad (k_r \sigma_s \ll 1)$
$\kappa_{\parallel} = \frac{\omega_r R_s}{4\sqrt{\pi} Q_s^2 (k_r \sigma_s)^3} \quad (k_r \sigma_s \gg 1)$ $(Z/n)_0 = R_s (\omega_0 / \omega_r)$	$\kappa_{\perp} \cong \frac{c}{2\sqrt{\pi} \sigma_s} \frac{R_{\perp}}{Q_{\perp}} \quad (k_r \sigma_s \gg 1)$
Resistive Wall [3.2.7]	
$s_0 = (2b^2 / Z_0 \sigma_{\text{cond}})^{1/3}$	
$w_{\parallel}(s) \cong \frac{-cZ_0 L}{4\pi\sqrt{2\pi} b^2} \left(\frac{s_0}{s}\right)^{3/2} \quad (s \gg s_0)$	$w_{\perp}(s) \cong \frac{cZ_0 s_0 L}{2\pi b^4} \sqrt{\frac{2s_0}{\pi s}} \quad (s \gg s_0)$
$Z_{\parallel}(k) \cong \frac{(1-i)Z_0 s_0 L}{4\pi b^2} \sqrt{k s_0} \quad (0 \leq k \ll 1/s_0)$	$Z_{\perp}(k) \cong \frac{2}{kb^2} Z_{\parallel}(k) \quad (0 \leq k \ll 1/s_0)$
$\kappa_{\parallel} \cong 1.2 \frac{cZ_0}{4\pi} \frac{L}{2\pi b^2} \left(\frac{s_0}{\sigma_s}\right)^{3/2}$	$\kappa_{\perp} \cong 0.58 \frac{cZ_0}{4\pi} \frac{2s_0 L}{b^4} \sqrt{\frac{s_0}{\sigma_s}}$
Extreme Anomalous Skin Effect [3.2.8]	
$s_0 = (Bb)^{3/5} / \sin(\pi/10)$	
$B = 3^{1/6} 2^{-4/3} \pi^{-1/3} Z_0^{-1/3} (l / \sigma_{\text{cond}})^{1/3} \cong 3.9 \times 10^{-7} m^{2/3} \quad (\text{Cu @ 4 K, specular reflection})$	
$w_{\parallel}(s) \cong \frac{-2cB Z_0 L}{3\pi \Gamma(1/3)b} s^{-5/3} \quad (s \gg s_0)$	$w_{\perp}(s) \cong \frac{2cB Z_0 L}{\pi \Gamma(1/3)b^3} s^{-2/3} \quad (s \gg s_0)$
$Z_{\parallel}(k) \cong \frac{(1-\sqrt{3}i)B Z_0 L}{2\pi b} k^{2/3} \quad (0 \leq k \ll 1/s_0)$	$Z_{\perp}(k) \cong \frac{2}{b^2 k} Z_{\parallel}(k) \quad (0 \leq k \ll 1/s_0)$
$\kappa_{\parallel} = 0.16 \frac{cZ_0}{4\pi} \frac{L}{\pi b^2} \left(\frac{s_0}{\sigma_s}\right)^{5/3}$	$\kappa_{\perp} \cong 0.21 \frac{cZ_0}{4\pi} \frac{2s_0 L}{b^4} \left(\frac{s_0}{\sigma_s}\right)^{2/3}$

### 3.2.3 Estimates of Instability Thresholds

To estimate the instability thresholds, we considered an approximate model of the storage ring impedance, including the long-range wakefield due to the longitudinal and transverse higher-order modes in the CESR-B cavities. The storage ring vacuum chamber is approximated by 720 m of aluminum with a vertical half-aperture of 12.5 mm. We also included 20 in-vacuum undulators, each with 3 m copper chambers of vertical half-aperture 2.5 mm. The geometric impedance due to cross-section changes in the vacuum vessel is approximated by longitudinal and transverse broadband resonators. The parameters for the resonators are based on experience at other storage rings [3.2.2, 3.2.9], especially APS and ESRF, as well as on the impedance calculations we have performed to date. We believe the model is conservative and that it may be possible to build NSLS-II with lower impedance. The details of the impedance model are presented in Table 3.2.2, and some key parameters needed in the estimation of instability thresholds are given in Table 3.2.3.

**Table 3.2.2 Impedance Model.**

CESR-B cavity higher-order modes (see Tables 3.2.4 and 3.2.5.)	$\beta_x = 20m$
720 m of aluminum with half-gap of 12.5 mm and $\beta_{av} = 7.6$ m:	$\kappa_{\parallel} = 4.0V / pC$ $\kappa_y = 0.68KV / pC / m$
60 m of copper with half-gap of 2.5 mm and $\beta_{av} = 2$ m:	$\kappa_{\parallel} = 1.3V / pC$ $\kappa_y = 5.6KV / pC / m$
Transverse broadband impedance with $f_r = 30$ GHz, $R_y = 1$ M $\Omega$ /m, $Q_y=1$ , and $\beta_{av} = 7.6$ m $\kappa_y = 19KV / pC / m$	
Longitudinal broadband impedance with $f_r = 30GHz$ , $R_s = 30k\Omega$ ,	$(\text{Im}Z_{\parallel} / n)_0 = 0.4\Omega$ $\kappa_{\parallel} = 35V / pC$

**Table 3.2.3 Parameters for Threshold Calculations**

Energy, $E$ [GeV]	3
Revolution period, $T_0$ [ $\mu$ s]	2.6
Momentum compaction, $\alpha$	$3.7 \times 10^{-4}$
Energy loss, $U$ [keV]	1172
RF voltage, $V$ [MV]	3.7
Synchrotron tune, $\nu_s$	0.0094
Damping time: $\tau_x, \tau_s$ [ms]	13, 6.5
Energy spread, $\sigma_{\epsilon_0}$ [%]	0.09
Bunch duration, $\sigma_{t_0}$ [ps]	15

#### 3.2.3.1 Transverse Mode Coupling Instability (TMCI)

An approximate relation [3.2.10] determining the threshold of the TMCI at zero chromaticity is given by

$$\frac{\Delta v_y}{\nu_s} = \frac{eI_0^{th}}{2E\nu_s\omega_0} \sum_j \beta_{y_j} \kappa_{y_j} \cong 0.7, \quad (3.2-15)$$

where  $I_0^{th}$  is the threshold bunch current,  $\beta_{y_j}$  is the average value of the vertical beta function in the  $j^{th}$  element, and  $\kappa_{y_j}$  is its kick factor.  $E = \gamma mc^2$  is the electron energy and  $\nu_s$  is the synchrotron tune. Consider

a current of 0.5 mA bunch. Using the NSLS-II parameters as described in Table 3.2.3, we find that to be below the TMCI threshold requires

$$\sum_j \beta_{y_j} \kappa_{y_j} < 180 \text{ KV} / \text{pC} . \quad (3.2-16)$$

Using the values of the kick factors and beta functions as specified in Table 3.2.2, we find that  $\sum_j \beta_{y_j} \kappa_{y_j} = 160 \text{ KV} / \text{pC}$ . Therefore, 0.5 mA bunches are below the TMCI threshold for zero chromaticity.

### 3.2.3.2 Longitudinal Microwave Instability

At very low single-bunch current, the longitudinal density is determined by the equilibrium between radiation damping and quantum fluctuations. As the bunch current increases, the longitudinal charge distribution is modified by the wakefield. Below the threshold of the microwave instability, the energy distribution remains unchanged, and the longitudinal charge distribution  $f_0(\tau/\sigma_{\tau_0})$  is determined by the time-independent solution of the Haissinski equation [3.2.11],

$$f_0(q) = A \exp \left[ -\frac{1}{2} q^2 + S \int_q^\infty dq' \int_{q'}^\infty dq'' f_0(q'') w(q'' - q') \right], \quad (3.2-17)$$

where the constant A is chosen to satisfy the normalization

$$\int_{-\infty}^{\infty} dq f_0(q) = 1 \quad (3.2-18)$$

In the case of a broadband resonator with shunt impedance  $R_s$ , resonant frequency  $\omega_s$ , and quality factor  $Q_s = 1$ , the scaled current is defined by

$$S = \frac{e I_0 R_s \omega_r}{E_0 v_s \omega_0 \sigma_\varepsilon} \quad (3.2-19)$$

and

$$w(q) = \exp \left( -\frac{q \omega_r \sigma_{t_0}}{2} \right) \left[ \cos(q \omega_r \sigma_{t_0}) - \frac{1}{2\sqrt{0.75}} \sin(q \omega_r \sigma_{t_0}) \right]. \quad (3.2-20)$$

In Figure 3.2.2, we show the Haissinski distribution for bunch currents of 0.1 mA and 0.4 mA.

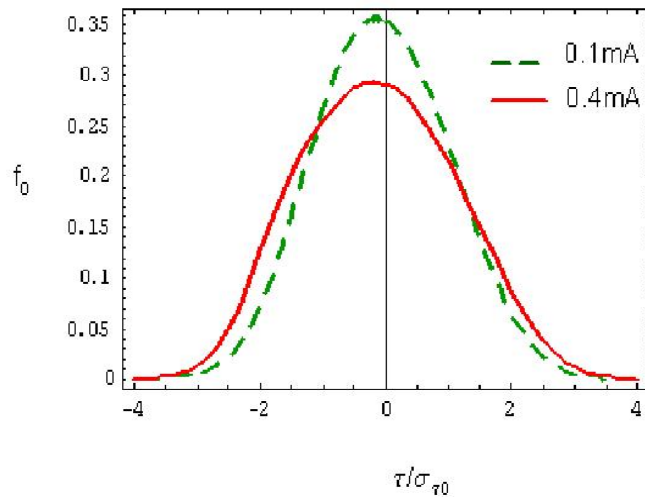


**Figure 3.2.2** Longitudinal distribution as determined from the Haissinski equations.

Once the current exceeds the microwave instability threshold, both the energy distribution and the charge distribution are modified and are no longer time-independent. In the case of a broadband resonator with shunt impedance  $R_s$ , resonant frequency  $\omega_s$ , and quality factor  $Q_s = 1$ , Oide and Yokoya [3.2.12] have shown that the single-bunch current threshold is given by

$$I_0^{th} = \frac{E v_s \sigma_\varepsilon}{e R_s (\omega_r / \omega_0)} S(\omega_r \sigma_{t_0}). \quad (3.2-21)$$

In Figure 3.2.3, we show the function  $S(\omega_r \sigma_{t_0})$  as determined by Oide and Yokoya (solid curve), and by tracking using the computer code ELEGANT [3.2.13] (symbols). A useful fit to the scaling function, in the regime  $x > 0.2$ , is given by

$$S(x) = 11 + 9.4(x - 0.7)^2. \quad (3.2-22)$$

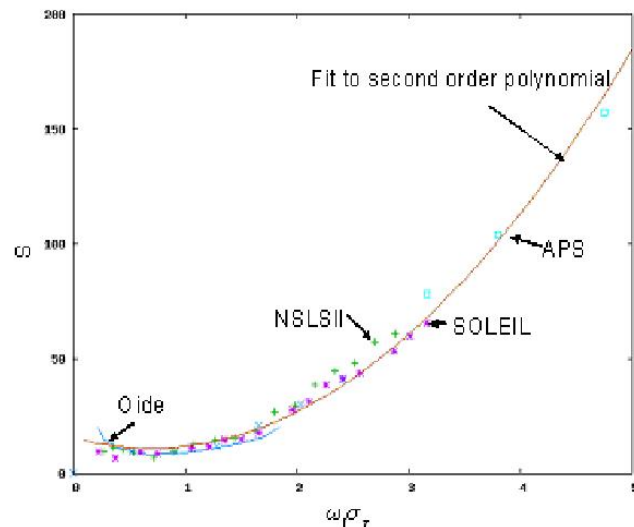


**Figure 3.2.3.** The scaling function  $S(\omega_r \sigma_{t_0})$  as determined by Oide and Yokoya (solid blue curve) and by tracking using ELEGANT (characters). The threshold is defined to be when the energy spread has increased by 5% over the zero current value.



In the limit when  $\omega_0 \sigma_{t0} \gg 1$ , the threshold condition becomes

$$I_0^{th} = 9.4 \frac{E v_s^2}{e \alpha (\text{Im} Z / n)_0} (\omega_0 \sigma_{t0})^3, \quad (3.2-23)$$

where  $(\text{Im} Z / n)_0 = R_s (\omega_0 / \omega_r)$ . This has the same form as the Boussard [3.2.14] criterion, except that in the Boussard case, the constant 9.4 is replaced by the smaller value  $\sqrt{2\pi}$ . The reason that the Boussard criterion gives too pessimistic a threshold is that it does not take into account the bunch lengthening due to potential well distortion.

In Figure 3.2.4, we show the dependence of the bunch length and the energy spread as calculated using the program ELEGANT. This shows that 0.5 mA bunches will suffer negligible increase in energy spread due to the longitudinal microwave instability.

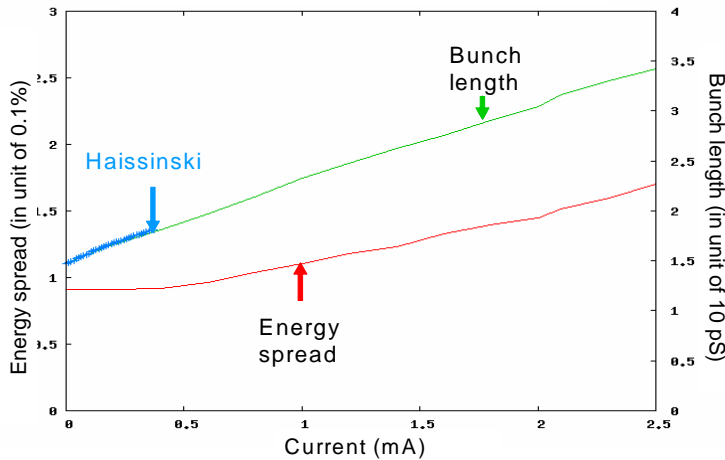


**Figure 3.2.4.** Bunch length and energy spread for broadband resonator. Resonant frequency  $f_y = 30$  GHz, shunt impedance  $R_s = 30$  k $\Omega$ , and  $Q_s = 1$ . This corresponds to  $(\text{Im} Z / n)_0 = 0.4$   $\Omega$ .

### 3.2.3.3 Transverse Coupled Bunch Instability Driven by Resistive Wall Impedance

As discussed in Section 3.2.3.1, the short-range part of the resistive wall impedance contributes to the single-bunch TMCI. The long-range tail contributes to the transverse coupled bunch instability. A rough approximation to the growth rate of the fastest growing transverse coupled bunch mode driven by the resistive wall impedance (at zero chromaticity) is given by

$$\frac{1}{\tau_{gr}} \cong \frac{e c I_{av} \beta_y}{2 E C} \text{Re} Z_{\perp}^{rw}(\omega_0) \frac{1}{\sqrt{1-q}}, \quad (3.2-24)$$

where  $C = 792$  m is the ring circumference,  $\beta_y$  is the average value of the vertical beta function in the resistive wall, and  $q = 0.28$  is the fractional part of the vertical tune. Equating the growth time to the radiation damping time provides an estimate of the instability threshold. Using the model parameters given in Tables 3.2.2 and 3.2.3, we find the threshold is at a total average current of 15 mA, far below the design value of 500 mA. Running at positive chromaticity will increase this threshold value.

Particle tracking [3.2.15] has been used to estimate transverse stability thresholds for coupled bunch modes. In these calculations we include both the long-range and short-range resistive wall wakefields as well as the short-range longitudinal and transverse wakefields, as described in Table 3.2.2. To keep the problem

manageable, we assume that all RF buckets contain identical bunches interacting via a single coupled bunch mode. A single bunch is tracked and the effect of other bunches is obtained by appropriate phase shifts under the assumption that the coherent frequency shift is small compared to the characteristic frequency width in the long-range transverse impedance. This should be an excellent approximation for the resistive wall impedance, which dominates the long-range transverse wake. The resistive wall impedance is due to 60 m of Cu with vertical aperture 5 mm and average beta function 2 m, in conjunction with 720 m of Al with aperture 25 mm and average beta function 7.6 m. The broadband transverse resonator has  $R_{\perp} = 1$  M-Ohm/m with  $Q_{\perp} = 1$  and 30 GHz resonant frequency at beta function 7.6 m. A longitudinal resonator with  $R_s = 30$  k-Ohm, resonant frequency 30 GHz, and  $Q_s = 1$  dominates the longitudinal impedance.

Three cases were simulated. Case 0 is a “stripped” case with no longitudinal wakes, no quadrupolar wakes (also referred to as detuning wakes), and no third-harmonic RF. Case 1 has the full suite of collective effects but no third harmonic cavity. Case 2 includes a perfect third harmonic cavity. The single-bunch threshold current as a function of vertical chromaticity is shown in Figure 3.2.5. In cases 1 and 2, a chromaticity of 4 allows for an average bunch current of about 0.5 mA and hence for an average stored current of 500 mA. This demonstrates the importance of running at positive chromaticity. Note also that bunch lengthening and enhanced synchrotron frequency spread introduced by the longitudinal wakefield and the third-harmonic cavity increase the effectiveness of positive chromaticity to stabilize the beam.

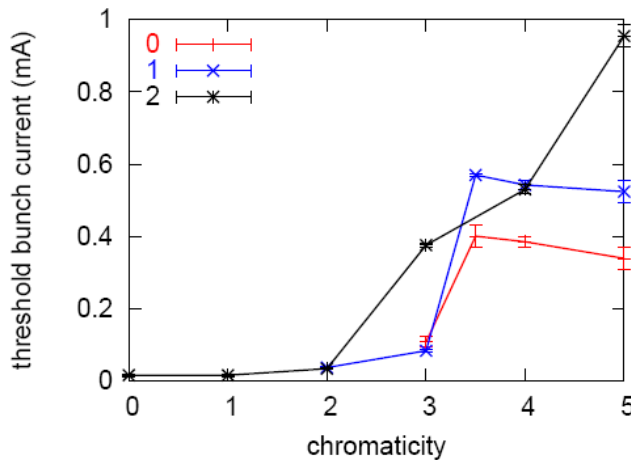


**Figure 3.2.5** Threshold single bunch current vs. chromaticity for: (0) no longitudinal wakes, no quadrupolar wakes, and only fundamental RF; (1) all the impedances but only fundamental RF; (2) all impedances as well as fundamental and third-harmonic RF.

### 3.2.3.4 CESR-B Cavity Longitudinal Impedance and Coupled Bunch Growth Rates

The longitudinal higher-order modes (HOM) in an RF cavity can result in coupling between bunches, leading to unstable synchrotron oscillations. In the case of  $M$  equally spaced and populated point bunches, the coherent synchrotron frequency  $\Omega_{\mu}$  of the  $\mu^{\text{th}}$  multi-bunch mode can be approximated by

$$\Omega_{\mu} - \omega_0 \nu_s = \frac{i e \alpha \omega_0 I_{av}}{4 \pi \nu_s E} \sum_{j=-\infty}^{\infty} (M j + \mu) Z_{\parallel} [(M j + \mu + \nu_s) \omega_0] \quad (3.2-25)$$

and

$$(\mu = 0, 1, 2, \dots, M - 1). \quad (3.2-26)$$

A 3D GdfidL [3.2.3] model has been created for the CESR-B cavity [3.2.16]. The model consists of the niobium cavity with the asymmetric beam tubes, warm-to-cold transitions, and ferrite-lined HOM dampers,

and it tapers to the 25×50 mm elliptical ring beampipes. The cavity has a fluted beam tube that allows the lowest dipole mode to be coupled out to the HOM damper. This made it essential to use a 3D model for calculating the HOMs. To benchmark such a complex model, C-Fish [3.2.17] and Superfish [3.2.18] models of the cavity with complex permittivity and permeability were created. The results were compared to GdfidL and to measured data on a ferrite-lined pillbox cavity that was measured on the bench.

The Superfish model approximates the fluted beampipe by a cylindrical tube with the same cutoff frequency. An outline of the cavity geometry with the field lines of the 1586 MHz mode is shown in Figure 3.2.6.

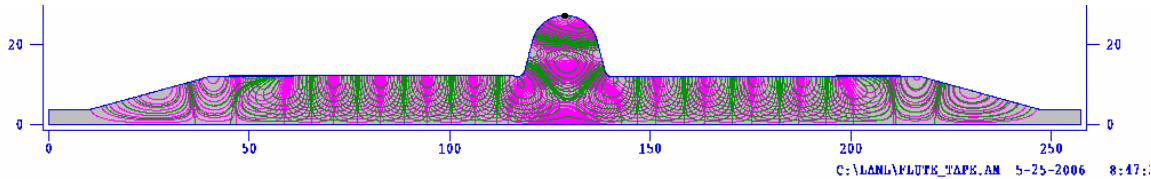


**Figure 3.2.6** CESR-B cavity geometry input to C-Fish.

The first eight HOMs calculated are given in Table 3.2.4. Superfish correctly calculates the surface resistivity of niobium as a function of frequency, but only takes the complex permeability and permittivity as a single input. The permittivity of the ferrite load is relatively constant and does not contribute significantly to damping the HOM, but the ferrite permeability properties vary considerably, so specific values (Table 3.2.4) closest to the HOM frequencies were calculated. The ferrite properties were obtained from the Canadian Light Source [3.2.19]. The measurements were made at several discrete frequencies in the band of interest.

**Table 3.2.4** CESR-B Higher-Order Longitudinal Modes.

Superfish			GdfidL		
Frequency (MHz)	Shunt Impedance (Ohms)	Q	Frequency (MHz)	Shunt Impedance (Ohms)	Q
952.4	112	222	950.55	8.14	350
973.32	57.07	332	976.62	54.6	420
1014.85	498	112	1014.38	505	150
1184.65	44.1	43	1181.5	13.2	60
1331.15	38.7	40	1361	65.6	20
1487.5	12.5	53	1481.5	46	40
1586.58	27.8	169	1580	7.5	30

We also performed studies of HOMs in CESR-B assembly using GdfidL code, shown in Figure 3.2.7. The studies took off from time-domain simulation of 1 pC charge passing through the structure. For the longitudinal impedance computation, the beam is moving on-axis, in comparison with the transverse impedance computation when the beam trajectory is shifted off-axis with an offset taken as 3×STEPSIZE. To get a result for the impedance, which is Fast Fourier Transforming of the wake function with higher frequency resolution, the wakepotential is computed up to an s-value of 50 meters. Parameters of the ferrite material are taken as  $\epsilon_r = 13.4$ ,  $\mu_r = 0.9$ ,  $\tan\delta_\epsilon = 0.02$ ,  $\tan\delta_\mu = 2.33$ ,  $\sigma_\epsilon = 0.05 \Omega^{-1}/\text{m}^{-1}$ , and  $\sigma_\mu = 46395 \Omega/\text{m}$  at a frequency of 2.8 GHz [3.2.19].

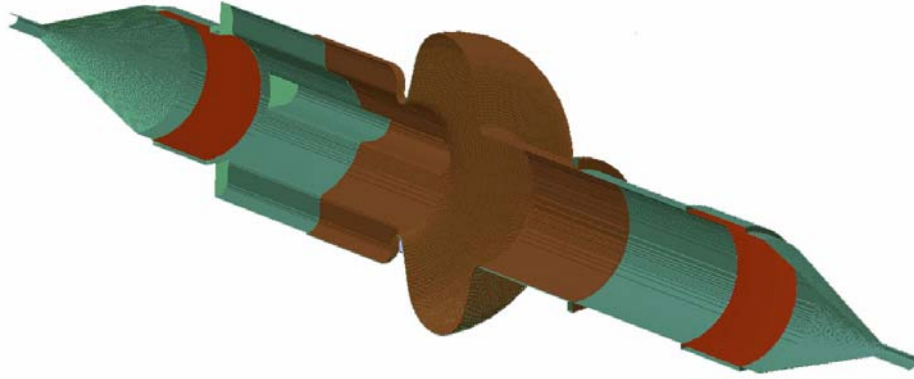


**Figure 3.2.7** 3D model of CCSR-B cavity assembly in GdfidL.

These parameters were used in ZAP [3.2.20] to calculate the growth rates for nominal ring and beam parameters. The maximum growth time was 120 ms for the sum of three cavity impedances, much longer than the longitudinal damping time of 6.5 ms, and so the beam is longitudinally stable for cavity HOMs.

To summarize the CCSR-B cavity studies, longitudinal CB growth rates were calculated for the first few HOM of the CCSR-B cavity and were found to be below the damping rate, even for three installed cavities without stagger tuning. However, the combination of small-bunch length exciting higher frequency modes and ferrite loss decreasing at higher frequency could lead to unstable modes whose growth rate exceeds the damping rate, so this analysis must be extended to higher frequencies. To enable this, we are pursuing measurements of the ferrite properties to 6 GHz with Ron Hutcheon, who provided the data below 3 GHz that were used in these calculations. This work must also be extended to the third harmonic cavities.

### 3.2.3.5 CCSR-B Cavity Transverse Impedance and Coupled Bunch Growth Rates

The transverse higher-order modes in an RF cavity can result in coupling between bunches, leading to unstable betatron oscillations. In the case of  $M$  equally spaced and populated point bunches, the coherent synchrotron frequency  $\Omega_\mu$  of the  $\mu^{\text{th}}$  multi-bunch mode can be approximated by

$$\Omega_\mu - \omega_0 \nu_x = -i \frac{ecI_{av}}{2E} \frac{\beta_x^{cav}}{C} \sum_{j=-\infty}^{\infty} Z_\perp [(Mj + \mu + \nu_y)\omega_0], \quad (3.2-27)$$

where  $\mu = 0, 1, 2, \dots, M-1$ ). The same GdfidL model used to compute the longitudinal cavity impedances was used to compute the transverse modes. The first 15 modes are listed in Table 3.2.5.

**Table 3.2.5 CESR-B Higher-Order Transverse Modes.**

Time domain #	Frequency [MHz]	$R_{\perp}$ [k $\Omega$ /m]	$Q_{\perp,load}$
$f_1$	608	2.2	60
$f_2$	653	3.1	60
$f_3$	681	15.6	70
$f_4$	769	1.6	30
$f_5$	864	1.03	50
$f_6$	917	0.72	40
$f_7$	964	0.66	30
$f_8$	1045	0.8	30
$f_9$	1146	1.17	30
$f_{10}$	1243	2.3	70
$f_{11}$	1299	0.36	160
$f_{12}$	1344	0.31	40
$f_{13}$	1405	0.33	70
$f_{14}$	1433	0.22	100
$f_{15}$	1464	0.44	70

The horizontal betatron function is 20 m at the RF cavities. These modes were used in ZAP [3.2.20] to calculate the transverse coupled-bunch growth rates. For 500 mA average current distributed uniformly in all the buckets around the ring and zero chromaticity, the coupled bunch growth time is 40 ms, which is longer than the radiation damping time of 13 ms. Therefore, the transverse cavity modes will not lead to unstable coupled-bunch betatron oscillations.

### 3.2.4 Impedance Budget

Extensive calculations have been performed of the wakefield and impedance produced by the storage ring components. Results of the calculations are summarized in Table 3.2.6, where we present the longitudinal kick factor (Eq. 3.2-4), the transverse kick factors (Eq. 3.2-12) and the imaginary part of the longitudinal impedance at low frequency divided by  $n = \omega/\omega_0$ , where  $\omega_0 = 2\pi \times 384.6 \text{ kHz}$ . The values given correspond to a single element. The number of times a given object is located in the ring is stated.

**Table 3.2.6 Calculated Impedance for Storage Ring Components.**

Object	Number of occurrences	$\kappa_{\parallel}$ V/pC	$(\text{Im}Z_{\parallel}/n)_0 \Omega$	$\kappa_x$ V/pC/m	$\kappa_y$ V/pC/m
Absorber	180	$3.4 \times 10^{-3}$	$9.2 \times 10^{-6}$	0.5	0.002
Bellows <sup>1</sup>	180	$8.7 \times 10^{-3}$	$124 \times 10^{-6}$	0.8	2
BPM	200	$20 \times 10^{-3}$	$47 \times 10^{-6}$	0.9	1.1
Cavity transitions/straight	2	3.5	$14 \times 10^{-3}$	25.4	57
500 MHz CESR-B cavity	4	0.31	----	0.17	0.17
1500 MHz CESR-B cavity	4	0.52	----	2.6	2.6
Dipole Chamber	60	$3.3 \times 10^{-5}$	$0.7 \times 10^{-7}$	$4.5 \times 10^{-3}$	0
Multipole Chamber	90	$0.5 \times 10^{-5}$	$0.1 \times 10^{-7}$	$0.7 \times 10^{-3}$	0
Flange <sup>1</sup>	300	$0.47 \times 10^{-3}$	$16 \times 10^{-6}$	0.141	0.141
Injection Region	1	TBD	TBD	TBD	TBD
SCU chamber geometric	TBD	$22.6 \times 10^{-3}$	$0.6 \times 10^{-3}$	61	257
SCU chamber ease (2.5 m)	TBD	$5.6 \times 10^{-3}$	----	13	26
IR chamber <sup>2</sup>	4	0.84	$2.1 \times 10^{-3}$	11.4	22.6
CPMU geometric	TBD	$95 \times 10^{-3}$	$1.1 \times 10^{-3}$	136	425
CPMU resistive wall (3.5 m)	TBD	$66 \times 10^{-3}$	----	112	225
720 m Al resistive wall	1	4.0	----	272	545
Scraper (Horizontal)	2	0.22	$1.4 \times 10^{-3}$	22	2
Scraper (Vertical)	2	TBD	TBD	TBD	TBD

The values for the geometric impedances were calculated using GdfidL with  $\sigma_s = 3$  mm. The resistive wall and extreme anomalous skin effect estimates were made with  $\sigma_s = 4.5$  mm. The bunch-length dependence of the wakefields will be determined in future work. <sup>1</sup>Values for bellows and flanges were calculated by Nagaoka [3.2.21] for SOLEIL with  $\sigma_s = 6$  mm. <sup>2</sup>The values for a simplified geometry of the far-infrared extraction chamber described in section 3.2.4.3.

The Al vacuum chamber is taken to be of length 720 m with vertical half-height 12.5 mm. The copper-plated RF shield for the in-vacuum permanent magnet undulator is 3 m long with vertical half-height of 2.5 mm. The superconducting undulator chamber is 2 m long with vertical half-height 2.5 mm and is cold copper in the extreme anomalous skin effect regime [3.2.8]. The vertical resistive wall wake of the elliptic chamber is taken to be 0.8 times the value for the circular chamber and the horizontal wake is 0.4 times the circular value [3.2.22]. Results not yet determined are indicated in the table.

### 3.2.4.1 Insertion Device Chambers

While most of the components listed in Table 3.2.7 are fairly common and have been successfully used in many machines, we feel that significant attention is warranted for studies and optimization of the impedance due to insertion device chambers. This need is based on experience at modern light sources, where installations of small-gap ID chambers have significantly affected beam dynamics [3.2.24], as well as on the requirements for NSLS-II, which is expected to have a large number of ID chambers ( $\sim 20$ ) with gap down to 5 mm beam stay-clear. Both the resistive wall component and the geometric component due to the transitions have been studied. Furthermore, in addition to the dipole impedances, which directly cause beam instabilities, we have estimated the quadrupolar component [3.2.25], which results in incoherent frequency shift and indirectly contributes to the instabilities through the Landau damping.

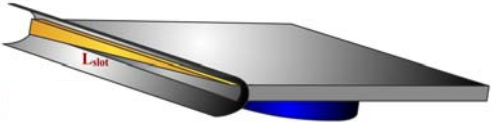
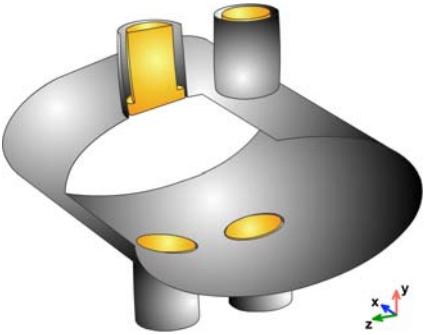


For the purposes of impedance budget we consider two representative ID chamber geometries: 1) a variable-gap, in-vacuum, permanent magnet undulator, and 2) a 5 mm fixed-gap elliptical chamber (4.2 K Cu inner surface) for a superconducting small-gap undulator.

Resistive wall contribution has been estimated analytically. While the inner chamber cross-sections are either complex H-like or elliptical shapes we have conservatively used the formulas in Table 3.2.1 for round

cross-sections. It is known [3.2.22] that as the chamber gets flatter (while height is kept fixed), the longitudinal impedance passes through a minimum equal to about 90% of the round-pipe value, while the transverse impedance monotonically approaches  $\sim 80\%$  of its round-pipe value. Copper coating and a minimum full gap of 5 mm were assumed for the estimates.

Geometric impedance contributions due to transitions [3.2.26] were calculated using EM code GdfidL [3.2.3] as well as checked against a recently developed analytical approach [3.2.25].

**Table 3.2.7 Description of Components.**

	<p><b>Absorber</b></p> <p>To protect the vacuum chamber and insertion devices in the ring from damage due to synchrotron radiation, photon absorbers are used. The model consists of a regular elliptical beampipe with a rectangular slot 10 mm high, 180 mm long, and 180 mm deep. A triangular copper burr is located inside the slot for synchrotron radiation absorption. It projects 5 mm inside the regular elliptical beampipe.</p>
	<p><b>BPM</b></p> <p>Due to excitation of resonant modes in the buttons, the impedance, kick factor, and loss factor depend very strongly on the BPM button geometry. The BPM button geometry can be optimized to reduce impedance contribution and heating, without losing its resolution. To estimate BPM contribution to the transverse and longitudinal impedance, buttons designed for the SOLEIL BPM were modeled on the regular elliptic beampipe for NSLS-II. Results of the transverse impedance were compared with results for the SOLEIL BPM geometry; in both cases, <math>50 \Omega/\text{m}</math> was computed.</p>
	<p><b>Dipole Chamber</b></p> <p>The dipole vacuum chamber for NSLS-II has an elliptical cross-section. Inside the chamber there is a slot 15 mm high. As was shown by Stupakov [3.2.23], the slot length does not affect the impedance. For this numerical computation, the slot length is taken to be 80 mm. The horizontal impedance of this geometry depends on beampipe radius and height of the slot.</p>
	<p><b>Scraper-H</b></p> <p>From the impedance estimations of other laboratories, horizontal or vertical beam scrapers can produce impedance comparable with that of a rectangular step or a tapered transition with a small angle of opening. Two scrapers of the presented geometry, one horizontal and the other vertical are under consideration for application in the NSLS-II ring.</p>

### 3.2.4.1.1 In-Vacuum Undulator

A 3D model of the IVU [3.2.26] is shown in Figure 3.2.8 (a, top). This model is motivated by the geometry of the X13 Mini-Gap Undulator [3.2.27] currently operating at the NSLS x-ray ring and has been tailored to meet the NSLS-II requirements. The device consists of two magnet arrays of width  $w_m = 100$  mm and thickness 34 mm, located inside a rectangular vacuum chamber of width  $w_{vc} = 180$  mm and height  $h_{vc} =$



170 mm. The tapered transition consists of two parts: 1) a fixed portion between the regular beampipe and the undulator vacuum chamber; and 2) a flexible-height portion with one end fixed to the interior of the undulator vacuum chamber and the other end fixed to the moveable magnet array. The flexible portion only consists of flat upper and lower conductive plates with no side walls. For simplicity in the 3D model, we used a continuous smooth taper of length 180 mm. Also, due to mesh limitations, we have shortened the magnet section length to 0.5 m.

Figure 3.2.8 (a, bottom) shows the transverse wakepotential for the considered geometry and 3 mm RMS bunch length. The wakepotential has a Gaussian-like part corresponding to mainly inductive broadband impedance, as well as a characteristic long-range tail.

The short-range wakefield in the IVU is predominantly determined by the tapers; the long-range wake depends on the cross-sectional geometry of the vacuum enclosure and the length of the magnet. The oscillations in the long-range part are due to multiple narrowband impedance resonances that are possible to characterize in terms of waveguide theory [3.2.28]. Due to limitations on the mesh, we have not yet been able to carry out a systematic study of the length dependence.

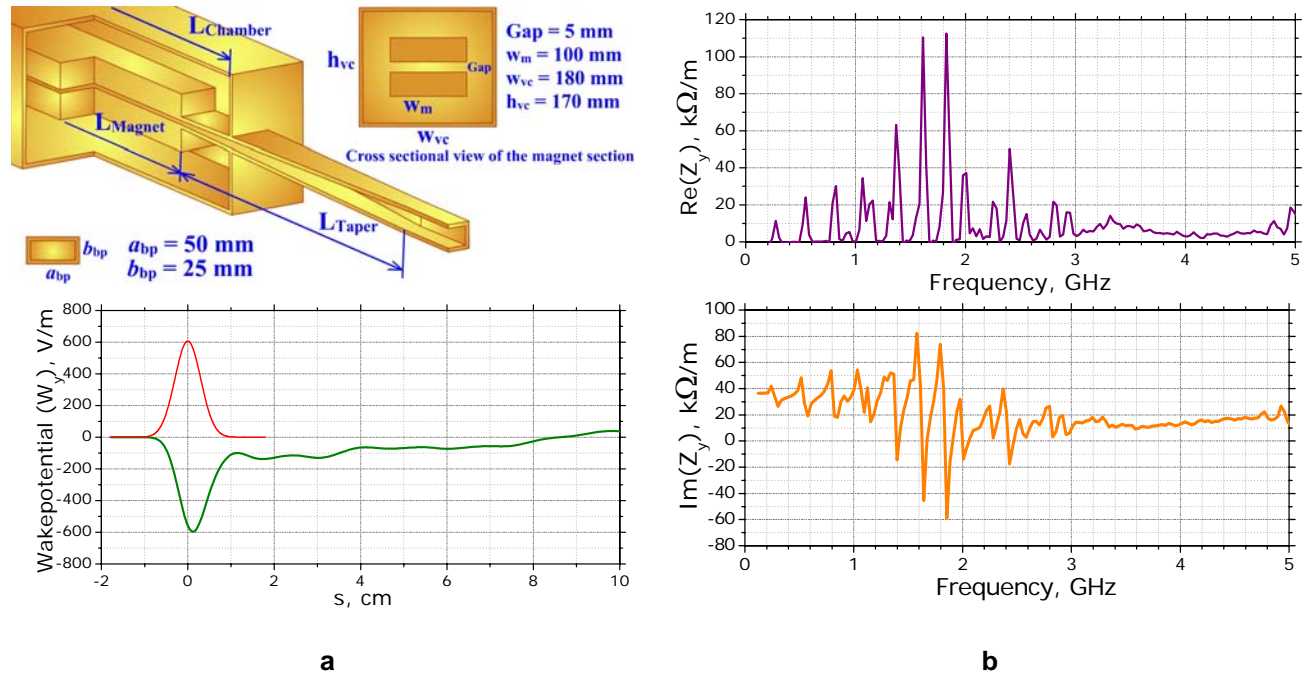


**Figure 3.2.8** (a, top) Geometry of CPMU with  $L_{\text{taper}} = 180$  mm; (a, bottom) Short-range transverse wakepotential of in-vacuum permanent magnet undulator chamber; (c, top and bottom) Low-frequency behavior of real and imaginary parts of the transverse impedance of CPMU. Impedances determined by FFT of the computed wakepotential up to  $s = 7$  m.

### 3.2.4.1.2 Superconducting Undulator

Similar calculations were performed for the elliptic vacuum chamber of a superconducting undulator. The geometry of the tapered elliptic vacuum chamber is shown in Figure 3.2.9 (a, top). The small-gap magnet region of the elliptic vacuum chamber for the superconducting undulator is fixed and has major axis  $2a_s = 15$  mm and minor axis  $2b_s = 5$  mm, with a magnet section length of 2000 mm. The tapers must smoothly transition between the magnet section and the regular beampipe, which has a major axis  $2a_b = 76$  mm and minor axis  $2b_b = 25$  mm.

Transverse impedance in the low-frequency limit and the kick factor for the tapered vacuum chamber are independent of the distance between the tapers. The inner section length was reduced to 100 mm for GdfidL



calculations. The resulting wakepotential for 3 mm RMS long bunch and the taper length of  $L_{\text{Taper}} = 180$  mm is shown in Figure 3.2.9 (a, bottom). It corresponds to  $\kappa_y = 190$  V/pC/m and  $\text{Im}Z_y(\omega \rightarrow 0) = 8.5$  k $\Omega$ /m. When we increased the taper length,  $\kappa_y$  and  $\text{Im}Z_y(\omega \rightarrow 0)$  decreased inversely proportional to  $L_{\text{Taper}}$ . The taper length of the elliptic vacuum chamber is chosen to optimize its contribution to the total impedance as well as space in the ring. Note that resonance peaks are observed inside the vacuum chamber in all cases of the transverse impedance calculations. These peaks are not resolved with a wakefield length of 0.3 m. A more detailed investigation of the electrodynamic properties of the tapered elliptic vacuum chamber uncovered the existence of trapped modes. These modes have been identified and classified [3.2.28]. In principle, these modes may affect multi-bunch dynamics and will be systematically studied.

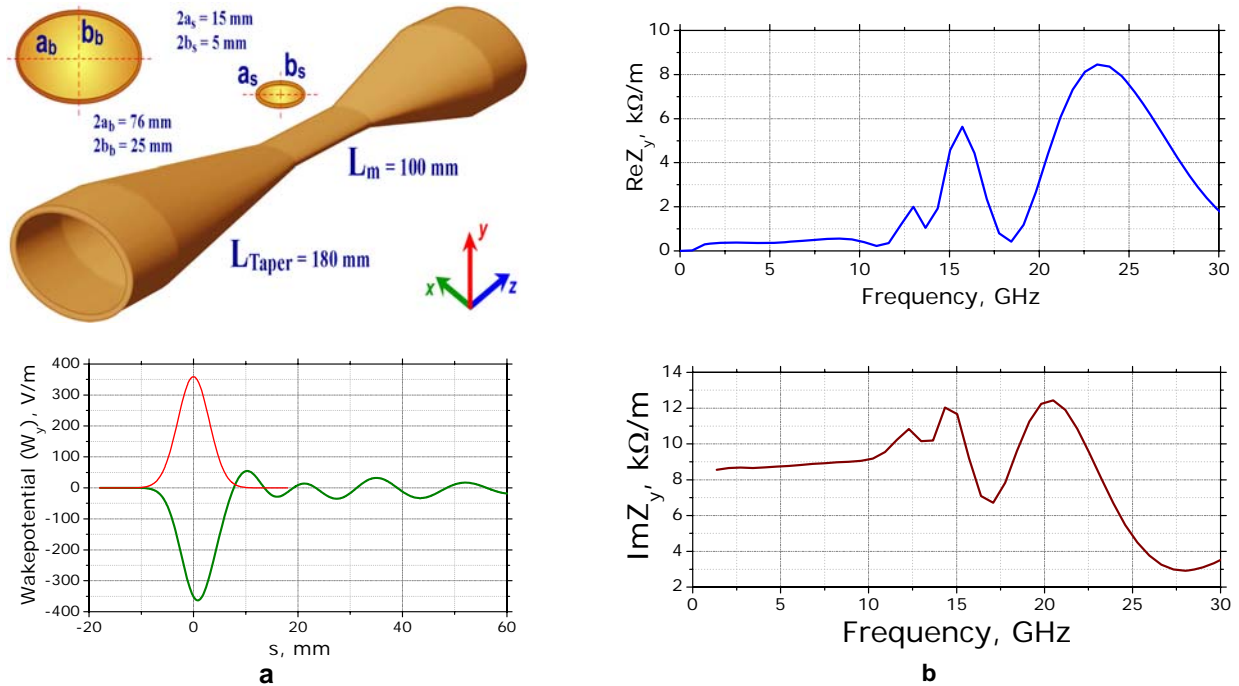


**Figure 3.2.9** (a, top) Tapered elliptical vacuum chamber for superconducting small-gap undulator ( $L_{\text{Taper}} = 180$  mm). (a, bottom) Transverse wakepotential; (b, top) Real part of the transverse impedance. (b, bottom) Imaginary part of the transverse impedance. Impedances correspond to FFT of the computed wakepotential up to  $s = 0.3$  m.

### 3.2.4.2 CESR-B Short-Range Wake

CESR-B [111] type superconducting cavities are considered for acceleration of the beam in the NSLS-II storage ring. Two main 500 MHz RF cavities and one 2-cell passive 1500 MHz bunch-lengthening harmonic cavity will be fitted in one long straight section. Two long straight sections are reserved in the ring for the RF system. The complicated nature of the RF cavities requires significant computational resources, to establish the longitudinal and transverse impedances for the whole assembly. In order to avoid computational complications, the coupling impedance in the whole assembly can be estimated as a sum the impedance of cavities and transitions [3.2.29, 3.2.30].

Calculated results for the 500 MHz main RF cavity with the attached round beam pipe of radius  $a=120$  mm on one side and the fluted beam pipe for Higher Order Modes (HOMs) coupling on the other (Figure 3.2.10a) are presented in Table 3.2.6 (beginning of Section 3.2.4). “Perfect matched layers” (or “port” boundary condition) is used on both sides of the cavity pipe for wakefield analysis. For simplicity, the RF coupler was not included in these computations. The coupling impedance of the rectangular slot in the round

beam pipe, which will be used for matching of the input power to the cavity, can be estimated analytically or can be computed separately and added to the total impedance of the cavity.

The loss factor of the main cavity for a 3 mm bunch length ( $\sigma_s$ ) is  $\kappa_{loss}=0.31V/pC$  ( $\sigma_s \ll a$ ). Two main cavities per straight contribute the loss factor of 0.62 V/pC. It is about 6 times smaller than the value for the cavity transitions per straight.

To estimate the contribution of the harmonic cavity to the total impedance of the ring we are using a scaled model of the CESR-B main cavity at frequency 1500 MHz. The loss factor of the harmonic cavity is increased by a factor of 1.7 ( $\kappa_{loss} \propto \sqrt{g}/a$ , where  $g$  is the gap of the cavity) due to reduction of the cavity dimensions by a factor of 3. The kick factor of the harmonic cavity is small compared to that due to the cavity transition. Assuming a small impact from the fluted pipes, the kick factor of the harmonic cavity can be scaled from that of the main cavity as  $\kappa_{\perp} \propto 1/a^3$  [222] in agreement with computed results in Table 3.2.6.

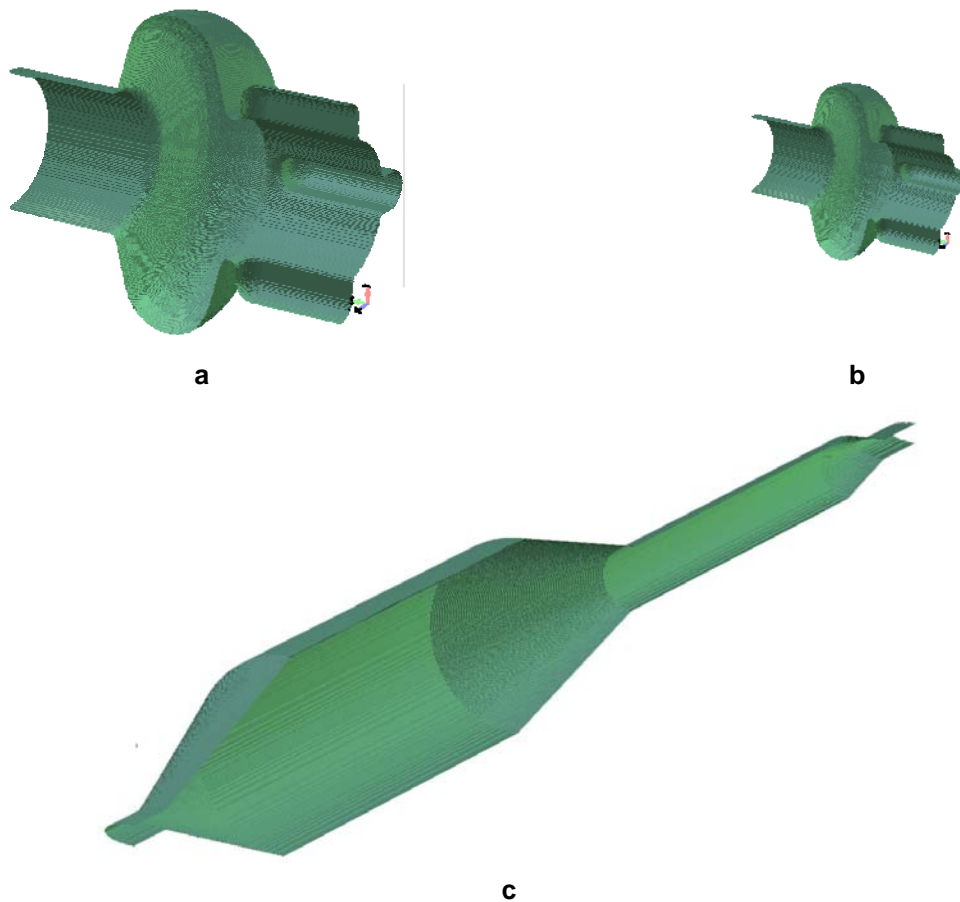


**Figure 3.2.10** 3D GdfidL models of the RF straight section.

**a)** 500 MHz main RF cavity. **b)** 1500 MHz harmonic RF cavity. **c)** Cavity transitions per straight.

Cavity transitions per straight consists of three smooth tapered transitions: regular vacuum chamber beam pipe – main cavity beam pipe, main cavity beam pipe – harmonic cavity beam pipe and harmonic cavity beam pipe – regular vacuum chamber beam pipe. Two longest tapers are taken to be 300 mm. The taper length between the beam pipe radius of the harmonic cavity (40 mm) and the regular vacuum chamber is 100 mm. For simplicity, the length of straight pipes between tapers is chosen to be 300 mm. Ferrite rings on both sides

of the RF cavities for HOM damping (narrow-band impedance) are not included in this analysis as they do not affect the short-range wakepotential (broad-band impedance).

Contribution of cavity transitions per straight to the broad-band longitudinal impedance in terms of the loss factor is significant ( $\kappa_{loss}=3.5\text{V/pC}$ ). This value is comparable with the values for 720 m aluminum resistive wall ( $\kappa_{loss}=4\text{V/pC}$ ) and for 200 BPMs ( $\Sigma\kappa_{loss}=4\text{V/pC}$ ) from impedance table. Cavity itself gives a smaller contribution to the longitudinal impedance. To minimize transition impedance, taper lengths between RF cavities will be lengthened to the extent allowed by the available space.

### 3.2.4.3 Infrared Extraction Chamber

To take out the synchrotron radiation in far-infrared region six dipole magnets will be designed with large gap. To be able to extract the light emission  $\sim 50$  mrad horizontal and  $\sim 25$  mrad vertical (full radiation opening angles of the collected emission in location of the extraction mirror) within a bending magnet of  $\rho=25$  m radius, the infrared (IR) chamber requires a full aperture of 67 mm vertical, 134 mm horizontal and a special trapezoidal slot extended vertically. The design of the far-IR chamber is shown in Figure 3.2.11. Since the IR-chamber has larger elliptical shape than the regular vacuum chamber (25 mm full height and 76 mm full width), smooth tapers are used to minimize the contribution to the longitudinal and transverse broad-band impedance. The IR-chamber will be installed inside of the wide-gap dipole magnet of 2.6 m long. Tapered transitions at each end of the structure, 300 mm and 100 mm long, are chosen to estimate the narrow-band impedance. They do not extend beyond the dipole magnet length and the taper length can be increased inside the dipole magnet to further reduce the broad-band impedance.

To direct the collected emission into the output port, the extraction mirror (copper color, 5 mm thick) is first modeled at the end of the trapezoid slot, 30 mm from the beam trajectory as shown in Figure 3.2.11 (zoomed part). Separation of the radiation from the electron beam is made more difficult due to the large bending radius of the NSLS-II dipoles. The mirror must be located close to the electron beam to collect the IR emission. Of particular concern is the narrow-band impedance which may be generated due to the mirror.

The narrow-band impedance computations are shown in Figure 3.2.11. The real part of the longitudinal impedance is presented for the IR-chamber with and without mirror. Set of resonant modes are generated into the chamber after the passing beam if the extraction mirror is inside. The mirror is seen by the beam and generated modes are trapped in a small pocket between the tapered transition and the mirror. These modes can cause couple bunch instability and heating of the chamber wall.

To avoid generation of resonant modes inside the chamber, we studied several variants of mirror position while maintaining the required extraction angles. One of the variants is shown in Figure 3.2.12. To avoid a pocket behind the mirror, we located the mirror at a point right after the widened cross-section had tapered back down to the regular dimensions. In this case, the extraction mirror is hidden behind the tapered transition in the region of the antechamber slot. This design eliminated the problem of resonant modes due to the mirror. It can be seen from the real part of the longitudinal impedance presented in Figure 3.2.12 (b). The narrow-band impedance of the complex IR-chamber was reduced down to the impedance of just a tapered structure.

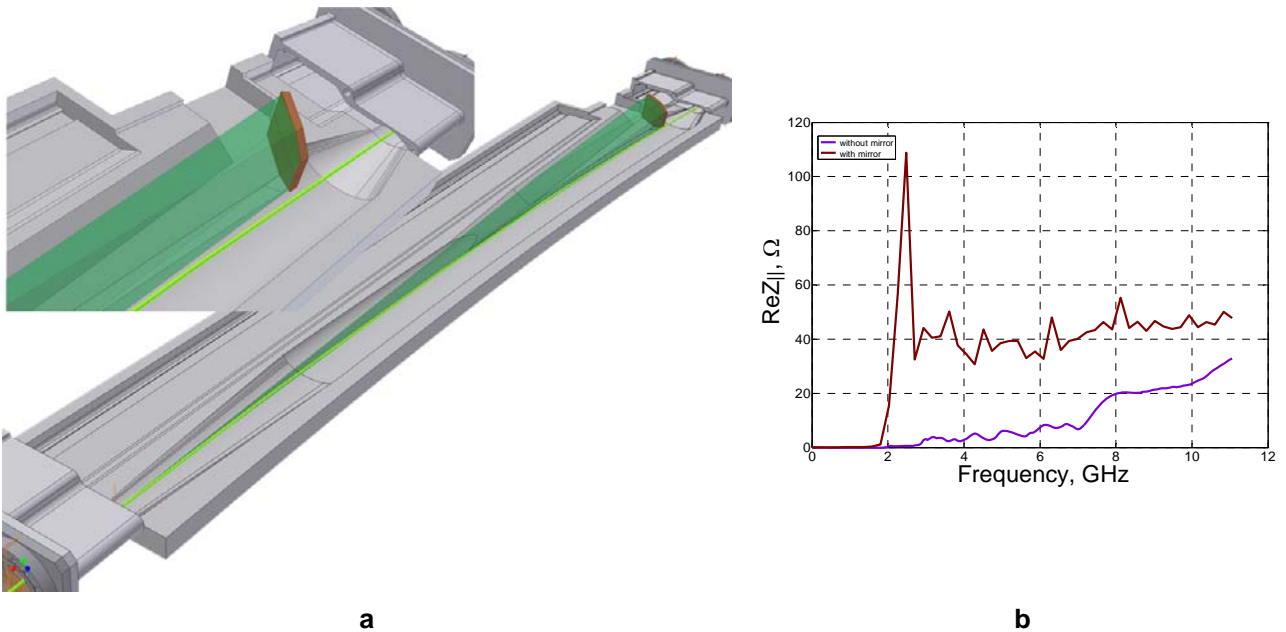


**Figure 3.2.11** Infrared extraction chamber for the dipole magnet with a large gap. **a)** Design of the IR chamber with a mirror in front of the tapered transition. The green line represents the electron beam and the green shaded region represents the IR radiation. **b)** Real part of the longitudinal impedance. Wine line and the purple line are calculations with and without extraction mirror inside the chamber respectively.

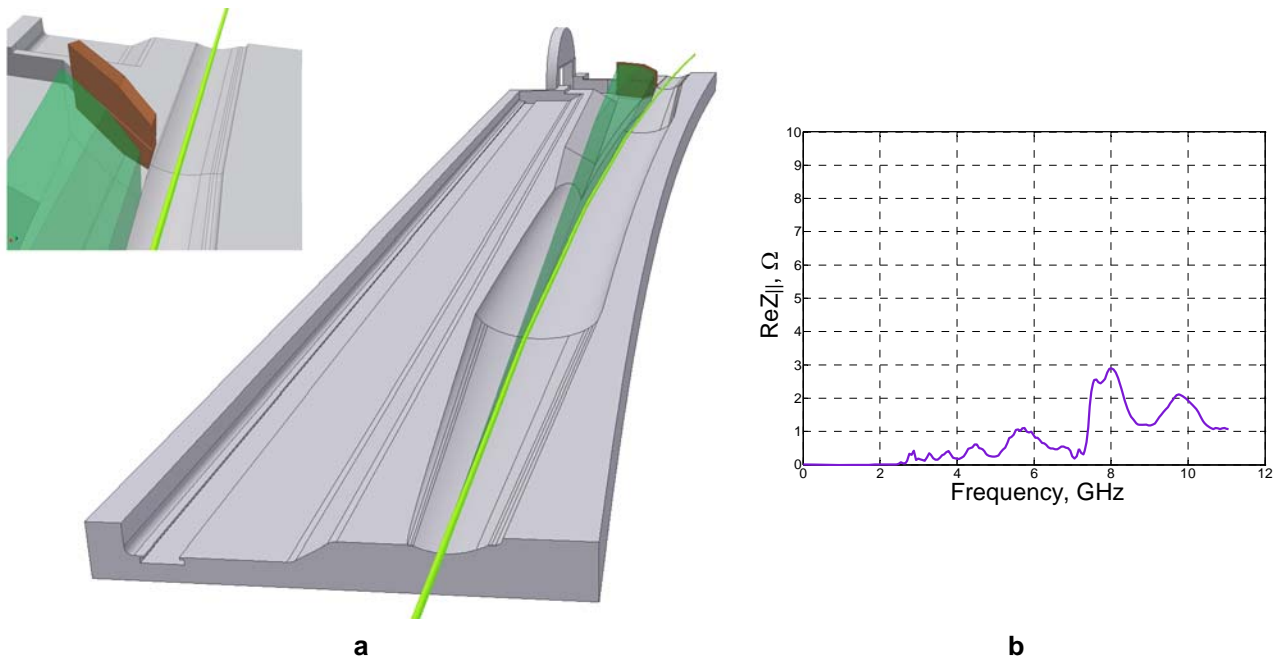


**Figure 3.2.12** Design of the infrared extraction chamber with the mirror at a point right after the widened cross-section. **a)** Mirror is located inside the regular vacuum chamber behind the tapered transition. **b)** Real part of the longitudinal impedance for the current design of the IR chamber with the extraction mirror.

To estimate the short range wake (broad-band impedance) of the IR chamber, we consider a simplified model. The full height and the full width of the tapered chamber are taken the same as for the real structure, 67 mm and 134 mm, respectively. Smooth tapered transitions, each 180 mm long, are located at both ends of

the chamber. The shorter taper length here is taken for reducing computational time. We modeled narrow and trapezoid slots, where the extraction mirror will be located. The trapezoid slot extends vertically away from the structure as shown in Figure 3.2.13 (c).

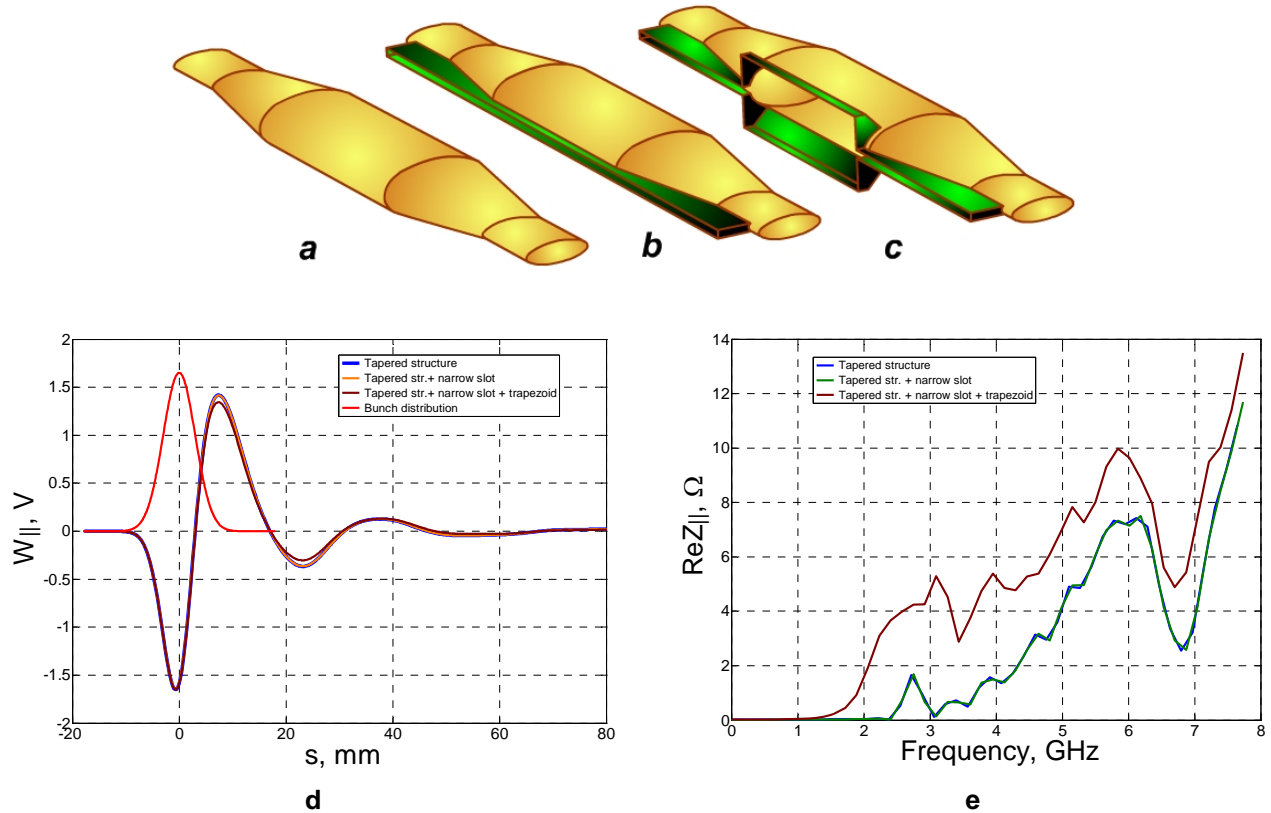


**Figure 3.2.13** Simplified model of IR-extraction chamber. **a)** Tapered elliptic chamber. **b)** Tapered elliptic chamber with narrow slot. **c)** Tapered elliptic chamber with narrow slot and trapezoidal slot. **d)** The longitudinal short-range wakepotential. **e)** The real part of the longitudinal impedance.

Computations of the longitudinal wakepotential for a  $\sigma_s = 3$  mm rms bunch length show that narrow and trapezoid slots do not significantly affect the short-range wakepotential (Figure 3.2.13d) and hence the loss factor. The narrow-band impedance due to tapered transitions is similar to the impedance of the real geometry with the extraction mirror at the right location. The amplitude of the resonant peaks in the simplified geometry is slightly higher due to shorter taper length.

This analysis was concentrated on verifying of the results obtained for the real geometry, which is a more complex geometry and has a large value for numerical computations. As a first step we eliminated the resonant modes (narrow-band impedance) due to the extraction mirror. The next step needs to be done, to estimate the broad-band impedance for the actual design geometry. It requires a lot of computational time. In Table 3.2.6 we present the results computed for the simplified geometries shown in Figure 3.2.13. The loss factor for these geometries is  $\kappa_{\text{loss}} = 0.84 \text{ V/pC}$ . Based on this preliminary study, the taper length for the actual design geometry will be increased to reduce the loss factor.

### 3.2.5 Intrabeam Scattering

Small-angle Coulomb scattering within a beam leads to the excitation of betatron and synchrotron oscillations of particles, which usually increases beam emittances in all phase planes. This effect, often called intra-beam scattering (IBS) or multiple Coulomb scattering, is proportional to the beam 3D phase-space density and depends strongly on beam energy, becoming more severe for high intensity, low energy machines.

When IBS is included, the steady-state beam properties with radiation damping are defined by

$$\varepsilon_x = \frac{\varepsilon_{x0}}{1 - \tau_x/T_x}, \quad \varepsilon_y = \frac{\varepsilon_{y0}}{1 - \tau_y/T_y}, \quad \sigma_p^2 = \frac{\sigma_{p0}^2}{1 - \tau_p/T_p}, \quad (3.2-28)$$

where subscript 0 indicates the beam properties in the absence of IBS,  $\tau_{x,y,p}$  stand for synchrotron radiation damping times, and  $T_{x,y,p}$  are the IBS growth times discussed below. These equations indicate that the IBS effect becomes important when IBS rates are significant in comparison with the radiation damping rates. Because the IBS growth times  $T_{x,y,p}$  depend on beam current as well as beam emittances, energy spread, and bunch length, the above equations are coupled, and solving them requires some iterative procedure. Sometimes a fourth equation is added that expresses the current-dependent relation of the bunch length to the energy spread, to account for the potential well distortion. If the vertical emittance is dominated by weak coupling (which is our expectation for NSLS-II), the effect simplifies to 2D, and the second equation is replaced by  $\varepsilon_y = \kappa \varepsilon_x$ , where  $\kappa$  stands for the coupling coefficient.

The basic theoretical framework of IBS effect was established long ago by Piwinski [3.2.31] and Bjorken and Mtingwa (B–M) [3.2.32] using two different approaches. These theories express IBS rise times  $T_{x,y,p}$  as complicated integrals of beam parameters, such as energy and phase space density, as well as lattice properties. The B–M theory has been extended to include arbitrary vertical-horizontal and vertical-longitudinal coupling [3.2.33]. The resulting growth rates are local quantities, and have to then be averaged around the lattice. Many accelerator physics codes include some variations of the B–M approach. In addition to these general procedures which are fairly computer intensive, there exist a number of more approximate formulations of IBS effect that simplify the treatment for certain parameter regimes. For example, Bane [3.2.34] has recently shown the equivalence of the Piwinski and B–M treatments in the regime applicable for high energy machines. In this regime, Bane has found that B–M results reduce to fairly compact expressions for IBS rise times, which we have found useful for NSLS-II.

The IBS approaches mentioned above result in growth times proportional to the so-called Coulomb log factor, equal to  $\ln(b_{\max}/b_{\min})$ , where  $b_{\max, \min}$  are impact parameters, which are not well defined. Often,  $b_{\max}$  is taken equal to  $\sigma_y$ . To fix  $b_{\min}$ , a so-called “tail-cut” procedure was suggested by Raubenheimer [3.2.35]. He pointed out that, since IBS results in non-Gaussian beam distributions, tail particles could be overemphasized; therefore, one must chose  $b_{\min}$  to eliminate interactions having collision rates smaller than SR damping rates.

The NSLS-II emittance is strongly dominated by the IDs and damping wigglers. Rather than assuming some fixed ID makeup, we have calculated IBS effects as a function of radiation losses in the machine, having  $\varepsilon_{x0}$  vary from the  $\sim 2$  nm bare lattice value down to about 0.4 nm. The zero-current vertical emittance  $\varepsilon_{y0}$  was fixed at the diffraction limit for 1 Å x-rays (8 pm-rad), corresponding to  $\kappa$  varying from  $\sim 0.5\%$  for bare lattice to about 2% for  $\varepsilon_{x0} = 0.4$  nm.

Most NSLS-II calculations have been performed with the code ZAP [3.2.20], which implements the 2D procedure of the B–M theory [3.2.32], i.e., the vertical emittance is assumed dominated by coupling. We used 500 mA for the total ring current, and assumed it uniformly distributed into 80% of the 500 MHz RF buckets. As we changed the amount of radiation losses, the RF voltage was adjusted to keep the RF energy acceptance constant at 3%. Electron beam parameters in the absence of IBS, used as input to ZAP (such as horizontal

emittance, energy spread, bunch length, and radiation damping times) were calculated analytically by scaling bare lattice values by the amount of radiation losses. The results given by ZAP are shown in Figure 3.2.14.

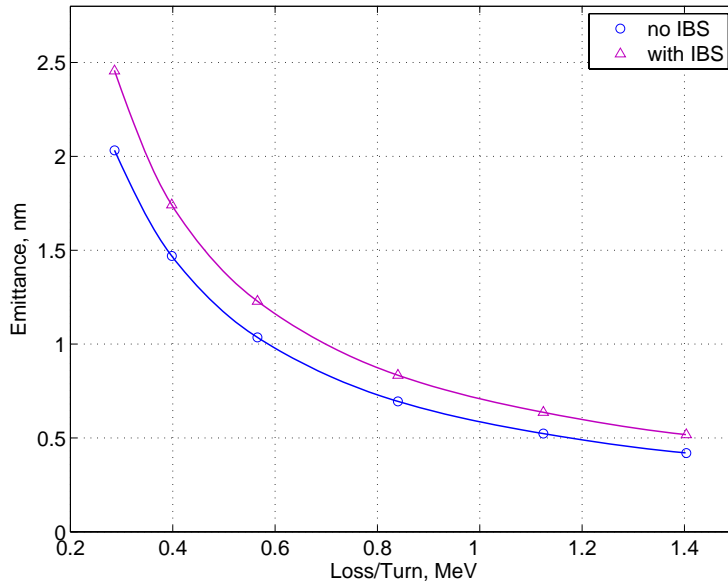


**Figure 3.2.14** Horizontal emittance vs. total SR loss.

Note that the IBS-induced relative emittance blow-up does not exceed 20%, and remains fairly independent of the amount of radiation losses (and hence the emittance). This implies that for smaller emittances, increased IBS rates due to denser bunches are offset by the increase in radiation damping. This is quite contrary to a more typical situation in a storage ring light source not dominated by IDs, where decreasing the emittance by adjusting the lattice (and hence keeping the SR rates fixed) can result in an increase of IBS-induced emittance blow-up. We have also found that the IBS rise times calculated by ZAP are in reasonable agreement (better than 50 %) with the estimates we have done using Bane's formalism.

Note that the results presented in Figure 3.2.14 are based on several conservative assumptions. First, calculations are performed at zero-current bunch length, while in reality the bunch will be longer, due to potential well distortion and the harmonic RF system. At even higher single-bunch currents, used in special operating modes, the microwave instability will result in an even stronger increase in bunch length as well as energy spread, reducing the IBS effect further. In addition, the calculations of Coulomb log that are used in ZAP use  $b_{\max} = \sigma_x$  and do not include the tail-cut procedure. As a result, the Coulomb log value ZAP assumes for NSLS-II parameters is about 17, while more recent estimates [3.2.33] that include the cut would reduce it to about 10.

We have also done some cross-checks of the bare lattice case using the SAD code from KEK [3.2.36]. SAD has been extensively benchmarked against the experimental results from the ultra-low emittance ATF storage ring. SAD does include the tail-cut, so it results in smaller IBS induced blow-up compared to ZAP. However, when scaled for the Coulomb log, the codes are in good agreement. SAD allows for full 3D treatment of IBS and will be used in the future to study the effects of vertical dispersion for NSLS-II.

To summarize, our calculations to date indicate that under pessimistic assumptions, IBS-induced relative emittance blow-up for NSLS-II should not exceed 20% at nominal bunch intensity and therefore it should not present a problem. Furthermore, we have found the magnitude of the blow-up to be fairly independent of the NSLS-II emittance, since the increased IBS rates for denser bunches are compensated by faster radiation damping. Future studies will include accounting for a more comprehensive ID makeup, considering the effects of vertical dispersion, and further developing some models of bunch lengthening.



### 3.2.6 Touschek Lifetime

The beam lifetime in most modern synchrotron radiation sources is limited by the Touschek effect, which describes the collision of two electrons inside a bunch, leading to momentum transfer from the transverse (usually horizontal) plane into the longitudinal direction. If the resulting longitudinal momentum exceeds the momentum acceptance of the accelerator, these particles are lost.

The Touschek lifetime is calculated as [3.2.37],

$$\frac{1}{\tau} = \frac{r_e^2 c q}{8\pi e \gamma^3 \sigma_s} \cdot \frac{1}{C} \cdot \oint_C \frac{F((\delta_{acc}(s)/\gamma \sigma_{x'}(s))^2)}{\sigma_x(s) \sigma_{x'}(s) \sigma_y(s) \delta_{acc}^2(s)} ds, \quad (3.2-29)$$

where  $r_e$  denotes the classical electron radius,  $q$  the bunch charge,  $\sigma_s$  the RMS bunch length,  $C$  the circumference of the storage ring, and  $\sigma_x(s)$  and  $\sigma_y(s)$  the RMS horizontal and vertical beam radii, including the dispersion term.

$$\sigma_{x'}(s) = \frac{\varepsilon_x}{\sigma_x(s)} \sqrt{1 + \frac{H(s) \sigma_\delta^2}{\varepsilon_x}} \quad (3.2-30)$$

is the RMS beam divergence for  $\alpha_x = 0$ , with

$$H(s) = \gamma_x \eta^2 + 2\alpha_x \eta \eta' + \beta_x \eta'^2 \quad (3.2-31)$$

the chromatic invariant. The function  $F(x)$  is defined as

$$F(x) = \int_0^1 \left( \frac{2}{u} - \ln \frac{1}{u} - 2 \right) \cdot \exp(-x/u) du. \quad (3.2-32)$$

While the Touschek lifetime depends linearly on the bunch length as well as on the vertical beamsizes, its dependence on the horizontal beamsizes (or emittance) is more complicated. For large horizontal beamsizes, the particle density of the bunch becomes very small, thus greatly decreasing the probability of two electrons colliding. On the other hand, a large horizontal emittance results in large horizontal momenta that can be transferred into the longitudinal plane due to a Touschek scattering event. The dependence of the resulting Touschek lifetime (for a bunch length of 4.5 mm) on horizontal emittance is illustrated in Figure 3.2.15. The result is that in the region of the design emittance for NSLS-II, the Touschek lifetime is not particularly sensitive to emittance. For a variety of reasons we will discuss, this estimate of Touschek lifetime is optimistic. Even so, for the design emittance, the lifetime is below the specified lifetime of 3 hours. Increasing the bunch length with a Landau cavity can provide the extra lifetime to meet the lifetime goal.



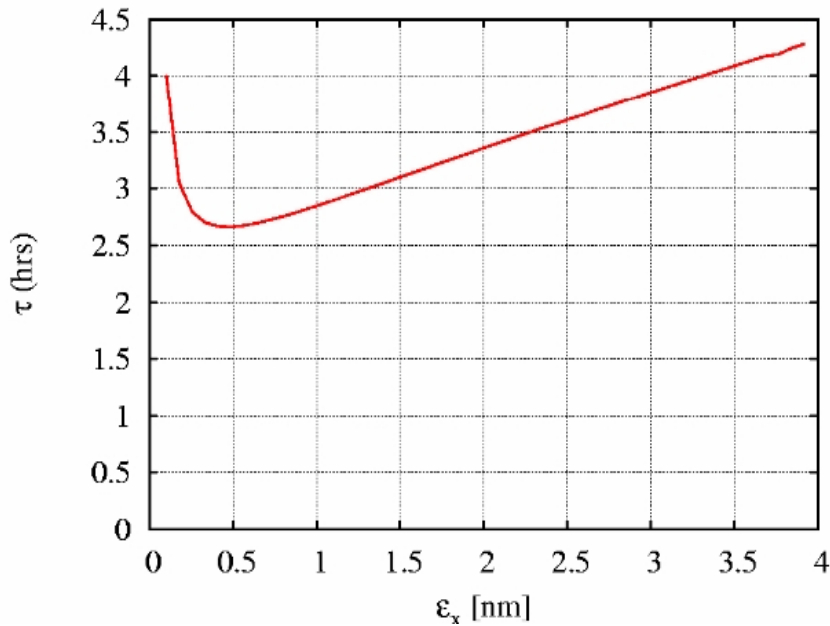


**Figure 3.2.15** Tauschek lifetime vs. horizontal emittance for 3% momentum acceptance and a 4.5 mm bunch length.

Experience at facilities like ALS and SLS has shown that nonlinear betatron coupling plays a significant role in limiting the momentum acceptance of the storage ring, especially in the presence of small vertical apertures due to small-gap insertion devices. Therefore, tracking has been performed using the TRACY-2 code. Since Tauschek scattering occurs near the center of the bunch, the momentum acceptance  $\delta_{acc}$  needs to be determined for particles starting at a longitudinal position  $s$  with coordinates  $x = x' = y = y' = 0$ . In general, this yields different momentum acceptances  $\delta_{acc}^+$  for positive and  $\delta_{acc}^-$  for negative momenta, resulting in different Tauschek lifetimes  $\tau^+$  and  $\tau^-$ . Based on these two results, the total Tauschek lifetime  $\tau_{tot}$  is computed as

$$\frac{1}{\tau_{tot}} = \frac{1}{2} \cdot \left( \frac{1}{\tau^+} + \frac{1}{\tau^-} \right). \quad (3.2-33)$$

The RF acceptance has been set to  $\pm 3\%$ . To achieve this for the bare lattice, an RF voltage of 2.5 MV is required. For the baseline case of 3 damping wigglers, a voltage of 3.1 MV is required. The RF acceptance determines the maximum achievable momentum acceptance. In fact there are a number of factors that can reduce the true momentum acceptance. Off-momentum particles below the RF acceptance can hit apertures that an on-momentum particle would not hit. This is due to the fact that off-momentum particles have a different orbit (from dispersion), and different tunes (from chromaticity). Further, as a particle executes damped synchrotron oscillations, it will sample a large region of phase space and tune space which can lead to the loss of the particle. The calculations shown here use 512 turns, or several synchrotron oscillations. Tracking for a full damping time ( $\sim 4500$  turns for 3 damping wigglers) should be performed to spot-check results. We have found that in some cases, this extra tracking time can decrease the momentum acceptance, and hence lifetime. In one case (very similar to the nominal case we present here), we found that the lifetime dropped from 2.5 hours to 2.2 hours when the number of turns was increased from 512 to 5000.

To get a realistic estimate of the momentum acceptance, a realistic lattice model is created from the design lattice and relevant non-linearities plus appropriate physical apertures are included. The lattice is non-linear due to the sextupoles, insertion devices and random and systematic higher order multipole errors. These are discussed further in the section on dynamic aperture. Here, we have taken the bare lattice and added 3 damping wigglers and 3 CPMUs, plus random and systematic multipole errors. The damping wigglers, in

addition, have higher harmonic content determined by fitting computed field maps to a Halbach basis. The systematic multipole errors come from modeling and measurements of quadrupoles and sextupoles borrowed from the SLS which are similar to our design magnets. The random errors come from measured values for the SLS magnets produced by the Budker Institute in Novosibirsk. The ID parameters used were as follows: for the damping wiggler, the peak field is 1.8 T, and the period length 9 cm, with 77 periods. For the CPMUs, the peak field is 1.2 T, and the period length 19 mm, with 160 periods.

Random misalignment and roll errors are added, including the systematic effects from the girders. The girders are misaligned randomly by 100  $\mu$ , and quadrupoles and sextupoles misaligned by 30  $\mu$  relative to the girder. The orbit is corrected by computing the beam response matrix and adjusting the corrector strengths to minimize orbit offset at the BPMs. In addition, we must correct the linear optics due to the perturbation caused by the damping wigglers. For these studies, the three damping wigglers were assumed to occur consecutively. Periodic distribution should also be considered.

The vertical emittance is determined by a combination of linear coupling and vertical dispersion. The random roll errors of 0.2 mrad for the quadrupoles and sextupoles and 0.5 mrad girder to girder cause coupling, but the equilibrium vertical emittance is still below the diffraction limited value of 8 pm ( $\epsilon_y = 1$  pm for the case used for the calculations of energy acceptance). An algorithm to increase vertical dispersion combined with coupling control/correction has been developed to control vertical emittance. The algorithm has been tested but is not included in these calculations. A vertical emittance of 8 pm is assumed here for the lifetime calculation.

After preparing the lattice by adding all the above errors, corrections and physical apertures (described below), the momentum acceptance around the ring is computed by tracking. The result for the nominal case is shown in Figure 3.2.16 (a). We see that the errors and apertures have not had a large impact and the lifetime has only dropped from 2.77 hours to 2.62 hours. Adding more insertion devices adds to the non-linearity and is expected to have an impact on momentum aperture.

As we have mentioned, beam loss can occur due to electrons hitting transverse physical apertures. Both vertical and horizontal apertures can decrease lifetime. First consider the horizontal case. A Touschek scatter in a dispersive region causes betatron oscillations throughout the ring. Considering uncoupled linear betatron dynamics, the amplitude of such oscillations is given by

$$x(s) = (\eta + \sqrt{H_0\beta_x})\delta \quad (3.2-34)$$

with  $H_0$  the dispersion invariant (3.2-31) at the position of the scatter, and  $\delta$  the resultant relative energy change of the particle. The maximum value is approximately twice the maximum dispersion times  $\delta$ . For  $\delta$  of 3% this can be as large as 27 mm. Figure 3.2.16 (b) shows the effect on lifetime of varying the horizontal aperture in the maximum dispersion region. We see that below 27 mm, the lifetime decreases. This shows the importance of maintaining the stay-clear aperture. Photon absorbers are one example of elements for which it would otherwise be desirable to be closer to the beam than the stay-clear specifications.

If we expect such large horizontal betatron oscillations to be stable, then clearly any coupling will cause vertical apertures to be a concern. The smallest vertical aperture is that of the CPMU gap of  $\pm 2.5$  mm. We have varied this gap size and computed the effect on the lifetime in Figure 3.2.16 (c). Below the nominal value of  $\pm 2.5$  mm, we see a decrease in lifetime.

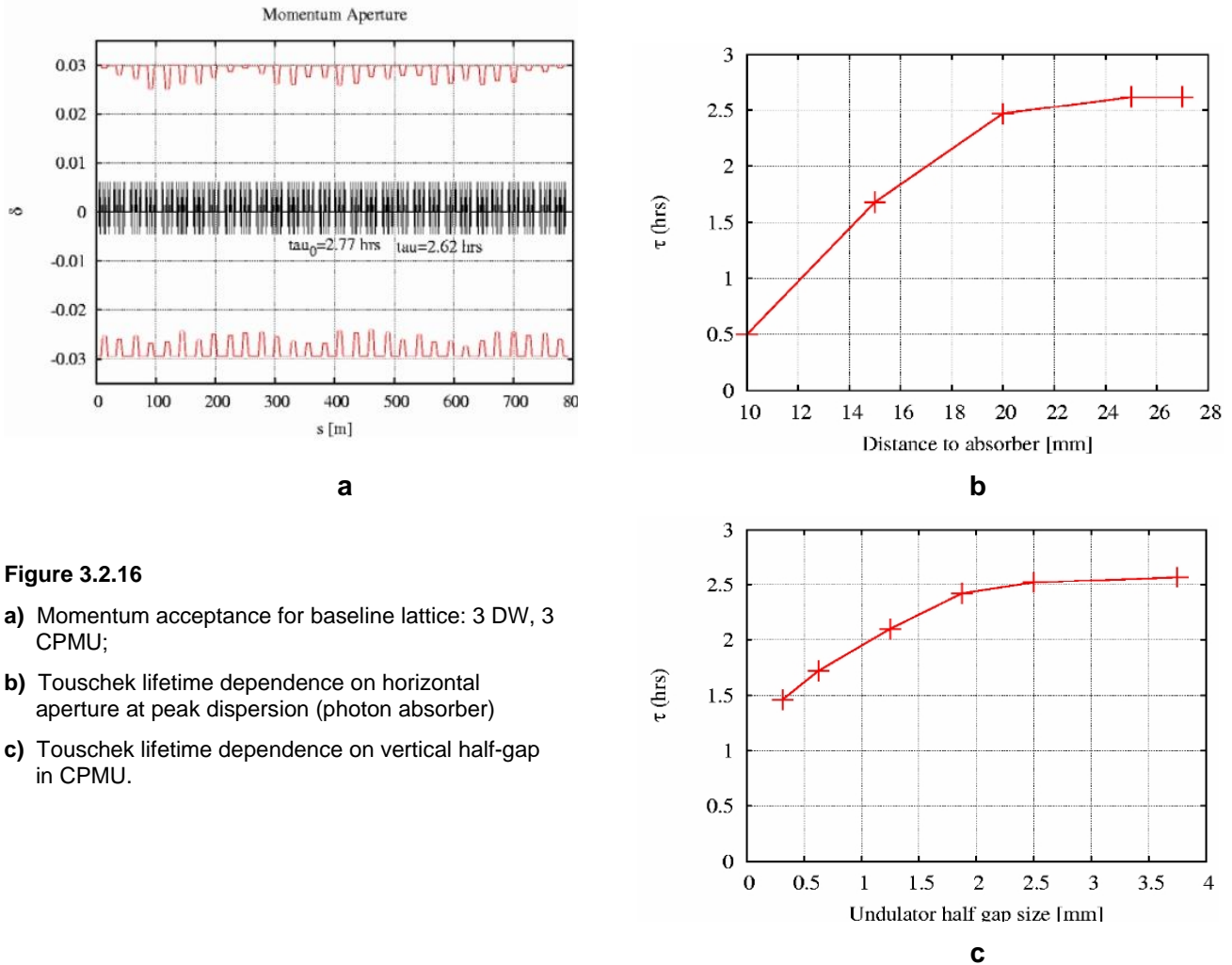


**Figure 3.2.16**

- a) Momentum acceptance for baseline lattice: 3 DW, 3 CPMU;
- b) Touschek lifetime dependence on horizontal aperture at peak dispersion (photon absorber)
- c) Touschek lifetime dependence on vertical half-gap in CPMU.

In conclusion, a realistic storage ring model is required to estimate the Touschek lifetime, particularly in order to compute the momentum acceptance. We are developing such a realistic model to be used together with dynamic aperture calculations to analyze limits on stay-clear apertures, magnetic and alignment imperfections, and other machine parameters such as chromaticity. Such studies are ongoing and must be continually updated as the sextupole settings and tunes continue to be optimized and the lattice design continues to mature. Further effects to be explored are the impact from additional insertion devices, especially from EPU's. Also, we will study more realistic ID modeling, inclusion of the dispersion wave to get a self-consistent model, and required stay-clear apertures. We also plan comprehensive studies including multiple seeds for the random errors. Finally, we emphasize that even if the momentum acceptance of 3% is achieved, we still require the bunch lengthening effect from the Landau cavity in order to achieve a Touschek lifetime of 3 hours.

### 3.2.7 Landau Cavity

Let us begin by reviewing the operation of a higher-harmonic, bunch-lengthening cavity (HHC) [3.2.38]. The fundamental cavity operates at an angular frequency,  $\omega_{rf} = h\omega_0$ , where  $h$  is an integer and  $\omega_0 = 2\pi/T_0$  is the angular frequency of revolution. Assuming the Landau cavity is operating at the  $n^{\text{th}}$  harmonic of the frequency of the fundamental RF, the voltage seen by an electron with temporal deviation  $\tau$  is

$$V(\tau) = V_0 \left[ \sin(\omega_{rf}\tau + \phi_s) + \kappa \sin(n\omega_{rf}\tau + \phi_n) \right]. \quad (3.2-34)$$

In the ideal operation of such a cavity, one chooses to satisfy the conditions

$$\begin{aligned} U_0 &= V_0 [\sin \phi_s + \kappa \sin \phi_n] \\ 0 &= \cos \phi_s + n\kappa \cos \phi_n \\ 0 &= \sin \phi_s + n^2 \kappa \sin \phi_n, \end{aligned} \quad (3.2-35)$$

where energy loss ( $U_0$ ) and gain are balanced, and the first and second derivatives of the waveform are set to zero, at zero phase. In this case, the voltage has the form

$$V(\tau) = \cos \phi_s \left( \sin \omega_{rf}\tau - \frac{1}{n} \sin n\omega_{rf}\tau \right) + \sin \phi_s \left( \cos \omega_{rf}\tau - \frac{1}{n^2} \cos n\omega_{rf}\tau \right). \quad (3.2-36)$$

Approximating this for small  $\tau$  yields the cubic form

$$V(\tau) \cong \cos \phi_s \left( \frac{n^2 - 1}{6} \right) (\omega_{rf}\tau)^3 + \sin \phi_s \left( 1 - \frac{1}{n^2} \right). \quad (3.2-37)$$

As we will operate the Landau cavity passively, i.e., powered only by the beam, we cannot satisfy all of the ideal conditions. A superconducting cavity, in particular, absorbs very little power, implying that  $\phi_n$  is fixed at  $-\pi/2$ , a few degrees from the ideal phase. Fortunately, this phase shift has little impact on the bunch profile. Figure 3.2.17 shows an unstretched bunch (blue) plotted with a stretched bunch (red) in a uniform fill with HHC detuning at +82 kHz.

A third-harmonic Landau cavity can be used to increase the electron bunch length without increasing the energy spread. This increases the Touschek lifetime and reduces the effect of intrabeam scattering on emittance. The nonlinear voltage resulting from the use of a Landau cavity results in a large increase in the dependence of the synchrotron tune on the amplitude of synchrotron oscillations. Energy transfer from potentially unstable resonant particles within a bunch to the surrounding non-resonant particles often provides a powerful mechanism for the suppression (Landau damping) of longitudinal coupled-bunch dipole modes. Also, the increase of bunch length can increase the stabilizing effect of positive chromaticity on the transverse dipole oscillations. The increased synchrotron tune spread can also help stabilize the higher-order head-tail modes.

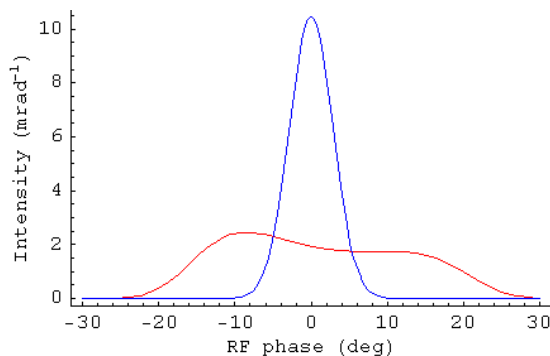


**Figure 3.2.17** An unstretched bunch (blue) plotted with a stretched bunch (red) in a uniform fill with HHC detuning at +80 kHz. The bunch lengths are 14.1 and 56.1 ps, respectively.

If, as expected, there is a gap in the fill for ion clearing, then there will be a periodic transient induced in the cavity fields, causing non-uniform bunch profiles across the bunch train [3.2.39, 3.2.40, 3.2.41]. This effect is proportional to the  $R/Q$ s of the cavities, which favors superconducting cavities due both to their lower  $R/Q$  and their higher sustainable fields (requiring fewer cavities). Away from the center of the bunch train, bunches are much shorter and are peaked near the local synchronous phase, which can be a distance from the center of the nominal bucket. These peripheral bunches have shorter Touschek lifetime. This effect was found at ALS [3.2.40] to significantly reduce the overall lifetime of the beam. Figure 3.2.18 shows the bunch profiles for a 90% fill pattern, harmonic-cavity detuning of +80 kHz, and a single gap, and with the gap split into four symmetrically spaced gaps.

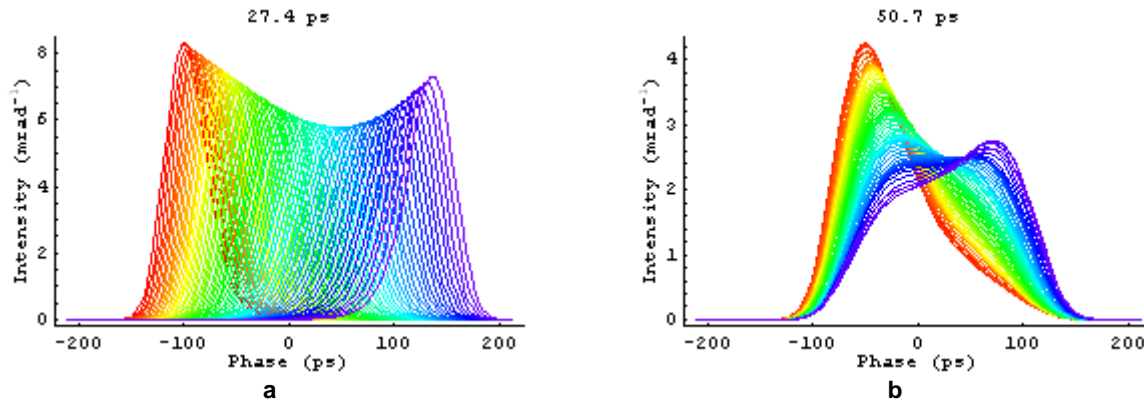


**Figure 3.2.18** Bunch profiles along the bunch train for a 90% fill fraction, harmonic-cavity detuning of +80 kHz, and a) a single gap in the train, and b) four gaps in the train. Each plot is labeled with the average RMS bunch length of the bunches. For reference, the unstretched bunch length is 14.1 ps and the stretched bunch length in a uniform fill is 56.1 ps.

With a single ion-clearing gap, the transient is severe, even with SC cavities (Figure 3.2.18a). The bunches are dispersed in phase with only modest stretching, reducing the field the beam is able to drive in the HHCs. The increase in bunch length is less than a factor of two. In this large ring, reducing the HHC detuning to bring up the field tends to increase the dispersion before increasing the field and stretching individual bunches. But breaking up the gap into several smaller gaps makes the ring appear to the cavities to be a smaller and is effective at increasing the average bunch length. In the case of four gaps, the increase in bunch length is by a factor of 3.6. The profiles of Figure 3.2.18b with four gaps appear similar to the bunch profiles measured at ELETTRA [3.2.42], which is one-third the size of NSLS-II. With an 80% fill fraction, the bunches are even shorter (Figure 3.2.19). Bunch lengths vary smoothly with increasing fill fraction to the 56.1-ns length at a 100% fill. Smaller fill fractions aggravate the variation of bunch shapes along the train.

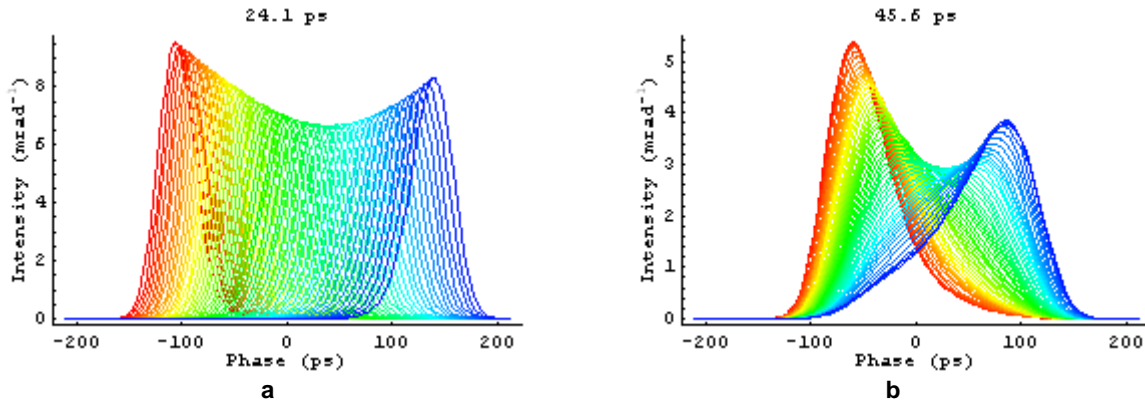


**Figure 3.2.19** Bunch profiles along the bunch train for a 80% fill fraction, harmonic-cavity detuning of +80 kHz, and a) a single gap in the train, and b) four gaps in the train. Each plot is labeled with the average RMS bunch length of the bunches. For reference, the unstretched bunch length is 14.1 ps and the stretched bunch length in a uniform fill is 56.1 ps.

Bunch lengths vary with position along the train, and tend to be greatest near the center. In Figure 3.2.20a, each trace corresponds to a particular cavity field set by the detuning, which is from +110 (violet) to 70 (red) kHz. As HHC fields increase, bunch lengths and lifetimes tend to increase; but bunches that become double peaked, however, can show large RMS bunch length but reduced lifetime. Bunch centroid phases (arrival times) also vary with position along the train. In Figure 3.2.20b, the phase along the train is plotted for a 90% fill and the same fields as in Figure 3.2.20a. The synchronous phase is a sensitive function of local shifts in the RF wave due to the  $(\omega_{rf})^3$  inflection; that sensitivity increases with increasing HHC field, even beyond the optimal HHC field.

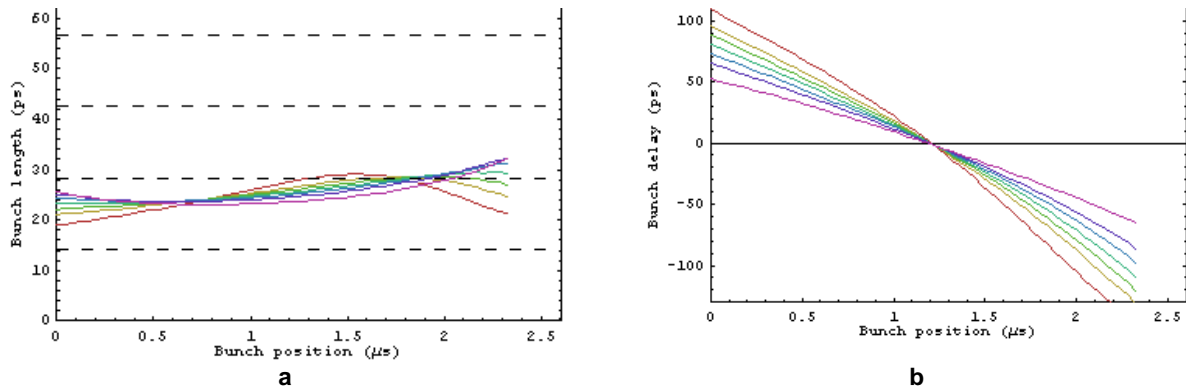


**Figure 3.2.20** Bunch lengths a) and delays b) along the bunch train for a 90% fill and a single gap. Each trace corresponds to a particular cavity detuning: +110 (violet), 100, 95, 90, 85, 80, and 70 kHz (red). In a), the dashed lines are drawn at multiples of the unstretched bunch length.

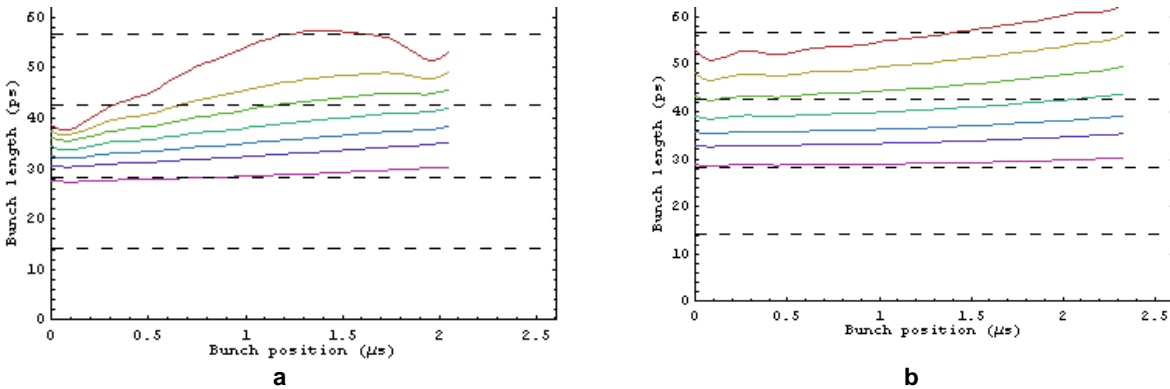


**Figure 3.2.21** Bunch lengths along the bunch train with four gaps in an **a)** 80% fill, and **b)** 90% fill. Each trace corresponds to a particular cavity detuning: in **a)**, +110 (violet), 100, 95, 90, 85, 80, and 70 kHz (red), and in **b)**, +110 (violet), 100, 95, 90, 85, 80, and 75 kHz (red). The dashed lines are drawn at multiples of the unstretched bunch length.

The HHC field required for nominal bunch stretching is 1.5 MV. Since the maximum sustained fields reached in HHCs developed to date are 0.5 MV per cell in 1500 MHz cavities, three cells are required, either in three single-cell cavities, or two double-cell cavities. The performance plots above were computed assuming four cells, perhaps in two cryostats. In practice, significantly longer lifetimes are achievable by operating the HHCs at fields slightly higher than the ideal described above, as the NSLS VUV ring is operated now. The useful fields are limited by the onset of higher-order longitudinal instabilities.

The Day-1 configuration employs a reduced number of damping wigglers and consequently requires less main- and harmonic-cavity fields. Since two harmonic-cavity cells are capable of providing 1.0 MV of the 1.1 MV nominally required during this phase, most of the benefit of the HHC is obtained from this one cavity. Since the impedance is only that of two main and two HHC cells, the impact of the bunch train on bunch profiles is reduced in proportion.

Compressed bunch operation for timing experiments is possible by detuning the HHC below the RF harmonic, instead of above. The bunch length at small single-bunch currents is reduced to less than half the bunch length without a harmonic cavity. But at finite currents, potential-well distortion by the ring's broadband impedance, and microwave instability, if present, inevitably increases the bunch lengths. The short bunch lengths may also permit higher-frequency, higher-order modes in the HHC and elsewhere to drive coupled-bunch instabilities. Short-bunch operation may drive the need for longitudinal feedback.

The potential for unstable coupled-bunch modes driven by the CESR-B SC cavity in unstretched bunches was investigated in Section 3.2.3.4. In stretched bunches, Landau damping is expected to provide additional damping. This was confirmed in Vlasov simulations of stretched bunches assuming an RF potential well giving the stretched bunch of Figure 3.2.17. In each run, bunches were simulated with a single HOM present, up to 6.3 GHz, and its threshold for instability in terms of impedance determined. At all frequencies, thresholds at least a few times higher than that given in Eq. 3.2-27 were determined. Results are shown in Figure 3.2.22.



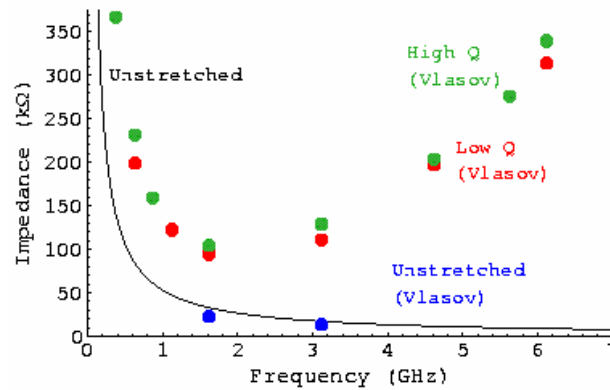


**Figure 3.2.22** Instability thresholds (at 500 ma) for coupled-bunch modes in a stretched bunch expressed in terms of impedance, for a high-Q-model HOM impedance (green points) and lower-Q-model HOM impedance (red points), in the phase-four commissioning phase of the machine. The solid line is from Eq. 3.2-27, and blue points are test Vlasov runs with unstretched bunches. Thresholds were determined by Vlasov simulations.

It is useful to construct linear time-independent models of the RF system and beam, which are then plugged into comprehensive models of the RF system and used to search for unanticipated behaviors [3.2.43]. Linear models are also useful for determining RF-system specifications, such as amplifier noise specifications, from beam-based noise specifications. But the stretched bunches of NSLS-II have a multiplicity of active degrees of freedom that shape their small-signal behavior as they interact with the rf system, and the Pedersen model [3.4.44] is not adequate to model them. As an alternative, computer simulations may be used to determine beam behavior, which is realistic to the degree to which the computer model captures the physics of the beams.

In this spirit, Vlasov simulations were used to determine impulse response functions, which were then Fourier transformed to their frequency-domain representations. The beam phase response to amplitude and phase modulation of the rf, which is the motion of the bunch centroid phase in response to excitation of the RF intensity and phase, is shown in Figure 3.2.23. Although only the beam phase response is shown, beam energy, main-cavity amplitude and phase, and HHC amplitude and phase responses are also determined by a single set of simulations. Very precise rational-function fits have been obtained using MATLAB's signal processing toolbox.

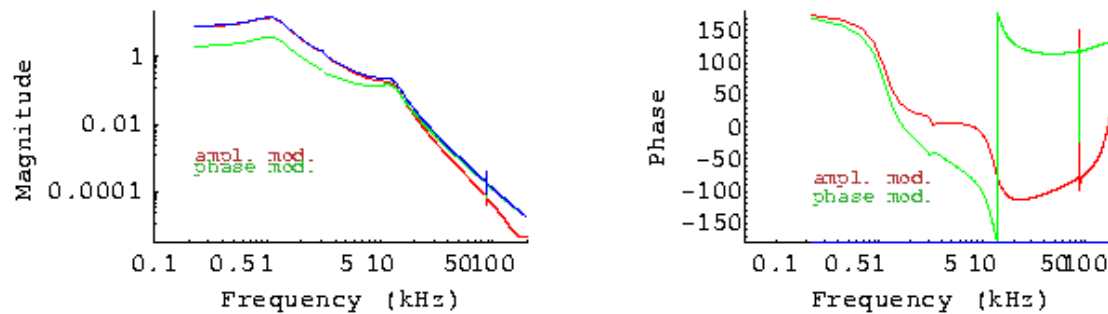


**Figure 3.2.23** Beam-phase response functions to amplitude and phase modulation. Red traces are for amplitude modulation, green traces for phase modulation, and blue traces for the root square sum of the two. The left plot shows the amplitudes of the response functions, and right plots show the phases. There are four main cavities, four HHCs, HHC detuning is -4 kHz, and the loaded Q of the main cavities is set to 90 k.



There is considerable structure in these response functions starting at about 1 kHz that suggests that the problem of designing an RF controller capable of suppressing noise at significant bandwidth will be difficult. It is hoped that detailed rational-function and RF system models will provide some guidance in this area.

NSLS-II can opt to use an active HHC, i.e., HHCs that are powered by conventional amplifiers, such as was done in the NSLS VUV ring. In this configuration, resistive and reactive power are applied to control the phase of the cavity relative to the beam, almost arbitrarily. But the numerical results presented above, and the example of the VUV ring, which uses an active system to set the cavity (a NC cavity) phase to  $-90$  degrees, show that the impact of the difference between  $-90$  degrees and the nominal phase for stretching, even in the uniform-fill case, is insignificant. And in a fill with a significant gap, the improvement in the profiles is swamped by the effect of the periodic transient. Furthermore, an active system would require development of a cavity with an input coupler, could introduce multipacting, and could complicate HOM suppression. For these reasons, a passive cavity has been selected for NSLS-II.

### 3.2.8 Conclusions

Using a simplified model of the storage ring impedance, we have estimated the instability thresholds for NSLS-II. The longitudinal motion is found to be stable. At zero chromaticity, the transverse resistive wall impedance will make the beam unstable at 15 mA average current. According to simulations, increasing the chromaticity above 4 should provide stability. However, there is concern about the effect on DA at higher chromaticity; therefore, we will also use a transverse feedback system.

We have made significant progress in calculating the impedance of the storage ring using GdfidL. The results obtained thus far are within the envelope of the model we have used to estimate thresholds. Thus, we believe our model is conservative. We plan to complete the calculation of the storage ring impedance and then use the numerically determined wakefields in a tracking code to determine the instability thresholds.

Calculations indicate that the increase of emittance due to intrabeam scattering should be less than 20%. For the present state of the lattice design, the 5 mm full vertical aperture of the in-vacuum undulators reduces the energy acceptance from 3% down to 1.5% at large-dispersion locations. This results in a Touschek lifetime of 2 hrs. We plan to investigate whether further optimization of the working point can reduce the nonlinear coupling and thus increase the Touschek lifetime. Use of a Landau third-harmonic bunch lengthening cavity is planned. This will reduce the effect of intrabeam scattering on the emittance, lengthen the Touschek lifetime to more than 3 hrs, and provide enhanced longitudinal and transverse stability.

### References

- [3.2.1] A.W. Chao, *Physics of Collective Beam Instabilities in High Energy Accelerators* (Wiley, NY, 1993).
- [3.2.2] See, e.g., K. Harkay, R. Nagaoka, J.L. Revol, and T. Nakamura, "A Preliminary Comparison of Beam Instabilities among ESRF, APS, and SPrinG-8 X-Ray Storage Ring Light Sources, Proc. EPAC2002, 1505 (2002).
- [3.2.3] W. Bruns, <http://www.gdfidl.de>.
- [3.2.4] G.V. Stupakov, "Wake and Impedance," SLAC-PUB-8683 (2000).
- [3.2.5] B. Zotter and S.A. Kheifets, *Impedances and Wakes in High-Energy Particle Accelerators* (World Scientific Publishing Co., Singapore, 1998).
- [3.2.6] A. Chao, S. Heifets, and B. Zotter, "Tune Shifts of Bunch Trains due to Vacuum Chambers Without Circular Symmetry," *Phys. Rev. ST-AB* **5**, 111001 (2002).
- [3.2.7] K. Bane, and M. Sands, "Short-Range Resistive Wall Wakefields," AIP Conf. Proc. **367**, 131 (1995).
- [3.2.8] B. Podobedov, "Extreme Anomalous Skin Effect Wakefields," unpublished.

- [3.2.9] Y.C. Chae, “The Impedance Database and its Applications to the APS Storage Ring,” Proc. PAC2005, 3017.
- [3.2.10] See, e.g., S. Krinsky, “Simulation of Transverse Instabilities in the NSLS-II Storage Ring,” BNL-75019-2005-IR.
- [3.2.11] J. Haissinski, *Il Nuovo Cimento* **18**, 72 (1973).
- [3.2.12] K. Oide and K. Yokoya, “Longitudinal Single-Bunch Instability in Electron Storage Ring,” KEK Preprint 90-10 (1990).
- [3.2.13] M. Borland, ELEGANT,  
[http://www.aps.anl.gov/Accelerator\\_Systems\\_Division/Operations\\_Analysis/software.shtml](http://www.aps.anl.gov/Accelerator_Systems_Division/Operations_Analysis/software.shtml)
- [3.2.14] D. Boussard, CERN LABII/RF/INT/75-2 (1975).
- [3.2.15] M. Blaskiewicz, “The TRANFT User’s Manual,” unpublished.
- [3.2.16] J. Kirchgessner, *Part. Accel.* **46**, 151 (1995).
- [3.2.17] M. de Jong et al., *J. Microwave Power Electromagnetic Energy* **27**, 136 (1992).
- [3.2.18] K. Halbach and R.F. Holsinger, “SUPERFISH-A Computer Program for Evaluation of RF Cavities with Cylindrical Symmetry,” *Part. Accel.* **7**, 213 (1976).
- [3.2.19] Mark deJong, private communication.
- [3.2.20] M.S. Zisman, S. Chattopadhyay, and J.J. Bisognano, “ZAP User’s Manual,” LBL-21270, UC-28 (1986), 168.
- [3.2.21] R. Nagaoka, “Numerical Evaluation of Geometric Impedance for SOLEIL,” Proc. EPAC2004, 2038.
- [3.2.22] K. Yokoya, “Resistive Wall Impedance of Beam Pipes of General Cross Section,” *Part. Accel.* **41**, 221 (1993).
- [3.2.23] G. Stupakov, “Coupling Impedance of a Long Slot and an Array of Slots in a Circular Vacuum Chamber,” *Phys. Rev. E* **51**, 3515 (1995).
- [3.2.24] E. Karantzoulis, V. Smaluk and L. Tosi, “Broad Band Impedance Measurements on the Electron Storage Ring ELETTRA,” *Phys. Rev. ST-AB* **6**, 030703 (2003).
- [3.2.25] B. Podobedov and S. Krinsky, “Transverse Impedance of Elliptical Cross-Section Tapers,” Proc. EPAC2006, 2973 (2006).
- [3.2.26] A. Blednykh, S. Krinsky, B. Podobedov, and J.M. Wang, “Transverse Impedance for Small-Gap Undulators for NSLS-II,” Proc. EPAC2006, 2973 (2006).
- [3.2.27] P. Stefan et al., “Small-Gap Undulator Research at the NSLS: Concepts and Results.” *Nucl. Instr. Meth. A* **412**, 161 (1998).
- [3.2.28] A. Blednykh, “Trapped Modes in an Elliptic Vacuum Chamber,” *Nucl. Instrum. Meth. A*.
- [3.2.29] P.J. Chou, “Numerical Analysis of Higher-Order Modes for Superconducting RF Cavity at SRRC,” Proc. Pac2003, 1368.
- [3.2.30] P.J. Chou, J. Chen, K.-T. Hsu, C.-C. Kuo, C. Wang, and M.-H. Wang, “Collective Effects in the TLS Storage Ring after the Installation of Superconducting Cavity,” Proc. PAC2005, 2360.
- [3.2.31] A. Piwinski Tech. Rep. HEAC 74, Stanford, 1974; See Also A. Piwinski in A. Chao and M. Tigner, *Handbook of Accelerator Physics*, World Scientific (1999) 125.
- [3.2.32] J. Bjorken and S. Mtingwa, “Intrabeam Scattering,” *Part. Accel.* **13**, 115 (1983).
- [3.2.33] K. Kubo and K. Oide, “Intrabeam Scattering Formulas for High Energy Beams,” *Phys. Rev. ST-AB* **4**, 124401 (2001).
- [3.2.34] K.L.F. Bane, “A Simplified Model of Intrabeam Scattering,” SLAC-PUB-9226 (2002).
- [3.2.35] T. Raubenheimer, *Part. Accel.* **45**, 111 (1994).
- [3.2.36] K. Oide, *SAD User’s Guide*.
- [3.2.37] A. Streun, “Momentum Acceptance and Touschek lifetime,” SLS Note 18/97.
- [3.2.38] A. Hofmann and S. Meyers, “Beam Dynamics in a Double RF System,” Proc. 11<sup>th</sup> International Conference on High Energy Accelerators, Geneva (Birkhauser Verlag, Basel, (1980), p 160.
- [3.2.39] N. Towne, “Stretched Bunch Shapes in the NSLS VUV Ring,” Proc. PAC1999 (1999) 2828.

[3.2.40]J.M. Byrd, S. De Santis, J. Jacob, and V. Serriere, “Transient Beam Loading Effects in Harmonic RF Systems for Light Sources,” *Phys. Rev. ST-AB* **5**, 092001 (2002).

### 3.3 Orbit Feedback System

#### 3.3.1 Requirements for Beam Stability

To realize the benefits of the high brightness and small beam sizes of NSLS-II, it is essential that the photon beams are exceedingly stable, assuring constant intensity after apertures, constant photon energy after monochromators, and minimal photon source size and highly precise steering accuracy for focusing on small samples. For example, in the common case of 1:1 focusing optics, positional stability of the photon beam on the sample is directly related to that of the electron beam. The position of the photon beam should be stable to a level of  $\Delta_y/\sigma_y \sim 10\%$ . We require beam motion of no more than 10% of beam size, particularly in the frequency range from  $\sim 10$  mHz to 100 Hz. This tolerance has been adopted by many synchrotron radiation laboratories. Since the minimum vertical beta function is about 1 m, when we take the vertical emittance as  $10^{-10}/4\pi$  m, the vertical beamsize is  $2.7 \mu\text{m}$  RMS. Therefore, the beam position stability should be  $\sim 0.3 \mu\text{m}$  in the short straight section.

#### 3.3.2 Fast Orbit Motion with Feedback Loop On and Off

For the NSLS-II ring with a DBA30 lattice as shown in Figure 3.1.1 (only half a super-period is shown), the performance of a fast, closed-orbit feedback system with 120 BPMs and 120 correction trims was calculated. The BPM and fast corrector positions used in this simulation are shown in Figure 3.3.1. The vacuum chamber at the fast correctors is made of stainless steel.

We averaged over 400 different sets of random numbers for positional deviation of all the quads, assuming they vibrate randomly with uncorrelated RMS displacement of  $0.2 \mu\text{m}$ . The resulting beam RMS motion  $\sigma_{\Delta y}$  is shown in blue in Figure 3.3.2. We used 60 out of 120 eigenvectors in this case.

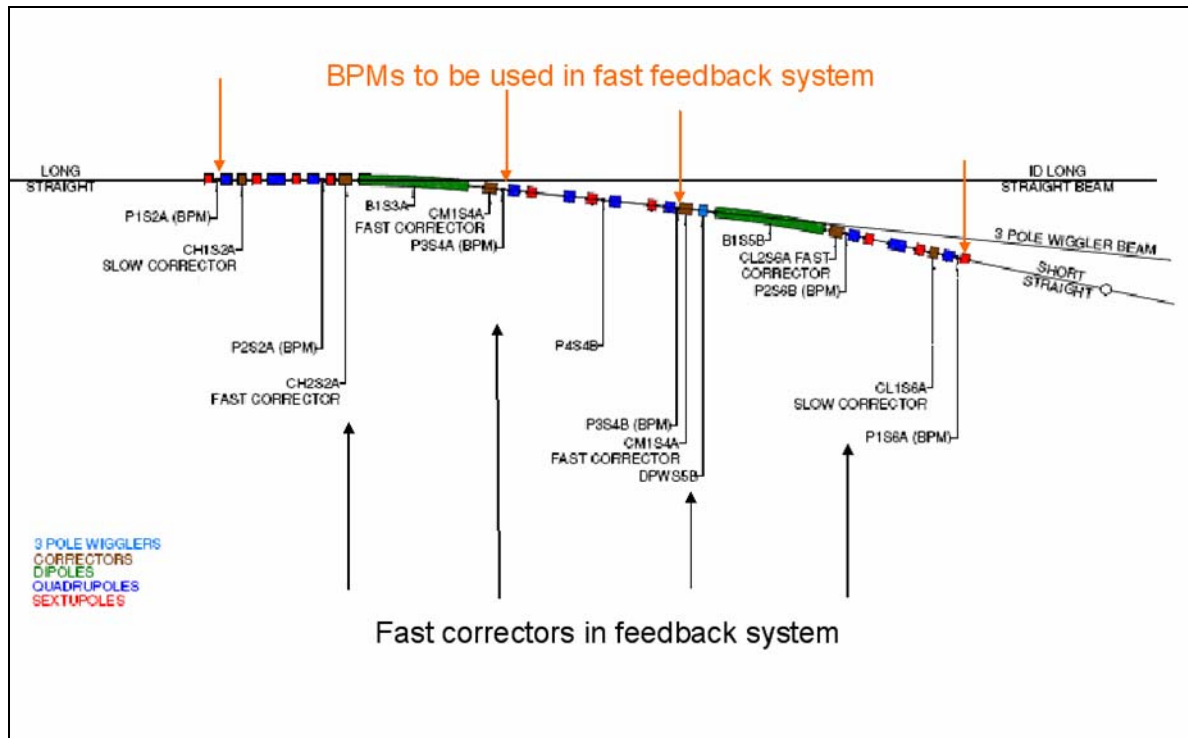
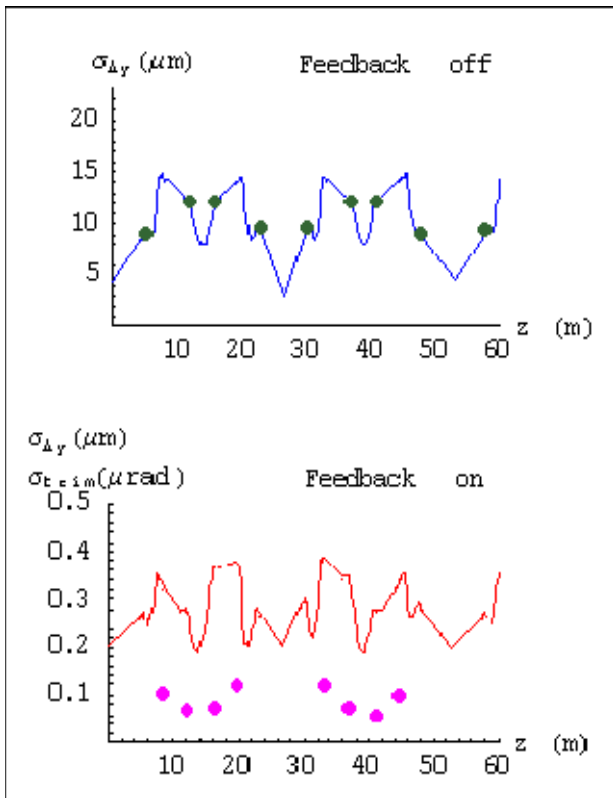


Figure 3.3.1 Positions of BPMs and fast correctors in one cell.

For each set of Gaussian random errors for the quad and BPM vibrations, all with RMS displacement of  $0.2 \mu\text{m}$ , the open-loop BPM signal was calculated assuming BPM electronic noise is  $0.2 \mu\text{m}$ . Then the SVD matrix was used to calculate the corrector strengths, and finally the orbit with the feedback loop closed with a gain of 100. After averaging over 400 random samples, the residual RMS beam motion shown in Figure 3.3.2 was obtained, represented by the red curve. The open-loop BPM signal and the corrector strength used in the feedback loop are marked by dark green and purple dots, respectively.

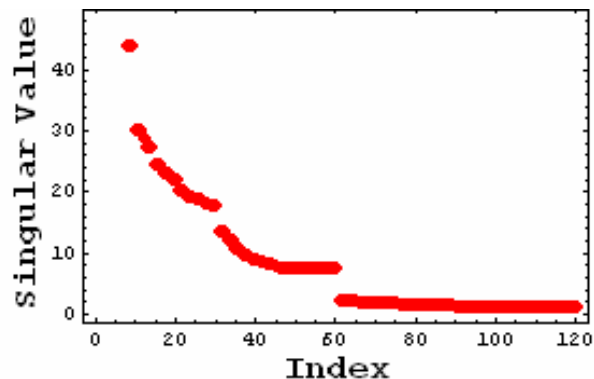
The height of the purple dots represents the RMS strength of the correctors, in units of  $\mu\text{rad}$ . The figure shows that the feedback loop reduces the beam motion at the center of the long straight section ( $z = 0$ ) from  $3 \mu\text{m}$  to  $0.2 \mu\text{m}$ . The maximum RMS corrector strength is on the order of  $0.14 \mu\text{rad}$ .



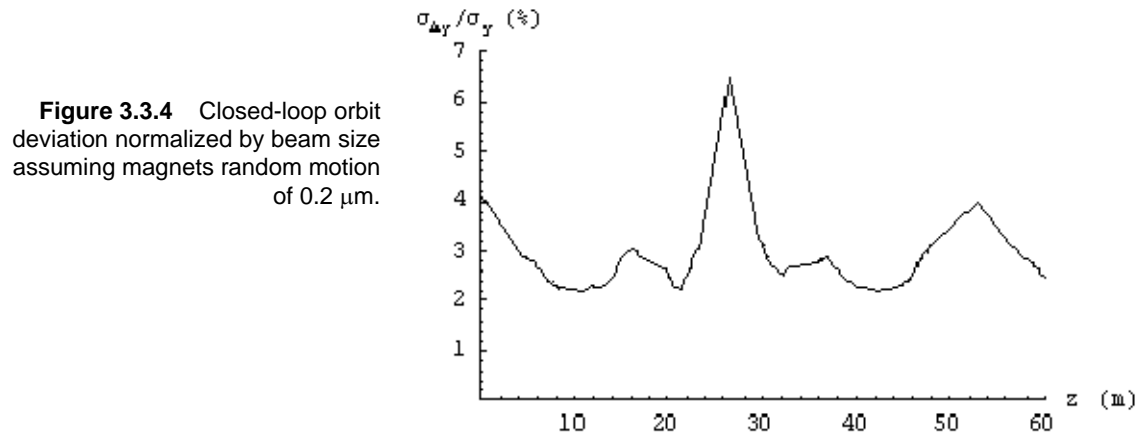
**Figure 3.3.2** Open (blue) and closed-loop (red) RMS orbit motion and RMS corrector strengths (purple dots) in the feedback loop. The  $z$ -axis is the distance along the ring circumference, in meters. The green dots are the RMS motion at the location of the BPMs in the feedback loop. 60 eigenvalues out of 120 are used in this simulation.

Figure 3.3.3 gives the singular value spectrum for the 4BPM, 4 trims feedback system, indicating the possibility of using 60 eigenvectors, or using 2 trims per cell in vertical plane. Simulations confirmed that both give similar performance.

**Figure 3.3.3** Singular values for the feedback system with four BPMs and four trims shows that using 60 eigenvectors should have similar performance to using all 120, and this is confirmed by simulation. It also indicates that good performance could be obtained using only two trims per cell (60 eigenvectors).



The tolerance on the floor motion required to keep beam motion within 10% of beamsize was determined using the following assumptions: 1)  $\epsilon_y = 0.1 \text{ nm}/4\pi$ , 2) all the quads and BPMs mounted on the girders have uncorrelated random vibration of  $0.2 \text{ }\mu\text{m}$ , and 3) the BPM electronic noise is  $0.2 \text{ }\mu\text{m}$ . Averaging over 400 samples gave the ratio of the vertical beam motion divided by the RMS beamsize as a function of  $z$  in the ring, shown in Figure 3.3.4. At the short straight section, the ratio of beam motion over beamsize is 6.4%. This implies that the tolerance for the quad vibration is more than  $0.3 \text{ }\mu\text{m}$  RMS. This calculation ignored the fact that for low-frequency ground motion, the movement of different components mounted on the girders can be correlated, since the sound wavelength at low frequency can be larger than the girder dimension. Actually, simulation for correlated movement of quads mounted on the same girder shows a reduced amplification factor, since the quads moving together tend to cancel each other [3.3.1]. The noise caused by ripples in the power supply corrector magnet current was also ignored. Compared with this effect, the orbit motion due to the vibration of BPMs is much more difficult to suppress. Actually, it is very difficult to reduce the beam motion to much less than the amplitude of the BPM vibration. Similar calculations for horizontal orbit show that if quads and BPMs have random vibration of RMS value  $0.2 \text{ }\mu\text{m}$  and BPM noise is  $0.2 \text{ }\mu\text{m}$ , the residual RMS value of beam motion is  $0.14 \text{ }\mu\text{m}$  at the straight sections. Since the horizontal beam size is much larger than the vertical beam size, the horizontal requirement is much easier to satisfy than the vertical.



The beam motion due to power supply noise in a digital feedback system is determined by the voltage corresponding to the last bit of the power supply and the power supply current noise itself [3.3.1, 3.3.2]. Similar to the vibration simulation, we find that if we require beam motion (due to trim noise at the beam waist where  $\beta_y = 1.26 \text{ m}$ ) to be less than  $0.1 \text{ }\mu\text{m}$ , the RMS trim noise should be less than 4 nrad. Hence the power supply should be accurate to  $4 \text{ nrad}/0.29 = 12 \text{ nrad}$ . If the maximum trim strength is 1 mrad, we need the last digit to be less than 12 ppm and the RMS noise should be less than 4 ppm.

### 3.3.3 Ground Movement at the NSLS-II Site

Figure 3.3.5 shows floor vibration measurement in January 2007 at three locations: CFN, field near CFN future NSLS-II site, and NSLS beamline. This data show that due to cultural activity the noise level is higher at the current NSLS site than CFN center and the field where the future NSLS-II is located. It shows that with improved floor design and construction, the vibration noise is much lower. In Figure 3.3.6, the inverse integrated PSD of floor vibration measurement at UV ring floor near entrance using seismic sensor shows RMS vibration amplitude within bandwidth from 0.5 Hz-100 Hz is less than  $0.1 \text{ }\mu\text{m}$ . Since the sound speed in concrete is 3 km/s, below 0.5 Hz, the ratio of sound wavelength over the storage ring diameter is sufficiently large that the effect of the vibration below 0.5 Hz is not critical.

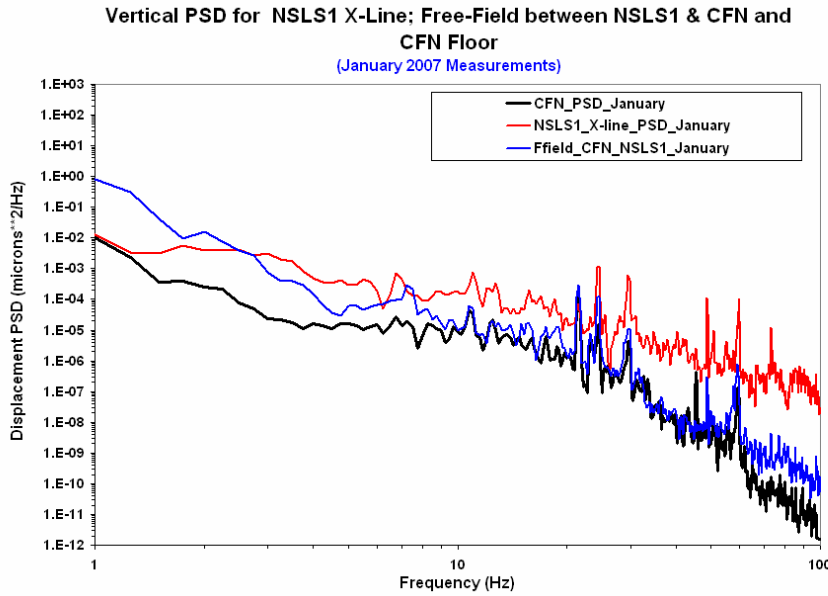


**Figure 3.3.5** Floor vibration measurement at three locations: CFN, field near CFN future NSLS-II site, and NSLS beamline X1.

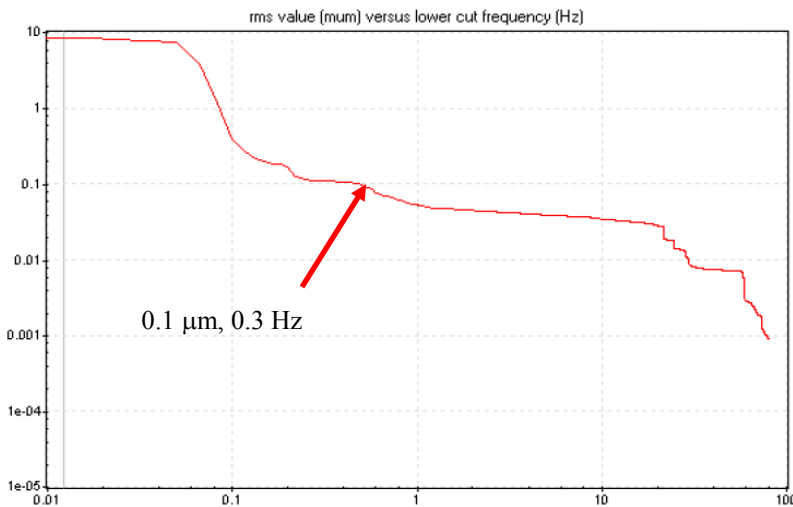


**Figure 3.3.6** Inverse integrated PSD of floor vibration measurement at UV ring floor near entrance using seismic sensor showing RMS vibration amplitude within bandwidth from 0.5 Hz-100 Hz is less than 0.1 μm.

### 3.3.3.1 Long-Term Ground Movement

As for long-term ground movement at the BNL site, measurements carried out at RHIC between 1997 and 2002 show the coefficient  $A$  in the ATL law is  $A \cong 3 \times 10^{-18} \text{ m}^2/\text{m/s}$  [3.3.4, 3.3.5]. Based on this, we estimate that the RMS movement within the 252 m diameter of NSLS-II over a half-year is about 110 μm.

We simulated the performance of the slow feedback system on long-term ground motion using the ATL law [3.3.6] at the NSLS-II site over a half year, with the same set of BPMs and correctors as mentioned in Section 3.3.2. The results are shown in Figure 3.3.7. In this specific example, the maximum ground movement was 107 μm, with an RMS value of 36 μm. The maximum relative movement between the beam and the ground was about 700 μm without feedback; with feedback, it was 48 μm with an RMS value of about 10 μm.

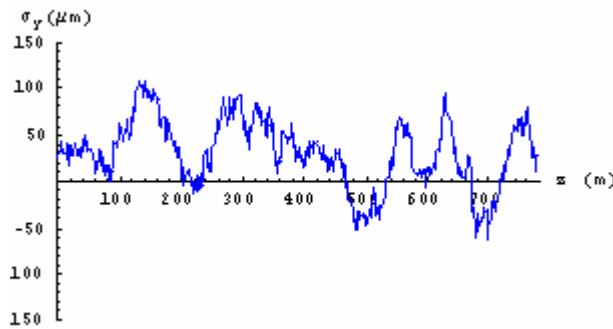
We averaged over 400 samples. The RMS residual movement has a mean value of  $9.3 \mu\text{m}$ . This is over half a year. When we scaled according to the ATL law, the residual RMS movement within a day should be reduced to about  $0.7 \mu\text{m}$ .

If the orbit is realigned every six months, then within that half year the required corrector strength for the global orbit correction is about  $0.1 \text{ mrad}$ . To leave a margin for error, the maximum strength of the corrector is specified to be  $0.5$  to  $1 \text{ mrad}$ . As shown in Section 3.3.2, this requires the last bit of the power supply to be  $30 \text{ ppm}$ .

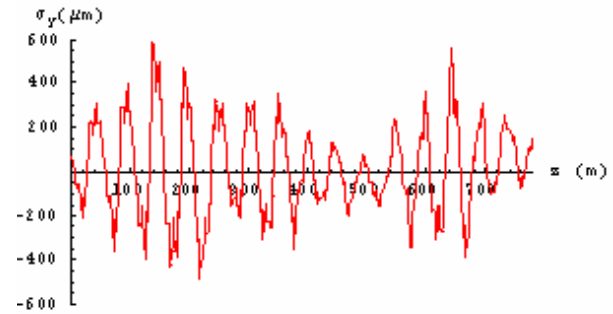
### 3.3.3.2 Temperature Stability

As we discussed in Section 3.3.2, the most stringent requirement on orbit stability is in the  $6.6 \text{ m}$  straight sections, where the BPM motion is required to be less than  $0.2 \mu\text{m}$  (see Figure 3.3.4). Due to thermal expansion of the girder and vacuum chamber support system, the air temperature stability in the storage ring tunnel is specified to be  $\pm 0.1^\circ\text{C}$ . We specify that the BPMs will move less than  $\pm 0.2 \mu\text{m}$ . To insure that in the short straight sections the orbit motion satisfy the stability requirement, we specify the BPMs at the ends of insertion devices in  $6.6 \text{ m}$  straight sections move less than  $\pm 0.1 \mu\text{m}$  with specially designed BPM supports. Our simulation shows that when those BPMs in the short straight sections move less than others, the feedback system also insure the orbit motion in those sections less than other sections correspondingly.

#### Feedback Loop Off

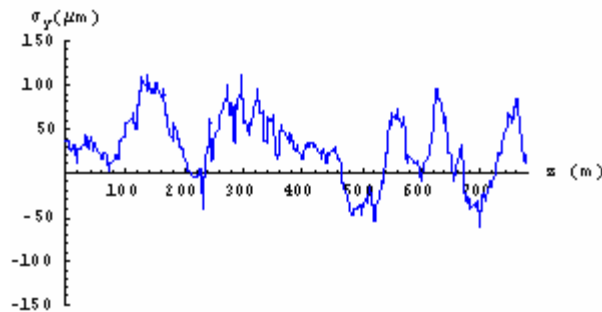


Floor motion around the ring. While the RMS of the relative displacement across the ring diameter for a large number of examples is  $110 \mu\text{m}$ , in this specific example the maximum movement is  $107 \mu\text{m}$ , and the RMS around the ring is  $36 \mu\text{m}$ .

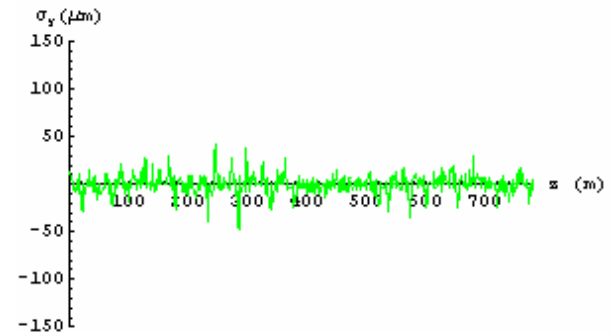


Electron beam motion (vertical) without feedback loop; maximum is  $600 \mu\text{m}$ .

#### Feedback Loop On



Electron beam motion with the feedback loop on follows the floor motion approximately.



Electron beam motion relative to floor (the difference between the two plots on the left) with the feedback loop on; maximum is  $48 \mu\text{m}$ , RMS  $10 \mu\text{m}$ .

**Figure 3.3.7** Simulated long-term ground motion and electron beam motion within half a year, with feedback system on and off. The horizontal axis is the distance along the circumference.



### 3.3.4 BPM Resolution and Noise Floor

A power density spectrum plot of measurement of orbit motion at NSLS using an RF BPM is reported in Figure 3.3.8, with beam motion shown in blue and the noise floor of the BPM in red. The plot shows that above 200 Hz, the beam motion is dominated by the noise floor. Hence, a feedback system with frequency higher than 200 Hz will not improve the orbit stability. The feedback system based on our BPM should have a cut-off point set below 200 Hz. Measurements at NSLS show that the vibration amplitude between 50 Hz and 200 Hz is less than 10 nm, which is negligibly small. Therefore, to relax the requirement on the feedback system bandwidth, the cut-off point is set at 60 Hz. A long-term drift test of the BPM offset is still needed, to show it is sufficiently small (lower than 0.2  $\mu\text{m}$ ). BPMs with better performance are available, and work in developing better BPMs is needed.

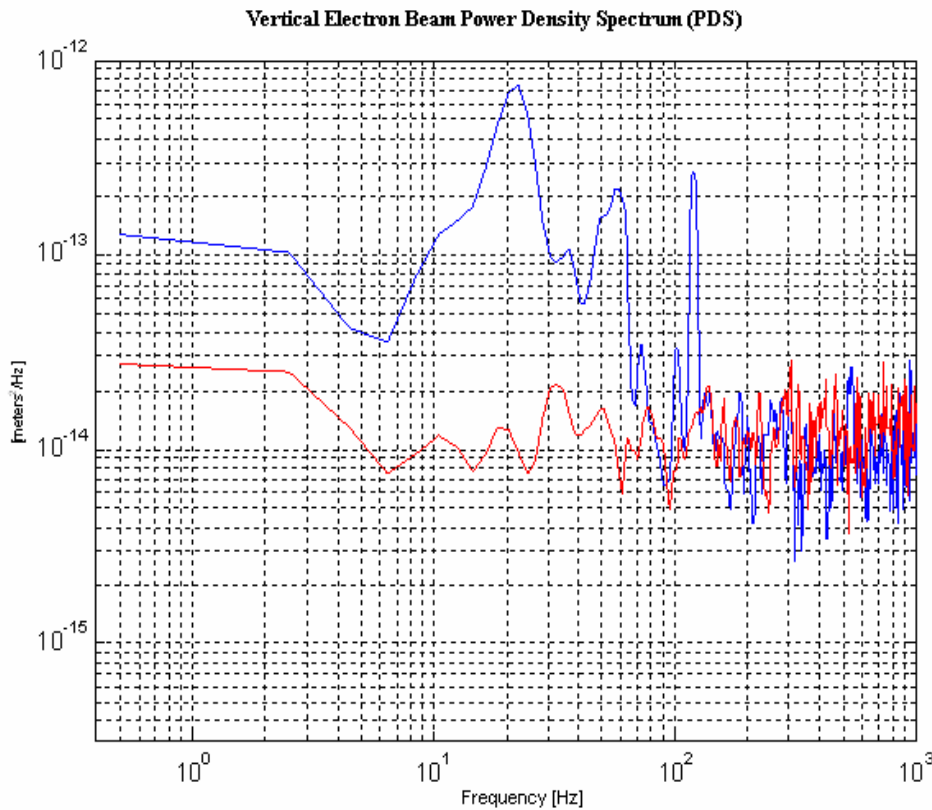


**Figure 3.3.8** Power density spectrum of beam motion.

### 3.3.5 Requirements for the Feedback System

Based on these considerations, the ground vibration of 0.2  $\mu\text{m}$  above 0.5 Hz satisfies the 0.3  $\mu\text{m}$  requirement determined by the feedback system performance calculation presented in Section 3.3.2. However, the BPM motion caused by thermal expansion poses the most stringent requirement on the temperature stability, we require the ring tunnel temperature stability to be within  $\pm 0.1^\circ\text{C}$ , and the BPM supports are designed such that they move less than  $\pm 0.2 \mu\text{m}$  within  $\pm 0.1^\circ\text{C}$ . In particular the BPM supports at the ends of the insertion devices in the 6.6 m sections are designed to move less than  $\pm 0.1 \mu\text{m}$  within  $\pm 0.1^\circ\text{C}$ .

As mentioned in Section 3.3.4, the measured beam motion coincides with the BPM noise floor for frequencies higher than 200 Hz (see Figure 3.3.8). In addition, since most of the motion comes below 60 Hz, it is desirable to design the feedback system PID circuit to reach a 60 Hz bandwidth.

Because eddy currents are proportional to the thickness and electrical conductivity of materials, only thin laminations (1 mm thickness) or air coils should be used for correctors and the low-conductive materials preferred for vacuum chambers. Eddy currents in vacuum chambers usually impose the most critical bandwidth limitation on the feedback loop [3.3.1].

When designing the feedback system bandwidth, it is crucially important to design the vacuum chamber and power supplies for all the correctors to be used in the fast global feedback system such that they have the same frequency response. Without excellent equalization, we may be forced to narrow the bandwidth of the feedback system or lower the gain of the system.

To maintain the dynamical aperture regardless of long-term ground movement requires the beam to stay within 50  $\mu\text{m}$  of the center of the sextupoles. According to the simulation based on the ATL law, described in Section 3.3.2, if the ring is regularly realigned, this can be achieved. RF frequency will also be used as an additional corrector to compensate for energy drifts.

## References

- [3.3.1] M. Borg, PAC '01, talk on IWBS'02, and EPAC 04 paper.
- [3.3.2] J. A. Carwardine and F. R. Lenkszus, "Real-Time Orbit Feedback at the APS," p.12, 1997 beam instrumentation workshop at SSRL.
- [3.3.3] Heiko Ehrlichmann, private communication (2/2006).
- [3.3.4] Vladimir Shiltsev, "Space-Time Ground Diffusion: The ATL Law for Accelerators," DESY-MPY, Notkestrasse 85, 22603 Hamburg, Germany.
- [3.3.5] Vadim Ptitsyn, private communication (7/2004).
- [3.3.6] A. Walski, and N.J. Walker, Proceedings of 2003 PAC.



### 3.4 Canting and Decker Distortion for the NSLS-II

Canting and Decker distortion are similar in that they both require additional trim dipoles placed in the ID straight. In both cases the dispersion must be constrained in the cell. Furthermore, the sum of the additional bend angles must be zero to ensure the beam orbit stays on the center of the multipole magnets. Therefore there are three constraints at the end of the bump:

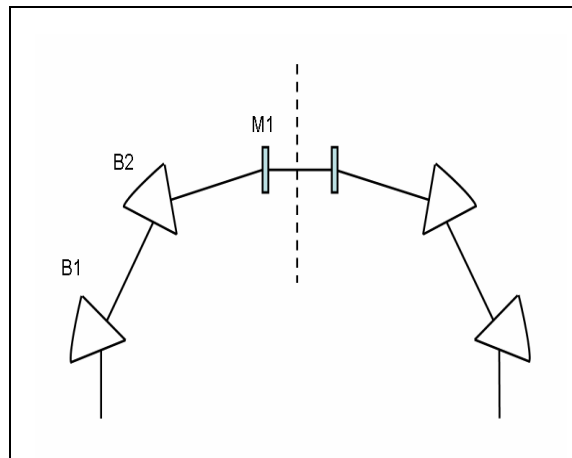
$$\begin{cases} \eta = 0 \\ \eta' = 0 \\ \sum \theta = 0 \end{cases} \quad (3.4.1)$$

It requires three independent knobs to satisfy these constraints. In addition, we require that the perturbation to the linear lattice must be small.

Decker distortion has proven effective in reducing the stray background radiation for the photon BPMs at the Advanced Light Source [3.4.1]. Even though the stability of the photon beam is directly related to that of the electron beam circulating in the storage ring, it is also affected by other factors, such as the electron trajectory in the insertion devices. Moreover, the long beamline amplifies small jitter of the electron beam. Hence including photon BPMs to the feedback loops helps keep the photon beam stable.

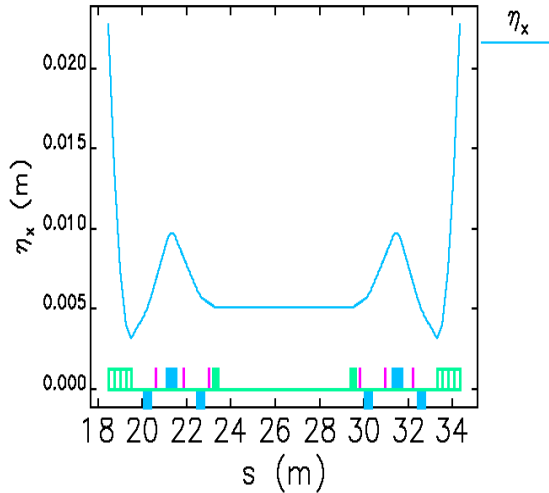
The characteristic radiation angle from the NSLS-II storage ring dipole is  $1/\gamma \sim 0.17$  mr; the dipole kick from the strongest quadrupole is about one milliradian if the beam is offset by 2 mm; therefore the distortion angle is determined to be 1~2 mr.

At APS, Decker distortion was implemented after the storage ring and the beam lines were built. In their case, moving the magnet girders was easier than moving the straights and the beam lines. Their approach was to add two trims to the front and the end of a cell and then move the entire cell except the straight section. For NSLS-II, we looked at other possible options, since we can design from the beginning. Instead of moving a cell, we found it is convenient to offset the ID straight with two trims and vary the cell magnets to fulfill the constraints. The diagram is shown in Figure 3.4.1. One can vary B1, B2, the main bending magnets, M1, the trim in the straight, and all the quadrupoles to form a dispersion bump. The downstream cell is reflection symmetric to the upstream one. We examined two solutions: in the first solution we vary only the dipoles and the trims; and in the second solution we also adjust the quadrupoles, but the field in only one main dipole is changed.



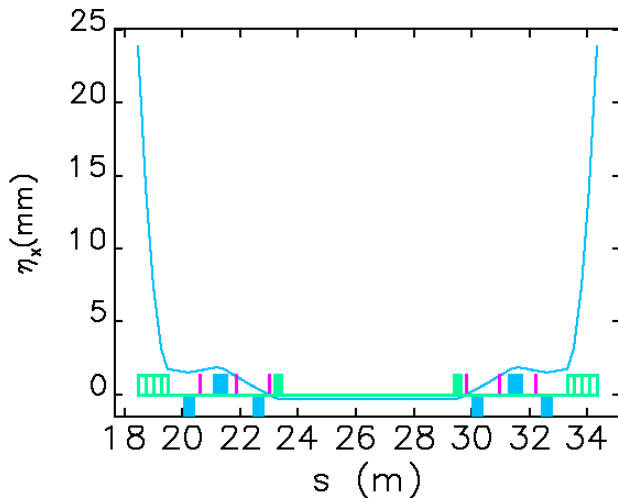
**Figure 3.4.1** Diagram of Decker distortion proposed for NSLS-II.

Figure 3.4.2 shows the first solution of Decker distortion for the NSLS II lattice. In this solution only the dipoles are varied. The bend angle adjustment in the dipoles and the trim is:  $\Delta\beta_1 = -1.727$  mr,  $\Delta\beta_2 = 0.727$  mr and  $M_I = 1$  mr. The quadrupole settings are not changed therefore the beta functions, the emittance and the tunes are kept the same. The dispersion in the long straight is constrained to zero. The dispersion departs from zero in the short ID straight and has the value 5 mm. Because of the symmetry and emittance constraints, the effect on the beam size and the emittance growth is negligible.



**Figure 3.4.2** Dispersion function in the dipole-only solution.

The second solution with variation of quadrupoles is shown in Figure 3.4.3. In this solution there is no need to change  $B_1$ . The parameters are:  $\Delta\beta_1 = 0$  mr,  $\Delta\beta_2 = -1$  mr, and  $M_I = 1$  mr. The relative quadrupole strength changes are small,  $|\Delta K_1 / K_1| \leq 0.015$ . The dispersion in the long straight is zero and it is about 0.3 mm in the short straight. This scheme has an advantage in that the girder between the two main dipoles does not have to be moved.



**Figure 3.4.3** The second solution: varying  $\Delta\beta_2$  and the quadrupoles.

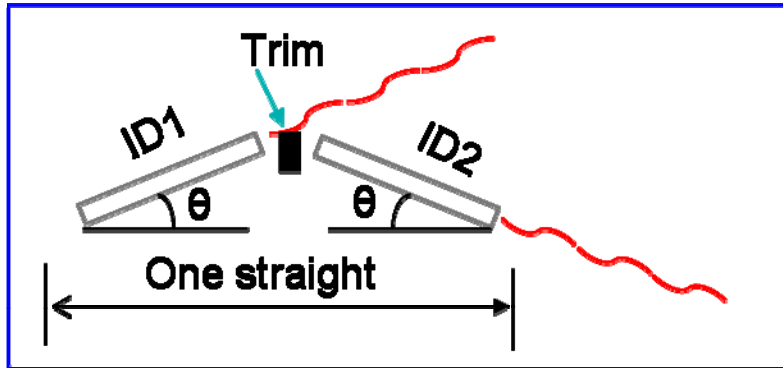


Figure 3.4.4 Diagram of canting.

The idea of canting is to split the radiation from one straight into two beam lines as is diagrammed in Figure 3.4.4. However, this also introduces external dispersion and the damping wigglers excite quantum fluctuations. The emittance growth is proportional to the dispersion invariant  $H = \gamma\eta^2 + 2\alpha\eta\eta' + \beta\eta'^2$ . It can be shown that if the dispersion function at the center of the straight is much less than  $\beta_c\theta$ , where  $\theta$  is half of the canting angle; i.e., if

$$\eta_c \ll \beta_c\theta, \quad (3.4.2)$$

then the dispersion invariant is minimized, and

$$H_{\min} \approx \beta_c\theta^2. \quad (3.4.3)$$

Therefore the emittance growth is proportional to the center beta function and square of the canting angle.

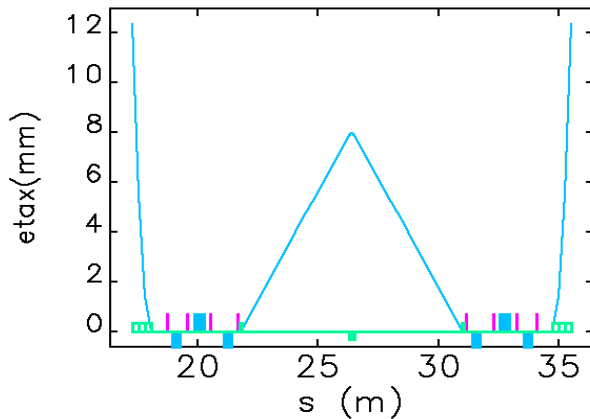
At commissioning, NSLS-II will have three 7 meter-long damping wigglers. The relevant parameters are  $\beta_w=1.8$  T,  $\lambda_w=9$  cmT, cm. One calculates the opening angle to be  $2\theta=2.6$  mr. It has been decided the maximum canting angle is 3.5 mr. With the minimized  $H_{\min}$ , the emittance growth is calculated as a function of the number of canted damping wigglers. The results are listed.4.1.

Table 3.4.1 Emittance Growth Due To 3.5 mr Canting.

	None canted	All canted	Growth factor
Emittance(nm)(21m)	0.9	0.96	1.068
Emittance(nm)(35m)	0.67	0.74	1.11
Emittance(nm)(56m)	0.51	0.59	1.16

The emittance growth for the baseline is only about 7% even if all three damping wigglers are canted. The emittance is less than 1 nm, which meets our design goal. Note the momentum spread is not affected by canting.

There are several choices to bend the electron orbit. A straightforward solution would be putting three trims in the straight. Such a solution is shown in Figure 3.4.5. The disadvantage of this solution is that 0.3~0.4 meters is needed for each trim; therefore the usable space for the insertion device is shortened.



**Figure 3.4.5** A straightforward solution for canting. Three trims are put in the straight as -2, 4, and -2 mr. The maximum dispersion is 8 mm.

The second option is to put only one trim in the center of the straight and vary the main dipoles and quadrupoles to satisfy the three constraints. A solution is shown in Figure 3.4.6. Note the negative dispersion in the center. This is because the dispersion invariant is minimized.

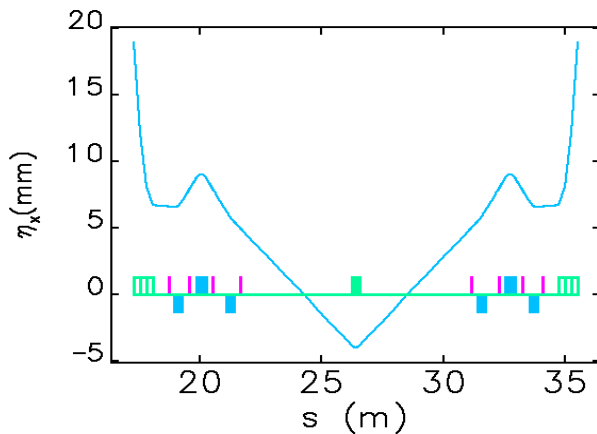


**Figure 3.4.6** A solution of canting the damping wigglers. The angles or the changes are:  $\Delta\beta_2 = -M_1 = -1.926$  mr. The quadrupole setting changes are  $|\Delta K_1 / K_1| < 0.01$ .

A third option would be to make special poles for the damping wigglers. One pole of the damping wiggler gives about 4 mr bending to the beam. If the end poles can be made longer, then the damping wiggler itself can bend the beam. This approach looks feasible and can save both space and cost on the magnets and power supplies.

## References

- [3.4.1] G. Decker and O. Singh, Phys. Rev. ST Accel. Beams 2, 112801 (1999).

### 3.5 Extra-Long Straights

The lengths of the normal short and long straight sections at the NSLS-II are 6.6 m and 9.3 m, respectively. Some experiments, e.g., inelastic scattering experiments, would benefit from long insertion devices with length as great as 10~12 m. Such long insertion devices require extra-long straights of 12~15 meters.

A straightforward way to create such long straights is to make a few special cells; however, this approach reduces the symmetry of the lattice to the number of the longer straights and affects the dynamic aperture of the beam. In order to restore the symmetry, Hara et al. proposed a  $2\pi$  transformer scheme[1]. The idea is to make the betatron phase advance a multiple of  $2\pi$  for the two matching cells and the extra-long straight; therefore the symmetry is restored. Note the periodicity number is two units less because of the excluding of the two matching cells. This idea was successfully implemented at SPring-8 in the year 2000. Four 27 m long straights were created this way.

Another issue for extra-long straights is that the vertical gap of the insertion device imposes a limiting physical aperture on the storage ring. Note the beta function in the straight is given by

$$\beta(s) = \beta_c \left[ 1 + \left( \frac{s}{\beta_c} \right)^2 \right], \quad (3.5.1)$$

where  $\beta_c$  is the beta function at the center of the straight.

The present physical aperture of NSLS-II is limited by the  $\pm 2.5$  mm gap of the in-vacuum undulator. In order not to diminish the physical aperture, the gap of the long undulator has to satisfy

$$h \geq 2.5 \sqrt{\frac{\beta_s(L/2)}{\beta_L(L/2)}}, \quad (3.5.2)$$

where  $\beta_s$  and  $\beta_L$  are the beta functions at the ends of the IDs in the short straight and the extra-long straight. Varying  $\beta_c$  to maximize the aperture, one gets

$$h \geq 2.5 \sqrt{\frac{L_U}{L_L}}, \quad (3.5.3)$$

where  $L_U$  and  $L_L$  are the lengths of in-vacuum undulator and the long undulator. Therefore, if the gap remains the same, an ID that is four times longer would reduce the physical aperture by two-fold. And it will be even worse if  $\beta_c$  is minimized for the purpose of higher brightness.

To focus the beta functions to small values while maintaining the physical aperture, quadrupole magnets can be added to the long straight to create segments. The quadrupoles are also helpful for matching the phase advance inside the long straight. Suppose the betatron phase advance of a normal straight is  $\Delta\Psi$ ; if the phase advance of the segmented extra-long straight is  $2\pi + \Delta\Psi$ , then the extra-long straight is the same as a normal straight, from the symmetry point of view.

One can show that the betatron phase advance in a magnet-free section is less than  $\pi$ . Hence, to obtain  $2\pi$  phase advance, a minimum of three sections are needed. To get a better understanding of the problem, we designed a solution for NSLS-II; the beta functions are plotted in Figure 3.5.1.



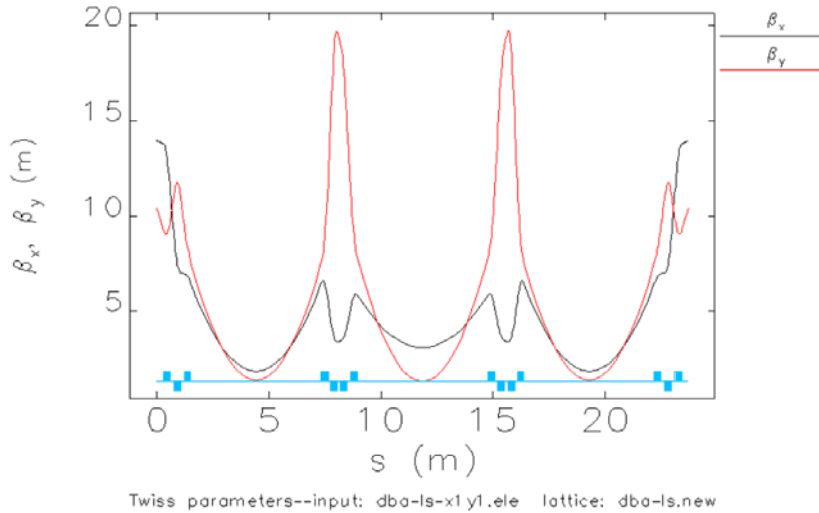


**Figure 3.5.1** A segmented extra-long straight solution for NSLS-II. It starts from the last magnet in the long straight of a normal cell. The total length is 23.7 m with three equal-length straights of 5.83 m each. The generated chromaticity is  $\Delta\zeta_x = -1.04$  and  $\Delta\zeta_y = -3.01$ . The beta functions at the center of the sections are  $\beta_x / \beta_y = 1.8/1.4, 3.0/1.3,$  and  $1.8/1.4$  m.

Because dispersion is zero everywhere in the extra-long straights, the generated chromaticity has to be corrected by the sextupoles in the other cells. Therefore the chromaticity in every cell cannot be corrected to zero. Because of this, the extra-long straight is not transparent to the off-momentum particles. One can show that if  $n$  extra-long straights are inserted into an  $m$ -period storage ring, then the ring is  $n < m$  fold symmetric for the off-momentum particles.

Proper selection of the working point and careful elimination of the higher-order terms might restore the dynamic aperture. However, the impact of extra-long straights on the stability of the dynamic aperture of off-momentum particles could not be studied in sufficient detail before the decision on the NSLS-II footprint could be made. Furthermore, there are issues, such as the deposition of high synchrotron radiation power on the extra-long undulator beam pipes. For this reason, an alternative approach to extra-long straights is envisioned, which could be implemented into the footprint of NSLS-II.

This idea is illustrated in Figure 3.5.2. Two cells are moved aside, converting the middle straight into an extra-long straight, the maximum length of which is about 18 m for the present lattice.

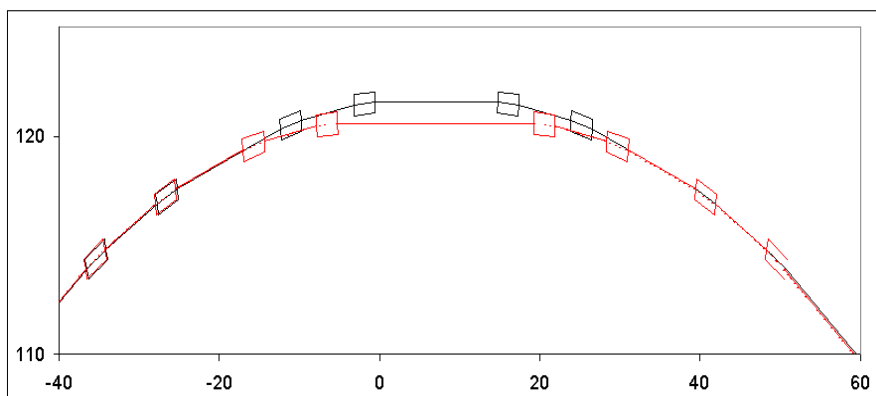


**Figure 3.5.2** Moving the cells to create an extra long straight.

This scheme would allow compensation of the chromaticity and nonlinear terms in the moved cells, and they can be transparent to the off-momentum particles if all the relevant higher-order terms are eliminated. The impact of such an insert on dynamic aperture is under study.

[3.5-1] M. Hara, T. Nakamura, T. Takada, and H. Tanaka, "Use of long straight sections of SPring-8," Rev. Sci. Instrum. 63 (1), p.355, 1992.

## 4 STORAGE RING SYSTEM

### 4.1 Storage Ring Magnets

#### 4.1.1 Parameters and Tolerances

The DBA lattice (30 cells with a super periodicity of 15) consists of 60 dipole magnets with uniform magnetic field and a maximum field of 4 kiloGauss at 3.0 GeV. The ring quadrupoles consist of a total of 300 magnets with two different lengths: 25 and 40 cm. These quadrupoles have a maximum gradient strength of 22 T/m at 3.0 GeV. The quadrupoles are individually powered, but the current lattice design assumes eight families. There are also 300 sextupoles magnets with two different lengths: 20 and 25 cm. These magnets, together with the correction magnets and BPMs, are listed in Section 6.1.1 and in Table 6.1.4.

#### 4.1.2 Preliminary Magnet Design

##### 4.1.2.1 Storage Ring Lattice Magnet Considerations

The magnet lattice is designed with a 30-cell DBA (double bend achromat) structure for a machine with 3.0 GeV full-energy top-off injection. The 792 m storage ring will contain more than 900 magnets. This quantity is comprised of 60 bending dipoles, 300 quadrupoles, 300 sextupole magnets, and 242 corrector magnets. To ensure acceptable dynamic aperture for the electron beam, the required magnetic field quality and alignment tolerances are the two primary considerations in the design. All the dipole magnets are connected in series and are energized by a single power supply. Individual trim power supplies will be used to provide  $\pm 3\%$  field adjustment. All quadrupoles will be individually powered and the sextupoles will be powered in nine families. Properties of the storage ring magnets are summarized in Table 4.1.1.

**Table 4.1.1 Storage Ring Magnet Specifications at 3.0 GeV.**

	Dipole		Quadrupole	Sextupole	Corrector	ID Corrector
	35 mm	90 mm				
Bending angle [deg]	6	6	0	0	$\pm 0.08$	$\pm 0.01$
Max. Clear bore aperture [mm]	35	90	66	68	150/100	35/80
Max. Dipole field [T]	0.4	0.4	0	0	0.04	**0.01
Field gradient [T/m]	0	0	22	0	*0.36	0
Max. Sextupole field [T/m <sup>2</sup> ]	0	0	0	500	0	0
Field quality in GFR - 20 x 40 [mm]	$1 \times 10^{-4}$	$1 \times 10^{-4}$	$2 \times 10^{-4}$	$5 \times 10^{-4}$	$1 \times 10^{-3}$	$1 \times 10^{-2}$
Nominal operating current [A]	360	360	108	190	20	20
Cooling type	water	water	water	water	air	air
Maximum temperature rise [°C]	10	10	10	10	20	20

\*Skew quadrupole component, 30 each required

\*\* at 100 Hz

In this section, we present designs of the individual magnets. Optimization and refinements will occur during the next phase of detailed design.

The following paragraphs in this section present a partial list of lattice magnet design considerations. For the preliminary design, these considerations are global in nature and will evolve into specific design parameters for the next phase of “reference” design.

- The average current density in the coil cross-section of the storage ring magnets was selected to be less than or equal to  $2 \text{ A/mm}^2$ , with typical current densities in the copper conductor of 3.5 to  $4.5 \text{ A/mm}^2$ .
- The temperature rise of cooling water across any magnet coil will be limited to about  $10^\circ\text{C}$ , with a pressure drop across each magnet of less than 4 bar.
- The magnetic alignment requirements of the multipoles exceed tolerances achievable by the normal optical survey method. Therefore, these magnets are aligned magnetically and then fixed to a rigid girder for installation in the storage ring tunnel.
- The storage ring magnet reference designs are being developed to minimize fabrication costs, provide high operational reliability, and minimize the power consumption by individual components as well as overall magnet systems.
- The magnet supports are designed so as to reduce vibration amplification by maintaining the resonance frequency of the multipole support assembly above that of the girder.
- The reference design will address a low-cost yet reliable means to integrate the multipole magnets into a vibrating wire magnet-to-magnet alignment system and a means to transfer magnetic field center locations precisely to survey targets on the magnet girder.
- Handling and rigging safety issues for magnet testing and installation will be addressed, and the reference design will comply with BNL’s Critical Lift Policy.
- Electrical and all other safety issues will be addressed in the next phase of detailed design. The design of the magnets, the power cabling, and the water cooling from the magnet-to-cable connections on the girders, as well as magnet instrumentation and controls, will be fully NEC and OSHA compliant.
- Magnetic lengths were optimized and drift space between the multipoles was increased to accommodate beam position monitors (BPMs) and corrector magnets without altering the lattice.
- Electrical, magnetic, and mechanical design optimization will be performed for the reference design of the relatively low-field-strength 0.4 T dipole magnet to assure high field quality requirements for the C-type magnet cross-section.
- Extensive 3D modeling and value engineering optimization is being performed for both the 22 T/m maximum quadrupole strength and the  $500 \text{ T/m}^2$  maximum sextupole strength. The goals are to 1) assure high field quality and extremely critical alignment requirements for both multipoles, 2) accommodate the synchrotron’s x-ray extraction lines and the vacuum chamber, and 3) minimize or eliminate the effects of crosstalk between neighboring magnets and correctors.

These preliminary designs and considerations will be refined by both the Laboratory and Industrial resources during the next phase of design, resulting in a “reference” design. The final magnet design will be developed by the magnet manufacturer, and reviewed and approved by the Laboratory prior to production. Extensive 2D and 3D magnetic modeling, mechanical design, and fabrication and assembly methods have been studied, resulting in the preliminary magnet designs that are described in the following sections.

#### **4.1.2.2 Dipole Magnet Preliminary Design**

##### **4.1.2.2.1 Scope and Physics Design Parameters**

A unique attribute of NSLS-II is the use of dipole magnets with apertures of two different sizes. This requirement is necessary to accommodate a significant and growing community of users who require lower

energy infrared and THz radiation. To serve this important community, a 90 mm aperture concept has been chosen, to allow the extraction of long-wavelength light from the dipole magnet [4.1.1, 4.1.2].

The NSLS-II storage ring will be equipped with six dipole magnets that have a gap of 90 mm, and 54 dipoles that have a gap of 35 mm. Each dipole will have a magnetic length of 2.62 m with a field 0.4 T at an electron energy of 3.0 GeV. The radius of curvature of the bending magnet is 25 m; it bends the electron beam  $6.0^\circ$  with a sagitta of 35 mm. The dipole magnets are C-type with a curved laminated flux return yoke (Figure 4.1.2).

A new extended pole (“nose”) design (Figure 4.1.3) releases a significant amount of physical space (~190 mm per magnet) and minimizes the challenges associated with a tight lattice. In most iron-dominated magnets, the magnetic length is larger than the yoke length but smaller than the coil length. The proposed NSLS-II design takes advantage of the fact that the nominal operating field of 0.4 Tesla is well below iron saturation. This allows the axial length of the iron pole to become as long as the coil length, thus making the magnetic length longer than the coil length. The proposed design makes the magnetic length larger than both the yoke length and the magnet mechanical length (including ends of the coil). The width of the iron pole is 100 mm.

Calculations of the magnetic field were made to optimize the pole contours and the quality of the magnetic field, which for a dipole magnet must have field non-homogeneity of  $\Delta B/B \leq \pm 0.01\%$  over a good-field region of 40 x 20 mm (Figure 4.1.2). All computed field harmonics in the entire range of operation (up to 0.48 T) are well below one part in  $10^4$  at 10 mm radius.

Investigations of beam dynamics have established that the good-field region accommodates the dynamic aperture. A list of the preliminary design dipole parameters is found in Table 4.1.2.

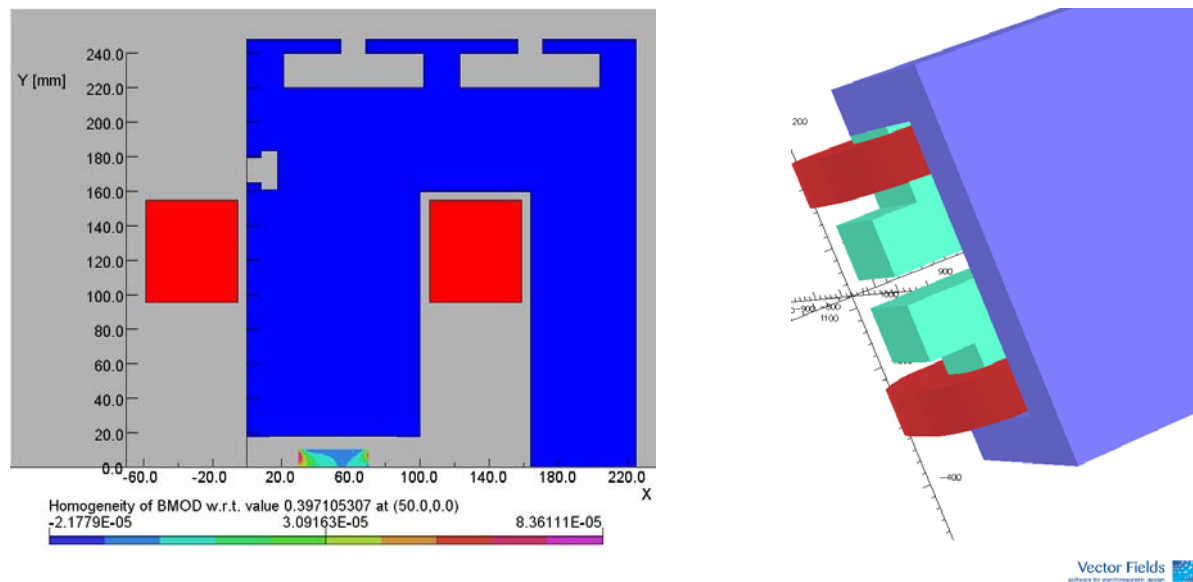


**Figure 4.1.2** Magnetic model of the Ring Dipole. 2D model with relative field errors in good field aperture is shown on the left and 3D model with extended pole (nose) on the right. The proposed design makes the magnetic length of the magnet longer than the mechanical length (including coil ends), and frees significant space in a tight lattice.

The storage ring dipoles are designed so that both aperture magnets may be connected in series with a single power supply. Implementation of Decker distortion and minor differences between the two aperture magnets shall be corrected by independently powered trim coils located on each dipole. The six large aperture

dipoles will be installed into the storage ring in pairs. Each pair shall comprise the adjacent bending magnets in a single cell, and there will be three cells equally distributed around the storage ring.

**Table 4.1.2 Dipole Magnet Preliminary Baseline Design Parameters.**

	35 mm Storage Ring Dipole	90 mm Storage Ring Dipole
Energy [GeV]	3.0	3.0
Bending angle [deg]	6	6
Clear bore aperture [mm]	35	90
Dipole field [T]	0.4	0.4
Field quality	$1 \times 10^{-4}$	$1 \times 10^{-4}$
Good-field region [mm]	40 x 20	40 x 20
Magnetic length [mm]	2,620	2,620
Nominal operating current [A]	360	360
Number of Ampere-turns	11,520	30,240
Number of turns / magnet	32	84
Total Inductance of the magnet [mH]	16	116
Current density in conductor [A/mm <sup>2</sup> ]	3.7	3.7
Max. temperature rise [°C]	10	10
Max. pressure drop [bar]	4.0	4.0
Voltage/magnet	11.4	32
Nom. power per magnet [kW]	4.2	11.5
Iron length Extended Pole/Return Yoke [mm]	2,585/2,415	2,530
Lamination thickness [mm]	1.5	1.5

#### 4.1.2.2.2 Mechanical Design of the Dipole

Fabrication and assembly concepts have been studied, resulting in the preliminary magnet designs that are shown in Figures 4.1.3 and 4.1.4. The laminated magnet yokes are composed of 1.5 mm-thick dry film epoxy-coated AISI 1006 low-carbon steel sheet. The permeability of the core material deviates by about 5% from the production value. The laminations must be shuffled to ensure a uniform magnetic property. The 35 mm dipole will have a self-supporting yoke assembly.

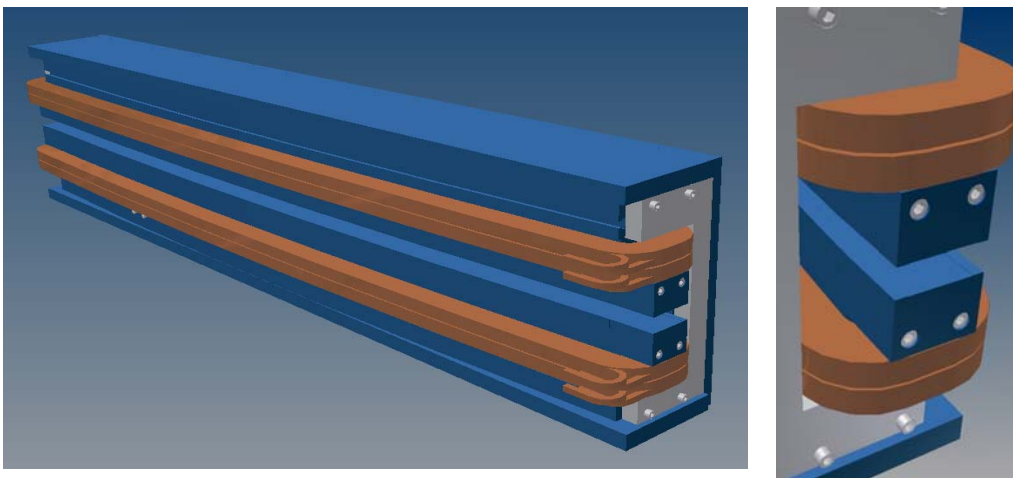


**Figure 4.1.3** Views of the 35 mm storage ring dipole , with close-up of novel nose ends pinned and bolted in place.

A precision stacking fixture will be used to register all the laminations to the magnet gap. The base of the fixture will be curved to generate the 25 m nominal core radius. The dipole laminations will be stacked in parallel, and straight tie bars will be inserted through clearance slots in the laminations. Prefabricated end packs will be added to either end of the yoke assembly. The tie bars are tensioned and the yoke assembly is cured. Straight steel stiffening plates are bolted together around the top, bottom, and back of the curved laminated core. The stiffener plates are then welded to the core to form a rigid yoke assembly. The dipole end packs will be tapped and pinned in preparation for adding the nose piece.

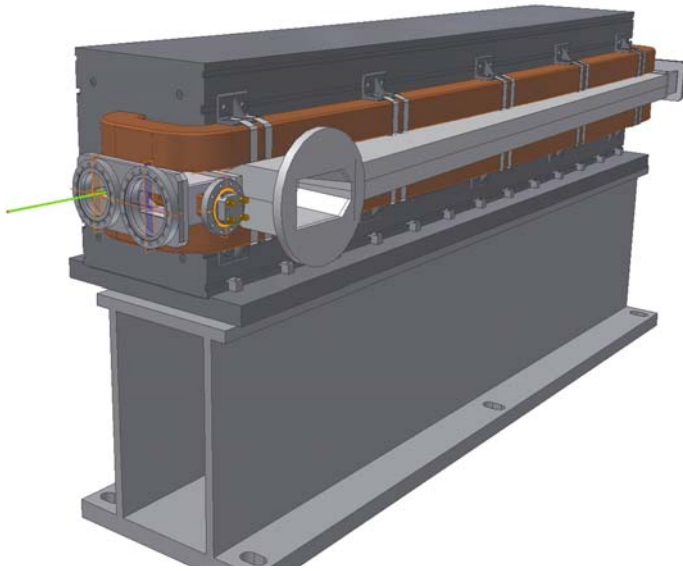


**Figure 4.1.4** The 90 mm aperture dipole design concept with an IR beam extraction vacuum chamber installed.

The coils for the 35 mm dipoles are made up of square hollow copper conductors, 13 x 13 mm, with an interior diameter of 9 mm. The coils for the 90 mm dipoles are made of the same rectangular hollow copper conductors. The water channels of the hollow conductor coil “pancakes” are connected in parallel to provide cooling adequate to restrict the increase in coil temperature to less than 10°C, and in the case of the 90 mm dipoles, to reduce pressure drop in the seven-turn, six-layer coils.

Fiberglass that is vacuum impregnated with highly radiation-resistant epoxy greater than 1.0 mm thick will provide interstitial conductor insulation. An additional 1.5 mm (minimum) of vacuum-impregnated epoxy fiberglass will provide ground plane insulation. The magnet will be high-potted up to 5 kV to detect defects in the insulation.

After the coils are assembled through the gap of the 35 mm dipole and secured, the core’s nose pieces will be precisely pinned and bolted to the laminated end packs at either end of the dipole yoke assembly. The nose pieces shape the dipole end fields to minimize end-field errors and to match the field profiles of the 90 mm dipole.

Dipoles of either aperture that are not used as IR sources will use a single dipole vacuum chamber design. The chamber will allow damping wiggler radiation to pass through. The larger aperture IR dipole vacuum chamber will have a minimum internal aperture of 70 mm.

The designed magnet cross-section will accommodate the vacuum chamber with a 2 mm clearance between the magnetic poles and either side of the vacuum chamber.

### 4.1.2.3 Quadrupole Magnet Preliminary Design

#### 4.1.2.3.1 Scope and Physics Design Parameters

Within the 66 mm aperture of the storage ring quadrupole magnet, the field gradient homogeneity in a region 40 x 20 mm is required to be better than 0.02%. The design geometry of the quadrupole is highly constrained by several factors:

1. Field quality and magnet alignment requirements as shown in Table 4.1.3
2. The geometry of the multipole vacuum chamber, and the need to accommodate its antechamber
3. The requirement to produce a low-cost magnet with very high reliability

To provide a path for synchrotron radiation exiting insertion devices, the antechamber and extraction ports must extend beyond the horizontal mid-plane of the magnet yoke. To assure symmetry, the horizontal back leg on either side of the quadrupole has been removed to accommodate the antechamber of the vacuum chamber. Therefore, the top and bottom halves of the quadrupole are not connected with a flux-return yoke; each half is connected mechanically with nonmagnetic metallic spacers that accommodate that vacuum chamber. This figure-8 style quadrupole has been known [4.1.3] and used successfully in previous machines, such as APS and SPEAR-3; cost savings are inherent in the design.

The quality of the field gradient in the full magnet aperture has been examined through 2D and 3D modeling using the OPERA code. The poles, shims, and end chambers are optimized to produce a quadrupole field with higher order systematic multipole components that meet the requirements shown in Table 6.1.9. Further modeling will be performed to assess the effects of value engineering and structural design optimization. R&D prototype magnets will be fabricated and magnetic measurements performed, to assess the effects of fabrication errors that contribute to random and additional systematic high-order multipoles. To assure that the total multipole harmonic content of the as-built reference design will meet the requirements of Table 6.1.9, magnet pole end chamfers are being modeled and actual optimization will be performed with the prototype quadrupole laminated end packs. Table 4.1.3 lists the preliminary design parameters.

**Table 4.1.3 Quadrupole Magnet Preliminary Design Parameters.**

	25cm SR Quadrupole	40cm SR Quadrupole
Energy [GeV]	3.0	3.0
Clear bore aperture [mm]	55	55
Maximum field gradient at 3.0 GeV [T/m]	12.8 / 8.3	22
Field quality	$2 \times 10^{-4}$	$2 \times 10^{-4}$
Good field region [mm]	40 x 20	40 x 20
Magnetic length [mm]	300	400
Nominal operating current [A]	95/ 146	160
Max. Number of Ampere-turns/pole	3686 / 5778	11520
Number of turns / magnet pole	39	72
Total resistance of the magnet at 30°C [ $\Omega$ ]	0.0529	0.129
Total inductance of the magnet [mH]	27	135
Max. Current density in conductor [A/mm <sup>2</sup> ]	4.2	4.6
Number of parallel cooling circuits	4	4
Temperature rise [°C]	7	10
Pressure drop [bar]	4	4
Voltage / magnet [V]	5 / 7.7	19.8
Iron core length [mm]	217	367
Lamination thickness [mm]	1.5	1.5
Quadrupole alignment tolerance [ $\mu$ m]	30	30

3-D OPERA code modeling of the figure-8 quadrupole with chamfering of the laminated end packs is shown in Figure 4.1.5. Further modeling will ensure that the requirements for higher-order multipoles (Table 6.1.9) are met.

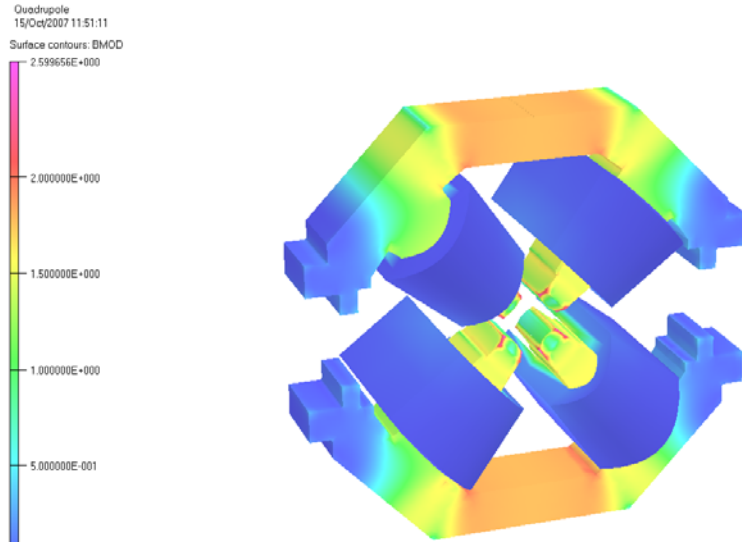


**Figure 4.1.5** OPERA model of an NSLS-II storage ring quadrupole magnet cross-section, for studying the effects of pole edge chamfering.

#### 4.1.2.3.2 Mechanical Design of the Quadrupole

Both halves of laminated iron yokes are composed of a single stamped and fine blanking lamination. The laminated magnet cores are made of low-carbon AISI 1006 steel sheet, 1.5 mm thick. A thin film of “B” staged (dry) heat-activated epoxy is applied to the lamination steel before blanking. The yoke is designed to allow the laminations to be shuffled.

End packs each having 12 laminations epoxied together are made using the Quadrupole yoke stacking fixture. The end pack stacking fixture is placed into an oven and heated until the lamination is full cured. Chamfers are precisely machined into the poles of these end packs.

The body of the quadrupole yokes are assembled using the same stacking fixture in shuffled packs about 18 mm thick. The packs are stacked with every other pack flipped in the stacking fixture. The chamfered end packs are secured to either end the center yoke section. While they are in the stacking fixture, a TIG weld bead is added to the outside of the iron to fix the packs together. The stacking fixture is compressed to a stop and heated until the epoxy between the laminations is fully cured.

The coils are wound on custom winding mandrills. Each coil has two layers of windings. For the majority of the quadrupoles, a single coil per pole is required. The conductor is a hollow square copper conductor 7.0 x 7.0 mm with a 4 mm diameter water channel and is wrapped with fiberglass.

The coil is wound in a manner that the first turn starts near the center of the length of conductor that is being wound. All NSLS-II coils are free from internal splices.

Vacuum impregnation is performed using an alumina-filled, high-radiation-resistant epoxy with a minimum thickness of 1.0 mm to provide interstitial conductor insulation. An additional 1.5 mm of alumina-filled epoxy fiberglass is applied to the outside of the coil to provide coil-to-ground plane insulation. The magnet coils will be high potted up to 5 kv to detect defects in the coil insulation system.



Value engineering of the quadrupole design to conform to lattice requirements has yielded three styles of coils. Most of the quadrupoles have four double-layer coils with four parallel water paths. Higher-field quads will have either a longer coil or additional coils per pole. Each coil shall represent an additional parallel water circuit. The increase in water temperature across any quadrupole magnet will be  $<1^{\circ}\text{C}$ . Figure 4.1.6 presents the mechanical design.

The quadrupoles will be supported from near the mid-plane so thermally induced strain in the magnet's iron poles and yoke will tend to act about the magnet's axis, maintaining its pre-surveyed location to  $\leq 10\ \mu\text{m}$  over its full range of excitation. A minimum clearance of 2.0 mm is maintained between the magnet poles and vacuum chamber to effect thermal and vibrating isolation between the two devices.

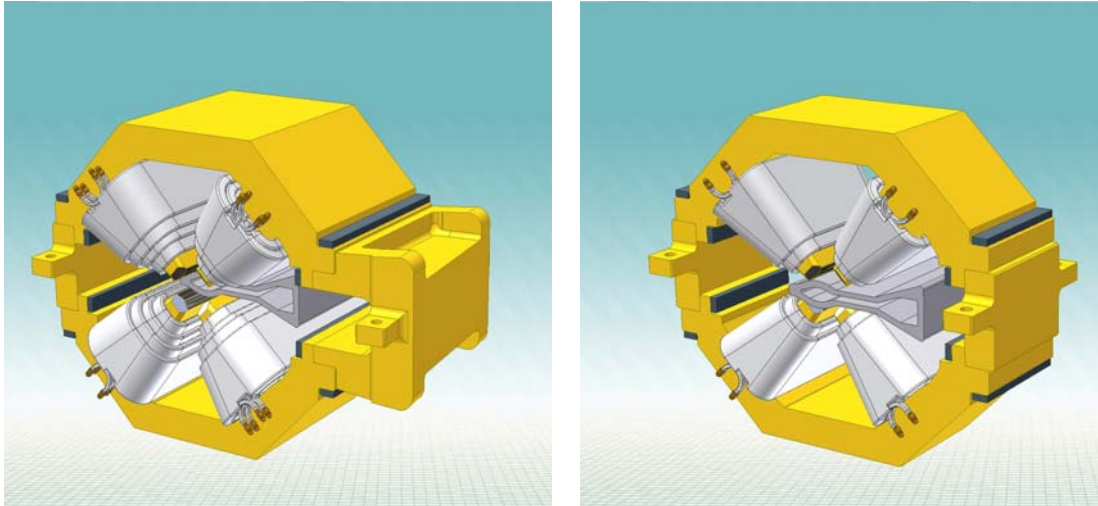


**Figure 4.1.6** Preliminary designs for the NSLS-II storage ring quadrupole magnet. **Left:** A high-field quadrupole with an antechamber clearance. **Right:** a symmetric low-to-moderate field quadrupole.

#### 4.1.2.4 Sextupole Magnet Preliminary Design

##### 4.1.2.4.1 Scope and Physics Design Parameters

The storage ring is equipped with 300 sextupole magnets. The sextupole field homogeneity in a region 40 mm x 20 mm is required to be better than 0.05%. The geometry of the vacuum chamber determines the bore radius of the sextupole magnet. The design of the sextupole magnet is constrained by the need to accommodate a vacuum chamber's antechamber.

The poles and shims are optimized with a 2D approximation. Additional 3D modeling was performed to ensure that the requirements for higher-order multipoles (Table 6.1.9) are met.

The field quality is optimized for standard and extended sextupole models (Figure 4.1.7). The field quality is consistent with the specified sextupole field throughout the required transverse region, and all harmonics below two parts in  $10^4$  at 45 mm reference radius, in the entire range of operation. The bore diameter of 68 mm was determined by specifications of field quality and the spatial constraint between the vacuum chamber and the poles and coil geometry. The base of the pole is widened to prevent saturation in that area at high field excitations. In a wide-aperture sextupole, the ideal symmetry is partially broken due to nonperfect return yoke geometry, and semi-allowed harmonics ( $b_0$ ,  $b_5$ ,  $b_7$ , etc.) are created. We have developed a new design method that minimizes these harmonics by moving up the pole located at 90 degrees by about  $\sim 35$  microns. Table 4.1.4 lists the preliminary design parameters for the sextupole magnets.

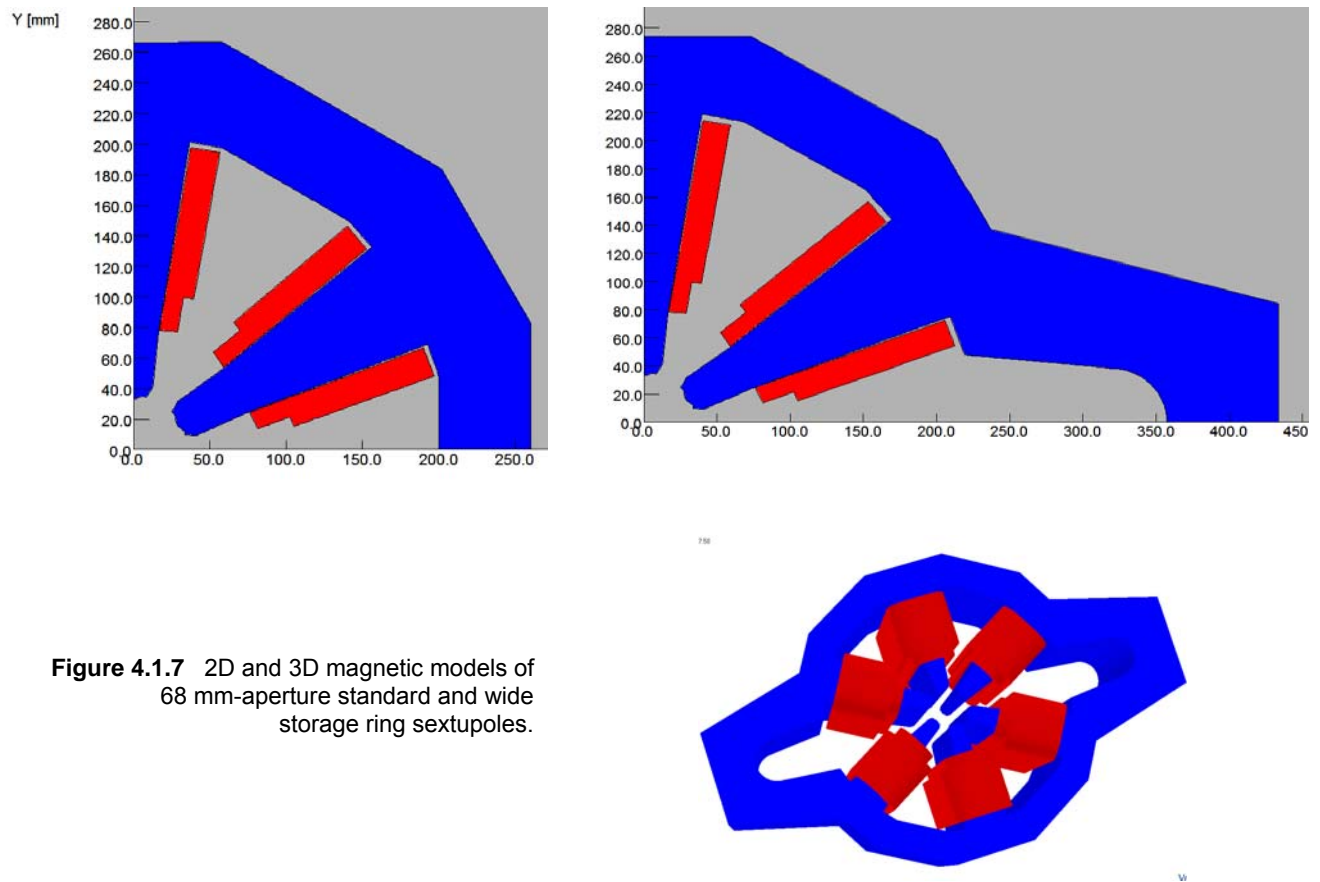


**Figure 4.1.7** 2D and 3D magnetic models of 68 mm-aperture standard and wide storage ring sextupoles.

**Table 4.1.4** Sextupole Magnet Preliminary Design Parameters.

	20cm Sextupole	25cm Sextupole
Clear bore aperture [mm]	68	68
Sextupole field [T/m <sup>2</sup> ]	300 / 400	400
Field quality	$5 \times 10^{-4}$	$5 \times 10^{-4}$
Good-field region [mm]	40 x 20	40 x 20
Magnetic length[mm]	200	250
Maximum operating current [A]	123 / 164	164
Max. Number of Ampere-turns/pole	3192 / 4255	4255
Number of turns / pole	26	26
Total resistance of the magnet at 30°C [ $\Omega$ ]	0.0293	0.0346
Total inductance of the magnet [mH]	8.8	11.0
Temperature rise [°C]	7.5	5.1
Pressure drop [bar]	4	4
Voltage / magnet	3.3 / 4.4	5.2
Iron length [mm]	179	228
Laminae thickness [mm]	1.5	1.5
Sextupole alignment tolerance [ $\mu\text{m}$ ]	30	30

#### 4.1.2.4.2 Mechanical Design of the Sextupole

The sextupole magnets for the storage ring come in two lengths. Most of the sextupoles have a magnetic length of 0.2 m. The mid-cell sextupole has a magnetic length of 0.25 m.

To maintain high field quality, minimize random errors, assure the long-term mechanical stability, and not eliminate the possibility of adding steering and skew quadrupole trims in the future, the mechanical design is based on a mid-plane parting surface. To perform magnet assembly, it was determined that a removable 90-degree center pole in each magnet half is feasible (Figure 4.1.8).

A minimum clearance of  $>1.5$  mm between the vacuum chamber and adjacent poles to maintain thermal and vibration isolation is maintained. The magnet cores are made from AISI 1006 low-carbon steel sheet. The laminations are coated with a thin film of “B” staged (dry) heat-activated epoxy. The yoke is designed to allow shuffling of laminations. The shuffled laminations are assembled in packs of ten laminations. Precision stacking fixtures are used to fabricate a series of end packs for both the two pole yoke and center-pole yoke subassemblies. After the end packs are oven cured, pin holes and chamfers are precisely machined into the pole tips. The body of the sextupole is composed of packs of shuffled laminations cured together inside a precision stacking fixture. The machined end packs are added to the mid yoke blocks in the stacking fixture. While in the stacking fixture, Tig weld beads are added to the yoke to secure the relative position of the packs.

Coils are composed of a double-layer stack of square copper conductor, 8.5 x 8.5 mm, with a 4.5 mm diameter water channel. The conductor is insulated with fiberglass. The coil is wound so the first turn starts the coil near the center of the length of conductor being wound. Vacuum impregnation is performed using alumina-filled high-radiation-resistant epoxy with a minimum interstitial conductor thickness of 1.0 mm. An additional 1.5 mm of alumina-filled fiberglass epoxy forms the ground plane insulation. The coils are high potted to 5 kv to detect defects in the insulation system. A coil center-pole subassembly is produced. A coil secured to the center-pole assembly is assembled in the yoke stacking fixture. Precision yoke end rings are assembled at either end of the sextupole core halves, and stainless steel rods with threaded ends are used to compress the yoke and end rings to precisely control yoke geometry. The end rings are used to position the center-pole relative to the two adjacent poles.

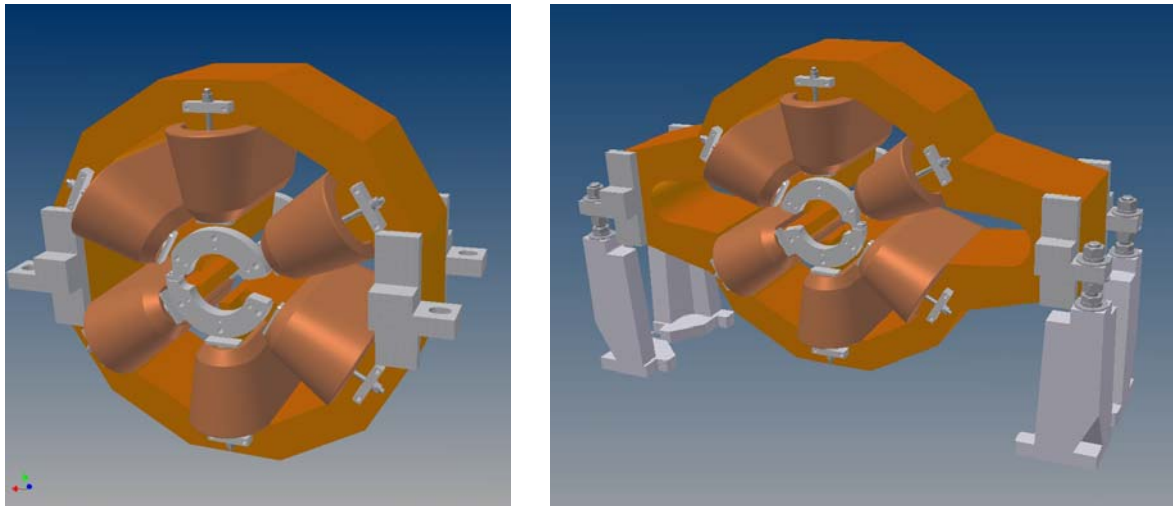


**Figure 4.1.8** Preliminary design of 68 mm aperture standard and wide storage ring sextupoles.

Brackets are pinned and bolted to the yoke back legs at the mid-plane, the yokes are assembled, and the end rings are used to locate the two halves of the poles about a common center. Studs are used in the brackets to secure the core halves together. At least three parallel water circuits are used to maintain  $\leq 10^\circ\text{C}$  temperature rise in the cooling water across the magnet.

#### 4.1.2.5 Correction Magnet Preliminary Design

In addition to the primary lattice magnets, the NSLS-II storage ring has corrector magnets. The correctors will be used to adjust the beam orbit and to correct for alignment errors. The correctors will also be used as part of both global and local feedback systems. The preliminary design calls for 242 correctors to be installed at the start of operation. Unlike other light sources where steering correction can be integrated into combined-function lattice sextupoles, the precise alignment and field quality requirements of the NSLS-II sextupoles largely prevent the use of combined-function sextupoles, making discrete correctors necessary.

There will be three types of corrector magnets. One type of global corrector will produce vertical and horizontal DC steering fields of up to 320 Gauss for  $\pm 0.8$  mrad vertical and horizontal steering of the 3.0 GeV electron beam. There will be 120 of these correctors located around the stainless steel bellows assemblies at either end of the lattice dipole magnets. These correctors will produce an oscillating field component from DC to less than 100 Hz for up to  $\pm 0.1$  mrad of vertical and horizontal dynamic steering. Another type of corrector, of similar design but with a smaller aperture, will be located around the aluminum vacuum chamber. A minimum of 60 of these correctors will produce both DC and an oscillating field component of greater than 5 Hz. The maximum operational frequency of these correctors will be determined as part of the NSLS-II R&D program, as we study and optimize the correctors' field interaction with the aluminum vacuum chamber. Thirty of these correctors will possess skew quadrupole windings to deliver a maximum DC field gradient of 0.36 T/m. 2D and 3D modeling studies of these correctors have been performed (Figure 4.1.9).

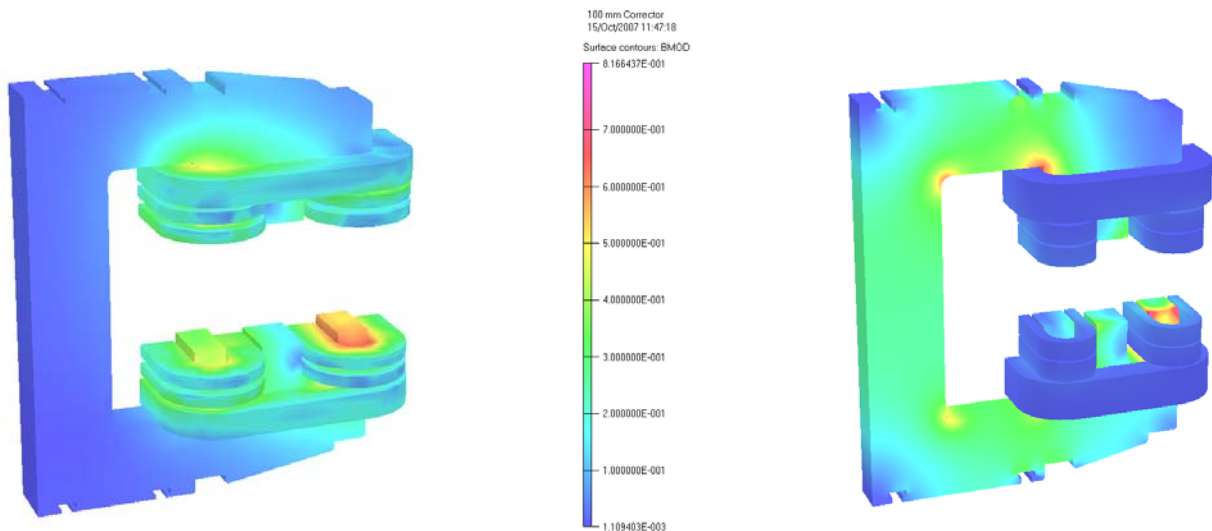


**Figure 4.1.9** OPERA models of NSLS-II storage ring corrector magnets.  
**Left:** Fast 156 mm aperture corrector. **Right:** Slow 100 mm aperture corrector.

A third type will be fast correctors, which will provide a maximum field of 100 Gauss at a frequency up to or exceeding 100 Hz. Twenty fast correctors will be used for local feedback. They will be located around stainless steel bellows or sections of stainless steel vacuum chamber at either end of an insertion device, such as an undulator. Silicon steel laminations 0.5 mm thick were selected for use in the corrector magnet flux return, to suit the charging rate. Table 4.1.5 lists the preliminary design parameters for the corrector magnets.

Many factors must be considered in the corrector magnet design. The design of a corrector magnet will be specific to its required function, the space constraints of the specific locations in the lattice, and how the corrector accommodates and interacts with the vacuum chamber design at its required location. Design options such as APS-style correctors are compact in size but tend to be rich in harmonics. Box-style correctors around the vacuum chamber have good field quality but tend not to use available space as efficiently and have larger stray fields. Analytical modeling of the C-shaped correctors revealed viable solutions for each corrector location.

**Table 4.1.5 Corrector Magnet Preliminary Design Parameters.**

	Fast Corrector	Slow Corrector	ID Corrector
Aperture [mm]	156	100	35/80
magnetic length [mm]	300	200	60/105
Iron core length [mm]	150	100	25
Max current at 3.0GeV	15	15	2
Max. DC voltage [V]	7.1/7.3 avg.	5.1/4.4 avg.	0.8/1.6
central field [T]	.028	0.04	0.0042
Max. NI/pole	2429/4188 avg.	2292/3360 avg.	180/360
J in copper [Amps./mm <sup>2</sup> ]	.35/1.4	.5/1.5	1.3

#### 4.1.2.5.1 Mechanical Design of the Corrector Magnets

The connector magnets are composed of  $\leq 0.5$  mm, track-insulated, silicon steel (M36) sheet. The laminations are stacked and glued together in a precision stacking fixture. A single C-style lamination is used to simplify the design and minimize cost. The yokes are oven cured and then the pole tips are machined to assure precise gap spacing. The mechanical design of the six-coil baseline 156 mm-aperture fast corrector and a four-coil alternative design are shown in Figure 4.1.10.

Coils are composed of solid Pyra ML-coated rectangular, solid conductors. The coils are vacuum impregnated with alumina-filled radiation-resistant epoxy. Aluminum chill plates are added between the coils. This technique is used to eliminate water-cooled conductor and the water-to-conductor electrical isolator relying on ground plane insulation to isolate the coils from the water cooling loop. The corrector produces both vertical and horizontal fields simultaneously. The vertical field (horizontal bending) is essentially air cooled, and the horizontal field is water cooled, via inter-coil chill plates. Coils are assembled onto the yoke through the core aperture. Threaded holes in the chill plates molded into the horizontal field coils are used to secure the coil package, via long screws, to brackets on the top and bottom of the magnet yokes.

The correctors come in two apertures: 156 mm and 100 mm. Screw quadrupole excitation coils with a molded-in, water-cooled chill plate can be added to the aperture of the 100 mm corrector and can be secured to the magnet aperture in a manner similar to that of the vertical and horizontal field coils. Skew quad trim coils can also be added to the sextupole at one location per superperiod.

Tee-slotted keyways in the magnet yoke are used to secure the corrector to a wedge-style spacer between it and the top of the girder.

Injection magnets such as septum and kicker magnets are discussed in Section 5.9.

## References

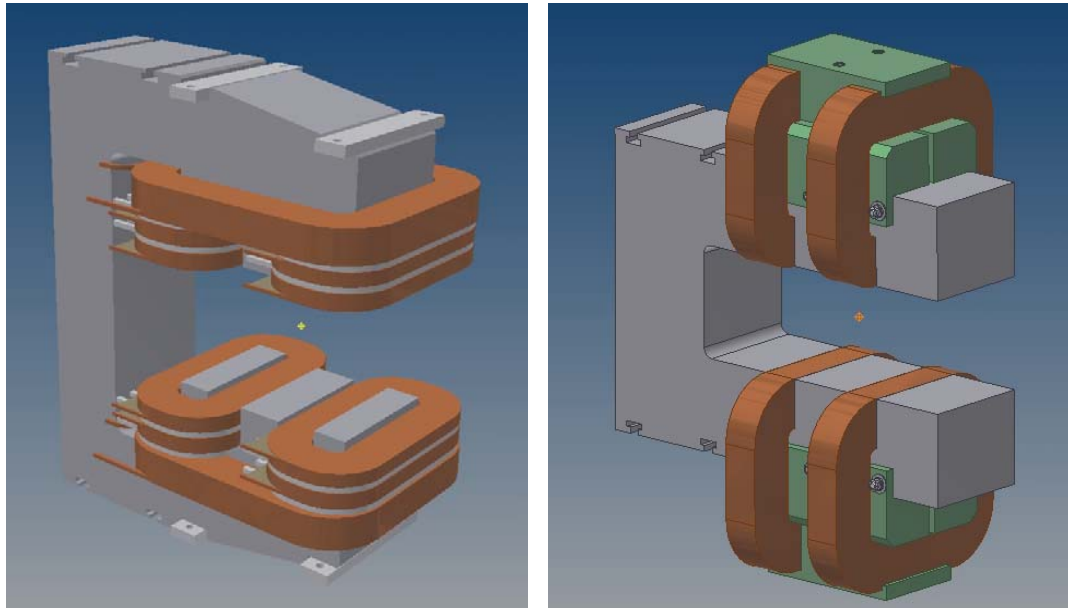


**Figure 4.1.10** Preliminary designs of 156 mm aperture baseline (**left**) and alternative (**right**) corrector magnet.

- [4.1.1] Creagh, D., et al., “An Infrared Beam-line at the Australian Synchrotron,” SRI-2006.
- [4.1.2] Katoh, M., et al., “Coherent Terahertz Radiation at UVSOR-II,” SRI-2006.
- [4.1.3] Danby, G.T., Jackson, J.W., IEEE Transactions in Nuclear Science, June, 1967.



### 4.2.3 Storage Ring Power Supplies

These power supplies are designed to stay at a fixed current except for the fast dipole correctors. The power supplies will be able to do simple ramps that will take 5 to 60 seconds from zero current to maximum current. These ramps can be software or hardware generated. The fast dipole correctors will be part of a beam-based feedback system. All power supplies will be located above the magnets in the equipment area. All power supplies will have at least a 20% margin in operating current. Listed below are the planned maximum numbers of power supplies that the storage ring will require. Some of the power supplies may have reduced quantities for day-one operation.

---

SR-MainDipole-PS	60 dipole magnets in a series circuit (54 small-aperture and 6 large-aperture magnets)
SR-LATrimDipole-PS	One shunt circuit to adjust current between large-aperture and small-aperture dipole magnets
SR-Quad-A-PS	150 individually powered quadrupole magnet circuits
SR-Quad-B-PS	60 individually powered quadrupole magnet circuits
SR-Quad-C-PS	90 individually powered quadrupole magnet circuits
SR-Sext-A-PS	35 pentant wide sextupole magnet circuits (7 of the 9 sextupole families)
SR-Sext-B-PS	10 pentant wide sextupole magnet circuits (2 of the 9 sextupole families)
SR-DipoleTrim-PS	60 dipole trim coil circuits – 30 planned for day-one operation
SR-SKQ-PS	30 skew quadrupole magnets circuits.
SR-BH-PS	60 intermediate speed horizontal dipole corrector magnet circuits
SR-BV-PS	60 intermediate speed vertical dipole corrector magnet circuits
SR-FGBH-PS	120 fast global horizontal correction dipole circuits
SR-FGBV-PS	120 fast global vertical correction dipole circuits
SR-FIBH-PS	120 fast insertion horizontal correction dipole circuits, 32 planned for day-one operation
SR-FIBV-PS	120 fast insertion vertical correction dipole circuits, 32 planned for day-one operation
Total slow power supplies	437 (407 planned for day-one operation)
Total intermediate-speed power supplies	120
Total fast power supplies	480 (304 planned for day-one operation)

---

#### 4.2.3.1 B PS – Main Dipole Power Supply

This circuit consists of 54 small-aperture dipole magnets and 6 large-aperture dipole magnets, for a total of 60 magnets (Figure 4.2.1). The small-aperture magnets are 0.032  $\Omega$  and 16 mH. The large-aperture magnets are 0.089  $\Omega$  and 116 mH. The operating current for both magnets is  $\sim$ 360 A for 3.0 GeV. The cabling between magnets and the return will use 650 MCM flexible copper cables with a resistance of 0.142  $\Omega$  and inductance of 1.4 mH. The power supply load is 2.404  $\Omega$  and 1.561 H (Figure 4.2.2).

The main dipole power supply is a unipolar, two-quadrant, current-regulated supply. It will use two 12-pulse SCR converters in series with the center point connected to ground. This configuration will reduce the voltage to ground at the magnet load and reduce the voltage rating on various converter components. Each converter will have a two-stage LCRL passive filter and a series pass active filter. This is required to reduce the ripple current to low levels (Figure 4.2.2). The power supply will be able run in the invert mode while ramping down. This produces a negative voltage.

A combined digital and analog control system will control the operation of the power supply. The power supply will have a precision current regulator using a Direct Current Current Transformer as the current feedback device. The digital controls will use a feed-forward system to improve overall reproducibility. A PLC will be used for state control (on/off commands and interlocks).



The large-aperture trim dipole power supply is used to adjust the current between the large- and small-aperture dipole magnets. The purpose of the power supply is to compensate for any systematic differences between the magnetic lengths of the two different dipole magnets. The current trim is done by having a shunt circuit connected across all the large-aperture magnets (Figure 4.2.2). This power supply will be designed to float off ground. It will use the same basic controls as the quadrupole power supplies except for needed control circuit isolation.

#### Main Dipole Power Supply Specifications

---

AC input power	3-phase 460 VAC ~683 AAC
DC maximum output current – I <sub>max</sub>	450 ADC
DC minimum output current – I <sub>min</sub>	~1 ADC
DC output voltage	1200 VDC
operating quadrants	2: (V+, I+) & (V-, I+)
small-signal – 3 db bandwidth	500 Hz
stability (8 h–10 s) – referred to I <sub>max</sub>	25 ppm
stability (10 s–300 ms) – referred to I <sub>max</sub>	15 ppm
stability (300 ms–0 ms) – referred to I <sub>max</sub>	10 ppm
absolute accuracy – referred to I <sub>max</sub>	100 ppm
reproducibility long term – referred to I <sub>max</sub>	25 ppm
current ripple – referred to I <sub>max</sub>	5 ppm 60 Hz and greater
resolution of reference current	18-bit ±1 LSB
resolution of current measured – fast sampling	16-bit ±1 LSB at 200 μsec
resolution of current measured – slow sampling	22-bit ±1 LSB at 16.67 msec

---

#### Large-Aperture Trim Dipole Power Supply Specifications

---

AC input power	3-phase 208 Vac ~ 12 AAC
DC maximum output current – I <sub>max</sub>	13 ADC
DC minimum output current – I <sub>min</sub>	~1 ADC
DC output voltage	300 VDC
operating quadrants	1: (V+, I+)
small-signal – 3 db bandwidth	100 Hz
stability (8 h–10 s) – referred to I <sub>max</sub>	100 ppm
stability (10 s–300 ms) – referred to I <sub>max</sub>	100 ppm
stability (300 ms–0 ms) – referred to I <sub>max</sub>	50 ppm
absolute accuracy – referred to I <sub>max</sub>	100 ppm
reproducibility long term – referred to I <sub>max</sub>	100 ppm
current ripple – referred to I <sub>max</sub>	10 ppm 60 Hz and greater
resolution of reference current	16-bit ±1 LSB
resolution of current measured – fast sampling	16-bit ±1 LSB at 200 μsec
resolution of current measured – slow sampling	22-bit ±1 LSB at 16.67 msec

---

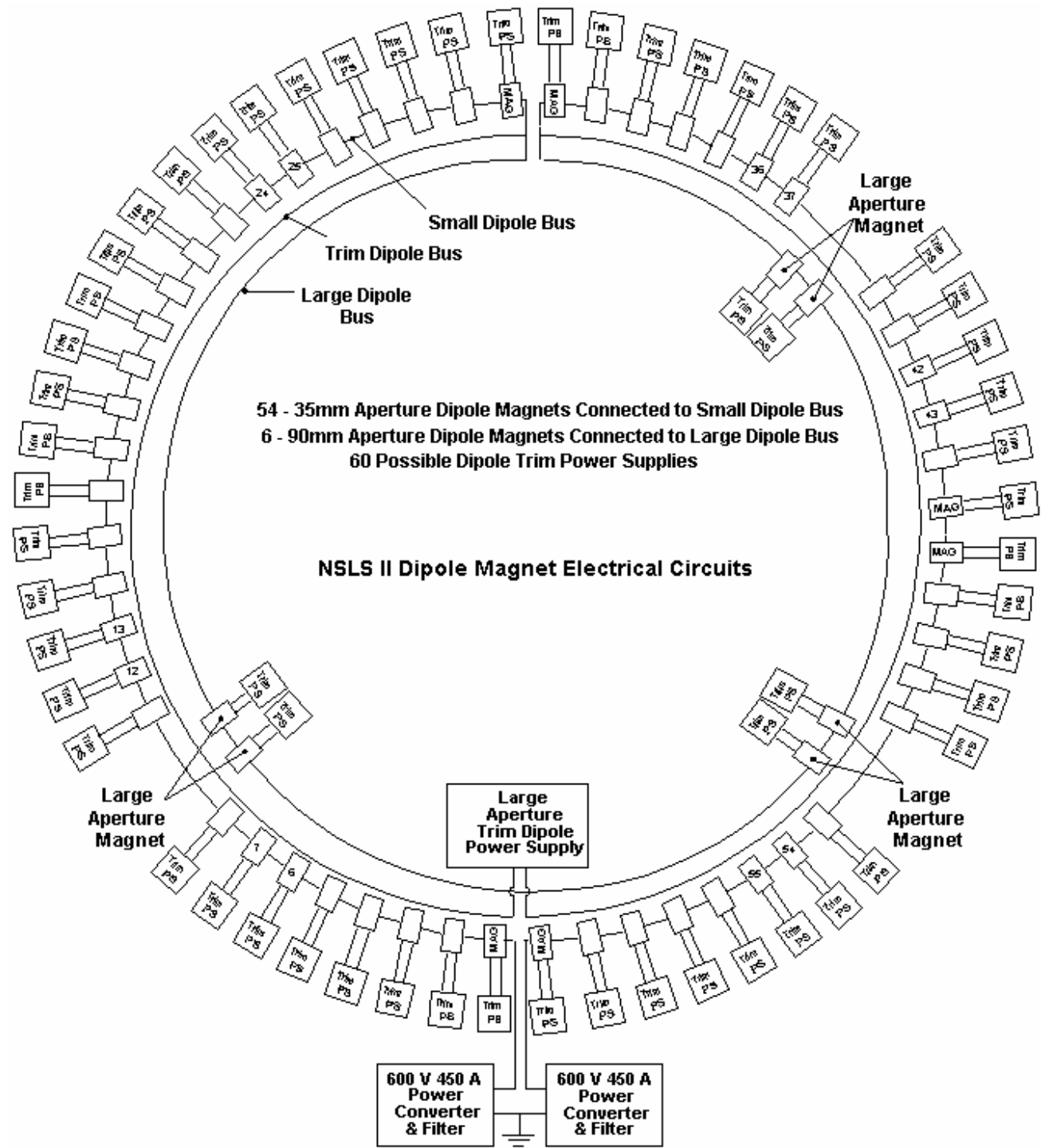


Figure 4.2.1 Storage ring dipole magnet circuit.

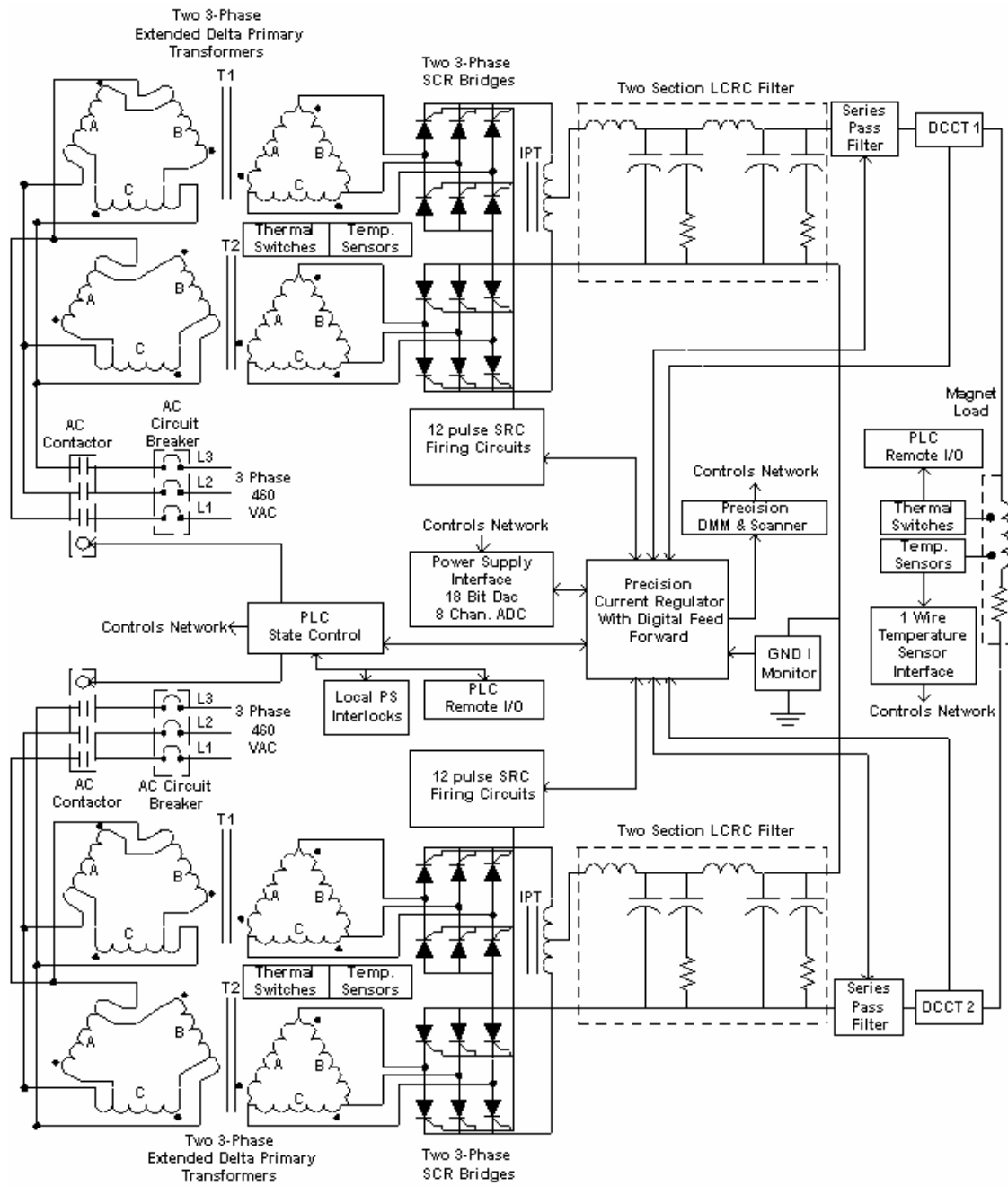


Figure 4.2.2 Dipole power supply block diagram.

#### 4.2.2 SR-Quad-A-PS, SR-Quad-B-PS, and SR-Quad-C-PS – Quadrupole Power Supplies

These circuits will use one power supply for each magnet. The quadrupole magnet load parameters require three power supplies for the different quadrupole magnet types. There are a total of 300 magnet circuits. The following table shows which power supply is used for each type of magnet and what are the power supply loads.

PS Type	Magnet	Operating Current	Load resistance	Load Inductance	Output Cable
Quad-A	Q1L,Q3L,QF,Q3H	146 A	0.058 $\Omega$	0.027 H	250 MCM
Quad-B	Q2L,Q2H	160 A	0.129 $\Omega$	0.135 H	250 MCM
Quad-C	QD,Q1H	95 A	0.058 $\Omega$	0.027 H	4/0 AWG

The cabling between the magnets and power supply will use flexible copper cables.

The power supply is a unipolar, single-quadrant, current-regulated switch-mode design. The power section is a commercial, voltage-controlled, switch-mode-programmable power supply with high output bandwidth ( $\sim 0.5$  kHz). These supplies have 3, 6.6, and 1.2 kW output power ratings. They fit in a standard 19-in. electronics rack and are only 3.5 and 1.75 inches high. These power supplies are air-cooled. A precision analog regulator to control the current will be developed in-house. The power supply will use a DCCT as the current feedback device. To minimize current ripple, an additional output filter can be used. An AC input module will turn the power supply on and off. A microcontroller will be used for state control (on/off commands and interlocks). See Figure 4.2.3 for a block diagram of the Quad power supply.

#### Quadrupole Power Supply Specifications

##### AC Input

PS Type	Voltage	Current	Phase
Quad-A	208 VAC	$\sim 11$ AAC	3
Quad-B	208 VAC	$\sim 23$ AAC	3
Quad-C	120 VAC	$\sim 14$ AAC	1

##### DC Output

PS Type	Voltage	Current	Power
Quad-A	16 VDC	185 ADC	3.0 kW
Quad-B	30 VDC	220 ADC	6.6 kW
Quad-C	10 VDC	120 ADC	1.2 kW

**Quadrupole Power Supply Specifications (cont.)**

DC minimum output current – I <sub>min</sub>	~0.5 ADC
operating quadrants	1: (V+, I+)
small-signal – 3 db bandwidth	100 Hz
stability (8 h–10 s) – referred to I <sub>max</sub>	100 ppm
stability (10 s–300 ms) – referred to I <sub>max</sub>	100 ppm
stability (300 ms–0 ms) – referred to I <sub>max</sub>	500 ppm
absolute accuracy – referred to I <sub>max</sub>	100 ppm
reproducibility long term – referred to I <sub>max</sub>	100 ppm
current ripple – referred to I <sub>max</sub>	15 ppm 60 Hz and greater
resolution of reference current	18-bit ±1 LSB
resolution of current measured – fast sampling	16-bit ±1 LSB at 200 μsec
resolution of current measured – slow sampling	22-bit ±1 LSB at 16.67 msec

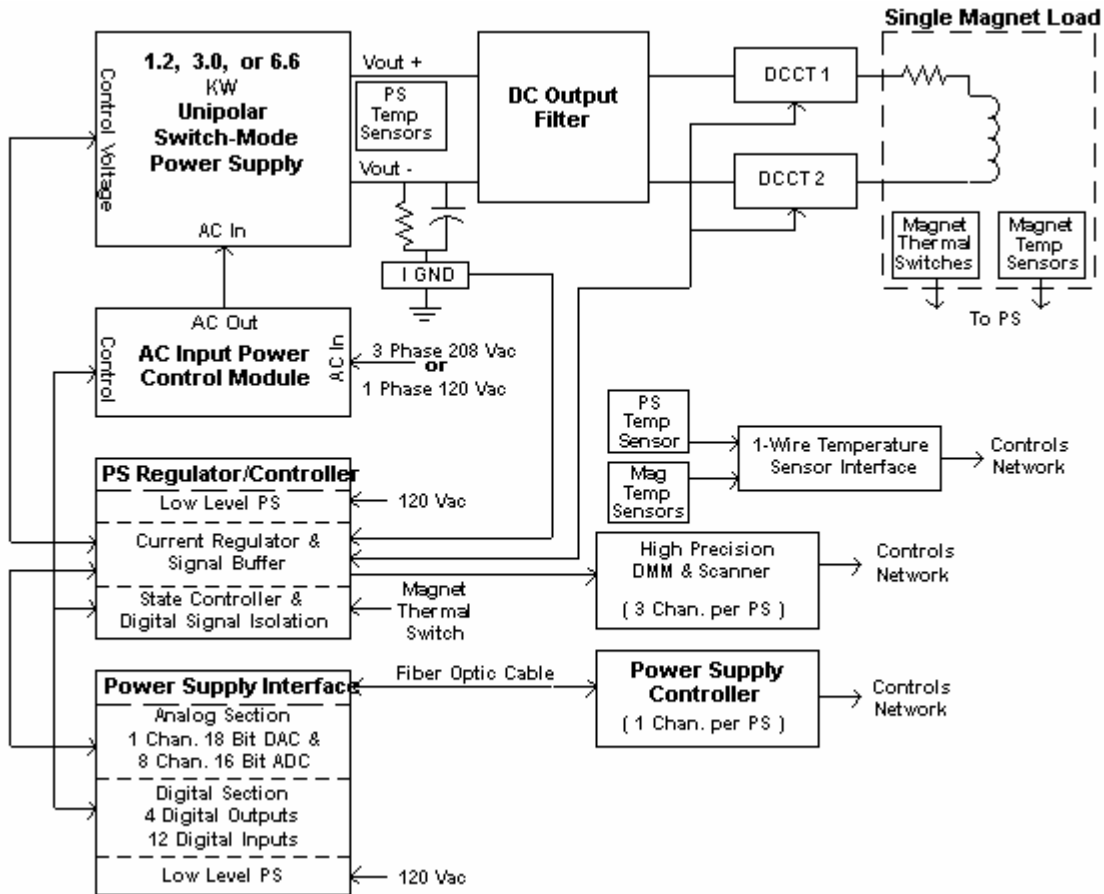


**Figure 4.2.3** Quadrupole power supply block diagram.

### 4.2.3 SR-Sext-A-PS and SR-Sext-B-PS – Sextupole Power Supplies

These circuits will use one power supply for each family of sextupole magnets in each pentant. There are nine families in each of the five pentants. There are a total of 45 magnet circuits. The sextupole magnet load parameters require two power supply types for the different sextupole magnet families. The following table shows which power supply is used for each sextupole families and what are the power supply loads.

PS Type	Sextupole Family	Operating Current	Load resistance	Load Inductance	Output Cable
Sext-A	SL1, SL2, SL3, SL4 SH1, SH2, SH3	123 A	0.246 $\Omega$	0.053H	250 MCM
Sext-B	SD	164 A	0.431 $\Omega$	0.106 H	250 MCM
Sext-B	SF	164 A	0.285 $\Omega$	0.066 H	250 MCM

The cabling between the magnets and power supply will be 250 MCM flexible copper cables. See Figure 4.2.5 for a connection diagram of sextupole families.

The supply is a unipolar, current-regulated switch-mode design, similar to that for the quadrupoles. The power section is a commercial, voltage-controlled, switch-mode-programmable power supply with high output bandwidth ( $\sim 0.5$  kHz). These air-cooled power supplies have an output power rating of 10 kW or 20 kW. They fit in a standard 19-in. electronics rack and are only 5.25 inches high for 10 kW and 10.5 inches high for 20 kW. A precision analog regulator to control the current will be developed in-house. The power supply will use a DCCT as the current feedback device. To minimize current ripple, an additional output filter will be used. An AC input module will turn the power supply on and off. A microcontroller will be used for state control (on/off commands and interlocks). See Figure 4.2.6 for a block diagram of the sextupole power supply.

#### Sextupole Power Supply Specifications

##### AC input

PS Type	Voltage	Current	Phase
Sext-A	208 VAC	$\sim 34$ AAC	3
Sext-B	208 VAC	$\sim 68$ AAC	3

##### DC output

PS Type	Voltage	Current	Power
Sext-A	60 VDC	167 ADC	10.0 kW
Sext-B	100 VDC	200 ADC	20.0 kW

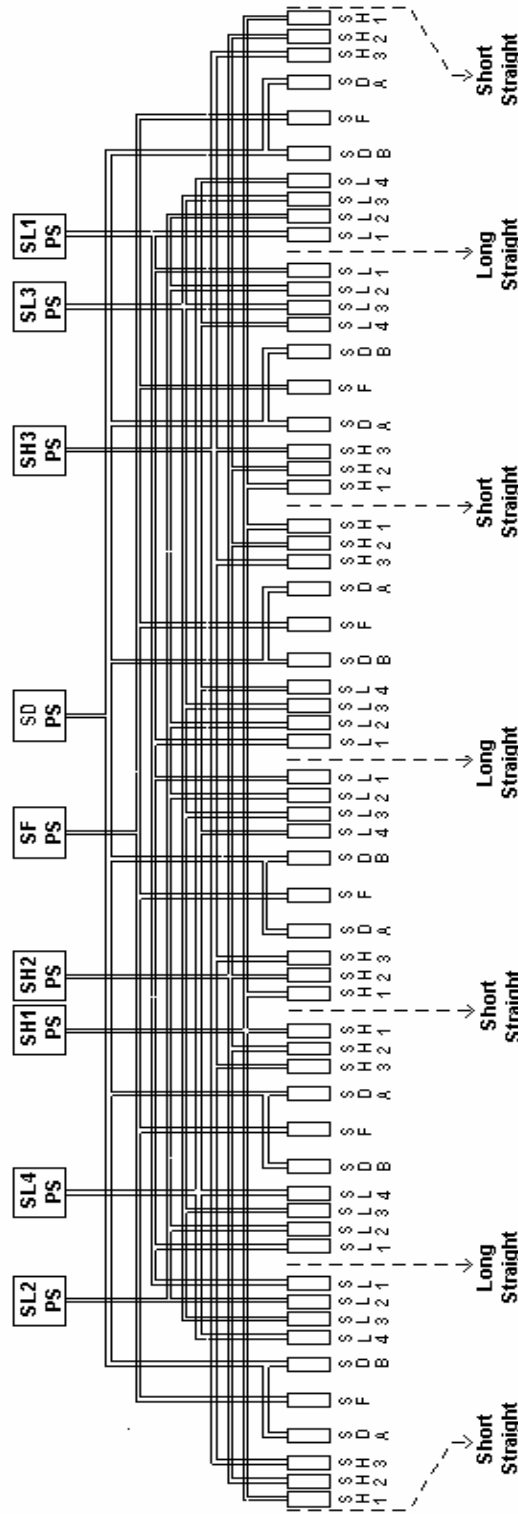
**Sextupole Power Supply Specifications (cont.)**

---

DC minimum output current – I <sub>min</sub>	~0.5 ADC
DC output voltage	12 VDC
operating quadrants	1: (V+, I+)
small-signal – 3 db bandwidth	100 Hz
stability (8 h–10 s) – referred to I <sub>max</sub>	100 ppm
stability (10 s–300 ms) – referred to I <sub>max</sub>	100 ppm
stability (300 ms–0 ms) – referred to I <sub>max</sub>	50 ppm
absolute accuracy – referred to I <sub>max</sub>	100 ppm
reproducibility long term – referred to I <sub>max</sub>	100 ppm
current ripple – referred to I <sub>max</sub>	15 ppm 60 Hz and greater
resolution of reference current	16-bit ±1 LSB
resolution of current measured – fast sampling	16-bit ±1 LSB at 200 μsec
resolution of current measured – slow sampling	22-bit ±1 LSB at 16.67 msec

---

# Pentant Wide Sextupole Power Supply Circuits



**9 Sextupole Power Supplies per Pentant**  
**45 Sextupole Power Supplies Total**  
**8 Six Magnet Circuits &**  
**1 Twelve Magnet Circuits**

**Figure 4.2.5** Connection diagram of sextupole families.



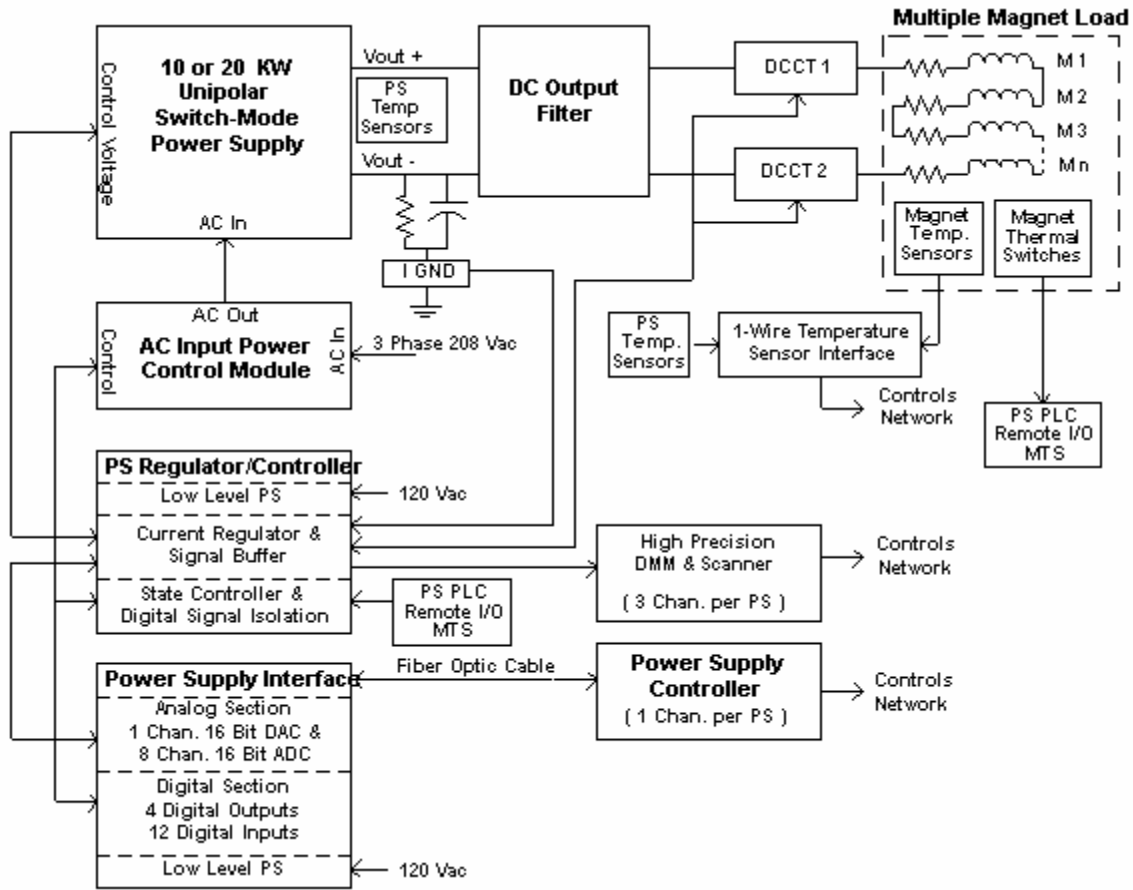


Figure 4.2.6 Sextupole power supply block diagram.

#### 4.2.4 SR-Dipole Trim-PS and SR-SKQ-PS – Dipole Trim Coil and Skew Quadrupole Power Supplies

The Dipole Trim PS circuit consists of the trim coil sets located in the dipole magnets. The coil set is 3.11  $\Omega$  and 26 mH for small-aperture dipole and 8.67  $\Omega$  and ~90 mH. The SKQ power supply circuit consists of a corrector coil that is still to be placed in the lattice; this coil is estimated at 3.0  $\Omega$  and 5 mH. The operating current for these power supplies is ~2 A for 3.0 GeV. The cabling from the coil set to the power supply will be # 10 AWG flexible copper, routed through the tunnel ceiling into the equipment area above the main tunnel. The cabling has a resistance of 0.153  $\Omega$  and an inductance of 0.1 mH. The worst-case power supply load is 8.82  $\Omega$  and ~ 0.09 H.

The bipolar, 4-quadrant, current-regulated linear power supply fits in a standard 19-in. electronics rack and is 5.25 inches high. A precision analog regulator to control the current will be used. The power supply will use a DCCT as the current feedback device. A microcontroller will be used for state control (on/off commands and interlocks).

##### B1 Trim PS and SKQ PS Power Supply Specifications

AC input power	1-phase 120 VAC ~2.4 AAC
DC maximum output current – I <sub>max</sub>	+5 ADC
DC minimum output current – I <sub>min</sub>	-5 ADC
DC output voltage	±20 VDC
operating quadrants	4: (V+, I+), (V-, I+), (V-, I-) & (V+, I-)
small-signal – 3 db bandwidth	10 kHz
large-signal bandwidth	~5 Hz
stability (8 h–10s) – referred to I <sub>max</sub>	100 ppm
stability (10 s–300 ms) – referred to I <sub>max</sub>	100 ppm
stability (300 ms–0 ms) – referred to I <sub>max</sub>	50 ppm
absolute accuracy – referred to I <sub>max</sub>	100 ppm
reproducibility long term – referred to I <sub>max</sub>	100 ppm
current ripple – referred to I <sub>max</sub>	10 ppm 60 Hz and greater
resolution of reference current	16-bit ±1LSB
resolution of current measured – fast sampling	16-bit ±1 LSB at 200 $\mu$ sec
resolution of current measured – slow sampling	22-bit ±1 LSB at 16.67 msec

#### 4.2.5 SR-BH-PS and SR-BV-PS – Intermediate Speed Horizontal and Vertical Corrector Coil Power Supplies

The BH and BV Corrector PS circuits consist of the corrector coil set located in an HVC magnet. Each coil set is  $\sim 0.34 \Omega$  and  $\sim 25$  mH. This coil set is estimated at  $3.0 \Omega$  and  $1$  mH. The operating current for both power supplies is  $\sim 15$  A for  $3.0$  GeV. The cabling from the coil sets to the power supplies will be # 10 AWG flexible copper cables, routed through the tunnel ceiling into the equipment area above the main tunnel. The cabling has a resistance of  $0.148 \Omega$  and an inductance of  $0.1$  mH. The worst-case power supply load is  $0.488 \Omega$  and  $\sim 25$  mH.

The BH and BV power supplies are bipolar, 4-quadrant, current-regulated linear PS that fit in a standard 19-in. electronics rack and are 5.25 inches high. A precision analog regulator to control the current will be used. The power supply will use a DCCT as the current feedback device. These corrector power supplies are part of an intermediate-speed beam position feedback system. A microcontroller will be used for state control (on/off commands and interlocks).

##### Corrector Coil Set Power Supply Specifications

AC input power	1-phase 120 VAC $\sim 7.3$ AAC
DC maximum output current – I <sub>max</sub>	+ 24 ADC
DC minimum output current – I <sub>min</sub>	– 24 ADC
DC output voltage	$\pm 25$ VDC
operating quadrants	4: (V+, I+), (V-, I+), (V-, I-) & (V+, I-)
small-signal – 3 db bandwidth	1 kHz
large signal – bandwidth	$\sim 5$ Hz
stability (8 h–10 s) – referred to I <sub>max</sub>	100 ppm
stability (10 s–300 ms) – referred to I <sub>max</sub>	50 ppm
stability (300 ms–0 ms) – referred to I <sub>max</sub>	25 ppm
absolute accuracy – referred to I <sub>max</sub>	100 ppm
reproducibility long term – referred to I <sub>max</sub>	100 ppm
current ripple – referred to I <sub>max</sub>	5 ppm 60 Hz and greater
resolution of reference current	18-bit $\pm 1$ LSB
resolution of current measured – fast sampling	16-bit $\pm 1$ LSB at 200 $\mu$ sec
resolution of current measured – slow sampling	22-bit $\pm 1$ LSB at 16.67 msec

#### 4.2.6 SR-FIBH-PS and SR-FIBV- PS Fast Insertion Horizontal and Vertical Corrector Power Supplies

The FIBH and FIBV fast insertion corrector power supply circuits consist of the corrector coil set located in a fast insertion HVC magnet. These magnets are located in the insertion region on either side of an insertion device. Each coil set is estimated at  $\sim 0.8 \Omega$  and  $\sim 10$  mH. The operating current for the power supplies is  $\sim 2$  A for 3.0 GeV. The cabling from the coil sets to the power supply will be # 10 AWG flexible copper, routed through the tunnel ceiling into the equipment area above the main tunnel. The cabling has a resistance of  $0.152 \Omega$  and inductance of 0.1 mH. The worst-case power supply load is  $\sim 0.95 \Omega$  and 0.010 H.

The FIBH and FIBV power supplies are bipolar, 4-quadrant, current-regulated linear power supplies that fit in a standard 19-in. electronics rack and are 5.25 inches high. A precision analog regulator to control the current will be used. The power supply will use a DCCT as the current feedback device. These corrector power supplies are part of a fast beam position feedback system. A microcontroller will be used for state control (on/off commands and interlocks).

##### Fast Insertion Corrector Power Supply Specifications

AC input power	1-phase 208 Vac $\sim 2.6$ AAC
DC maximum output current – I <sub>max</sub>	+ 5 ADC
DC minimum output current – I <sub>min</sub>	- 5 ADC
DC output voltage	$\pm 20$ VDC
operating quadrants	4: (V+, I+), (V-, I+), (V-, I-), & (V+, I-)
small-signal – 3 db bandwidth	10 kHz
large signal – bandwidth	100 Hz
stability (8 h–10 s) – referred to I <sub>max</sub>	100 ppm
stability (10 s–300 ms) – referred to I <sub>max</sub>	50 ppm
stability (300 ms–0 ms) – referred to I <sub>max</sub>	25 ppm
absolute accuracy – referred to I <sub>max</sub>	100 ppm
reproducibility long term – referred to I <sub>max</sub>	100 ppm
current ripple – referred to I <sub>max</sub>	5 ppm 60 Hz and greater
resolution of reference current	18-bit $\pm 1$ LSB
resolution of current measured – fast sampling	16-bit $\pm 1$ LSB at 200 $\mu$ sec
resolution of current measured – slow sampling	22-bit $\pm 1$ LSB at 16.67 msec

#### 4.2.7 SR-FGBH-PS and SR-FGBV-PS Fast Global Horizontal and Vertical Corrector Power Supplies

The FGBH and FGBV fast global corrector power supply circuits consist of the corrector coil set located in a fast global HVC magnet. This magnet is located over stainless steel bellows on both sides of the dipole magnets. This magnet serves as an alignment and fast orbit position corrector. This requires the power supply to have both high voltage and current. The operating current for the power supplies is  $\sim 15$  A for 3.0 GeV. The coil resistance is  $\sim 0.5 \Omega$  and coil inductance is  $\sim 0.10$  mH. The cabling from the coil sets to the power supply will be # 10 AWG flexible copper, routed through the tunnel ceiling into the equipment area above the main tunnel.

The FGBH and FGBV power supplies will use a switch-mode, bipolar, four-quadrant, current-regulated power supply. It will fit in a standard 19-in. electronics rack. A precision analog regulator to control the current will be used. The power supply will use a DCCT as the current feedback device. These corrector power supplies are part of a fast beam position feedback system. A microcontroller will be used for state control (on/off commands and interlocks). See Figure 4.2.7 for a block diagram of the fast global corrector power supply.

##### Fast Global Corrector Power Supply Specifications

AC input power	120 VAC $\sim 14$ AAC
DC maximum output current – $I_{max}$	+ 24 ADC
DC minimum output current – $I_{min}$	- 24 ADC
DC output voltage	$\pm 45$ VDC
operating quadrants	4: (V+, I+), (V-, I+), (V-, I-), & (V+, I-)
small-signal – 3 db bandwidth	5 kHz
large signal – bandwidth	100 Hz
stability (8 h–10 s) – referred to $I_{max}$	1,000 ppm
stability (10 s–300 ms) – referred to $I_{max}$	50 ppm
stability (300 ms–0 ms) – referred to $I_{max}$	25 ppm
absolute accuracy – referred to $I_{max}$	100 ppm
reproducibility long term – referred to $I_{max}$	100 ppm
current ripple – referred to $I_{max}$	5 ppm 60 Hz and greater
resolution of reference current	20-bit $\pm 1$ LSB
resolution of current measured – fast sampling	16-bit $\pm 1$ LSB at 200 $\mu$ sec
resolution of current measured – slow sampling	22-bit $\pm 1$ LSB at 16.67 msec

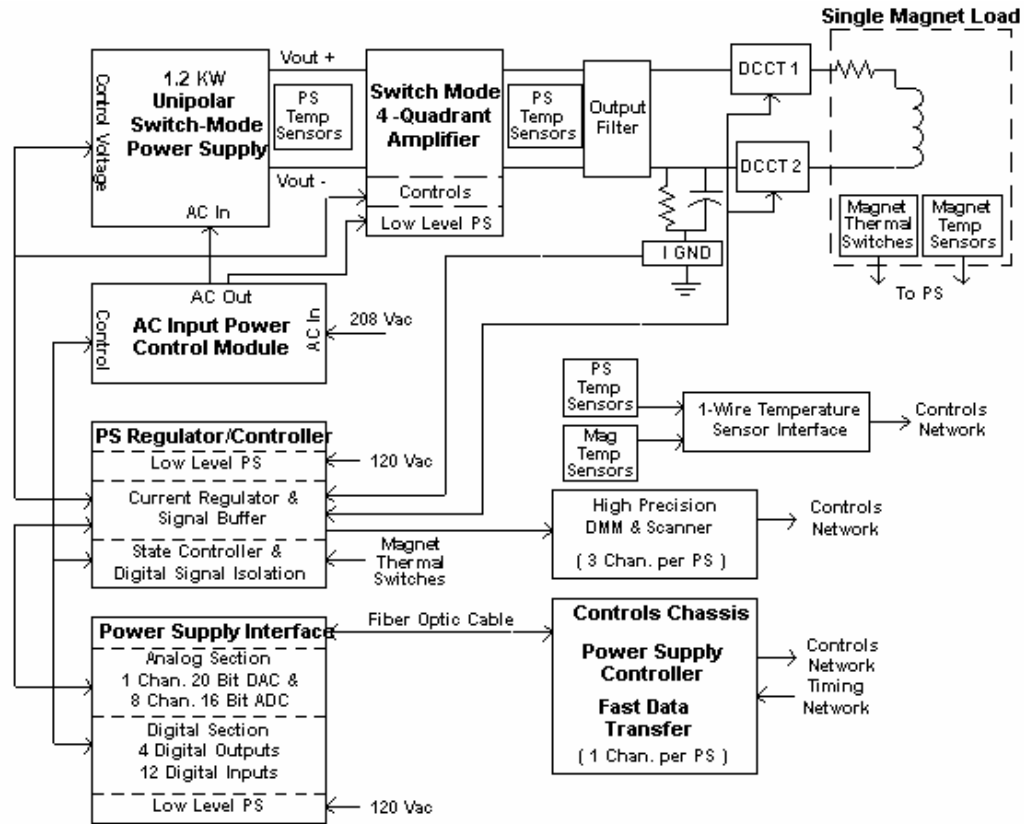


Figure 4.2.7 Block diagram of the Fast Global Corrector power supply.

### **4.2.8 Power Supply Interlocks**

All power supplies will have sufficient interlocks that will prevent the power supply from becoming damaged due to changes in cooling conditions, AC power disturbances, and nonstandard operating conditions.

All magnet coils will have an over-temperatures interlock if there is a change in cooling and/or operating conditions. Temperature interlock for magnets that are part of ring- and pentant-wide circuits will be interfaced to a ring-wide interlock system. This system will use a PLC with remote I/O modules located in every cell. The system will monitor all the thermal switches on these magnets and route the interlock signal to the appropriate power supplies.

All power supplies will have an electrical safety interlock that will prevent the power supply from turning on if the machine safety system requires it.

### **4.2.9 Power Supply Instrumentation**

Redundant DCCTs will be used to confirm the power supply current reproducibility.

High-precision DMMs and scanners will be used to monitor the power system current, the redundant current sensor, and the analog current set point. This equipment will ensure long-term stability and reproducibility.

Temperature monitoring of the magnet coils and power system environment will be accomplished using low-cost digital temperature sensors. With such systems, a problem can be identified before it becomes an emergency, making it possible for repairs to be scheduled more conveniently.

### **4.2.10 Power Supply Controls**

The Power Supply Interface has a precision DAC for generating the reference current and a multi-channel ADC for inputting PS signals. The PSI also has digital I/O for state control and status readbacks of the PS.

A VME device card will be used to communicate between the control system and the PSI. This card will be located in a control system's VME chassis that will be mounted in one of the power supply system racks. This card will generate the reference current profiles, input analog data, and perform digital state control and status readbacks. The output of the device card is a fiber optics cable that connects to a PSI.

The other controls will include the operation of the high-precision DMM and scanner and readout of the digital temperature sensors.

### **4.2.11 Electrical Safety**

All power supplies will conform to the latest BNL safety requirements, especially concerning arc flash protection. Whenever possible, NRTL-listed equipment will be used.

### **4.2.12 Cable Tray and Cable Routing**

The cable tray for the magnet circuits will be located in the equipment area above the main tunnel. The cable will drop through the tunnel ceiling at two locations in each cell, where it will connect to two dipole magnets. There will also be a tray inside the main tunnel only in the area of the cell. This tray will be located over the storage ring magnets. The single cables will be installed with a twist to prevent pickup from noise sources. All cables will be tray-rated cables. Power supply cables will be arranged to minimize pickup from other circuits. All power cables will be separated from signal cables. The quadrupole, sextupole, and corrector

cables will be routed through conduit in the main tunnel ceiling. The cable going through the conduit will run in the cable tray in the tunnel until it is connected to the magnet. All cables and trays will meet NEC codes.

See Figure 4.2.8 for a block diagram of the cable and tray for one cell.

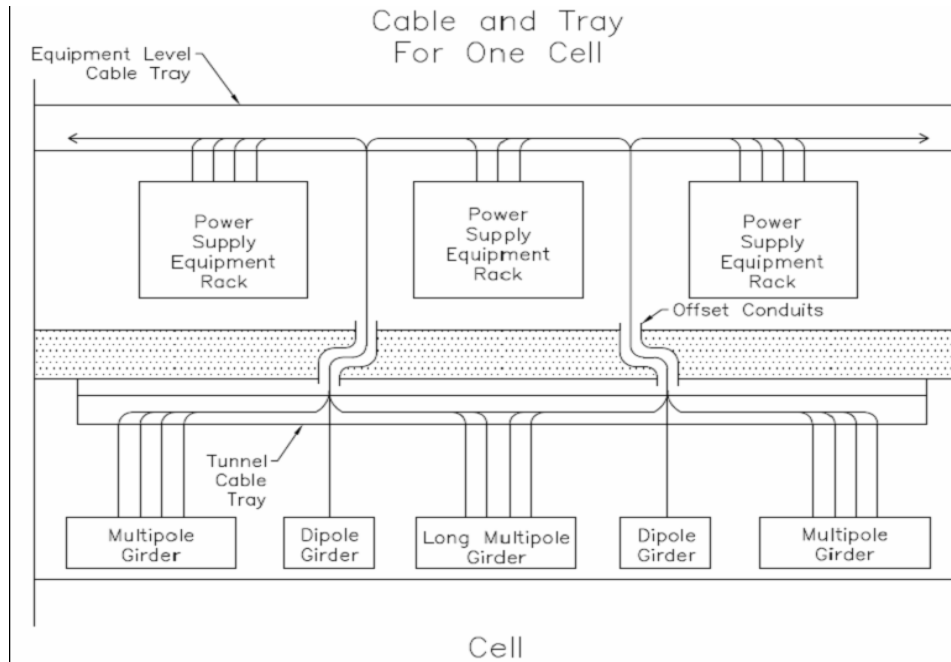


**Figure 4.2.8** Block diagram of the cable and tray for one cell.



### 4.2.13 Power Supply Racks

All storage ring power supplies except for the dipole will be mounted in sealed Nema 12 electronics racks. These racks will have a maximum of six 3kW power supplies installed in them. These racks will also have power supply controls and instrumentation installed in them. At each cell location there are 11 power supply racks (Figure 4.2.9). The power racks will be located above the magnets they supply.

Three PS Rack Configuration

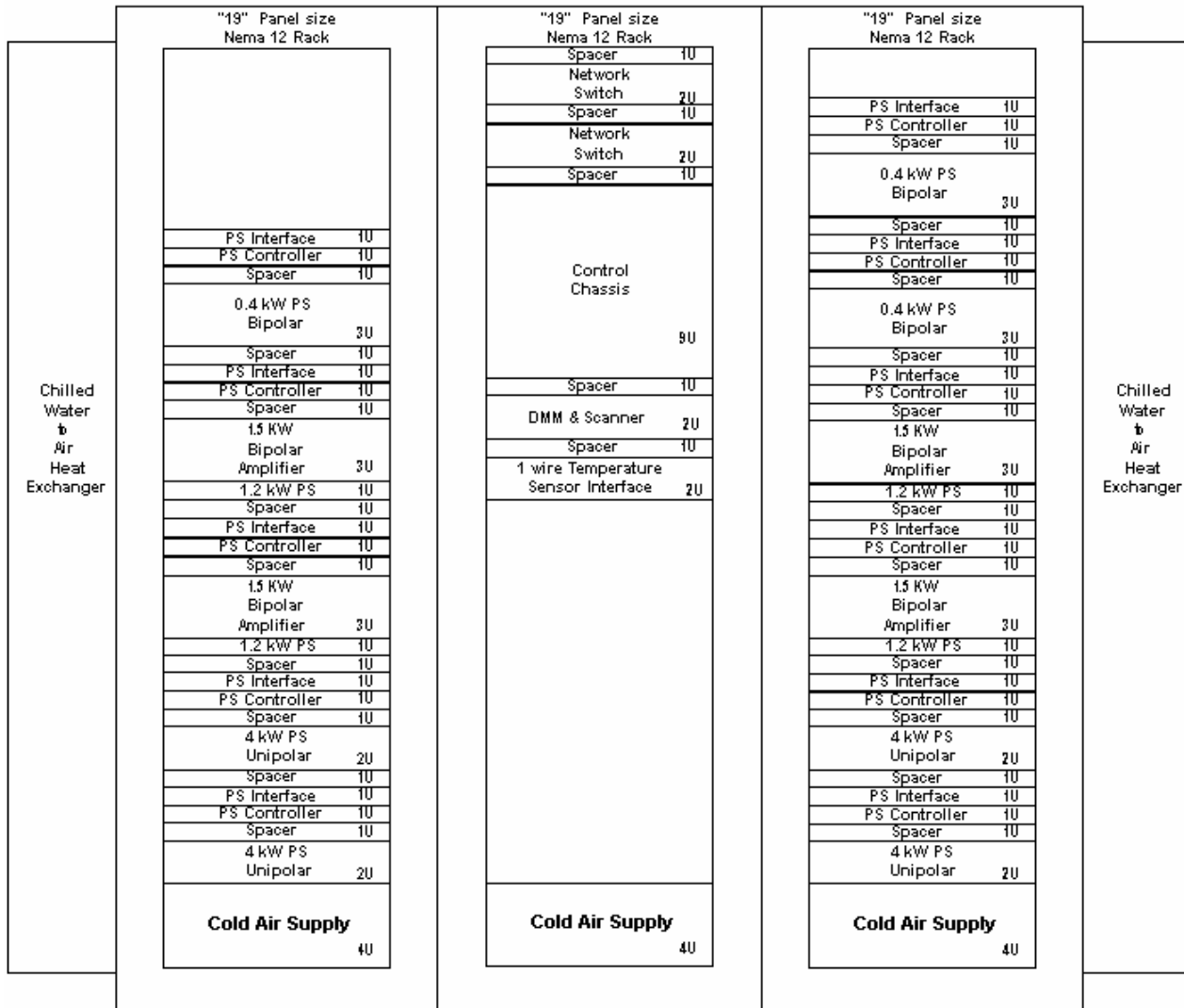


Figure 4.2.9 Magnet power supply rack layout.

A water-to-air heat exchanger will cool a set of three or four racks. Cooled air will flow through the power supplies and circulate back to the heat exchanger. The heat exchanger will use chilled water and have the outlet temperature regulated (Figure 4.2.10).

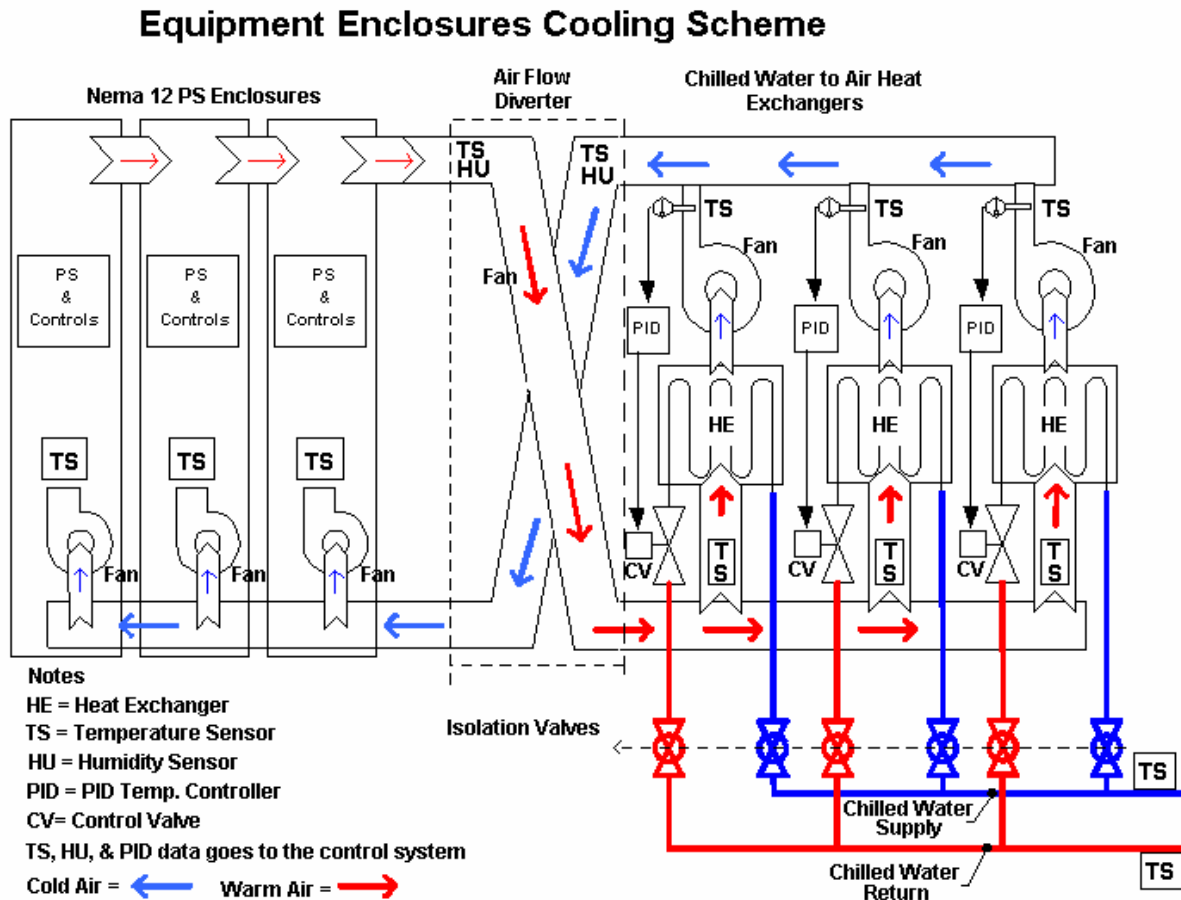


Figure 4.2.10 Rack cooling scheme.



## 4.3 Magnet–Girder Support System

### 4.3.1 Scope

This section describes alignment tolerances, stability requirements, and preliminary design of the storage ring magnet support system. Specifications for magnet alignment and stability are established from analysis of the storage ring nonlinear dynamics. Functional requirements of the girder supports are presented and design features for meeting these requirements are discussed. Various sources of ambient motion affecting the stability of the support system are identified and design solutions to mitigate their effects are discussed.

### 4.3.2 Alignment Tolerances and Stability Requirements

The alignment tolerances for the ring magnets impact the ring performance in several ways. Magnet alignment is necessary to be able to store the electron beam with the design emittance and lifetime (i.e., sufficient dynamic aperture, DA). First, there is a relative magnet-to-magnet alignment tolerance to a line relative to the rigid girder. Second, there is an alignment tolerance specified for the transverse position of the ends of the girder and its roll angle and longitudinal position (six parameters), as it is installed in the tunnel. The girder misalignment introduces a correlated offset of the magnets. For this preliminary design, we took the achievable magnet-to-magnet alignment values from recently commissioned light sources as our specification and calculated the impact on the DA. Future studies will further explore sensitivity to these tolerances, along with the tolerance on magnetic field errors. The current tolerances are listed in Table 4.1.1. The impact of tolerance errors is discussed in Section 4.1.1.

The stability of closed-orbit position is critical to providing a constant flux in the user beamlines (i.e., intensity through slits and mirror systems). There are several sources of steering that cause large closed-orbit motion (relative to the user beamline): power supply fluctuations, energy modulations, and alignment variations due to vibrations of the magnets. We only consider the last effect here. The magnet motions that are of most concern are those of the quadrupole transverse position, dipole longitudinal position, and roll angle. This closed-orbit motion is the result of the large COAF, discussed in Section 4.1, which determined the magnitude of beam motion per unit of transverse motion of the quadrupoles, assuming that all quadrupole motions were uncorrelated in location around the ring, as well as uncorrelated in time. Here we discuss in more detail the time variation of the beam orbit due to quadrupole and dipole motion and the impact this has on the user beam.

To estimate the magnitude of the resulting orbit motion, we need to know how the quadrupoles are shifted around the ring. This depends on the noise source that generates this motion, as well as its coupling to the magnets through their support system (girders and floor). The simplest model of these magnet vibrations is just the random fluctuations of the magnet centers by a common tolerance level and assuming this impact will be the same at any frequency of vibration. This tends to overestimate the impact on the beam motion, since it ignores correlations that will smooth the distortions, as well as the synchrotron radiation damping that will damp the beam to the shifted closed orbit. This latter effect will mean that for frequencies greater than  $F_{x,y} \approx 1/\tau_{x,y}$ , where  $\tau_{x,y}$  are the transverse damping times, the effective beam emittance will grow, while the centroid orbit shift will be reduced from that estimated from the random closed-orbit shift calculation.

We place a limit on the amplitude of magnet motion to be that which contributes to an RMS orbit shift equal to 10% of the RMS beam size in that plane. These sizes are shown in Table 4.3.1 for beam at the center of the two ID straight sections (long and short, LID and SID):

**Table 4.3.1 Beam size at the center of the ID straights for 0.5 nm-rad (x) and 0.008 nm-rad (y) emittance.**

Long ID	Long ID	Short ID	Short ID	TPW
$\sigma_x, \sigma_y$	$\sigma_x, \sigma_y$	$\sigma_x, \sigma_y$	$\sigma_x, \sigma_y$	$\sigma_x, \sigma_y$
$[\mu\text{m}], [\mu\text{rad}]$	$[\mu\text{m}], [\mu\text{rad}]$	$[\mu\text{m}], [\mu\text{rad}]$	$[\mu\text{m}], [\mu\text{rad}]$	$[\mu\text{m}], [\mu\text{m}]$
107.7 4.64	4.8 1.67	29.6 16.9	3.1 2.58	175 12.4

The closed orbit at the center of the short straight section for 2,000 random seeds is shown in Figure 4.3.1, for the ring quadrupoles shifted by Gaussian random values with RMS values of ( $\Delta X = 0.157 \mu\text{m}$  and  $\Delta Y = 0.022 \mu\text{m}$ ). Each point represents a different sampling of the random fluctuations of the quadrupole centers at any frequency with that amplitude, and includes all of the nonlinear elements in the calculation.

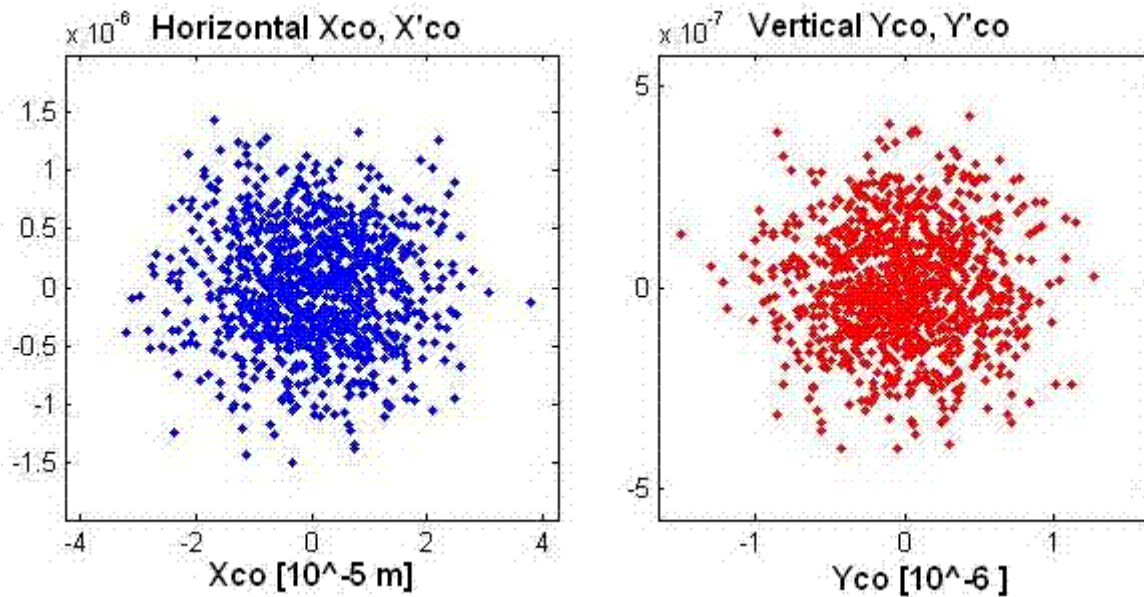


**Figure 4.3.1** The horizontal and vertical closed-orbit in the LID straight for 2,000 seeds with RMS random quadrupole center shifts of  $\Delta X = 0.157$  and  $\Delta Y = 0.022 \mu\text{m}$ .

The RMS horizontal and vertical beam orbit shifts were 19.4 and 0.5  $\mu\text{m}$ , respectively, or 10% of the RMS beam size in the LID. These RMS values give a very conservative tolerance for quadrupole vibration tolerances. At frequencies above the damping frequency,  $F_{x,y}$ , this calculation gives an estimate of the emittance dilution.

$$\Delta\epsilon_x / \pi = \frac{1}{n} \sqrt{\sum x^2 \sum x'^2 - (\sum x x')^2} \quad (4.3-1)$$

where  $x$  and  $x'$  are closed orbit and slope from each seed and the sum is over all seeds. The effective emittance dilution shown in Figure 4.3.1 is only 1% horizontal and 1% vertical of the emittance plane, or  $\Delta\epsilon_x = 5.1 \text{ pm}$  and  $\Delta\epsilon_y = 0.09 \text{ pm}$ , representing a small increase in the damped beam emittance.

Since the dipole magnets do not have gradients, their transverse motions have little impact on the closed-orbit motion. However, longitudinal position fluctuations of the dipoles will also create a horizontal beam

motion and the roll angle will create a vertical closed-orbit motion. Using a similar random distribution analysis, we set a tolerance level for the RMS fluctuations of the dipole longitudinal position,  $\Delta S < 2 \mu\text{m}$ , and the dipole roll angle of  $\Delta\theta < 0.1 \mu\text{rad}$ . These tolerances, together with the quadrupole levels set above, contribute increases of the RMS closed-orbit motions of 11% and the effective emittance dilution of

$$\Delta\epsilon_x = 5.6 \mu\text{m} \text{ and } \Delta\epsilon_y = 0.12 \mu\text{m}. \quad (4.3-2)$$

Because the magnets are not supported independently but on girders, magnetic center fluctuations will be correlated. In Section 7.1.1 the effect of random misalignment of the girders was considered and the closed-orbit Girder Amplification Factor was computed to be 3 to 5 times less than the COAF for the quadrupoles, for independent fluctuations. The GAFs in the long ID straight sections are  $34 \mu\text{m}$  (H) and  $7.8 \mu\text{m}$  (V). In the short ID straight sections the GAFs are  $9.4 \mu\text{m}$  (H) and  $4.3 \mu\text{m}$  (V). To maintain an RMS closed-orbit fluctuation of  $\sim 10\%$  of the RMS beam size in the LID would require random girder fluctuations of less than  $0.31 \mu\text{m}$  (H) and  $0.061 \mu\text{m}$  (V). The tolerances for the SID would be  $0.31 \mu\text{m}$  (H) and  $0.0072 \mu\text{m}$  (V). This shows the reduction in tolerance levels for vibrations coming from the correlation of the magnet vibrations, compared to the random quadrupole tolerance, and that the random model tends to yield a worst-case tolerance level estimate for vibrations.

Another model for quadrupole magnet center fluctuations attempts to include a magnet-to-magnet spatial correlation based on a ground movement model of a plane wave passing through the ring. This model was implemented in the accelerator design code BETA-ESRF [4.3.1]. The horizontal and vertical quadrupole motions are then calculated from the amplitude and wavelength ( $\lambda$ ) of the wave. The increase in the effective emittance can be calculated from the closed-orbit shift around the ring using Eq. (4.3-1). Since there will be a dependence on the direction of the wave relative to straight sections, several phases relative to the lattice orientation have been considered, to estimate the maximum impact. The wavelength varies as a function of frequency, which depends on the knowledge of the speed of propagation. We assumed  $V = 270 \text{ m/sec}$  for both S and P waves (see Section 4.3.3.5.1 for measurement for the BNL site). The impact on the beam's closed-orbit shift is then estimated by displacing the center of each quadrupole on the corresponding point of the plane wave. The effective amplitude of the closed-orbit distortion is estimated by sampling the closed orbit around the ring, instead of for different seeds. No consideration for the girders is taken, nor is there any damping of the wave or the beam assumed. Figure 4.3.2a shows the tolerance level for the horizontal (pressure, P) wave amplitude versus frequency ( $f = V/\lambda$ ), for an effective emittance dilution that is 1% of the beam emittance, or  $5 \mu\text{m}$ .

Figure 4.3.2b shows the tolerance level for the vertical (shear, S) wave amplitude versus frequency ( $f = V/\lambda$ ), for an emittance dilution that is 1% of the beam emittance, or  $0.08 \mu\text{m}$ . Clearly, as the wavelength exceeds the ring diameter of  $248 \text{ m}$  ( $f < \sim 2 \text{ Hz}$ ), the entire ring moves in phase and the closed-orbit impact becomes small; the tolerance becomes quite large. Above  $20 \text{ Hz}$  (H) and  $10 \text{ Hz}$  (V), the amplitude tolerance becomes almost independent of frequency, about at the levels where  $\Delta X = 0.08 \mu\text{m}$  and  $\Delta Y = 0.04 \mu\text{m}$ .

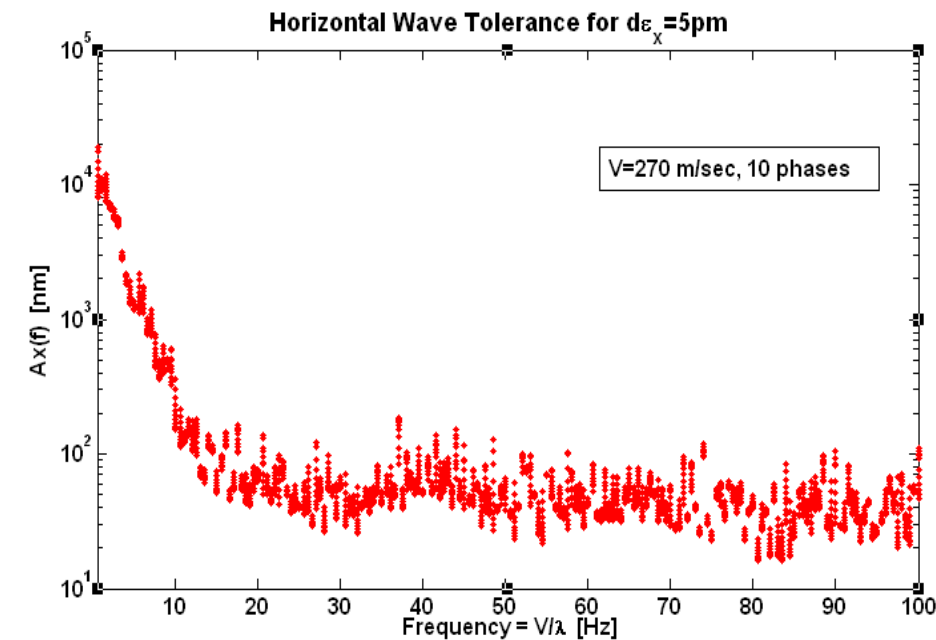


**Figure 4.3.2 a** The tolerance level for a horizontal wave amplitude, in nm, yielding a 5 pm emittance dilution, assuming a wave velocity of 270 m/sec.

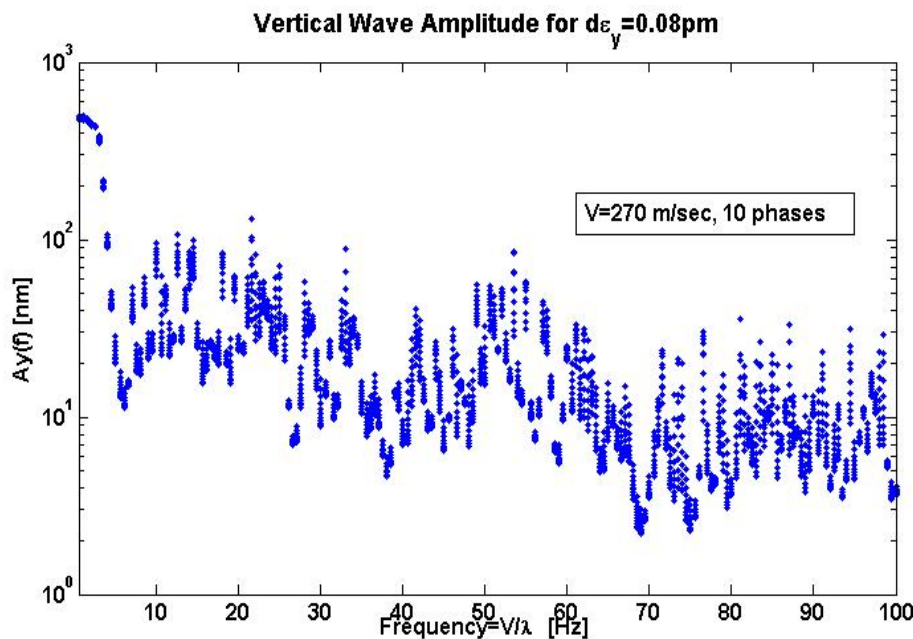


**Figure 4.3.2 b** The tolerance level for a vertical wave amplitude, in nm, yielding a 0.08 pm emittance dilution, assuming a wave velocity of 270 m/sec.

At frequencies below the 2 Hz level, clearly this model will yield very large tolerances, since all the ring magnets move together. In the low-frequency range (up to ~50 Hz), the global feedback system will take out most of the closed-orbit motion independent of the source term, to a level limited by the BPM and corrector electrical noise level. Above 50 Hz, the centroid motion becomes less obvious, but the beam emittance will be diluted by the effective emittance resulting from the magnet motion.

In summary, the magnet stability tolerances estimated with these models show the worst-case being the random model for the  $\sim 10\%$  vertical beam size. However, the effective emittance contribution of this is 1% of the beam emittance and could be relaxed at least by a factor of 2, to about  $0.050 \mu\text{m}$ . These tolerance limits, for the magnets only, are listed in Table 4.3.2. All other tolerances are readily achievable with careful design of girders and the accelerator floor. However, a global feedback system is planned, to ensure that orbit stability is achieved even if these tolerances cannot be achieved. Based on the calculations in Section 6.3, this feedback system will handle random quadrupole fluctuations as large as  $0.3 \mu\text{m}$  vertically.

**Table 4.3.2 Magnet Stability Tolerances for AC Closed-Orbit Stability, without Feedback Correction.**

Tolerance Limits	$\Delta X$ RMS Quads	$\Delta Y$ RMS Quads	X (LID) RMS	Y (LID) RMS	X (SID) RMS	X (SID) RMS
Random motion	$<0.157 \mu\text{m}$	$<0.022 \mu\text{m}$	$10.5 \mu\text{m}$	$0.48 \mu\text{m}$	$3.2 \mu\text{m}$	$0.30 \mu\text{m}$
Random girder motion	$<0.31 \mu\text{m}$	$<0.072 \mu\text{m}$	$10.6 \mu\text{m}$	$0.5 \mu\text{m}$	$3.0 \mu\text{m}$	$0.30 \mu\text{m}$
Plane wave $<5\text{Hz}$	$>2 \mu\text{m}$	$>0.1 \mu\text{m}$	$10.5 \mu\text{m}$	$0.5 \mu\text{m}$	$3.0 \mu\text{m}$	$0.30 \mu\text{m}$
Plane wave $>10\text{Hz}$	$\sim 0.08 \mu\text{m}$	$\sim 0.04 \mu\text{m}$	$10.5 \mu\text{m}$	$0.5 \mu\text{m}$	$3.1 \mu\text{m}$	$0.28 \mu\text{m}$
Additional limits	$\Delta S$ RMS Dipole	$\Delta\theta$ RMS Dipole				
Random motion	$\leq 2 \mu\text{m}$	$\leq 0.1 \mu\text{rad}$	$10 \mu\text{m}$	$0.48 \mu\text{m}$	$3.2 \mu\text{m}$	$0.30 \mu\text{m}$

### 4.3.3 Preliminary Design of the Magnet–Girder Support System

#### 4.3.3.1 Functional Requirements

The storage ring girders in a cell provide common mounting platforms for different set of magnets, as shown in Figure 4.3.3. Multipole magnets are mounted on girders in sections numbered 2, 4, and 6. Dipoles are mounted on separate girders in sections numbered 3 and 5, because of their height difference and less stringent alignment and stability requirements.

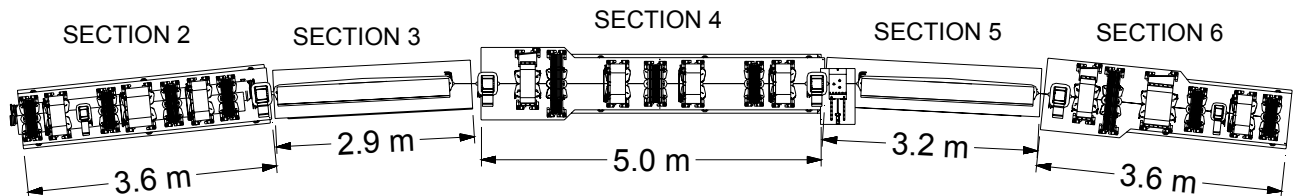


**Figure 4.3.3** NSLS-II girders in one cell of the storage ring.

General functional requirements of the magnet–girder support system are given as follows:

1. Raise the centers of the magnets to the nominal beam height of 1 m. This height was chosen based on stability considerations that are discussed in Section 4.3.2.
2. Provide a stable platform for assembling and aligning the magnets outside the tunnel. The stringent alignment tolerances can only be met by precision alignment techniques (see Section 4.3.3.3) requiring out-of-tunnel assembly and alignment. The magnet alignment must remain unperturbed during the transportation and installation of the magnet–girder assemblies in the tunnel.



3. Meet girder-to-girder alignment requirements, both during the initial alignment and subsequently to compensate for long-term floor settlement.
4. Meet dynamic stability requirements under expected ambient floor motion, flow-induced vibrations, and temperature fluctuations of the tunnel air and process water.

In addition, the overall width of the magnet–girder support system must be less than 1 m, for ease of transportation and assembly in the tunnel. The support design must also be cost effective without sacrificing speed of installation and alignment.

#### 4.3.3.2 Main Preliminary Design Features

In many recent light sources the girders have been precisely fabricated with very stringent top surface tolerances ( $\sim 15 \mu\text{m}$  flatness) and with T-slot type alignment features. Magnets, built with equally tight tolerances, are fastened directly to the girder's top surface without an interface of alignment hardware. After a careful examination of this approach, we decided to design NSLS-II girders and magnets with conventional tolerances, and to use a vibrating-wire alignment technique for aligning the magnets to within  $\sim 30 \mu\text{m}$  tolerance.

A typical girder with its mounting pedestals is shown in Figure 4.3.4. The nominal length is 2.9 to 3.2 m for the dipole girders and 3.6 to 5.0 m for the multipole girders. The girders are approximately 0.8 m wide and 0.5 m high. They are fabricated by welding commercially available plates and channels of thicknesses ranging from 1 to 2 inches. After welding, the girders are stress-relieved by commercial vibratory stress-relief equipment.

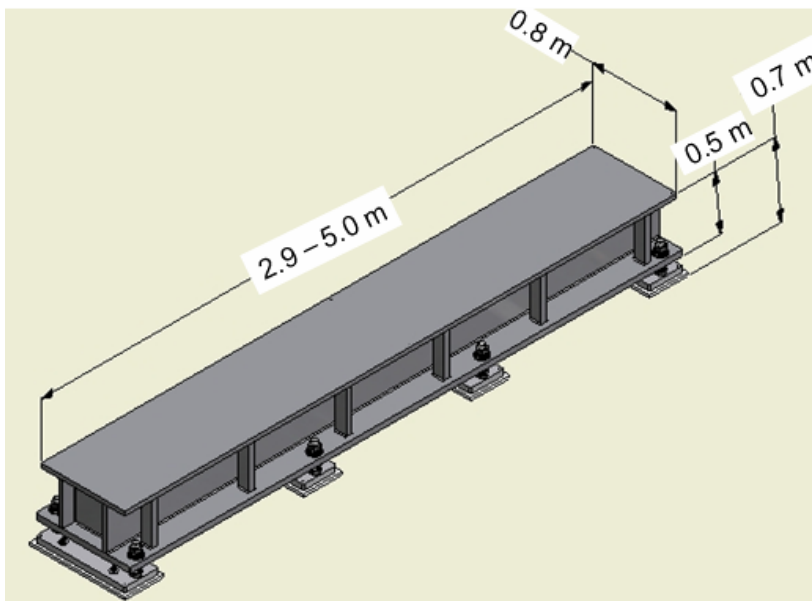


**Figure 4.3.4** Preliminary design of the NSLS-II storage ring girder.

The girders are mounted on four 2-inch-thick pedestals that are grouted to the floor with nonshrinking epoxy grout. For mounting and height adjustment, eight 2 inch-diameter bolts with spherical washers are used. The girder is thus over-constrained in order to minimize static deflection and to raise the first natural frequency of the magnet–girder assembly. A similar over-constrained scheme has been used successfully at SPring-8 [4.3.2] and will be implemented at the ALBA light source [4.3.3].

#### 4.3.3.3 Magnet–Girder Assembly and Alignment

NSLS-II lattice magnets have magnetic alignment tolerances that exceed mechanical assembly tolerances and the ability of conventional alignment techniques to locate the magnetic components within the required

tolerances. Therefore, a vibrating wire alignment technique, originally developed at Cornell University [4.3.4] and subsequently adopted at SLAC, will be used. It has been shown that this technique is capable of aligning magnets to within  $10\ \mu\text{m}$  with respect to an axis defined by the wire.

In this alignment technique, an oscillator drives a sinusoidal current in a thin wire ( $\sim 150\ \mu\text{m}$  diameter) stretched through the apertures of all the magnets on a girder while a particular magnet being measured is powered (see Figure 4.3.5).

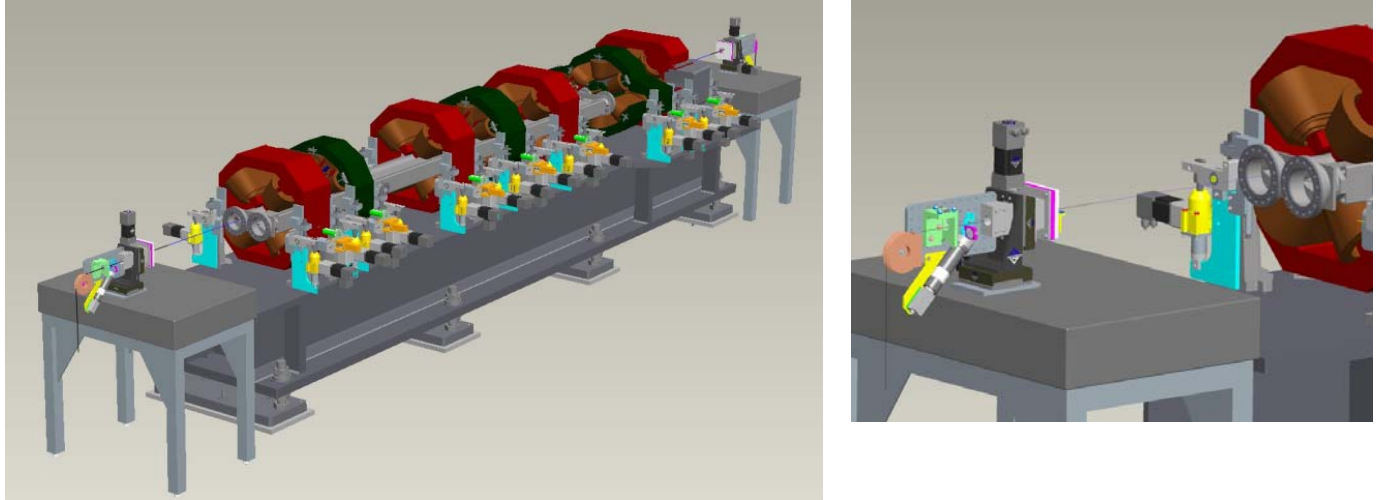


**Figure 4.3.5** Left: Vibrating wire alignment system mounted on the girder. Right: Special brackets with wire movers, wire locators, and laser tracker fiducials are attached to either end of the girder.

The presence of any transverse magnetic field at the wire position exerts a sinusoidal force on the wire, causing it to vibrate. The vibrations in the wire in the transverse plane are detected by a pair of sensors (one for each axis). By carefully selecting the drive current frequency to match one of the resonant frequencies of the wire, even very small fields may produce easily detectable wire motion. For measuring average center over the length of the magnet, the resonant mode chosen is the one having an anti-node roughly at the center of the magnet being measured. The transverse field profile in the aperture of the magnet can be measured by recording the amplitude of wire motion as a function of the transverse position of the wire. In the case of a quadrupole, a linear dependence of field with horizontal and vertical position is seen, from which the magnetic axis (defined as the point where the field is zero) can be determined in the coordinate system defined by the wire translation stages. In the case of the sextupole magnets, the field profile is parabolic and the magnetic center is defined as the point where the field gradients (or equivalently, the quadrupole terms) are zero. The magnets are then moved such that the magnetic centers lie on the line joining the two end points of the wire, and are locked into place. Due to the long length ( $\sim 6$  to  $7$  m) of the wire, there is a significant sag ( $\sim 600\ \mu\text{m}$ ) which must be precisely measured and corrected for while adjusting the magnet positions. It has been shown that the sag can be computed to sufficient accuracy from the measured fundamental resonant frequency. In the case of the quadrupoles, it may be necessary to carry out the measurements at two or more different excitation currents to eliminate any errors caused by background fields, such as the earth's field or remnant fields in the yokes of other un-powered magnets on the girder. Laser trackers are then used to transfer the positions of the wire ends (defining the axis to which all magnets are aligned) to the fiducials on the girder.

The following magnet assembly and alignment plan has been developed Upon receipt individual dipole, multipole, and corrector magnets will be subjected to an incoming test and inspection regimen. Inspections will include dimensional checks, electrical tests and magnetic measurements. Magnetic measurements shall

be performed or certified by BNL's magnet division for every lattice magnet. Magnets will then be stored until needed for girder assembly. Initially, the magnets will be installed and aligned on the girder with a laser tracker. The top-half of the multipole magnets will then be taken off and the vacuum chamber will be installed. The ends of the chamber will be sealed with Mylar caps. The caps will have small holes in either end to allow the ends of the vibrating wire to protrude through while a positive purge of dry nitrogen gas is maintained. After the top half of the magnets are reassembled, their iron cores will be supported on precisely computer-controlled positioners as shown in Figure 4.3.5. The roll angles of the magnet cores will be brought to within  $\pm 0.2$  mrad tolerance by using magnet positioners and digital inclinometers. The girder is then installed in the vibrating wire test stand built in a clean temperature-controlled laboratory and all magnets are aligned to a common straight line as described above. The magnets are then tightly fastened to their supports legs.

To determine the feasibility of maintaining the magnet alignment during this fastening process, a bolting test fixture was fabricated using a Swiss Light Source magnet of the size and weight comparable to that of the NSLS-II magnets. Using electronic indicators, ten trials of positioning and then bolting the magnet were performed to replicate the procedure that will be required with the magnet mover system. Location data and time per trial were recorded. The tests proved that it is relatively quick (<10 minutes per magnet) and easy (standard fine thread hardware, no special tools nor experienced labor) to obtain a stable positioning of the magnet vertically to within 5 microns, and laterally to within 10 microns of the desired theoretically "perfect" position. Thus real magnetic alignment of the multipoles to within 20 microns on a rigid girder appears feasible.

#### 4.3.3.4 Installation of Magnet–Girder Assemblies

A transporter system with self-contained air pads will be used to transport the girder–magnet assemblies from the alignment laboratory into the storage ring tunnel for final installation.

During the early phases of girder installation, the multipole girders will be installed prior to the dipole magnets. The wire support brackets will be left attached for the entire installation process. The air pad system will cushion any shocks to the girder during transport to prevent shifting of the magnets from their aligned positions. The girder transporter will locate the girder over the eight pedestals studs that will affix the girder to the tunnel floor.

Instrumented torque wrenches will be used in conjunction with laser trackers to precisely offload the girder from the air pads onto the pedestals' studs. Once the girder is fixed to the floor and prior to dipole installation, in-situ vibrating wire measurements will be repeated to confirm alignment of the magnets. These measurements will be discontinued when it is established that the magnet alignment was not disturbed during transportation and alignment.

#### 4.3.3.5 Mechanical Stability of the Magnet–Girder Support System

Sources affecting the mechanical stability of the support system include ground settlement, ambient floor motion, flow-induced vibrations, and thermal transients. These sources can be categorized in terms of the frequency range—*fast* when greater than a few Hz or *slow* when operating at frequencies lower than one Hz. Sources are also categorized based on the time-scale of the excitation, as being short (<1 hour), medium-term (<1 week), or long-term (>1 week). Short-term sources include natural and cultural ground vibrations, flow-induced vibrations, and power supply jitters. Thermal transients due to temperature changes of the cooling water or the tunnel air, as well as gravitational and tide effects, constitute medium-term sources. Floor settlement or seasonal temperature changes, which may have direct impact on the alignment of components, are considered to be long-term effects. Cultural noise or human activity is typically observed in the frequency range of 1 to 100 Hz. Ground motion from ocean waves or tides is centered at about 0.2 Hz.

#### 4.3.3.5.1 Medium- and Long-Term Stability

Over the years, various studies have been performed at the BNL site and in the vicinity of NSLS-II to characterize the subsurface conditions. Drill-core data show that the soil at the site consists mainly of medium coarse sand with traces of silt and, in some cases, traces of clay and gravel. The shear wave velocity in the top sand layer is about 270 m/sec. The bedrock lies at a depth of approximately 430 m beneath the site. Therefore, the BNL site is classified as a very deep site with relatively soft soil. The soil consisting of glacial sands is well settled and, based on the drill-core results, exhibits limited scatter in key properties (coefficient of variation  $\sim 0.18$ ). This is important, in that the differential movement (or settlement) in the soil supporting NSLS-II is expected to be of the order of  $10 \mu\text{m} / 10 \text{ m} / \text{year}$ . To ensure that this is the case, a detailed study of ground settlement based on finite element analysis will be performed, taking into account both the site soil conditions and the facility layout.

#### 4.3.3.5.2 Short-Term Stability

##### Short-Term Stability – Ambient Ground Motion

Ambient ground motion measurements near the NSLS-II site were taken from August 31 through September 1, 2006. Data measured at the following locations at BNL were used for a comparison of the NSLS-II site with the ALS, ESRF, and SPring-8 sites:

1. Microscopy suite of the Center for Functional Nanomaterials (CFN)
2. Foundation of a light stand near CFN, not stiffened by the presence of the building
3. A remote location near the northeast corner of BNL
4. Experimental hall of NSLS directly beneath the X1 beamline

The RMS (4–50 Hz) amplitudes of the ground motions in vertical, north–south, and east–west directions are given in Table 4.3.3. The most important value is that of the microscopy laboratory at CFN, where the RMS amplitudes are 20 nm or lower in all directions. The lower values, compared to those at the free-field at CFN and at the remote northeast BNL location, are indicative of the stiffening effect of the CFN building and the floor. The ambient ground motion at the floor of NSLS X1 beamline is considerably higher at 18 and 30 Hz, due most likely to rotating mechanical equipment.

**Table 4.3.3 RMS (4-50 Hz) Ground Motion near the NSLS-II Site.**

Location	Time	Vertical (nm)	North–South (nm)	East–West (nm)
Microscopy lab at CFN	7:30 pm	20	12	19
Free-Field at CFN	11:40 pm	24	41	38
Remote location near the northeast corner of BNL	Noon	21	25	26
Beamline X1 at NSLS	Midnight	71	12	13

Figure 4.3.6 shows the vertical log mean of site vibrations at the NSLS-II site expressed as PSD, compared with similar data from ALS, ESRF, and SPring-8. Shown also are PSD spectra measured at NSLS beamline X1 just after midnight, the “free-field” location near CFN, and the microscopy suite at CFN identified by the black arrow. The legend indicates the RMS amplitude using summation between 4 and 50 Hz, except for the NSLS-II log mean, which is summed with a 6 Hz lower cutoff because of contamination by the instrumentation noise floor at lower frequencies. The RMS amplitudes for ALS, ESRF, and SPring-8 were calculated in the 2 to 100 Hz band.

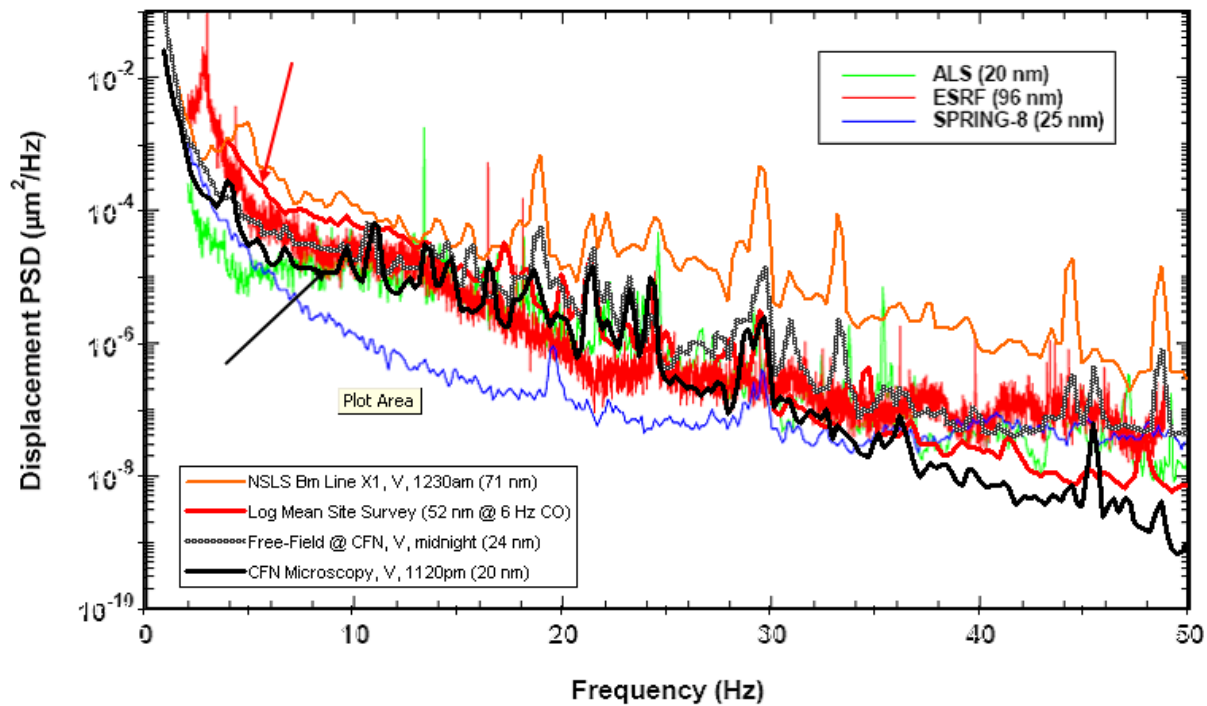


**Figure 4.3.6:** Comparison of PSDs of vertical ground motions at various locations near the NSLS-II site and at ALS, ESRF, and SPRING-8 light sources [4.3.5].

The vibration measurements indicate the presence of local noise sources at ~18 and 30 Hz in the NSLS building. Further vibration measurements are planned to identify and eliminate these local sources of vibration. In addition, the CFN measurements show that the installation of the NSLS-II storage ring and experimental hall will significantly stiffen the site. The floor vibration levels of the NSLS-II storage ring are then expected to be comparable to those of the other light source facilities.

#### 4.3.3.6 Resonant Frequencies of the Girder Support System

Although the NSLS-II magnet–girder assembly fastened to the pedestals is a complex dynamical system, its important design features can be understood by a simple 1-D oscillator shown in Figure 4.3.7a.

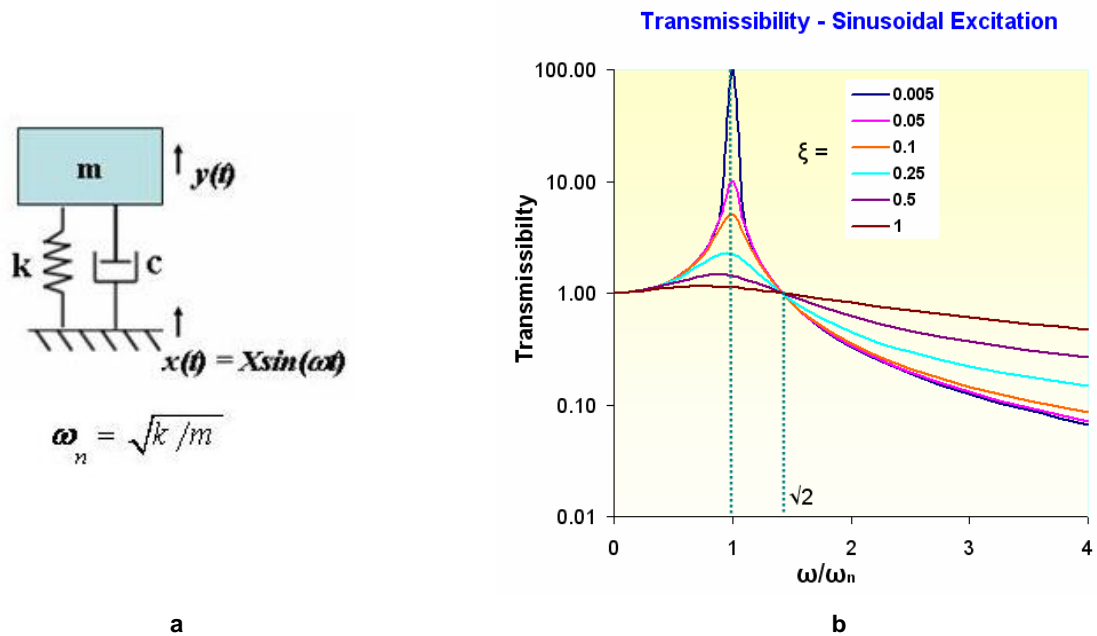


Figure 4.3.7 a) 1-D oscillator; b) transmissibility plot.

For such an oscillator, the natural frequency is

$$\omega_n = \sqrt{k/m} \quad (4.3-3)$$

and the vibration amplification (or transmissibility) is given by

$$\text{Transmissibility} = Y/X = \sqrt{\frac{4\xi^2(\omega/\omega_n)^2 + 1}{[1 - (\omega/\omega_n)^2]^2 + 4\xi^2(\omega/\omega_n)^2}} \quad (4.3-4)$$

where the fraction of critical damping,  $\xi$ , is given by

$$\xi = \frac{c}{2\sqrt{mk}} \quad (4.3-5)$$

Transmissibility curves, obtained from Eq. 4.3-4 for different values of critical damping,  $\xi$ , are plotted in Figure 4.3.7b. There is no significant vibration amplification (transmissibility  $\approx 1$ ) when the natural frequency,  $\omega_n$ , is substantially greater than the excitation frequency,  $\omega$ . The ambient ground motion reduces sharply as  $1/\omega^4$ , as shown in Figure 4.3.6, and its amplification above 30 Hz can be ignored. Several investigations have been carried out on the dynamic response of the magnet-girder support systems using vibration measurements and finite element modal analyses. These studies have shown that it is quite difficult to raise the lowest natural frequency of the support system to greater than 20 Hz if elaborate alignment mechanisms are used either between the girder and its pedestals or between the girder and the magnets. When such alignment mechanisms are used, then the internal structural damping ( $\xi = 0.02$  to  $0.04$ ) of the support

system is insufficient to reduce the floor motion amplification to an acceptable level. External damping devices, either active or passive, are then used, such as viscoelastic damping pads at APS and ESRF.

For the NSLS-II magnet–girder support system, a lowest natural frequency of greater than 50 Hz will be obtained by eliminating elaborate alignment mechanisms, and by lowering the beam height to 1 m. Short, stiff threaded rods will be used for height adjustment only. The alignment of the girders will be achieved by precise but removable alignment mechanisms. Finite element model analysis of the NSLS-II magnet–girder assembly shows that the lowest two natural frequencies are 58.8 Hz and 74.4 Hz. The corresponding mode shapes, rolling and twisting of the girder, are depicted in Figure 4.3.8.

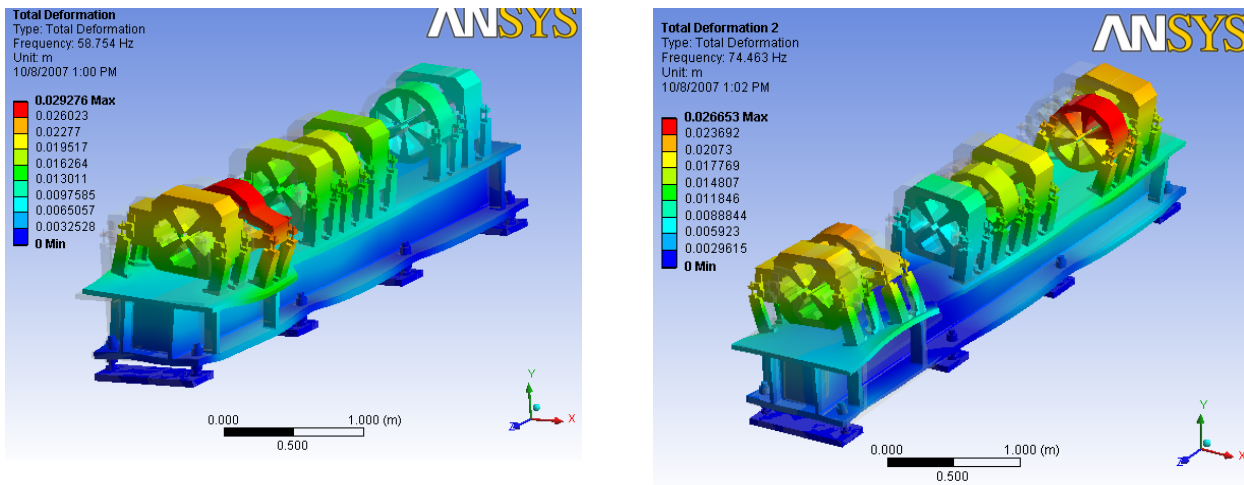


**Figure 4.3.8** Mode shapes of the NSLS-II magnet–girder assembly. **Left:** First mode shape, rolling,  $\omega_1 = 58.8$  Hz. **Right:** Second mode shape, twisting,  $\omega_2 = 74.4$  Hz.

#### 4.3.3.7 Flow-Induced Vibrations

Flow-induced vibrations of the water headers can be transmitted to the magnets and the vacuum chambers [4.3.6] by flexible hoses and pipes. The effects of flow-induced vibrations will be mitigated by paying close attention to several useful design guidelines, namely:

1. Locate all rotating equipments including fans, blowers, compressors, and pumps outside the storage ring tunnel, preferable tens of meters away from the tunnel floor and ceiling.
2. Keep low flow velocities (less than 2 m/s) in the process water headers.
3. Design header supports to minimize their vibration, such as by integrating viscoelastic dampers in the headers hangers, or by attaching headers directly to the ceiling.
4. Arrange water flow circuits and connection fittings such that sharp bends are eliminated. Special attention is to be given to the routing and clamping of the hoses and tubes that connect the magnets and vacuum chambers to their respective headers.

Analytical models and vibration measurements will be employed to ensure that flow velocities required to regulate the temperature of the vacuum chambers do not induce unacceptable level of vibrations.

#### 4.3.3.8 Thermal Stability

Ambient temperature variations will result in displacements of both the magnets on the girders and the BPMs on the vacuum chambers [4.3.7]. To ensure acceptable thermal deformations of the ring components, process water and tunnel air temperatures will be maintained to within  $\pm 0.05^\circ\text{C}$  and  $\pm 0.1^\circ\text{C}$ , respectively, of



their nominal values, 25.0 °C. Air-conditioning temperature cycling of ~1-hour duration will be maintained in order to take advantage of the thermal inertia of the support system. The girders will be thermally insulated to further reduce the effects of temperature transients.

Lowering the beam height from 1.4 m to 1 m would reduce the vertical thermal expansions of the assembly proportionately. In addition, over-constraining each girder to its pedestal at eight locations would minimize thermal bending effects.

To investigate the effect of temperature transients, FE thermal analyses were performed for the girder, magnets and vacuum chamber assembly. For the analyses, the fluctuations in the temperature of the tunnel air and the cooling water flowing through vacuum chamber were approximated by linear increase and decrease over 15 minutes corresponding to 1-hour temperature cycle. For modeling heat transfer by air convection, a film coefficient value of 8 W/m<sup>2</sup> °C and 1 W/m<sup>2</sup> °C was applied on all external surfaces and internal girder's surface, respectively. The lower film coefficient value was applied on the internal girder's surface to include the effect of stagnant air condition.

For modeling heat transfer by process water a film coefficient value of 15,000 W/m<sup>2</sup> °C was applied. For girder insulation a glass-wool material with a thermal conductivity of 0.03 W/m °C was considered in the analysis.

Figure 4.3.9 shows the temperature distribution in girder, magnets and vacuum chamber assembly. The maximum temperature change in the girder and magnets is limited to ~ 0.01°C due to the effects of thermal mass and girder insulation. For the vacuum chamber, however, the temperature change is ~ 0.05°C, the same as the change in the water temperature.

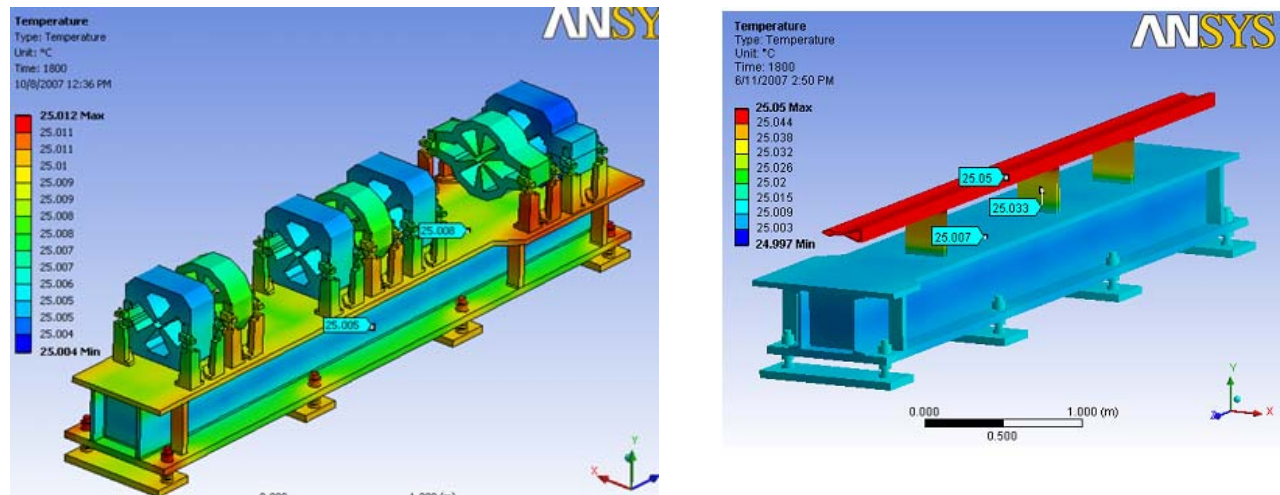


**Figure.4.3.9** Temperature distribution in the girder, magnets and vacuum chamber assembly.

Vertical deformations for the girder, magnets and vacuum chamber assembly corresponding to the calculated temperature distribution are shown in Figure 4.3.10. The FEA results indicate that the RMS vertical misalignment between the magnets is 0.013 μm, which is less than the design tolerance of 0.025 μm. For the vacuum chamber, at the BPM locations next to the Invar support stands, the maximum vertical displacements are about 0.14 μm as compared to the mechanical stability budget of 0.2 μm for the chamber-mounted BPMs.



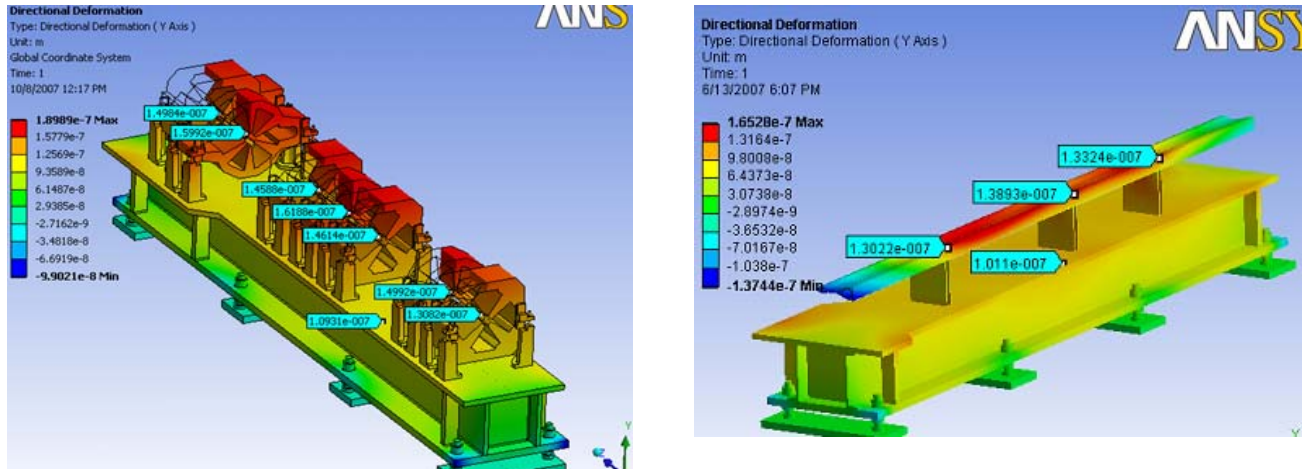


Figure 4.3.10 Vertical thermal deformations of the girder, magnets and vacuum chamber assembly.

#### 4.3.3.9 Stability of the User BPM Support System

Compared to the chamber-mounted BPMs, the BPMs at the two ends of the insertions devices (user BPMs) as well as X-BPMs in the front ends have even more stringent mechanical stability requirements. The vertical and horizontal RMS displacements of the latter BPMs are specified to be less than  $0.1 \mu\text{m}$  and  $1 \mu\text{m}$ , respectively. We are considering BPM support stands made from carbon fiber composite on which the BPM blocks are supported at their mid-planes (see Figure 4.3.11). A carbon fiber composite can have thermal coefficient of expansion as low as  $0.2 \mu\text{m}/\text{m}/^\circ\text{C}$ . With the tunnel air temperature fluctuations controlled to within  $\pm 0.1 \text{ }^\circ\text{C}$ , the vertical displacement of 1 m high support stand can be maintained to about  $\pm 0.02 \mu\text{m}$ . The carbon fiber composites are, however, weak in the transverse (thickness) direction which can result in a system with very low natural frequency. Typical Young's moduli along the principal and transverse directions are 120 GPa and 7.5 GPa, respectively. From our preliminary discussions with vendors, we have been assured that the vendors can supply us with a 10-inch diameter carbon fiber composite that will meet the thermal design specification ( $< 0.1 \mu\text{m}$ ) and the natural frequency requirement ( $> 50 \text{ Hz}$ ).

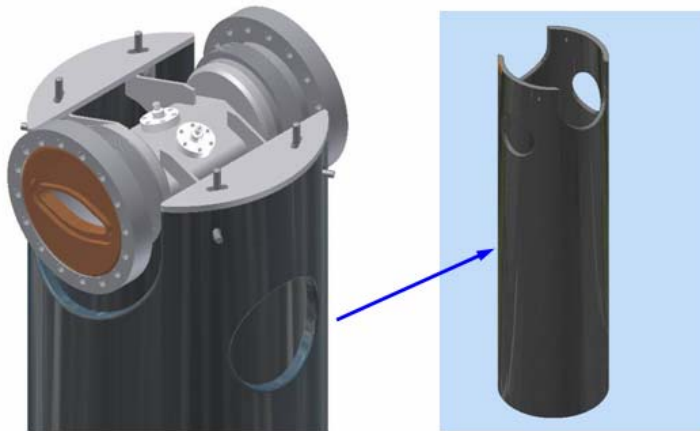
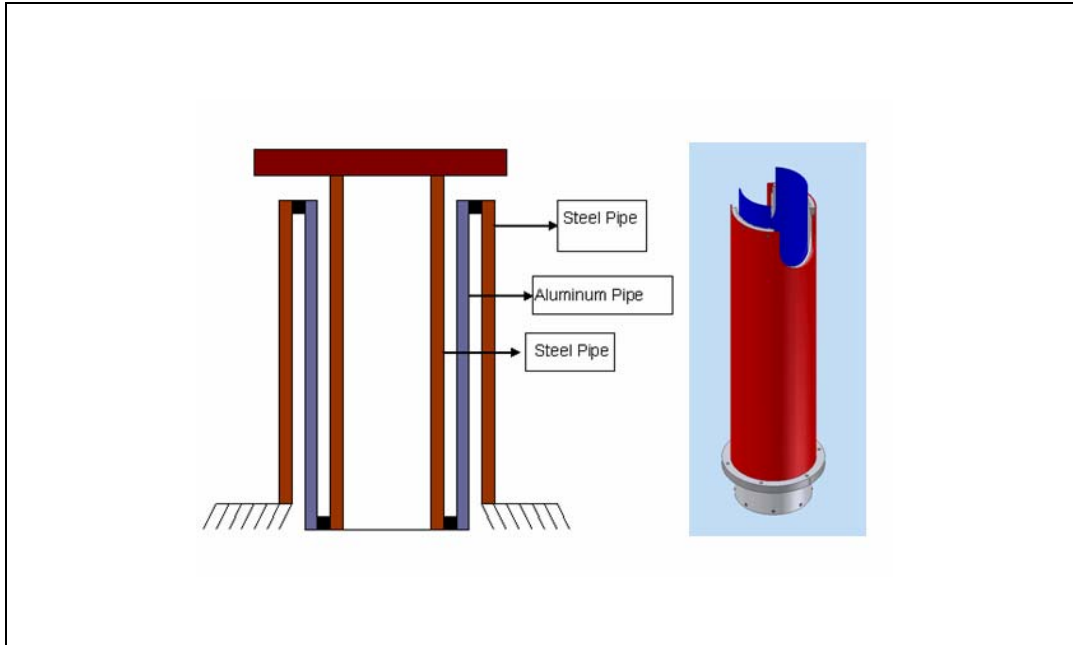
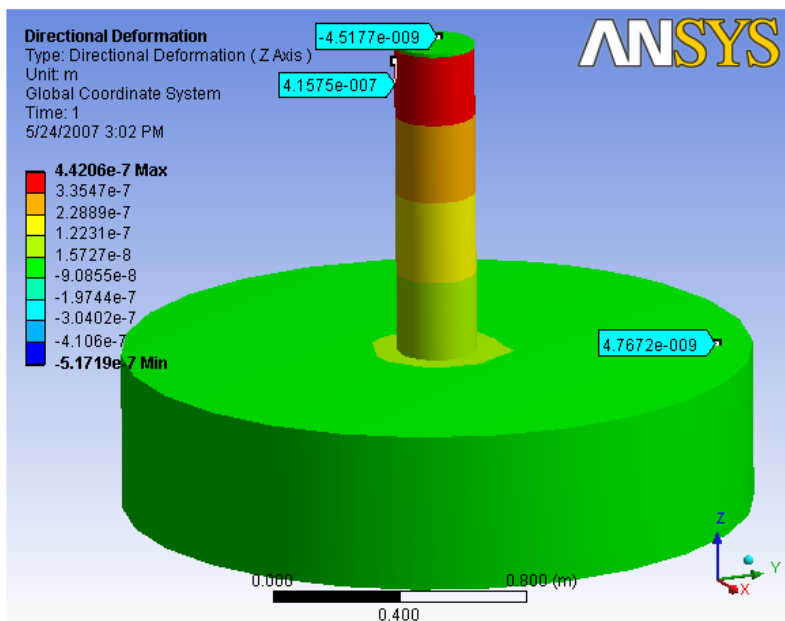


Figure 4.3.11 User BPM support stand with a BPM block mounted at its mid-plane.

A second design option for the user BPM support stands consists of a system of aluminum pipe sandwiched between two structural steel pipes. A schematic of this design is shown in Figure 4.3.12. In this design, the aluminum pipe counteracts the expansion of the steel pipes, and by carefully adjusting the lengths and diameter of each member it is possible to get zero thermal expansion at the BPM support point as indicated by the FEA thermal results (vertical displacement = 0.005  $\mu\text{m}$ ) shown in Figure 4.3.13.



**Figure 4.3.12** User BPM support stand consisting of aluminum and steel pipes



**Figure 7.3.13** Maximum thermal deflection at the user BPM support point = -0.0045 microns.

Vibration FEA analysis results for this design are shown in Figure 4.3.14. The lowest natural frequency for the system is 45 Hz which corresponds to vibration (swaying) in the horizontal direction. The RMS horizontal displacement (2-50 Hz,  $1\sigma$ ) is calculated to be  $0.026\ \mu\text{m}$  as compared to the specification of  $1\ \mu\text{m}$ .

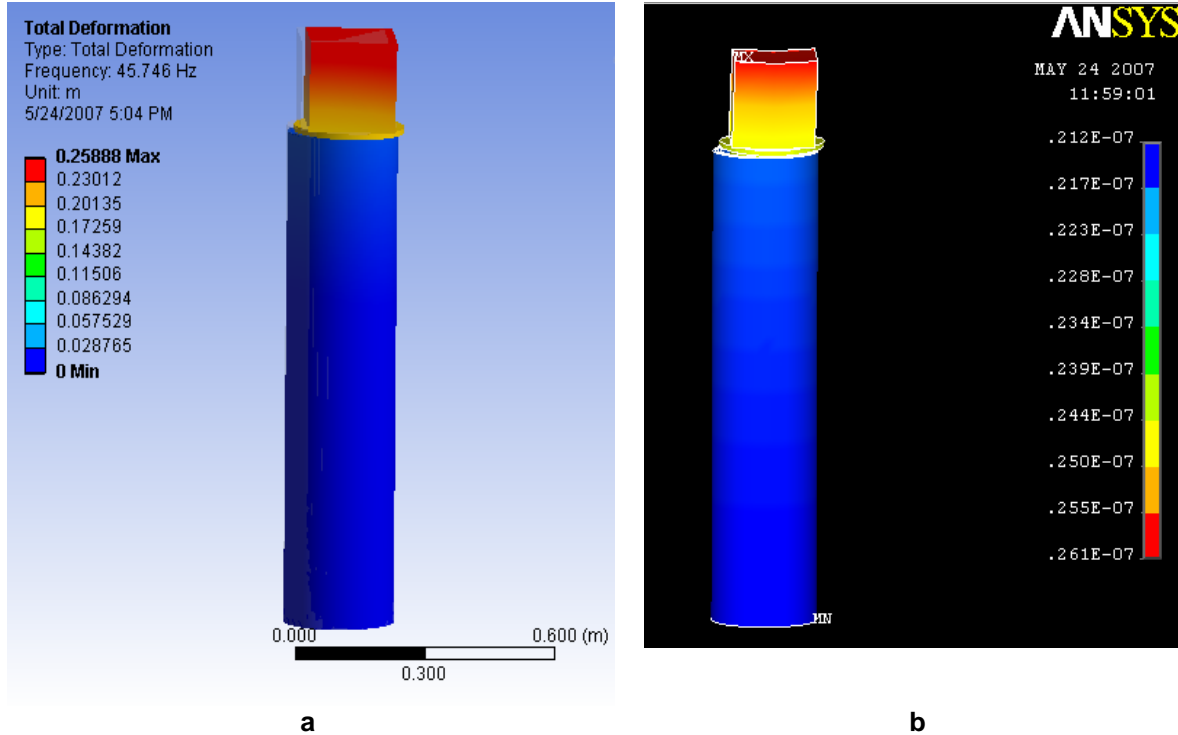


Figure 7.3.14 **a:** Modal analysis of user BPM support stand -natural frequency = 46 Hz,  
**b:** Random vibration analysis of user BPM support stand-RMS displacement = 26 nm

#### 4.3.3.10 R&D Program on Stability of the Magnet–Girder Support System

To further improve the mechanical stability performance of the girder support system, the following R&D tasks will be undertaken:

- real-time online measurements and analysis of the NSLS-II ambient ground motion.
- optimization of the stiffness of the magnet–girder assembly (A prototype assembly will be built for this purpose.)
- use of viscoelastic damping devices
- characterization and mitigation of the flow-induced vibrations of the magnets and the vacuum chambers
- investigation of the effect of process water and tunnel air temperatures on the field quality of the storage ring magnets
- assessment of insulating materials to reduce the effects of thermal transients in the tunnel

## References

- [4.3.1] BETA USERS' GUIDE by L. Farvacque, T.F. Gunzel, J.L. LaClare, A. Ropert.
- [4.3.2] K. Tsumaki and N. Kumagai, "Vibration Measurement of the SPring-8 Storage Ring," IEEE, PAC, 2001.
- [4.3.3] L. Nikitina and Y. Nikitin, private communication on ALBA girders, August 13, 2006.
- [4.3.4] A. Temnykh, "The Magnetic Center Finding using Vibrating Wire Technique," CBN 99-22, Cornell University, May 26, 1999.
- [4.3.5] S. Sharma, C. Doose, G. Portmann, L. Zhang, K. Tsumaki, and D. Wang, "Ground Vibration Problems at the Light Sources," 22<sup>nd</sup> Advanced ICFA Beam Dynamics, SLAC, Nov. 6-9, 2000, SLAC-WP-18, pp. 37-48.
- [4.3.6] Nakazato, et al., "Observation of beam Orbit Fluctuation with Forced-Vibrating Magnets and Vacuum Chambers," MEDSI2002, Chicago, IL 2002.
- [4.3.7] L. Emery, "Measurements of Thermal Effects on the Advanced Photon Source Storage Ring Vacuum Chamber," MEDSI2002, Chicago, IL, 2002.



## 4.4 Beam Chambers and Vacuum Systems

### 4.4.1 Scope

The storage ring vacuum system provides adequate and low impedance aperture for the circulating electron beam, and low pressure for long beam lifetime and low bremsstrahlung radiation. The storage ring vacuum system includes all vacuum chambers, vacuum pumps, vacuum valves, bake-out systems, and vacuum instrumentation and control. The storage ring vacuum system extends throughout the storage ring from the booster injection line-storage ring interface to the photon exit gate valve at the front end transitions to the user beamline.

During the start-up and beam commissioning of the storage ring, no insertion devices will be installed or positioned at the designated straight sections. Therefore, straight beam pipes with same cross section as the cell multipole chambers will be installed at these straight sections. Some appendage vacuum components such as rf-shielded gate valves, bellows, pumps, vacuum gauges and residual gas analyzers, will be installed at the designated straight sections together with the insertion devices after the initial beam commissioning.

Many components such as photon absorbers, beam scrappers, insertion devices, etc. require or share storage ring vacuum, but only the components whose main purpose is to maintain, monitor, and control storage ring vacuum are included in detail here. The other components are described in their respective sections.

The average pressure with beam is designed to be less than  $1 \times 10^{-9}$  Torr with main residue gas being hydrogen. At this pressure level, the beam lifetime due to bremsstrahlung and Coulomb scattering is longer than 40 hours. The stored beam lifetime for 500 mA operation will be limited to 2–3 hours by the Touschek lifetime due to the scattering loss of electrons in the bunch. However, localized pressure bumps will produce bremsstrahlung radiation and damage the beam line components, and have to be suppressed.

To achieve the low thermal outgassing and low photon-stimulated desorption (PSD), all the vacuum vessels and appendage vacuum components will be made from ultra high vacuum compatible materials. All the vacuum components will be carefully prepared, cleaned, and conditioned using UHV compatible processes. In-situ bake will be implemented to further lower the thermal outgassing and PSD.

### 4.4.2 Mechanical Design

#### 4.4.2.1 Design Overview

There are 30 cells in the storage ring. Each vacuum cell consists of five basic chambers; an upstream matching multipole chamber, a dipole chamber, an arc section multipole chamber, a second dipole chamber, and a downstream matching multipole chamber. There are RF-shielded bellows connecting the chambers together. There is a straight section, either 6.6 m or 9.3 m long between the cells, for insertion devices and for special components such as RF cavities, injection devices, damping wigglers, and so forth. A typical vacuum cell layout is shown schematically in Figure 4.4.1. The dipole chambers are approximately three meters long and the straight chambers for the multipole magnets 3 to 5 m long. All-metal, RF-shielded gate valves will be employed to isolate each of the 30 cells and the straight sections between cells.

Most of the storage ring cell chambers will be made of extruded aluminum with a cross-section similar to that of the APS chambers [4.4.1]. Regular or bi-metal Conflat flanges with copper gaskets will be used throughout the vacuum systems, except for the flanges and seals for beam position monitor buttons, where Helicoflex delta seals will be employed. Water-cooled copper or Glidcop absorbers will be positioned in the

storage ring vacuum chambers to absorb the unused photons and heat loads, and to protect the un-cooled flanges and bellows. The entire vacuum cells will be in-situ bakeable to 130°C to remove adsorbents, such as water, and contaminants on the inner surface. Vacuum bake for the aluminum chambers will be at 120°C using pressurized hot water circulated within the cooling water channels. Alternative bakeout and conditioning approaches, such as super dry hot nitrogen flush and non-evaporable getter (NEG) strip heating, will be explored for their benefit and applicability. External heating jackets will be used for the bakeout of the appendage vacuum components.

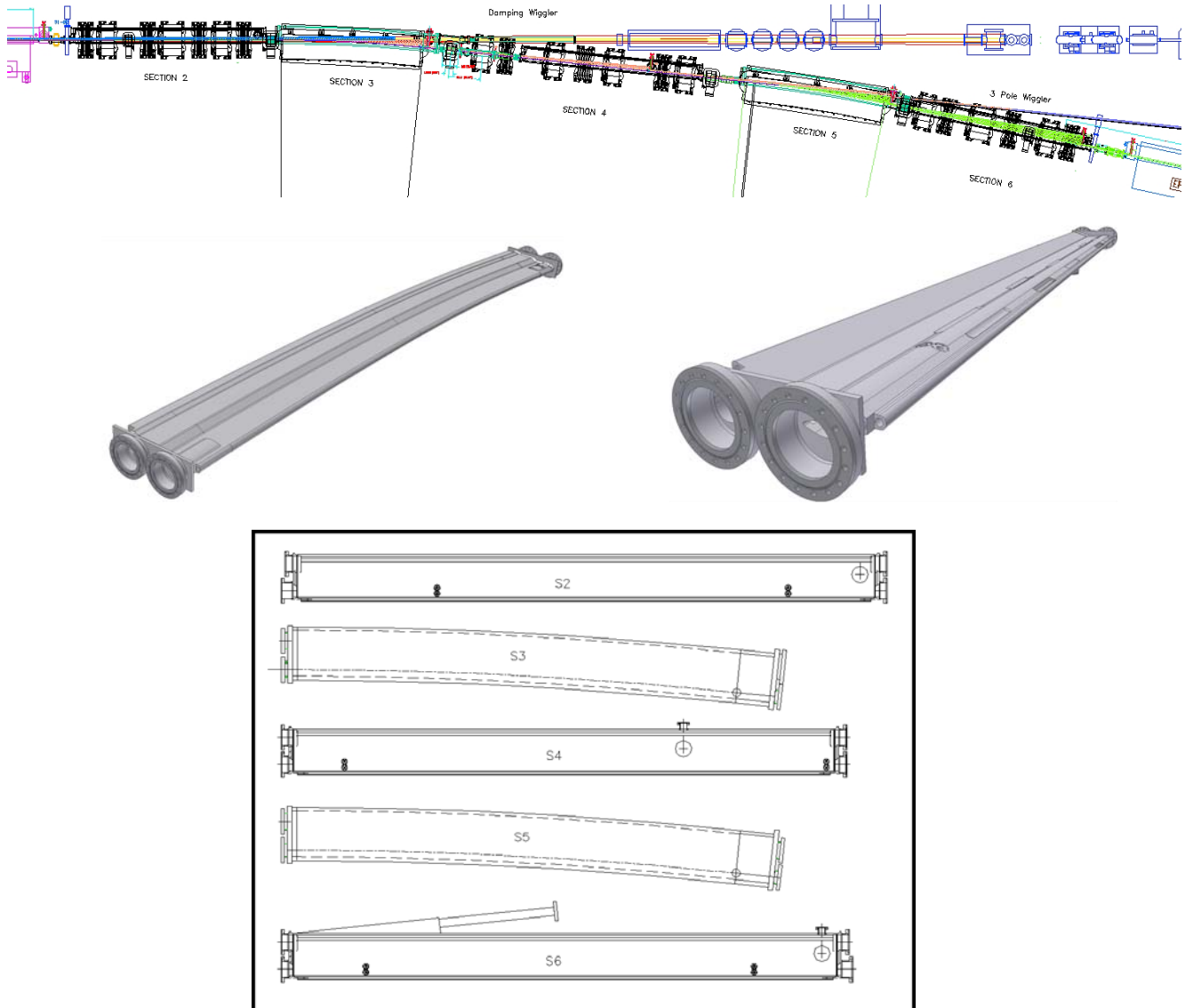


**Figure 4.4.1** The layout of the five cell vacuum chambers in a typical storage ring cell with two photon exit ports; the 3D models of dipole chambers, and the arc multipole chamber; and the top view of the five chambers in each cell.

To achieve fast conditioning after intervention, sufficient pumping capacity is needed. Following rough pumping and in-situ bakeout, the vacuum cell chambers will be pumped by sputter ion pumps, non-evaporable getters (NEGs), and titanium sublimation pumps (TSP) as their main UHV pumping. The vacuum chamber design must provide provisions for stability during bakeout and with sufficient precision for accurately locating the vacuum chambers and BPM buttons after bakeout. Three chamber supports made of Invar will be employed for each cell chamber, one fixed support in the middle and two flexible supports at the

ends. The impedance of the vacuum chamber should be low enough so as not to excite higher-order mode resonances. Smooth cross-sectional transitions between components are required, as are flexible interfaces such as RF-shielded bellows between cell chambers and insertion devices.

#### 4.4.2.2 Vacuum Chamber Design

The electron beam vacuum chambers differ according to their location within the storage ring. The vacuum chambers will provide adequate ports for heat absorbers, BPM buttons, pumps and exit ports to the front ends. A pronounced antechamber design similar to that of APS [4.4.1] will be used to allow adequate aperture for the exiting photon beams and to better distribute vacuum pumping capability. The cell vacuum chambers, as shown in Figures 4.4.2 and 4.4.3, contain two distinct but connected channels; the beam channel portion must be continuous, but the antechamber portion may be interrupted at various locations for vacuum valves, bellows, absorbers, insertion device chambers, and other devices where the mechanical requirements constrain the use of the antechamber. Ports emanating from the aluminum cell chambers will have aluminum-stainless bi-metal Conflat flanges which joint to the standard mating Conflat flanges using regular copper gaskets. The internal beam channel cross-section will be elliptical, 25 mm vertical by 76 mm horizontal, to allow sufficient beam-to-chamber clearance, except at absorbers. The absorbers will be inserted horizontally from the antechamber side wall and positioned 22 mm to 27 mm from the beam channel center to intercept a portion of the photon fans from the bending magnets. The antechamber is also sized for distributed NEG pumping and to fit within the multipole magnets.

The photon exit slot connecting the beam channel and antechamber is sized as large as possible to provide adequate aperture for photon fans and sufficient vacuum pumping conductance. However, the vertical height of this slot is restrained by magnet pole gaps and by the minimum required wall thickness under atmospheric pressure load when the chamber is under vacuum. The chamber cross sections inside the dipole, quadrupole and sextupole magnets are shown in Figure 4.4.2. There will be 2 mm clearance between chambers and magnet poles and coils at the closest points, except at corners of sextupole poles, to count in the chamber fabrication tolerances, to allow the alignment of BPM buttons and the adjustment of the chambers and supports. The extruded chamber cross sections and the cross sections after machining are given in Figure 4.4.3. The multipole chamber inside the sextupole magnets will be machined down to a minimum wall thickness of 3.1mm to accommodate the 68 mm sextupole pole gaps. The 3D finite element analysis of the stress and deflection due to atmospheric pressure load of the multipole chambers at the sextupole location are shown in Figure 4.4.4. The maximum stresses is 64 MPa, and the maximum deflections are less than 0.6 mm. The yield strength of the extruded aluminum A6063 T5 is 145 MPa, therefore providing a safety factor of > 2. The analysis for dipole chamber gives a maximum stress of 42 MPa, a safety factor of > 3, and maximum deflection of 0.55 mm.

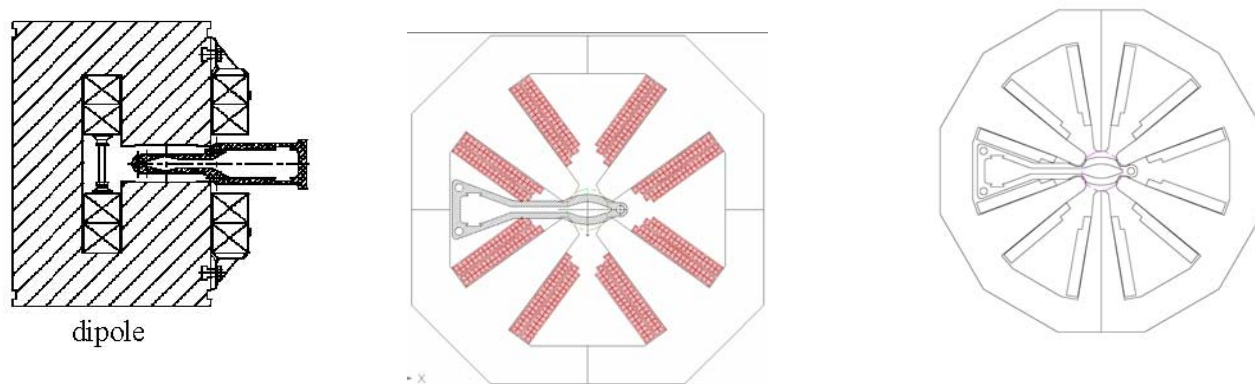


**Figure 4.4.2** Storage ring vacuum chambers and magnet cross-sections at dipole, quadrupole, and sextupole interfaces. The beam channel will have an aperture of 25 mm (V)×76 mm (H). The clearance between chamber outer surface and the magnet poles will be 2 mm or more.



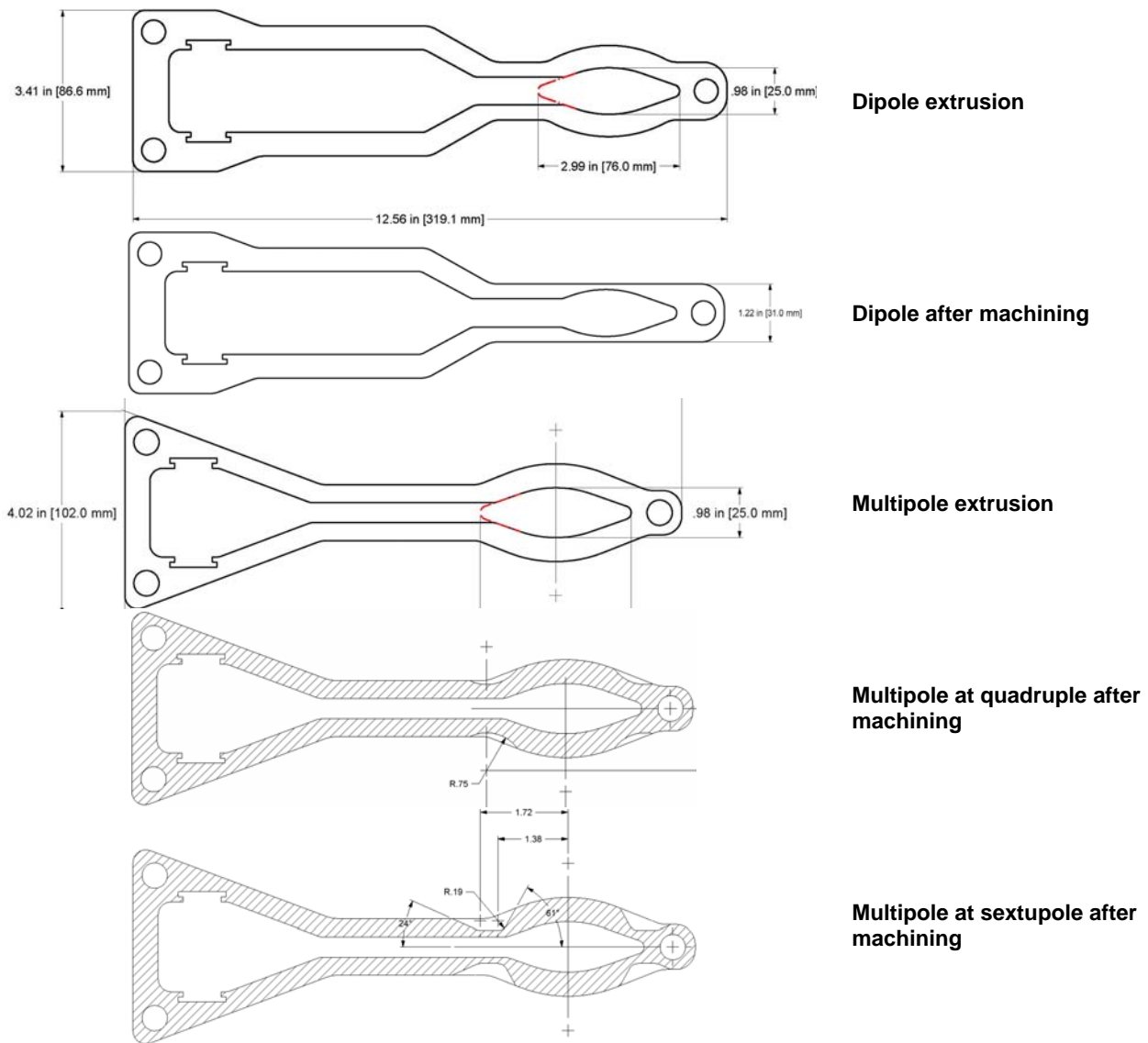
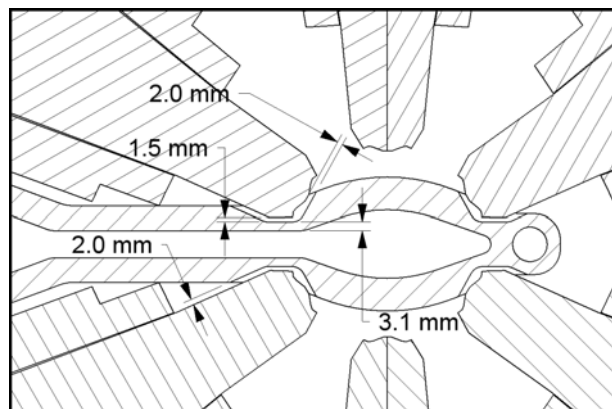


**Figure 4.4.3** Storage ring vacuum chamber cross sections after extrusions and after machining, at dipole, quadrupole, and sextupole interfaces. The minimum wall thickness at the sextupole location is ~3.1 mm, and 3 mm inside the dipole magnet.



**Multipole chamber cross section inside sextupole**

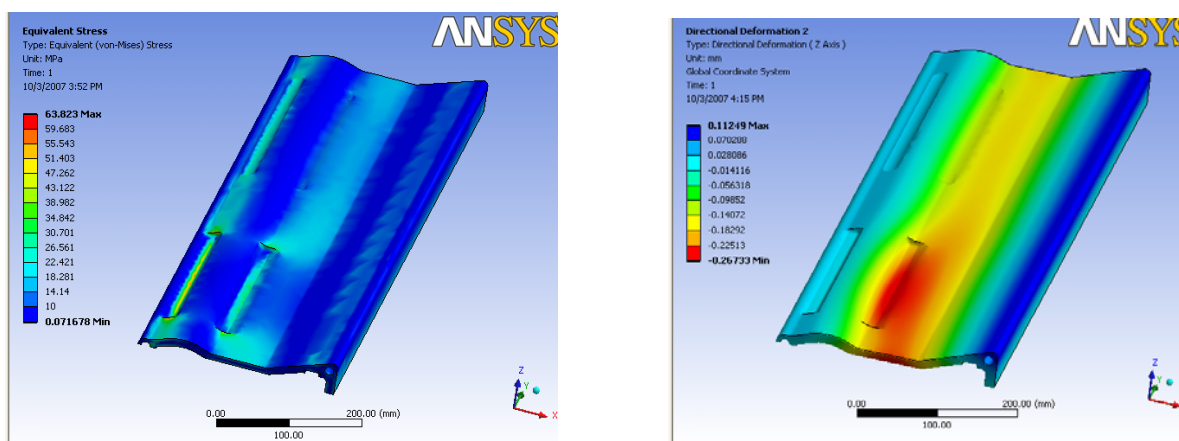


**Figure 4.4.4** Top: the cross sectional view of the multipole chamber at sextupole magnet pole location: **Bottom**: 3-D finite element analysis of the deflection and stress of the multipole chamber at the sextupole pole tip locations, where the minimum wall thickness is 3.1 mm. **Bottom left**: The maximum deflection due to atmosphere pressure load is found to be 0.28 mm $\times$ 2; and **Bottom right**: the maximum von Mises stress at this single point is 64 MPa, within the maximum allowable stress of 145 MPa for extruded aluminum A6063 T5.

As shown in Figure 4.4.1, there are five extruded cell chambers in each cell, named S2-S6 chambers (the straight section chambers are named as S1 chambers). The cross sections and the exact length of the cell chambers, and the locations of various absorbers within, must be developed to provide adequate apertures for both the electron beam and the photon fan, while protecting un-cooled components such as flanges and bellows. Detailed ray tracing analysis was carried out for both bending magnet radiation fans of  $\pm 52$  mrad, and for damping wiggler radiation fans of  $\sim \pm 3$  mrad. The radiation fan from other insertion devices has divergence of  $\ll \pm 1$  mrad and will clear through the cell chambers and the connecting bellows into the front ends. Ray tracing also provides the distribution of the power and power density and the number of photons intercepted by various absorbers, allowing detailed thermal analysis of the absorbers, and pressure profile distribution in the electron beam chamber.

A portion of ray tracing at downstream end of the first bending magnet is shown in Figure 4.4.5, where  $\sim 40\%$  of bending magnet fan is intercepted by the crotch absorber. Approximately 20% of the bending fan will enter the front end, together with the DW fan, through the opening in the crotch absorber. The remaining 40% of the bending fan travels downstream through the connecting bellows to S4 multipole chambers, where it is trimmed further by the two flange absorbers. The percentage of the bending fan intercepted by each absorber depends on the distance from the tip of the absorber to the beam center line, which provides

adequate protection to the downstream beam pipes, flanges, and bellows. The typical distance used for ray tracing is 25 mm; however, some are at 23 mm, 27 mm, or further, depending on the shielding requirement and dynamic aperture requirement. A list of bending radiation absorbers in a typical superperiod is given in Table 4.4.1, together with their distance from the center of the long straight, the position from the beam center, and the power and photons intercepted. The power and density are used for thermal analysis of the absorbers, while photon flux on the absorbers is used to derive pumping requirements and the pressure profile in the electron beam channel.

The DW fan passing through the crotch absorber must be clipped immediately before traveling down the front end, due to its divergence and distance (over 10 m) from the DW. This is accomplished using a DW absorber with side walls at inclined angles  $\sim 5^\circ$  to limit the maximum power density, and thus the temperature of the absorbers to below 300C. Depending on the canting angles of the DW, 15 – 30% radiation power (or 10 – 20 kW) will be absorbed here. The DW fan will be further clipped by fixed masks in the front end prior to entering the beamline.

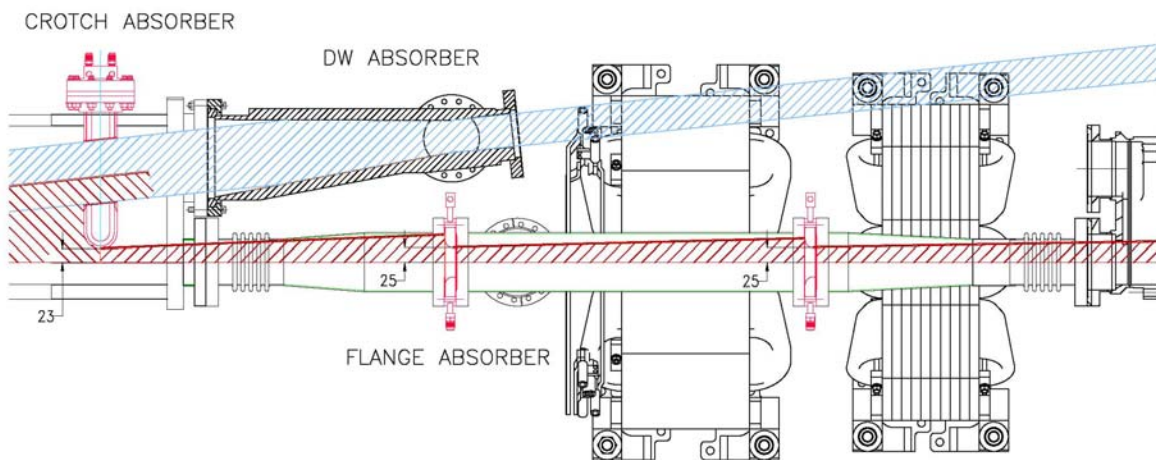


**Figure 4.4.5** Chamber and absorber layout at the downstream end of the S-3 chamber (the first bending chamber), showing both the bending magnet radiation fan and the damping wiggler fan. The crotch absorber has an opening for passing the damping wiggler fan into the front end while intercepting some bending radiation.

**Table 4.4.1** List of absorbers in each superperiod with their distance from the center of the long straight section, position from the beam center, angle of the bending magnet fan intercepted, total power, and the number of photons intercepted.

Section #	Absorber Type	S (m)	X (mm)	BM Fan on Absorber (degree)	Power 3 GeV (watt)	# hv 3 GeV
S6	Stick		25			
S1-LS	Stick	0.00	22	0.210	84	7.1E+17
DW	Stick		37			
S3	Crotch	11.04	23	2.459	983	8.3E+18
S4	Flange	11.55	25	0.851	340	2.9E+18
	Flange	12.20	25	0.549	220	1.9E+18
	Stick	15.78	27	0.659	264	2.2E+18
S5	Crotch	20.28	25	3.611	1444	1.2E+19
S6	Stick	23.64	25	1.969	788	6.7E+18
S1-SS	Stick	24.61	22	0.086	34	2.9E+17
EPU	Stick	29.13	32	0.115	46	3.9E+17
S2	Stick	32.95	25	0.092	37	3.1E+17
S3	Crotch	36.14	23	3.366	1346	1.1E+19
S4	Flange	36.66	25	0.851	340	2.9E+18
	Flange	37.31	25	0.549	220	1.9E+18
S4	Stick	40.89	27	0.659	264	2.2E+18
S5	Crotch	45.38	25	3.611	1444	1.2E+19
S6	Stick	49.03	25	1.998	799	6.8E+18

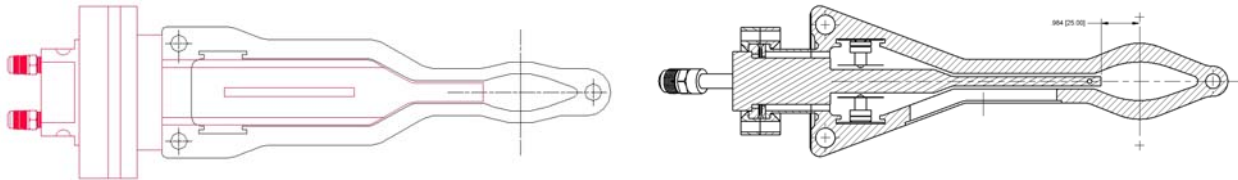


**Figure 4.4.6** Conceptual design of the crotch absorbers and the stick absorbers as inserted from the side ports through the antechamber and photon exit slot. Most absorbers are positioned at 25 mm from the center of the electron beam channel, with a few positioned from 22 mm to 37 mm away.

**Table 4.4.2 Types and numbers of cell vacuum chambers, absorbers, and RF-shielded bellows in the NSLS-II storage ring.**

Description - Type	Length (m)	Quantity
Cell chamber – Bending – S3, S5	3	60
Cell chamber – Straight – S2	4	30
Cell chamber – Straight – S4	3.5	30
Cell chamber – Straight – S6	3.5	30
Cell – RF shielded Bellows	0.2	150
Cell - Absorber		225
ID - Absorber		45
ID chamber – EPU	~4	5
ID chamber – Damping wiggler chambers	~4	16*
ID – SRF cavity	~7	2
ID – Injection kickers + septum	~7	1
ID chamber – Empty 6.6 m straight	~5	10
ID chamber – Empty 9.3 m straight	~7	8*
ID – RF-Bellows	-0.2	-60

\* Two 4 m beampipes will be used at each 9 m long straight.

#### 4.4.2.3 Pumping at the Photon Absorbers

There are approximately eighteen photon absorbers, as listed in Table 4.4.1, in each superperiod to intercept and absorb unused photons from the two bending magnets. The absorbers are located as far from the source of the photons as practical, to reduce the power density, and thus the peak temperature on the absorber surface. Sputter ion pumps with titanium sublimation pumps (TSP) will be located at the absorbers to remove as much desorbed gas as possible, thus minimizing the amount of gas diffused back to the beam channel. The maximum gas load from bending magnet photons intercepted by each crotch absorber is estimated to be  $\sim 2 \times 10^{-6}$  Torr-l/s, as described in Section 4.4.3.2, and can be handled with the combination of a sputter ion pump and titanium sublimation pump. The absorber for the DW radiation fan will intercept more than 10 kW of photons, resulting in a gas load of  $> 3 \times 10^{-5}$  Torr-l/s. This high gas load at the DW absorber may be pumped by the combination of a sputter ion pump and a NEG cartridge pump, which has higher capacity than a titanium sublimation pump. Typical absorbers as inserted into the cell chambers from the side ports through the antechamber and the photon exit slot are shown in Figure 4.4.6. The crotch absorbers will be located at end of the dipole chambers where no NEG strips are present. Some stick absorbers are located in the middle of cell chambers or straight section chambers, and have to pass through the NEG strips mounted in the antechamber. Insulating coatings will be applied to the outer surface of the stick absorbers to provide electrical isolation during NEG strip conditioning and activation.

#### 4.4.2.4 Injection Kicker Chambers

Kicker magnets require special ceramic vacuum chambers. The four ceramic chambers will be located in the injection straight section, upstream and downstream of the injection septum magnet to correct the electron beam path as needed during injection to the storage ring. These chambers will be specially designed so that they are able to 1) withstand the stresses of fast magnet actuation, 2) resist fatigue, and 3) maintain vacuum integrity. The internal surface of the ceramic chambers will be coated with a conductive film to reduce impedance for the beam image current and prevent charge buildup [4.4.2]. The film must be thin to minimize the eddy current induced by the fast-pulsing kicker field, so as not to disturb the injected beam.

#### 4.4.2.5 Photon Exit Ports

There are two photon exit ports at each vacuum cell to extract photon beams to the user beamlines: one at straight chamber S4 for the photon beam originating from the upstream insertion device; and the second at the upstream end of straight chamber S6 for photons from the three-pole wiggler or bending magnet #2. The downstream end of these exit ports will have bending magnet photon shutters to intercept the photons before the front ends and beamlines are installed, or when the beamlines are not in use. Pneumatic gate valves will be located downstream of the photon shutters to allow vacuum isolation of the storage ring and front ends for maintenance and troubleshooting. The exit port chambers will be made of stainless steel. Sputter ion pumps with TSP will be placed at the photon shutters to remove the desorbed gas molecules. A bremsstrahlung radiation stop will be installed downstream of the gate valve prior to front end installation, to protect the equipment and personnel at the experimental floor.

#### 4.4.2.6 RF-Shielded Bellows, Flanges, and Ports

To reduce the broadband impedance of the vacuum chamber wall and to minimize the localized HOM heating, the inner cross-section of the electron-beam chamber should be maintained as smooth as possible. High transverse impedance may cause beam instability, which might put an upper limit on the stored current. The changes in cross-sections of the beam chamber should vary smoothly, with an angle of inclination less than  $1/9$  for tapered transitions. The height of the steps should be less than 1 mm, in general, and less than 0.5 mm at small-aperture ducts for insertion devices. For vacuum components with cavity-like or discontinuous structure, such as flange joints and bellows, RF contact fingers will be installed to reduce the impedance and provide a smooth path for the beam image current. The opening of the thin slits of these fingers should allow enough pumping of residual gases that have been outgassed from the surface behind the slits. Calculations will be made to optimize the design of the thin slits while minimizing the impedance of the chambers. Slots or screens, if deemed necessary, will be implemented at the ion pump ports to reduce impedance and still provide adequate pumping conductance. Only commercially available RF-shielded gate valves will be used along the storage ring beam channel.

Two types of RF-shielded bellows will be studied for their finger contact force, flexibility, cost, and vacuum and RF properties: the single-finger type with hydro-formed bellows used at APS [4.4.3], and the double-finger type with welded bellows used at B-factories and a few synchrotron radiation facilities in Asia. They are shown in Figure 4.4.7. The welded bellows will allow more compression and lateral movement than the hydro-formed ones. The double-finger design may not be as reliable as the single-finger type, but does offer lower contact resistance. The magnetic permeability of both welded and formed bellows must be measured and the eddy current effect calculated, since fast corrector magnets will be mounted over the stainless steel bellows. The welded bellows will cost more than the formed ones.

Explosion-bonded bi-metal transition Conflat flanges, made from 316L stainless steel and A6061-T6 aluminum plates, will be used for the aluminum chambers throughout the storage ring. These Conflat type flanges with aluminum weld neck will be tungsten-inert-gas welded to the cell chambers using a robotic welding machine. They have the standard stainless steel knife-edge sealing face for the copper gaskets and are commercially available. They will form reliable, leak-tight joints with other bi-metal flanges and standard stainless steel flanges of adjacent chambers, bellows and other appendage vacuum components, such as vacuum pumps and gate valves. The bi-metal joints can be in-situ baked up to 250°C.

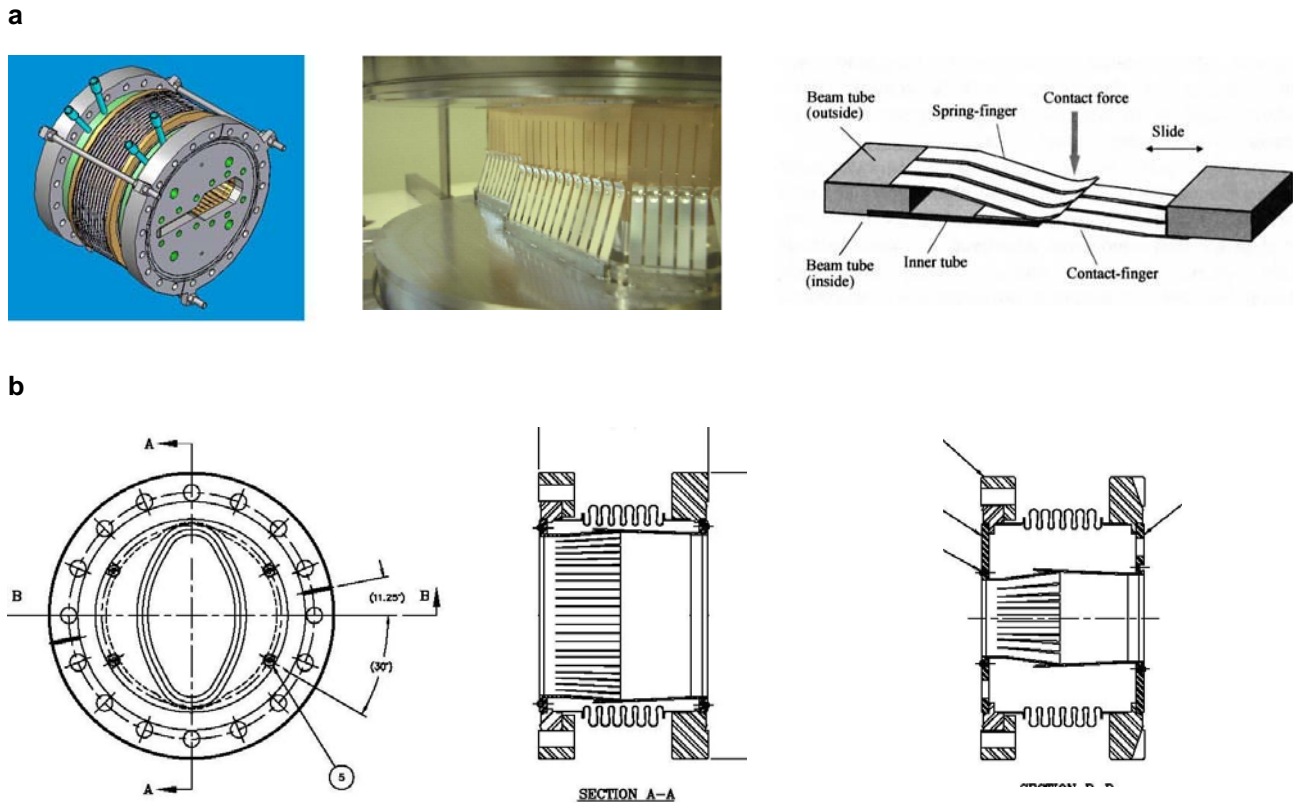


**Figure 4.4.7.** Two types of RF-shielded bellows: (a, upper row) the ones with welded bellows used in B-factories and BEPC-II with single or double fingers; and (b, lower row) the APS type with single fingers and hydro formed bellows.

### 4.4.3 Pressure Requirements and Distribution

As mentioned earlier, an average beam channel pressure of less than  $1 \times 10^{-9}$  Torr is needed. This pressure will provide ample beam-gas lifetime with minimal radiation and beam loss effects. Beam losses generate radiation according to electron current, energy, and vacuum pressure. At pressures greater than  $10^{-8}$  Torr, both the stored beam lifetime and the life of many vacuum pumps will be reduced. Titanium sublimation and NEG pumps have lifetimes that are directly related to the operating pressure; therefore, maintaining this vacuum level in the storage ring improves vacuum component life, stored beam life, and minimizes the amount of radiation produced from bremsstrahlung scattering.

The beam gas scattering loss in the NSLS-II storage ring will depend largely upon the interaction of the beam with heavier residual gas molecules such as CO, CO<sub>2</sub>, and Ar due to bremsstrahlung and Coulomb scattering. The gas density inside the vacuum chamber is determined by the installed pumping and by the surface condition of the vacuum chambers and the absorbers, which is bombarded by photons generated by the circulating electron beams. During initial ring commissioning, there are severe limitations on the achievable beam current and stored beam lifetime, caused by large pressure increases due to high photon-stimulated desorption (PSD) yield. Experience gained during early commissioning of the NSLS x-ray ring showed that residual gas spectra obtained with no stored electrons were typical of a well-baked UHV system. Hydrogen constituted approximately 95% of the residual gas at that time, and the average vacuum was in the  $10^{-10}$  Torr range. The composition of the desorbed gases during initial operation of the x-ray ring was ~ 43% H<sub>2</sub>, ~ 25% CO, and ~ 16% each of CO<sub>2</sub> and CH<sub>4</sub>. After three months of additional beam conditioning, the



PSD rate dropped by a factor of five, and the CO, CO<sub>2</sub>, and CH<sub>4</sub> peaks represented much smaller percentages of the total desorbed gas. The PSD yield versus beam conditioning dosage for copper and aluminum chambers [4.4.4, 4.4.5], as measured at NSLS, is shown in Figure 4.4.8. Typical desorption yields after 100 A.hr beam conditioning are used in the pressure simulation. The beam lifetime did not show a corresponding increase with the reduced desorption rate, mostly due to Touschek effect.

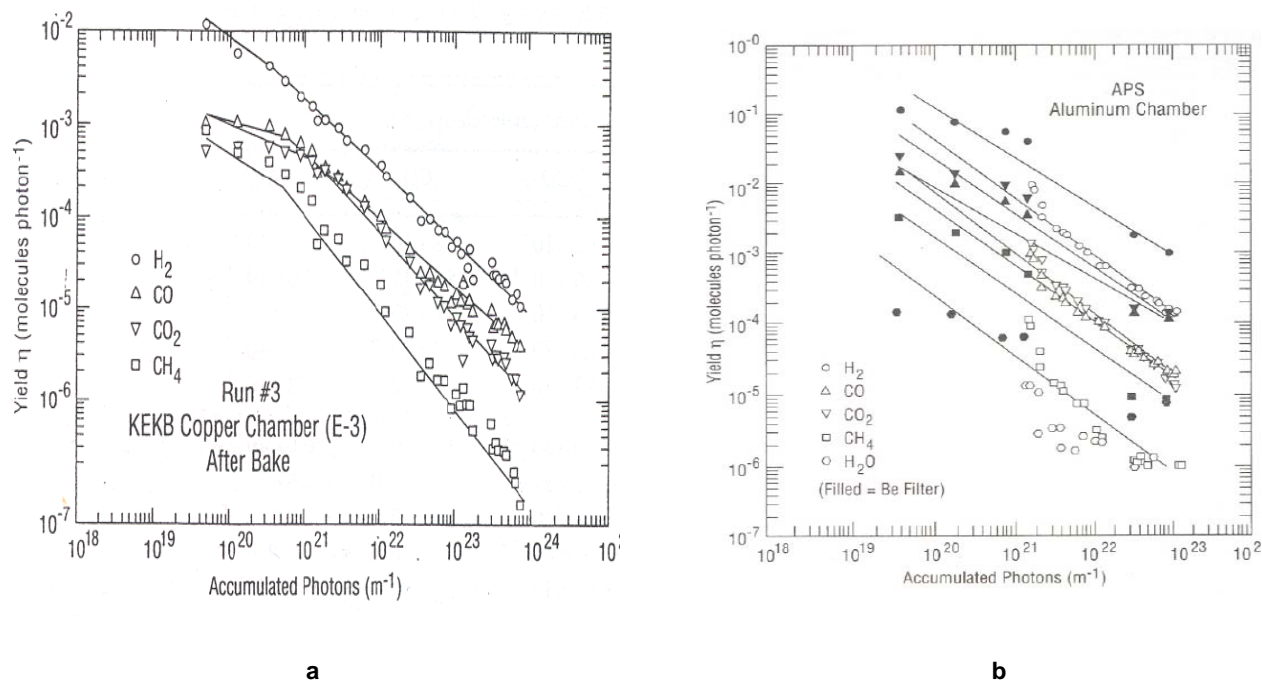


**Figure 4.4.8** Comparisons of PSD yields with photon dosages for copper and aluminum. **a)** PSD yields for a 1 m pure copper sample beam chamber at KEKB. **b)** PSD yields for a 1 m extruded aluminum sample beam chamber at APS.

Most of the NSLS-II storage ring vacuum chambers will be fabricated from extruded aluminum and may be exposed to low levels of bending magnet photon radiation due to scattered photons. Almost all unused photons will be intercepted by water-cooled copper and GlidCop absorbers. After proper conditioning with photons, the PSD yields for copper, stainless steel, and aluminum will be at the same levels.

The 25×76 mm electron beam channel is vacuum pumped using distributed NEG strips in the ante chamber connected by a narrow pumping slot. Two NEG strips are installed in the extruded ante chamber and have a combined pumping speed of 240 l/s/m. The NEG pumps only chemically active gases. Sputter ion pumps (SIP) are employed to pump the inert gases not pumped by the NEGs. The SIPs are located under the photon absorbers where the majority of PSD occurs. The SIPs provide ~ 200 l/s pumping speed and are part of a combination SIP/TSP. The TSP provides an additional 500 l/s of pumping for active gases.

Linear conductance of the electron beam channel is ~ 8 l/s/m. The photon exit slot in the chamber extrusion between the ante chamber and the beam channel in dipole chamber is 15 mm high which limits the NEG pumping speed to about 135 l/s/m, in the beam channel. The slot in the multipole extrusion is 10 mm high, which yields a conductance of approximately 45 l/s/m in the beam channel.

#### 4.4.3.1 Static Vacuum: Thermal Outgassing

The static pressure distribution in the storage ring will be determined by the amount of thermal outgassing from the internal surfaces in the vacuum chambers. These outgassing rates will depend on the construction



materials used and their preparation. After precision cleaning, the chambers will be vacuum-baked and may be glow-discharge conditioned to reduce outgassing and remove contaminants prior to their final assembly into the storage ring magnets and girders. All the chambers and vacuum components in the vacuum cell will be in-situ baked, to reduce the thermal outgassing as well as the PSD yields. Most of the internal vacuum surfaces along the storage rings are aluminum. The contribution of other materials to the thermal outgassing load is much smaller than that of aluminum wall. Vacuum-baked aluminum outgassing of  $1 \times 10^{-12}$  Torr-l/s/cm<sup>2</sup> is used for thermal gas load modeling. The thermal gas load is estimated to be  $1 \times 10^{-8}$  Torr-l/s/m.

#### 4.4.3.2 Dynamic Vacuum: Photon Stimulated Desorption

During operations with stored electrons, specially designed water-cooled Glidcop absorbers will intercept most unused synchrotron radiation. The PSD rate  $\eta$  for vacuum-baked copper and Glidcop has been studied at NSLS [4.4.4] and at other laboratories. An  $\eta$  value of  $1 \times 10^{-5}$  molecules per photon is used for the modeling calculations [4.4.6]. The total photon flux from the storage ring dipole magnets is calculated using  $N_p$  (ph/s) =  $8 \times 10^{+20}$  [E(GeV)] [I(Amperes)]. For 3 GeV and 500 mA, the total photon flux is  $1.2 \times 10^{+21}$  ph/s. Using these values and converting to gas load yields  $3 \times 10^{-4}$  Torr-l/s (or  $\sim 5 \times 10^{-6}$  Torr-l/s per bending magnet). The undulator radiation will have a narrow fan. It will mostly be collimated and intercepted down at the front end and beamline, and will produce little gas load to the storage ring beam channel. In contrast, the damping wiggler radiation will have a relatively wide fan. Approximately 15% of the DW radiation will be intercepted by the crotch absorber located upstream of the S4 multipole chamber, equivalent to  $\sim 1 \times 10^{+20}$  ph/s by each DW. Assuming the same  $\eta$  value of  $1 \times 10^{-5}$  molecules per photon, this corresponds to an additional gas load at photon exit port of  $3 \times 10^{-5}$  Torr-l/s from each DW.

#### 4.4.3.3 Dynamic Pressure Distribution

The pressure rise with beam operation will be determined by the PSD of gases from internal surfaces of the vacuum chamber, and the amount of dynamic pumping. Most synchrotron radiation will be intercepted by water-cooled Glidcop absorbers. The pressure distributed in a super-period of 52 m was calculated using both Molflow [4.4.7] and Vaccum [4.4.8] software. The storage ring pressure distribution in the beam channel with no beam current, with 500 mA stored beam current, and with damping wigglers is plotted in Figure 4.4.9. PSD yield of  $1 \times 10^{-5}$  mol/ph, reached after approximately 100 amp-hours of beam conditioning, is used in the calculation. The design average pressure of less than  $1 \times 10^{-9}$  Torr can be reached with the current pumping scheme of distributed NEG, lumped ion pumps, and TSP. However, the DW absorber, as shown in Figure 4.4.5, does produce a sharp, but localized peak up to 10 nTorr, assuming 15% of the DW radiation be clipped here. The pressure peak will be proportionally higher if more DW fans are to be clipped here. The significant increase in bremsstrahlung radiation at this location could damage the downstream equipment and may require additional shielding. The importance of the distributed pumping by NEG strips is clearly illustrated in Figure 4.4.10. The reduction of the lumped pumping speed at the absorbers from 500 l/s to 100 l/s, due to long manifold or saturation of TSP film, only increase the average pressure by two folds. The average pressure increases by over ten folds when the NEG strip pumping is eliminated, perhaps due to saturation or fails to activate. To further illustrate this point, the NEG strips at short straight are left intact in the simulation, which generate a local pressure of  $\sim 0.1$  nTorr.

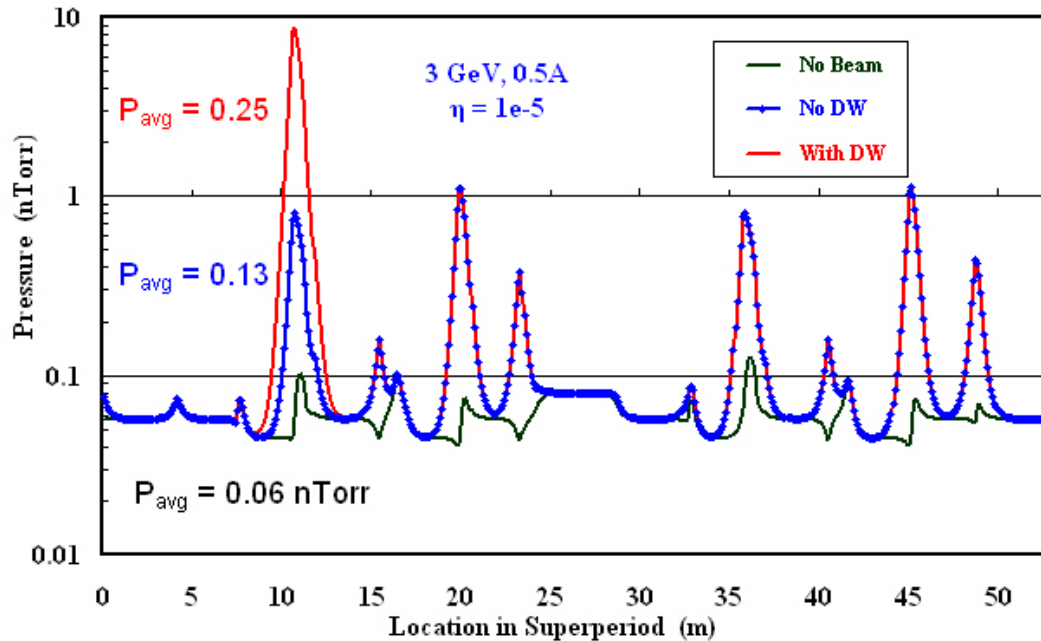


**Figure 4.4.9** Pressure distribution inside the electron beam channel in one superperiod, without beam (black), with 500 mA (blue line and circles), and with damping wigglers (red line). The average pressure is about 0.1 nTorr without damping wiggler, ~ 0.3 nTorr with damping wiggler. However, the localized pressure at wiggler absorber is peaked at 10 nTorr.

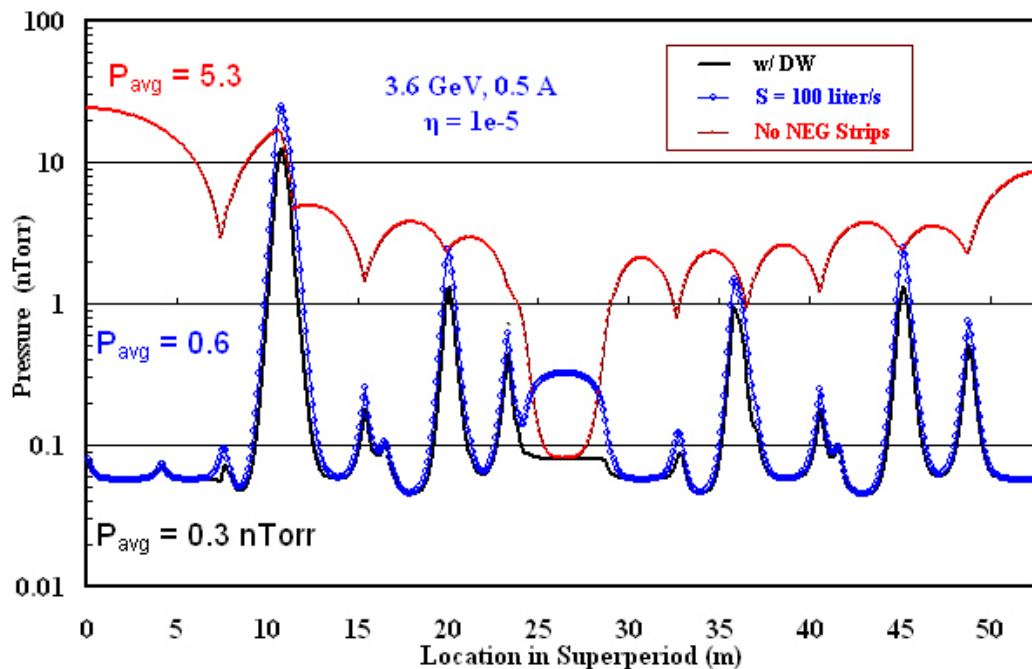


**Figure. 4.4.10** Pressure distribution inside the electron beam channel in one 52 m superperiod with damping wigglers. The blue curve represents the pressure when the lumped pumping speed (IP+TSP) at absorbers is reduced from 200 l/s to 100 l/s. The red curve is when the NEG strips are not activated and the average pressure exceeds 5 nTorr.

#### 4.4.4 Vacuum Chamber Materials, Fabrication, and Treatment

Most of the storage ring vacuum chambers will be constructed from extruded A6063-T5 aluminum. This alloy was selected based on a comparison of various properties for commonly used vacuum chamber materials for electron storage rings, as described below.

##### 4.4.4.1 Selection of Chamber Materials

There are three common UHV materials suitable for the vacuum chambers of the electron storage ring: stainless steel, aluminum alloys, and OFHC copper, with stainless being preferred for a few new SR facilities in Europe, and aluminum for the new ones in Asia and the U.S. Copper was chosen for storage rings with high energy and high power density, such as the B-factories at SLAC and KEK, and also for its high thermal conductivity and radiation shielding properties. However, copper has the disadvantages of high material and fabrication costs. For the 3 GeV NSLS-II, radiation shielding and thermal conductivity requirements are not as critical as in the higher energy machines. Moreover, most synchrotron radiation from bending magnets will be removed by discrete copper or Glidcop absorbers. Therefore, copper has not been considered a preferred chamber material. The choice between stainless and aluminum for the NSLS-II cell chambers is based on experience at NSLS and APS, plus aluminum's vacuum and mechanical properties, ease of fabrication, and relatively reasonable cost.

One major difference between NSLS-II and other new SR facilities of comparable energy is the large bending magnet radius. The photon fan from the bending magnet will have a small dispersion and will be easily intercepted by discrete absorbers. This allows a narrow chamber geometry design; therefore, the cell chambers can be fabricated from extruded aluminum with uniform cross-sections. The need to accommodate the distributed NEG pumping also favors extruded aluminum, since an antechamber can easily be produced by aluminum extrusion. The cost of extrusion is considerably lower than that of chambers made of stamped stainless plates or machined aluminum plates, although the cost of machining the external chamber profile to fit the magnet poles and the various access ports will be significant. A few important arguments concerning the choice of material are listed and further discussed below.

**Table 4.4.3 Electron Storage Ring Chamber Materials and Their Critical Properties.**

Specifics	Aluminum	Stainless	Copper
Initial PSD rate	High	Low	Average
Mechanical strength	Acceptable	Excellent	Good
Thermal expansion	Large	Small	Small
Thermal conductivity	Excellent	Poor	Excellent
Weldability	Good	Excellent	Good
Beam impedance	Low	High	Low
Bi-metal flanges	Yes	No	Yes
Cooling channels	Extrusion	Brazed	Brazed
Fabrication cost	Low	Average	Expensive
Ease of in-situ bake	Good	Poor	Good
Radiation shielding	Poor	Average	Excellent

The outgassing of unbaked aluminum is higher than that of stainless, but an in-situ baked aluminum surface has similar or lower outgassing than that of stainless. The initial PSD rate of an aluminum surface is higher than those of copper and stainless. However, aluminum conditions faster and will reach the same PSD rate at a modest integrated beam dosage. The high thermal conductivity of aluminum offers distinct advantages over stainless, both during the in-situ bake and during normal operation. No conductive coatings or strips are needed on aluminum to reduce the chamber wall impedance, whereas stainless chambers may need copper strips and absorbers in certain locations and for mis-steered beam. Therefore, our preferred

material to form the cell chambers through extrusion is aluminum A6063-T5 alloy. Stainless-to-aluminum bi-metal Conflat flanges will be welded to the aluminum chambers, and standard copper seals can be used to form reliable joints between the chambers, bellows, and appendage components.

#### 4.4.4.2 Vacuum Facility

To ensure the necessary chamber surface properties, cleanliness, mechanical quality, and leak tightness, vacuum facilities will be needed for cleaning, welding, assembling, and evaluating the vacuum chambers and other vacuum components for the storage ring and injectors. A dedicated chemical cleaning facility is required to clean the long chambers and other vacuum components. It will consist of four long, stainless steel tanks and a gantry crane capable of handling chambers up to 6 m long and 200 kG in weight. These tanks will provide ultrasonic cleaning with hot water, commercial bio-degradable cleaning agents, and de-ionized water rinse, and are suitable for aluminum, copper, inconel, and stainless chambers and materials. The exact cleaning recipe and process will be based on the chamber material and experience developed at other SR facilities such as NSLS and APS. Programmable robotic welding stations with laminar flow hoods will be set up to weld the cleaned chambers, the sub-assemblies, and the flanges. A Class 1000 clean room with  $\sim 100 \text{ m}^2$  floor space is needed for the assembly of the chambers with distributed NEG strips, ion pumps, gauges, absorbers, BPM buttons, and other components.

A facility with these capabilities was established at Argonne National Laboratory for the construction of the Advanced Photon Source. The NSLS-II project plans to use the ANL/APS facility for the production, chemical cleaning, and automatic welding of the cell chambers of the NSLS-II vacuum system. Should this prove impractical for some reason, equivalent facilities will be established at BNL. Even if the ANL vacuum facility is utilized, a small chemical cleaning facility is still needed at BNL for storage ring and beamline vacuum components. The clean room and vacuum bakeout/evaluation stations are still required at BNL for the final assembly and evaluation of the cell chambers. If we do not utilize the APS facility and need to establish all of the capabilities at BNL, then  $\sim 2,000 \text{ m}^2$  of space would be required. If the ANL facility is used for production, cleaning, and welding, then  $\sim 1,400 \text{ m}^2$  would be required. Building 905 at BNL has been identified as the preferred location for the BNL vacuum facility. This building has more than  $2,500 \text{ m}^2$  of space, as well as overhead cranes, and is available for use by the NSLS-II project.

#### 4.4.4.3 Fabrication, Assembly, and Evaluation

Most of the storage ring chambers will be made of extruded aluminum. Immediately after extrusion, the long chamber sections will be stretched to obtain the uniform cross-section and to meet the dimensional requirement. They will then be cut to the designed length. The bending chambers will be formed to the curvature on a hydraulic press with dies or rollers of correct radius. To preserve the internal cross-sections, the inner volume of the bending chambers will be filled with DI water and frozen prior to the bending/forming operation. The extruded chambers will be machined at industrial vendors to the appropriate external profiles and to add photon exit ports, access ports for BPM buttons, pumps, absorbers, and other vacuum components. The chambers will then be cleaned at the chemical cleaning facility and sealed in an aluminum bag filled with dry nitrogen gas for storage and further processing.

The aluminum chambers and flange adaptors are welded together with tungsten-inert-gas welding processes, using programmable robotic welding machines. The relative humidity of the laminar hoods over the welding zones will be reduced to less than 50% during welding to minimize oxide growth at the heat zone and to ensure weld integrity. Following welding, the vacuum chambers will be pumped down with a turbomolecular pump (TMP) backed by a dry mechanical pump, then checked for leaks using a leak detector with minimum helium sensitivity of  $5 \times 10^{-11}$  Torr-l/s. Specific procedures for repairing each type of weld leak will be developed to ensure that the quality of the chambers is not compromised. The cooling water channels will be leak-checked with vacuum and by sniffing while pressurized. The welded chambers are then brought

into the Class 1000 clean room for assembly of peripheral components, such as BPM buttons, NEG strips, pumps, absorbers, and gauges. The chamber end flanges will then be capped with blank flanges.

The assembled chambers will be installed at the evaluation stands for final leak checking and bakeout at 130°C using temporary ovens. The vacuum level and the residual gas composition will be closely monitored during the bakeout, using vacuum gauges and residual gas analyzers (RGA), to ensure that the chambers remain leak-tight and are free of contaminants. All the pumps, gauges, BPM buttons, absorbers, and thermocouples are to be activated and measured to ensure their proper operation during and after the bakeout cycle. The possible use of a DC glow-discharge system to clean internal surfaces with an Ar/O<sub>2</sub> mixture during bakeout will be investigated for its merit versus the technical complexity and cost. After bakeout, the chambers will be either at storage vacuum or back-filled with dry nitrogen for the subsequent assembly into magnets/girde and installation in the SR tunnel.

#### 4.4.4.4 Installation, Alignment, and In-Situ Baking

During the machining of the vacuum chambers, all mounting holes for the survey fiducials will be checked against the beam channel cross-sections and the BPM mounting surfaces. To ensure precision alignment, the design of the vacuum chambers and the proposed alignment schemes will be reviewed and approved by the diagnostics, accelerator physics, and alignment and support groups. The required precision of the chamber alignment is  $\leq 0.5$  mm in general, and  $\leq 0.1$  mm for special parts such as the BPM buttons. The assembled and tested chambers will be installed into the split magnets and aligned using built-in adjustment bolts of the fixed support plates mounted on the girder. After the installation and alignment of individual chamber/magnet girders in the tunnel, the end capping flanges will be removed and the RF-shielded bellows will be installed and connected to the next cell chambers. Two sector gate valves will be mounted and supported on the end flanges of the S2 and S6 chambers of each cell. The magnet buses, cooling water lines, and vacuum equipment cables will then be connected prior to final measurement, pump down, leak check, and in-situ bakeout.

The in-situ bakeout of the storage ring cell in the tunnel will be carried out with pressurized hot water provided by the storage ring utility system. Additional heating jackets, heating tapes, and thermal insulation are needed for large appendage components, such as gate valves, ion pumps, etc., to ensure uniform temperature distribution, especially at large flange joints where uneven temperatures may result in seal failure and vacuum leaks. The supports for the chambers and the pumps must be adjusted to allow thermal expansion during the bake, while still maintaining and protecting the mechanical stability of the entire system. Three Invar plates, one fixed in the middle and two flexible at the ends, will mount and support each cell chamber on the girder. The storage ring cell will be pumped down with a turbomolecular pump backed by a dry mechanical pump during the bakeout. The vacuum level and gas composition will be continuously monitored using cell vacuum gauges and RGAs during the bakeout. The temperature of the chambers will be raised slowly by the hot water system and the heating jackets, and controlled by the bakeout programmable logic controller with inputs from the installed thermocouples on the chamber surface. The entire vacuum cell will be baked at 120°C for ~ 40 hours to remove absorbed water and other contaminants from the surfaces. The sputter ion pumps, the titanium sublimation pumps, the NEG strips, and NEG cartridges will be degassed during the bake, then activated during the ramp down of the bake. The bakeout of the whole cell will be completed in ~3 days, from Day 1 to Day 3, and can be comfortably fitted in a normal work week while still leaving sufficient time for any necessary remedial actions. The vacuum cell will be leak-checked again after the bake, using the cell RGA. The fixed support points on the chambers will be checked and adjusted to their original positions by the survey group to ensure that all the critical components, such as the BPM buttons are properly aligned.

## 4.4.5 Storage Ring Vacuum Pumping

The types and sizes of the pumps to be used at NSLS-II will be standardized throughout all the machine areas as much as possible, to lower the unit cost and to ease routine maintenance in the future. The selection of the pumps will be based on the experience gained from existing pumps used in NSLS and other similar SR facilities.

### 4.4.5.1 Roughing Pumps

A set of TMPs backed by dry mechanical pumps will be used to rough down the vacuum section from ambient pressure to high vacuum, and during in-situ bake before turning on the in-line ultra high vacuum pumps. The TMPs will be connected to the vacuum sections through small, manually operated, all-metal angle valves. TMPs with magnetic or ceramic bearings of ~100 l/s size backed by dry pumps of ~5 l/s are deemed sufficient, since the ultimate pumping speed at the vacuum chambers is limited by the conductance of the chambers, the angle valve, and the flexible hose. TMPs will be manually valved out once the sector reaches ultra high vacuum. Each of the TMP stations will be equipped with vacuum gauges and electro-pneumatic valves to quickly and effectively isolate the TMP from the vacuum section in the event of pump or power failure. A dozen TMPs will be needed during the first phase of NSLS-II construction for component testing and leak checking. These TMPs, due to limited operating lifetime under heavy usage, will be replaced with newer models during NSLS-II commissioning and operation. A list of TMPs required for the operations at the storage ring is given in Table 4.4.4.

**Table 4.4.4 List of Vacuum Pumps and Gate Valves for the Storage Ring and Font Ends.**

	IP 200 l/s	TSP 500 l/s	NEG Lumped 500 l/s	NEG strips*~100 l/s/m	TMP portable	Gate valves
SR	150	150	60	150	10	60
Exit port	60	60	0	0	4	60
ID	60	60	60	27	4	
Total	270	270	120	177	18	120

\*Each chamber will have a pair of 3–5 m NEG strips for a total length over 1 km.

### 4.4.5.2 Ultra High Vacuum Pumps

After initial rough down and in-situ bakeout of the vacuum sectors, the system pumping will be transferred from TMPs to ultra high vacuum pumps, including SIPs, TSPs, NEG cartridges, and NEG strips. TSPs and NEGs have high pumping speed for active gases such as CO, CO<sub>2</sub>, H<sub>2</sub>O, and H<sub>2</sub> with equilibrium pressure down to 10<sup>-12</sup> Torr; they, however, will not pump inert gases (CH<sub>4</sub>, C<sub>2</sub>H<sub>6</sub>, etc.) nor noble gases (He, Ne, Ar, ...). Sputter ion pumps will remove inert and noble gases as well as active gases.

Triode-type SIPs have better pumping speed for noble gases, but they tend to have higher leakage current and are harder to rebuild after electrode saturation. A few noble diode SIPs, with tantalum cathode plates and similar pumping speed as triode pumps for noble gases, will be used to supplement the regular diode-type SIPs, thus avoiding so called “argon instability.” Ion pumps of 30 l/s and 200 l/s will be used throughout NSLS-II, with the 30 l/s pumps used at conductance-limited areas such as booster synchrotron and beam transport lines; and the larger pumps at SR absorber and shutter locations. These SIPs will have large anode cells to retain sufficient pumping speeds down to the 10<sup>-10</sup> Torr range. A DESY-style high-voltage feedthrough, which is less prone to radiation-induced corrosion at the brazing joint, will be used for the ion pumps. Commercial dual ion pump controllers with local and remote capabilities will power and monitor the SIP, by interfacing with the PLC and control computers, through hard wires and Ethernet linkage, respectively. Ion pump currents will supplement the vacuum gauges to provide pressure distribution over the whole ring. However, due to the buildup of leakage current in the ion pump elements, the reliable pressure

reading from ion pumps is limited to the mid  $10^{-10}$  Torr range. A list of ion pumps for the storage ring is given in Table 4.4.4.

The large volume of active gases desorbed from the photon absorbers can be efficiently removed from the SR by localized TSPs of  $\sim 500$  l/s, thus minimizing the quantity of gases diffused back to the electron beam channel. Alternatively, at absorbers for damping wigglers, with a modest increase in cost, TSPs may be replaced with NEG cartridges of comparable pumping speed but higher capacity before needing reactivations. Both TSPs and NEGs can be activated and reactivated locally or remotely. However, TSPs have the advantage of only generating a brief gas burst during their short sublimation period, while NEG activation takes longer, during which time a large amount of hydrogen is produced and should be removed by portable TMP stations.

Distributed NEG pumping in the form of NEG strips, similar to those employed at the APS storage ring, is planned for use in all cell vacuum chambers. This is deemed efficient to provide linear pumping to the beam channel through the photon exit opening. Dual strips will be mounted on the top and bottom of the antechamber. There will be sufficient clearance between the two mounted NEG strips to allow the passage of photons, even when a beam mis-steers, and for the insertion of stick absorbers. The mounting of the dual strips will be carefully designed and thoroughly tested to eliminate any potential electrical faults during in-situ bake and NEG activation. The NEG activation is at  $400^{\circ}\text{C}$  for 30 minutes and will be achieved with resistive heating of the NEG strips with  $\sim 70$  ampere current, carried out at the end of in-situ bakeout or during the machine maintenance period. The two NEG strips together will provide more than 240 l/s per meter pumping speed for active gases such as CO and  $\text{H}_2$  even after pumping  $\sim 0.1$  Torr-l per meter of active gases, corresponding to a few months of beam operation at  $10^{-9}$  Torr pressure.

Some of the ID vacuum chambers will have very small gaps of a few mm, resulting in very limited linear conductance. In these cases it is not effective to simply rely on the lumped pumps located at both ends of the chamber. Sputter-coated NEG thin film has been applied to the inner surface of ID chambers at several SR facilities, notably at ESRF, where over 20 ID chambers have been coated and in operation for more than 5 years, and at Soleil, where most straight chambers have been NEG coated. For narrow-gap undulators at NSLS-II, NEG coating will be considered during the design stage; if appropriate, it will greatly simplify the pumping system design. For long straight sections that are not occupied by insertion devices, distributed NEG strips together with ion pumps and titanium pumps will be installed to maintain ultra high vacuum.

## **4.4.6 Vacuum Measurement and Control**

### **4.4.6.1 Monitoring and Control Methodology**

The vacuum level in the storage ring, the front ends, and the beamlines will be monitored and interlocked with the ion pump current and with vacuum gauge readings. Residual gas analyzers will also be used for online monitoring and diagnosis. Each vacuum sector will have a convection-enhanced Pirani gauge and two ionization gauges as the primary vacuum gauges. Additional vacuum gauges will be installed to protect the RF cavities and kickers. Vacuum devices such as gauge controllers, ion pump controllers, and RGA - with local and remote capabilities - can be operated through front-panel switches. Their communication with the equipment control system will be through RS232 or Ethernet links for remote monitoring and control. It is anticipated that most of the vacuum controllers will be off-the-shelf items purchased through competitive bids from qualified vendors.

Due to the high level of radiation in the SR tunnel, controllers for vacuum systems will be placed in satellite electrical racks located at mezzanine above the storage ring tunnel. Electrical power for vacuum diagnostics and controllers will be standard 115 VAC and 60 Hz. Since vacuum pumps and associated vacuum equipment surrounding the ring vacuum chambers are subjected to synchrotron and bremsstrahlung radiation, radiation-resistant cables and appropriate routing will be employed to minimize radiation damage.

#### 4.4.6.2 Vacuum Gauges

One primary vacuum gauge, a convection-enhanced Pirani gauge, will be installed in each vacuum sector to provide pressure readings ranging from atmospheric pressure down to  $10^{-4}$  Torr. It will also be used for other vacuum equipment protection and interlocking. Two ion gauges, either Bayard-Alpert ion gauges or inverted-magnetron cold cathode ion gauges, will be installed at each SR vacuum section as the primary UHV gauge. The same type of ion gauge will be used for injectors, beam transport lines, front ends, and user beamlines. Both types of ion gauges have a useable pressure-sensing range down to  $10^{-11}$  Torr and they have been implemented successfully at various synchrotron radiation facilities. CCGs have the advantage of overlapping the lower end of the Pirani gauge range and can be operated through long cables for signal transfer, thus eliminating the needs of locating electronics nearby. CCG tubes do not have built-in hot filaments and are therefore less susceptible to mishandling and filament breakage during startup and commissioning. The accuracy of CCG readings is normally at  $\pm 50\%$ . Moreover, it is difficult to degas CCGs once they are contaminated. CCGs are still our choice at this point in the design process. The numbers of vacuum gauges in each area of the storage ring are listed in Table 4.4.5.

**Table 4.4.5 Number of Gauges and Residual Gas Analyzers in Areas of the Storage Ring.**

	TCG*	Ionizing Gauge	Residual Gas Analyzer
SR	30	60	34
Front end	30	60	60
ID	30	60	10
<b>Total</b>	<b>90</b>	<b>180</b>	<b>104</b>

\*TCG = convection-enhanced Pirani gauge

Interference with the gauge readings due to the presence of copious electrons, photons, and photoelectrons has been observed at many SR facilities. Therefore, if practically achievable, the gauge tubes will be mounted on elbows at shielded ports on the antechambers to minimize interference and erroneous pressure readings. The gauge tubes will also be installed in areas with minimal stray electrical and magnetic fields. Radiation-hardened material such as Kapton-insulated cables will bridge the short distance between the chamber gauge ports and the cable tray to ensure system reliability. Kapton cables are bakeable up to 200°C. Microprocessor-based multi-gauge controllers will be used to power the vacuum gauges and to provide system monitoring and control through RS232 or an Ethernet bus. The gauge controller will be hardwired to PLCs to interlock gate valves, other beam components and subsystems.

#### 4.4.6.3 Residual Gas Analyzers

Quadrupole-type RGAs will be installed to measure the partial pressures of residual gas species at selected locations in the injectors, storage ring, front ends, and user beamlines. Their use will help to identify sources of residual gases, including photon-desorbed gas from chamber walls and absorbers, air leaks, cooling water leaks, oil back-streaming, specialty gases back-streamed from the beamlines, and other contaminants. RGAs, with electron multiplier, will have partial pressure sensitivity down to the  $10^{-13}$  Torr range. Due to the high cost, RGAs may only be installed at some vacuum sections during the initial phase of NSLS-II operation. The RGAs' quadrupole mass filter RF box, which contains sensitive electronics, may be located near the head and needs to be shielded from synchrotron radiation. The PC-based control units for RGAs, however, will be located at the satellite control racks, to allow easy access for online analysis and maintenance. The number of RGAs estimated for the storage ring and front ends is listed in Table 4.4.5.

#### 4.4.6.4 Vacuum Control and Equipment Protection Systems

The vacuum control system has to 1) monitor and control all the vacuum equipment including gauges, pumps, valves, etc., to ensure that they are operating properly in their appropriate ranges; 2) collect and



archive the data for instant display and alarm and for off-line analysis; and 3), most importantly, interlock and protect the storage ring and injector from harm before damage develops.

The vacuum control system will interface directly with each vacuum device, and as part of the storage ring equipment control and protection systems (EPS). Due to high radiation levels in the storage ring tunnel, all the vacuum devices and the vacuum control system will be located at the satellite control racks. They will be backed by uninterruptible power supplies. Vacuum devices include gauge controllers, ion pump controllers, chamber and absorber temperature readouts, cooling water flow sensors, and gate valve solenoids. They can be operated via front-panel switches and with the machine control system through RS232 or Ethernet links for high-level monitoring and control. The low-level vacuum controls, consisting of several dedicated PLCs with digital and analog I/O modules, take inputs from the vacuum devices and send out commands through dry contact circuits. The PLCs, with their own microprocessors and operating systems, will be programmed by vacuum system experts and provide the logic for the operation and control of the vacuum devices.

For gate valve control, the PLCs will use a voting scheme, with inputs from the setpoint contacts of several gauges and pumps, to initiate valve interlock and closure, therefore minimizing false triggering due to the malfunctioning of a single gauge or pump. The PLC for the water flow and temperature monitoring system, with direct inputs from thermocouples and flow meters, will read and compare those with the pre-set values. An out-of-range alarm from this PLC will trigger an output to the EPS to abort the beam, thus preventing overheating of the chamber wall or absorbers, due to either the malfunction of the cooling water system or abnormal beam steering. The PLC outputs for the flow meters, the temperature readouts, and gate valve status will be part of input arrays to the EPS, which will be used to determine if conditions are unacceptable. When warranted, the EPS will initiate a fast beam abort by interrupting the low-level RF power to the accelerating cavities. The stored beam would coast inward to a scraper and be lost in a fraction of millisecond.

## References

- [4.4.1] J. Noonan, J. Gagliano, G.A. Goepfner, R.A. Rosenberg, and D.R. Walters, "APS Storage Ring Vacuum System Performance," Proc. PAC97, p 3552-5 (1998).
- [4.4.2] C. Doose, L. Emery, and S.H. Kim, "Investigation of the Surface Resistivity Tolerance of the Kicker Ceramic Vacuum Chamber at APS," Proc. PAC01, p1491-3 (2001).
- [4.4.3] J. Jones, S. Sharma, and D. Bromberek, "APS SR Flexible Bellows Shield Performance," Proc. PAC99, p 3095-7 (2000).
- [4.4.4] C.L. Foerster, C. Lanni, and K. Kanazawa, "Measurements of photon stimulated desorption from thick and thin oxide of KEKB collider copper beam chambers and a stainless steel beam chamber," *J. Vac. Sci. Technol. A* **19**, 1652 (2001).
- [4.4.5] C.L. Foerster, C. Lanni, J. Noonan, and R.A. Rosenberg, "Photon stimulated desorption measurements of an extruded aluminum beam chamber for the Advanced Photon Source," *J. Vac. Sci. Technol. A* **14**, 1273 (1996).
- [4.4.6] V. Anashin, et al., "Photodesorption and Power Testing of the SR Crotch-Absorber for BESSY-II," Proc. EPAC98, p. 2163 (1999).
- [4.4.7] R. Kersevan, "MOLFLOW User's Guide," Sincrotrone, Trieste Technical Report, ST/M-91/17 (1991).
- [4.4.8] M.K. Sullivan, "A Method for Calculating Pressure Profiles in Vacuum Pipes," PEP II AP Note No. 6-94, March 1994. (Vaccalc is a software using the finite differential method for pressure calculation.)

## 4.5 Beamline Front Ends

### 4.5.1 Scope

The beamline front ends connect the storage ring to the user beamlines and provide radiation protection to personnel. Most of the front-end components generally reside within the storage ring's shield wall, outboard of the dipole vacuum chamber. The major components of the beamline front-ends are photon masks, shutters, heat absorbers (such as beam-defining apertures and/or slits), fast valves (or other shock wave protection devices), vacuum isolation valves, pressure isolation sensors, and diagnostics. Vacuum chambers are also included; however, the chambers are often part of the individual front-end components. Other components, such as filters, may be included depending on the application. The front end usually starts at the exit to the dipole vacuum chamber and extends to a beryllium window or a differential pump, where the user vacuum is isolated from the machine vacuum. If a beryllium window is used, it generally is positioned as close as is practical to the outer end of the storage ring shield wall. Also to be considered as important front-end components are radiation shields, i.e., safety shutter shields and bremsstrahlung shields. Vacuum pumps, vacuum sensors, and diagnostics (e.g., for Residual Gas Analysis, to activate fast valves, etc.), heater tape and provisions for bakeout, as well as the vacuum valves, are included in the front ends—even though these components are generally considered part of the vacuum system. Support tables and stands made of structural steel are provided to support the front-end components at the nominal 1m beam height.

Only six beamline front ends will be installed in the initial scope of the project: three in-vacuum undulators (IVUs), two damping wigglers (DWs), and one elliptically polarized undulator (EPU). The project scope also includes engineering and design effort for the bending magnet (BM) and three-pole wiggler (3PW) front ends. The preliminary design of the front end described below can be adopted, with appropriate modifications for beam power and beam size, to all front ends.

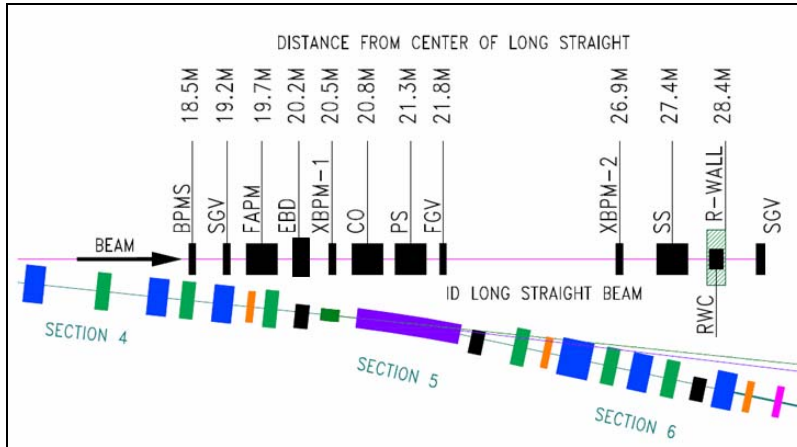
### 4.5.2 Standard Front End Design

Figure 4.5.1 shows the preliminary layout of a typical front end with its main components and their approximate locations from the center of a long straight. The first component is a bending magnet photon shutter (BMPS) which intercepts bending magnet photons when there is no front end or when a front-end is under maintenance. A slow gate valve (SGV) is the next component provided to separate the storage ring vacuum from the front-end vacuum. Until a complete front end is available for installation, the BMPS and SGV are locked in closed position, and an out-of-vacuum lead stop is provided downstream of the SGV to stop bremsstrahlung radiation.

The next component is an e-beam deflector (EBD), which prevents the injected beam from accidentally entering the beamline hutch during top-off injection. The EBD consists of permanent magnet blocks that provide a vertical field of 1.1 T over a 20cm length with a pole gap of 14 mm. The EBD is designed to deflect a 3GeV beam horizontally into the stationary tungsten blocks of the safety shutter (see below), located at ~7 m downstream. The beam is deflected at this location by 15 cm, which is 5 cm more than the horizontal beam aperture provided in the tungsten blocks.

A pair of photon BPMs (XBPM-1 and XBPM-2) is used to deliver a stable beam to the user's end station by providing beam position data to the global feedback system. Next to XBPM-1 is a lead collimator (CO), which collimates the angles of bremsstrahlung radiation to minimize the size of tungsten blocks required in the safety shutter (SS) and the amount of supplemental lead in the ratchet wall (R-WALL). The uncooled tungsten blocks in the safety shutter are protected by a water-cooled photon shutter (PS) that is inserted in the beam path before the safety shutter is actuated. A fast gate valve (FGV) in the front end is provided to intercept the pressure shock wave in the case of a vacuum breach in the beamline. Another slow gate valve is

usually provided downstream of the ratchet wall collimator (RWC) to separate front end vacuum from the beamline vacuum. Some front ends will be provided precision X-Y slits between FGV and XBPM-2, at the request of beamline users. All components of a front end requiring actuation (SGV, FGV, PS, SS, and X-Y slits) will be remotely operable.



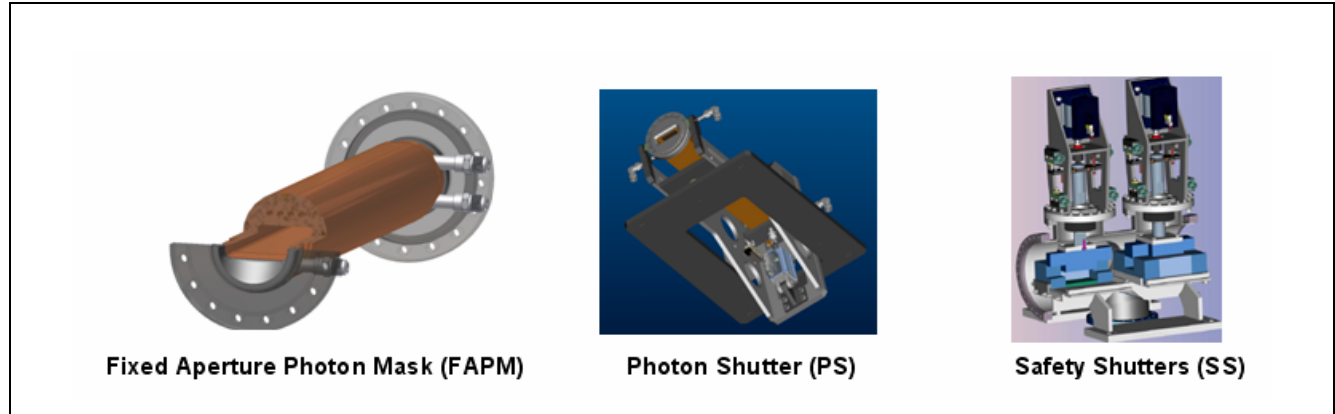
**Figure 4.5.1** Typical layout of a front end. From left to right: bending magnet photon shutter (BMPS), slow gate valve (SGV), fixed aperture photon mask (FAPM), e-beam deflector (EBD), first photon BPM (XBPM-1), lead collimator (CO), photon shutter (PS), fast gate valve (FGV), second photon BPM (XBPM-2), safety shutter (SS), ratchet wall collimator (RWC), and slow gate valve (SGV).

The power densities of the NSLS-II insertion devices, shown in Table 4.5.1, are lower than those at the APS Undulator-A (130 kW/mrad<sup>2</sup> at 100 mA). We plan to adopt the APS designs of the front end components with appropriate modifications for the aperture requirements of each beamline.

**Table 4.5.1 On-axis power densities of NSLS-II insertion devices (3 GeV, 500 mA).**

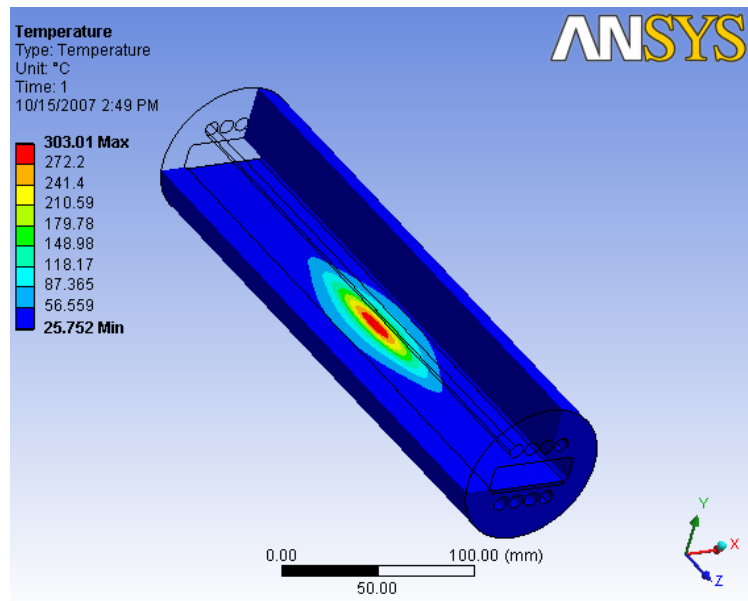
	Name						
	U20	U19	U45	U100	DW-1.8T	SCW	3PW
Type	IVU	CPMU	EPU	EPU	PMW	SCW	PMW
On-axis power density (kW/mrad <sup>2</sup> )	62.33	77.86	40.03	26.33	55.30	25.60	0.28

Figure 4.5.2 shows the typical APS designs for the three critical components: FAPM, PS, and SS. The heat-absorbing surfaces of the FAPM are designed from a single, solid piece of Glidcop, ~0.5 m long, to handle the high heat flux of the insertion devices. Water-cooling channels are gun-drilled in Glidcop block before machining for the beam aperture with 4° taper and brazing of the Conflat flanges. The design of the PS is very similar to that of the FAPM except that its downstream end can be lowered by an actuator to intercept the photon beam. In the design of the APS safety shutter, two independently movable tungsten blocks are lowered to interlock with the fixed tungsten blocks, thus closing the beam aperture and as well a line-of-sight escape for bremsstrahlung radiation. Only one set of tungsten blocks is being considered in the NSLS-II design, with the provision of redundant position switches for the movable tungsten block, and more restrictive access to the beamline hutches.



**Figure 4.5.3** Typical designs of the APS front end components. Left to right: fixed aperture photon mask (FAPM), photon shutter (PS), and double safety shutter (SS).

FE analyses were performed for all front end components. The most critical component is the photon shutter which is located at  $\sim 20$  m from the center the IVU in the short straight. It intercepts x-rays at an incidence angle of  $4^\circ$ . The analysis results (Figure 4.5.4) show a maximum temperature of  $303^\circ\text{C}$  is at the center of the beam footprint. In comparison, the acceptable temperature rise in Glidcop is  $\sim 400^\circ\text{C}$ , based on its thermal fatigue life.



**Figure 4.5.4** Temperature profile in the photon shutter located at 19 m from the center of an IVU.

### 4.5.3 Vacuum Components/Enclosures

The front end vacuum chambers and ducts will be constructed from 304L stainless steel and will be joined to adjacent components using commercially available Conflat flanges, copper gaskets, and UHV hardware. Fabrication of chambers and ducts will be from stainless steel utilizing TIG-welded construction.

Because the front ends share the storage ring vacuum, front-end and SR vacuum pressures must be compatible. A pressure of  $10^{-9}$  Torr therefore must be maintained in the beamline front ends during machine

operations. To achieve these pressures, we will use a combination of UHV components and procedures, in addition to bakeout of the front-end subsystem. The chambers and beam ducts will be designed to withstand a bakeout temperature of 200°C, to accelerate the release of gases. We expect that an integral bakeout system will be incorporated in the beamline front end, to enable the capability of in-situ bakeout.

Only all-metal commercially available gate valves will be used in the front ends. An all-metal right-angle valve will be located between the photon shutter and the fast-closing valve. Attached to this valve will be a fitting with both an ion gauge and an RGA to monitor the total and partial pressures of the front-end vacuum. At the remaining port of the cross, a valve will be installed (to be used in combination with the right-angle valve) to allow for venting and pump-down when replacing either the ion or RGA gauge filaments. Additionally, installation of a vacuum valve between the fast-closing valve and the XBPM-2 is planned, to allow for separate venting/pump-down of the downstream portion of the front end. The fast gate valve should close in less than 15 msec and have a leak rate of less than  $7.5 \times 10^{-10}$  Torr-l/s when closed. Two ion pump/titanium sublimation pump combinations are planned, located strategically in each beamline front end. To minimize any residual gas species generated by the photon beam impinging on a surface, a 400 L/s ion pump/TSP pair will be installed near the photon shutter locations. An additional 400 L/s ion pump/TSP pair will be installed at the safety shutter, due to the relatively long distance (~5 m) between the photon shutter and safety shutter.

#### 4.4.3.2 Radiation Protection

At times during storage ring operations, it will be necessary to access the experimental hutch (for example, to set up equipment and change samples). The remotely actuated safety shutter device is provided (see Figure 7.5.1) to stop brehmsstrahlung radiation, thus providing protection from ionizing radiation for personnel downstream of each shutter. From calculations, a thickness of 20 cm of tungsten is required to attenuate the brehmsstrahlung radiation in the forward direction. Ray-tracings will be done to determine the transverse dimensions of the tungsten shielding. Additionally, lead collimators will be provided in each front end to confine the radiation cone in the downstream experimental area. From calculations, a thickness of at least 30 cm of lead for the collimators will be required to attenuate the brehmsstrahlung radiation in the forward direction. As with the tungsten shield of the safety shutter, ray-tracings will be performed to determine the minimum transverse dimensions of lead required.

A byproduct of the brehmsstrahlung/lead collimator interaction is the production of neutrons that ultimately must be shielded. The concrete used in the shielding wall is a very effective neutron shielding material; however, there will be beampipe penetrations through the shield wall that must be considered. Void volumes between the shield wall and front-end beampipe penetrations will be filled with concrete and lead, to terminate the transit of photons and neutrons beyond the shield wall. For exit ports with no front end, the shield wall window will be completely filled with concrete.

#### 4.4.3.4 Interlocks

The Personnel Protection System (PPS) will monitor the position of the safety shutter to provide personnel at the beamline safety from prompt radiation. The Equipment Protection System (EPS) will control the sequencing and control of front-end devices and prevent damage from occurring. The EPS will prevent damage to front-end components by sensing position, water flow, and vacuum, then taking action by operating components or dumping the beam, when appropriate.

To protect the storage ring vacuum from any inadvertent pressure rise due to front-end or beamline component failures, various interlock sequences will be implemented. Two possible scenarios in which an air-to-vacuum leak in the front end would corrupt the SR vacuum are mentioned here as examples: 1) a slow air-to-vacuum leak due to faulty bellows or a leaking weld in a vacuum chamber, and 2) a catastrophic vacuum leak due to a failure in a beamline.

If monitoring of the vacuum quality indicates a slowly increasing pressure, the origin of this pressure rise will be investigated and repaired during a regularly scheduled maintenance period. Should the pressure in the front end reach the ion gauge set point of approximately  $5 \times 10^{-7}$  Torr, the EPS will first signal the insertion device on the offending beamline to open its gap, thereby eliminating the high heat flux on any front-end components. The bending magnet photon shutter will then be actuated to provide dipole radiation protection to the uncooled isolation valve when it has been moved into the closed position. Finally, first the photon shutter and then the safety shutters will be the last devices instructed to close. With the storage ring isolation valve in the closed and sealed position and PPS in place, ring operations will be allowed to continue unhindered by the vacuum leak in the front end. The front end or beamline experiencing such vacuum difficulties would be repaired during a regularly scheduled maintenance period. Note that all of these front-end actions will be taking place in the background while facility operations continue unhindered.

In the case of a catastrophic leak, once the fast-closing valve is triggered by a pressure exceeding  $5 \times 10^{-6}$  Torr in the front end or beamline, the EPS will send the appropriate signals to dump the stored electron beam. Triggering of the FV will simultaneously close the BMPS, isolation gate valve, and safety shutters. Operations may resume when proper sealing of the isolation gate valve has been verified and the vacuum leak in the front end or beamline has been isolated from the SR vacuum.



## 4.6 Storage Ring RF Systems

The large dipole radius (25 m) and the medium energy (3 GeV) of NSLS-II result in very low radiated energy from the bending magnets (288 keV/turn). This increases the effectiveness of eight damping wigglers to reduce the bare emittance of 2.1 nm-rad to 0.5 nm-rad. The RF system power requirement for NSLS-II is determined primarily by the power radiated by the damping wigglers. This makes it possible for us to stage the RF system installation to parallel the installation of damping wigglers and user insertion devices.

The small momentum compaction (0.0037), an RF frequency of 500 MHz, and high RF voltage result in small bunch lengths of ~4 mm. This contributes to a short Touschek-dominated lifetime of <2 hours. To improve lifetime to greater than 3 hours, a third harmonic bunch lengthening cavity is included in the baseline design.

The storage ring RF system consists of the 500 MHz Superconducting RF cavities, their associated klystron tube amplifiers and power supplies, the passive SCRF third harmonic Landau (bunch lengthening) cavity, the liquid helium cryogenic plant, and the master clock, frequency synthesizers, digital cavity controllers, and RF distribution system that make up the low-level RF.

### 4.6.1 Physics Requirements and Design Parameters

The RF system must provide sufficient momentum acceptance (bucket height) so as not to be the limiting factor in the storage ring acceptance. In addition, with the small momentum compaction of the low emittance lattice leading to very short bunches, and the accompanying short lifetime, a third harmonic (1500 MHz) RF system is used to lengthen the bunches to increase the Touschek lifetime from <2 hours to >3 hours. The Landau cavity also increases the dependence of the synchrotron tune on the oscillation amplitude providing Landau damping, which can suppress bunch instabilities. The required RF power is the sum of the beam radiated power in the dipoles, damping wigglers, and user IDs. There is no unique approach to meeting the RF requirements; in fact, the frequency choice of 500 MHz is within a broad range of frequencies in which RF sources and cavity designs exist and that would meet the physics requirements. Three frequencies within this broad range, 352 MHz, 476 MHz, and 500 MHz, have been used successfully in third-generation light sources. The operating frequency of 500 MHz has been selected here due to the availability of existing SCRF cavity designs, commercial RF transmitters, and the large number of 500 MHz systems in use at light sources around the world. This translates into mature technologies and lower development costs. A summary of the ring parameters related to the design of the RF system is shown in Table 4.6.1.

**Table 4.6.1 RF and Beam Parameters for the NSLS-II Storage Ring.**

RF frequency [MHz]	499.68
Circumference [m]	792
Harmonic number	1320
Loss per turn (assuming 5 undulators, 21 m of DW, and dipole losses) [keV]	816
RF acceptance [%]	3
Accelerating voltage [MV]	3.3
Momentum compaction	$3.7 \times 10^{-4}$
Bunch charge [nC]	1.25
Number of buckets filled with charge	1056

The radiation from dipoles and an assumed complement of five undulators and 21 m of damping wigglers result in an energy loss per turn of 816 keV, corresponding to 408 kW power loss at the design current of 500 mA. A 3% momentum acceptance ( $\Delta p/p$ ) is specified to ensure sufficient Touschek lifetime of the storage



ring. For 816 keV/turn energy loss, this corresponds to an RF voltage of 3.3 MV (see Figure 4.6.1). As insertion devices and damping wigglers are added as the user program is built out, the loss per turn increases to more than 1.6 MeV, and a voltage of 4.8 MV is required to maintain the 3% bucket height.

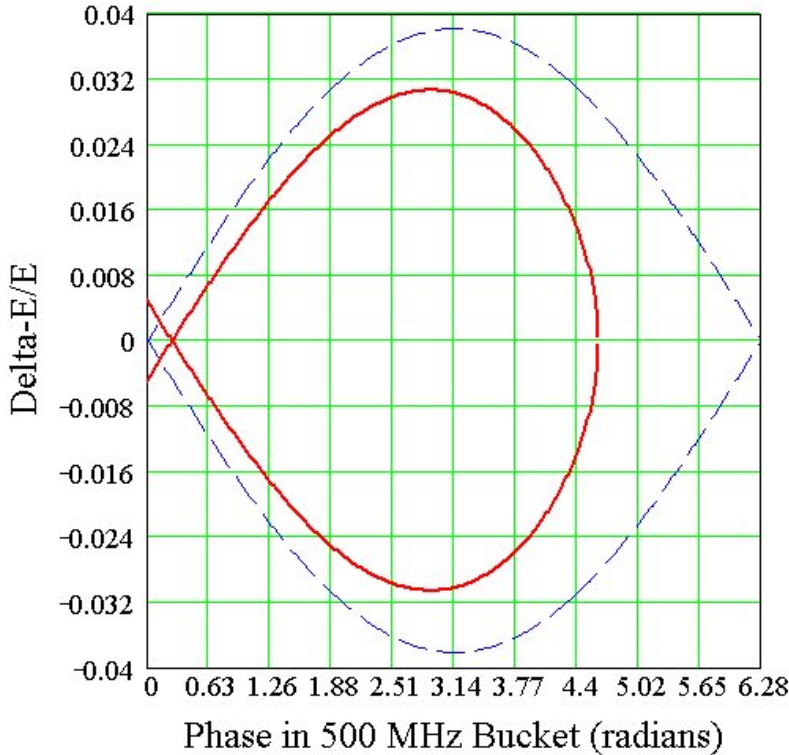


**Figure 4.6.1** RF separatrix for 3.3 MV RF field with (red trace) and without (blue trace) 816 keV/turn radiation losses. The 3% RF acceptance is easily met with two CESR-B cavities.

Thus, the evolution of the RF power requirements over the life of the facility must be taken into account. Table 4.6.2 outlines the initial machine configuration, the capabilities of the RF system, and a reasonable extrapolation as to how this might evolve as insertion devices are added. The exact scenario will be driven by the user requirements and is not fixed at this stage of the machine design.

**Table 4.6.2 RF Power Requirements for Dipole Losses and Various Example Insertion Device Configurations for one, two, and four RF systems installed.**

RF power requirements	Phase 1: Capability of installed RF (270kW/cavity)		Phase 2: Adding 2nd cavity plus purchase 300-kW Transmitter		Phase 3: Add 3 <sup>rd</sup> and 4 <sup>th</sup> RF station (cavity + transmitter)	
	#	P (kW)	#	P (kW)	#	P (kW)
Dipole	-	144	-	144	-	144
Damping wiggler (9.23 kW / m, 7 m each)	0	0	3	194	8	517
IVU (2.7 kW/m, 3 m each)	3	24	[6]	66.6	[10]	111
[CPMU] (3.77kW/m, 3m each)						
EPU (4.1 kW/m, 4 m each)	1	12	4	48	5	60
Total		180		452		832
RF power available for additional ID's		90		88		248
Total Available RF power		270		540		1080

The initial RF system will consist of two CESR-B cavities, each powered by a 310 kW transmitter. Three cavities will be purchased with the third cavity to be used as a spare in the event of a cavity failure. Two installed cavities can provide up to 5 MV, which exceeds the voltage requirement of 4.8 MV even for the full complement of insertion devices and the 56 m of damping wigglers envisioned for NSLS-II. However, the power coupler is capable of delivering only ~270 kW of beam power, and so the ring is limited to four damping wigglers and 10 user IDs (or equivalent) by the initially available RF power. Installing a third cavity and transmitter will support a full complement of eight damping wigglers, resulting in the ultimate horizontal emittance of 0.5 nm-rad. Two 500 MHz cavities and one 1500 MHz harmonic cavity (to be described in Section 4.6.3) fit into a single 8 m straight. A second RF straight is reserved for the third and potentially fourth CESR-B cavity and second 1500 MHz cavity, to meet the evolving power requirements of NSLS-II as more user IDs are added.

#### 4.6.1.1 Impedance Analysis and Beam Stability

The high beam loading due to 500 mA average stored current requires highly damped structures to prevent beam instabilities. In this regard, the B-factory cavity designs of KEK, PEP-II, and Cornell are attractive and have been studied in detail.

The narrow band cavity impedances have been calculated using the codes GdfidL, SUPERFISH, and CLANS [4.6.1, 4.6.2, 4.6.3]. These codes calculate the longitudinal shunt impedance as

$$R_{sh} = \frac{\left[ \text{Re} \left( \int E_z(z) e^{ikz/\beta} dz \right) \right]^2}{2P}, \quad (4.6-1)$$

where P is the power dissipated in the cavity,  $E_z$  is the longitudinal electric field either on axis (monopole modes) or displaced with a radial offset corresponding to a dipole mode, quadrupole mode, etc. Here, k is the wave number ( $\omega/c$ ), and  $\beta$  is the ratio of beam velocity to that of light.

The cavities also have transverse impedances that can couple strongly to the beam. The transverse shunt impedance of a cavity is given by the integral of the force acting on the beam, as

$$Z^\perp = -i \left( \frac{\int_0^L (\vec{E} + \vec{v} \times \vec{B})_\perp ds}{\beta \cdot I_{av} \cdot a} \right), \quad (4.6-2)$$

where L is the cavity length,  $I_{av}$  is the average bunch current, and  $a$  the offset of the beam from the cavity axis. The beam must couple energy into the higher-order transverse mode through the electric field ;hence, there is a relation between the longitudinal and transverse impedances. The broadband impedance model uses the Panofsky-Wenzel relation,

$$Z_\perp = \frac{c}{\omega \Delta^2} \cdot Z_\parallel^{(\Delta)}, \quad (4.6-3)$$

where  $\Delta$  is the offset at which the longitudinal impedance is calculated. The cavity impedances have been calculated for the PEP-II, KEK-B, and CESR-B cavities [4.6.4, 4.6.5, 4.6.6]. All three cavity designs can meet the NSLS-II requirements in terms of attainable RF voltage and beam power delivered. The SCRF approaches of KEK and Cornell result in lower installed RF power requirements and more efficient operation, attain much lower HOM impedances, and require fewer cavities to achieve the voltage specification. This is particularly important when additional insertion devices are installed that will increase the RF voltage

requirement to  $\sim 5$  MV. The choice for NSLS-II has been narrowed to either the KEK-B cavity or the Cornell CESR-B cavity. Further studies on cost, reliability, and future upgrade potentials in the preliminary design phase will lead to the final choice. For the purposes of this document, the CESR-B cavity is baselined in order to present self-consistent calculations of system parameters such as RF power and cryoplant requirements, coupled bunch growth rates, system mechanical layouts, and cost. Details of the HOM impedances and coupled bunch growth rates are given in Section 6.2.3.

To meet the initial requirements of 3.3 MV accelerating voltage and 408 kW beam power, two RF cavities with individual klystron transmitters are to be installed. A third cavity to be used as a test cavity / spare will be purchased as part of the baseline machine. It is expected that this cavity will be installed in a future upgrade as additional insertion devices increase the beam power requirement to beyond  $2 \times 270$  kW, a soft limit of the power couplers in the CESR-B cavities. The CESR-B cavity parameters are given in Table 4.6.3.

**Table 4.6.3 CESR-B Cavity Parameters.**

Frequency [MHz]	499.68 +/- 0.2
Electric field (normalized to 0.3m) [MV/m]	>8 MV/m
Accelerating Voltage (beam energy gain) [MV]	>2.4 MV
Unloaded Q (at 8MV/m)	> $7 \times 10^8$
Static heat losses [W]	<30 W
Dynamic heat losses (at 4.5k and 8MV/m) [W]	<120 W
Maximum power transferred to beam [kW]	>250 kW
Loaded Q	$1 \times 10^5$

In addition to coupled bunch instabilities caused by higher order modes in the cavities, the fundamental and harmonic RF systems can cause instabilities where all of the bunches oscillate in unison, the so-called Robinson instabilities. The classical Robinson analysis [4.6.7] is particularly relevant for short and compressed bunch operation of the machine. The resistive Robinson instability is not excited by the cavities. This is due to the fact that the main cavities are detuned below resonance to compensate for beam loading, which strongly damps phase oscillations, while the harmonic cavities' very high quality factor greatly reduces the resistive part of their impedance at the synchrotron frequency, and hence their excitatory (or damping) influence on phase oscillations.

The second observation concerns the reactive Robinson instability. In this instability the static bunch distribution is an unstable fixed point of the longitudinal dynamics, and a perturbation of the bunch pushes it with some growth rate away from that distribution, subsequently damping to one of two stable distributions. In the absence of harmonic cavities, the bunch is marginally unstable. The addition of inductively detuned harmonic cavities for stretched bunches tend to suppress this problem; capacitively detuned harmonic cavities for compressed bunches aggravate the instability. In unstretched or compressed operation, however, the unmitigated instability results in only a small phase shift of the bunch due to the narrow potential well. But for stretched bunches the potential well is wide and flat, and the instability results in gross distortion of the bunches, which must be addressed. A simple cure, first recognized by Miyahara [4.6.8], is to introduce a small-bandwidth feedback of the RF system to the beam. Simulations also show that a reduction of the main-cavity impedance using RF feedback suppresses the instability, although too much feedback excites a higher-order oscillatory instability.

Although glossed over in the discussion to this point, with stretched bunches the classical Robinson picture is not so simply applicable; more involved analyses, such as those by Bosch et al. [4.6.9], and numerical simulations are required to assess the stability of higher-order modes of these bunches. As was just mentioned, the use of RF feedback, which allows the adjustment of the impedance of the main cavities, is a means by which some manipulation of bunch stability is possible. Our experience with the NSLS VUV ring

also shows that short-range wakes can have an impact on the stability of stretched bunches, which is further complicated by the varying bunch profiles along the train.

## 4.6.2 500 MHz RF System

### 4.6.2.1 500 MHz Cavities

The CESR-B cavity consists of a bulk niobium SCRF single cell with waveguide coupler, a special fluted beampipe to extract the lowest frequency dipole modes, warm-to-cold transition spool pieces for thermal isolation, water-cooled C48 ferrite HOM dampers, and long tapers to transition from the 240 mm cavity bore to the elliptical beampipe. The CESR-B cavity is a “single-mode” cavity. All higher-order modes with the exception of the TM<sub>110</sub> dipole mode propagate through the cylindrical beampipe. A fluted beampipe at the opposite end of the cavity has a lower cutoff frequency to allow the TM<sub>110</sub> to propagate to the ferrite load. This has only a small effect on the fundamental mode. This allows a shorter attenuation length in the beam tube and a more compact cavity. The cavity assembly is shown in Figure 4.6.2. The layout of two CESR-B cavities plus a single Super3HC harmonic cavity in a single straight is shown in Figure 4.6.3.

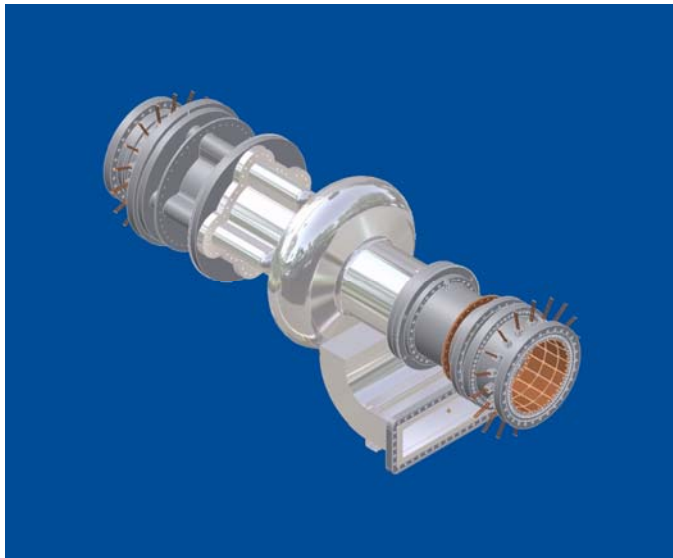


**Figure 4.6.2** The CESR-B bare cavity assembly.

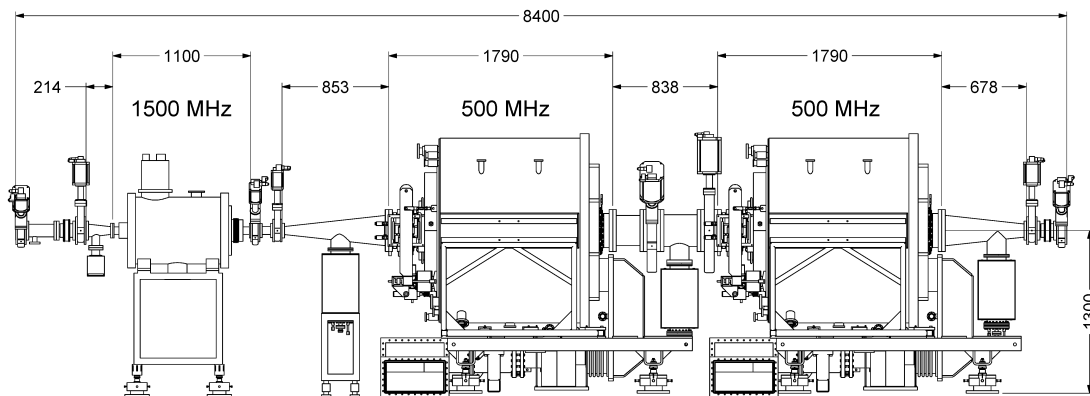


**Figure 4.6.3** Layout of two 500 MHz cavities plus one 1500 MHz Landau cavity in a single straight. The tapers from the large cavity beampipe to the ring beampipe are 678-853 mm long, limited by the available length in the straight of 8.4 m. A second RF straight is reserved for additional cavities.

### 4.6.2.2 HOM Damper

The HOM damper consists of C48 ferrite tiles brazed to water-cooled copper backing plates that form a spool piece outside the cryostat. The ferrite is several 500 MHz attenuation lengths away from the SC cavity. There is power dissipated in the ferrite from two sources. First, there is dissipation of the fundamental 500 MHz field driven by the transmitter. This has been calculated with CFISH [4.6.2, 4.6.10] to be less than 100 W at 2.5 MV cavity voltage. Second, the beam also loses energy from wakefields. This loss is given by

$$P_{loss} = k_{\parallel} \cdot \frac{I_0^2}{n} T_0. \quad (4.6-4)$$

For NSLS-II,  $T_0 = 2.6 \mu\text{s}$ ,  $I_0 = 0.5 \text{ A}$ , and  $k_{\parallel} (\sigma_s = 4 \text{ mm}) = 3.6 \text{ V/pC}$ , resulting in a  $P_{loss} = 2.3 \text{ kW}$ . In the worst case, all of this power is lost in the ferrite, which is still a factor of 4 lower than the design limit.

### 4.6.2.3 KEK-B Cavity Option

The superconducting cavities developed for the KEK-B factory are being considered as an option for NSLS-II, for several reasons. The most significant advantage is the higher power per coupler, which has been demonstrated at KEK to be greater than 400 kW. In principle, two KEK cavities could meet the power requirements for the full complement of damping wigglers and user insertion devices,  $\sim 800 \text{ kW}$ . The waveguide feed at the top of the cryostat makes the tunnel installation easier, and the coupling can be optimized for various beam currents and cavity voltages by simple spacers on the antennae coupling mounting flanges, as opposed to the fixed coupling of the waveguide feed for the CESR-B approach. A layout of two KEK-B cavities in an 8 m straight is shown in Figure 4.6.4.

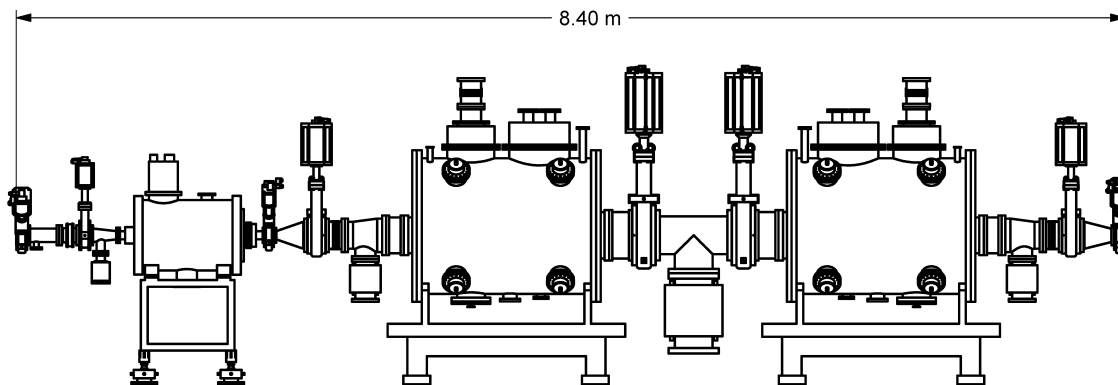


Figure 4.6.4 Installation of two KEK-B SCRF cavities in an 8.4 m (available length) straight.

### 4.6.2.4 RF Transmitter

The power couplers for SCRF cavities have a wide statistical variation in their power handling capability. Although they have been engineered for high power handling by proper thermal and electrical design, they are prone to multipacting, a resonant electron-avalanche effect that can impose a hard limit on power transmission and cause failure by local heating due to electron loading. The multipacting depends on the secondary-emission coefficient of the surface, which in turn depends on the properties of the bulk material, usually copper or niobium, and surface contaminants, which are usually cryo-pumped organics from the machine vacuum. These contaminants can be present at start-up or accumulate over a period of time, degrading performance and requiring, in the worst case, the cavity to be warmed up with a mild bake to drive off the condensed gases. Experience with the CESR-B cavities has shown transmitted power per coupler in the range of 250–330 kW. A transmitted power of 270 kW is assumed for meeting machine requirements and placing a limit on installed RF power. In addition to the energy losses due to radiation in dipoles, damping

wigglers, and undulators, the RF power transmitter and coupler must provide for the HOM losses that are excited by the beam. We are exploring ways of increasing the power per coupler, and will factor this into the preliminary design and choice of transmitter power.

The coupling of the waveguide to the cavity in the ideal case is adjusted so that the cavity presents a matched load to the RF source at the normal operating current and energy. Since there is a phased installation of cavities and insertion devices, this optimal coupling varies over the life of the machine. The KEK-B cavity has an adjustable antennae coupler that, in principle, can be changed to follow the optimal coupling. In practice, this must be done in a clean room environment and may be of limited value.

For an aperture-coupled cavity such as the CESR-B, coupling is set during the design and manufacture. Usually coupling is set so the generator is matched to the cavity at the highest expected beam-loading (beam power) of 270 kW. This minimizes the requirement on installed RF power. For the staged installation of insertion devices (RF power required) and RF cavities there is not a single minima, and it is necessary to balance the mismatch over the different phases. For an approximate match to the conditions in Phase 3 in Table 4.6.2, the maximum reflected power in the other three phases is ~10.5 kW. Alternatively, we can choose the coupling to be slightly over-coupled in the case of the highest beam-loading, and accept. In order to reduce the residual reflected power during commissioning and staged insertion device installation, we have the option of installing a 3-stub waveguide tuner between the circulator and the cavity.

There will be variation of the impedance presented by the cavities to the beam at different times of the machine's life due to the varying number of cavities and insertion devices. RF feedback can be used to reduce (or increase) this impedance; this option is being studied and system layout designed to minimize loop delay to allow its implementation. A minimum transmitter power of 275 kW is required to meet the sum of the radiated, HOM, and reflected power demands. To allow for the case of coupler improvement (coupler is limited by multipacting, not power limitations) or system aging (degradation of klystron output power), the transmitter will be designed for a minimum of 310 kW, allowing up to ~280–300 kW per coupler.

A single 300 kW klystron amplifier will drive each of the main ring cavities through a 350 kW rated circulator and load. Klystrons that meet or exceed this power level are available from three vendors: CPI, Toshiba, and Thompson. The klystron beam power will be provided by a Pulse Step Modulation switching power supply at 55 kV and 12 A. The PSM switching power supplies have the benefit of low stored energy, and fast turn-off capability of the IGBTs eliminating the need for a crowbar circuit to protect the klystron. The power supply will have redundant switching cards built in, and will operate at full capacity even with several card failures. The RF transmitter will have local control via PLC, with system parameters and control available to the main control system via an Ethernet link. The PLC will also monitor the PSM switch modules, so that failed modules are logged and transmitter repairs can be scheduled for the next maintenance period. The main ring power systems with a rating of 300 kW are beyond the power limit of air-cooled coaxial cable, and will be implemented in WR1800 waveguide. A layout of the RF straight with the associated RF transmitters is shown in Figure 4.6.5.

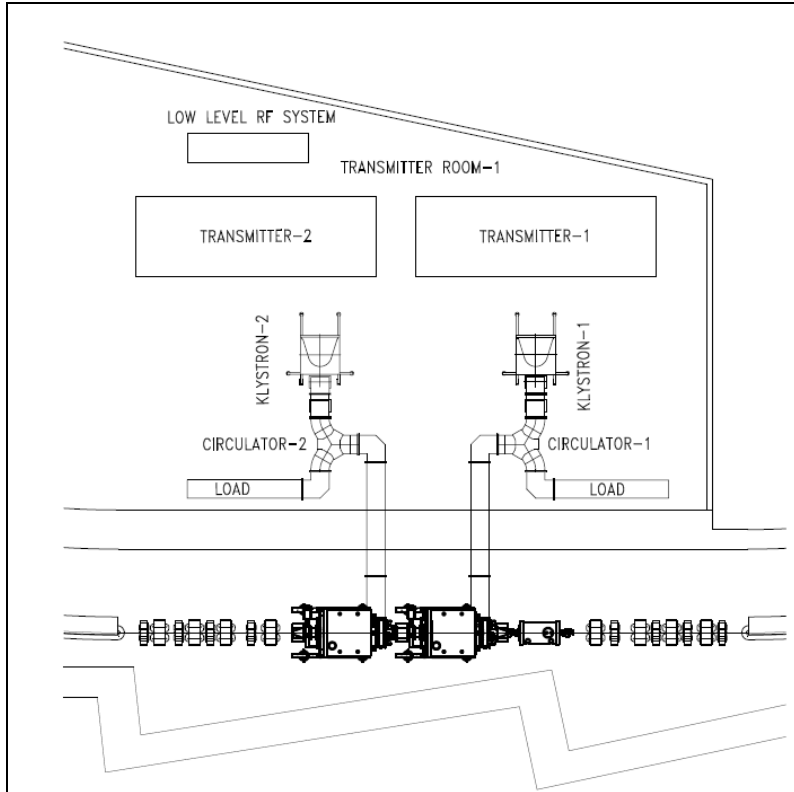


**Figure 4.6.5** Layout of an RF straight section with two 500 MHz cavities and their klystron transmitters and a single 1500 MHz harmonic cavity.

An alternative approach of combining several Inductive Output Tube (IOT) amplifiers to obtain the necessary RF power has been developed at other facilities [4.6.11, 4.6.12]. IOT systems have higher efficiencies and some limited failure tolerance. Likewise several hundreds of high-power transistors can be combined to provide the required power. SOLEIL has recently commissioned such a system at 352 MHz [4.6.13]. Both of these options will be explored in detail during the R&D phase.

### 4.6.3 1500 MHz Harmonic Cavity System

A passive 1500 MHz SCRF cavity, such as the BESSY scaled CESR-B [4.6.14] or Super3HC [4.6.15] scaled SOLEIL cavity, has been studied for the Landau cavity in NSLS-II. Both of these cavities can achieve  $\sim 0.5$  MV per cell, with the BESSY cavity containing a single cell, and the Super3HC containing two cells per cavity. The details of the impact of the Landau cavity have been discussed in Section 6.2.7 on collective effects. Here we will discuss the hardware and system configuration. For this purpose, two cells (1 cryo-module) of the Super3HC design is in the baseline design.

The nominal voltage and phase of the harmonic cavity is that which cancels the slope and second derivative with respect to time of the total RF field. This results in bunches lengthened by approximately the ratio of the harmonic-to-main cavity frequencies. The field required of the harmonic cavity is approximately the reciprocal of that ratio times the main-cavity field, although slightly less due to the non-zero main-cavity synchronous phase that is a consequence of the beam's radiation loss. In practice, this harmonic-cavity field is pushed slightly higher to provide additional stretching, striking a balance between improved lifetime and the eventual onset of longitudinal instabilities. Furthermore, the use of a gap in the ring's fill pattern for ion clearing results in perturbations of the potential wells that vary along the train. As a result, the lengths of most bunches are shortened by these perturbations and the average lifetime is reduced. For these reasons, the harmonic-cavity field and phase require further investigation. Simulations shown in Section 6.2.7 give a

maximum in bunch length for ~1.1 MV of third-harmonic voltage for the initial fundamental cavity voltage of 3.4 MV. This can be met with a single Super3HC cavity. As the number of damping wigglers and user insertion devices increases, the fundamental mode voltage increases to 4.8 MV and an additional third-harmonic cavity will be necessary for optimal bunch lengthening.

#### 4.6.4 Low-Level RF and Beam Control

The specifications of the RF system amplitude and phase requirements are derived in part from the user requirements that the transverse motion of the photon beam is to be <10% of the RMS beam size, and the increase in photon beam size due to emittance dilution of the electron beam is to be <10%. The relation of the photon beam size and jitter to electron beam size and jitter is influenced by the design of a particular insertion device and beamline, which might impose a tighter tolerance on the electron beam stability. The stability required from the RF system to limit the transverse jitter of the electron beam to 10% beam size is derived below. This will be expanded to study the effect on the photon beam in the next phase of design.

#### 4.6.4 Low-Level RF and Beam Control

The specifications of the RF system amplitude and phase requirements are derived in part from the user requirements that the transverse motion of the photon beam is to be <10% of the RMS beam size, and the increase in photon beam size due to emittance dilution of the electron beam is to be <10%. The relation of the photon beam size and jitter to electron beam size and jitter is influenced by the design of a particular insertion device and beamline, which might impose a tighter tolerance on the electron beam stability. The stability required from the RF system to limit the transverse jitter of the electron beam to 10% beam size is derived below. This will be expanded to study the effect on the photon beam in the next phase of design.

##### 4.6.4.1 RF Tolerances Imposed by User Experiments

Timing experiments, such as the IR experiments run at NSLS currently, require that the timing jitter of the bunch be less than 5% of the RMS bunch length over the frequency range of 500 Hz to 50 kHz. This corresponds to a phase error of 0.16 degree for a 10 ps bunch, or a corresponding momentum jitter of 0.005% due to synchrotron motion.

The majority of users are not concerned with timing experiments but require small and stable photon beam size. The vertical photon beam divergence for a experiment using a higher harmonic of an Insertion Device (ID) is given by<sup>1</sup>

$$\sigma_{y'}^2 = \frac{\lambda_n}{2L} \sqrt{1 + 16n^2 N_w^2 \sigma_\delta^2} + \frac{\varepsilon_y}{\beta_y}, \quad (4.61)$$

where  $n$  is the harmonic of the ID being used,  $N$  the number of periods,  $L$  the length of the ID,  $\sigma_\delta$  the momentum deviation,  $\varepsilon_y$  the vertical emittance of the electron beam, and  $\beta_y$  the vertical beta function of the lattice at the insertion device location.

For NSLS-II,  $\varepsilon_y \sim 8 \times 10^{-12}$  nm·Rad and  $\beta_y \sim 1$  m at the ID straights,  $L \sim 3$  m,  $N \sim 100$ . Because of the  $n^2$  dependence, the worst case is for  $n \gg 3$ , where the two terms on the right hand side of Eq. (1) are comparable. Thus, using Eq. (4-5.1), for a 10 % increase in beam size, the momentum jitter must be 44% of the inherent momentum spread—or equivalently, a phase jitter of 1.4 degrees.



A third limit on momentum spread is due to longitudinal energy oscillation leading to filamentation and increase in beam size. With a momentum kick  $\Delta p/p$  to the bunch, an electron would have a longitudinal oscillation:

$$\delta(t) = \left( \frac{\Delta p}{p} \right) \sin \nu_s \omega_0 t + \delta_0 \sin \nu_s \omega_0 (t + t_0). \quad (4-5.2)$$

Because of the longitudinal tune spread the two terms will de-cohere and become

$$\delta(t) = \left( \frac{\Delta p}{p} \right) \sin \nu_s \omega_0 (t + t_1) + \delta_0 \sin \nu_s \omega_0 (t + t_2), \quad (4-5.3)$$

where  $t_1$  and  $t_2$  are two random numbers. Averaging over  $t_1$ ,  $t_2$  and  $\delta_0$  we arrive at

$$\sigma_\delta = \sqrt{\frac{1}{2} \left( \frac{\Delta p}{p} \right)^2 + \sigma_{\delta,0}^2} = \sqrt{1 + \frac{1}{2} f^2} \sigma_{\delta,0}, \quad (4-5.4)$$

where  $f = (\Delta p/p)/\sigma_\delta$  is the relative kick factor. For a 10% increase in  $\sigma_\delta$ ,  $f \sim 0.65$  or  $\Delta p/p = 6.5 \times 10^{-4}$ . The corresponding phase jitter is given by

$$\Delta\phi = \frac{h\alpha_c}{\nu_s} \frac{\Delta p}{p}, \quad (4-5.5)$$

where  $h$  is the harmonic number (1320),  $\alpha_c$  is the momentum compaction factor = .00037,  $\nu_s \sim 0.0087$ , and  $\Delta\phi = 2$  degrees.

The transverse electron beam size and position are related to the momentum spread and average momentum, respectively. The beam size is given as

$$\sigma_{x,y} = \sqrt{\beta_{x,y} \epsilon_{x,y} + (\eta_{x,y} \sigma_\delta)^2}. \quad (4-5.6)$$

The residual dispersion  $\eta_y$  is of the order 1 mm and the second term is negligible in beam size. Vertical position is given as  $y = y_0 + \eta_y \langle \delta \rangle$ . The allowed centroid jitter is 10% of the beam size or  $0.3 \mu\text{m}$ ; therefore, the average momentum jitter should be less than  $3 \times 10^{-4}$ , with a corresponding phase jitter of 0.95 degrees. These limits are summarized in Table 4.6.1.

**Table 4.6.1** Longitudinal beam stability requirements

	Phase jitter (°)	Momentum jitter ( $\Delta E/E \times 10^{-4}$ )
Timing-dependent experiments	0.16	0.5
Vertical divergence (from momentum jitter)	1.4	4.4
10% increase in $\sigma_\delta$ due to filamentation	2.0	6.5
Vertical centroid jitter (due to residual dispersion)	0.95	3
Dipole, TPW Beam lines (Position stability due to momentum jitter)	0.32	1

Due in large part to the near zero dispersion in the ID straights which mitigates the effect of momentum jitter, the tolerance on the RF is dominated by the IR timing experiments.

The magnitude of the effect on the beam of RF phase and amplitude noise depends on whether the source of the RF jitter is random or harmonic (systematic). Sources of noise are broadly classified into continuum sources possessing a continuous and slowly varying (with respect to frequency) spectral density, and spurious sources that possess spectral lines, possibly varying in time. Examples of the former are the continuum component of synthesizer phase noise, amplifier shot noise, and the continuum components of other active devices in the RF system. Examples of the latter are line related and power-supply switching noise, microphonics, and vibration. To assess the impact of, and derive tolerances for, RF-system noise sources, we need to determine the beam's sensitivity to noise from identified sources and derive a tolerance budget. The sensitivities are to be determined by modeling the RF system's linear response to these sources. Noise magnitudes in existing machines are a starting point for noise intensities, from which sensitivities are used to determine where noise tolerances need to be tightened. This work is in progress, and will be expanded in the preliminary design phase. Digital low-level RF systems have achieved less than 0.1 degree phase and 0.1% amplitude stability [4.6.16], these tolerances should be sufficient for NSLS-II.

#### 4.6.4.2 Master Oscillator and Ring Frequency Synthesizers

The low-level RF and beam control design is at a preliminary stage of defining specifications and architecture. Unlike the power systems, which stay relatively static over long periods of time during the life of the machine and should be transparent to the user, the LLRF and beam control requirements may change several times as the machine evolves, so the design must be flexible. To this end a digital architecture is used.

An ultra stable Master Oscillator at the fundamental RF frequency is distributed to the storage ring, booster and linac RF stations as well as other systems such as bunch feedback systems and beam diagnostics. The Master Oscillator is software tunable to allow for a radial (frequency) loop to stabilize the beam orbit against slow drifts caused by diurnal or annual variations in machine circumference. The RF frequency is nominally  $499.68 \text{ MHz} \pm 20\text{kHz}$  to cover seasonal variations, machine studies (measurement of chromaticity, etc). For the sake of clarity in the description of the low level RF it will be assumed to be 500 MHz. The Master Oscillator is mixed with an IF frequency generated from the same master oscillator. The (RF+IF) frequency is used as a local oscillator for the up/down conversion of the 500 MHz RF signals. An example of such a system is shown in Figure 4.6.6. An IF frequency of 50 MHz is chosen resulting in a 550 MHz LO frequency. This has the advantage of having a common subharmonic in the ring revolution frequency ( $F_{\text{rev}}$ ) of 379KHz for both the RF ( $\div 1320$ ) and LO ( $\div 1452$ ). Thus, the  $F_{\text{rev}}$  can serve as a synchronization clock on system power-up for all of the ring, booster, and linac controllers as well as serve as a bunch zero clock for timing. The 10 MHz frequency standard for the Master Oscillator will be available as an external time base for other systems.

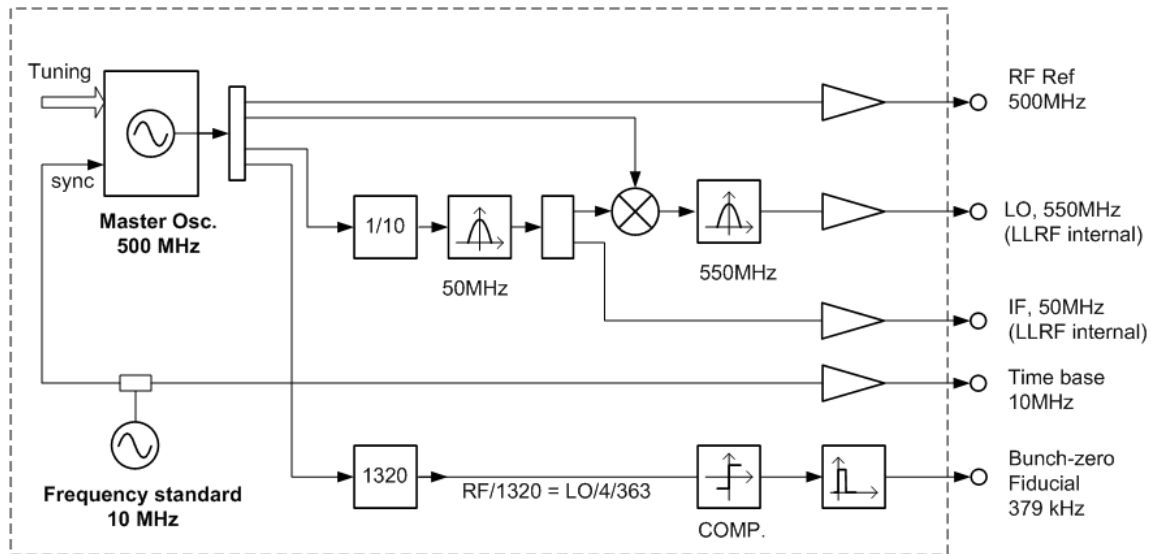


Figure 4.6.6 Master oscillator.

#### 4.6.4.3 Cavity Controllers

The cavity-amplifier system has several nested feedback loops to control the amplitude and phase of the RF cavity fields in the presence of beam-loading, mechanical perturbations to the cavity, and residual klystron noise due to power line/DC power supply ripple. The innermost loop is the tuner loop, which tunes the cavity resonance in order to present a purely resistive impedance to the klystron, thus minimizing klystron power. This loop, which is closed around a mechanical tuner, is slow—on the order of 1 Hz. Next is an RF feedback loop that is used to adjust the impedance of the main-cavity accelerating mode. In order to stabilize the cavity fields against fast perturbations, an amplitude and phase loop around the klystron-cavity chain is implemented. Although these can be independent loops, it is more effective to combine them in a common In-phase and Quadrature (I/Q) modulation loop, due to the coupling of the loops by cavity detuning for beam loading.

In addition to the above RF, amplitude, phase, and tuner loops, it may be necessary to implement other loops. A loop for zero-order coupled-bunch-mode feedback from the beam to the RF system to damp Robinson or higher-order longitudinal instabilities may be necessary. A klystron scalar phase loop to reduce the DC power supply induced the klystron, and possibly a feed-forward loop on the anode modulation of the klystron for maximizing klystron efficiency under different operating conditions, may also prove useful.

With the exception of direct RF feedback, the above loops can be implemented in either analog or digital hardware. Analog systems have the advantage of being simpler and less expensive to produce, and have higher speed and bandwidth. Their disadvantages include the lack of flexibility in changing loop characteristics for varying beam loading, slightly less phase and amplitude accuracy, and DC shifts that are more difficult to control. Digital implementation has the advantage of flexibility, in particular of being able to synthesize the loop filters digitally so that the feedback loops can be programmed for different machine states. Higher accuracy can be achieved, and DC drifts are easier to control. This comes at the price of higher complexity, and requires an additional skill set in high-speed digital design. Careful attention must be paid during the design stage to design in “digital probes” and other debugging tools to monitor and allow trouble shooting of the digital feedback loops.

To maximize the performance of the RF system and allow simple optimization and upgrades over the life of the machine, a digital implementation is our choice for NSLS-II.

The low-level RF cavity field control will be via a digital I/Q modulator-demodulator incorporating up and down conversion, ADCs and digital-to-analog converters (DACs) interfaced to the digital baseband signal processing, a Field Programmable Gate Array (FPGA) state machine, and interface to the control system. Similar systems have been designed for both hadron and electron machines in recent years [4.6.18, 4.6.19].

Although the booster and linac RF systems are simpler since they do not have the tight RF specifications of the storage ring, and harmonic cavities are easier because they are passive with only tuner control, we will use identical ring controllers throughout, with up and down conversion from 500 to 1500 and 3000 MHz. The only difference will be how the control loops are programmed and their control system graphical user interfaces. This makes the control system integration easier to manage with I/O, yet memory buffers for fault analysis, development tools, and maintenance identical.

The controller is derived from the LBNL LLRF4 design [4.6.20]. Five RF input channels support measurement of the forward, reflected, transmitted, and reference phase RF signals plus a beam pickup signal. The 14-bit input ADCs are clocked at 68.75 MS/s derived by a divide by eight from the 550 MHz LO. Two Direct Digital Synthesizers (DDS) built into the FPGA provide two output IF frequencies via DACs clocked at 137.5 MHz (LO divide by four). These are up-converted to the cavity drive and an RF calibration signal.

A conceptual design of the digital controller is shown below in Figure 4.6.7.

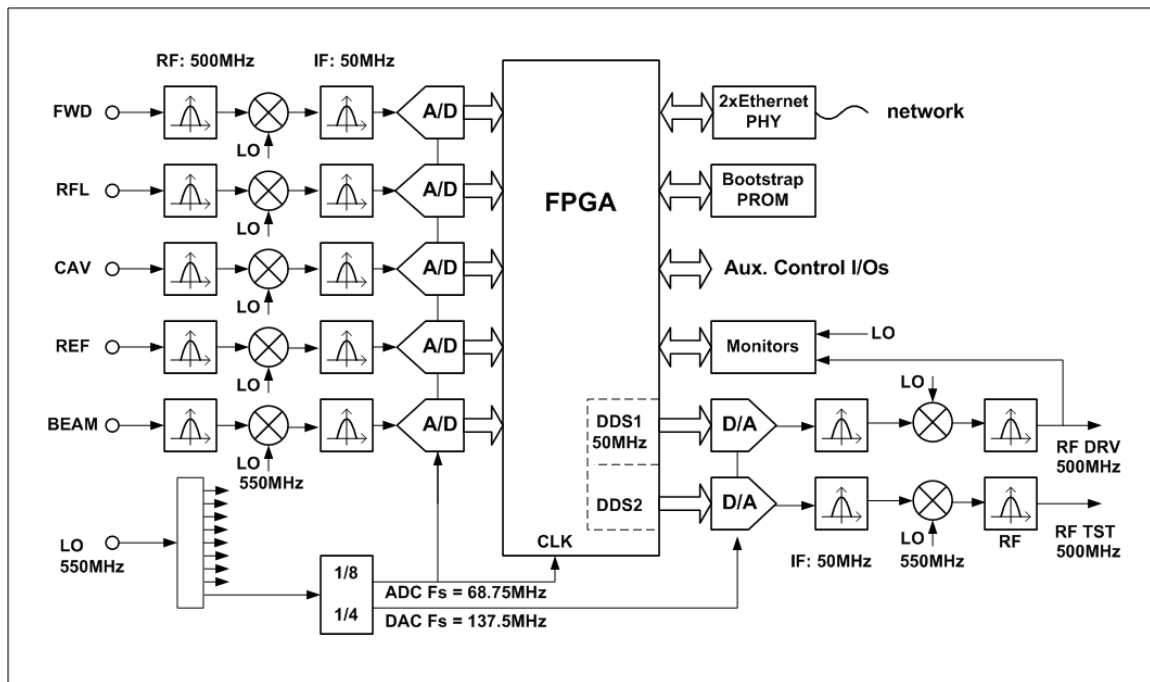


Figure 4.6.7 500 MHz Cavity controller.

Feedback algorithms within the FPGA logic will provide low frequency stabilization of the RF fields, with the phase auto-zeroed to the phase reference line. It will also adjust the fundamental RF cavity dynamic impedance for maximum stability, using information from a beam phase pickup and from the landau cavity fields.

In addition to the fast RF loops, a slower cavity tuning loop measures the phase shift between the cavity input and output, and adjusts the cavity tuner for optimum phase (usually coinciding with minimum reflected RF power). The landau cavity, since it is a passive cavity, has only this tuner loop. In order to use the same cavity controller, an additional LO frequency of 1000 MHz (2x RF frequency) will be used to down-convert

from 1500 to 500 MHz, from which point the hardware will be identical to the fundamental system. A fully built-out RF straight is shown in Figure 4.6.8 below.

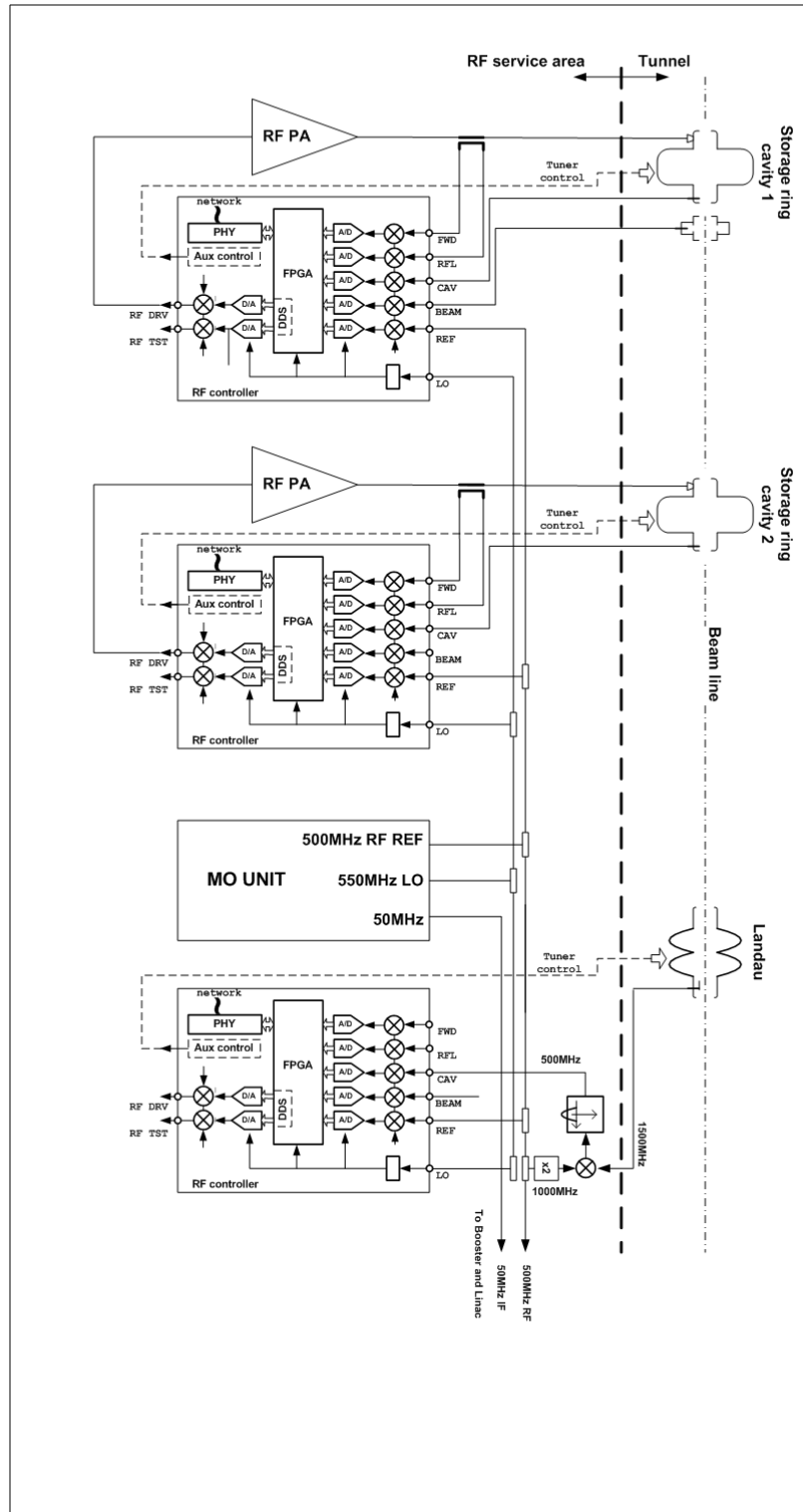


Figure 4.6.8 Storage ring system configuration.

The booster RF is very similar to the ring RF, with the exception that beam phase feedback is not expected to be included. Since the 500 MHz RF reference and the 50 MHz LO are distributed from point to point, the 550 MHz LO must be generated at the booster. It is shown in Figure 4.6.9. Identical up/down conversion from 50 MHz IF to 500 MHz RF will be used, as in the storage ring.

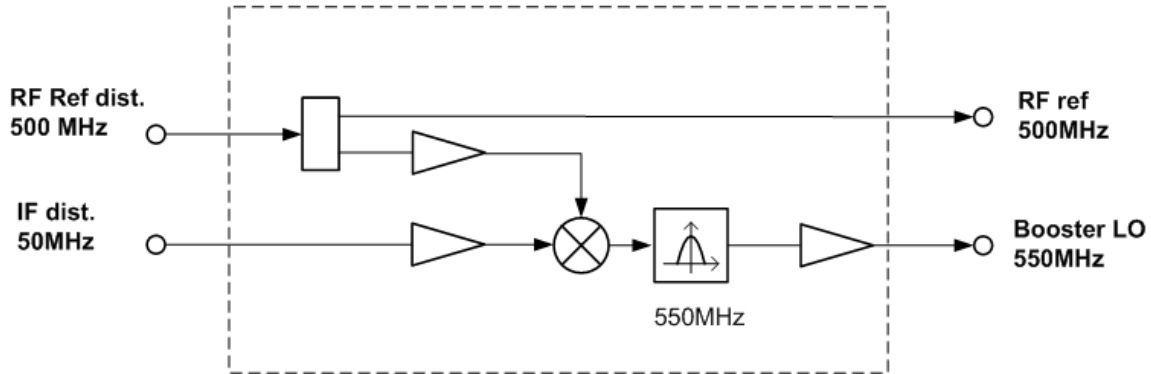


Figure 4.6.9 Booster LO generation.

The linac consists of a 500 MHz subharmonic buncher, a 3000 MHz pre-buncher with independent amplifier (and hence controller), and three klystron amplifiers. The first klystron output is split and drives a final buncher through a high-power attenuator/phase shifter and the first accelerating structure directly. The second and third klystrons drive their respective accelerating structures directly. Thus, one 500 MHz and four 3000 MHz systems need RF control. Again, to use identical RF cavity controllers the 3000 MHz signals are up/down-converted with a double conversion using 2500 MHz and 550 MHz LO frequencies. The LO generation is shown in Figure 4.6.10.

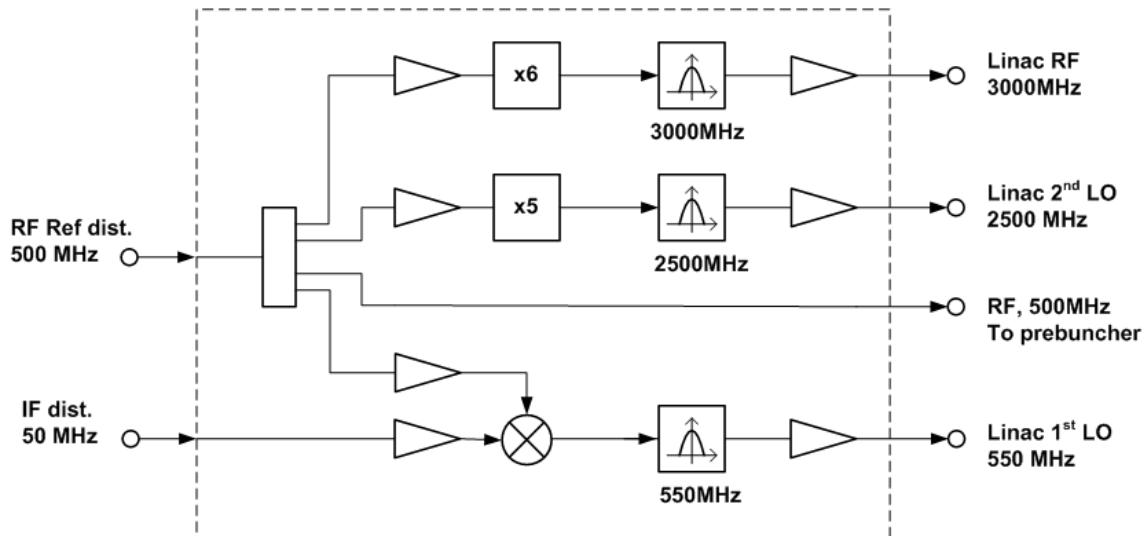


Figure 4.6.10 Frequency synthesis at the linac.

The controllers' 50 MHz IF frequency is first up-converted to 500 MHz using the 550 MHz LO, as in the 500 MHz systems. Then it is up-converted to 3000 MHz using the 2500 MHz LO. A system schematic is shown in Figure 4.6.11.

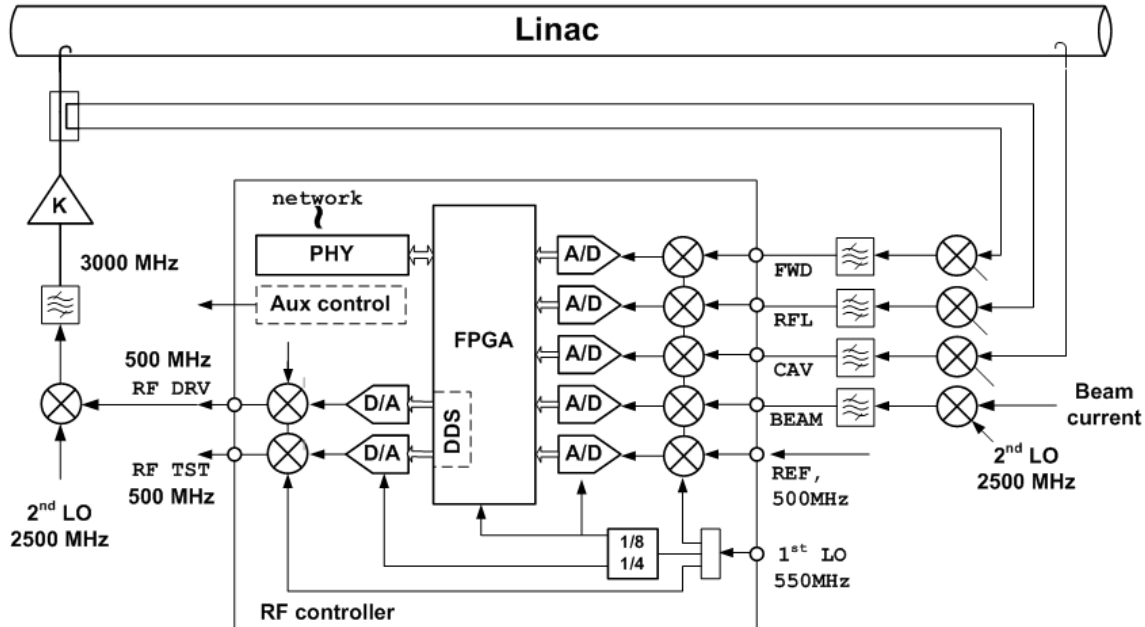


Figure 4.6.11 Linac up/down conversion and controller architecture.

## References

- [4.6.1] W. Brauns, [www.gdfidl.de](http://www.gdfidl.de)
- [4.6.2] K. Halbach and R. F. Holsinger, "SUPERFISH - A Computer Program for Evaluation of RF Cavities with Cylindrical Symmetry," *Particle Accelerators* **7** (1976) 213-222.
- [4.6.3] D. Myakishev, "CLANS2 - A Code for Calculation of Multipole Modes in Axisymmetric Cavities with Absorber Ferrites," *Proceedings of the 1999 Particle Accelerator Conference, NYC*.
- [4.6.4] R. A. Rimmer et al., "An RF Cavity for the NLC Damping Rings," *Proceedings of the 2001 Particle Accelerator Conference*.
- [4.6.5] S. Mitsunobu et al., "Status and Development of Superconducting Cavity for KEK-B," *Proceedings of the 1997 Particle Accelerator Conference*.
- [4.6.6] J. Kirchgessner, *Part. Accel.* **46**(1):151 1995.
- [4.6.7] K.W. Robinson, CEAL-1010, Cambridge Electron Accelerator, Cambridge, MA (1964).
- [4.6.8] Y. Miyahara et al., "Equilibrium Phase Instability in the Double RF System for Landau Damping," *NIM A-260* (1987) p 518-528.
- [4.6.9] R.A. Bosch et al., "Robinson Instabilities with a Higher-Harmonic Cavity," *Phys Rev ST-AB* **4**, p. 74401 (2001).
- [4.6.10] M. de Jong et al., *J. Microwave Power Electromagnetic Energy*, **27**:136-142, 1992.
- [4.6.11] M. Jensen et al., "First Results of the IOT Based 300 kW 500 MHz amplifier for the Diamond Light Source," *PAC 2005, Knoxville, TN*.

- [4.6.12] F. Perez et al., “New Developments for the RF System of the ALBA Storage Ring,” EPAC 2006, Edinburgh, Scotland.
- [4.6.13] P. Marchand, et al., “High Power (35 kW and 190 kW) 352 MHz Solid State Amplifiers for the SOLEIL Synchrotron,” PAC 2005, Knoxville, TN.
- [4.6.14] Hanspeter Vogel, ACCEL. Private communication.
- [4.6.15] M. Svandrlík, et al., “The Super-3HC Project: An Idle Superconducting Harmonic Cavity for Bunch Length Manipulation,” EPAC 2000.
- [4.6.16] S. Simrock, “Digital Low-Level RF Controls for the Future Superconducting Linear Colliders,” PAC 2005, Knoxville, TN.
- [4.6.17] C.W. Horrabrin, and D.M. Dykes, “Diamond Low Power RF System,” EPAC 96.
- [4.6.18] J.M. Brennan et al., “RHIC RF beam control,” EPAC-2001.
- [4.6.19] M. Liepe, S. Belomestnykh, et al., “A New Digital Control System for CESR-C and the Cornell ERL,” PAC 2003, Portland, OR.
- [4.6.20] <http://recycle.lbl.gov/llrf4/>





## 4.7 Cryogenic Systems

### 4.7.1 Cryogenics System Overview

A helium closed-cycle cryogenic system is necessary to provide liquid helium to the Superconducting Radio Frequency (SRF) cavities. Baseline operation will require two 500 MHz (fundamental) and one double cell, 1500 MHz (harmonic) SRF modules which must be maintained at approximately 4.5K during operation of the storage ring. An identical configuration will be required for full operation at later date. Therefore, the cryogenic plant is sized versatile to accommodate sufficient cooling capacity for eventual full operation, four 500 MHz and two 1500 MHz SRF modules. The cryogenic system includes a refrigerator/liquefier cold box, a main compressor and a recovery compressor with oil removal systems, One LHe dewar, one valve box, liquid helium (LHe) and liquid nitrogen (LN2) transfer lines, gaseous helium (GHe) storage tanks, and a GHe management system, instrumentation, controls, and safety devices. Each 500 MHz and 1500 MHz module has 500L and 60L storage capacities, respectively, and runs with 400L and 50L He during operation.

### 4.7.2 Factors Influencing Cryogenic System Design

#### 4.7.2.1 Single versus Multiple Refrigerators

The refrigeration system needs to have high reliability with near-zero unscheduled downtime. Using risk and failure analysis criteria, a study to determine the source of unavailability was undertaken in the past by the TESLA collaboration at DESY, with results shown in Table 4.7.1 in the order of their occurrence frequency.

**Table 4.7.1. Rating of refrigerator system unavailability.**

Rating	Topic	Example	Multiple Refrigerators
1	External Utility Failure	Electrical power, cooling water, instrument failure	No advantage
2	Blockage by frozen gas or impurities	Air and/or water vapor	Somewhat larger risk tolerance provided
3	Operational problems	Operators, controls, instrumentation,	Greater risk due to more system complexity
4	Single component failure not leading to total plant shutdown	Electrical motor burnout, compressor bearings, leaking oil pump seal, turbine bearing trouble	No advantage over component redundancy within a single refrigerator
5	Catastrophic component failure leading to plant shutdown	Loss of insulation vacuum, rupture of heat exchanger, oil spill into cold process piping	Would have a positive effect

The information in this table suggests that major downtimes are likely to occur as a result of catastrophic component failure; the effect of any of the other four occurrences is relatively negligible. Therefore, we selected a single refrigerator with a full inventory of spare critical components. Also, we will develop procedures that follow the manufacturer's recommended maintenance schedule.

#### 4.7.2.2 Partial versus Full Loads

The reliability factor is increased by designing refrigerators that are capable of operating efficiently at partial load. When the accelerator is operated at reduced load, or when all modules are not in use, the electrical power and utility usage will be proportionally reduced. This could be achieved in two ways, operating the cold box (CB) without a LN2 pre-cooler during the baseline operation and by automatically

varying the speed of the compressor (and therefore mass flow rate of the main compressors) by incorporating a variable frequency driver (VFD) system.

#### 4.7.2.3 With or Without Gas Purity Monitoring System

Gas impurities have an adverse effect on R/L efficiency. Air, for instance, solidifies at approximately 50K. Small solidified air particles can damage the expansion turbine, which runs at a high rotational speed; thus the concentration of impurities in the helium gas must be maintained at less than 10 ppm. The R/L internal dual 80K absorbers, coupled with a constant gas purity monitoring system, will serve as the main source of purification and as the feedback system. No external purifier has been considered, since a redundant internal adsorber with automatic reactivation and switch-over features is judged to be cost effective and the reliability is not compromised.

#### 4.7.2.4 Heat Load Budget

There are two types of heat loads: static which come from thermal conduction and radiation, and dynamic which result from beam operation. The static heat loads of the SRF cavity cryostats are based on measured values of similar cryostats in other synchrotron facilities. The dynamic heat loads are calculated based on physics requirements. Heat loads associated with transfer lines, valve boxes, dewar losses, and other components are combination of estimated values based on information provided by vendors, engineering calculations, and professional judgment. Table 2 itemizes the estimated static and dynamic heat loads of the superconducting cavities and associated cryogenic components at 4.5K for both baseline and full operation.

The projected LN2 required by the R/L pre-cooler heat exchanger and other components heat shields is listed in Table 4.7.2 for both the initial and full system.

**Table 4.7.2 Liquid nitrogen consumption estimates.**

Component(s)	Per Cavity [L/hr]	Two Cavities + 1 Harmonic [L/hr]	Four Cavities + 2 Harmonic [L/hr]
500 MHz cavity	10	20	40
Harmonic cavities	10	10	20
Cold Box		23	45
RF valve box	–	12	24
Transfer lines (1 W/m), 50 m	-	2	4
Subtotal		67	133
Margin (20% of subtotal)		14	27
Total		81	160

The waveguides of each 500 MHz and 1500 MHz cavity require 0.134 g/s and 0.174 g/s of cold helium for cooling, respectively (Table 4.7.3). These are the liquefaction load to the R/L, and are equivalent to 4 L/hr and 5.2 L/hr of liquid helium. Therefore the liquefaction loads for the baseline and full operation are 13.2 L/hr and 26.5, L/hr, respectively.

**Table 4.7.3 Heat loads budget and refrigeration sizing.**

Cryo-Plant Heat Load Baseline Budget	Per Cavity	2 Cav. + 1 harm (Baseline)	4 Cav. + 2 harm (Full Operation)
Number of Harmonic 1500MHz RF (X)	1	1.00	2
Number of 500MHz RF (Y)	1	2.00	4
Total Number (Z)	1	3.00	6
500MHZ Cavity Operation		3.3MV/2	5MV/4
Q (*10 <sup>9</sup> )		0.75	0.75
<b>Background Heat Load</b>			
Cavity beamtubes (RBT + FBT)*Y	13.8	27.60	55.2
Cavity Waveguide (conduction)*X	5.3	10.60	21.2
Waveguide cooling (0.134 g/s)*X	13.4	26.80	53.6
Cavity Rad. LN2 to Lhe (No MLI)*X	8.1	16.20	32.4
Harmonic (17.0W + 0.171 g/s)*Y	34.1	34.10	68.2
40, 80m Xfer Lines (0.2W/m)	8.0	8.00	16.0
2*1.6*Y*5m Xfer Line (1.6W/m)	16.0	48.00	96.0
Dewar Loss (static, Dynamic)	5.0	10.00	10.0
(Z*5W) SRF Valve Box; He only	5	15.00	30
Background TOTAL	108.7	196.30	382.6
150% background TOTAL	163.1	294.50	573.9
<b>Dynamic Heat Leak</b>			
V <sup>2</sup> /(89*Qo), 10 <sup>9</sup> )		81.60	93.6
Harmonic Cavity	22.0	22.00	44.0
TOTAL	22	103.60	137.6
150% TOTAL	33	155.40	206.4
<b>Standby/CD, Beam-off Load, W</b>			
Margin, 900 W R/L OP. W	791.3	703.70	517.4
Margin, 900 W R/L OP. Percent (%)	728.0	358.50	135.2
Available Liquefaction, LPH	197.8	175.90	129.4
Recover 400 Litters, Hours	2.0	2.30	3.1
<b>Standby/CD, 150% Beam-off Load, W</b>			
Margin, 900 W R/L OP. W	737.0	605.60	326.1
Margin, 900 W R/L OP. Percent (%)	452.0	205.70	56.8
Available Liquefaction, LPH	184.2	151.40	81.5
Recover 400 Litters, Hours	2.2	2.70	4.2
<b>Beam-on Grand Total Load, W</b>			
Margin, 900 W R/L OP. W	769.3	600.10	379.8
Margin, 900 W R/L OP. Percent (%)	588.6	200.10	73.0
Available Liquefaction, LPH	192.3	150.00	95.0
Recover 400 Litters, Hours	2.1	2.70	4.2
<b>Beam-on, 150% Grand Total Load, W</b>			
Margin, 900 W R/L OP. W	704.0	450.20	119.7
Margin, 900 W R/L OP. Percent (%)	78.2	50.00	13.3
Available Liquefaction, LPH	176.0	112.50	29.9
Recover 400 Litters, Hours	2.3	3.60	13.4
<b>100% Refrigeration, W</b>			
100% Liquefaction, g/s (Linde)	7.5		
100% Liquefaction, 1ph (Linde)	225.0		

#### 4.7.4 Design Approach

The main storage ring RF systems will initially consist of two 500 MHz (fundamental) cavities and one 1500 MHz (harmonic) Superconducting RF cavity. The cryogenic system must operate continuously for at least a full year before scheduled downtime. The design goal, therefore, was to provide a highly reliable and stable cryogenic system supported with required monitoring, alarms, interlocks, safety devices, and control system. As the cryogenic system must supply LHe to all of the RF cavities, redundancy of vulnerable components was considered, to ensure that continuous operations can be maintained effectively.

Total refrigeration cooling requirements were based on two sets of operating conditions: an initial baseline, and eventual full operations. Note that the cooling requirements for the full operation condition is approximately doubled compared with the baseline, since identical static loads are the dominant factor (Table 4.7.2). Therefore, the cryogenic system must minimally provide refrigeration power of 299.9W during baseline operation and 520.2W for the eventual full operating conditions. The Refrigerator–Liquefier (R/L) is oversized (150% margin) to enhance reliability and account for contingencies on additional heat loads that may develop during detail design.

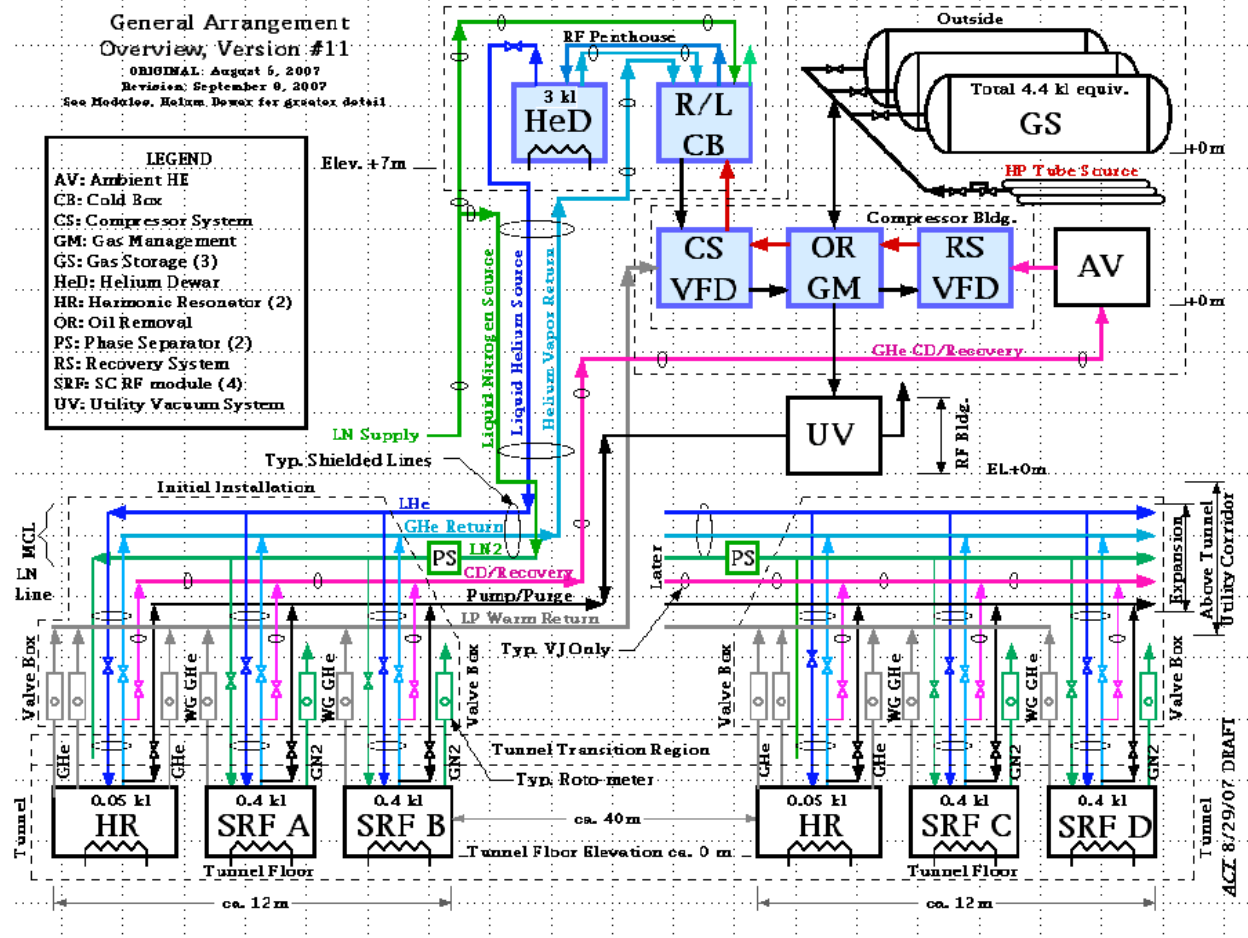
The SCRF modules are planned to be situated in two neighboring straight sections of the storage ring, 50 m apart in two groups of three SRF cavities: two 500 MHz fundamental cavities and one 1500 MHz harmonic cavity.

The SRF cryogenic system General Arrangement (GA) shown in Figure 4.7.1 depicts the full operating condition with capability to run at baseline. The design approach is primarily based on commercial helium R/L CB, main and recovery compressors, Variable Frequency Drivers, oil removals, helium dewars, and gas management systems. The design of the transfer lines, warm pipes, valve box, and control system will be defined during detailed system design.

General Arrangement considerations define distribution lines of equal length, locating the source LHe dewar at the approximate center of the 50 m (i.e., 25 m laterally from each module group). The distribution/return lines are listed in Table 4.7.4.

**Table 4.7.4 Distribution of Source/Return Lines**

Lines Description	Source/Return
Liquid Helium, 4.4K saturated	LHe dewar
Helium Vapor Return	Cold Box
Liquid Nitrogen, saturated at 25 psig	Phase Separator
Cool-down/Recovery:	
Warm-up, power failure	Cold Box or Ambient Vap
W Pump and Purge, utility vacuum	Utility Vacuum System
LP Warm Return, e.g., vapor cooled	Compressor Suction
Nitrogen exhaust, vents to atmosphere	Valve Box Vent



Lines a, b, and c are arranged so the liquid nitrogen flow radiation-shields the He lines, and all are contained in a common insulating vacuum jacket. The CESR creators of this arrangement have dubbed this configuration, as implemented with VCR and Conflat fittings at the ends of each section, the Multi-Channel Line (MCL).

The Cool-down and Recovery line, d, provides for temporary flows and may be efficiently provided as a standard, standalone, and relatively inexpensive vacuum-jacketed transfer line commonly used for liquid nitrogen. The recovery flows (loss of power, rapid warm-up), are diverted from the cold box to an ambient vaporizer (which may be augmented with an electrical heater for extreme cold weather conditions) to assure that the recovery compressor suction stays sufficiently warm.

The Pump and Purge line, e, will be sized for efficient pumping speed with the specified Utility Vacuum System pumping speed. The Utility Vacuum System vacuum pump will be, for line size considerations and costs, located in the RF building near the tunnel straight section middle.

The Low Pressure (LP) return line, f, collects and returns GHe from the waveguide and other warm-return flows to the compressor suction.

The cryostats' LN2 shield is vented to the outside tunnel with a gaseous nitrogen exit temperature sensor and a modest flow control.

Isolation and removal of a warmed module from an otherwise cold system in standby situation will require absolutely tight shutoff valves and the necessary procedures to verify their tightness. The safe

installation and operation procedure will be developed during detail design. However, clearly, all of the Valve Box valves will be normally in closed position, i.e., “fails closed” in the event of loss of signal or power. The operation of all essential components (such as control valve signals) will be hooked to the emergency power system in case of main power failure. Full descriptions of each subsystem are given in the following sections.

#### 4.7.5 SRF Modules, System Layout

The two 500 MHz (fundamental) and one double-cell 1500 MHz (harmonic) SRF modules will occupy a single straight section. A designated space in the adjacent long straight section is planned for identical configuration for the fully built-out machine. These two neighboring straight sections are near the linac and the control room.

The cold box and the LHe dewar is planned to be located in a mezzanine deliberately placed almost at equal distance from each straight section. The valve box(es) will be located on the tunnel’s roof, connected to the LHe via MCL and the modules via single VJ lines.

The compressor room, gas management buffer tanks, and LN2 dewar will be in a area detached from the main building to isolate induced vibration and noise.

Another room adjacent to the cryogenic and power supply rooms is planned for testing SRF modules prior to installation, for troubleshooting, and for R&D purposes.

Currently, four rooms are dedicated to the RF power supplies and cryogenic systems. These rooms will be adjacent to the RF straight sections, minimizing the waveguide length and heat load from the helium transfer lines between the cryogenic room and SRF modules. Two power supply rooms are directly adjacent to each RF straight section. The cryogenic room houses the refrigerator, LHe dewar, inter-connecting transfer lines, multi-channel distributing manifolds, and local control system. The adjacent RF test room is dedicated for pre-installation testing and R&D purposes.

#### 4.7.6 Refrigerator-Liquefier (R/L) Cold Box

For long term reliability with minimum maintenance, commercial R/L with gas bearing turbines will be used. Furthermore, the R/L shall be capable of operating over a large range of loads as required by the project. Comprehensive interaction with the potential vendors during this design stage has been conducted to insure best match between the system performance and operation requirements. The Linde LR280 R/L, shown in Figure 4.7.2, together with a variable frequency driven compressor (ESD441), is found to meet the present application and is used for illustration. Other potential vendors also have R/Ls of very similar characteristics.

As shown in Table 4.7.2, the expected heat load is 520 W for eventual full operation, to run four 500MHz and two 1,500MHz cavities simultaneously (with a 1.5 safety factor, the load could be 780 W). Thus, a 900W refrigerator is considered the best commercially available R/L system. For baseline operation, the expected heat load is 300 W (450 W with a 1.5 safety factor). The 900W refrigerator must be turned down to 450 W during baseline operation and to preferably to as low as 300 W in order to minimize operating costs. The excess refrigeration that can’t be turned down must be “burned” by a heater added to the LHe dewar to provide an artificial load; this is admittedly an inefficient solution.



Figure 4.7.2. Typical R/L cold box.

The Linde LR280/ESD441 is a 900W cooler at 4.4K, with three-turbines whose refrigeration can be turned down to 640 W by turning off the LN<sub>2</sub>, and by another 50% to 320 W by the use of a Variable Frequency Drive (VFD). The capacity curve for refrigeration vs. liquefaction is given in Figure 4.7.3. That almost meets the refrigeration requirements outlined above and seems an acceptable refrigeration turndown solution. However, a serious consideration has been made for the liquefaction component of the load, and especially in any case without LN<sub>2</sub> (elaborated below). Note that the large, single R/L system solution is the most cost effective of all those considered, provided that it can demonstrate a successful (operational and cost effective) turndown capability.

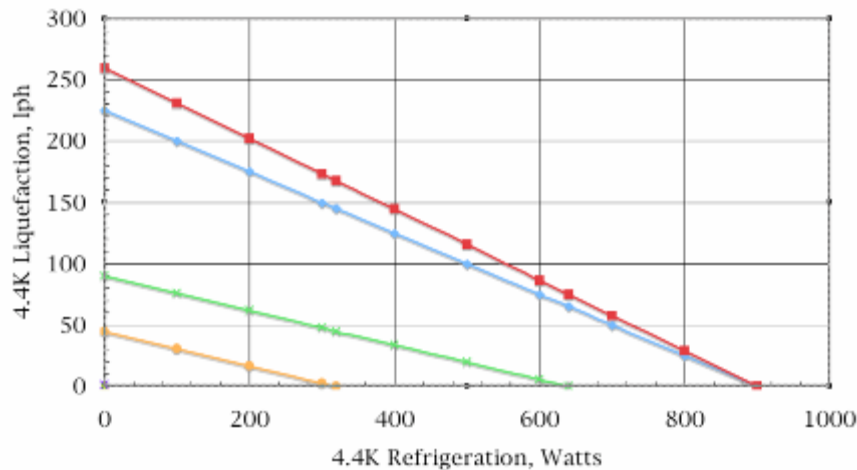


Figure 4.7.3 Liquefaction vs. refrigeration for LR280.

Red represents R/L with LN<sub>2</sub> and assumed 100 W/g/s.

Blue represents R/L with LN<sub>2</sub> and supplied data by Linde.

Green represents R/L without LN<sub>2</sub> and data supplied by Linde.

Orange represents R/L without LN<sub>2</sub> at 50% VFD, estimated by Linde.



#### 4.7.6.1 Special Turndown Consideration

The turndown refrigeration capability of the R/L is very desirable in the current application to efficiently address the initial half-system operation. Unfortunately, a major turndown mechanism, the removal of the LN<sub>2</sub>, seriously cripples the liquefaction capability in the face of a small yet substantial liquefaction load. That means that the sum of the liquefaction loads presented to the R/L operating without LN<sub>2</sub> is a far greater burden than that operating with LN<sub>2</sub>.

A possible solution of modulating (load tracks) of the LN<sub>2</sub> pre-cooling with the load for turndown (rather than just turn it “off”), will be examined during the detailed design. The first order approach to modulated LN<sub>2</sub> cooling would be to leave the LN<sub>2</sub> “on” while turning the VFD down. the 900W unit should be able to turn down to ~450 W (VFD to 50% speed/flow) in that way. A similar VFD turndown to 40% (assuming it is possible to turn down from 60 Hz to 24 Hz) speed/flow might get close to 360 W. At the 360W level, the excess refrigeration available in the half-system will be quite small in full operation, and the excess power costs too small to be of concern.

#### 4.7.6.2 Main Compressor System

All potential suppliers of the R/L use an oil screw compressor manufactured by Kaeser (Figure 4.7.4). Two ESD441 type compressors (one as hot standby) will provide the required 80 g/s flow at 15 bar absolute for the 900W R/L. The compressor skid consists of a bulk oil separator, a gas cooler, two stages of coalescers, an adsorber, and an oil cooler. The oil cooler is used to cool oil from the bulk oil separator for re-injection to the compressor.

Each compressor will be equipped with a Variable Frequency Driver (VFD), housed in an external cabinet. The drive motor of the compressor package is capable of varying speed between 20 Hz to 60 Hz (corresponding to one-third to full flow).

The screw compressors are low-vibration machines that normally do not require massive foundations. Vibration dampers, however, will be identified and implemented at the time of installation. All compressors will be housed in a separate building away from the main building to eliminate any possible vibration transmittal.

#### 4.7.6.3 Recovery Compressor System

A smaller screw compressor, 12 g/s mass flow, will be used to pump boil-off helium to storage tanks in case of a power failure. This recovery compressor is to be equipped with uninterrupted power supply and automatically start. This compressor will have same pressure characteristics as the main compressor. The start time of emergency power will be about 20 s, to avoid the difficulty of starting at high suction pressure.



**Figure 4.7.4** Typical Kaeser helium compressor.

### 4.7.7 Liquid Helium Dewar

The LHe dewar is the repository of the stored LHe heat of vaporization and concurrently the cooling source for the LHe cooled loads. Most of the R/L load is a refrigeration load; the condensed liquid is evaporated at the load and the returned cold vapor is utilized to create new liquid in a continuous R/L loop. A small portion of the R/L load, the waveguide heat intercept of the 500 MHz cavities and all the beam tube conduction and radiation cooling of the 1500 MHz cavities are in liquefaction loads ( i.e., LHe is evaporated, warmed to room temperature and returned directly to the compressor suction).

The He dewar capacity has been set at 3,000 liters to 1) contain liquid inventory needed at any one time; 2) store liquid for limited period deficit (loads larger than the available refrigeration of rapid filling) operations; and 3) as a repository for recondensed and accumulated liquid in anticipation of its protracted, excessive, use. Helium operating inventory is 400 liters per SCRF CESR-B and an assumed 50 liters per Harmonic Resonator module, for a total of  $1,600+2(50) = 1,700$  L. An operating storage level of 500 to 1,000 L would provide the space for a 3,000L dewar to recover the entire cavity inventory as liquid (desirable in a short-term scenario), with a margin for the significant mass of saturated He vapor in a mostly empty dewar. See Table 4.7.4 for the system inventory.

**Table 4.7.4 Helium system inventory.**

Nominal inventory, liquid helium (liters equiv.)	250 psig ASME gas storage	3,000 liter 1% LHe dewar	4+2 cryostats cap. = 1.7 kl	HP Source, standby trailer
Warm	>3,500	0	0	$\geq 1,200$
Standby	1,000	2,500	0	$\geq 1,200$
Operate	1,000	800	1,700	$\geq 1,200$
Shutdown	>3,500	0	0	$\geq 1,200$

The He dewar will be specified as a required part of the R/L vendor supply to include the R/L connecting lines, an auxiliary inlet/outlet(s) (for feeding the dewar from an external source, should this be necessary), the dewar's heat leak rate, heaters, and instrumentation and control system. See Figure 4.7.5 for a schematic of a LHe dewar.

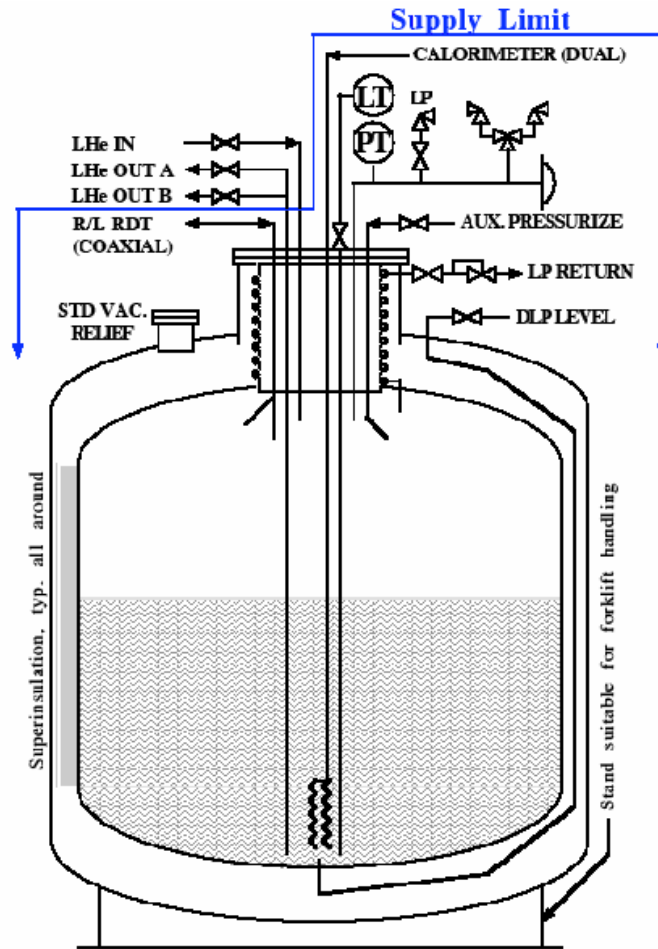


Figure 4.7.5 Schematic of the LHe dewar.

### 4.7.8 Liquid Nitrogen Dewar

A 10,000-gal LN<sub>2</sub> dewar will supply LN<sub>2</sub> to the SRF cryogenic plant. This dewar will be filled from the facility's LN<sub>2</sub> storage tank via a vacuum-jacketed line with automatic fill control system. A LN<sub>2</sub> Phase Separator will assure a single-phase flow to the SRF module at a constant pre-set pressure to support steady SCRF module shield and intercept cooling flows. The single phase and isothermal cooling at a constant (phase separator regulator controlled) pressure will contribute to predictable and reliable module liquid nitrogen cooling performance.

### 4.7.9 Gaseous Helium Storage Tanks

The warm gas storage water volume of about 6,250 scf (46,875 gal) will be sufficient to provide storage for an equivalent of 3,500 LHe to 14 bar pressure. Two 30,000 or three 20,000-gal tanks will have sufficient volume with room to spare. The total capacity of either these options is  $14 \times 60k / 7.5 / 25 = 4,480$  liquid liters equivalent.

These tanks will be designed for an internal pressure of 20 bar and external pressure of 1 bar. The maximum operating pressure is about 15 bar and the minimum operating pressure is estimated at 2 bar. The design specifications will include all appropriate ASME Boiler and Pressure Vessel Codes, Section VIII,

Divisions I (Unfired Pressure Vessels) and IX (Welding and Brazing Qualification), and Safety Relief Valves. Material and other geometric features will be detailed before purchasing.

One 30,000-scf HP gas trailer (capacity ~1,200 liquid liter equivalent) can serve as a continuous warm (no maintenance) standby storage.

#### **4.7.10 Gas Management**

Helium inventory in the refrigeration system is automatically adjusted by the gas management system as the refrigeration/ liquefaction load changes. The gas management system will consist of typically two control valves. One valve automatically sends excess helium to the buffers (for example, during quenches or warm-ups) One valve adds helium to the system from the buffer tank when the liquefaction capacity is higher than flow recovered from loads.

These two valves work in concert with the bypass recycle valve, which automatically recycles excess flow from compressor discharge to suction. These two valves maintains proper amount of helium in the system according to variation in liquefaction or refrigeration rate of the R/L. A frequency driver will reduce the total cycle mass flow rate in case of excess flow from the compressors.

Pressure transmitters and indicators with analog or digital output will be installed on both the discharge and suction lines near the main compressors. Similar transmitters will be installed near the suction side of the distribution valves boxes. Safety relief valves shall be installed in both the suction and discharge line of the compressor.

Sufficient instrumentation ports with shut-off valves will be placed on both the discharge and suction lines in the compressor room and also on the high-pressure line near the refrigerators/liquefiers. The makeup/recovery control valves will be in the compressor room. Several other smaller ports will be located on both the discharge and suction lines of the compressors and oil removals for gauges, sensors, and gas sampling purposes.

##### **4.7.10.1 Vacuum-Jacketed (VJ) Liquid Helium Transfer Lines**

Single Channel Line (SCL) and Multi-Channel Lines (MCL) vacuum-jacketed cryogenic transfer lines will be used to transfer liquid or cold GHe among various components such as to/from the main LHe dewar, SRF distribution valve box, and SRF modules. These vacuum-jacketed lines will be constructed of high-quality seamless stainless steel tubing. The lines and mating connections will have minimum heat leak and will resist damage from thermal expansion and contraction.. The use of copper tubing to carry LN2 for cooling radiation shields will be permitted, provided the design conforms to all applicable codes.

In addition to combined pump-out/burst ports, the line will have pressure and temperature transmitters with digital or analog output signals for monitoring and interlock purposes.

##### **4.7.10.2 Vacuum-Jacketed Liquid Nitrogen Transfer Lines**

Different sizes of the LN2 transfer lines will require transferring appropriate flow rate among inter-connecting components. The fill line between the outside main LN2 tank and the SRF LN2 dewar located near cryogenic plant will be vacuum jacketed (reduce the cool-down consumption and added enhance safety) capable of handling large flow rate of 400 L/hr at 4 bar head pressure. The interconnecting lines between the SRF LN2 dewar and cryogenic equipment (L/R, valve box, LHe transfer lines, heat shields, SRF modules) will be designed as rigid and flexible lines with heat leak to be less than 0.5 W/m at 80K (exclusive of valves

and bayonets). The insulating vacuum space of the lines will take into account the relative humidity factor, dew point, and seasonal temperature variations to ensure it is condensation free at all times.

Suitable keep-full valves will be installed along the fixed lines to ensure single-phase liquid flow to designated components when pressure stability is essential (e.g., SRF modules). An insertion of a LN2 phase separator before the SRF modules will insure pressure stability requirements of cavities. Similar to LHe transfer lines, these lines will also have pressure and temperature transmitters with digital or analog output signals for monitoring and interlock.

#### 4.7.10.3 Warm Piping

In addition to vacuum jacketed lines, there are three sets of piping for warm helium:

- One suction line to transfer low-pressure helium gas from SRF modules (waveguides), valve boxes, to compressor's suction.
- one discharge line to transfer high-pressure helium gas from the main/recovery compressors to oil removals, and to either the refrigerators/liquefiers cold box or gaseous storage tanks
- one makeup/recovery line between suction/discharge of the compressors and GHe storage tanks.

These lines will be sized and designed according to the flow rate, allowable pressure drop and operating pressure and temperature conditions. Seamless Stainless Steel tubing/pipes, 304 or 304 L, will be used and constructed in conformance with all applicable codes.

#### 4.7.10.4 Power Failure Considerations

Cryogenic systems are susceptible to damage from abrupt power losses. Loss of electrical power could cause an unexpected system shutdown which would require continuous operation of the recovery compressor to recover generated boiled-off GHe to the helium storage tanks. The recovery compressor, main helium dewars, cryogenic distribution valve box, and the cryogenic electronics of the SRF modules require a sufficient source of emergency power, as does the Oxygen Deficiency Monitoring systems, which must have an Uninterruptible Power Supply (UPS) system. A 50 KW emergency power generator is dedicated to the cryogenic system.

The demands of He inventory recovery in the case of a protracted (greater than 10 minutes) power failure is shown in Table 4.7.5.

**Table 4.7.5 He inventory recovery demand during protracted (>10 min.) power failure.**

LHe, Cool Time	Units	500 MHz	1500 MHz	LHe dewar
Operating Volume	Liters	400	50	800
Quant. LHe liters	Liters	1600	100	800
HOV Available	Joules	3.65E+06	2.28E+05	1.82E+06
Unit LHe Load	Watts	40.6	34.1	5.0
LHe Load, total	Watts	162.4	68.2	5
Self Cooled	Hours	6.24	0.93	101.33

#### 4.7.10.5 Ambient Vaporizer

Power outages are most likely to create the largest recovery flow rates. An Ambient Vaporizer (AV), capable of handling  $\sim 288$  l/h ( $\sim 10$  g/s) cold GHe flow to warm-up the temperatures for safe operation of the compressors will be used.

#### 4.7.10.6 Valve Boxes

Two valve boxes are eventually required for full operation condition. One located near each RF straight sector location. One MCL (two total) will transfer both LHe and LN<sub>2</sub> to each of the two VB(s) (one for the baseline condition). Individual transfer lines, most likely flexible type, will be provided between each VB and the individual SRF modules.

A tentative 15 valve-arrangement package in a horizontal rectangular enclosure is shown in Figure 4.7.6. A total of 12 valves, three LHe feeds, three GHe returns, three helium cool-downs, and three LN<sub>2</sub>s is required per GA at this stage.

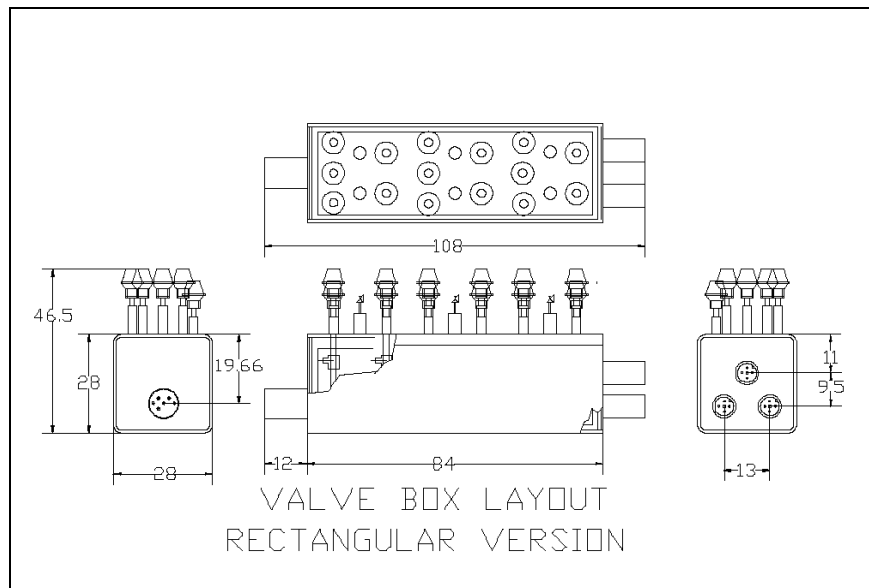


**Figure 4.7.6** Tentative valve box arrangements.

#### 4.7.10.7 Operating Modes

Process provisions for the complete installation/operation cycle must support the SCRF module operating modes as follows:

1. Independent Module Connection
2. Independent Pressure Test and Leak Check
3. Independent Pump and purge
4. Independent Liquid Nitrogen Cool-down
5. Independent Liquid Helium Cool-down and Fill
6. Independently Establish Readiness for Stable Operation
7. Independent Isolation and/or Warm up

#### **4.7.10.8 Independent Module Connection**

Although the SCRF modules have common feed and return manifolds, their inline isolation valves within the valve box (fully closed and secured) can create a complete isolation from all other modules. All transfer lines between the modules and the valve box will have separate vacuum with mating bayonets for installation.

#### **4.7.10.9 Pressure Test and Leak Check**

Each module upon complete connection shall be pressure tested and leak checked for safe operation. Only when these operations are successfully accomplished can a module be considered ready for pump and purge.

#### **4.7.10.10 Pump and Purge**

Each module shall be pumped and purged to strict criteria to protect the system from impurities. System contamination can dramatically undermine and/or preclude the designed performance of an otherwise reliable system.

#### **4.7.10.11 Liquid Nitrogen Cool-down (To about 200K)**

The LHe cool-down is accomplished by activating the module's liquid nitrogen shield and intercept flows. The radiation shield isolates, and the intercepts reduce, the conduction to the He temperature cold mass from the ambient world, providing cooling. After ~48 hours (in the case of routine CESR operation of a similar system), the module can be cooled to 200K by this arrangement. The cooling progress slows dramatically below 200K. That temperature value is the suggested benchmark to initiate the second and final stage He cool-down to 4K. Finally, the module is filled with liquid helium and the operating level is established and continuously maintained in automatic mode.

#### **4.7.10.12 Liquid Helium Cool-down to 4.5K and Fill**

The standard cool-down procedure accumulates liquid using the available liquefaction capacity and then consumes the liquid heat of vaporization and sensible heat (where appropriate) to cool the load. If the cool-down rate consumes liquid at a rate greater than liquid can be produced by the R/L, the main compressor pumps the excess mass to warm gas storage for later liquefaction. To put the issue in quantitative terms, the excess consumption over liquefaction could easily reach as high as 200 L/h, or about 6.7 g/sec, well within the recovery compressor's capability.

The recovery compressor can be seen to connect to provide cool-down and recovery directly via the CD/Recovery line and an ambient vaporizer outside of the gray dotted lines, as shown in the Figure 4.7.7 block diagram.

If the recovery compressor is to do a lot of standby or variable flow pumping it should be fitted with a VFD that simply reduces the RPM whenever the bypass valve opens and increases the RPM when it is closed. Supervisory logic can decide when it is useful to turn it on and off outside of the hard-wired power failure recovery function.

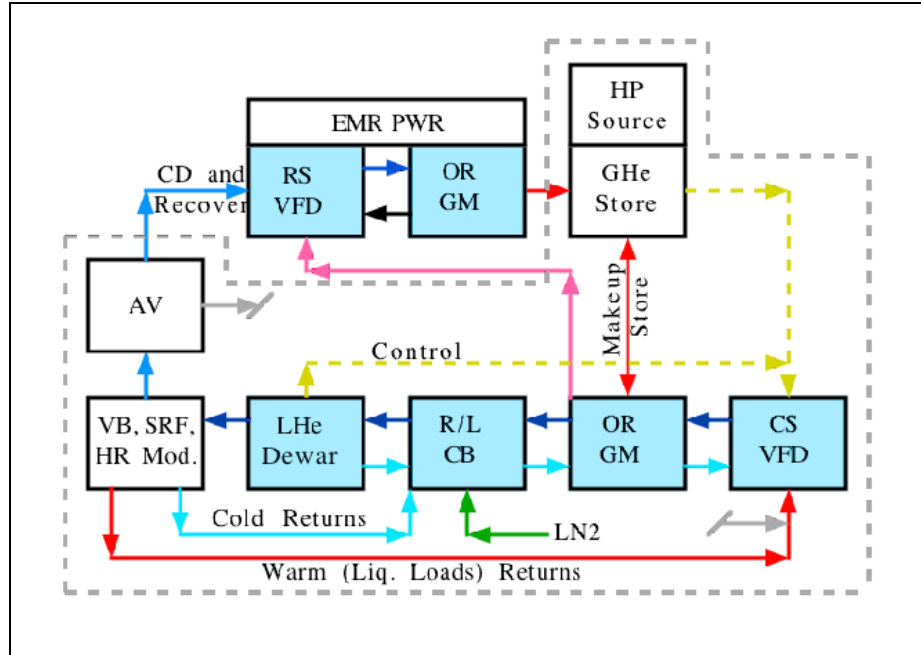


**Figure 4.7.7** Compressors and gas management block diagram.

#### 4.7.11 Establish Readiness for Stable Operation

Upon completion of cool-down to 4.5 K, each module is filled with 400 L of liquid helium or 80% of total volumetric capacity. The helium vessel's pressure, temperature and liquid level will be maintained at operating values and controlled by the local control system with monitoring and set-points accessible from the EPICS accelerator control system. The system is ready for operation when all pre-set parameters have been met and all safety interlocks are fully operational.

##### 4.7.11.1 Independent Isolation and/or Warm up

###### 300 K main SRF modules warm-up

This process isolates and warms-up the main SRF modules to ambient temperature, while the Main Cryogenic plant is cold. The liquid helium of the main SRF modules will boil-off by using cryostats DC (within 3 hrs) and recovered to the cold return line via the cryogenic distribution valve box and R/L cold box back to the compressor suction and gaseous helium tanks. The warm-up may include the cryogenic distribution valve box and main modules feed lines.

###### 10-20 K main SRF modules warm-up

The main SRF modules is warmed in the same manner as the 300K warm-up, but only up to 10K to get rid of the magnetic flux trapping in the superconducting state by warming the niobium bulk cavity temperature higher than its critical temperature or up to 20K for RF window conditioning. The liquid nitrogen in the radiation shield flows continuously.

###### 300 K Main Cryogenic Plan and main SRF modules warm-up

The main SRF module and Main Cryogenic Plant are both warmed to room temperature. The LHe dewar will, in general, continue to store liquid helium, but may be warmed as well.



### 300 K Main Cryogenic Plan awarm-up, cold main SRF modules

The Main Cryogenic Plant may be quickly warmed and then colled down to operating temperature again while the main SRF module is kept cold by liquid transfer from the liquid helium dewar.

#### 4.7.12 Equipment Elevations

A study of He System Head vs. Location for locating the R/L,d LHe dewar and the valve box either at floor level or elevated to the tunnel roof was conducted, with results shown in Table 4.7.6.

**Table 4.6.7 Various Equipment Location options.**

Item/Case	Cold Box	LHe dewar	Valve Box	SRF Cryostat
Case A	HB Floor	HB Floor	HB Floor	Beam
Case B	HB Floor	HB Floor	Tunnel Roof	Beam
Case C	Tunnel Roof	Tunnel Roof	Tunnel Roof	Beam
Case D	Penthouse	Penthouse	Tunnel Roof	Beam

In the first case, A, the equipment is located on the High Bay (HB) floor. The second case, B, puts only the valve box on the tunnel roof. The third case, C, puts the cold box and the He dewar on the tunnel roof along with the valve box. The last case, D, puts the cold box and the LHe dewar on the penthouse level and keeps the valve box on the tunnel roof.

The cold box and LHe dewar can be at an elevated level, centralized between two straight sections, to provide a large (in LHe terms) LHe dewar liquid head (Figure 4.7.8). The elevated location allows gravity to help transfer LHe from the dewar to the valve box and cryostat below, without the need to significantly pressurize the dewar, as would otherwise be required.

The valve boxes will be located on the tunnel roof directly above each straight section joined to the LHe dewar independently, by independent MCL(s).

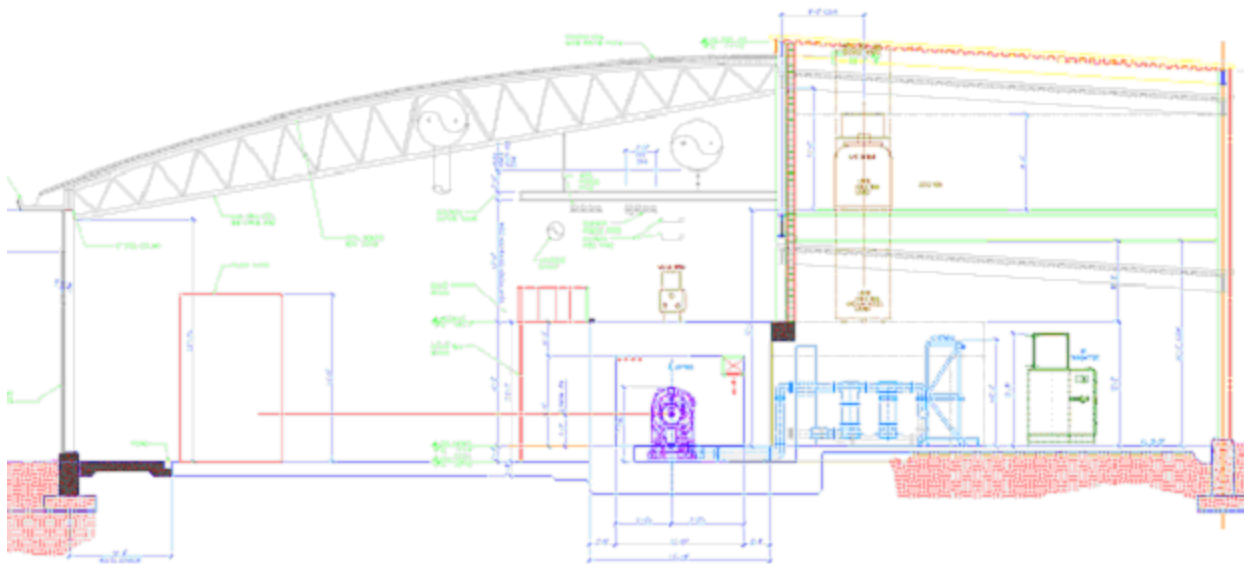


**Figure 4.7.8.** SRF Cryogenic system, elevation view.

The He dewar system head vs. different locations possibilities are tabulated in Figure 4.7.9. As a case in point, the dewar liquid head (see last entry in the first data column) of 1.531 psi is reduced by the cryostat liquid head (see the last entry in the cryostat column) of 0.240 psi, to provide the dewar-to-cryostat head of 1.291 psi. This is a respectable and constant LHe transfer pressure difference. Consequently, the R/L, LHe dewar, and valve box are planned to be on an elevated mezzanine with (sufficient overhead clearance), due to the highly technical advantage that case D represents. An alternative to this elevated equipment arrangement is to use a subcooler for stable LHe transfer throughout the system.

### NLS-II He System Head vs. Locations

Reference	Units	Dewar L	Dewar G	Cold Box	Cold Box	Valve Box	Cryostat
Helium		4.424K	4.424	313K GHe	300K GHe	4.424K	4.424K
Pressure		1.2	1.2	1.05 atm	13 atm	1.2	1.2
Density	g/cc	0.12080	0.02053	0.00016	0.00210	0.12080	0.12080
Density	kg/m <sup>3</sup>	120.800	20.530	0.164	2.101	120.800	120.800
Normalized		738.665	125.536	1.000	12.847	738.665	738.665
Location		HB Flr	HB Flr	HB Flr	HB Flr	HB Flr	Beam
Service El.	m	1.500	1.500	2.600	2.600	1.500	1.397
Ref. Head	kg/m <sup>2</sup>	181.200	30.795	0.425	5.463	181.200	168.758
Ref. Head	psi	0.257	0.044	0.001	0.008	0.257	0.240
Location		HB Flr	HB Flr	HB Flr	HB Flr	Roof	Beam
Service El.	m	1.500	1.500	2.600	2.600	5.640	1.397
Ref. Head	kg/m <sup>2</sup>	181.200	30.795	0.425	5.463	681.337	168.758
Ref. Head	psi	0.257	0.044	0.001	0.008	0.968	0.240
Location		Tunnel	Tunnel	Tunnel	Tunnel	Tunnel	Beam
Service El.	m	5.640	5.640	6.740	6.740	5.640	1.397
Ref. Head	kg/m <sup>2</sup>	681.337	115.793	1.102	14.161	681.337	168.758
Ref. Head	psi	0.968	0.165	0.002	0.020	0.968	0.240
Location		Pent	Pent	Pent	Pent	Tunnel	Beam
Service El.	m	8.917	8.917	10.017	10.017	5.640	1.397
Ref. Head	kg/m <sup>2</sup>	1077.151	183.062	1.638	21.045	681.337	168.758
Ref. Head	psi	1.531	0.260	0.002	0.030	0.968	0.240

Figure 4.7.7. Helium system head vs different locations.

#### 4.7.13 Instrumentation and Control

The functional analysis, consisting of the startup, shutdown, and regular and exceptional operating modes of the refrigerator will be written by the cryogenics engineer and then translated into the PLC logic for control of the refrigerator. This PLC must communicate with the PLCs embedded in the cold box, compressor, and cryo-module systems. In addition, there must be a seamless integration with the EPICS control system, allowing full control, monitoring, and history logging.

##### 4.7.13.1 Oxygen Deficiency Hazard Monitoring and Control System

Oxygen Deficiency Hazards are present when atmospheric oxygen content falls below 19.5% by volume. The BNL Standard Based Management System has strict guidelines in compliance with the Occupational Safety and Health Administration Respiratory Protection Standard 29CFR1910.134, Table 4.7.8.

The main potential sources of reduced oxygen are from unplanned discharge of cryogenics into confined spaces. Liquefied gases such as helium and nitrogen have the potential to cause ODH conditions, since expanded gases can displace air rapidly when released to the atmosphere.

For NSLS-II, a complete ODH analysis is required for each area (tunnel, cryogenic room, and compressor room), for all possible scenarios, in order to plan and put appropriate controls and measures in place. For the purpose of this report, an ODH classification of 1 is assumed, which among several requirements mandates the implementation of personal oxygen monitoring systems.

**Table 4.7.8. ODH Control Measures.**

Environmental Controls	ODH Class				
	0	1	2	3	4
1. Warning signs	■	■	■	■	■
2. Ventilation			■	■	■
3. ODH-Qualified Personnel Controls					
4. Medical approval as ODH-qualified		■	■	■	■
5. ODH training	■	■	■	■	■
6. Personal oxygen monitor		■	■	■	■
7. Self-rescue supplied atmosphere respirator		■	■	■	
8. Multiple personnel in communication			■		
9. Unexposed observer				■	■
10. Self-contained breathing apparatus					■

Gas monitoring systems, such as Safe T Net 410 (up to four channels), have been considered for installation in each area. These microprocessor-based controllers are designed to accept up to four combustible oxygen transmitters. Features include digital readout display, LED alarm indication, 4 to 20 mA output, individual low and high alarm, and relay signals for interlock purposes.

#### 4.7.14 Preventive Maintenance Programs

The overall availability of the cryogenic system is defined as the ratio of the actual delivery time to the scheduled operating time. Synchrotron light source facilities are normally operated continuously, 24 hours per day, seven days a week, excluding short studies or maintenance periods and one or two extended periods of machine maintenance per year when the facility is shut down for preventative maintenance, upgrades, and repairs. This is necessary to decrease the number of unscheduled breakdowns. Routine preventive maintenance must therefore be conducted according to the manufacturers'

## 4.8 Beam Scrapers and Photon Absorbers

### 4.8.1 Beam Scrapers

Two pairs of electron beam scrapers will be used for accelerator physics measurements of the aperture and beam lifetime limits. The thickness must be  $\sim 5X_0$  (radiation lengths) for the electron beam. The horizontal blades must be in the same plane and adjustable from full open (vacuum chamber width) to the chamber centerline with a resolution of  $\sim 1 \mu\text{m}$  and a reproducibility of  $\sim 5 \mu\text{m}$ . One location for the horizontal scrapers is in one of the dispersion regions next to the BPM and the SF2 sextupole, where there is high  $\beta_x$  and dispersion. The second location for horizontal scrapers is in the SID between the QL2 and SL2 sextupoles, the maximum  $\beta_x$  for the ring. The two vertical scrapers will be placed near the high  $\beta_y$  in the dispersion region (drift space at  $\Delta\mu_y \sim \pi/2$  from the injection septum) and the LID (drift space at  $\Delta\mu_y \sim 2\pi$  from the injection septum). These scrapers will provide controlled physical apertures to prevent large-amplitude particles (from the injector) from hitting the small-gap undulators, later in the ring. The scrapers will also provide defined apertures for understanding the dynamic aperture and lifetime in the ring.

#### 4.8.1.1 Preliminary Design

To maximize their effectiveness as well as to simplify their engineering design, the two pairs of beam scrapers required will actually consist of four separate units: two horizontal and two vertical scrapers. These scrapers will serve as protective devices for the IDs. They will also be used as diagnostic tools during the commissioning phase and during machine studies.

Previous reports [4.8.1] have indicated that Touschek scattering is the dominant source of ID damage. Work done at APS has shown that scrapers should be located in a low-emittance lattice to effectively protect the IDs. This suggests that the horizontal scrapers should be installed where there is adequate dispersion at the scrapers as well as a large horizontal beta function. Touschek scattering presumably not only imparts a large energy deviation, but also induces large betatron oscillations for the scattered particles. A significant concern, however, is that the scrapers may compromise injection efficiency—or worst yet, may even produce more ID damage if the injected beam hits the scrapers, creating a shower that propagates to the IDs. To address this concern, we will carefully study the development work done at APS.

All four units planned for NSLS-II will share the same engineering design and be built identically—the horizontal and vertical scrapers differing only in the final mounting and installation. Each unit will have two jaws or blades that can move independently from one another, each being driven by precisely controlled stepping motors. The blades will be made of Glidcop, a dispersion-strengthened copper with excellent thermal and electrical properties at elevated temperatures. Each of the blade assemblies will have a water-cooling circuit to minimize thermal expansion of the blades when they are hit by the dipole radiation fan.

Furthermore, to minimize impedance problems, the shape of the blades will be determined by detailed numerical simulation. These studies are still in progress and the results are preliminary. Figures 4.8.1 and 4.8.2 show two views of the design of an existing scraper at APS. The NSLS-II scraper design will be based on this APS design, with appropriate modifications to match the chamber geometry. Figure 4.8.3 shows a preliminary layout of the possible NSLS-II scraper.

Each scraper unit will be mounted directly on the vacuum chamber and the adjustable blades can be repositioned remotely. Once they are in the desired position, however, they must stay in place within the required tolerance.

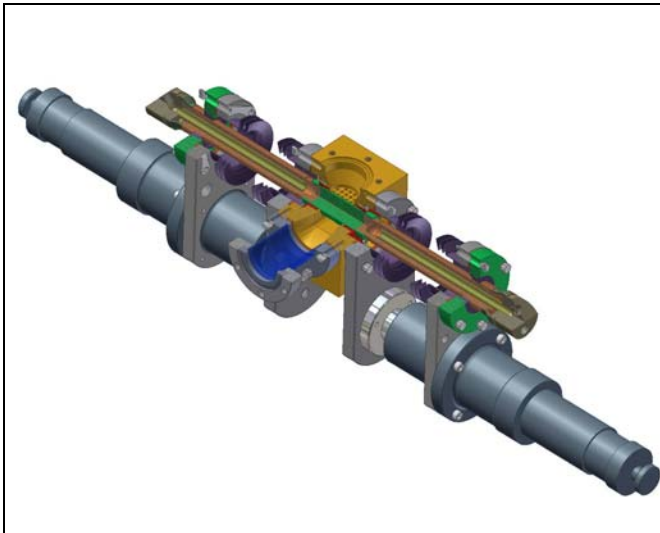


**Figure 4.8.1** (top left) Sectional view of APS scraper assembly, round blades (closed).

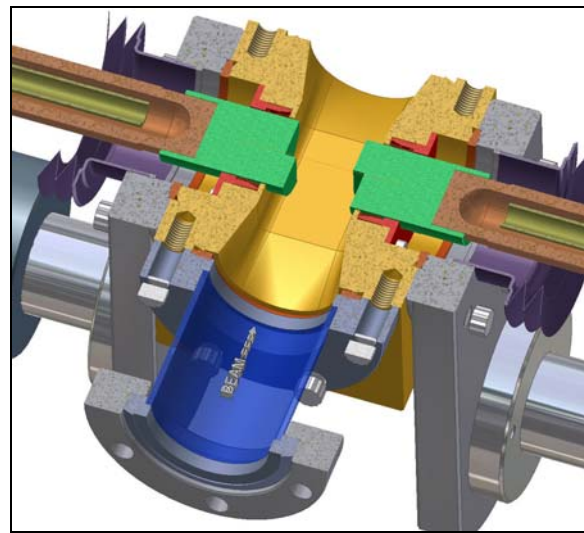
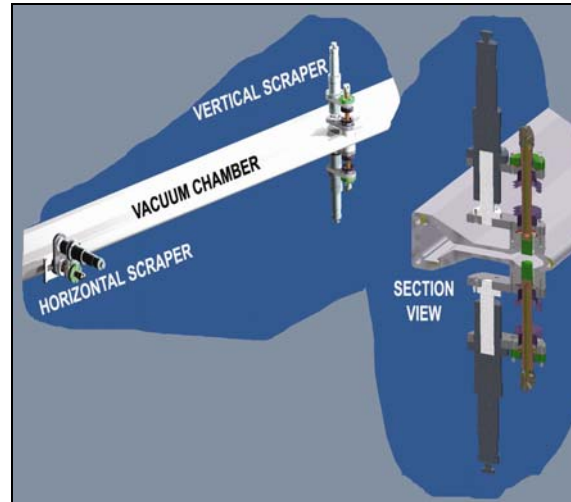


**Figure 4.8.2** (top right) Sectional view of APS scraper assembly, blades partially opened.

**Figure 4.8.3** (right) Preliminary layout of NSLS-II scraper (two views)



## 4.8.2 Photon Absorbers

Discrete photon absorbers will be installed in the vacuum chambers to protect their uncooled surfaces from the radiation fans of the bending magnets and IDs. Shielding the vacuum chambers from radiation fans also minimizes their thermal distortions and leads to better thermal stability of the BPMs attached to the chambers. To protect the chambers from exposure to unintentional beam deviations, BPM interlocks at insertion devices will be set at  $\pm 0.25$  mrad [4.8.2]. The positional error budgets consisting of orbit error, mechanical, and survey tolerances will be set at  $\pm 2$  mm.

The peak power densities of the bending magnets, damping wigglers, and the in-vacuum undulators (IVU) are  $0.088$  kW/mrad<sup>2</sup>,  $55.30$  kW/mrad<sup>2</sup>, and  $62.33$  kW/mrad<sup>2</sup>, respectively, for a 500 mA beam at 3 GeV. The power density of the BM is uniform in its horizontal fan of  $104.7$  mrad ( $6^\circ$ ) except at the edges. For the DW and IVU devices, the vertical and the horizontal power density profiles are shown in Figure 4.8.4 and Figure 4.8.5 respectively.

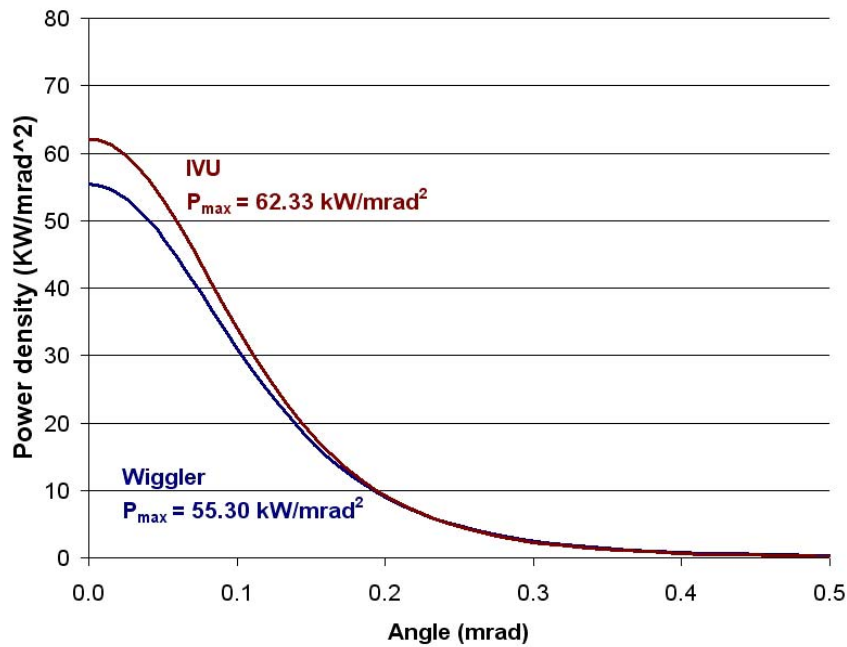


**Figure 4.8.4** Vertical power density profiles,  $P/P_{\max}$ , of damping wiggler and IVU.  $P_{\max}$  is obtained at 500 mA beam current.

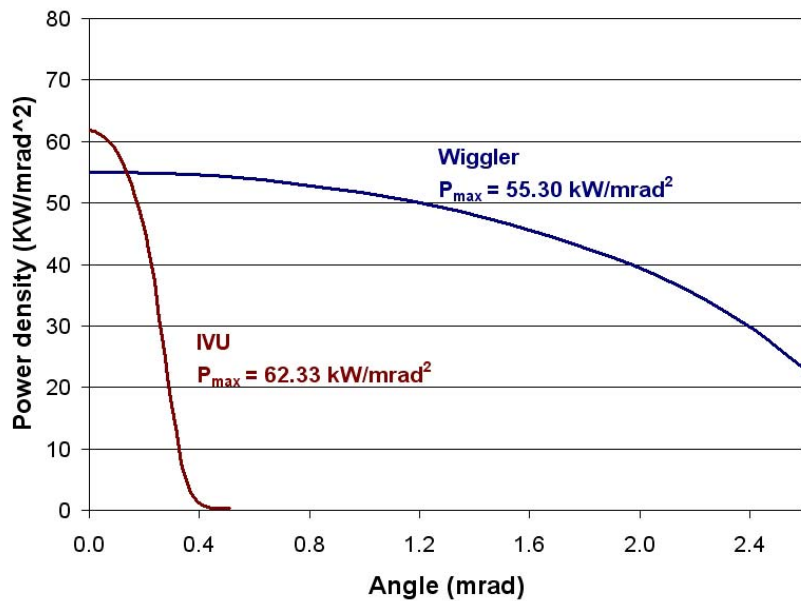


**Figure 4.8.5** Horizontal power density profile,  $P/P_{\max}$  for damping wiggler and IVU.

The IVU radiation fan is narrow in both directions and can be extracted with adequate clearance through the 76 mm (H)  $\times$  25 mm (V) apertures of the straight vacuum chamber in Section 2 and the 15 mm slot of the dipole chamber in Section 3. The BM and DW radiation fans in at the downstream end of Section 3 dipole chamber, however, require clipping by two absorbers, namely, a crotch absorber and a wiggler absorber (see Figure 4.8.6). Because of the high power density of the DW radiation, these absorbers clip the outer edges of the DW horizontal fan just enough to allow the clipped fan to be extracted to the front end.

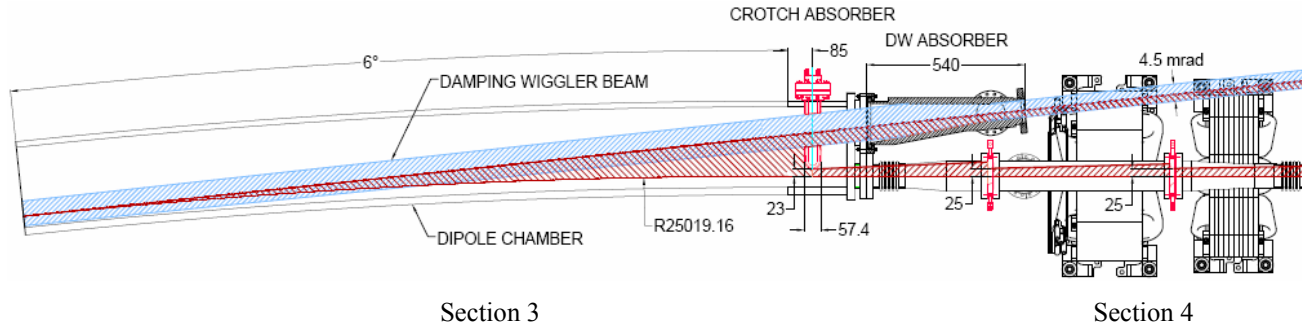


**Figure 4.8.6** Clipping of BM and DW x-ray fans by crotch and wiggler absorbers in at the downstream end of the Section 3 dipole chamber. The BM radiation fan (blue color) partially overlaps the DW radiation fan (red color).

#### 4.8.2.1 Preliminary Designs of Photon Absorbers

Figure 4.8.7a shows a 3D model of the crotch absorber inside the vacuum chamber. The absorber is made from a Glidcop® block with brazed water-cooling channels of OFHC copper. Also brazed to the Glidcop block are a stainless-steel flange and a water manifold. A rectangular slot in the center of this block allows DW or IVU radiation fans to pass through without interception. The crotch absorber is inserted into the downstream aperture of the dipole vacuum chamber in Section 3 such that its nose tip is 5 mm inside the aperture (i.e., 30 mm outboard from the center of the aperture). The tip intercepts a total of 840 W of beam power with a maximum power density of 12 W/mm<sup>2</sup>. A thermal analysis of the crotch absorber was carried out using ANSYS software. The results, plotted in Figure 4.8.7.b, show a peak temperature of 200°C, which is lower than the maximum allowable temperature of 400°C for Glidcop.

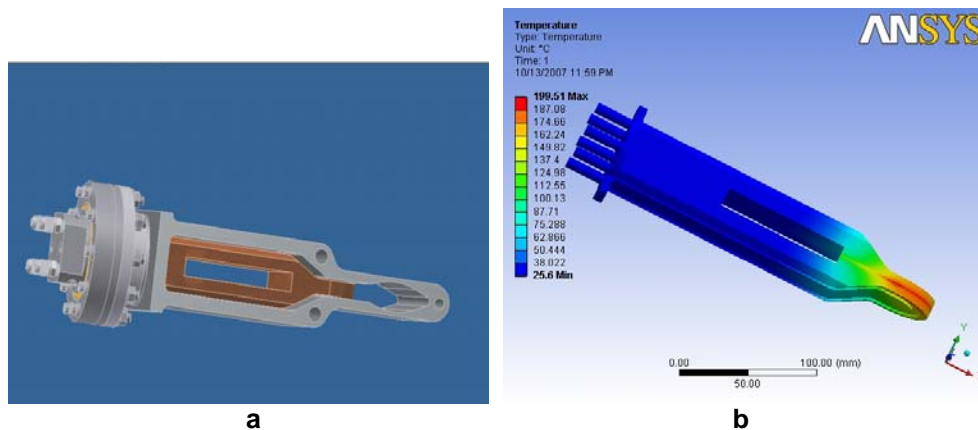


**Figure 4.8.7** Crotch absorber. a) a 3-D section inside the vacuum chamber. b) temperature contours from an ANSYS FE analysis with a peak temperature of 200°C.

The damping wiggler absorber, shown in Figure 4.8.8a, fits in the ~ 600 mm space between Section 3 and 4 on the outboard side. The upstream end of the absorber is brazed to a flange that mates with the flange of the chamber in Section 3. The downstream end is cantilevered inside a bellows assembly to allow for thermal expansions of the chambers during bakeout. Two water cooling channels are provided on each vertical side of the Glidcop block to absorb power from the outer extents (0.35x2 mrad) of the horizontal DW x-ray fan (5.2



mrad) at a grazing incidence of  $6^\circ$ . The total power intercepted by the two vertical sides is 4 kW, with a peak power density of  $22 \text{ W/mm}^2$ .

An ANSYS FE thermal analysis of the wiggler absorber predicted a peak surface temperature of  $214^\circ\text{C}$ . The temperature profile, plotted in Figure 4.8.7b, shows high temperatures directly under the beam footprint.

Assuming a water flow of 2 GPM in each of the cooling channels, the average bulk water temperature rise will be  $5.5^\circ\text{C}$ .

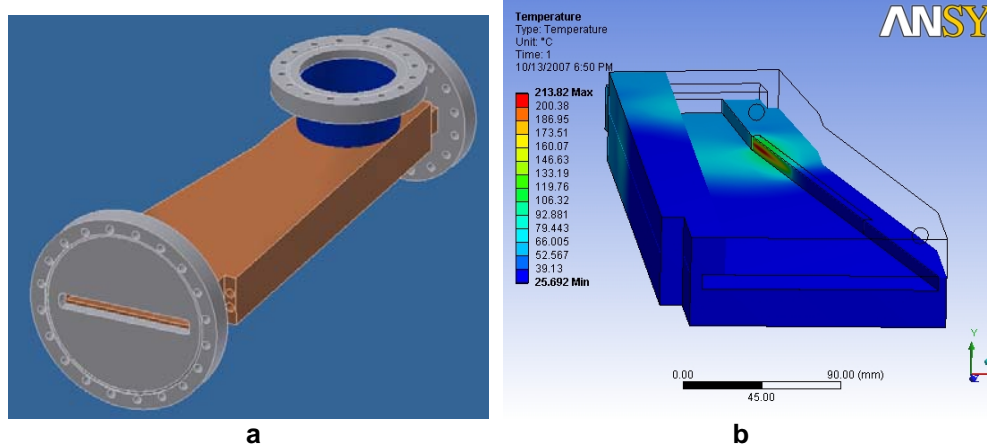


**Figure 4.8.8** Damping wiggler absorber. **a)** 3D model showing Glidcop block and flanges. **b)** Temperature contours from an ANSYS FE analysis with a peak temperature of  $214^\circ\text{C}$ .

Another crotch absorber will be used in Section 5 with a slot width that will allow the user-specified width of the dipole radiation fan to exit to the front end. Additionally, counter-flow and flange absorbers (Figure 4.8.9) will be used in Sections 2, 4, and 6 to intercept unused dipole radiation fans.



**Figure 4.8.9** Counter-flow and flange absorbers for the storage ring vacuum chambers.

## References

- [4.8.1] Borland, M. "ID Protection with Fast-Moving Scrapers," OAG-TN-2004-050, November 11, 2004.
- [4.8.2] V. Ravindranath, S. Sharma, B. Rusthoven, M Gosz, L. Zhang, and J. Biasci, "Thermal Fatigue Life Prediction of Al-15," proceedings, MEDSI-2006 Workshop, SPring-8, Himeji, Japan, May 24-26, 2006.





## 4.9 Storage Ring Diagnostics and Instrumentation

### 4.9.1 Introduction

State-of-the-art advanced diagnostics and instrumentation systems are required for a smooth and rapid commissioning and for productive and successful operation of the NSLS-II storage ring. This section provides a list of the monitored parameters, technical solutions with some alternative variants, and the required specifications to achieve these goals. Table 4.9.1 shows a summary of these various instrumentation components.

**Table 4.9.1 Beam Diagnostics and Instrumentation for Storage Ring.**

Monitor	Quantity	Function
4-button pick-ups	188	Beam position, dispersion, response matrix, turn-by-turn dynamics
Photon BPMs	1 per installed undulator	Photon beam position
DC current transformer	1	Beam current, lifetime
Emittance monitor	1	Transverse emittances
Fast current transformer	1	Filling pattern, beam current
Transverse feedback system	1	Suppress beam instabilities, tune monitoring
Pinhole camera	1	Transverse beam size, energy spread
Optical ports for visible radiation	2	To provide light for streak camera, FireWire camera, fill pattern and beam current
Streak-camera	1	Bunch length, beam dynamics
FireWire camera	1	Transverse beam characteristics
Fluorescent screen	1	Injection position, profile
RF-drive stripline and amplifier	1	Betatron tune
Beam oscillations monitor	1	Frequency components of longitudinal and transverse beam motion
P-i-n diodes loss monitors	60	Beam loss pattern
Scintillator loss monitors	10	Beam loss
X and Y beam scrapers	2	Machine studies, halo
Diagnostics undulator	1	Energy spread, beam divergence, momentum compaction factor

As a basic policy, whenever possible, we will pursue the utilization of commercial off-the-shelf devices to reduce cost as well to achieve better reliability. Most of the existing diagnostics equipment today already satisfies the basic requirements for NSLS-II and only a few, if any, need further development.

Full utilization of the micron-size electron beam requires sub-micron resolution of the orbit monitoring system, to provide the required position stability. Priority consideration will be given at the earliest stages of design to provide instruments for the detection and remedy of factors that affect beam quality.

### 4.9.2 Physics Design and Parameters

The following beam parameters will be monitored during regular operations:

- closed orbit (accuracy better than 10% of beam size)
- working point (tune for both planes with  $10^{-4}$  resolution)
- circulating current (0.1% accuracy) and beam lifetime (1% accuracy)
- injection efficiency
- filling pattern (1% of maximal bunch charge)
- emittance for both planes (10% relative accuracy)

- energy spread
- individual bunch length (2 psec resolution)
- position of the photon beam for the insertion devices
- coherent bunch instabilities
- distribution of beam losses around the ring

During beam studies the following parameters will be measured:

- linear optics, including  $\beta$ -functions (1% accuracy) and betatron phase advance ( $2\pi \times 10^{-3}$  or better)
- dispersion for both planes (1 mm accuracy)
- chromaticity for both planes (with accuracy 0.1)
- coupling (0.05% absolute accuracy)
- momentum compaction (1% relative accuracy)
- beam-based alignment of quadrupoles and sextupoles (30 microns or better)
- synchrotron frequency
- RF system parameters (cavity voltages and phasing)
- vacuum chamber impedances

### 4.9.3 Intercepting Diagnostics

A fluorescent screen in the injection straight will provide information on the shape and position of the injected beam and will assure proper matching of the beam optics. It is included in the baseline design. The screen will have two positions. The first position will be used to observe the incoming beam from the booster. In the second position, a special hole will allow the injected beam to enter the storage ring, and the beam shape will be observed after one turn. The screen material will be cerium-doped yttrium aluminum garnet (YAG:Ce), which has excellent resolution (about 30  $\mu\text{m}$ ) and radiation stability [4.9.1]. The estimated horizontal beam size coming from the booster is  $\sigma_x = 360 \mu\text{m}$ , and vertical size for 10% coupling is  $\sigma_y = 95 \mu\text{m}$ . If the spatial resolution of the YAG:Ce flag is found to be inadequate, then optical transition radiation can be used.

To avoid impedance problems, the screen assembly will be designed to ensure a smooth vacuum chamber wall when the screen is fully retracted. Spring-loaded RF-fingers will be used to provide electrical contact in order to avoid trapped modes for the wake fields. A typical screen assembly used at APS is shown in Figure 4.9.1, and the RF fingers are shown in Figure 4.9.2. To use this design we will need only to modify the vacuum chamber aperture to match the NSLS-II geometry.

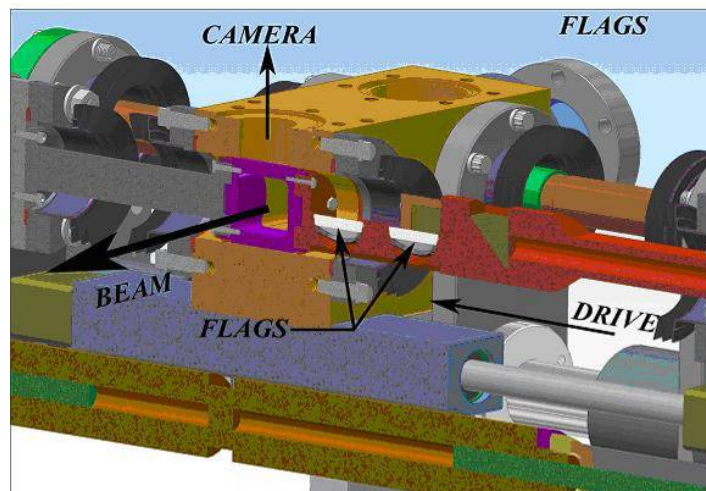


**Figure 4.9.1** Design of the screen used for the diagnostic of the electron beam injected into the storage ring at APS. We will modify the vacuum chamber aperture to match the NSLS-II geometry.

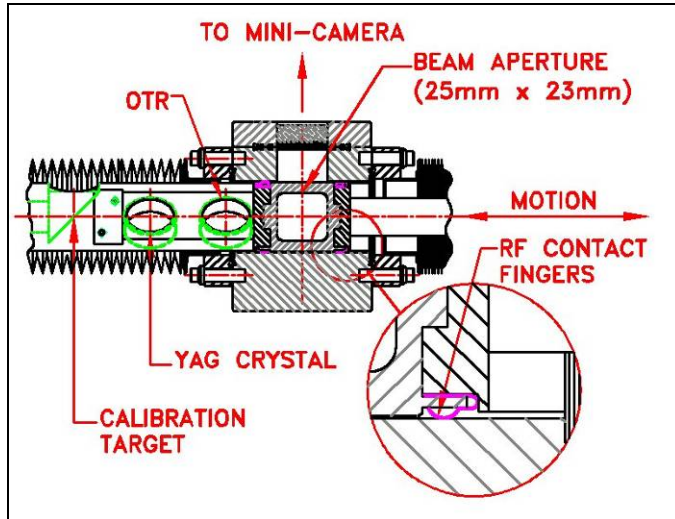


**Figure 4.9.2** Spring-loaded RF fingers (see detail) provide smoothness in the vacuum chamber. Electrical contact avoids trapped modes for the wake fields.

## 4.9.4 Circulating Current

### 4.9.4.1 Filling Pattern Measurement

To maintain uniform fill and to mitigate dependence of the BPM receivers on the filling pattern, a fast current transformer (FCT), included in the baseline design, will provide electrical signal proportional to the charge of individual bunches. Figure 4.9.3 shows a typical FCT that can be directly mounted on the beam chamber with a ceramic break. FCT-WB-082-20:1 model by Bergoz has 1.75 GHz bandwidth with a 200 psec rise time [4.9.2]. The FCT will be placed over a ceramic break and provided with RF-shielded housing. Fast ADC sampling of the voltage with 500 MHz on the top of each pulse will make charge distribution available to the control system. The information obtained will be used in the top-off algorithm. The signal from the FCT can be used as input for the top-off safety interlock, based on the monitoring of circulating current. Summing found charges for all bunches will provide an alternative means for measuring total beam current.



**Figure 4.9.3** Bergoz Fast Current Transformer.

### 4.9.4.2 Measurement of Circulating Current

A DC current transformer will monitor the stored current in the baseline design. The Bergoz New Parametric Current Transformer (NPCT) is the latest evolution of the Unser transformer [4.9.2], commonly known as DCCT, developed at CERN in 1966 by Klaus B. Unser. It is shown in Figure 4.9.4.

NPCT has large dynamic range and high bandwidth, making it a versatile device for measuring lifetime and injection efficiency. It is insensitive to a synchrotron revolution frequency and bunch fill pattern, with residual modulator ripple being eliminated, thus enabling full bandwidth operation down to a very low current.



**Figure 4.9.4** Bergoz NPCT (New Parametric Current Transformer).

The NPCT-115-C30-HR-H model has a radiation-hardened sensor and four ranges ( $\pm 20$  mA,  $\pm 200$  mA,  $\pm 2$  A,  $\pm 20$  A) with remote control by TTL signals. Wide operational range allows utilization of NPCT starting at commissioning and during regular operations without compromising the requirements for accuracy. Its resolution is better than  $1 \mu\text{A}/\text{Hz}^{1/2}$ . Such a small noise will allow measurement of the expected 60 hours lifetime for 25 mA circulating in one minute with 2% accuracy (assuming a 1 Hz sampling rate). The high bandwidth of the DCCT will allow measurements of the steps in the current after injection, and therefore provide a means of continuously monitoring injection efficiency.

The DCCT will be placed in the dedicated enclosure, providing shielding for RF noise as well as magnetic fields. The microwave absorbers and ferrite will be placed inside in order to suppress wake fields produced by the circulating electron beam.

## 4.9.5 RF Diagnostics

### 4.9.5.1 RF Beam Position Monitors

The optics of the NSLS-II storage ring are shown in Figure 4.9.5. In the baseline design there will be six beam position monitors (BPMs) equipped with receivers for each cell. Straights with insertion devices, however, will be provided with two additional instrumented BPMs.

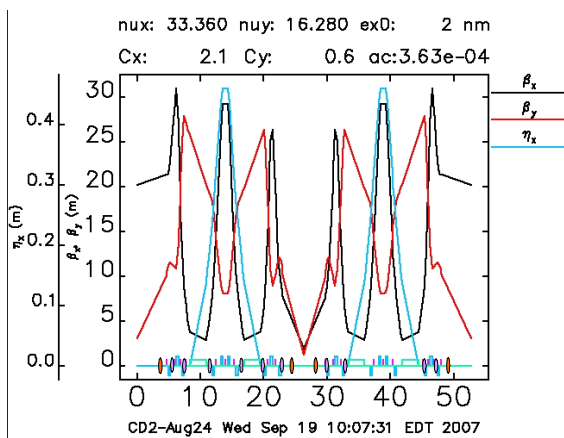


**Figure 4.9.5** NSLS-II superperiod. Baseline BPMs are shown as lavender ellipses and user BPMs as orange ellipses.

The high-precision pick-up electrodes will utilize button design and will be diagonally incorporated into the aluminum extrusion vacuum chamber. Figure 4.9.6 shows the cross-section of the basic construction of the four-button pick-up electrodes. An average current of 500 mA circulating in the storage ring is expected to produce  $-1.1$  dBm signal into  $50 \Omega$  load at 500 MHz. This estimate is done for a button, shown in Figure 4.9.7, with 5 mm radius and capacitance of 4 pF. The buttons are spaced with a distance to the beam of 20 mm. The scaling parameters for both vertical and horizontal directions are estimated to be around 10 mm for the present geometry; more precise sensitivities will be established during preliminary design.

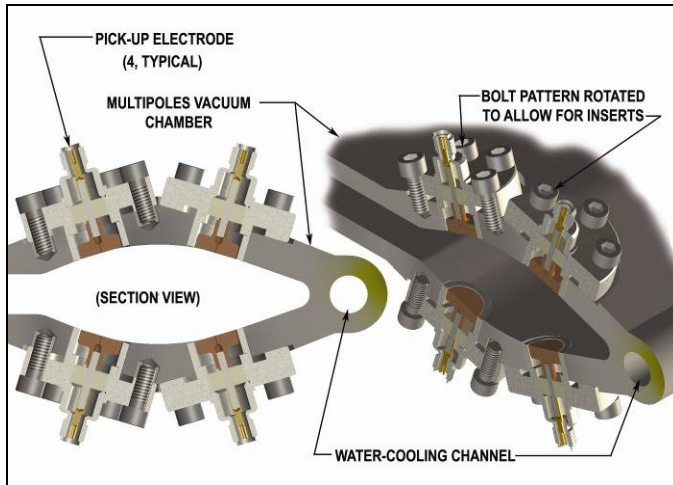
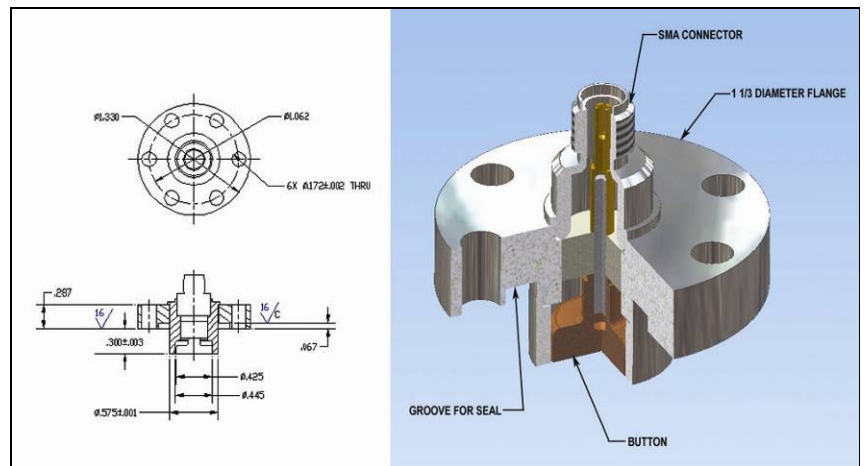


**Figure 4.9.6** Four-button, two-plane pick-up electrodes mounted on the vacuum chamber.

**Figure 4.9.7** Design of the BPM button for the storage ring.



Libera Brilliance modules, manufactured by Instrumentation Technologies [4.9.3, 4.9.4] and shown in Figure 4.9.8, can be used to process the signal from the BPM buttons. The RMS uncertainty of the beam position is expected to be below  $0.2 \mu\text{m}$  in 1 kHz bandwidth for the geometry shown. The digital design of the receivers provides the possibility of turn-to-turn beam position measurements with  $1 \mu\text{m}$  accuracy. The chamber with BPM buttons will be mounted on a girder by precisely machined supports, to provide high stability. Small alignment errors, as well as electrical offsets and errors in the BPM system, will be accounted for at the commissioning using beam-based alignment, which will be straightforward, thanks to the individual power supplies.



**Figure 4.9.9** Libera Brilliance by Instrumentation Technologies.



The NSLS-II storage ring utilizes very strong sextupoles. This makes it very important to have the orbit of the circulating beam as close as possible to the magnetic centers of the sextupoles. We will rely on highly accurate relative alignment of the sextupoles and quadrupoles on the same girder. In addition, a beam-based alignment procedure will be used for the sextupoles.

To provide the necessary beam stability, not only electrical noise in the BPM electronics should be considered but also mechanical motion of the vacuum chamber. For the most demanding beamlines, the high-stability BPMs will be placed on special, extra-stable posts (Figure 4.9.9), which will minimize positional changes of the vacuum chamber caused by changes in the ambient temperature. Shielded bellows will relieve the tension from the adjacent vacuum ducts. A more detailed description can be found in Section 4.3.2.

**Figure 4.9.9** Design of the high-stability BPM support.



#### 4.9.5.2 Tune Monitor

In the baseline design, the vertical and horizontal betatron tunes will be monitored using a network analyzer [4.9.5, 4.9.6]. The analyzer's source will be connected to the excitation striplines through the buffer amplifiers. The signal from the receiver pick-up electrodes will be combined with hybrids to produce vertical or horizontal signals, which will be down-converted below the revolution frequency and fed to the input of the network analyzer (Figure 4.9.10). Such an approach allows utilization of the maximal driving strength of the striplines and makes measurement of the tunes less sensitive to changes in the revolution frequency.

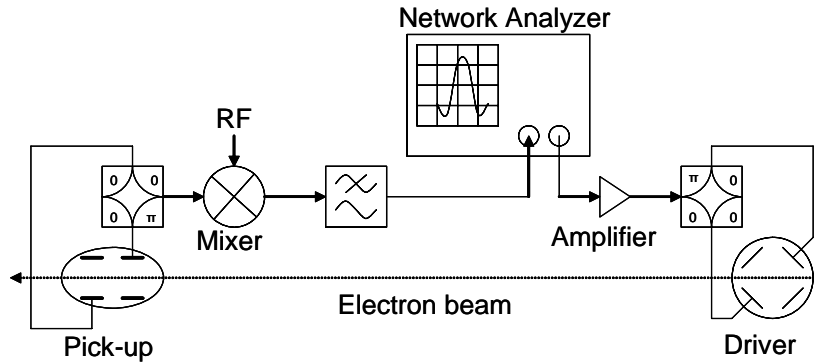


**Figure 4.9.10** Layout of the tune measurement system.

As a back-up, we can use the turn-by-turn data provided by the orbit monitoring system with electron beam being excited by the pingers located in the injection straight. Another solution that can be implemented after ring commissioning is utilizing the phase-locked loop.

The tune monitor should provide betatron frequency resolution of  $10^{-4}$  (or better) to obtain 1% accuracy in the  $\beta$ -functions, with up to five-fold difference in the  $\beta$ -functions for different planes with 0.05 allowable tune change. High precision of the tune measurements will facilitate beam-based alignment of the sextupoles, as well. Such parameters need to be reached even with chromaticities as high as 5.

#### 4.9.5.3 Beam Oscillations Monitor

The signal from a dedicated set of pick-up electrodes will be connected to an RF spectrum analyzer (Figure 4.9.11). The sidebands observed can be used to analyze electron beam motion. Summing the signal from opposite electrodes helps to eliminate components with transverse oscillations, while maintaining the signal with phase motion of the electron bunches, which allows measurement of the synchrotron frequency. The difference signal will be used to observe transverse oscillations of the electron beam. This diagnostic instrument is included in the baseline design due to its usefulness during commissioning.

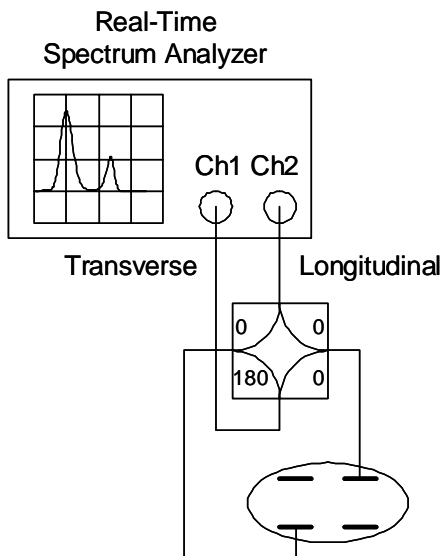


**Figure 4.9.11** System for the observation of beam oscillations.



### 4.9.5.4 Transverse Feedback System

The resistive wall wake can destabilize the electron beam in the storage ring. Increasing the chromaticity may not be sufficient, due to limitations on sextupole strength resulting from loss of the dynamic aperture required for beam lifetime and injection. The required stability can be provided by a digital bunch-by-bunch transverse feedback system [4.9.7, 4.9.8]. A broadband signal measuring the position of the individual bunches will be provided by the button-shaped pick-up electrodes. It will be sampled with a fast ADC (sampling rate 500 MHz). A digital filter will calculate the desired correction signal, which is generated by a DAC. The correction kicks are fed through a broadband amplifier and drive the electron beam using the second stripline. We are considering using a Libera Bunch-by-bunch system as an integrated unit, which provides all necessary analog-to-digital and digital-to-analog conversion with FPGA processing [4.9.8] (Table 4.9.2). In the baseline design the transverse feedback will be employed only for the vertical plane. However, the design can be easily expanded for the horizontal plane by the addition of another processing module.

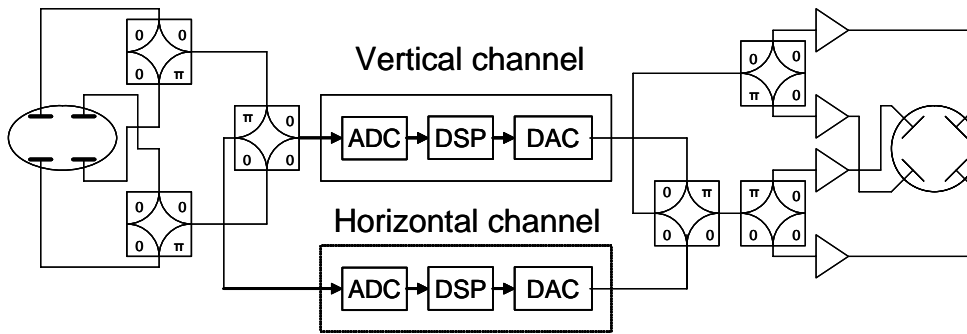


Figure 4.9.10 Conceptual layout of the transverse feedback system.

Table 4.9.2 Parameters of the transverse feedback.

Feedback parameters	vertical	horizontal
Measurement range	±0.15 mm	±1.5 mm
Resolution	0.3 micron	0.5 micron
Kick strength per turn	0.5 microrad	0.3 microrad
Minimal damping time $T_{min}$	90 microsec	2.6 msec
Added noise for $T=T_{min}$	0.01 microns	0.09 microns

The length of the 50 Ω striplines will be 15 cm (one-quarter of the RF wavelength). The striplines will be installed in the drift space on the arc where  $\beta_x=4.6$  m and  $\beta_y=19.1$  m. 100 W amplifiers will produce an electric field of 5 kV/m on the 38 mm vertical gap. Together with the magnetic field, the stripline will produce a deflection angle of 0.5 microradians for 3.0 GeV electron beam.

## 4.9.6 Synchrotron Radiation Diagnostics

### 4.9.6.1 Overview

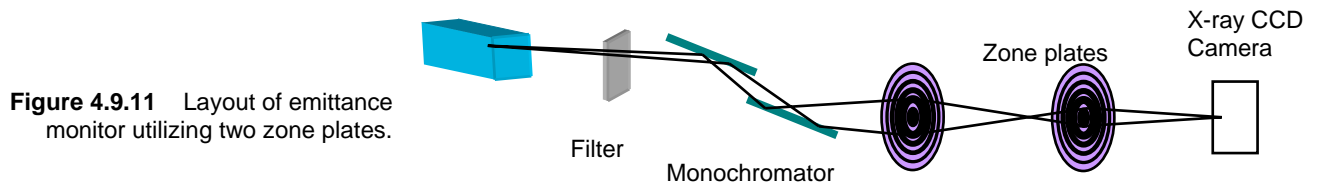
This section describes diagnostics for the NSLS-II storage ring that utilize visible and x-ray synchrotron radiation generated in a bending magnet and an x-ray undulator. Table 4.9.3 shows the types and quantities of diagnostics for the storage ring.

**Table 4.9.3 Complement of the Optical Diagnostics for the NSLS-II Storage Ring.**

Monitor type	Quantity	Function	Range	Resolution	Bandwidth
Emittance monitor	1	Horizontal emittance	0.5-2.5 nm-rad	5 pm-rad	100 Hz
		Vertical emittance	8 pm-rad	1 pm-rad	
Streak-camera	1	Bunch length	10 – 50 ps	2 ps	8 Hz
Pinhole camera	1	Beam size	10x30 microns	4 microns	30 Hz
		Energy spread	0.2 – 2%	0.01%	
Photon BPM	1 per beamline	Position of ID radiation	10 mm	0.001 mm	2 kHz
Diagnostics undulator with pinhole camera	1	Horizontal emittance	0.5 – 2.5 nm-rad		
		energy spread	0.2 – 2%		
		momentum compaction factor	$10^{-4}$		
FireWire camera	1	Beam profile		640x480	120 fps

### 4.9.6.2 Emittance monitor

For measuring the ultra low vertical emittance of the storage ring, we included in the baseline design the direct imaging of the electron beam with two zone plates. This method was developed at KEK [4.9.9] for measuring ultra small beam sizes. A double crystal monochromator selects the observation wavelength,  $\lambda$ . The first zone plate focuses the monochromatic beam to small spot, while the second zone plate magnifies the image, making it suitable to observe by X-ray CCD camera. The optical setup is shown in Figure 4.9.11.



### 4.9.6.3 Bunch Length Measurement

A double-sweep streak-camera Optronis model SC-10 [4.9.10], shown in Figure 4.9.12, will be used to measure the longitudinal beam dynamics. Its versatility and high sensitivity make it an excellent choice for monitoring the bunch length with high resolution and studying beam instabilities. The streak camera will be equipped with IOV-10 input optics. The bialkali photocathode with  $8 \text{ mm} \times 2 \text{ mm}$  area provides low dark noise (below  $50 \text{ e}^-/\text{cm}^2/\text{s}$ ). The parameters of the streak camera are shown in Table 4.9.3. The synchroscan feature provides low-phase jitter for synchronous summing of signals and tracking phase dynamics. The dual sweep is also available. The readout will be performed with a fiber optically coupled CCD camera (ANIMA-PX/25).

The OptoControl software will enable us to access all streak camera parameters and to control the camera operation. A 100 MHz Ethernet (TCP/IP) interface is integrated with the control system. For additional image analysis, the OptoAnalyse software is available. This program allows the use of sophisticated image acquisition algorithms and provides various tools for temporal or spatial analysis. The photon counting combined with drift and jitter correction makes possible long-term measurements with high sensitivity and high temporal resolution.

**Table 4.9.3 Optronis SC-10 Streak Camera Parameters.**

Spectral response characteristics [nm]	350 to 700
Synchroscan frequency (factory setting) [MHz]	40 – 250
Temporal resolution (FWMH) [ps]	2
Sweep range	300 ps to 4 ns
Camera resolution [pixels]	1360x1024
Frame rate [Hz]	8
Dynamic range [bit]	12

The streak camera will be shared with the booster. An optical beamline from the booster will be used to transport a beam of synchrotron radiation from the booster bending magnet to the streak camera. An alternative solution is to use C5680 synchroscan streak camera by Hamamatsu.



**Figure 4.9.12** View of the SC streak camera family.

#### 4.9.6.4 Photon Beam Position Monitors

Photon beam position monitors (PhBPMs) manufactured by FMB-Berlin (shown in Figure 4.9.13) are being considered for monitoring radiation from the insertion devices [4.9.11]; the blades, of course, will be designed and optimized to suit the requirements of NSLS-II. The PhBPMs are based on a development by Dr. Karsten Holldack at BESSY. The information obtained on the position of the photon beam will be incorporated into the orbit feedback system to provide the beam stability required for user applications. In the baseline design we have one PhBPM per beamline. The PhBPM assembly will be mounted on a stable post and its location (elevation and transverse position) will be adjusted with 2D translation stages (Figure 4.9.14). Similar devices at APS enable pointing stability of the photon beam with peak-to-peak drift of less than 2  $\mu$ rad over six days [4.9.12].

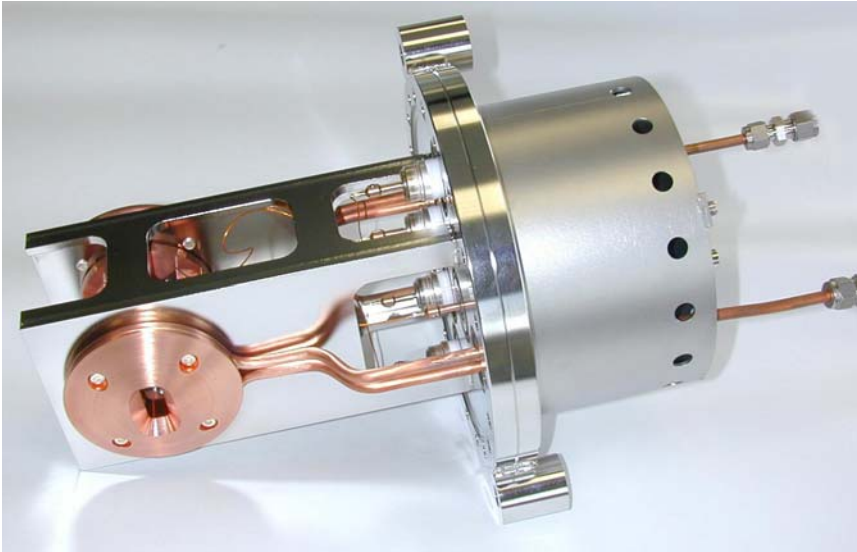
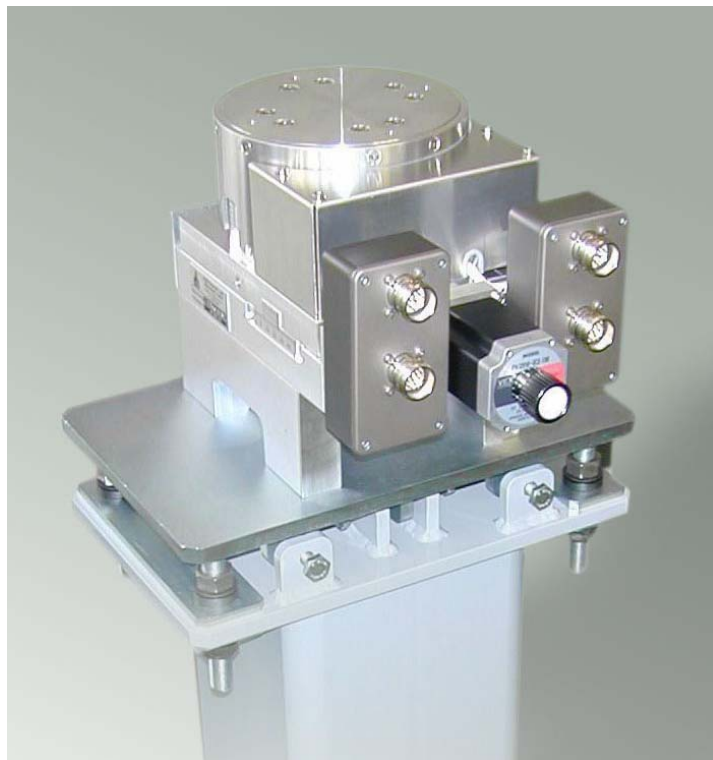


**Figure 4.9.13** Photon beam position monitor.

**Figure 4.9.14** Photon beam position monitor on the support column with motorized stage.

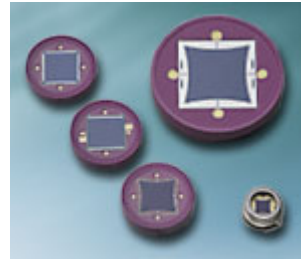


#### 4.9.6.5 Diagnostics with Visible Synchrotron Radiation

An IEEE1394 camera will be used to observe the visible radiation from the electron beam. Such an approach eliminates the need for a frame-grabber and makes display of the beam on the control computer straightforward. The camera has an external trigger capability and exposure control from 10  $\mu$ sec to 5 sec.

Position-sensitive photodiodes which provide signal based on the location of the center of gravity of the optical beam can be incorporated into the orbit feedback system to monitor beam stability for IR users, as well as results of image processing. The model S2044 (the smallest object in Figure 4.9.15) has 0.6  $\mu$ m sensitivity and 0.3  $\mu$ sec rise time.

**Figure 4.9.15** Position-sensitive diodes by Hamamatsu.



#### 4.9.6.6 Diagnostics Undulator

The diagnostics undulator will allow independent measurement of the energy spread and horizontal emittance. The momentum compaction factor can be also measured. We plan to utilize one of the user beamline undulators in a 5m straight; therefore, this tool is not included in the baseline design.. This beamline will be equipped with an additional high-resolution fluorescent screen and a retractable pinhole (Figure 4.9.16). Use of the radiation from the undulator for diagnostic purposes will be restricted to periods when it is not needed by the users.

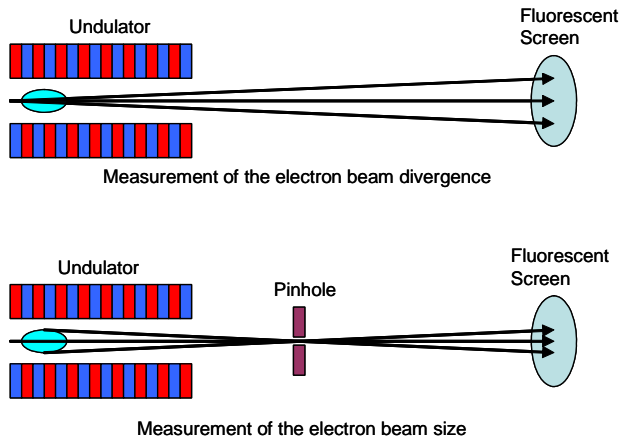


**Figure 4.9.16** Beam diagnostics with undulator radiation.

The  $\beta$ -functions in the straight are  $\beta_{x\min} = 2.5$  m and  $\beta_{y\min} = 1.2$  m. The U20 undulator that we propose to use has a 20 mm period and 3 m length. To measure the divergence of the electron beam, the transverse profile of the undulator radiation will be monitored. To increase system resolution, small undulator  $K$  values will be utilized. These will also help to minimize the power from higher harmonics and avoid distorting the power profile. For  $K = 0.3$ , the power density of the 3<sup>rd</sup> harmonic is two orders of magnitude below the power density of the main harmonic. For this value of  $K$ , the fundamental wavelength of the undulator radiation will be 0.29 nm and the divergence due to a diffraction will be  $\sigma'_{ph} = \sqrt{\lambda/L} = 9.8 \mu\text{rad}$ , which compares favorably with the horizontal divergence of the electron beam:  $\sigma'_e = \sqrt{\epsilon_x/\beta_x} = 14.1 \mu\text{rad}$  for 0.5 nm-rad emittance.

Inserting a pinhole, which can be realized as a slit, will enable measurement of the horizontal beam size. Knowing the divergence and beam size will enable us to directly measure the beam emittance, independent of the  $\beta$ -function.

Analysis of the width of the undulator spectrum provides information on the energy spread of the electron beam. It is also possible to measure the momentum compaction factor by observing the shift of the undulator spectrum with revolution frequency [4.9.12].

## 4.9.7 Other Diagnostics

### 4.9.7.1 Beam Loss Monitors

NSLS-II will utilize a distributed beam loss monitoring system based on p-i-n diodes, which are commercially available from Bergoz [4.9.2] (Figure 4.9.17). Two beam loss monitors per cell will be used for monitoring the spatial distribution of beam losses.



Figure 4.9.17 Beam loss monitor by Bergoz.

The loss monitors have a pulse output (one pulse per lost particle) and are insensitive to the synchrotron radiation photons. The monitors are small and can be easily relocated to the region of interest. CosyLab has developed interfaces for easy integration with the control system [4.9.13].

For the temporal distribution of the lost particles (on the scale of one turn) we plan to use ten scintillation detectors (Figure 4.9.18). They can be also be used for monitoring the losses of injected electrons near the injection and RF straights.

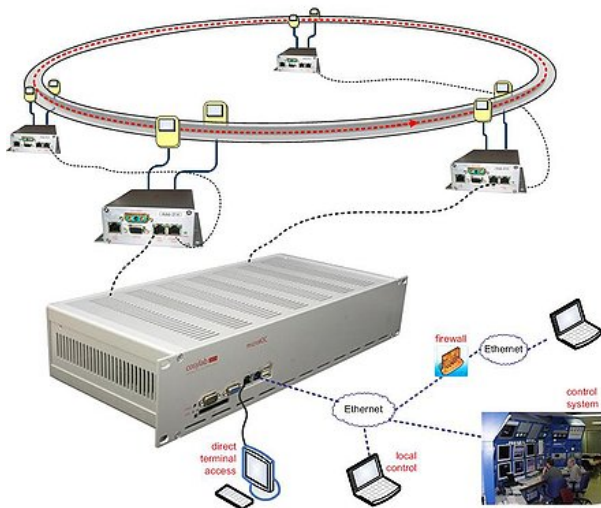


Figure 4.9.18 MicroIOC with signal conditioners for Bergoz beam loss monitors.

### 4.9.7.2 Scrapers

Two pairs of two-plane adjustable-position scrapers will be installed on the ring to be used both as protective devices as well as diagnostic instruments for accelerator studies. More details are described in Section 4.7. One set of scrapers (horizontal and vertical) will be installed in the dispersive section to measure the energy distribution of the electron beam. Another set will be installed in a straight section with zero dispersion in order to have information on the transverse size of the electron beam, and to eliminate possible beam halos capable of affecting the insertion devices.

### 4.9.7.3 High-Level Accelerator Modeling

Extracting data on the storage ring lattice from the experimental data [4.9.14] requires high-level accelerator modeling, described in the control system section. High-level accelerator modeling will also be used in the development of a real-time orbit feedback system and for coupling correction. Such high-level applications will necessitate a storage ring simulator for the offline testing and debugging of the software being developed.

A procedure was developed and experimentally verified for measuring accelerating voltage in the RF cavity [4.9.15]. The method is based on the observation of a phase shift between the electron beam and electrical field in the cavity when amplitude of the field varies. This procedure also makes it possible to measure relative phases between multiple cavities installed on the storage ring.

## References

- [4.9.1] E.D. Johnson, W.S. Graves, and K.E. Robinson, "Periscope Pop-In Beam Monitor," Proc. of Beam Instrumentation Workshop 1998, AIP Conf. Proc. 451, pp. 479–484.
- [4.9.2] <http://www.bergoz.com>
- [4.9.3] R. Ursic et al., "Holy Trinity of the Instrumentation Development," Proc. of the 11th Beam Instrumentation Workshop, Knoxville 2004.
- [4.9.4] U. Mavric, "Innovative RF Design Unites Benefits of Multiplexed and Multichannel System," Proc. of the 11th Beam Instrumentation Workshop, Knoxville, 2004.
- [4.9.5] A.S. Fisher, "Instrumentation and Diagnostics for PEP-II," Proc. Beam Instrumentation Workshop 1998, AIP Conf. Proc. 451, pp. 95–109.
- [4.9.6] A. S. Fisher, M. Petree, U. Wienands, S. Allison, M. Laznovsky, M. Seeman, and J. Robin, "Upgrades to PEP-II Tune Measurements," Proc. of Beam Instrumentation Workshop 2002, AIP Conf. Proc. 648, pp. 267–274.
- [4.9.7] M. Dehler, R. Kramert, P. Pollet, and T. Schilcher, "Commissioning Results of the Multi Bunch Feedback System at SLS," Proc. of EPAC 2004, pp. 2508–2510.
- [4.9.8] J.M. Koch, G. Naylor, E. Plouviez, and F. Epaud, "Beam Diagnostic Features of the ESRF Multibunch Feedback," Proc. DIPAC 2007.
- [4.9.9] K. Iida, et al., "Measurement of an Electron-Beam Size with a Beam Profile Monitor Using Fresnel Zone Plates," Nucl. Instr. and Meth. A506 (2003), pp. 41-49.
- [4.9.10] <http://www.optronis.com>
- [4.9.11] G. Decker and O. Singh, "Beam Stability at the Advanced Photon Source," Proc. of PAC 2005, pp. 3268–3270.
- [4.9.12] B. Yang, M. Borland, and L. Emery, "High Accuracy Momentum Compaction Measurement for the APS Storage Ring with Undulator Radiation," CP546, Beam Instrumentation Workshop 2000, American Institute of Physics, pp. 235–241.
- [4.9.13] <http://www.CosyLab.com>
- [4.9.14] J.A. Safranek, "Beam-based Accelerator Modeling and Control," Proc. of Beam Instrumentation Workshop 2000, AIP Conf. Proc. 546, pp. 23–5.
- [4.9.15] I. Pinayev, Characterization of the RF System of NSLS X-ray Ring, Proceedings of PAC'07.



## 5 Radiation Sources

This chapter describes the radiation sources to be provided in the NSLS-II baseline configuration. Continuing the tradition established by the existing NSLS, they span a very wide spectral range, from the far IR, down to 0.1 meV (equivalent to  $1 \text{ cm}^{-1}$ ), to the very hard x-ray region, more than 300 keV. This is achieved by a combination of bending magnet sources, covering the IR, VUV, and soft x-ray range, three-pole wiggler sources extending into the hard x-ray range, and insertion device sources, covering the soft x-ray through very hard x-ray range. They will achieve world leading levels of time average brightness and flux from the far IR through to  $\sim 20$  keV, only being surpassed above  $\sim 20$  to 25 keV by the performance of synchrotrons operating at higher energy (6 to 8 GeV).

As discussed in elsewhere in this report, the NSLS-II lattice contains 30 DBA cells, or 15 superperiods with alternating straight section lengths. The beta function values at the centers of the shorter straight sections will be quite low, especially in the vertical plane, and the longer straights will have somewhat higher beta function values. The resulting horizontal and vertical electron beam sizes and divergences in the center of the two types of straights, as well as in the center of the bend magnets and three-pole wigglers, are given in Table 5.1.1. These beam sizes and divergences are very small, especially in the insertion device straight sections. The beta functions also determine the allowed minimum vertical gap of an undulator and non-linear dynamic effects constrain the maximum length of the undulator,  $L$ . The minimum undulator gap and the undulator lengths for the devices described in this chapter were all chosen to satisfy these constraints.

All of the source properties described in this chapter assume a fully-damped horizontal emittance value of 0.5 nm-rad. This is the performance value for the NSLS-II storage ring when operating with a full complement of eight 7 m damping wigglers. The initial emittance value will be greater than this value, owing to operation with fewer damping wigglers, as discussed in Chapter [xx].

**Table 5.1.1 Electron Beam Size and Divergence at NSLS-II.**

Type of source	Low- straight section (6.6m)	High- straight section (8.6m)	0.4T Bend magnet	1T three-pole wiggler
$\sigma_h$ [ $\mu\text{m}$ ]	28.	99.5	44.2 (35.4-122)	136
$\sigma_h'$ [ $\mu\text{rad}$ ]	19.	5.5	63.1 (28.9 – 101)	14.0
$\sigma_v$ [ $\mu\text{m}$ ]	2.6	5.5	15.7	15.7
$\sigma_v'$ [ $\mu\text{rad}$ ]	3.2	1.8	0.63	0.62

### 5.1 Insertion Devices

The goal in choosing the set of principal insertion device parameters is to provide a wide overall spectral coverage with insertion devices that target the photon energy ranges of interest for the experimental programs. It is expected that other parameter choices besides those outlined here may be specified to meet the needs of the science program as it evolves over time.

The set of insertion devices described included in the baseline configuration of NSLS-II consists of hard x-ray and soft x-ray undulators, x-ray damping wigglers, and high-energy superconducting wigglers. Their spectral brightness, flux, power, spatial and angular output properties, and polarization performance are described. These IDs produce high-brightness radiation spanning a large photon energy range, from the soft x-ray ( $\sim 200$  eV) to the very hard x-ray ( $\sim 300$  keV). An R&D program focused on developing the required magnetic and mechanical design of these devices is presented in Chapter [xx]. Their effects on the properties of the NSLS-II storage ring and other accelerator physics issues are presented in Chapter [xx].



**Table 5.1.2: Insertion Devices included in the Baseline Configuration of NSLS-II**

Type of Device	Purpose	Usage	Quantity
Damping Wiggler: 90 mm period (DW90), 1.8T, 2 × 3.5-m long	Broadband	Machine/User	3
In-Vacuum Undulator (IVU): 20mm period (U20), 1.81T, 3-m long	Hard X-ray	User	3
Elliptically-polarized undulator (EPU): 45mm period (EPU45), 4.33T, 2 × 2-m long, canted by ~0.25 mrad	Soft X-ray	User	1
Three-Pole Wiggler: 1.0T, 20cm long	Broadband	User	≤15

The complement of insertion devices included in the NSLS-II baseline configuration is listed in Table 5.1.2. This set is not meant to be complete for the built-out NSLS-II facility. Rather, these devices represent a set that attempts to optimize the performance of the beamlines included in the NSLS-II baseline configuration. These IDs have been chosen consistent with the philosophy of building beamlines dedicated to a given technique, which requires that the source also be individually optimized for each application, as appropriate.

[[remove paragraph?? Other types of undulators and/or wigglers besides those discussed in this Chapter will also be considered during the preliminary engineering design phase of the project. These will include in-vacuum EPUs, to reach smaller magnetic gaps and thereby cover wider photon energy ranges, and quasi-periodicity, for both planar undulators and EPUs. In addition, revolver concepts, figure-8 type undulators, and long-period electromagnetic undulators will be considered. These concepts are discussed further in the description of the undulator R&D program in Chapter 12.]]

## 5.1.1 Planar Undulators

The hard x-ray undulators at NSLS-II will be planar designs and will produce linearly polarized radiation.

### 5.1.1.1 IVU – U20

The baseline NSLS-II hard x-ray undulator is an In-Vacuum Undulator (IVU) with a period of 20 mm, referred to as U20. This device will be operated at room temperature and is based on the mini-gap in-vacuum undulator design and development pioneered at NSLS and now utilized at SR sources around the world.

## 5.1.2 Elliptically Polarized Undulators

The NSLS-II soft x-ray insertion devices will be elliptically-polarized undulators. EPUs provide full ellipticity control of the radiated output from circular through linear, while only marginally reducing the brightness of the linearly polarized output, compared to pure planar undulators of the same period. In addition, these EPUs can also provide linearly polarized output with the polarization axis oriented either horizontally, vertically, or anywhere in between. As discussed in the soft x-ray beamline Section [xx], these properties are extremely useful for separating various contributions to a given signal in an experiment.

### 5.1.2.1 Soft X-ray EPU – EPU45

The total length of the EPU45 undulator is specified as 4 m, corresponding to a single long device. However, this corresponds to only one of two proposed operating modes for these devices. In fact, for the soft x-ray beamlines discussed in Chapter [xx], this 4 m total length would be comprised of two ~2 m EPUs and the appropriate steering magnets and diagnostics would be placed between the sections to allow a small (~0.25 mrad) canting angle for the electron beam between them. As described in more detail in Chapter [xx],

this configuration will allow the two undulator sections to be set to two different polarizations, e.g., left circular and right circular, or horizontal linear and vertical linear. The angular separation provided by the canting will then permit fast switching between the chosen polarizations of the two EPU's, thereby enabling various types of polarization-sensitive experiments to be performed with high sensitivity, as provided by lock-in detection methods for example. The accelerator issues associated with these, and other, canting angles are discussed briefly in Section [xx] and will be addressed in more detail in the technical design phase of this project.

### 5.1.3 Wigglers

Classes of experiments that require continuous x-ray spectra, sizable x-ray beams, or very hard x-rays, such as EXAFS, powder diffraction, x-ray topography, x-ray standing waves, high pressure, and x-ray footprinting, to name some, will benefit from the availability of x-ray beamlines that view damping wiggler sources. Superconducting wigglers will be the preferred source for experiments requiring very hard x-rays, up to ~300 keV. All wiggler sources at NSLS-II are expected to be in high demand.

#### 5.1.3.1 Damping Wiggler – DW90

The damping wigglers will produce the highest flux of any NSLS-II source out to ~30 keV and will also have excellent brightness. They are expected to be the premier source for experiments above ~5 keV that do not require the ultra-high brightness and extremely small beams produced by the hard x-ray undulators.

#### 5.1.3.2 Three-pole Wiggler – TPW

The three-pole wigglers, to be inserted just upstream of the downstream bend magnet in the super-period, will produce a very useful hard x-ray bend-magnet-like spectrum. With a critical energy of 6 keV, the three-pole wigglers will produce usable hard x-ray flux out to ~25 keV. The emitted horizontal angular fan from these devices is 2 mrad wide.

#### 5.1.3.3 Superconducting Wiggler – SCW60

The highest energy photons will be produced by very high field, short period, wigglers. The radiation will be broadband with high power at high x-ray energies, covering the 20 to 300 keV energy range. The baseline SCW60 device has a period length of 60mm and a wiggler field of 3.5T. This combination of period and magnetic field has been demonstrated technologically at ELETTRA and MAX lab. Specifications of other high magnetic field SCWs that are currently in service at medium energy synchrotrons are listed in Table 5.1.3.

**Table 5.1.3 Some Working SCWs Similar in Specifications to Proposed and Alternative NSLS-II Wigglers.**

Facility	Manufacturer	Field(T)	Period (cm)	# full-field poles
NSLS X17	Oxford	6	17.4	5
BESSY II	Novosibirsk	7	14.8	13
CLS	Novosibirsk	4.2	4.8	25
ELETTRA	Novosibirsk	3.6	6.4	45
MAX lab	Custom	3.5	6.1	47

Increasing the SCW60 magnetic field will be the subject of NSLS-II R&D, so that its flux and brightness are as high as possible. A target magnetic field value is 6.0T, which represents an SCW design that pushes the limit of presently achievable current density. The SCW60 will outperform other NSLS-II radiation sources at

energies above 30 keV. The target deflection parameter,  $K$ , is chosen to be high enough to generate a large horizontal beam profile of more than 0.5 m at 50 m from the source point. This allows splitting of the fan into multiple experimental hutches.

## 5.2 Bend Magnets

The NSLS-II bending magnets will have a relatively low critical energy (2.4 keV), and will be excellent sources for low photon energies, below 10 keV. It is expected that the available bend magnet ports will be allocated primarily to VUV and soft x-ray uses, as well as infrared uses. Those classes of experiments that require access to harder sources of bend-magnet-like x-rays (energy  $>\sim 5$  keV) are better suited to three-pole wigglers (TPW), described in section 5.1.3.2 above.

The NSLS-II bend magnets and three-pole wigglers will provide very stable beams. The relatively low emitted power from these sources simplifies the cooling requirements on the optics, although it does not eliminate the need to provide cooling. The brightness provided by the NSLS-II dipole sources will be two orders of magnitude higher than that of the present NSLS dipoles (extending up to  $\sim 12$  keV) and their flux will also show some improvement (extending up to  $\sim 4$  keV), as shown in Table 5.2.1. Indeed, the NSLS-II bend magnets will provide almost twice the flux of the ALS conventional bend magnets (i.e., not the superbends) and offer even larger improvements in source brightness. Thus, aspects of the very successful ALS research programs based on bend magnet illumination can be developed at NSLS-II, although the distribution of beamlines and end stations will be determined by the strengths and interests of the NSLS-II user community. The NSLS-II 3 three-pole wiggler sources will have essentially the same critical energy as the present NSLS dipoles, but will be more than an order of magnitude brighter and produce a factor of 1.5 to 3 times greater flux (see Table 5.2.1).

**Table 5.2.1 Comparison of Bend Magnet Sources**

Energy	NSLS-II Bend Magnet		NSLS-II Three-pole-wiggler		ALS Conventional Bend Magnet		NSLS X-Ray Bend Magnet		NSLS VUV Bend Magnet	
	Flux	Brightness	Flux	Brightness	Flux	Brightness	Flux	Brightness	Flux	Brightness
1000 eV	$3.3 \times 10^{13}$	$1.5 \times 10^{16}$	$3.3 \times 10^{13}$	$2.7 \times 10^{16}$	$2.1 \times 10^{13}$	$1.5 \times 10^{15}$	$1.4 \times 10^{13}$	$1.3 \times 10^{14}$	$6.0 \times 10^{12}$	$1.1 \times 10^{13}$
100 eV	$2.5 \times 10^{13}$	$8.0 \times 10^{15}$	$1.9 \times 10^{13}$	$1.3 \times 10^{15}$	$1.5 \times 10^{13}$	$7.5 \times 10^{14}$	$8.0 \times 10^{12}$	$7.0 \times 10^{13}$	$1.3 \times 10^{13}$	$9.0 \times 10^{13}$
10 eV	$1.3 \times 10^{13}$	$3.7 \times 10^{15}$	$9.3 \times 10^{12}$	$6.0 \times 10^{14}$	$7.2 \times 10^{12}$	$3.4 \times 10^{14}$	$3.8 \times 10^{12}$	$2.8 \times 10^{13}$	$7.7 \times 10^{12}$	$4.4 \times 10^{12}$
1 eV	$5.9 \times 10^{12}$	$1.7 \times 10^{15}$			$3.4 \times 10^{12}$	$1.6 \times 10^{14}$	$1.8 \times 10^{12}$	$1.3 \times 10^{13}$	$3.7 \times 10^{12}$	$2.0 \times 10^{12}$
0.1 eV	$2.8 \times 10^{12}$	$8.0 \times 10^{14}$			$1.6 \times 10^{12}$	$7.3 \times 10^{13}$	$8.4 \times 10^{11}$	$6.1 \times 10^{12}$	$1.8 \times 10^{12}$	$9.4 \times 10^{11}$

ALS parameters assume top-off mode operation at 500 mA stored current. Flux is in units of ph/s/0.1%BW and brightness is in units of ph/s/0.1%BW/mm<sup>2</sup>/mrad<sup>2</sup>.

The special considerations required for collecting infrared radiation produced by the bend magnets are discussed in detail in Section 5.4.

### 5.3 Parameters and Performance of Radiation Sources

The basic parameters characterizing the IDs, bending magnet, and three-pole wiggler sources are listed in Table 5.3.1. In the case of the NSLS-II bend magnet and TPW, the total power value is actually the power per horizontal mrad.

**Table 5.3.1 Basic Parameters of NSLS-II Radiation Sources for Storage Ring Operation at 3.0 GeV and 500 mA**

	U20	EPU45	DW90	SCW60	Bend Magnet	Three-pole wiggler
Type	IVU	EPU	PMW	SCW	Bend	PMW
Photon energy range [keV]	Hard x-ray (1.9–20)	Soft x-ray (0.180 – 7)	Broadband (<0.010 - 100)	Very hard x-ray (<0.010 – 200)	Soft and low-energy x-ray (<0.010 – 12)	Hard x-ray (<0.010 – 25)
Type of straight section	Low- $\beta$	Low- $\beta$	High- $\beta$	Low- $\beta$		
Period length, $\lambda_u$ [mm]	20	45	90	60		
Total device length [m]	3.0	4.0	7.0	1.0		0.25
Number of periods	148	89	75	17		0.5
Minimum magnetic gap [mm]	5	10	12.5	15		28
Peak magnetic field strength in linear mode, B [T]	1.03	1.03	1.80	3.5	0.40	1.12
Max $K_y^*$ , linear mode	1.81	4.67	15.20	19.61		
Peak magnetic field strength in circular mode, B [T]		0.68				
Max $K_h = K_y^*$ , circular mode		2.87				
Minimum $h\nu$ fundamental [keV]	1.62	0.183				
$h\nu$ critical [keV]			10.8	21.0	2.39	6.7
Maximum total power [kW]	9.1	12.09	64.6	34.9		
Horizontal angular power density [kW/mrad]					0.023	0.064
On-axis power density [kW/mrad <sup>2</sup> ]	65.4	40.03	59.3	26.1	0.088	0.25

\* $K = 0.934 B[T] \lambda_u[cm]$ ; effective K values listed

#### 5.3.1 Brightness

For many experiments, especially those involving imaging or microscopy, where, for example, the beam must be focused down to a small spot, the key figure of merit of user radiation sources is their time average brightness. This is the flux output per unit bandwidth, per unit source area, and per unit solid angular divergence. Undulators and wigglers are excellent sources of high brightness radiation. The brightness of the baseline set of radiation sources for NSLS-II is shown in Figure 5.3.1. For the undulators, the tuning curves of harmonics 1, 3, 5, 7, and 9 are shown. These tuning curves show the variation of the peak brightness of the undulator harmonics as the magnetic field strength, and hence K parameter, is varied from  $K_{max}$ , listed for each undulator in Table 5.3.1, down to  $K_{min} \sim 0.4$ .

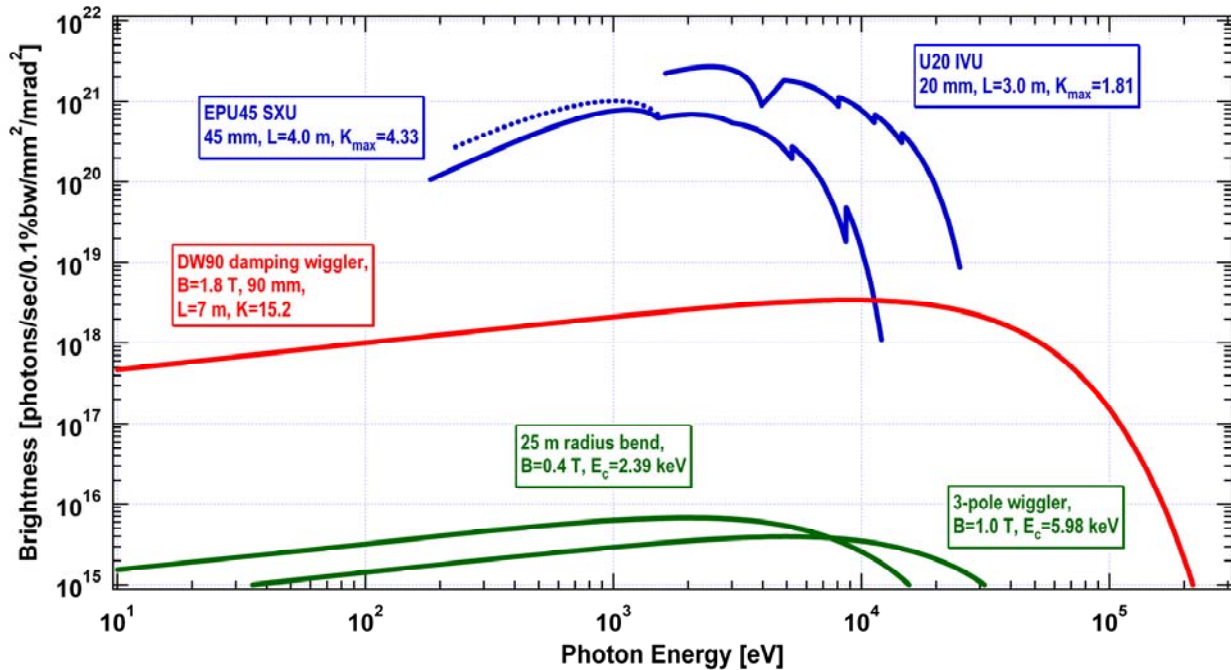


**Figure 5.3.1** Brightness vs. photon energy for the baseline radiation sources at NSLS-II. Ring parameters: 3.0 GeV, 0.5 A,  $\varepsilon_h=0.5$  nm,  $\varepsilon_v=0.008$  nm, energy spread=0.001; Straight section parameters: low- $\beta$ :  $\beta_h=2.02$  m,  $\beta_v=1.06$  m; high- $\beta$ :  $\beta_h=20.8$  m,  $\beta_v=2.94$  m;  $\alpha_h=\alpha_v=\eta_h=\eta_v=\eta'_h=\eta'_v=0$ ; Bend magnet parameters:  $\beta_h=2.62$  m,  $\beta_v=20.3$  m,  $\alpha_h=1.75$ ,  $\alpha_v=-0.952$ ,  $\eta_h=-0.129$  m,  $\eta'_h=-0.102$ ,  $\eta_v=\eta'_v=0$ ; Three-pole wiggler parameters:  $\beta_h=3.87$  m,  $\beta_v=35.2$  m,  $\alpha_h=2.01$ ,  $\alpha_v=-1.56$ ,  $\eta_h=0.168$  m,  $\eta'_h=-0.105$ ,  $\eta_v=\eta'_v=0$ .

The brightness of the U20 hard x-ray undulator is the highest of any devices in the NSLS-II baseline configuration. This is due in part to the short period length of this device, thereby increasing the number of periods contributing to the flux output, and in part to the short output wavelengths compared to the soft x-ray undulator (EPU45). For diffraction-limited undulator radiation, which characterizes a good portion of the range of these two undulators, the brightness varies inversely as the square of the output wavelength. Note that the brightness of the U20 hard x-ray undulator exceeds the  $10^{21}$  ph/s/0.1%BW/mm<sup>2</sup>/mrad<sup>2</sup> level.

The wigglers provide broadband, high brightness sources of x-ray radiation. Each of the wigglers shown in Figure 5.3.1 covers nearly the entire photon energy range shown. The superconducting wiggler SCW60 is optimized for very high-energy x-ray work (i.e., above  $\sim 60$  keV), while the damping wiggler DW90 is a high-flux, hard x-ray source with smooth spectral output extending down through the soft x-ray and VUV photon energy ranges.

Figure 5.3.1 shows the source brightness of the EPU45 soft x-ray undulator in two polarization modes: helical (or circular), shown as dotted lines, and linear, shown as solid lines. The circular polarized mode has intensity only in the fundamental and is slightly brighter than the linearly polarized mode at the same energy. It is expected that this mode will be used for all work below 2 keV, unless linearly polarized light is specifically required.

The NSLS-II bending magnet spectral brightness curve is also shown in Figure 5.3.1. The bending magnet spectrum is a bright source which extends from the infrared to the hard x-ray. This source will be useful up to a few times the critical energy of 2.39 keV, i.e., up to  $\sim 10$  keV. The bending magnet brightness peaks at  $\sim 2$  keV, making it an ideal broadband source in the soft x-ray (0.1–2 keV) and low-energy x-ray (2–5 keV) ranges.

The three-pole wiggler (TPW) source has a critical energy of 6 keV, making it a very useful continuum hard x-ray source up to  $\sim 25$  keV. The TPW spectral brightness curve is shown in Figure 5.3.1. The emitted horizontal angular fan from these devices is 2 mrad wide.

### 5.3.2 Flux

For those experiments which do not require a very collimated and/or focused beam, the photon spectral flux is the key figure of merit. This is the number of photons per unit bandwidth per unit time, i.e. it is an angle-integrated quantity. For undulators, flux values typically quoted are integrated over the central angular cone, which contains essentially all of the usable flux from these devices. For wigglers and bend magnets, the flux value typically quoted is integrated over all angles vertically and over 1 mrad horizontally. The horizontal angular dependence of bend magnets is uniform over its horizontal extent and, for wigglers, is maximum on axis and falls to zero at  $\pm K/\gamma$ . For large-radius storage rings such as NSLS-II, the usable horizontal angular range will be determined by physical apertures in the beamline front end. The maximum horizontal angular range deliverable by NSLS-II insertion device front ends will be  $\sim 6$  mrad [check]. The corresponding value for bend magnets will be  $\sim 5$  mrad [check], whereas the three-pole wigglers will produce a 2 mrad-wide horizontal angular fan. Figure 5.3.2 shows the flux for the NSLS-II radiation sources. The maximum flux is  $\sim 6 \times 10^{15}$  ph/s/0.1%BW, reached by all three baseline insertion devices (DW90, IVU20, and EPU45) at the peaks of their output spectra ( $\sim 0.2$  keV,  $\sim 2$  keV, and  $\sim 3$  keV, respectively). As has been said previously, the bend magnets at NSLS-II will be superlative sources of high brightness and high flux radiation in the VUV and soft x-ray energy range. The three-pole wiggler sources are bend-magnet-like sources which extend into the hard x-ray energy range. Both the bend magnet and three-pole wiggler flux spectra peak at  $\sim 4 \times 10^{13}$  ph/s/0.1%BW, per horizontal mrad.

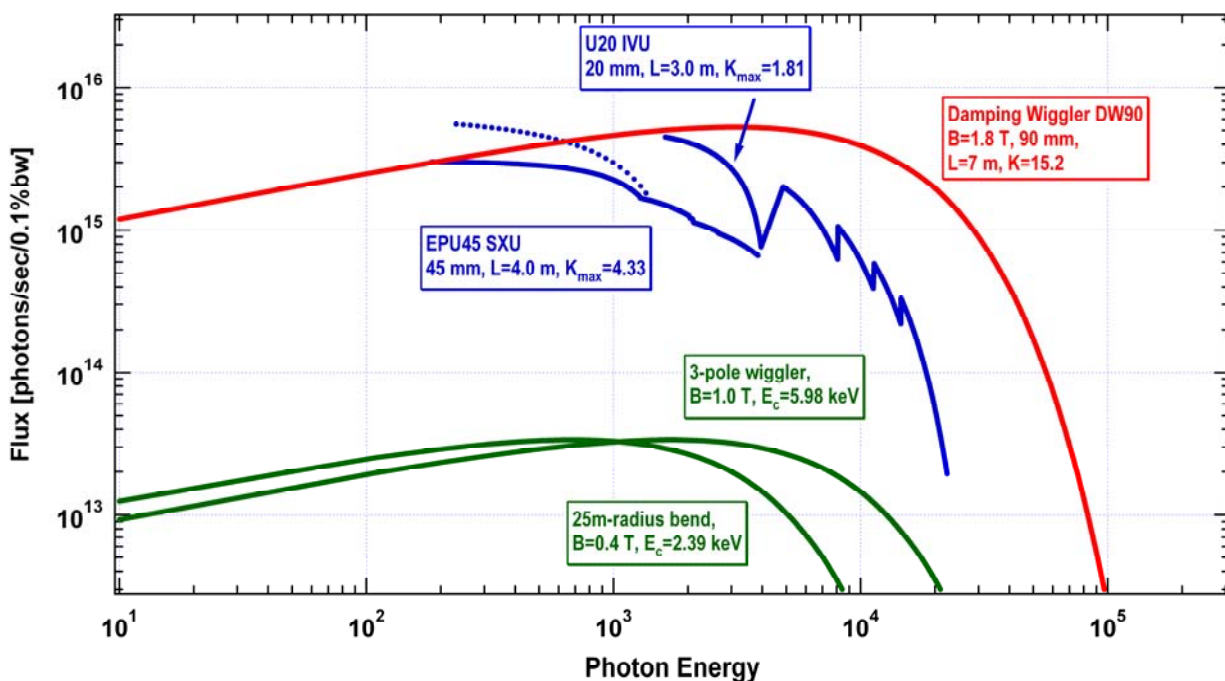


**Figure 5.3.2** Flux output of baseline radiation sources at NSLS-II vs. photon energy. See the caption to Figure 5.3.1 for a listing of accelerator parameters used to calculate the flux curves shown here.”

### 5.3.3 Power

Table 5.3.1 gives the maximum total output power of the NSLS-II radiation sources and Figure 5.3.3 shows how the total output power output of the undulators varies as their  $K$  value is changed from  $K_{\min}$  (taken to be  $\sim 0.4$ ) to  $K_{\max}$ , as given in Table 5.3.1. For reference, the corresponding energy of the photons' radiation in the fundamental as a function of  $K$  is also given. The photon energy of harmonic  $n$  is  $n$  times that of the fundamental.

The total power radiated by the undulators at their maximum  $K$  settings (i.e., at minimum magnetic gap) is in the 8–13 kW range. The total power output from the NSLS-II wigglers is higher than that of the undulators, at nearly 65 kW, while that of the NSLS-II bend magnets and TPWs is very much less, at only  $\sim 23$  W and 57W per horizontal mrad, respectively (see Table 5.3.1). Figure 5.3.3 also shows that the total output power at a given value of  $K$  increases by about a factor of two when operating in circular mode ( $K_h = K_v \neq 0$ ) compared to linear mode ( $K_h = 0, K_v \neq 0$ ) for the EPU. The engineering challenges of handling the high heat loads in the insertion device front ends are detailed in Section [xx].

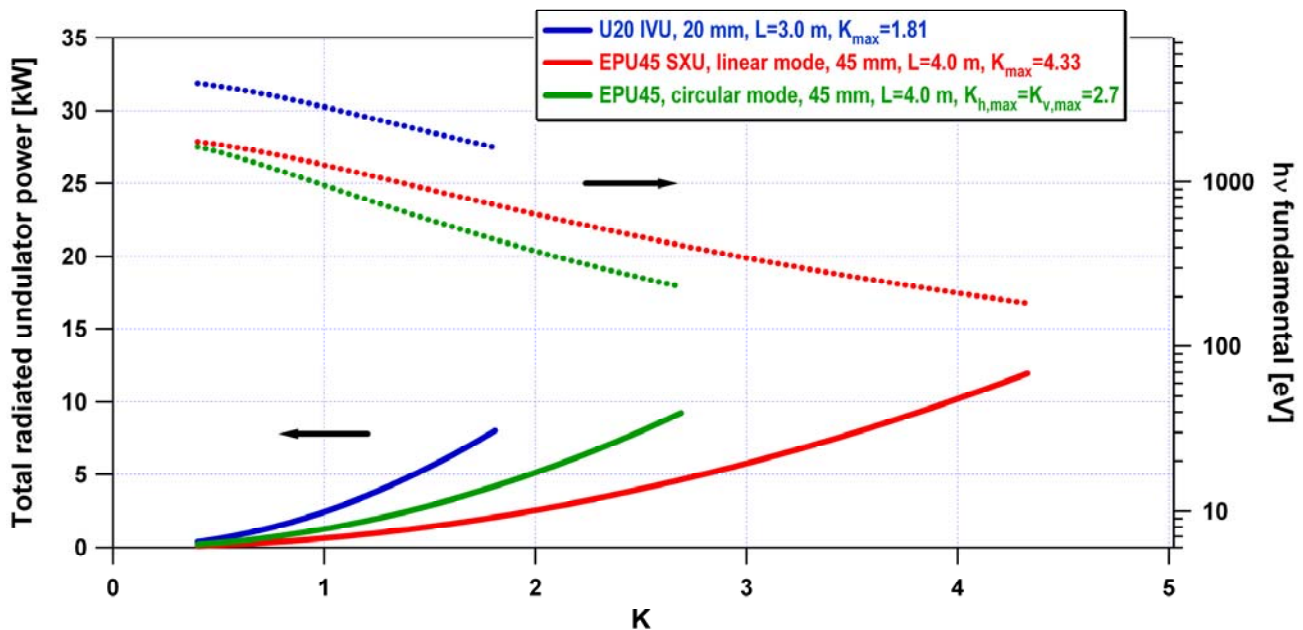


**Figure 5.3.3** Total output power (left-hand axis) and fundamental output energy (right-hand axis) of the baseline NSLS-II undulators as a function of the undulator parameter,  $K$ .

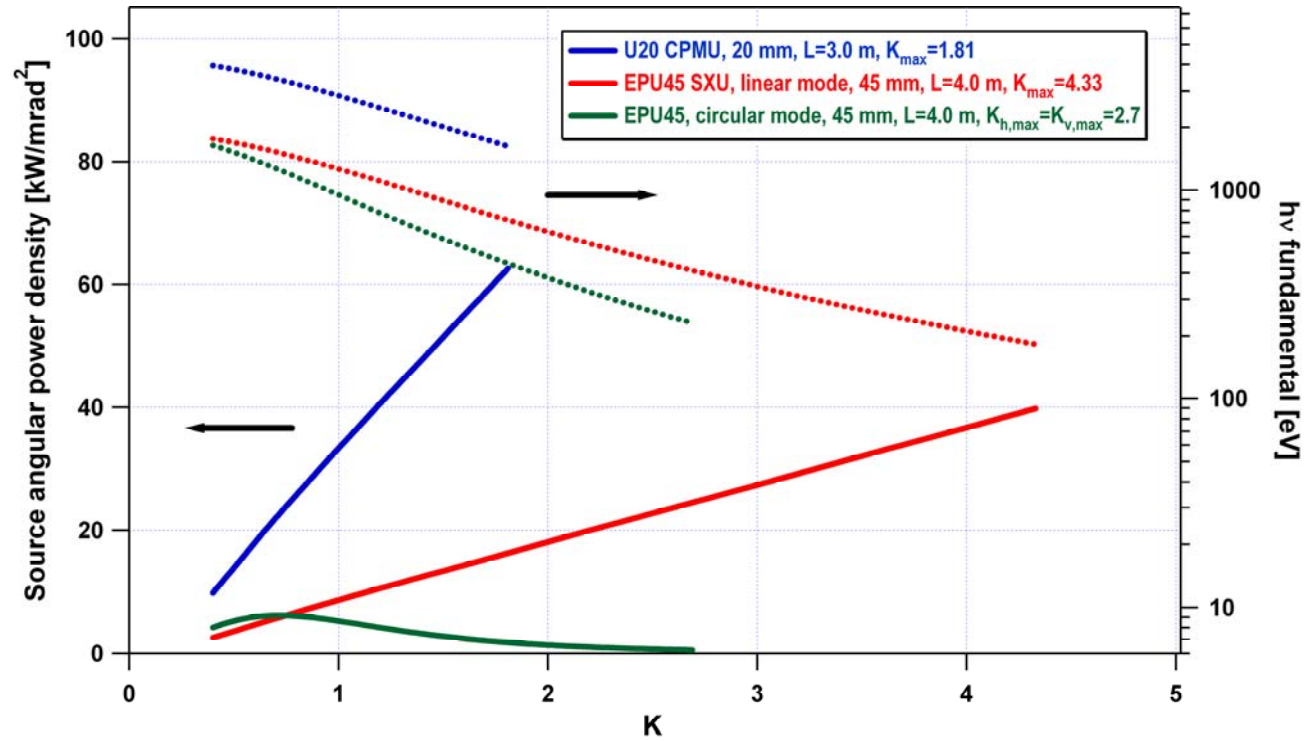
### 5.3.4 Power Density

Table 5.3.1 gives the maximum (on-axis) angular power density of the NSLS-II radiation sources; Figure 5.3.4 shows how the maximum angular power density of the undulators varies as their  $K$  value changes from  $K_{\min}$  (taken to be  $\sim 0.4$ ) to  $K_{\max}$ , as given in Table 5.3.1. For reference, the corresponding energy of the photons radiated in the fundamental as a function of  $K$  is also given. The energy of harmonic  $n$  is  $n$  times that of the fundamental. The maximum undulator angular power density radiated by the undulators at their maximum  $K$  settings (i.e., at minimum magnetic gap) varies from 40 to 65 kW/mrad<sup>2</sup>. The wiggler angular power density output is in the 25–55 kW/mrad<sup>2</sup> range, while the bend magnet and TPW values are again very much less, at 88 W/mrad<sup>2</sup> and 220 W/mrad<sup>2</sup>, respectively.

Figure 5.3.4 also shows that the EPU45 output angular power density in circular polarization mode is much lower than in linear polarization mode, and has a different dependence on  $K$ . This is primarily because in circular mode there are no higher harmonics, just the fundamental. An advantage of the circular



polarization mode is the lower output power density, which simplifies the design and operation of high energy-resolution beamlines by reducing the thermal deformations of the optical elements (see Chapter [xx]).



**Figure 5.3.4** Angular power density (left-hand axis) and fundamental output energy (right-hand axis) of the baseline NSLS-II undulators as a function of the undulator parameter,  $K$ .

### 5.3.5 Photon Beam Size

The  $1\text{-}\sigma$  effective photon beam size of the NSLS-II undulators is shown in Figure 5.3.5 as a function of photon energy. The lowest, straight (on a log-log graph) gray lines show the “natural” photon beam size, which is the size of a diffraction-limited photon beam for a zero emittance (and therefore zero size) electron beam. This diffraction-limited, “natural” photon beam size  $\sigma_{photon}$  is given by

$$\sigma_{photon} = \frac{1}{4\pi} \sqrt{2L\lambda} \quad (5.1-2)$$

One measure of the effective photon beam size,  $\sigma_{eff}$ , is given by the quadrature sum of the electron ( $\sigma_{electron}$ ) and photon,  $\sigma_{photon}$ , contributions:

$$\sigma_{eff} = \sqrt{\sigma_{electron}^2 + \sigma_{photon}^2} \quad (5.1-3)$$

The red and blue curves show  $\sigma_{eff}$  for the EPU45 SXU and U20 IVU undulators, respectively, in the vertical and horizontal planes, as labeled. Clearly, the undulator radiation is nearly diffraction-limited in the vertical plane over a wide photon energy range, from the far-infrared to  $\sim 2$  keV. The deviation of the effective source size from the natural, diffraction-limited value is due to the contribution of the small, but finite, electron beam



size. The effective beam size in the horizontal plane is approximately an order of magnitude greater than the natural, diffraction-limited value at 10 keV, but at 10 eV and below is nearly diffraction-limited.

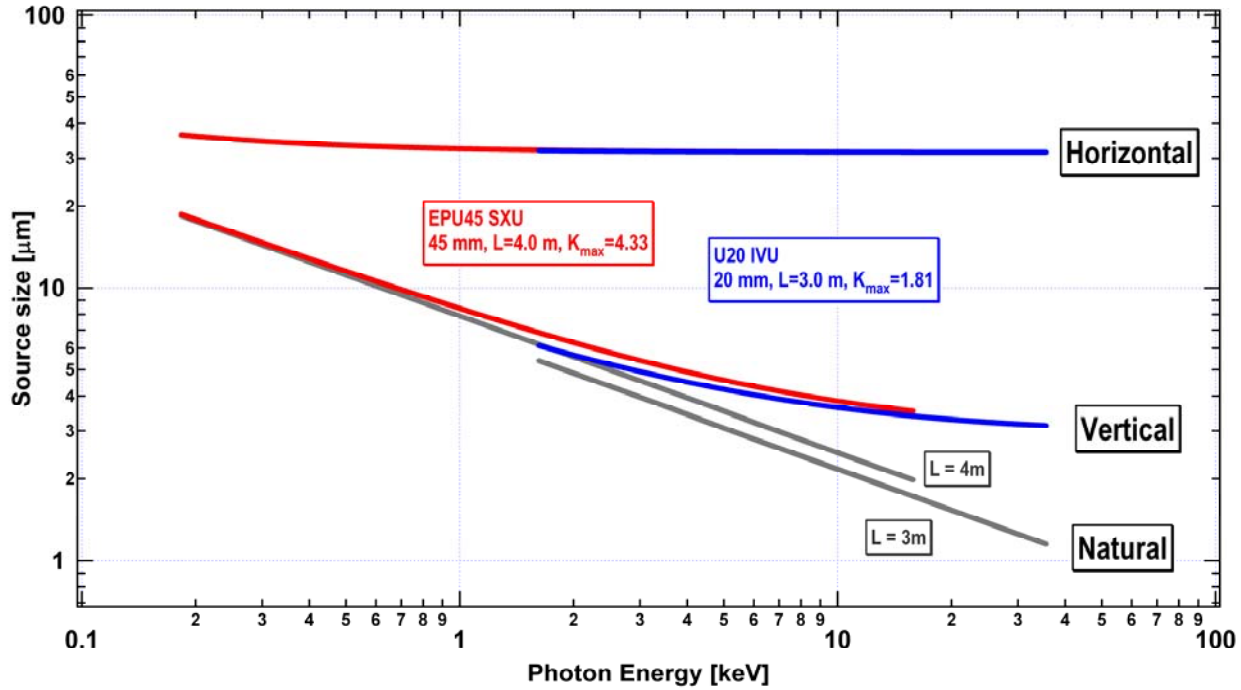


**Figure 5.3.5** Photon beam source size in the horizontal and vertical directions for the NSLS-II undulators. The straight (gray) lines represent the corresponding diffraction-limited values (i.e., the zero electron beam emittance limit).

### 5.3.6 Photon Beam Angular Divergence

The 1- $\sigma$  effective photon beam angular divergence of the NSLS-II undulators is shown in Figure 5.3.6 as a function of photon energy. The lowest, straight (on a log-log graph) gray lines show the “natural” photon beam angular divergence, which is the angular divergence of a diffraction-limited photon beam for a zero-emittance (and therefore zero angular divergence) electron beam. The diffraction-limited, “natural” photon beam angular divergence  $\sigma'_{photon}$  is given by

$$\sigma'_{photon} = \sqrt{\frac{\lambda}{2L}} \quad (5.1-4)$$

and the effective photon beam angular divergence  $\sigma'_{eff}$  is again given by the quadrature sum of the electron ( $\sigma'_{electron}$ ) and photon ( $\sigma'_{photon}$ ) contributions:

$$\sigma'_{eff} = \sqrt{\sigma'_{electron}{}^2 + \sigma'_{photon}{}^2} \quad (5.1-5)$$

The red and blue curves in Figure 5.3.6 show  $\sigma'_{eff}$  for the EPU45 SXU and U20 IVU undulators, respectively, in the vertical and horizontal planes, as labeled. As in Figure 5.3.5 for beam size, Figure 5.3.6 shows that the angular divergence of the undulator radiation from NSLS-II undulators is nearly diffraction-limited in the vertical plane, and only somewhat less so in the horizontal plane, over the wide photon energy range from the far-infrared to  $\sim 2$  keV. The deviation of the effective source angular divergence from the natural, diffraction-limited, value is due in part to the contribution of the tiny, but finite, beam angular divergence of the NSLS-II electron beam. In the horizontal plane, the effective beam angular divergence is

approximately a factor of 2 or 3 greater than the natural, diffraction-limited, value at 10 keV, but is nearly diffraction-limited at 10eV.

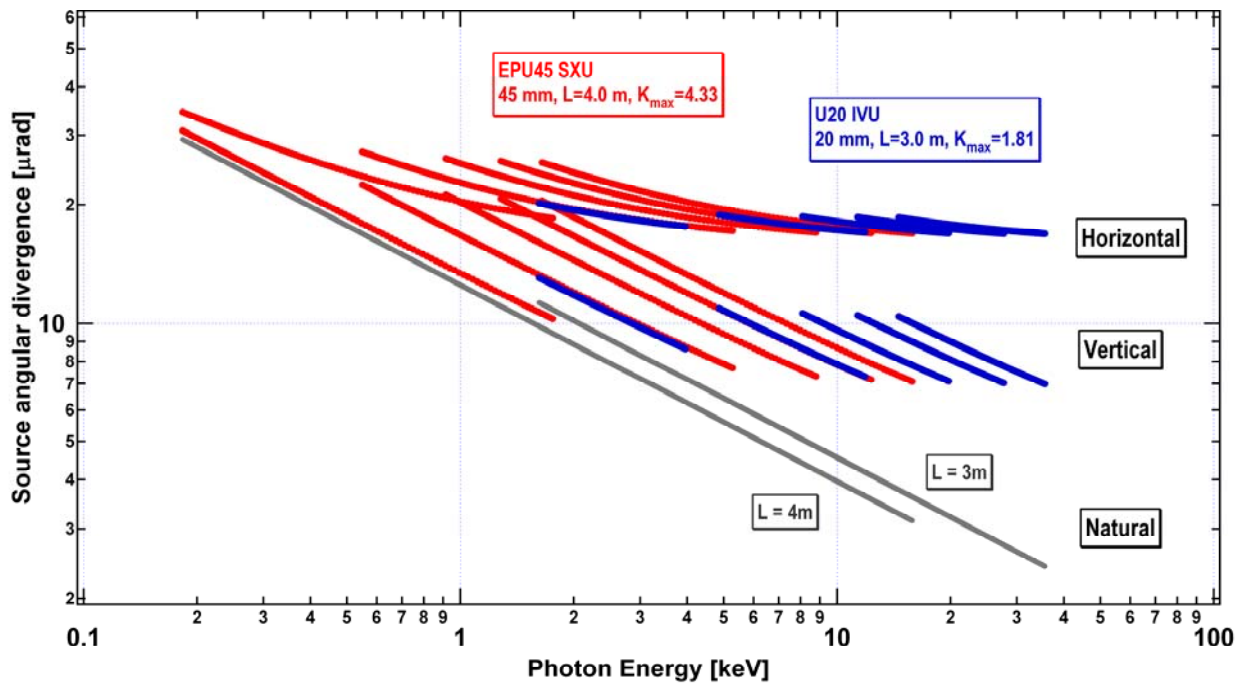


**Figure 5.3.6** The angular divergence in the horizontal and vertical directions of the photon beam for the NSLS-II undulators. The straight (gray) lines represent the corresponding diffraction-limited values (i.e., the zero electron beam emittance limit).

The angular divergence is also limited by the finite energy spread of the electron beam. A noteworthy feature of Figure 5.3.6 is that the angular divergence of the various harmonics for a given undulator is approximately equal to that of the fundamental of that undulator. That is, it appears, empirically, that the angular divergence of undulator harmonic  $n$  is given by

$$\sigma'_n \approx \sqrt{\frac{\lambda_1}{2L}} \quad (5.1-6)$$

for  $n = 1, 3, 5, 7, \text{ or } 9$ , in both the horizontal and vertical planes. This value is  $\sqrt{\lambda_1/\lambda_n} = \sqrt{n}$  times larger than the zero-emittance angular divergence.

Thus, the limiting factor governing the vertical angular spread of the  $n > 1$  harmonics of NSLS-II undulators is the finite energy spread of the electron beam, which for the fully-damped case is  $\delta E/E \sim 0.001$ . This effect is stronger for the hard x-ray undulator (U20) than for the soft x-ray undulator (EPU45), but clearly affects both.

## 5.4 Infrared

The intrinsic infrared brightness of most synchrotron storage ring sources is determined entirely by the circulating beam current. This is certainly the case for the low emittance electron beam of the NSLS-II storage ring, and the goal of 500 mA beam current is very attractive from the standpoint of infrared performance. The ring is designed for an extremely stable beam; an important characteristic for the standard

rapid-scan interferometric techniques employed in most infrared spectroscopies. But designing an optical extraction configuration that preserves the brightness, while meeting mechanical and accelerator design constraints, can be quite difficult. Typically, the large angular collection needed to achieve an acceptable performance involves nonstandard construction geometries for the dipole chambers. These, in turn, can affect the beam impedance and lead to instabilities. A careful impedance analysis will be integral to the design of any dipole chamber intended for extracting infrared radiation, and efforts are underway to treat this issue quantitatively.

It is well known that dipole (bending) magnets produce infrared radiation by two distinct mechanisms: the conventional synchrotron radiation (bending magnet radiation) is produced in the body of the magnet, whereas edge radiation is produced as electrons enter or exit a dipole's magnetic field [5.4.1]. Infrared beamlines have been built to utilize one or the other of these source types, and sometimes both. For reasons outlined later in this section, we plan to meet most of the source requirements using bending magnet radiation, but also plan to collect and extract edge radiation. The beamline design and performance analysis described in Chapter 11 will take both source types into account.

### 5.4.1 Bending Magnet Source

The collection efficiency for conventional dipole bend radiation is determined by the natural opening angle for synchrotron radiation in the long wavelength limit. For a wavelength  $\lambda$  and bend radius  $\rho$ , the RMS half-angle is defined as:

$$\theta_{\lambda} = \left( \frac{3}{4\pi} \frac{\lambda}{\rho} \right)^{1/3}. \quad (5.4-1)$$

From this expression we see that the large bending radius ( $\rho \sim 25$  m) of NSLS-II dipoles causes the infrared to be emitted into angles 2.35 times smaller than for the existing NSLS VUV/IR ring ( $\rho \sim 1.9$  m). Thus, the performance for NSLS-II with 38 mrad extraction would be identical to a 90 mrad extraction from the VUV/IR ring. A study of the NSLS-II dipole design indicates that a horizontal extraction of 50 mrad is achievable (plus an additional 5 mrad on the “negative side”, useful for collecting edge radiation). This is based on an infrared extraction where the second dipole in a DBA cell is used in order to stay clear of any potential insertion device beamline (Figure 5.4.1). The large bending radius makes extraction increasingly difficult as one continues toward the second half of a dipole, giving rise to the 50 mrad horizontal collection limit.

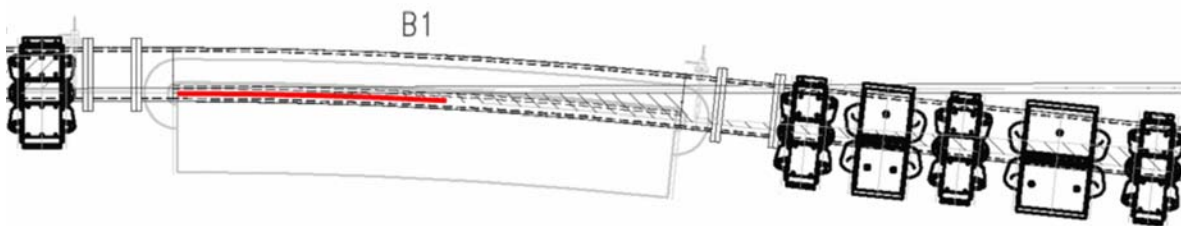


**Figure 5.4.1** Drawing of the second dipole magnet in the NSLS-II DBA 30 lattice. Red line indicates the candidate IR source orbit segment. Approximately 50 mrad of horizontal collection appears feasible, including the zero degree segment for edge radiation.

The standard NSLS-II dipole bending magnets allow a vertical chamber dimension of  $\sim 25$  mm and represent another constraint for infrared, limiting the vertical collection to approximately 16 mrad (the value varies from 12 mrad up to 20 mrad due to the large source depth). While this is adequate for mid-infrared spectroscopy as used in chemical imaging, it limits the performance for far-infrared spectroscopy due to the relatively large angles into which this radiation is emitted. Therefore, we are planning for a second dipole

magnet design for use on far-infrared ports. This dipole would have a ~60 mm (or larger) gap and would accept a dipole chamber providing an average 32 mrad of vertical collection (and potentially up to 48 mrad with a larger dipole gap). The need for such a large aperture port becomes even more apparent when one considers the shielding effects of a conducting dipole vacuum chamber. The subject has been treated most thoroughly by Bosch [5.4.2] who confirmed (theoretically) that bending magnet radiation is suppressed for wavelengths greater than an effective cutoff value given by  $\lambda_c=(h^3/\rho)^{1/2}$  where  $h$  is the chamber height and  $\rho$  is the bending radius. The large bending radius of NSLS-II, combined with a standard chamber height of 25 mm, results in a cutoff wavelength of 800  $\mu\text{m}$ , effectively removing the portion of the THz spectral range most important for magnetospectroscopy. This provides another compelling reason for a larger dipole chamber and 60 mm gap dipole magnet. Indeed, increasing the dipole gap an additional 30 mm (to accept a 75 mm vertical height chamber) would shift the cutoff wavelength to beyond 4 mm. In all cases, the detailed dipole chamber design and transitions will require careful study in terms of electron beam impedance and potential instabilities. Our initial impedance analysis for a 50 mm high chamber appears promising and suggests that an even larger (75 mm) chamber would be feasible. However, more detailed calculations will be needed for actual chamber mechanical designs to ensure no instability problems will arise.

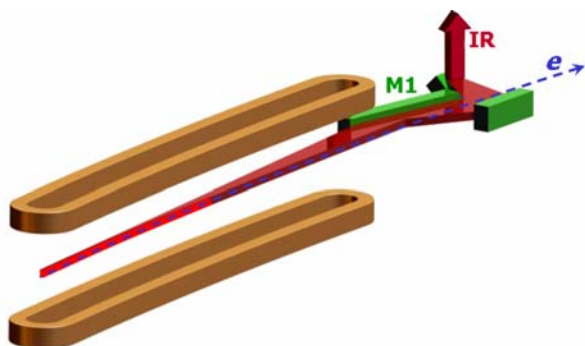


**Figure 5.4.2** NSLS-II Infrared Dipole Radiation Extraction. The bright red segment marks the electron beam segment serving as an infrared source. The radiation is collected by a long mirror (M1) and reflected out of the dipole chamber by a second and third mirror combination.

The extraction arrangement for NSLS-II is proposed to have the 1<sup>st</sup> mirror optic integrated into the dipole chamber construction. The metal mirror can be made to be electrically contiguous with the chamber wall to minimize impedance effects. The oblique angle of incidence and soft x-ray spectrum from the large NSLS-II dipole bending radius limits the local power load on this optic to well under 1 kW/cm<sup>2</sup>, such that a special slot or cooling mask may not be required (Figure 5.4.2). Finite element analysis will be performed on candidate mirror materials (e.g., aluminum or copper) to confirm that this heat load can be directly managed without significant optical distortion of the surface. Initial studies of the required optical figure for this 1<sup>st</sup> mirror suggest that a simple toroidal shape will suffice, allowing conventional diamond turning to be used in its construction (Figure 5.4.3). The remaining optical elements can be either conventional aluminized glass or diamond-turned aluminum to meet specific optical design requirements.

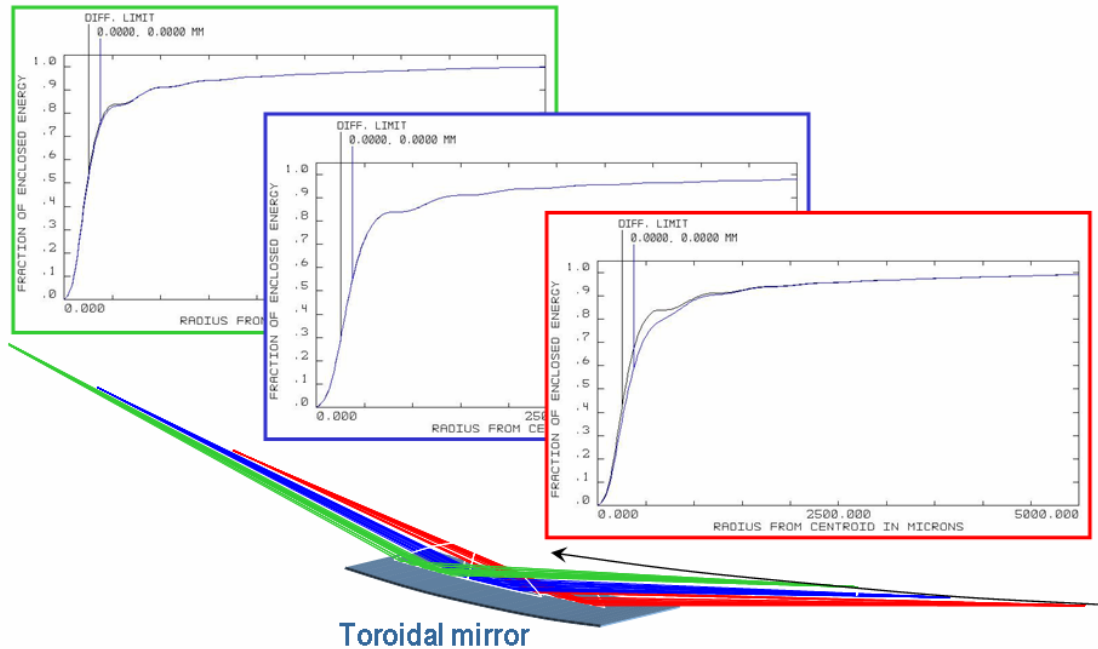


**Figure 5.4.3** Extraction Optical Performance. ZEMAX optical analysis for a toroidal first mirror optic when used to focus a dipole bend/arc source at a wavelength of  $6\ \mu\text{m}$  (mid-infrared). Near diffraction limited performance is achieved along the entire source length.

A detailed performance comparison for these NSLS-II dipoles and the existing VUV/IR ring dipoles can be made using the standard expressions for dipole synchrotron radiation in the low frequency limit. The flux calculations can be compared to results from other synchrotron radiation source codes such as SPECTRA [5.4.3] or SRW [5.4.4] to check for consistency. Though some of these calculations are for the photon flux, they can be used for comparing brightness whenever the source's physical dimensions are smaller than the diffraction limit (the case for all IR wavelengths on NSLS-II, and IR wavelengths longer than 10 microns for the existing NSLS VUV/IR ring). We find that all three calculations agree to within 10% for the intrinsic flux of dipole radiation when multiparticle coherence and chamber shielding effects are ignored. Note that one can convert from units of  $\text{ph/s}/0.1\% \text{BW}$  to watts per wavenumber, multiplying by  $2 \times 10^{-20}$ . Calculation results are shown in the Figures 5.4.4 and 5.4.5, along with a calculation for an existing port on the VUV/IR ring, indicating that NSLS-II can serve as a highly competitive, and indeed, world-leading, storage ring source for infrared.

Details of these calculation results show that an extraction based on a conventional NSLS-II dipole (average of 16 mrad vertical and 50 mrad horizontal) will be sufficient for mid-infrared spectroscopy, including microprobes and imaging. We envision two options for such mid-infrared extractions. In one option, the beam is divided horizontally to simultaneously serve two or three mid-infrared microprobe end stations. The three collections (in order of entering the dipole) would be (H×V)  $15 \times 12$  mrad,  $15 \times 16$  mrad, and  $20 \times 20$  mrad. The varying vertical aperture is due to the changing distance between the first collecting mirror and the collected source segment as a function of horizontal position (angle). The performance for any of these extractions exceeds the present performance of the NSLS VUV/IR ring over most of the mid-infrared. Only at the long wavelength (low frequency) end of this spectral range are the three extractions distinguishable, with the  $20 \times 20$  mrad outperforming the other two. But it should be noted that the initial  $15 \times 12$  mrad collection also includes the zero-degree component, giving this the added feature of edge radiation (not included in the brightness calculation). In the other option, the entire horizontal swath is fed into a single microspectrometer end station based on a focal plane array detector for large area imaging, as

described in Chapter 11. The detailed optical system for matching the source to the instrument will be the subject of further research.

In the far-infrared, the brightness for a conventional dipole (16 mrad average vertical extraction) continues to fall away from the ideal value and below the present performance for the NSLS VUV/IR by a factor of 5 at  $25 \text{ cm}^{-1}$  ( $400 \text{ }\mu\text{m}$  wavelength). The degradation below  $10 \text{ cm}^{-1}$  becomes even more severe when the shielding effect of the 25 mm high dipole chamber is taken into account. Note that the shielding effect for dipole radiation is a complex subject, and we have taken it into account using a simplified approach. In this approach, it is assumed that radiation unable to couple into a propagating waveguide mode of the chamber is completely lost, and is roughly equivalent to truncating the effective near-field source size to a dimension equal to the chamber height (see [5.4.2], condition 2 for strong shielding). A large-gap dipole enables greater vertical collection efficiency and also shifts the shielding cutoff to lower frequencies. This is illustrated in the brightness calculations of Figure 5.4.5, which includes curves for the standard NSLS-II dipole extraction ( $50 \times 16$  mrad) plus two candidate large-gap dipole extractions ( $50 \times 32$  mrad based on a 50 mm high dipole chamber, and  $50 \times 48$  mrad based on a 75 mm high dipole chamber). Also shown is the existing performance for the NSLS VUV/IR ring's  $90 \times 90$  mrad ports plus the very large port beamline at the UVSOR facility (Okazaki, Japan) that represents the most competitive far-infrared beamline elsewhere in the world. (Note: This does not take into account the coherent THz synchrotron radiation mode of operation developed at BESSY and proposed for CIRCE by the ALS/Lawrence Berkeley Lab.) The  $50 \times 48$  mrad configuration would maintain the NSLS lead in the area of incoherent THz synchrotron radiation, and provide excellent ports for studying aspects of coherent synchrotron radiation production, a subject of great interest for future source development. Any of these ports would offer excellent mid-infrared performance.

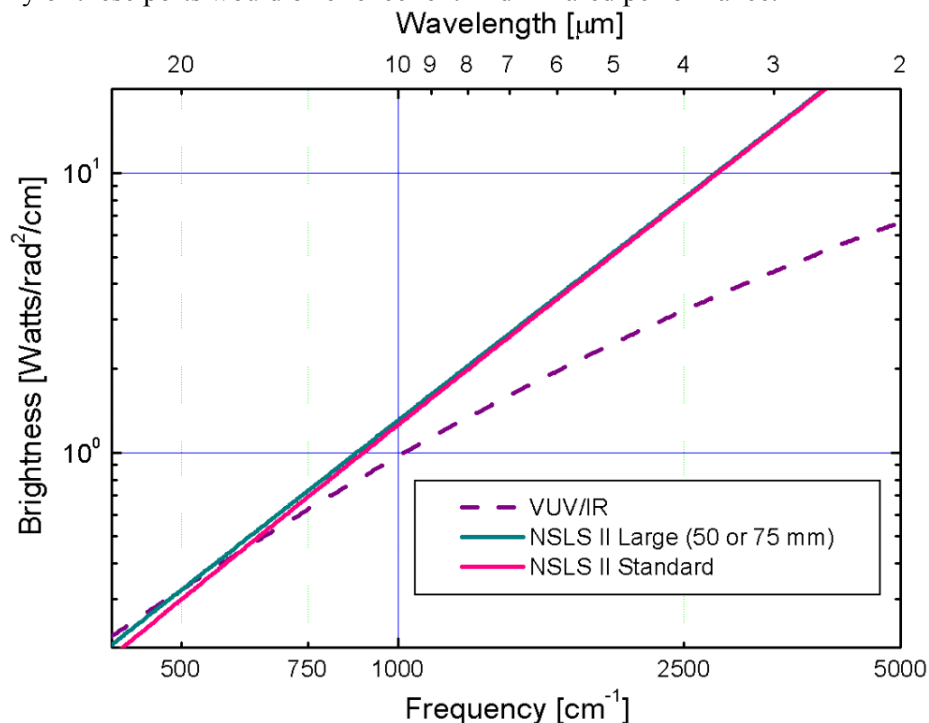


**Figure 5.4.4** Calculated NSLS-II brightness for the mid-infrared spectral range, comparing the existing VUV/IR ring with the two proposed for NSLS-II extractions. Note that the lower emittance of NSLS-II leads to brightness improvements over much of this spectral range and that the standard dipole chamber height of 25 mm is sufficient for this spectral range.



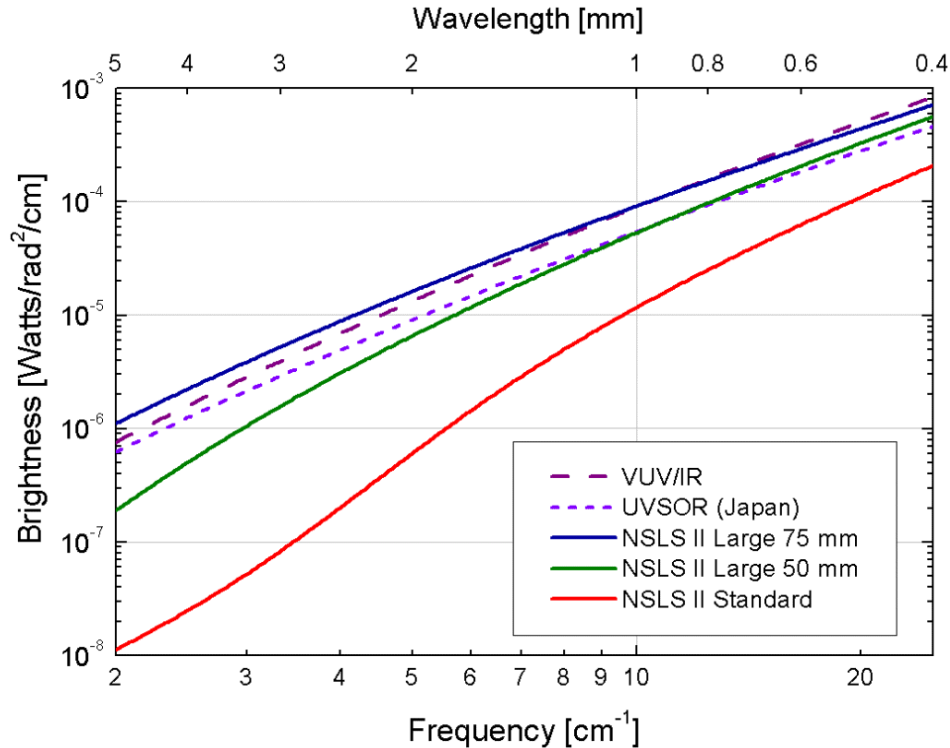


**Figure 5.4.5** Calculated NSLS-II brightness for the very far-infrared spectral range, comparing the existing VUV/IR ring with three collection geometries for NSLS-II having vertical dipole chamber heights as shown, plus a high-performance beamline at UVSOR. The cutoff effect of the standard-gap dipole chamber and 16 mrad collection can be clearly seen for wavelengths greater than 1 mm.

## 5.4.2 Dipole Edge Source

The proposed infrared extraction geometry allows for collection of the zero-degree segment from the dipole (in line with the upstream straight section), including  $\sim 5$  mrad on the opposite side. This will allow for the extraction of dipole edge radiation [5.4.1]. Dipole edge radiation has characteristics similar to transition or diffraction radiation, e.g., radial polarization. In contrast to bending magnet radiation, the far-field angular distribution for edge radiation is contained mostly within a cone of angle  $\theta = 1/\gamma$ . This implies an effective source size of  $\lambda\gamma$  and a very long formation length of  $\lambda\gamma^2$  such that computations designed exclusively for the far-field are no longer accurate. An added complication stems from the fact that dipole edges typically occur in pairs, leading to a ring-like interference pattern that depends on wavelength. The SRW code [5.4.4] includes near-field terms suitable for calculating edge radiation in the ideal case where the ring chamber has no shielding effect on the radiation. An example result from SRW is shown in Figure 5.4.6, and illustrates both edge radiation (ring-like pattern at right) and bend radiation (broad smear extending to left). The actual projection of the beam onto the first mirror optic will be stretched horizontally about a factor of 3 compared to these views (due to the  $75^\circ$  angle of incidence for the radiation).

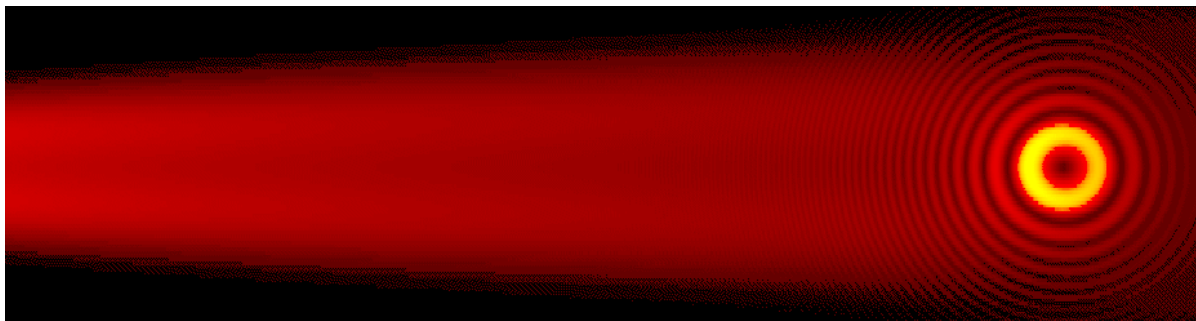


**Figure 5.4.6** SRW analysis for 55 mrad (-5 to +50) horizontal and 12 to 20 mrad vertical collection of 6  $\mu\text{m}$  wavelength infrared radiation produced in the leading section of an NSLS-II dipole bending magnet. The ring pattern is due to interference from the back edge of the previous dipole, located 5.6 meters upstream (distance between dipole edges in a DBA cell). The broad stripe of radiation extending to the left is the conventional bending magnet radiation.

Though a few infrared beamlines based on edge radiation exist (e.g., at ANKA/Karlsruhe, SRC/Wisconsin, and ESRF/Grenoble), the detailed performance at long wavelengths has not been formally demonstrated. There are two reasons to be concerned about the long wavelength performance. First, the radius of the first constructive interference ring moves outward with increasing wavelength such that the collection through a finite aperture will suffer. Second, the large effective source size is expected to cause a shielding (waveguide) cutoff when the wavelength exceeds  $h^2/R$ , where  $h$  is the chamber height and  $R$  is the distance from the source to the collecting aperture [5.4.2]. Our extraction aperture would be situated approximately 3 meters away from the source point and, with a nominal chamber height of 25 mm, the cutoff would begin at a wavelength of  $\sim 200 \mu\text{m}$  such that a significant portion of the very far-infrared would be lost. Edge radiation also introduces complications for mid-infrared microspectroscopy and imaging due to its radial polarization. The source itself is point-like, making it less suitable for illuminating large area focal plane array detectors that are expected to become the standard approach for delivering large area, high-resolution images. For these reasons, our infrared extraction will be based primarily on conventional bending magnet radiation, but we will have the opportunity to exploit the unique characteristics of edge radiation where beneficial.

## References

- [5.4.1] R.A. Bosch et al., *Rev. Sci. Instr.* **67**, 3346 (1996); Proceedings of the Ninth Nat'l Conf. on Synch. Rad. Instrum., Argonne, IL, (1995.)
- [5.4.2] R.A. Bosch, *Nucl. Instrum. & Meth. Phys. Res. A* **482**, 789 (2002).
- [5.4.3] T. Tanaka and H. Kitamura, *J. Synch. Rad.* **8**, 1221 (2001)
- [5.4.4] O. Chubar and P. Elleaume, *Proc. of the EPAC98 Conference*, 1177 (1998).
- [5.4.5] G.L. Carr, *Vibrational Spectroscopy* **19**, 53 (1999); R.P.S.M. Lobo, et al., *Rev. Sci. Instrum.* **73**, 1 (2002).





## 5.5 Conceptual Magnetic Designs for the IDs

In Section 5.1 we specified the types of insertion devices that are needed to meet user requirements and to achieve the unprecedented brightness goals of NSLS-II. We presented the optical performance and spectral characteristics of these IDs. They are based on proven designs, and in some cases push the state of the art in what we believe to be rational and realizable extensions of existing technology. In this section we present conceptual magnetic designs of the various ID types that will meet the performance requirements and constraints. We also identify and describe the R&D and prototyping needed to verify each design concept, to resolve any unknowns, and to test advanced concepts for future upgrade paths. We describe novel mechanical concepts that may simplify ID designs and/or improve their performance. Finally, we describe magnetic measurement systems that will be developed to verify and optimize ID performance.

Section 5.5.1 deals with the damping wiggler, which is also used as a broadband source.

Section 5.5.5 discusses tunable, planar, hard x-ray sources, specifically the mini-gap, in-vacuum undulator (IVU) as a baseline device, and its most recent evolution, the cryo-permanent magnet undulator (CPMU).

Section 5.5.3 describes variable polarization devices for soft x-rays and vacuum ultra-violet. The baseline design is an Apple-II type machine. An alternative HiSOR-type design was considered.

Section 5.5.4 addresses using a permanent magnet three-pole wiggler (3PW) to meet the needs of the current users of hard X-ray bending magnets at NSLS.

In Section 5.6, the IDs to be installed or considered in later stages of beamline construction will be discussed. Those devices are the superconducting wigglers (both low- and high-temperature types), superconducting undulator, quasi-periodic undulator, and revolver-type undulator. Also discussed in Section 5.6 is the development of an insertion device Magnetic Measurement Facility (MMF).

### 5.5.1 Damping Wigglers

Earlier we defined two key parameters of the damping wigglers (DWs): the operating peak field of 1.8 T and an eventual total length of 56 m. The peak field value was chosen to be high enough to radiate sufficient power for adequate emittance damping, but not so high as to create excessive energy spread. The DWs are also useful as high-flux, high-brightness broadband sources in the hard x-ray range.

The initial installed length of DWs will be 21 m, composed of six wigglers, each 3.5 m long. A third key design parameter is the minimum magnetic gap. The estimated vertical stay-clear aperture at  $\pm 3.5$  m from the center of long straight section is 9.5 mm. Allowing for beamtube wall thickness of 1 mm, plus 0.5 mm clearance between the beamtube and the magnet poles, we obtain a minimum magnetic gap of 12.5 mm. From empirical design formulas developed by Elleaume for various planar undulator (wiggler) technologies [5.7.15], we find that 1.8 T peak field can be produced at that gap by a conventional PM-hybrid wiggler with a period of 90 mm, using high-field NdFeB magnets ( $B_r = 1.2$  T) and vanadium permendur poles. However, the total radiated power from such a wiggler is less than that by the device with ideal sinusoidal field due to longitudinal higher harmonics contents. Therefore, special care is needed to optimize the field profile. Unlike users of undulator radiation, wiggler users expect a broad, dipole-like spectrum. Therefore, minimizing phase errors is not important. Shimming of DWs is concerned mainly with trajectory straightness and multipoles. In fact, gap taper, or variation in pole periodicity are sometimes introduced in wigglers intentionally to spoil coherence and to smooth the spectrum.

DWs must meet the same integrated dipole and multipole error specifications imposed on all IDs. However, since they will operate at fixed gap, these errors can be shimmed out more easily than in variable-

gap IDs, without concern about gap-dependence. The next sections discuss some additional design considerations for DWs.

### 5.5.1.1 Dynamic Field Integral

The integrated field seen by sinusoidally wiggling electrons [5.5.1.1] is

$$\int B_y ds \approx \frac{-L}{2k^2 B \rho} B_y(x_i) \frac{dB_y(x_i)}{dx}, \quad (5.5.1-1)$$

where  $L$  is the device length,  $k_w$  is the  $2\rho$ /period length,  $\rho$  is the radius of curvature of the trajectory, and  $x_i$  is the horizontal displacement of the electron. This is called dynamic field integral, and it scales as ID period squared and as the derivative of the transverse field roll-off. An important aspect of optimization of long-period wiggler magnetics is how to determine the necessary transverse pole width to minimize the effect of the dynamic field integral effect while minimizing attractive force, which is proportional to the magnet area, and keeping the cost as low as possible. Beam tracking reveals the detrimental effect of this integral on the beam dynamics. However, ordinary magnetic measurement method in straight line is incapable of measuring this effect. Therefore, careful modeling effort is required for long period device.

### 5.5.1.2 Attractive Force and Size/Cost Challenges of the Damping Wigglers

For NSLS-II, the damping wigglers will be used as a broadband source. The design calls for 7 m of damping wiggler in an 8 m straight. In reality, it is easier to combine two 3.5 m devices. The approximate attractive force of a planar device is given as follows:

$$F_{ID} \approx \frac{B_y^2 WL}{4\mu_0}, \quad (5.5.1-2)$$

where  $W$  is the horizontal width of poles or magnets,  $L$  is the total length of the device, and  $\mu_0$  is the permeability of the vacuum. With  $W = 80$  mm and  $B_{oy} = 1.8$  T, the attractive force per meter is about 60 kN. A variable-gap device must have a structure that is rigid enough not to create intolerable multipole components due to deflection. As this is an out-of-vacuum device, many different designs have worked properly in storage rings.

Wigglers of this type, from 2 to 4 meters in length, have been designed and build to specification by industry for many synchrotron light sources. The mechanical structures to support and control the gap of these wigglers are generally massive and expensive for variable gap device. However, NSLS-II DW is designed to operate at a fixed gap, no strict parallelness of magnet arrays is required at other gap positions. On the other hand, the available cross section of a device for NSLS-II is substantially smaller than other equivalent facility due to the lower beam height (1.0 m compared to 1.2-1.4 m for most of facilities in the world) and due to the need to have extra space in the tunnel for emergency evacuation. A detailed design study will consider alternative magnet configurations that could lessen the need for these massive structures while maintaining the structural rigidity. The goal of this project is to design a magnet configuration that can utilize a relatively compact, lower-cost magnet support system that ultimately could reduce the cost of these wigglers significantly.

### 5.5.1.3 Non-Sinusoidal Field Effect

Another issue for long-period undulators is the deviation from sinusoidal field, which effectively reduces the deflection parameter. (This is not an issue for wigglers, where the critical energy depends on peak field only.) We examine a hybrid undulator with side magnets and permendur poles with the parameters shown in Table 5.5.1.1.

**Table 5.5.1.1 U90 Wiggler Parameters.**

Period length [mm]	90
Nominal peak field [T]	1.8
Remanent field ( $B_r$ ) [T]	1.20
Gap [mm]	12.5
Magnet horizontal size [mm]	140
Magnet vertical size [mm]	95
Main Pole horizontal size [mm]	80
Main Pole vertical size [mm]	75
Air gap [mm]	0.1
Chamfer (magnet) [mm]	2.0
Chamfer (pole) [mm]	1.5
Corner cut (magnet) [mm]	3.0
Gap offset (magnet) [mm]	0.25

By varying the pole thickness while keeping fixed the total period length, we have calculated the peak magnetic field (induction) and effective  $K_y$ , as shown in Table 5.5.1.2. When the pole thickness is reduced from 21 to 19 mm, the peak field increases from 1.80 to 1.85 T and effective  $K_y$  decreases from 15.2 to 15.1. This indicates that the field deviates too much from the sinusoidal form.

**Table 5.5.1.2 Comparison of Peak  $K_y$  and Effective  $K_y$  with Varying Pole Width (Period Length=90 mm)**

Pole Thickness (mm)	Peak Field (T)	Peak $K_y$	Effective $K_y$
19	1.85	15.6	15.1
20	1.83	15.4	15.2
21	1.80	15.2	15.2
22	1.75	14.7	15.1

The effective K value should be close to the peak K value of a sinusoidal wave of peak amplitude of 1.8T to obtain equal amount of radiated power assumed in emittance reduction calculation. The following quantity was numerically calculated over one period to compare the value with sinusoidal field.

$$P_{per} = \int_L^{-L} B_y^2 ds \quad (5.5.1-3)$$

where  $L$ =period length /2. With pole thickness of 21 mm, the effective field appears to be closest to that of ideal sinusoidal field.  $P_{per} = 1.01 P_{per}$  (ideal).

### 5.5.1.4 Baseline Damping Wiggler Design

A hybrid structure with side magnets and permendur poles has been chosen for the NSLS-II device. Soft iron poles are significantly cheaper than permendur but produce slightly lower field. Figure 5.5.1.1 is an isometric rendering of the W90 magnet arrays by Radia. The side magnets shown in magenta have identical size; two different sized magnets are shown in green. Pieces in yellow represent permendur poles. Figure 5.5.1.2 shows the end view of the array.

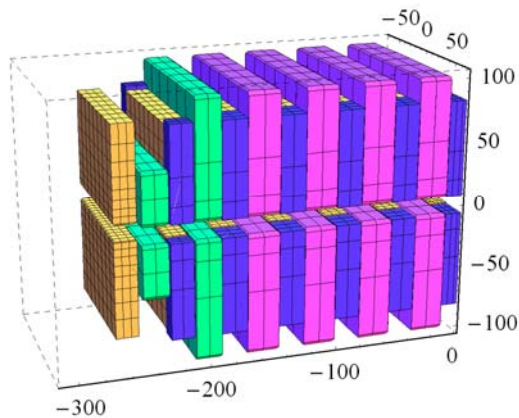


**Figure 5.5.1.1** Magnet arrays of W90. Only the first few periods are shown, for clarity. Units are millimeters.

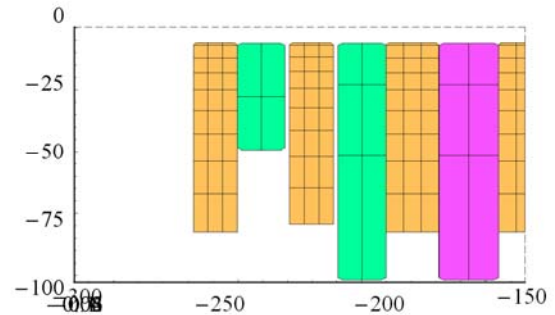


**Figure 5.5.1.2** End view of W90.

The field and trajectory computed from the model are plotted in Figure 5.5.1.3, for a gap of 12.5 mm. The trajectory is calculated by a particle-tracking Runge-Kutta routine. The particle is launched with zero offset and angle ( $x = 0$ ,  $x' = 0$ ), and its position and angle are calculated every 2.5 mm (36 points per period). The amount of change in the first integral can be easily compensated by external coils.

a

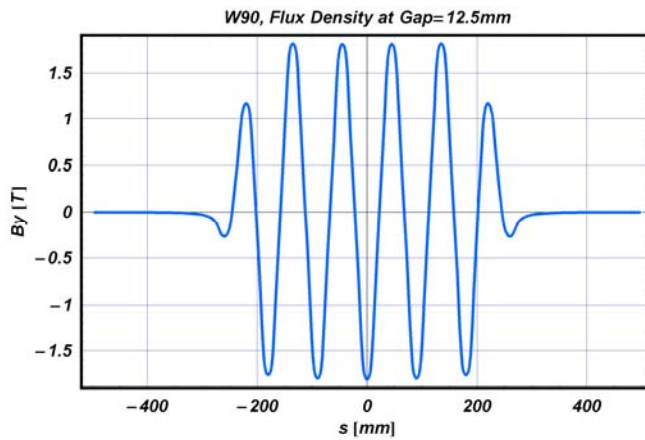
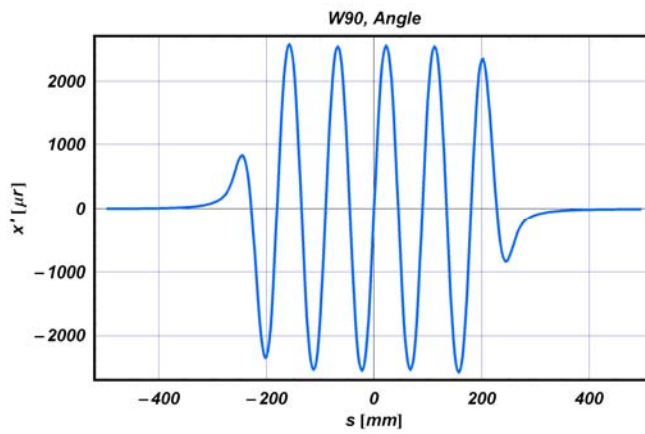


**Figure 5.5.1.3** Field, angle, and trajectory plots for the five-period model of W90.

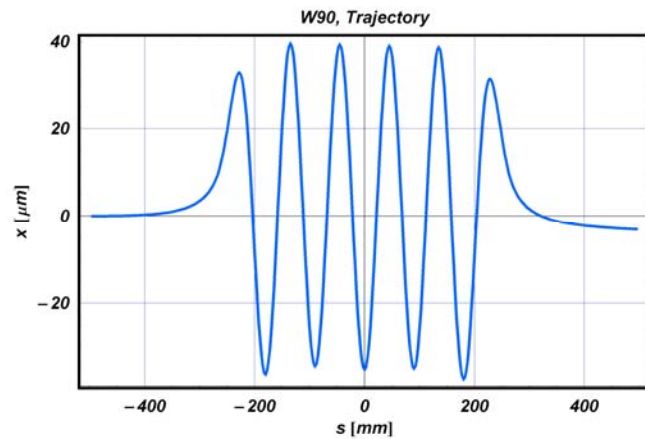
a) Vertical magnetic flux density at a gap of 12.5 mm.

b



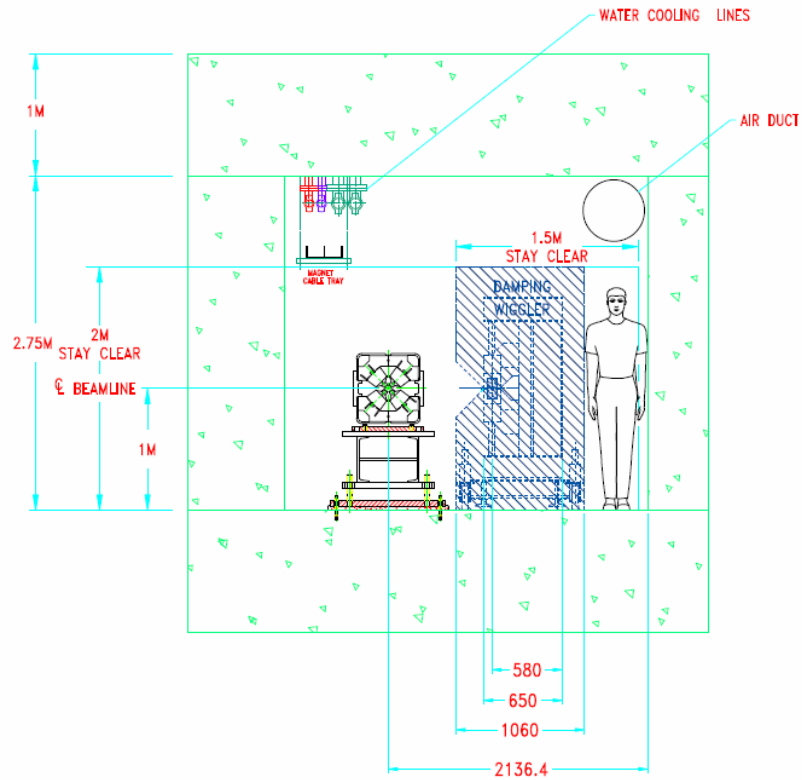
b) Horizontal angle at a gap of 12.5 mm.

c



c) Horizontal trajectory at a gap of 12.5 mm.

**Figure 5.5.1.4** Available cross section of NSLS-II DW.



There is one challenging requirement for all NSLS-II insertion devices. That is an unusually restricted transverse cross section available for the devices. Firstly, the NSLS-II beam height is only 1.0 m compared to 1.4 m at many U.S. facilities and 1.2 m at some European and Japanese facilities. Secondly, the horizontal size is limited due to safety requirements which demand certain space in the tunnel during device transport. The external dimensions of the NSLS-II DW must conform to the envelope shown in Figure 5.5.1.4. Preliminary FEA analysis with 63 kN/m attractive force was carried out by STI Optronics, Inc. The result is shown in Figure 5.5.1.5, where the units for transition are shown in inches. These deformations translate approximately 3.9 mrad of roll angle for each strongback, which can be compensated for operating gap.

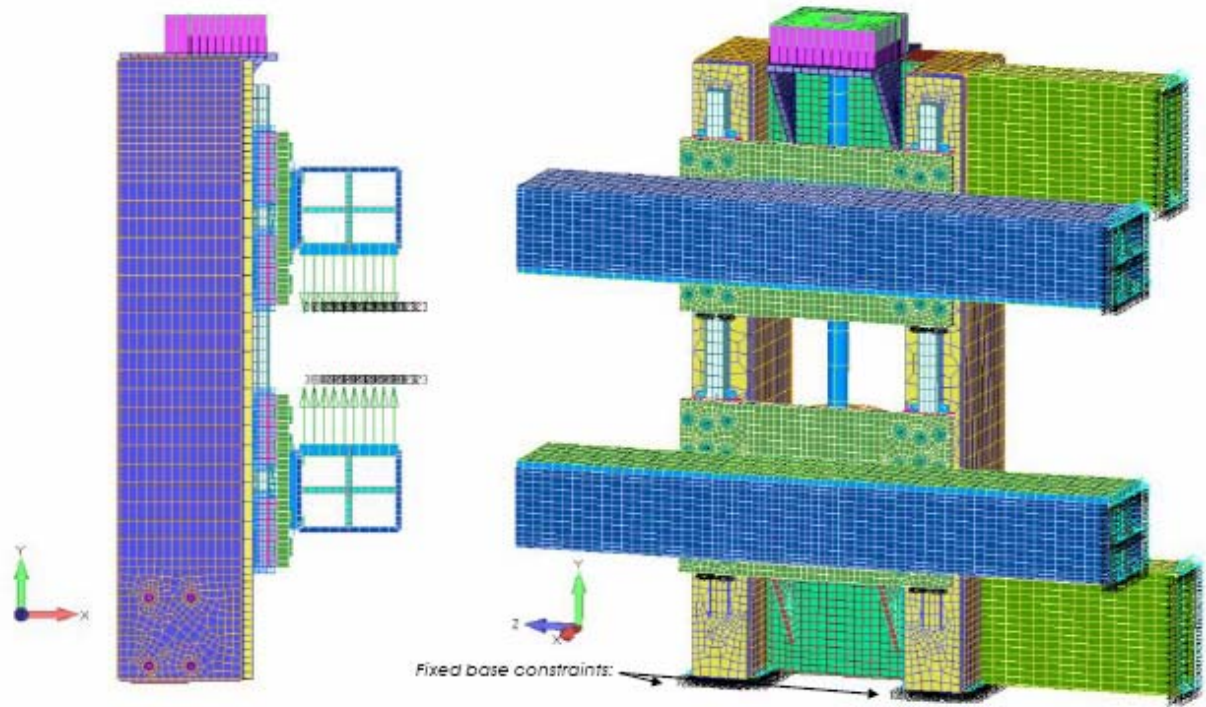


Figure 5.5.1.5 FEA analysis model

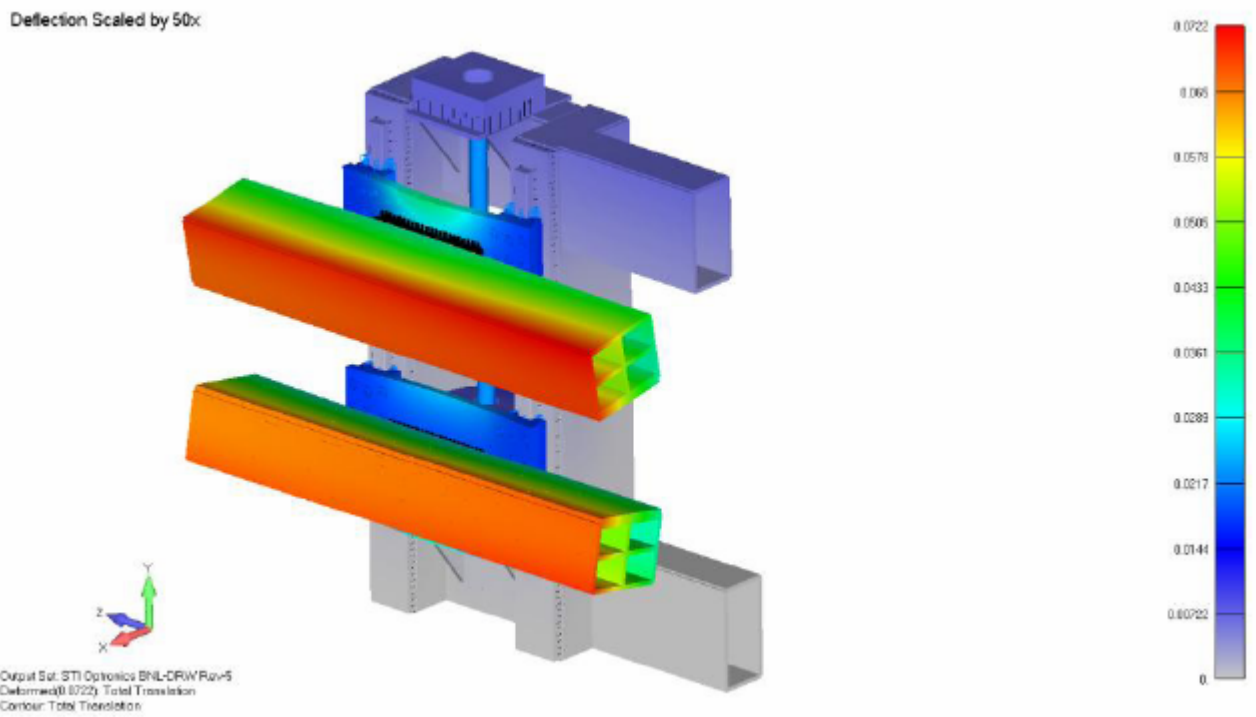


Figure 5.5.1.6 Displacement plot



### 5.5.1.5 R&D Elements for DW Development

Superconducting devices, especially HTS versions, can be considered as an alternative choice for DWs. However, unlike user devices, these DWs are an integral part of the light source lattice and any failure would result in the degradation of emittance, which affects all the users in the facility. Therefore, it is essential to achieve extremely high reliability for the SCWs to be considered as an alternative for PM-based DWs. Extensive reliability studies will be necessary if this option is pursued.

Another subject is a novel gap separation mechanism, which should simplify the mechanical structure of the device. Attractive force for wiggler magnets is much larger than that by an undulator, so conventional structures tend to be very rigid and heavy in order to avoid deflection. As NSLS-II DWs are presumed to be fixed-gap devices, no strict requirement for gap parallelness is required for the open position. One option is the scheme employed at the Source Development Laboratory at BNL, which utilizes inner and outer cages with roller bearings. Other possibilities will be considered.

### References

- [5.5.1.1] J. Safranek, et al., Nonlinear dynamics in a SPEAR wiggler, *Phys. Rev. ST, Acc. and Beam*, Vol. 5, p.010701 (2002).

## 5.5.2 Tunable Hard X-ray Sources

A decade ago, the hard x-ray region of the spectrum by undulators could only be covered at high-energy machines, such as ESRF, APS, and SPring-8. The advent of a mini-gap, short-period in-vacuum undulator, dubbed IVUN [5.5.1.1] in 1997 at the National Synchrotron Light Source has had a lasting impact on the design of synchrotron light source facilities all over the world. With the use of mini-gap, short-period undulators, a medium-energy ring ( $\sim 3$  GeV) can now produce tunable hard x-rays between 2 keV and 20 keV. Many years of successful operation of IVUs at SPring-8 [5.5.2.1], NSLS, and, more recently, at SLS and ESRF have demonstrated the reliability of IVUs. The NSLS currently has three IVUs in operation.

A long-standing concern in the ID community has been that the permanent magnets in small-gap IVUs would be gradually demagnetized and degraded by radiation, due to their proximity to the electron beam and exposure to synchrotron radiation. The conservative approach has been to use  $\text{Sm}_2\text{Co}_{17}$  magnets, rather than NdFeB magnets, because its lack of boron ought to make  $\text{Sm}_2\text{Co}_{17}$  more radiation resistant. However, after many years of successful operation at SPring-8, NSLS, and SLS without any signs of demagnetization, NdFeB IVUs with proper magnets having high intrinsic coercivity ( $H_{cj}$ ) have proven to be quite radiation resistant. The newest high-remanence, high  $H_{cj}$  grades of NdFeB (such as NEOMAX AH series), developed for use in hybrid car motors, should be particularly robust and radiation resistant. We have used this high-temperature NdFeB in our most recent IVU and have based our PM ID designs for NSLS-II on this same magnet material.

Curiously, some out-of-vacuum undulators at APS have experienced localized demagnetization, particularly those with smaller aperture vacuum chambers. Detailed simulations and radiation measurements suggest that the main source of the demagnetizing radiation could be the tapered part of the aluminum vacuum chamber itself. Thus, out-of-vacuum IDs, such as the elliptically polarized undulators, may be more vulnerable to demagnetization than IVUs. Another contributing factor may be that the magnet grade used in APS undulators does not have particularly high enough  $H_{cj}$  and therefore does not withstand even localized radiation-induced heat.

Advantages of IVUs over fixed-chamber, out-of-vacuum IDs besides performance advantage are 1) that the former can be opened to provide a wide aperture during machine commissioning or beam studies, and 2) the lack of neutron-producing materials at transitions would mitigate magnet demagnetization.

A subject that needs further study is the impedance of the variable-gap IVUs. Earlier in this report, it was shown that the H-shaped space created by the gap space and the chamber forms a waveguide that contributes to transverse impedance. The RF transitions at the extremities of an ID must be properly tapered to reduce the geometric impedance. Modeling and RF measurements of real IVUs will be part of the design effort.

### 5.5.1 IVU (Baseline Device)

Room-temperature in-vacuum undulators are now considered to be a mature technology. Earlier concerns about demagnetization of permanent NdFeB magnets for IVUs are less of a concern now with proper magnet selection after many years of successful operation at SPring-8, NSLS, and SLS without any signs of demagnetization. The baseline design for a hard x-ray undulator for NSLS-II is based on a short-period linear undulator of the room temperature IVU type. This is the U20 device described in Chapter 5.

### 5.5.2 CPMU (Future Option)

For the future upgrade option, cryogenic permanent magnet undulator (CPMU) is considered. The enhancement is based on the fact that NdFeB magnet has a negative temperature coefficient of about  $-0.1\%/K$  at  $20^\circ\text{C}$  for the remanent field ( $B_r$ ), and also  $-0.5\%/K$  for the intrinsic coercivity ( $H_{cj}$ ). Therefore, one can expect higher field and higher radiation resistance simply by cooling the magnet array to lower temperature.

However, NdFeB exhibits a spin orientation below somewhere around 150K and its  $B_r$  starts decreasing as the temperature goes below this value [5.5.2.3]. An obvious advantage of operating NdFeB at the plateau around 150K (in addition to gaining 11 to 13% higher field), is greatly reduced sensitivity of the field to temperature gradients.

To test the effect of cooling NdFeB undulators, we measured our decommissioned 0.3 m Prototype Small-Gap Undulator in dry ice at  $-71^\circ\text{C}$ , and demonstrated that the field increased as expected at  $-0.1\%/^\circ\text{C}$ , or about 9% when cooled down by  $\sim 90^\circ\text{C}$ . However, this measurement did not reach the plateau in the  $B_r$  vs. temperature that is expected at around  $-120^\circ\text{C}$ . Analysis of the Hall probe data showed no significant increase in phase error, or in trajectory error, except in the end terminations. We also measured a 10-pole 13.5 mm period PM-hybrid prototype in dry ice with similar results.

The SPring-8 and ESRF recently compared warm and cold measurements of a 1 - 2 m long CPMU. They found that while the fields increased as expected, magnetic field errors scaled and tracked with temperature as well. This suggests that a CPMU can be shimmed at room temperature, and it will remain optimized when it is cooled. This also supports the notion that a CPMU is inherently “fail-safe,” in that it will still work well, albeit over a reduced tuning range, even if the cryocooling fails. If this result holds true for a hybrid CPMU, we will save an enormous amount of time in the magnetic shimming and spectral optimization of CPMUs by avoiding multiple cool-downs and warm-ups during the iterative shimming process. An important R&D task will be to verify by cold and warm measurements that field errors track with temperature in a hybrid CPMU as well.

### 5.5.2.1 “Cryo-Ready” MGU Installed in NSLS

NSLS has recently constructed and installed a 1 m long “cryo-ready” MGU for beamline X25 (18 mm period,  $B_y = 0.95$  T at 5.6 mm gap) [5.5.2.4]. It has provision for cryogenic cooling by circulating cold He gas from a refrigerator through channels embedded in the magnet array platens. For the test we were able to cool it to 130K by circulating boil-off  $\text{N}_2$  gas. This test demonstrated that the mechanical features designed to accommodate the large differential thermal contraction of the cold magnet arrays relative to the warm vacuum vessel worked. We mapped the undulator before and after thermal cycling and found no measurable magnetic changes.

### 5.5.2.2 Optical Gap Measurement

First-order gap control is performed using four external stepper motors with a linear encoder feedback system that positions each magnet girder to a mean reproducibility of 1 micron. The 1 m magnet length required multiple structural feed-throughs in the vacuum envelope to assure continuity between rigid external structural girders and the in-vacuum magnet girders. However, magnetic and mechanical measurements indicated that gap-dependent nonlinear magnetic forces, environmental temperature gradients, and operational conditions caused deflections of the in-vacuum magnet girders exceeding specifications. The external linear encoders could not measure these effects, and correction by the primary gap control system would be ineffective. The CPMU direct measurements of the magnet gap differed by greater than 1 mm with respect to the gap, as inferred by the external linear encoders. These measurements indicated that relying exclusively on a conventional external linear encoder-based control system is insufficient under extreme conditions, and a direct means of gap measurement and a secondary means of gap control are necessary to maintain micron control of the magnet girders over the full range of environmental and operational conditions. An LED-based system (e.g., Keyence LS-7030) that has a measurement accuracy of  $\pm 2 \mu\text{m}$  and repeatability of  $\pm 0.15 \mu\text{m}$  can be employed to provide a secondary means of gap control, to permit correction over the regime of these tertiary effects for up to 100 microns of nonlinear gap control. Very fine taper/bow control can be achieved by embedding temperature-controlled heaters for each post. This method successfully worked for the X25 MGU at NSLS. This feature is important even for RT-IVU to maintain very low phase errors. The effect of array deformation on phase error is examined in Section 5.5.2.4.

### 5.5.2.3 Optimizing the Device Design

Table 5.5.2.1 shows the possible combinations of period length, achievable peak field, and effective values of deflection parameter ( $K_{y \text{ eff}}$ ) at the undulator gap of 5 mm for a conventional room temperature IVU (20°C) and cold (-120°C) in-vacuum devices calculated by the same Radia [5.5.2.5] model used for the X25 MGU. These are all hybrid structures with vanadium permendur poles. Magnet type used in calculation for warm device is NEOMAX-32AH,  $B_r = 1.12\text{T}$  and  $H_{cj} = 33\text{kOe}$ . This material was recently used for a similar device at Australian Light Source. Due to the much shorter beam lifetime and higher current for the NSLS-II storage ring than the NSLS x-ray ring, many more lost electrons will be produced as a demagnetization source. Therefore, more conservative material must be chosen compared to the NSLS MGUs. The magnet for cold type is NEOMAX-42AH  $B_r = 1.29\text{T}$  at 273K  $\rightarrow 1.45\text{T}$  at 120K, and  $H_{cj} = 24\text{kOe}$  at 273K  $\rightarrow >40\text{kOe}$  at 120K. In this table, the effective K value for the non-sinusoidal field is calculated as

$$K_{x,y \text{ eff}}^2 = 2 \left\langle \gamma^2 \frac{v_{x,y}^2}{c^2} \right\rangle, \quad (5.5-1)$$

where  $c$  is the speed of light in vacuum,  $\gamma$  is the Lorentz factor, and  $v$  is the velocity of the electrons.

**Table 5.5.2.1** Period-Length vs. Maximum Flux Density and Effective K Value for IVU at Room Temperature and 150K.

Period Length (mm)	Warm ( $B_r = 1.12\text{ T}$ ) $B_{\text{peak}}$ (T)	Warm $K_{\text{eff}}$	Cold ( $B_r = 1.45\text{ T}$ ) $B_{\text{peak}}$ (T)	Cold $K_{\text{eff}}$
16.0	0.76	1.11	0.98	1.43
17.5	1.87	1.37	1.11	1.74
19.0	0.97	1.63	1.21	2.03
20.0	1.03	1.81	1.26	2.22
21.0	1.10	1.99	1.31	2.40

All of the NSLS MGUs have severe limitations in their length. Therefore, the ideal magnetic termination at the extremities has to be compromised in order to increase the number of full-field-strength periods. Hybrid devices tend to have an inherently larger gap dependence of integrated field strength, due to the nonlinear characteristics of pole materials and anisotropy of permanent magnets. Various termination schemes that minimize the gap dependence for pure permanent magnet devices have been developed [5.7.9]. However, designs for hybrid devices have limited effectiveness. End effects tend to be less important for small-gap undulators than for large-gap, high-field wigglers.

### 5.5.2.4 Minimizing Phase Error

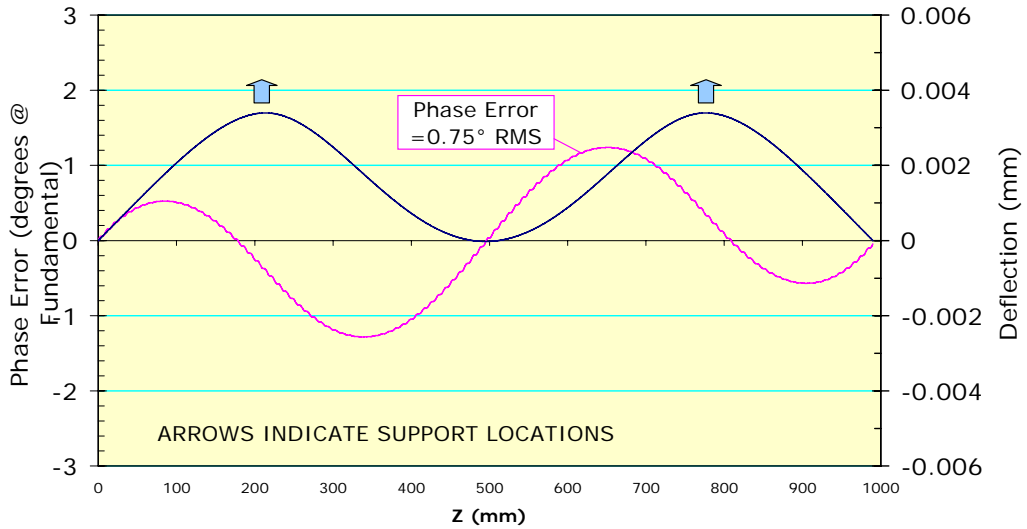
A critical requirement for short-period, in-vacuum MGUs in a medium-energy storage ring is retaining high spectral brightness, up to the 7th or even the 9th harmonic. Loss of spectral brightness is well correlated with optical phase error. Phase error can be defined as the cumulative path length difference between the electron's actual trajectory and an ideal trajectory, expressed in degrees of phase at the fundamental optical wavelength. Cumulative optical phase error of 2° RMS is considered state of the art and will be the target for all NSLS-II undulators. This is an especially challenging requirement for small-gap, short-period IDs, as shown below.

Phase error arises from three sources: 1) systematic gap error, 2) trajectory wander, and 3) random phase errors. We will next describe the techniques we have developed and use routinely to minimize phase error from these three sources.

Systematic phase error can be caused by a) bowing of the magnet arrays due to attractive magnetic forces, b) gap taper, and c) nonflatness of the magnet mounting surfaces. These are long-range gap variations, on the scale of many undulator periods, which cause a gradual variation of field amplitude, wiggle amplitude, and

therefore trajectory path length, without trajectory steering. To obtain a mechanical tolerance budget for these effects in the X25 MGU, we started with a finite-element analysis of an initial mechanical design for the magnet support beams, suspended on two hangers, under a distributed magnetic load of 8,000 N (due to the peak field of 1 T at a 5.6 mm gap). The resulting deflection profile was scaled to a field amplitude profile, which was numerically integrated to obtain the trajectory and, finally, a cumulative phase error profile. Figure 5.5.2.1 is a plot of the gap error (blue) and resulting cumulative phase error (magenta) vs. longitudinal position Z. The peak-to-valley deflection of 3 microns results in a RMS phase error of 0.75°. The figure shows that two supports per meter can induce a phase error of 0.75 degrees, due to deflection resulting from B = 1 T. Solid aluminum platens are assumed in this simulation.

**Figure 5.5.2.1**  
Phase error created by the mechanical deflection of aluminum magnet platens, due to the magnetic force of B = 1T.



The phase error created by 3.3 microns of linear tapering in 1 m is presented in Figure 5.5.2.2.

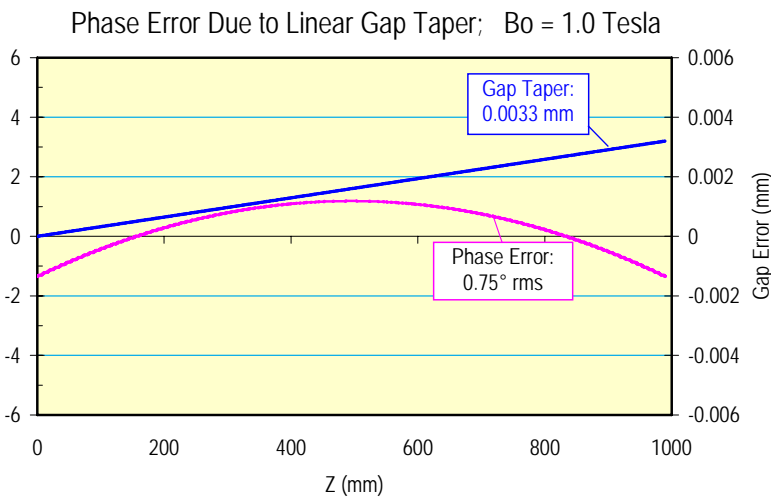


**Figure 5.5.2.2** Phase error created by linear gap taper. B<sub>0</sub> = 1.0T.

*Trajectory wander* is caused by local, random field amplitude errors, which cause the trajectory to deviate from a straight line. The longer path is reflected in a phase error. Local steering errors can also accumulate over the length of the undulator as both integrated dipole (first integral error) and trajectory offset (second integral error). We routinely use the Pulsed Wire technique to quickly visualize the trajectory in undulators, identify the location and magnitude of steering errors, and apply steering shims to correct them. The pulsed

wire easily displays both the horizontal and vertical components of a trajectory, including the contribution of the Earth's field.

*Random phase errors* are nonsteering errors that remain following trajectory straightening and the removal of systematic phase errors. In a PM-hybrid undulator, random phase errors are mainly caused by variations in the strength of individual magnets, as well as by pole positioning errors. To minimize these, the individual magnets are first measured, then sorted, paired, selected, and assigned to specific locations in the arrays. Various manual and computer-aided sorting and selection algorithms have been developed and are considered standard practice.

*Earth's field* causes significant trajectory deflection in long undulators. The measured local Earth's field is about 0.4 Gauss with an inclination of about 14° from the vertical. The vertical component contributes an integrated (horizontally deflecting) dipole error of about 40 Gauss-cm/m. In a 3 m long CPMU, that adds up to a nontrivial dipole error of 120 Gauss-cm. The horizontal component is about 0.1 Gauss and oriented toward magnetic North. The effective (vertically deflecting) dipole error is <10 Gauss-cm/m and depends on the azimuthal orientation of the ID in the ring. The effect of Earth's field is readily visible on the pulsed wire as a parabolic trajectory component. It can be compensated by distributed trajectory shimming, or with external Helmholtz coils. In the X25 MGU we added a pair of 10-turn horizontal coils around the undulator vacuum vessel, powered by the end-pole trim supply from the old X25 wiggler previously residing at that location. Using the pulsed wire, we determined the optimal current to cancel Earth's field in the X25 MGU to be about 3.5 A. The small horizontal component was not compensated.

Other error specifications, such as maximum first and second integral and allowable integrated multipole requirements, will be specified before the engineering design phase.

### 5.5.2.5 Effect of Magnetic Field Errors on the Undulator Harmonics

The performance of real undulators is known to be poorer than the ideal case owing to magnetic field errors, despite valiant efforts to minimize such errors. It is generally accepted that the parameter which best relates magnetic field errors to spectral output is the RMS phase error  $\phi$ . The RMS phase error  $\phi$  is defined as the RMS path length difference between the real and ideal electron trajectories. It is calculated at the poles of the undulator and normalized to the wavelength of the fundamental harmonic ( $n = 1$ ). (At higher harmonics ( $n > 1$ ), the RMS phase error is  $n\phi$ .) To date there has been no complete analytic treatment of the spectral effects of the phase errors. It has been argued that, for a zero-emittance electron beam, the relative on-axis brightness of the odd undulator harmonics  $n = 1, 3, 5, \dots$  emitted by an undulator with uncorrelated and Gaussian distributed phase errors is given by

$$B(n, \phi)/B(n, 0) = e^{-n^2 \phi^2} \quad (5.5.2-2)$$

where  $\phi$  is the RMS phase error.

Recently, we have found empirically that this formula tends to underestimate the effect of phase errors for real undulators. For the two LCLS undulators discussed below, the expression above for a zero-emittance beam can be made to agree reasonably well with the result derived from magnetic measurements only if the RMS phase error is increased by ~20% from the measured value ( $\phi \rightarrow 1.2\phi$ ). This is a large "correction" factor; more accurate results can be obtained by feeding the measured magnetic field profiles directly into undulator codes, such as UR or SPECTRA. Moreover, there is no analytical formula for phase error effects when the emittance needs to be taken into account, so we need to resort to numerical calculations.

Simulations were performed using measured magnetic field data from a set of undulators with RMS phase errors spanning a range from 2.0° to 3.7°. The measured magnetic field profiles and the storage ring parameters for NSLS-II were used as inputs to the undulator code UR in order to simulate realistic undulator spectral performance. If the results are a well-behaved function of phase error, one can then make a

determination of the maximum tolerable RMS phase error required to achieve a particular level of undulator spectral performance. As discussed below, the results confirm the intuition that achieving a  $2^\circ$  RMS phase error, or better, is important for maintaining high spectral brightness for the high NSLS-II harmonics (7, 9, and 11). These results also confirm the idea that the phase error effects become more significant as the ring emittance decreases.

#### 5.5.2.5.1 Relative On-Axis Brightness for Harmonics 7, 9, and 11 vs. RMS Phase Errors for NSLS-II Undulators

Computer simulations of the relative on-axis brightness as a function of the RMS phase error were performed using the NSLS-II emittance and real measured magnetic fields of three undulators. Comparisons were made to the spectral performance of the same undulators with hypothetical ideal magnetic fields. The results are detailed below and show, for example, that the 9<sup>th</sup> harmonic undulator radiation degrades by about 15% if the RMS phase error increases from  $2.0^\circ$  to  $3.0^\circ$ .

#### Conditions

The NSLS-II storage ring parameters for a 5 m-long low- $\beta$  insertion device straight section were used for these simulations. The following parameter values were used: emittances  $\epsilon_h=0.55$  nm,  $\epsilon_v=0.01$  nm, energy spread  $\delta E/E=0.1\%$ , and  $\beta$ -functions  $\beta_h = 2.7$  m,  $\beta_v=0.945$  m. The resultant electron beam sizes and divergences are  $\sigma_h=38.5$   $\mu\text{m}$ ,  $\sigma_v=3.1$   $\mu\text{m}$ ,  $\sigma_h'=14.2$   $\mu\text{rad}$ , and  $\sigma_v'=3.2$   $\mu\text{rad}$ .

The following three undulators were studied:

- Linac Coherent Light Source undulator number 1 (LCLS #1), period length=3.0 cm, 113 periods; K and  $\phi$  measured at 6.8 mm gap: K=3.50 and  $\phi=3.54^\circ$
- Linac Coherent Light Source undulator number 2 (LCLS #2), period length=3.0 cm, 113 periods; K and  $\phi$  measured at 6.8 mm gap: K=3.49 and  $\phi=4.21^\circ$
- APS short undulator A (APS #40), K = 2.80, period length = 3.3 cm, 62 periods; K and  $\phi$  measured at 10.5 mm gap: K = 2.80 and  $\phi = 3.68^\circ$

Numerical calculations of the on-axis brightness for these three undulators were performed. In order to study the dependence on the RMS phase error, the LCLS undulator fields were scaled in both field strength (uniformly to a lower value) and period length to simulate a change of the RMS phase error (the RMS phase error decreases when the K value becomes smaller). Very minor adjustments to the on-axis view angle were applied, and as such, those fields represent real devices with true magnetic field errors. It is worth noting that for the LCLS undulators, the period length was scaled from 3.0 cm to 1.9 cm to simulate a shorter period-length undulator, such as the NSLS-II U19 CPMU hard x-ray undulator. This procedure allowed us to study undulators which have RMS phase errors covering the range  $2.0^\circ$  to  $3.7^\circ$ .

#### Results

The on-axis brightness of the 7<sup>th</sup>, 9<sup>th</sup>, and 11<sup>th</sup> harmonics, relative to the brightness of the corresponding harmonics of a hypothetical, ideal magnetic field undulator, is plotted in Figure 5.5.2.3 for the three undulators described above, simulated for their performance in the NSLS-II storage ring. The relative brightness of the 3<sup>rd</sup> and 5<sup>th</sup> harmonics is much closer to 100% and is not shown in this figure.

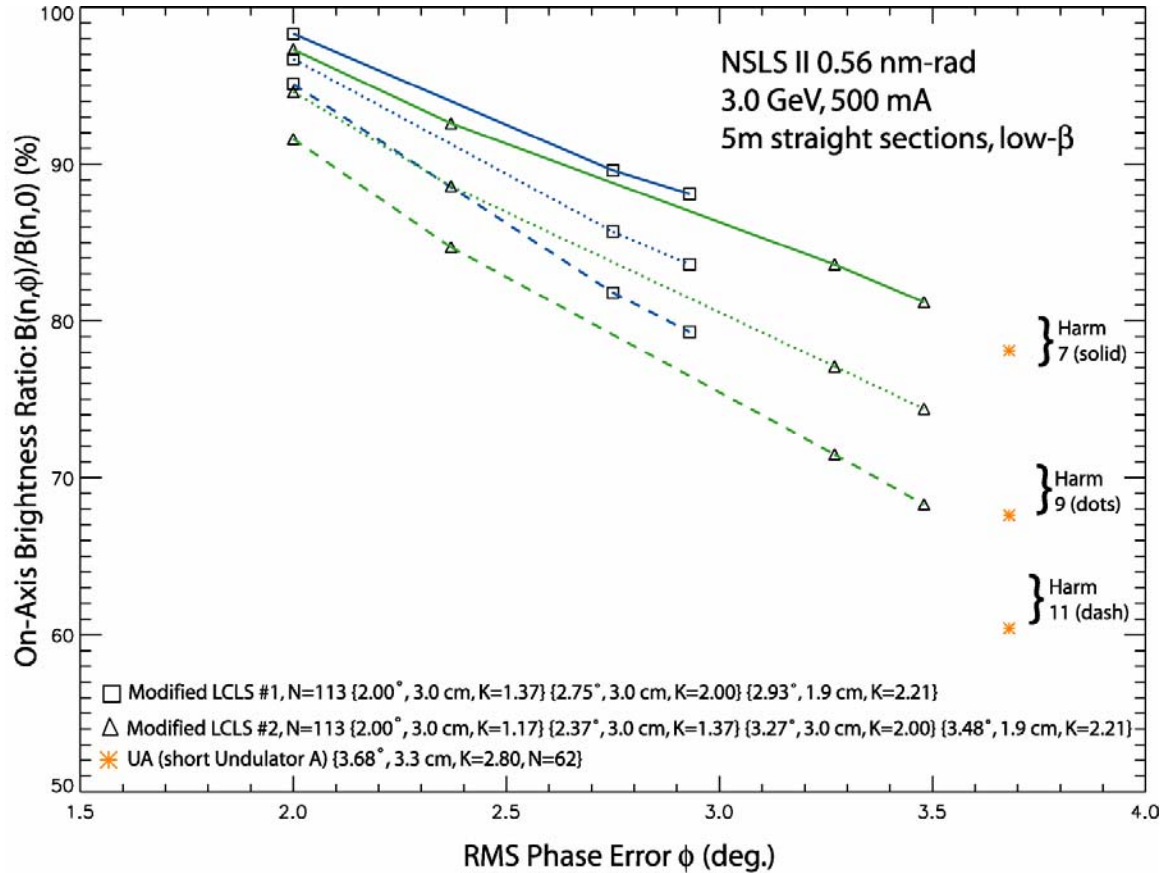


**Figure 5.5.2.3** On-axis brightness of the 7<sup>th</sup>, 9<sup>th</sup>, and 11<sup>th</sup> harmonics of three undulators relative to the brightness of the corresponding harmonics of an ideal magnetic field undulator, as a function of the RMS phase error.

The key results of these simulations are as follows: improving the RMS phase error from  $3.0^\circ$  to  $2.0^\circ$  changes the relative brightness of the 7<sup>th</sup> harmonic from 86 to 98% ( $\Delta_7 = 12\%$  points), the 9<sup>th</sup> harmonic from 81 to 96% ( $\Delta_9 = 15\%$  points), and the 11<sup>th</sup> harmonic from 75 to 93% ( $\Delta_{11} = 18\%$  points).

## Conclusions

The relative brightness of the NSLS-II undulator harmonics depends sensitively on the RMS phase error. The higher the harmonic number and the higher the RMS phase error, the faster is the rate of reduction. The rate of reduction is somewhat sensitive to the actual distribution of phase errors for real devices, but is much less sensitive to the actual  $K$  value or the undulator period length. For example, by improving the RMS phase error from  $3.0^\circ$  to  $2.0^\circ$ , the 9<sup>th</sup> harmonic would gain about 15%.

The effect of phase error becomes greater as the emittance of the storage ring decreases. For example, the performance drop for NSLS-II undulators would be 2 to 5% greater for harmonics 7–11 than for the same devices at APS, as a result of the smaller emittance of NSLS-II.

Future work on this subject should include simulations using the measured fields from recently built undulators around the world, including the 18 mm period undulator installed at NSLS beamline X25 in December 2005, which has a period length very close to the U19 CPMU proposed for NSLS-II and has a measured RMS phase error close to  $2^\circ$ .



### 5.5.2.6 Baseline IVU Magnetic Design

The base design for the NSLS-II hard x-ray planar device is derived from the NSLS cryo-ready undulator developed for X25. The X25 mini-gap in-vacuum undulator has an 18 mm period length, a minimum magnetic gap of 5.6 mm and length of 1 m, and is designed to be operated at 150 K. The NSLS-II U20 IVU will have a minimum gap of 5 mm and will be 3 m long, but most of its other requirements are similar to those for the X25 MGU. The main parameters are given in Table 5.5.2.1

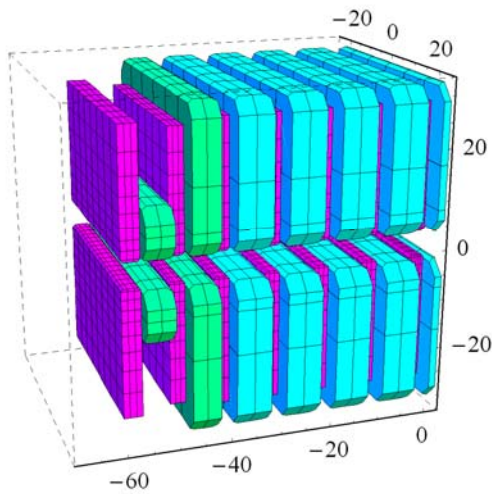
Table 5.5.2.2 shows the expected mechanical tolerances of the magnetic arrays.

**Table 5.5.2.2 Mechanical Tolerances.**

Item	Tolerance
Magnet/pole width [ $\mu\text{m}$ ]	$\pm 100$
Magnet height [ $\mu\text{m}$ ]	$\pm 25$
Magnet thickness [ $\mu\text{m}$ ]	$\pm 25$
Pole height [ $\mu\text{m}$ ]	$\pm 25$
Pole thickness [ $\mu\text{m}$ ]	$\pm 10$
Pole-to-pole flatness [ $\mu\text{m}$ ]	$\pm 10$
Period [ $\mu\text{m}$ ]	$\pm 10$
Magnet array pitch/yaw/roll (relative) [ $\mu\text{rad}$ ]	$\pm 25$
Magnet array horizontal/vertical rack [ $\mu\text{m}$ ]	$\pm 5$
Gap control [ $\mu\text{m}$ ]	$\pm 5$
Gap repeatability [ $\mu\text{m}$ ]	$\pm 5$

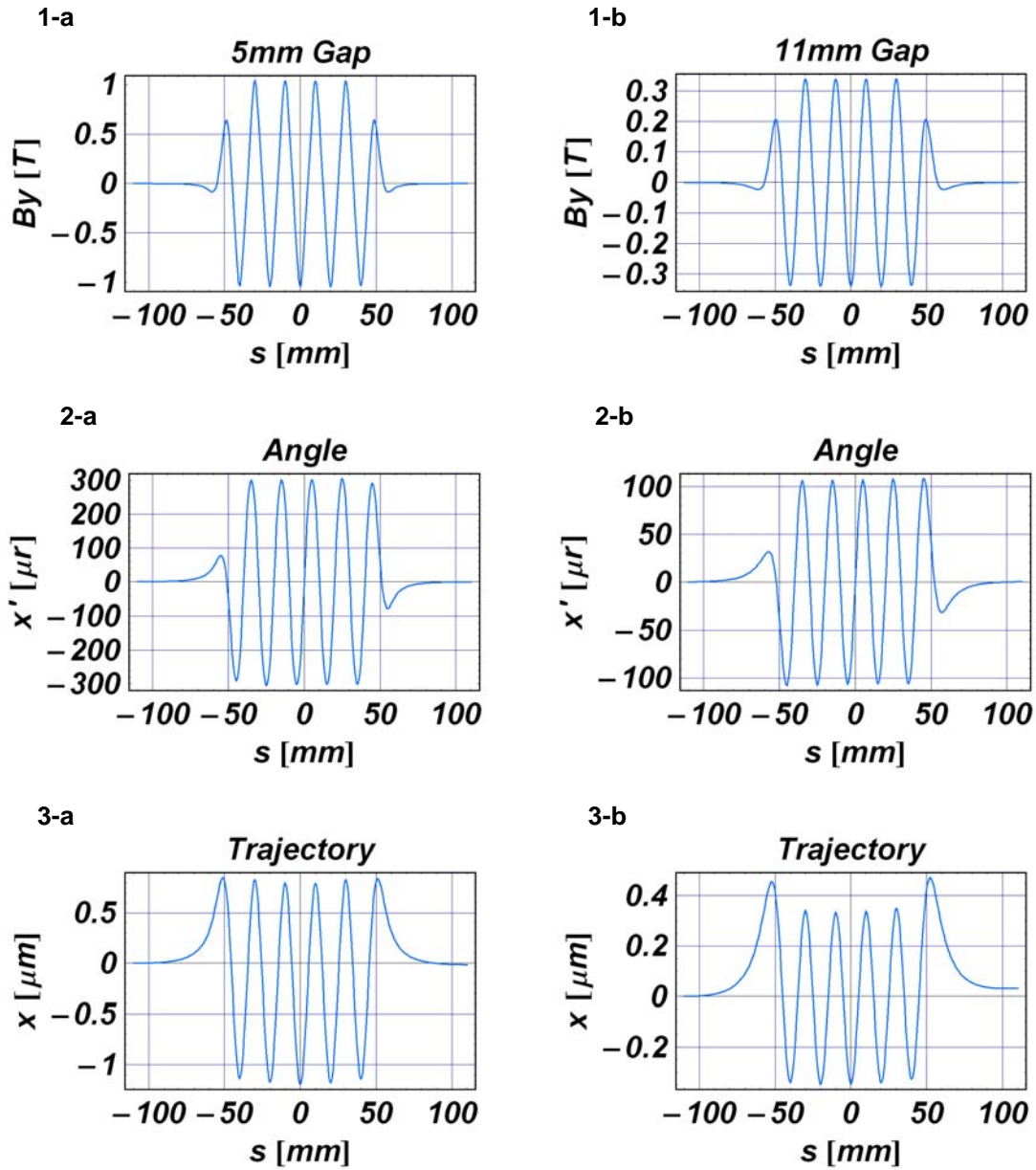
The phase error for the device is required to be less than two degree RMS. Slight tapering, platen bowing, and other factors must be carefully controlled to achieve this level of phase error. As mentioned above, a novel gap measurement system using a commercial, high-precision, LED-based optical micrometer was incorporated in the X25 MGU to back up the linear encoders and to correct for gap changes due to differential contraction during cryogenic operation. The system monitors the magnet gap optically through viewports at either end of the MGU, ensuring gap accuracy of  $\pm 2 \mu\text{m}$ .

Figure 5.5.2.4 shows an isometric rendering of the MGU magnet arrays by Radia. Blue magnets have identical size and two different sized magnets are shown in green. Pieces in magenta represent perpendicular poles.



**Figure 5.5.2.4** MGU magnet arrays. Only the first few periods are shown, for clarity. Units are millimeters.

The Radia simulations shown here were performed with a symmetrical model so the angular kick could be estimated. In the actual device we are likely to use an anti-symmetric structure to minimize the residual first integral. The values of magnet susceptibilities used are  $\chi_m$  (para) = 0.02,  $\chi_m$  (perp) = 0.42. The field and trajectory computed from the model are plotted in Figure 5.5.2.5 for gaps of a) 5.0 mm and b) 11.0 mm. The trajectory is calculated by a particle-tracking Runge-Kutta routine. The particle is launched with zero offset and angle ( $x = 0$ ,  $x' = 0$ ), and its position and angle are calculated every 0.53 mm (36 points per period). The gap dependence of the first integral is shown in Figure 5.5.2.6. The amount of change in the first integral found here can be easily compensated by external coils.



**Figure 5.5.2.5** Gap dependence. Field, angle, and trajectory plots for the 7-period model for (column a) minimum gap (5.0 mm) and (column b) maximum operating gap (11.0 mm).

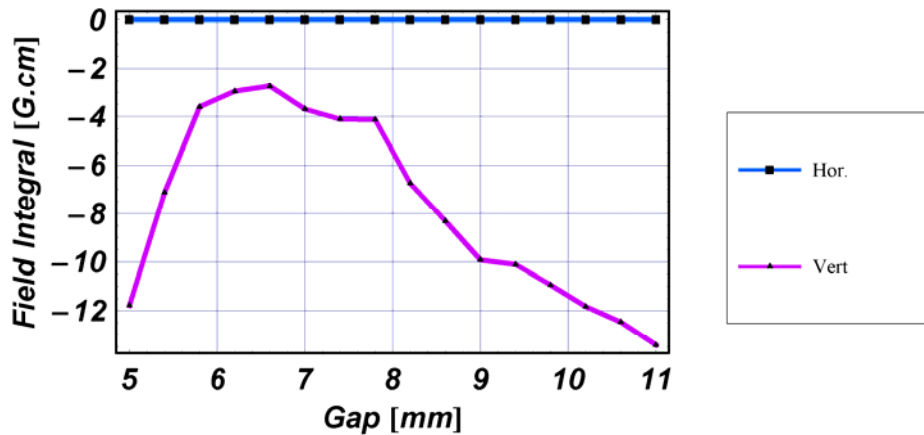


**Figure 5.5.2.6** Gap dependence of the first integrals simulated for U20. Due to symmetric model structure, horizontal field integral dependence does not appear.

### 5.5.6 Vacuum and Mechanical Systems Development

A 3 m device will be constructed with three 1 m modules that are similar to the X25 MGU. The vacuum chamber is rectangular and opens along its length to facilitate magnetic field measurements and shimming. Most of the required vacuum components are mounted to this cover for easy access and for a cost-effective design. These components include ion pump/titanium sublimators, getter pumps, an RGA analyzer, a glow discharge cleaning system with associated pumping and view ports, an ion gauge, and bleed-up ports. The X25 system successfully achieved a pressure of less than  $5 \times 10^{-10}$  Torr, including magnets, after bakeout. The conceptual design in a CAD model is shown in Figure 5.5.2.7.

Techniques first demonstrated in the cryo-ready X25 MGU will be optimized and incorporated for the NSLS-II development program for the control system of the IVU. Systems such as an in-vacuum gap separation system will be modeled that can provide precision gap control with negligible effects from external temperature fluctuations and ultimately demonstrate a cost-effective alternative to more conventional gap separation and control systems.

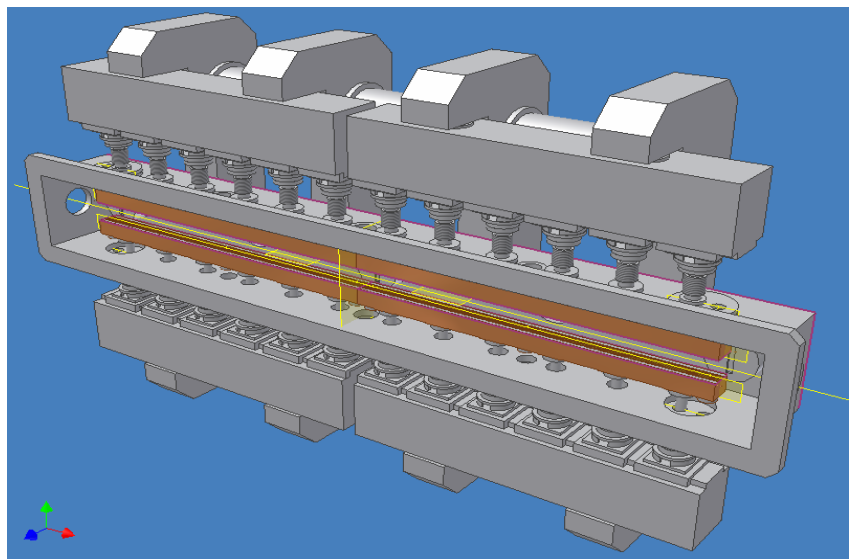


**Figure 5.5.2.7** Conceptual design of U20.

## References

- [5.5.2.1] T. Tanabe, et al., “Development of an In-Vacuum Minipole Undulator Array for National Synchrotron Light Source In-Vacuum Undulator,” *Rev. Sci. Instrum.* 69 (1), pp 18 – 24, (1998).
- [5.5.2.2] H. Kitamura, “Recent development of insertion devices at SPring-8,” *Nuc. Instr. & Meth. A* 467-468 (2001) p 110.
- [5.5.2.3] M. Sagawa, et al., “Magnetic properties of rare-earth-iron-boron permanent materials,” *J. Appl. Phys.* 57 (1985) pp 4094.
- [5.5.2.4] T. Tanabe, et al., “X-25 cryo-ready in-vacuum undulator at the NSLS,” AIP SRI2006 conference proceedings (to be published).
- [5.5.2.5] O. Chubar, P. Elleaume, and J. Chavanne, *J. Sync. Rad.* 5, pp. 481–484 (1998).

### 5.5.3 Variable Polarization Device for Soft X-ray

The variable polarization undulator, also known as an elliptically polarized undulator, EPU, is becoming more popular, as its impact on beam dynamics can now be controlled to an acceptable level. Currently, no in-vacuum EPU has been constructed, because of the difficulty of having moving parts and a strong force in a UHV environment. Therefore, the baseline design for NSLS-II will be the permanent magnet out-of-vacuum EPU45 and EPU100 devices described in Section 5.1, but R&D may be carried out to investigate in-vacuum EPU designs.

Various schemes to generate variably polarized light from an insertion device have been proposed. An electromagnet-based design that switches the polarity cannot cover the required photon energy range (250 eV–2 keV). The most popular design, based on PM technology, is the Advanced Planar Polarized Light Emitter (APPLE ) type [5.5.3.1]. It has been popular because it can generate all the possible polarization states with the minimum number of magnets. However, it also has a few deficiencies. Strong multipole components inherent to the design would reduce the dynamic aperture of the machine. This effect is due to the fact that horizontal field and vertical field are coupled, so static optimization for different gap and phase is difficult. In long-period devices, the electron's wiggle amplitude can be large enough for the field rolloff to affect the trajectory and result in a so-called "dynamic field integral," which is not measured by stretched wires or long coils. Recent efforts by various laboratories have mitigated these problems for limited types of operations [5.5.3.2 ].

There is an alternative design proposed for HiSOR by SPring-8 [5.5.3.3]. It separates the magnets for horizontal and vertical field, for ease of tuning as well as more moderate skew multipoles, at the expense of weaker achievable horizontal field. Detailed tracking studies will be carried out to decide which type of device is appropriate for NSLS-II.

Another concern for NSLS-II EPUs is the possible demagnetization of the permanent magnets by the use of the APS-style narrow gap vacuum chamber. Improvements to the vacuum chamber design will be investigated in order to minimize the source of radiation at the extremities of the chamber.

#### 5.5.3.1 Anisotropy of Permanent Magnets

Rare-earth magnets used for insertion devices have permeability close to unity, so that, to first order, the magnetic induction from individual magnet blocks can be superposed to obtain the total field. However, more careful analysis shows that there is anisotropy in those magnets. The components of the permeability that are parallel to the preferred direction of magnetization (easy axis), and perpendicular to this direction, are different and larger than unity. The magnetic susceptibility  $\chi_m$  and polarization  $J$  are defined as follows:

$$B = \mu H = \mu_0 \mu_r H = \mu_0 (\chi_m + 1) H , \quad (5.5.3-1)$$

$$J = \mu_0 \chi_m H \quad (5.5.3-2)$$

where  $B$  is magnetic induction,  $H$  is magnetic field strength,  $\mu_0$  the permeability of vacuum, and  $\mu_r$  is the relative permeability defined for convenience.

The permeability can vary at different points on the hysteresis curve. For example, the value at the beginning of magnetization is termed initial permeability, and the largest gradient in the B-H curve is called maximum permeability. What is important in a magnetic circuit is the reversible or recoil permeability, which is the slope of a minor loop in the second quadrant. The recoil permeability is usually approximated by the slope of the major loop at  $H = 0$ . For NEOMAX 42AH, the susceptibility is estimated by the slope of the J-H curve around  $H = 0$ . The estimated values of susceptibilities from these curves are:

$$\chi_m (\text{para}) = 0.02, \chi_m (\text{perp}) = 0.42. \quad (5.5.3-3)$$

These values indicate that in the region where the magnetic flux lines deviate from the preferred direction of magnetization, the material can be nonlinear. For planar insertion devices, this region corresponds mostly to end sections, which determines the gap dependence of the field integral, in practical terms. However, in most EPUs, the field directions inside magnets vary greatly, depending on the array phase. For the CPMU these values will need to be measured at the operating temperature, in order to be more precise.

### 5.5.3.2 Advanced Options (Outside Baseline Project Scope)

In-vacuum EPU is still an R&D subject. The performance of any type of ID strongly depends on the available minimum magnetic gap. A 2.5 m long in-vacuum EPU may be developed in this program. BNL will assemble magnet and pole materials, develop in-vacuum gap separation and magnet module axial position actuators, and procure a vessel and undulator support system. Using the facilities in the Undulator Development Laboratory in Building 832, measurements and characterization of the EPU fields under various gaps and phases will be made, as well as field corrections. The in-vacuum EPU could then be installed for the X-1 beam line of NSLS I to verify performance prior to the move to NSLS-II. The goal of this development is to advance the state of the art in EPU technology, to demonstrate the first in-vacuum EPU, to resolve the uncertainty in the methods of measurement and shimming of EPUs to permit reliable and cost-effective operation, and to perfect a new class of insertion device, the in-vacuum EPU, that can be offered to meet the needs of NSLS-II users.

To switch the helicities at higher than 1 Hz, a tandem structure is needed so that light with opposite helicities is produced simultaneously for various switching schemes. In this case, each ID is located away from the center and the required beam stay-clear gap would increase. If a slower switching frequency is tolerated, one longer device with mechanical phase change is possible. Another possibility is to set up two helical undulators in tandem and have a phase shifter between them to change the resulting polarization [5.5.7.4]. In this case, two helical undulators can be in-vacuum type if limited tuning range can be tolerated. Table 5.5.3.1 shows the characteristics of an APPLE-II type EPU.

**Table 5.5.3.1 Characteristics of an APPLE-II Type EPU. Assumed Br of the magnets is 1.35 T.**

Period Length (mm)	Magnetic Gap (mm)	Helical Mode Peak Field (Bx = By)	Effective Kx / Ky	Linear Mode Effective Ky
40	6.5	0.87	3.2	4.87
42	8	0.77	3.0	4.76
45	10	0.68	2.87	4.67
45	11	0.62	2.6	4.38

### 5.3.3 EPU45 (APPLE-II) (Baseline Design)

One possibility is to install twin devices in an 8 m straight section. Assume that we can have a 5 mm vertical aperture for a 3 m device placed at the center of the 5 m straight, with vertical beta function equal to 1 m at the insertion center. In this case, the ring aperture (A) is:

$$A = \frac{\text{gap}}{\sqrt{\beta(\text{end})}} = \frac{\text{gap}}{\sqrt{\beta_0 + \frac{(\text{end})^2}{\beta_0}}} = \frac{5\text{mm}}{\sqrt{(1+1.5^2)m}} = 2.77\text{mm} / \sqrt{m}. \quad (5.5.3-4)$$

We must verify that this is sufficient, but once we determine that this is acceptable, the required aperture  $y$  for an insertion device of length  $L$  placed at the center of a straight with beta-function  $\beta_0$  at the center is determined to be

$$y = A \sqrt{\beta_0 + \frac{(L/2)^2}{\beta_0}} \quad (5.5.3-5)$$

For the 8 m straights  $\beta_0 = 3$  m, we find the required vertical aperture is 7.4 mm at the half length of 3.5 m. An 8 mm aperture chamber at APS allows 2.5 mm extra for the magnetic gap of their insertion device. Therefore, we will assume that the magnetic gap of the NSLS-II insertion device is close to 10 mm.

The minimum photon energy to be covered is 250 eV. An EPU45 with an APPLE-II type configuration shows the characteristics listed in Table 5.5.3.2. Here, the remanent fields of the NdFeB magnets are assumed to be 1.35 T.

**Table 5.5.3.2 APPLE-II Type EPU45 Parameters.**

Period length [mm]	45
Peak field (helical mode: v/h) [T]	0.68 / 0.68
Effective K	2.87
Minimum photon energy in helical mode [eV]	206
Minimum gap [mm]	10
Magnet horizontal size [mm]	50
Magnet vertical size [mm]	45
Remanent field ( $B_r$ ) [T]	1.35

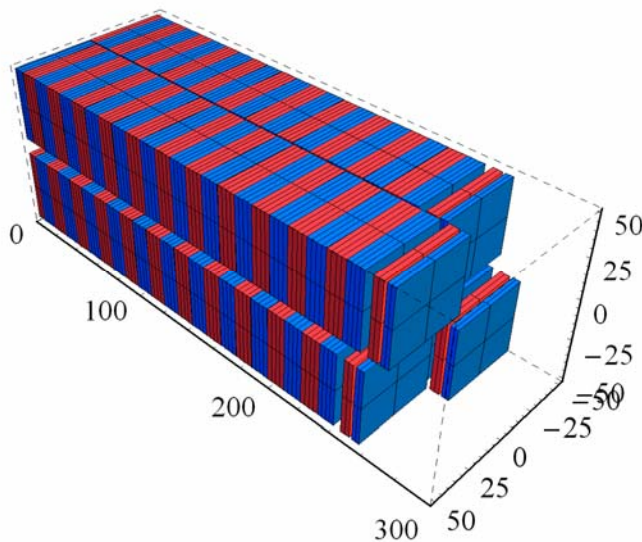


**Figure 5.5.3.1** Magnet arrays of EPU45. Only the first few periods are shown for clarity. Units are millimeters. Vertically magnetized magnets are in red and horizontally magnetized magnets are in blue.



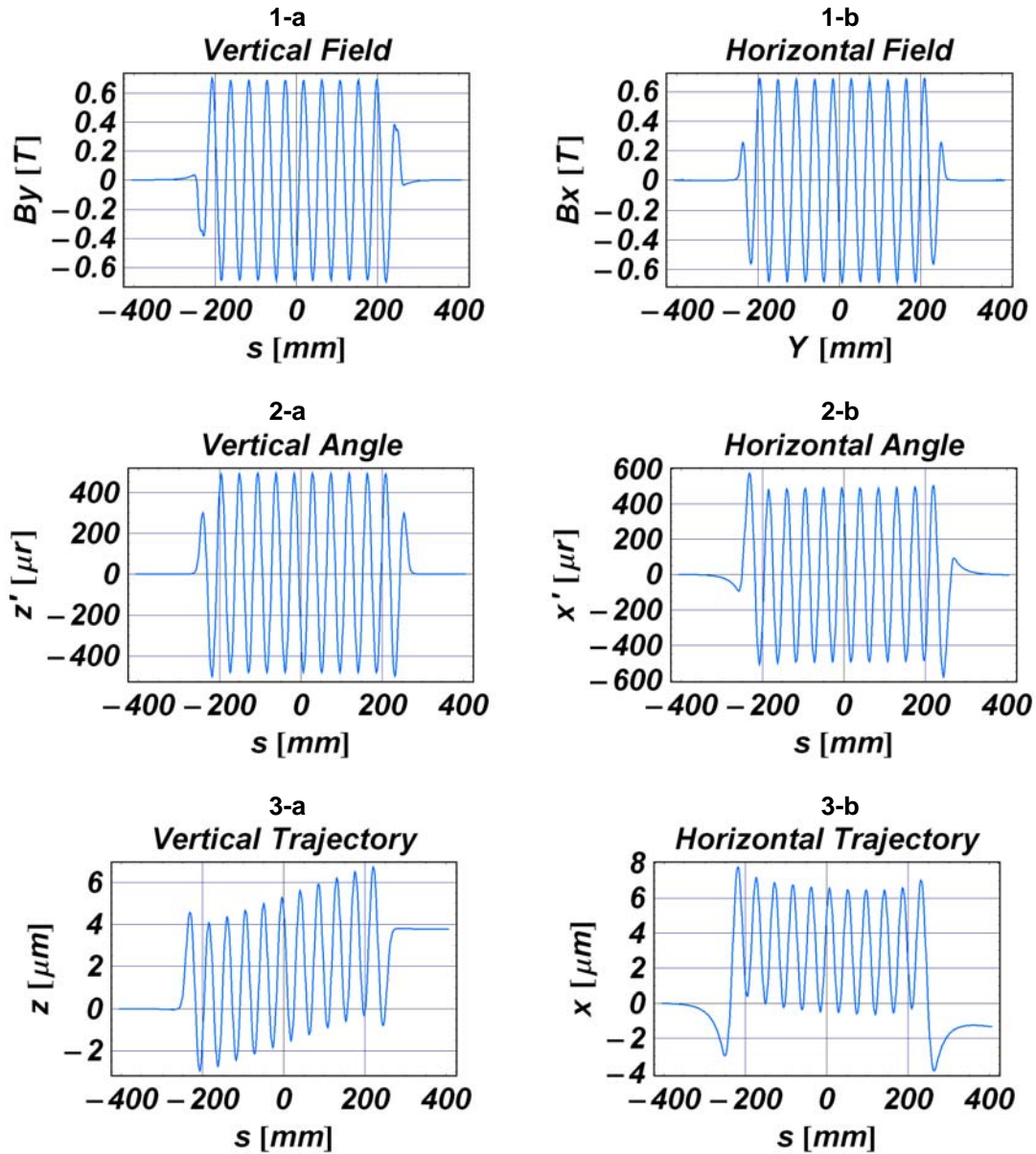


**Figure 5.5.3.2** Field, angle and trajectory plots for the 11-period model of EPU45 in helical mode. a) vertical field, horizontal angle, horizontal trajectory and b) horizontal field, vertical angle, and vertical trajectory at a gap of 10 mm.

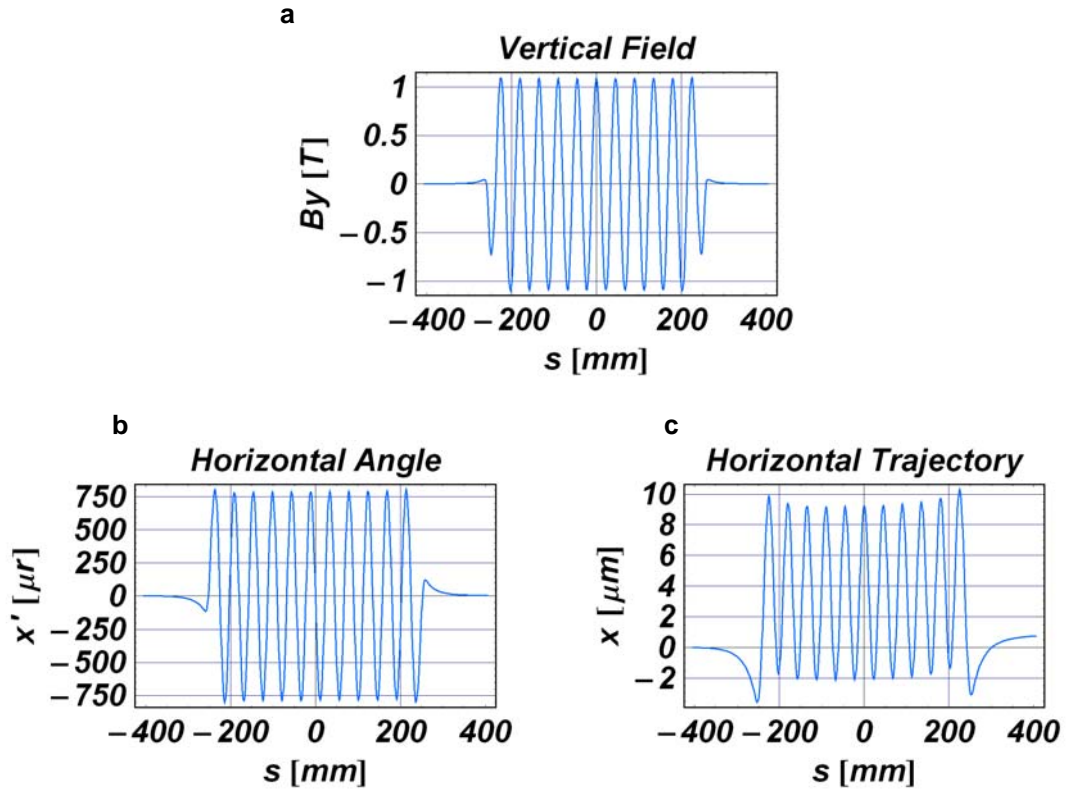


**Figure 5.5.3.3** Field, angle, and trajectory plots for the 11-period model of EPU45 in linear mode. a) vertical field, b) horizontal angle, c) horizontal trajectory at a gap of 10 mm.

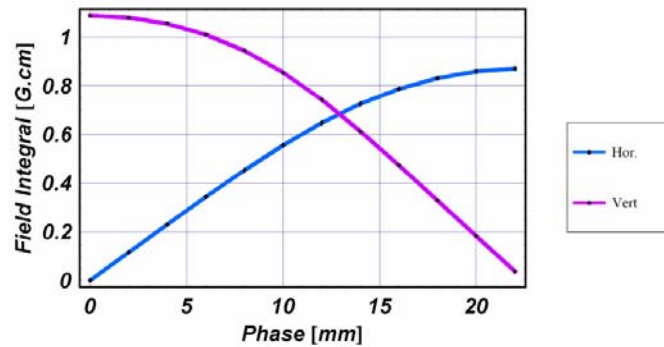


Figure 5.5.3.4 Fields vs. phase.

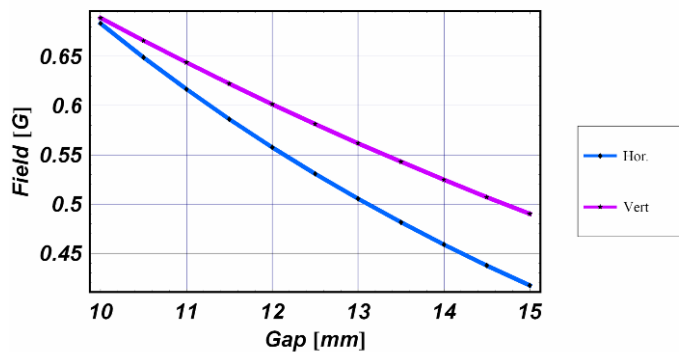


Figure 5.5.3.5 Fields vs. gap in helical mode.

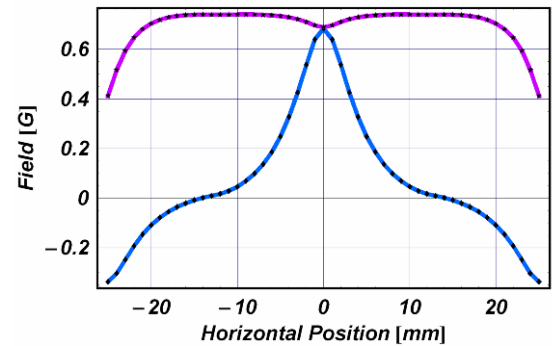
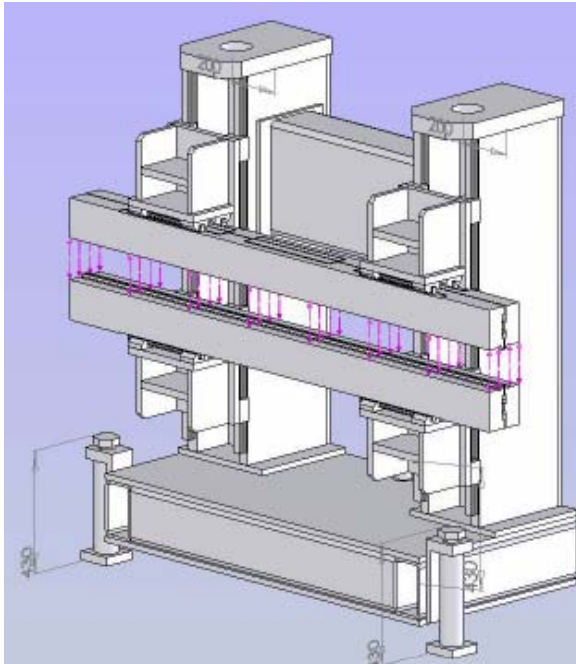


Figure 5.5.3.6 Fields vs. horizontal position at the origin in helical mode.

### 5.5.3.3.1. Mechanical Analysis

The small available transverse cross section of a device is also a concern for EPUs. Mechanical analyses have been conducted with slightly different parameters from EPU45. The chosen period length is 49 mm, and the minimum gap of 11 mm was selected due to cost and technical reasons. It was found that the maximum attractive force in gap direction is approximately 25000N, and that for phase direction is 15000N. The FEA analyses were done by Danfysik A/S as a part of the advanced conceptual design contract.



**Figure 5.5.3.7** Applied force directions (magenta arrows).

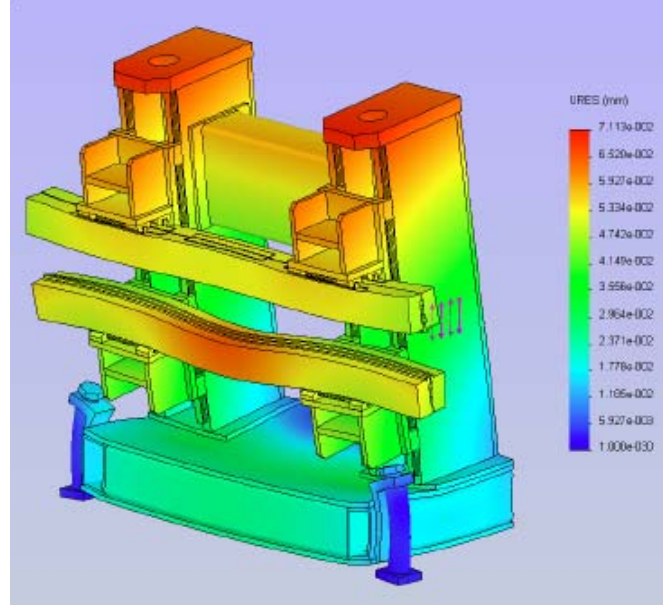


**Figure 5.5.3.8** Displacement in vertical direction

**Attractive force** (12500N for each jaw and opposite directions)

The displacement plot shows that the maximum displacement is 0.071 mm at the top of the undulator, due to the weight of the motor and magnets. The maximum displacement between girders is approximately 0.013 mm. This amount will influence the achievable phase error in planar mode if one requires phase error better than 5 degrees, which is conventional for a commercially available Apple-II device.

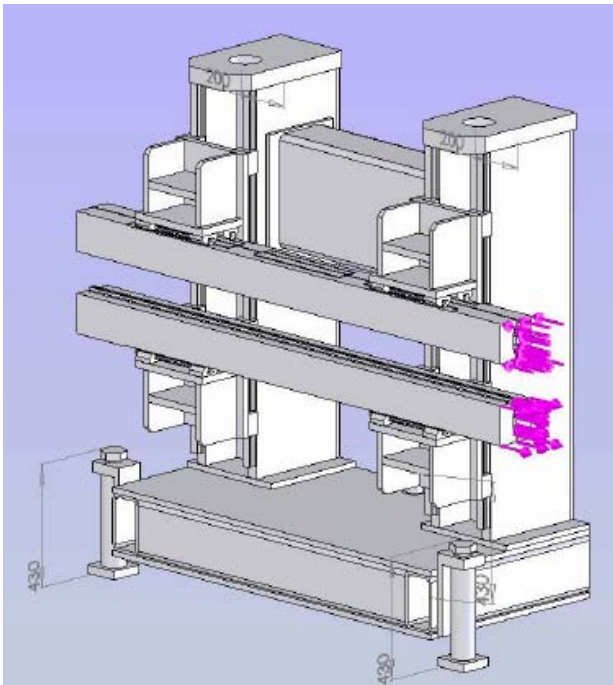


Figure 5.5.3.9 Applied force directions

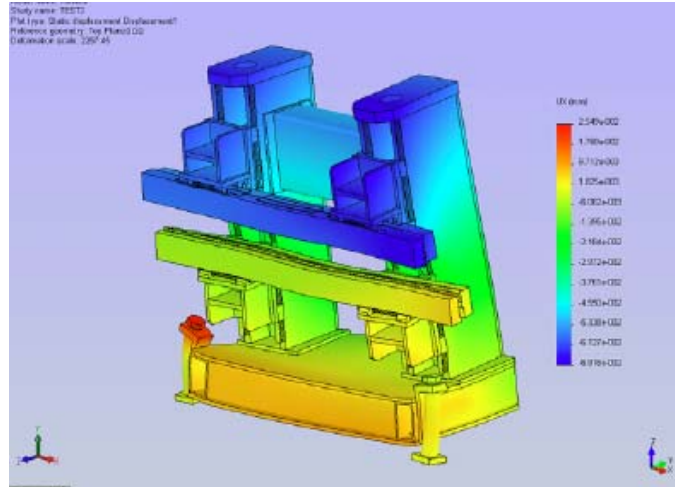


Figure 5.5.3.10 Displacement in longitudinal direction

#### Moment load (14700N per upper/lower jaw )

The maximum displacement in phase direction is found to be 0.062 mm. This amount can be easily compensated by the phase motion control.

#### 5.5.3.4 EPU52 (HiSOR) Magnetic Design (Backup Option)

To alleviate a highly sharp horizontal field profile and the coupling of vertical and horizontal fields from the same magnet, a new design with three magnet arrays in each jaw has been proposed and implemented at UVSOR and HiSOR in Japan. Unlike the APPLE-II design, one array in the center produces vertical field and two arrays on the sides generate horizontal field. Therefore, each type can be separately shimmed to perfection upto |The horizontal field profile is more benign than that from APPLE-II. The parameters for the HiSOR design are shown in Table 5.5.3.3, and a Radia drawing shows the design (Figure 5.5.3.11).

Table 5.5.3.3 HiSOR-Type EPU52 Parameters.

Period Length	52 mm
Peak Field (helical mode: v/h)	0.53 / 0.53T
Effective K	2.49
Minimum photon energy in helical mode	240 eV
Minimum gap	10 mm
Side Magnet Size (H/V)	50 / 45 mm
Center Magnet Width	14 mm
Remanent Field (Br)	1.35T

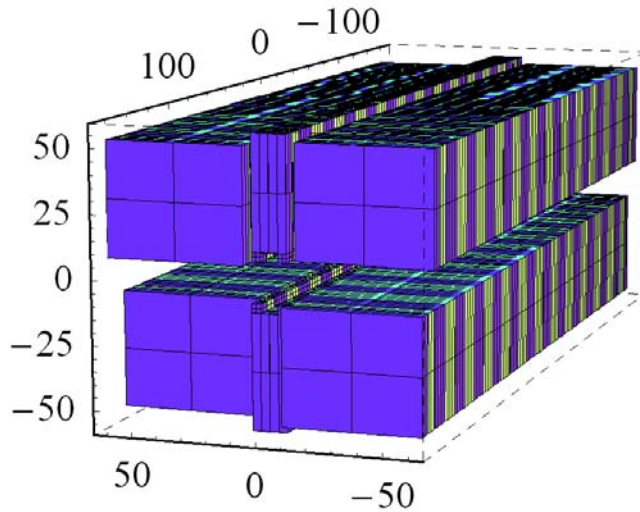


**Figure 5.5.3.11** Magnet arrays of HiSOR-EPU52. Only the first few periods are shown, for clarity. Units are millimeters. Vertically magnetized magnets are in light green and horizontally magnetized magnets are in purple.

One disadvantage of the HiSOR design is that the maximum horizontal field is weaker than that of the APPLE-II for the same period length, due to the increased distance between the two arrays. Hence, slightly longer period length is required to obtain the same photon energy as with the APPLE-II design. If vertical linear polarization is needed, the vertical arrays can be shifted out of phase. However, some longitudinal components remain at the extremities, and tracking studies are needed to determine the detrimental effect.

The grooved-shape magnets in the center arrays improve the vertical field uniformity (Figure 5.5.3.13).

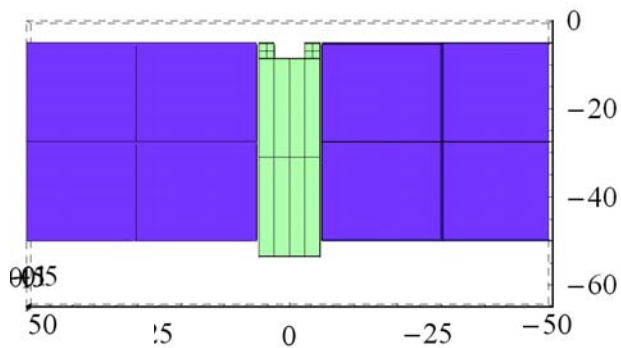
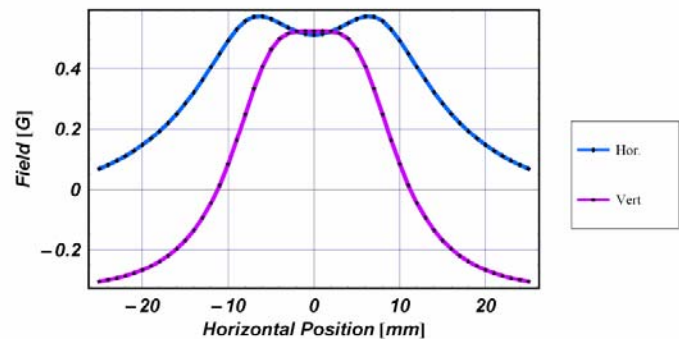


**Figure 5.5.3.12** Cross-section of a magnetic array. Light green is for the vertical field and purple is for the horizontal.

**Figure 5.5.3.13** Field profile vs. horizontal position in helical mode.





## References

- [5.5.3.1] S. Sasaki , et al., “A new undulator generating variably polarized radiation,” *Jpn. J. Appl. Phys.* 31 (1992) L1794.
- [5.5.3.2] J. Bahrt, et al., “Preparing the BESSY APPLE-undulators for top-up operation,” AIP SRI2006 conference proceedings (to be published).
- [5.5.3.3] A. Hiraya, et al., “Undulator at HiSOR—A compact racetrack-type ring,” *J. Sync. Rad.* (1998) 5, pp 445.
- [5.5.3.4] T. Hara, et. al., “SPring-8 twin helical undulator,” *J. Sync. Rad.* (1998) 5, pp426.

## 5.5.4 Three Pole Wiggler

### 5.5.4.1 Requirement

The NSLS-II three-pole wiggler (3PW) should be capable of producing the minimum of 2 mrad of fan angle above 1 T field. Field profile must be designed so as to minimize the emittance increase. Eq. (5.5.4.1) gives a rough estimate of emittance increase.  $\varepsilon_0$  represents the initial emittance,  $N$  is the number of device, and  $B_w$  is the vertical field of the wiggler.

$$\varepsilon_w = \frac{\varepsilon_0 + 0.4 N \int ds |B_w(s)|^3}{1 + 0.04 N \int ds B_w(s)^2} \quad (5.5.4-1)$$

Figure 5.5.4.1 shows field, angle, and trajectory plots for the NSLS-II 3PW.

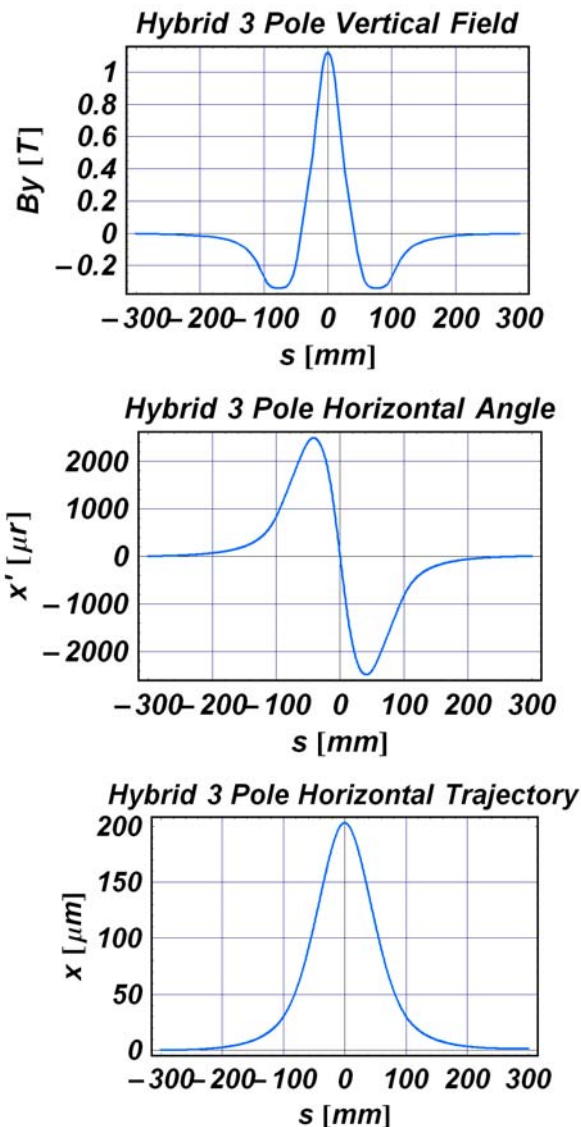


**Figure 5.5.4.1** Field, angle, and trajectory plots for NSLS-II 3PW.

a) Vertical magnetic flux density at a gap of 12.5 mm

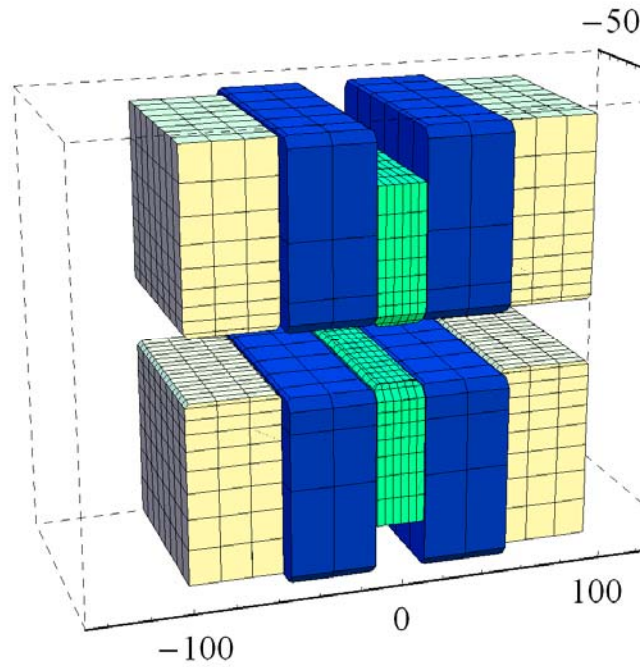
b) Horizontal angle at a gap of 12.5 mm

c) Horizontal trajectory at a gap of 12.5 mm

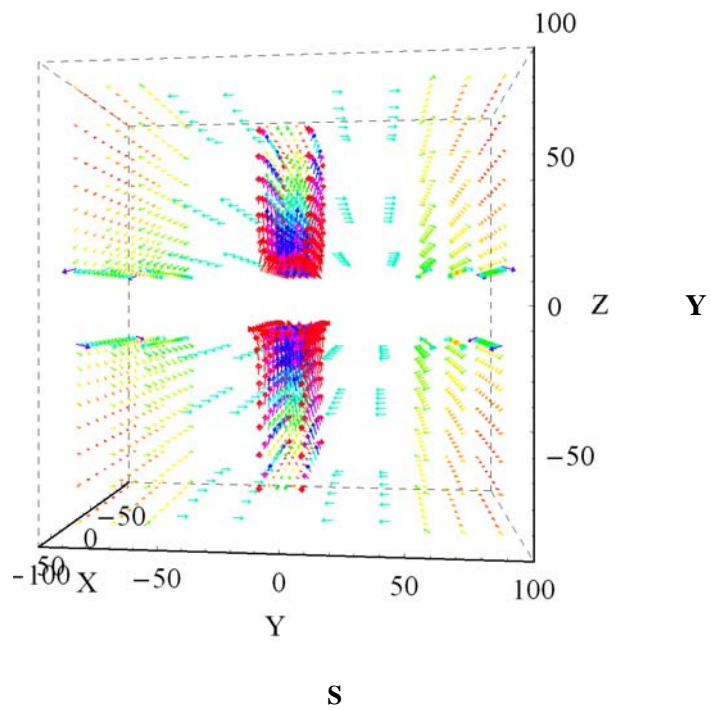


Figure 5.5.4.3 shows the preliminary magnetic structure of the 3PW and the distribution of magnetic flux density in the circuit. The magnetic gap in the center poles is 28 mm.

**Figure 5.5.4.3** Magnetic structure of 3PW. Section in blue is NdFeB permanent magnet, green section is vanadium permendur and light yellow part is made of low-carbon steel.



**Figure 5.5.4.3** 3PW magnetization vector plot.



**Figure 5.5.4.4**  
Isometric view of conceptual 3PW

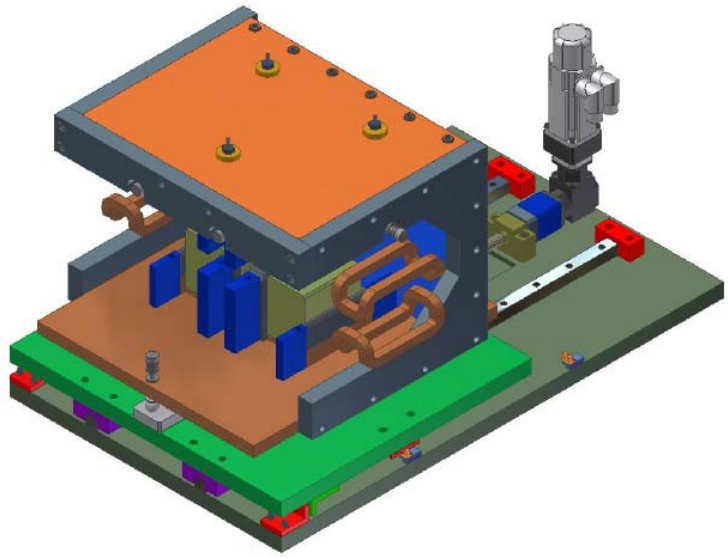


**Figure 5.5.4.5**  
Side view of 3PW.

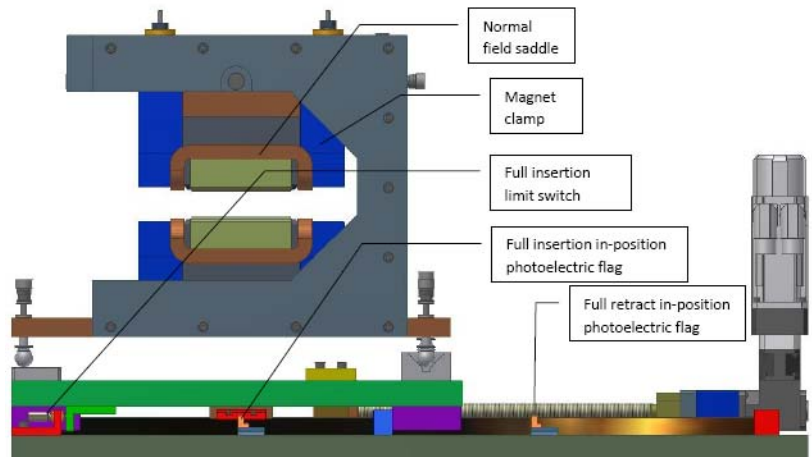
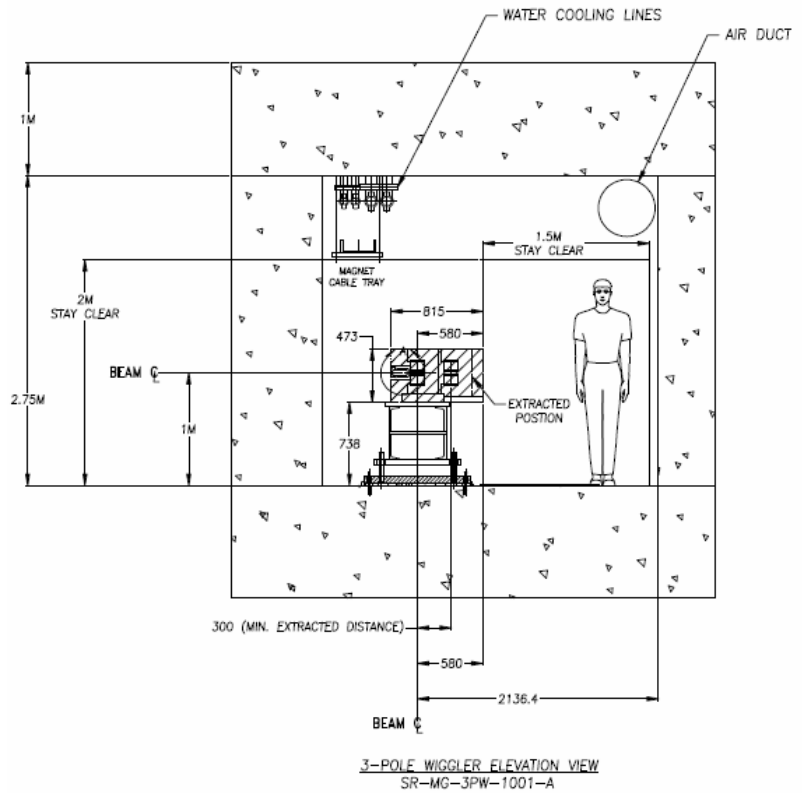


**Figure 5.5.4.6** Tunnel cross section for 3PW location.





## 5.6 R&D Subjects and Insertion Devices for Future Consideration

In this section we briefly discuss three other types of insertion devices that will be explored in our R&D program. If these prove feasible, they would provide a number of benefits and will be considered for future installation at NSLS-II.

### 5.6.1 Magnetic Measurement Facility

Even though conventional insertion devices can be manufactured by industry, their ability to precisely measure the produced field is not in the state of art. Higher performance IDs to meet extremely high beam stability requirement must have very small field errors. Therefore it is essential that this project has its own insertion device magnetic measurement facility, in which each delivered device is certified and corrected if necessary. Due to handling of UHV components for IVUs, Class 10000 clean room with temperature controlled area must be secured for the measurement bench.

#### 5.6.1.1 Requirements

Here are various requirements for the NSLS-II MMF:

- 1) clean area for insertion device assembly/staging
- 2) storage areas for insertion device parts and materials
- 3) temperature stabilized ( $\pm .2^{\circ}\text{C}$ ) clean-room (maybe class 10000) for magnetic survey, with gantry for overhead crane (twin 2-ton chain hoists), 7m Hall probe mapping bench, pulsed-wire test area, flowing water NMR for Hall probe calibration, and the associated electronic systems
- 4) machine shop, fully equipped, with storage for tooling
- 5) an area for winding superconducting insertion devices, with storage for parts
- 6) an area to setup and operate the Vertical Test Facility and also a Horizontal Test Facility for surveying superconducting insertion devices.
- 7) an area outside the main building—maybe an affixed structure--for bead blasting and polishing equipment, a hood for spraying paint, and an oven for curing coatings
- 8) office space with windows/emergency egress
- 9) an area for loading and unloading trucks

#### 5.6.1.2 Building 832

Building 832 will be used to process, assemble, test and survey room temperature and cold permanent magnet undulators, and superconducting insertion devices and their associated hardware. Materials, supplies and magnet assemblies will be moved in and out of the building through the south-facing roll-up door. The large, 30 ton overhead crane will be used on occasion as required. Custom tooling/jigs for wire winding and special parts for the insertion devices and for the survey lab, will be fabricated in the shop. Parts will be polished and coated in the 'affixed structure' setup for that function. Areas will be set aside for the storage of permanent magnets, superconducting wire, basic hardware and other necessary ID parts and supplies. An area will be configured for winding superconducting insertion devices. In the back part of the high-bay area, the Vertical Test Facility, and later a Horizontal Test facility, will be setup for testing those superconducting designs. The permanent magnet type insertion devices will be assembled in the assembly/staging area. They will then be moved into the temperature stabilized clean-room for magnetic survey and field corrective

shimming. Cold measurement for CPMUs will also be conducted in this area. The finished devices will then be moved, maybe by flatbed trailer, to the ring for installation.

### 5.6.2 New Magnetic/Pole Materials

An avenue of further development of CPMUs is to investigate other rare-earth magnets that do not exhibit the spin re-orientation transition at 150K. For example, PrFeB has similar Br as NdFeB at room temperature, but its Br continues to increase further all the way down to 4K. PrFeB would permit use of liquid nitrogen to cool the CPMU to 77K and thereby attain an additional 5 to 7% increase in field. NEOMAX produced a few research samples of PrFeB several years ago, and again just recently. Although the material is not available commercially, we are discussing with NEOMAX and with SPring-8 the possibility of a funded PrFeB development project.

We will also investigate the use of exotic pole materials, such as oriented dysprosium, with a reported saturation flux density up to 3.5 Tesla at cryogenic temperatures. This opens the possibility of a CPMU built with PrFeB magnets and Dy poles, operating at 77K or lower with significantly higher performance than with NdFeB and permendur poles. This may ultimately reduce or eliminate the need for the complexity of superconducting undulators. This project will draw on the expertise in dysprosium and permanent magnet materials at the BNL Materials Science Department. If development of both PrFeB magnets and oriented Dy poles is successful, a short prototype undulator magnet module could be constructed and tested in our existing Superconducting Undulator Vertical Test Facility.

### 5.6.3 In-Vacuum Magnetic Measurement Systems

Two types of measurement systems are used to characterize the field quality of an insertion device at the magnetic measurement laboratory at NSLS. The first is a pulsed-wire measurement system that can be used to check the trajectories in both horizontal and vertical directions. It is also used to find the correct coil current of a Helmholtz coil to cancel the earth field. The second type is a Hall probe mapping system. The Hall probe scan is done “on-the-fly,” starting from a precise home position, acquiring the desired number of samples per undulator period.

One of the challenges for CPMU development is to establish an accurate low-temperature field measurement system. For properly designed undulators, the differences in field quality between room temperature and low temperature are expected to be small. However, it is essential that the field quality be verified at the actual operating temperature. A vertically oriented cryogenic magnetic measurement apparatus for prototype undulator models up to 0.4 m in length has been developed and used at NSLS [5.6.1]. In order to measure full-length devices in a horizontal orientation, a new measurement scheme must be developed. The magnetic measurement should be done in the vacuum vessel at the cold operating temperature, but not necessarily in UHV. Figures 5.6.1 and 5.6.2 delineate the concept of an in-vacuum, in-situ Hall probe mapper based on square chamber design. It is mounted on the large rectangular front flange of the chamber. Hall probe position accuracy is maintained by a laser tracker and piezo controller. ESRF and SPring-8 have independently developed in-vacuum Hall probe mapper based on their cylindrical shape vacuum chamber. It is essential to establish our method of precise field measurement to produce the state of the art insertion device such as CPMU.

For field integral measurements, an in-vacuum moving wire system has already been developed by ACCEL and ESRF. A similar mechanism can be used for a pulsed-wire system.

There is no convenient way to make in-situ (i.e., in-vacuum) field error corrections unless a remote-control magnet adjustment mechanism is incorporated in the magnetic arrays. In the absence of this development, field error correction must be performed iteratively, where each iteration requires a lengthy series of warm-up, venting, measurement, adjustment, pump-down, and cool-down steps. Our goal is minimize the number of such iterations by 1) designing the mechanical components to minimize the

systematic field errors resulting from warm-up and cool-down, and 2) developing an efficient scheme of warm shimming and cold measurement. Ideally, field errors may track with temperature, so shimming at room temperature may suffice.

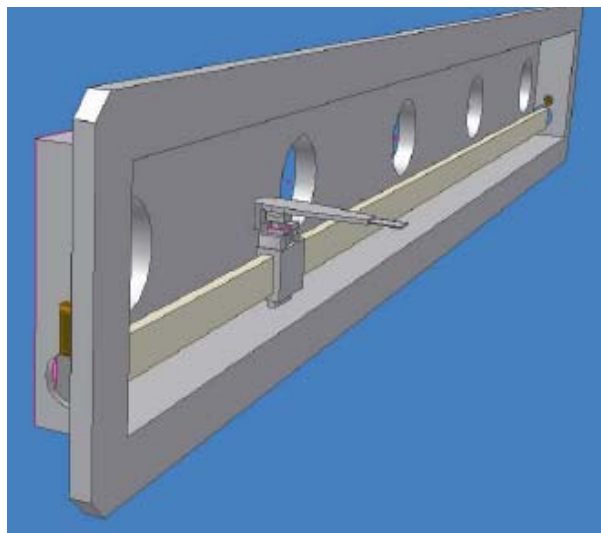


**Figure 5.6.1** Hall probe mapper mounted on the flange cover.

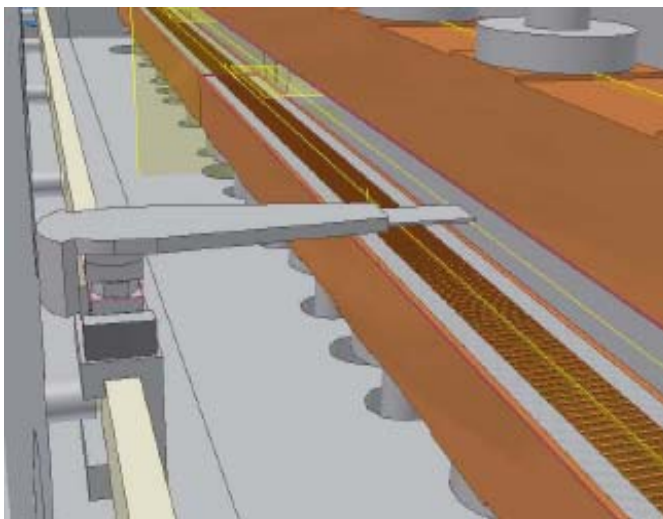


**Figure 5.6.1** Mapper position with respect to the magnet arrays.

This system will be designed to be used primarily in the measurement laboratory but can also be used to perform in-situ measurements of insertion devices in remote locations such as a synchrotron tunnel. This system will incorporate a horizontal vacuum chamber that could accommodate either a CPMU or HTSCU that is 3+ m long and that demonstrates efficient installation of in-situ shimming and measurement of the magnet modules without the need for chamber reassembly. A cryogenic Hall probe, pulsed/vibrating wire, and moving wire will be investigated. The research phase will demonstrate the incorporation of an in-vacuum measuring system with the vacuum vessel and precision gap separation mechanisms.

The goal of this development is to demonstrate cryogenic undulator measurement concepts that will ultimately be used in the characterization, shimming, and in-situ measurements of all the production in-vacuum and cryogenic insertion devices.

#### 5.6.4 Quasi-Periodic Undulator

Undulators designed to produce tunable vacuum ultra-violet and soft x-rays are of necessity long-period devices with period lengths of 40 to 100 mm or more. Because the characteristic K-parameter is proportional to the product of peak field and period, long-period undulators have necessarily high K values. Planar and elliptical undulators with high K-values produce spectra rich in harmonics (primarily odd-integer harmonics, since even harmonics are suppressed on-axis). In fact, the first few harmonics produced by high-K IDs have higher brightness and generate more SR power than the fundamental. If the user's monochromator is tuned to the fundamental, unwanted harmonics corresponding to higher orders of the monochromator pass through the exit slit unimpeded, polluting the monochromatic light and imposing an excessive heat load on optical components.

The Quasi-Periodic Undulator [5.6.2] was developed to overcome this problem. As the undulator's field amplitude pattern is altered, integer harmonics can be suppressed and replaced by noninteger harmonics. The latter do not coincide with higher orders of the monochromator and do not pass through the exit slit. The transmitted light is then purely monochromatic, and sensitive optics are protected. The monochromator must still absorb the unwanted harmonic power somewhere, but this can be accomplished by cooled absorbers at

the exit slit. As with a conventional undulator, the monochromator can be tuned to any of the noninteger harmonics of the QPU to extend the spectral coverage of the instrument.

The QPU concept has been applied to both planar and APPLE-II type IDs. In circular polarization mode, the APPLE-II generates only fundamental radiation on-axis, so the QPU is of no benefit in that case. But in planar and elliptical modes, the quasi-periodicity helps manage the harmonic power and improves spectral purity, as described above. Special care must be taken to absorb the radiated heat in vertical direction in helical / elliptical mode for long period device due to large value of  $K_x$ .

### 5.6.5 Superconducting Wiggler

Higher photon energies (above 20 keV) can be effectively covered by a superconducting wiggler at NSLS-II. For a field range of 3.5 T, 60 mm period length, and a 10 mm magnetic gap, low-temperature SCW technology is now well established. However, achieving 6.0 T with the same period and gap will be a challenging task. In contrast, devices based on the use of high-temperature superconductors are a very promising approach for medium-field wigglers and would reduce the cost of both construction and operation. However, the current density now available for HTS wire remains inadequate to produce the necessary field. Thus, the baseline design for the NSLS-II SCW will be the SCW60 device described in Chapter 5, which is based on conventional LTS technology, but R&D will be carried out to investigate HTS wiggler designs.

### 5.6.6 Superconducting Undulator

The first superconducting undulator in an electron storage ring was installed at LURE, Orsay in 1979. Since then, various devices for FELs have been developed [5.6.3]. In the past fifteen years, IVUs have been the primary device for short-period undulators. One of the reasons for not using SCUs in the storage ring is the difficulty of opening the necessary gap for injection. A new SCU with a variable gap mechanism has been in operation at ANKA [5.6.4] for the past few years. It has a rather complicated two-vacuum vessel structure, one vacuum for UHV and the other for insulation. The vessels are separated by 300 $\mu$ m stainless steel foil. The required performance was barely achieved due to 1) excessive heat load, which reduced the critical current achievable, and 2) a structural problem that contributed to the degradation of phase errors.

SCUs with conventional NbTi wire face serious problems to reduce the heat load onto the device's cold mass to a level manageable with modern cryocoolers. Unfortunately, state-of-the-art cryocoolers have a cooling capacity of less than a few watts at 4K. What is needed is a different type of LTS wire that can withstand higher operating temperatures. One approach is to use Nb<sub>3</sub>Sn; this is being pursued by the ALS group [5.6.5]. This type of wire is best suited for high-field applications. However, it is difficult to create the precise structure required for undulators, due to the wind and react process. Another approach is to use APC NbTi wire, which is supposed to be operated at much higher current density than conventional NbTi wire. Using this approach, extra space for heat shielding may be available for a fixed-gap vacuum chamber.

Even with these developments, SCUs based on LTS technology will still have substantial thermal challenges. It may be that SCUs will not be viable until future developments in HTS technology make it possible to manufacture an HTS device. There is reason to be optimistic about this, and the NSLS-II project will monitor HTS industry developments.

Another issue for SCUs is field correction. Extra wiring to correct phase errors has been attempted, but distributed integrated multipole corrections appear to be difficult. They might require correction at the end of the device. These also are issues for future development.

The initial phase of this work was supported by two SCU-related LDRDs along with investigations to take advantage of new developments in the field of applied superconductivity.

One of the activities in this project is to demonstrate the capability for industry to produce lengths of APC NbTi and optimized Nb<sub>3</sub>Sn superconductor that could be used to produce up to 1M long SCUs. Conductor



produced in this project can be used to produce 1/3 meter undulator prototype magnets that could be tested in the VTF.

In addition, this project will aggressively investigate films coated with high-temperature superconductors such as YBCO, MgB<sub>2</sub>, and other advanced materials, and determine the feasibility for their possible use in future SCUs and SCWs. Direct deposition methods for thick-film and multiple-layer superconducting for use in HTS magnet assemblies will be investigated in the first year. If feasible, these materials will be integrated into SCU shimming concept prototypes in the second year. This project will also investigate the design and demonstration of a superconducting EPU prototype that can be tested and measured in the VTF in year 2 or 3. The goal of this project is to demonstrate a variety of viable materials, manufacturing, and magnet design concepts for use in a NSLS-II SCU, and ultimately establish reliable superconducting insertion device technology that can be offered to meet the needs of NSLS-II users.

### 5.6.7 Revolver Type

If one type of magnetic array cannot satisfy the user's requirement, two or more different arrays could be used interchangeably, in a "revolver" type undulator system [5.6.6]. In-vacuum revolver type systems have also been developed. Revolver designs have been built at SPring-8 and ESRF and are operating reliably. In-vacuum revolver undulator was also developed by SPring-8 and installed at Pohang Light Source in Korea. This is a subject for future consideration, depending on the user requirements.

### References

- [5.6.1] D. Harder, et al., "Magnetic measurement system for the NSLS superconducting undulator vertical test facility," Proc. 2005 Particle Accelerator Conference, Knoxville, USA (2005).
- [5.6.2] S. Sakaki, et al., "Conceptual design of quasiperiodic undulator," *Rev. Sci. Instrum.* 66 (2), p 1953 (1995).
- [5.6.3] G. Ingold, et al., "Fabrication of a high-field short-period superconducting undulator," *Nuc. Instr. & Meth. A* 375 (1996) p. 451.
- [5.6.4] A. Bernhard, et al., "Planar and Planar Helical Superconductive Undulators for Storage Rings: State of the art," Proc. 2004 European Particle Accelerator Conference, Lucerne (2004).
- [5.6.5] S. Prestemon, et al., "Design and evaluation of a short period Nb<sub>3</sub>Sn superconducting undulator prototype," Proceed. 2003 Particle Accelerator Conference, Portland, U.S.A. p 1032 (2003).
- [5.6.6] H. Kitamura, et al., "Recent developments of insertion devices at SPring-8," NIM-A, 467, (2001), pp 110.



## 6 CONTROL SYSTEM

### 6.1 Introduction and Scope

The control system for NSLS-II is designed to convey all monitor, control, model-based, and computed data from all accelerator, facility, experimental, safety, and operations subsystems to accomplish supervisory control, automation, and operational analysis. The scope of the control system extends from the interface of the equipment being controlled through to the designers and operators of the accelerator facility, as well as synchrotron beamline experimenters and staff. The control system includes all hardware and software for global systems such as timing, deterministic data communication, network communication, control room operations, automation and optimization. The control system includes the computers and software required to implement and integrate all subsystems including: diagnostics, power supply control, low level RF, vacuum, personnel protection, equipment protection, undulator, experimental beamlines, and conventional facilities

To provide this comprehensive monitoring, control, and automation, the NSLS-II control system must scale to support 100,000 physical I/O connections and 350,000 computed variables that can be correlated to analyze events and provide data for all control aspects. It must support 1 Hz model-based control, 110 kHz power supply digitization, 500 MHz RF control, 5 KHz orbit feedback, and 20 millisecond equipment protection mitigation. It also must provide 5 Hz updates to operators of up to 1,000 chosen parameters, provide coherent turn-by-turn orbit data for up to  $2^{10} = 1,024$  consecutive turns (for FFT), archive up to 6,000 parameters at a rate of 0.5 Hz continually, latch the last 10 seconds of data from all parameters in the storage ring when a fault is detected in the Machine Protection System (MPS), archive up to 1,024 consecutive turn by turn data for 1,000 parameters at a rate of 10 Hz, and provide pulse-to-pulse beam steering in the linac at 1 Hz.

Our proposed client-server architecture is depicted in Figure 6.1.1. Different levels of access and control reside at distinct layers. At the highest layer (layer 3), access is provided for activities that do not involve moment-by-moment control or monitoring of the accelerator. Layer 3 includes high level physics modeling, making use of live data and data stored in the site Relational Database (RDB in the figure). Experimental activities that do not require synchronization with the ring also reside at layer 3. Layer 2 contains accelerator operation and monitoring activities. Layer 1 contains dedicated equipment controllers, which in turn interface to specific equipment through point-to-point protocols (event system, deterministic data communication hardware for Fast Orbit Feedback). Layer 0 contains remote, slow, independent, reliable control that requires synchronization with the accelerator no faster than 2 Hz such as facility control, vacuum control, or Personnel Protection.

Communication between subsystems takes place via four distinct buses as indicated. Fast Feedback, MPS, and Global Synchronization buses supply information as implied for the needs in a deterministic and reliable fashion of these control operations. Asynchronous information flow which does not require specific transfer rates is achieved by Channel Access Protocol. This is the most global communication standard in the system and, accordingly, most devices in every layer are identified as channel access clients, servers, or both.

The standard two-layer client server architecture ensures scalability and avoids performance limitations. NSLS-II controls must be built upon a proven tool kit with well-defined interfaces at both the server and client to enable integration and development. It should enable the use of hardware and software already developed for specific light source requirements. The core of the Experimental Physics and Industrial Control System (EPICS) has been chosen as the basis for the control system. The advantages in three key areas drove this decision: large user base in the accelerator community, functionality for accelerator-related systems, and support for the required hardware interfaces.

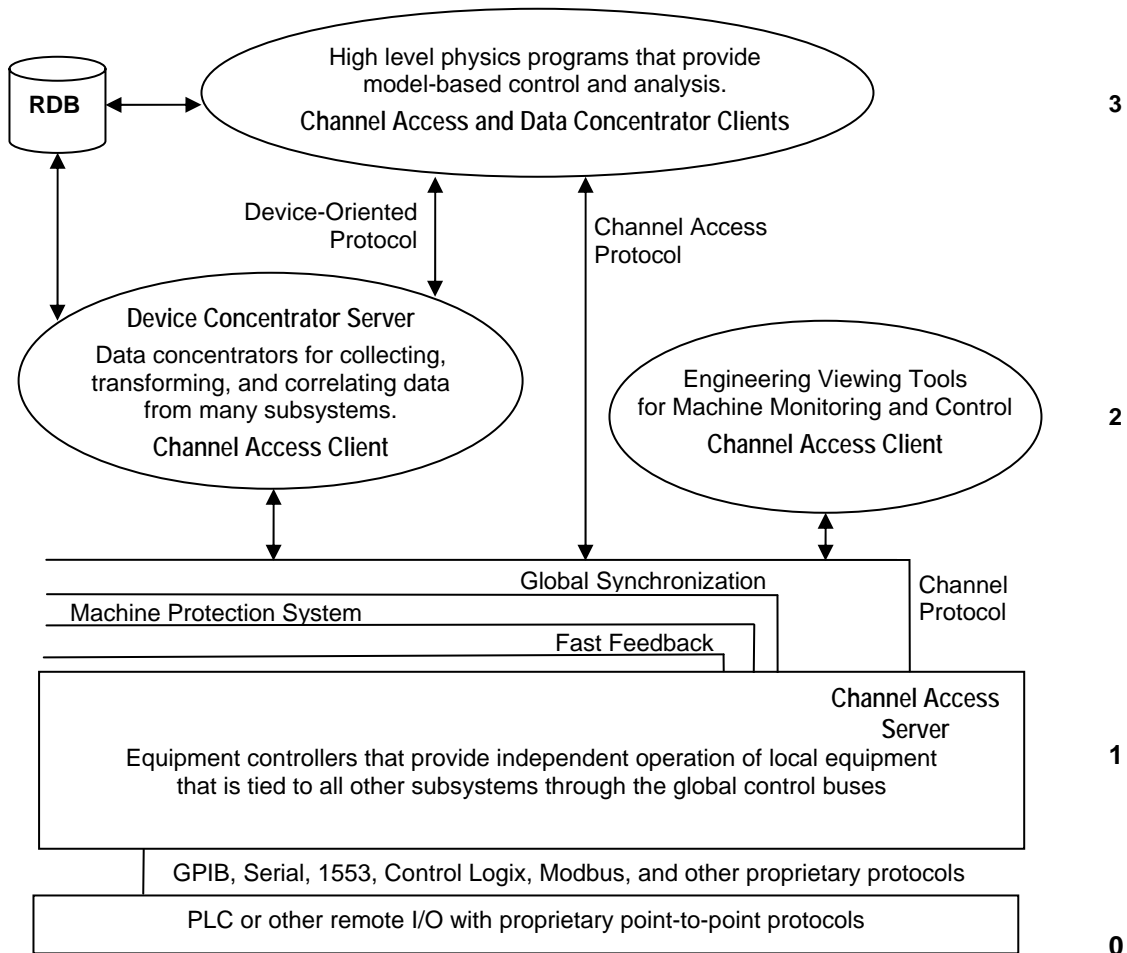


Figure 6.1.1 NSLS-II software architecture.

## 6.2 Control System Requirements

### 6.2.1 Technical Requirements

The control system must be modular, incrementally upgradeable, scalable, and extendable. Expansion of the control system to accommodate the build-up of the accelerator and beamlines from early testing, through installation and commissioning, and during the life of the facility, should not impact the performance. The control system must be available to support all aspects of the project schedule, from component tests during prototyping to beam characterization and optimization at commissioning. To achieve this, the NSLS-II control system is based on open standards and commercial off-the-shelf equipment, whenever possible. Developments needed by NSLS-II are to be accomplished in a manner that meets the project schedule, budget, and performance needs, with consideration for knowledge transfer to the wider accelerator community.

## Machine Control

Machine control supports linac control that is synchronized to the master timing system to fill the booster ring with 80 nanosecond pulse trains made up of 40 micro bunches of 2 ns length each. Pulse-to-pulse timing jitter will be less than 80 ps at the 1 Hz rate. The pulse is ramped up to the correct energy in the booster ring over 400 ms. It is then injected into the storage ring. The revolution rate for the booster and storage ring is 2.6  $\mu$ s. Manual control of orbit trims, quadrupoles, sextupoles, and insertion devices is asynchronous. These are controlled by the operators, accelerator physicists, high level applications, or users. In particular,  $\sim$ 10 Hz write/read is suitable for “turning knobs” for a power supply. The only “fast” process is the fast orbit feedback system with 5 KHz bandwidth (and feedback systems for coherent bunch instabilities of order MHz). To summarize, the beam bunches in the ring and the injection process are synchronous to the RF, but everything else has its own time scales. Model-based control is used to correct steering, the orbit, tune, linear chromaticity, optics, etc. in the storage ring at 1 Hz.

## System Reliability

The control system must have 99.99% availability, 24 hours per day, 365 days per year. Control system modifications that add new functionality will be performed during scheduled down times. New functionality for the operational facility will be tested on equipment test stands before installation. The cryogenic control must achieve even higher standards. Failures or modifications to the cryogenic control system must not result in the loss of temperature control for greater than 15 minutes. Subsystems will be designed to meet system reliability goals using high reliability technology, where required. This includes the use of an uninterruptible power supply, programmable logic controllers, battery backup, and redundant power supplies for VME crates. All subsystems will be designed to achieve operational reliability goals.

## Security and Integration across Operator Base

The system must manage access requirements for the different classes of user. It must also incorporate appropriate tools to guarantee security of its computers and network systems. The source of the data should be irrelevant from the point of view of any software designer or user. For example, it should be possible to display data from the control system, from the associated relational database and from an accelerator model on one full-screen synoptic.

### 6.2.2 Software Requirements

Control system applications must be designed to enable future upgrades to be incorporated economically. Well defined interfaces to support the modular upgrade/replacement of code is a key component for this requirement. The EPICS architecture provides these interfaces at all levels implemented in EPICS. The software used to implement Fast Orbit Feedback (FPGA code) and the software used to implement High Level Applications will attempt to accomplish this same level of modularity.

## Code Maintenance

All code, control system tools, and applications will be placed under source/release control. A standard tool will be used to control the version of software running and to keep previous versions and an audit trail for changes to released and commissioned software. Accelerator components and signal lists such as: magnetic lengths, min/max currents, calibration coefficients for currents vs. gradients, diagnostics channels, and configuration parameters also will be kept and their versions managed. The data that are also needed by accelerator models are to be kept in a similarly controlled relational database.

## Open Standards, Integration, and Ease of Use

The control system will use open standards and an open architecture. The long life expectancy of an accelerator complex implies that the control system will need to evolve to incorporate upgrades and new technology. The control system must enable seamless integration of systems at both the server and client side through well-defined APIs. It is beneficial for the applications that comprise the NSLS-II control system to have a consistent look and feel. Related functions should be linked, to reduce the number of mouse clicks a user has to perform. For example, trends could be accessed by clicking on a process value hotspot displayed on a plant synoptic value. All control system facilities that need to be accessed directly will be accessible via menus, where the menu titles give a clear indication of the facility being called up. It should never be necessary for a user to remember the name of a program or of data files in order to use the system.

Context-sensitive online help facilities should be designed into the system, where feasible. Conscientious attention to common-sense ergonomics during application development will clearly pay dividends for long-term ease of use and will minimize familiarization and training costs for new operators. Production of a concise Style Guide document at an early stage in the development cycle of the project will provide a good ethos for addressing these issues.

### 6.2.3 Architecture Requirements

The four-layer EPICS-based client-server architecture illustrated in Figure 6.1.1 implies further design considerations for its implementation:

#### Network

The connection of the control system layers will use standard network components. These should be in a redundant configuration and include provision for network evolution, i.e., the development to the latest network standards. Control system network security is to include physical security that limits access to the control network from outside, using gateways and firewalls. It requires appropriate types of password and key protection within the control network with access control to manage who is controlling which operation.

#### Operator Interface

The operator interface will be either workstations or PCs running Linux. The control system should seamlessly integrate with office systems through a gateway process to maintain security.

#### Equipment Interface

The equipment interface will provide the physical connection to the equipment being controlled through a variety of interfaces. The preferred standards will include VME because of physical and electrical performance, Compact PCI where higher performance backplanes or lower point count make this more cost effective, and PLC I/O for applications where equipment safety is required and speed is not. The control system includes all VME crates and processors, any network hardware required for integrating instrumentation, the timing/event system, all hardware used for fast feedback, and all the crates and processors used to integrate the I/O. Except where noted, the intelligent device controllers, I/O, and PLCs are provided by the subsystem. The notable exceptions are the controllers for the undulator equipment and the non-BPM diagnostics in the Storage Ring. The network cables and cables to implement the global buses are the responsibility for the control system.

## Relational Database

The control system must include a relational database as a central repository for all configuration information. This should include all static information about accelerator components such as coefficients to calculate field magnetic strength from current. Consideration should be given to extending the database to include all technical information to enable subsequent support and maintenance. At the application level, there should be a unified and seamless interface to both the static and dynamic data.

## 6.3 Identification of Control System User Groups

The control system must support several user groups, each with varying requirements.

### Accelerator Operators

Accelerator operators are the principal managers and users of the control system. It must be a complete and consistent interface for them to perform any function in the accelerator complex. The data and interfaces must be consistent in how data is presented and how equipment is seen to behave. The operation of the accelerators requires real-time control and monitoring of the equipment, archiving, alarm handling, sequencing, backup and restore for routine operation. For these users, alarm and error messages should be supported by information regarding recommended courses of action. The control system should allow the automation of plant operating tasks. It should provide applications that encourage and facilitate the keeping and passing of operation logs, particularly from shift to shift.

### Accelerator Physicists

The accelerator physicists' requirements for the control system include all the routine operations of the control system together with the ability to integrate programs developed to support different accelerator models. Functionality is required to allow easy acquisition of data produced as part of an experimental run, and to provide the ability to switch between different accelerator models. Data retrieved from the control system must be acquired with sufficient time accuracy to enable accurate correlation.

### Technical Groups

The technical groups require diagnostics to enable maintenance such as calibration and fault finding. Access to the control system is required in the main Control Room, local to the equipment, and potentially in the offices, laboratories and off-site. Applications must provide all diagnostic information necessary to assist in commissioning and debugging of equipment. They must provide useful fault diagnosis facilities to assist with plant equipment maintenance and maintenance of the control system itself (both hardware and software). An easy interface to databases of equipment properties, manufacturers, documentation, cabling data and fault histories is required, as well as access to information clearly identifying the geographical location of equipment and a system of fault prediction facilities to allow for scheduled maintenance of components likely to fail.

### Beamline Staff and Experimenters

The end users of the experimental station require a straightforward graphical interface to the control system. They also require good integration of control system parameters with the experimental control and data acquisition systems. This is particularly necessary in the case of synchronizing scanning of a sample with changing a parameter on an insertion device in the storage ring, e.g., the gap of an undulator. Experimenters require clear information on light source status, performance, and timing signals, and may require remote access (i.e., from off site) to experiments and beam-lines.

## Control System Engineers

Control system engineers require current and archived data on the status and behavior of the entire control system. Information required includes CPU loading, network loading, application monitoring (for frozen/crashed applications), connectivity status, and reports of any control system faults.

## Facility Managers

The control system should be capable of producing operating reports and statistics in a form that can then be imported into software applications (i.e., spreadsheets, web-based tools, etc.) used by management. Information required could include the number of hours of beam time supplied to users and unplanned beam dump statistics – how often these events occur, time taken to restore beam, reason for beam dump, and signs of common modes of failure.

## Public Users and Staff

A wide range of other groups will require information from the control system. These include technical and scientific groups on and off site. These groups should be served through a web service as the user interface.

## 6.4 EPICS Toolkit

EPICS is the result of a collaboration of control groups, across a number of research organizations, to produce a tool kit to build distributed control systems. The resultant tool kit reduces software development and maintenance cost by providing: configuration tools in place of programming, a large user base of proven software, a modular design that is expandable, and well defined interfaces for extension at all levels.

Worldwide, EPICS has a very large user base for a variety of accelerators, detector systems, astronomical projects, and industrial processes. Most recently, EPICS has been successfully deployed at the Diamond Light Source, the Spallation Neutron Source at ORNL, and the Australian Synchrotron Project. It is being used for the LINAC Coherent Light Source at SLAC, the Shanghai Light Source, and the multi-faceted accelerator facility JPARC at Jaeri.

The use of EPICS on a diverse range of projects means that there is a large base of drivers and hardware support already available. The existence of these makes interfacing of the underlying systems less dependent on software development.

The EPICS tool kit is supported through the collaboration with software distribution and documented through the web. There are EPICS training courses run each year by many groups in the collaboration, and there are two EPICS workshops rotating through the U.S., Europe, and Asia each year; a number of individuals and companies are also available to provide support and training.

### 6.4.1 Structure of an EPICS Control System

EPICS embodies the standard client server model for a distributed control system, and shown in Figure 6.4.1. The user consoles are one class of client that receives and processes information. The servers are the source of information and in the general case, the interface to the equipment being controlled. The clients and servers are physically connected using network technology and they communicate with the EPICS protocol Channel Access.



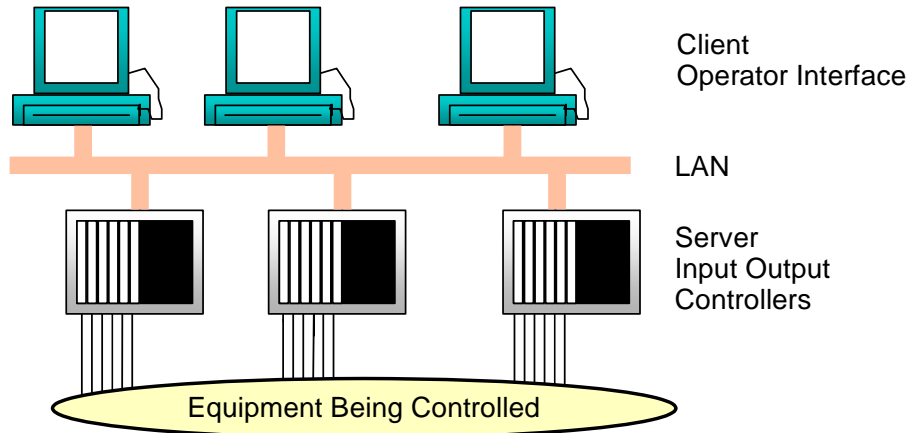
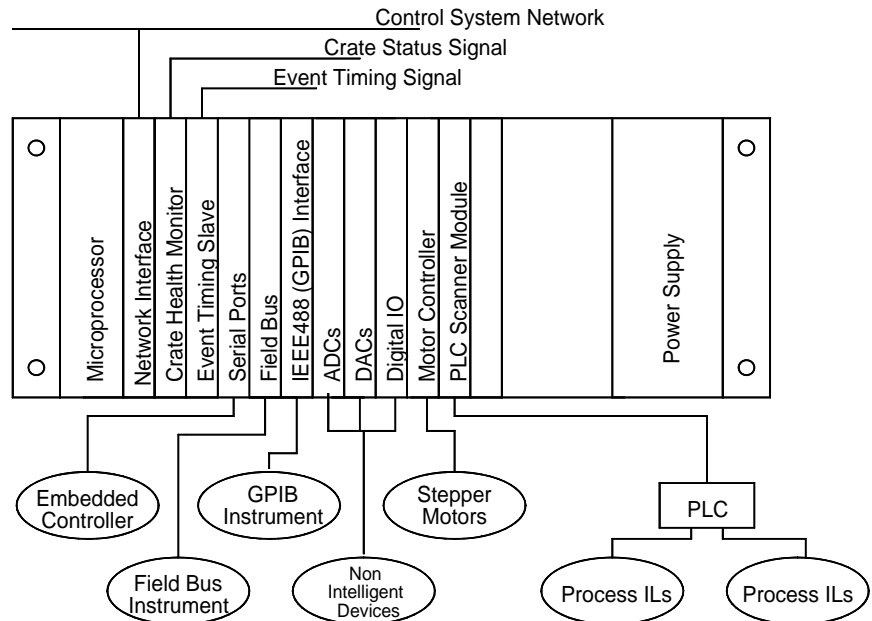


Figure 6.4.1 EPICS model.

### 6.4.2 EPICS Servers

The physical realization of EPICS servers is typically as multiple embedded VME systems, which are called IOCs, Figure 6.4.2. IOCs interface to the equipment being controlled, for which EPICS supports a large range of physical interface standards, protocols, and devices. IOCs also support the use of an event timing signal, to time-stamp transactions and enable synchronous acquisition or control across multiple IOCs.

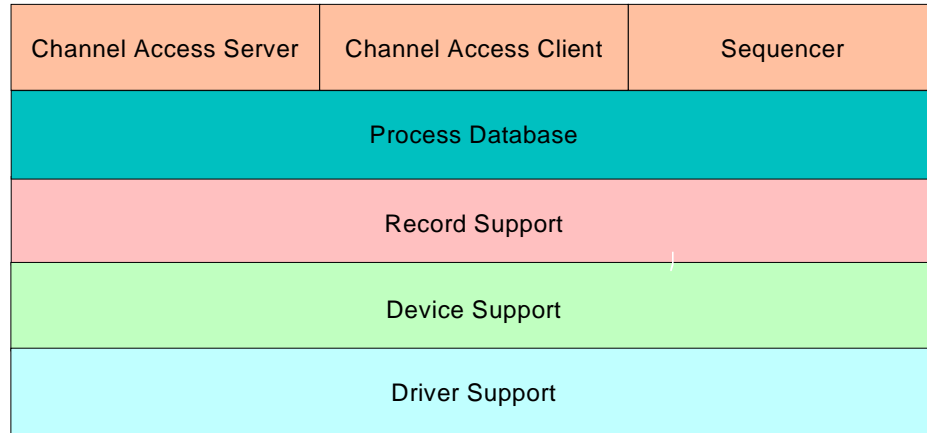
Figure 6.4.2 Example EPICS IOC.



### 6.4.3 Server Side Processing

Within the IOC, the CA server communicates with the Process Database, which uses the Record Support, Device Support, and Driver Support layers to interface to the plant, Figure 6.4.3. The communication from the EPICS client, over CA to the database, can be by synchronous call and reply or by the client establishing a monitor whereby the server asynchronously serves the data. The update of monitors can be on a periodic basis, on change of data, or on external event.

**Figure 6.4.3** EPICS IOC data model.



The process database is a memory resident database that defines the functionality of the IOC. The database uses the Record Support layer to perform the processing necessary to access IO, perform data conversion, check alarms, and update monitors. The IO operations are carried out through the Device Support layer, which handles equipment specific protocols, and through the Driver Support layer, for the hardware interfaces. The structure provides support for interfacing to embedded controllers, field buses, IEEE488 (GPIB), DACs, ADCs, Digital IO, stepper motors, PLCs, power supplies, and a range of instrumentation.

Within the Input/Output Controller there is also a CA client to facilitate IOC-to-IOC communication. This is realized by linking process information from one process database to a process database on another IOC.

An IOC also contains a Sequencer to perform Finite State Machine control on the process database. The sequencer logic is defined as SNL, which is compiled to C code, then to an executable to run on the IOC. This allows for easy production on complex sequences, such as switching through the steps in bringing on a piece of equipment.

A standalone version of the CA server is available, which can be integrated into other systems without the process database and support layers. This facilitates integration of self-contained systems into EPICS, one example being the integration of LabView systems.

#### 6.4.4 EPICS Clients

The client side of EPICS is realized on either Unix workstations or PCs running Windows and is called the OPERator Interface (OPI).

In the standard EPICS model, the OPI application programs interfaced directly to the CA client. This has limitations in that it only provides access to the dynamic control data through the CA API and so limits seamless integration of data from other sources, e.g., a RDB. The EPICS toolkit provides a suite of applications for the OPI. Among the choices for the core tools are: a synoptic user interface for control and monitoring (EDM), an Alarm Handler, an Archiver for recording and retrieving the historical state of the control system, a backup and restore facility to take snapshots of parameter settings, a knob manager to provide attachment of physical knobs to parameters and a parameter plotting tool. There is support within EPICS for the scripting languages Jython, Matlab, Tcl/Tk, Perl, and LabView. Data can be further served up to web pages through a CGI server.

## 6.4.5 EPICS Development Environment

The functionality of a control system built with EPICS is defined in three places: the Operator Interface, the Process Database, and the Sequencer logic. EPICS provides a number of tools to develop each of these which do not require software development. The OPI applications can be produced by a number of interface-generating tools, one of which is EDM. These tools allow for control objects to be placed on pages and animated with a connection to the control parameters. There are both text and graphical tools to produce the Process Database, which involves selecting records and drivers, and linking them to process data and alarms. The Sequencer logic is produced from SNL, which can be defined as text or, more recently, in a graphical form.

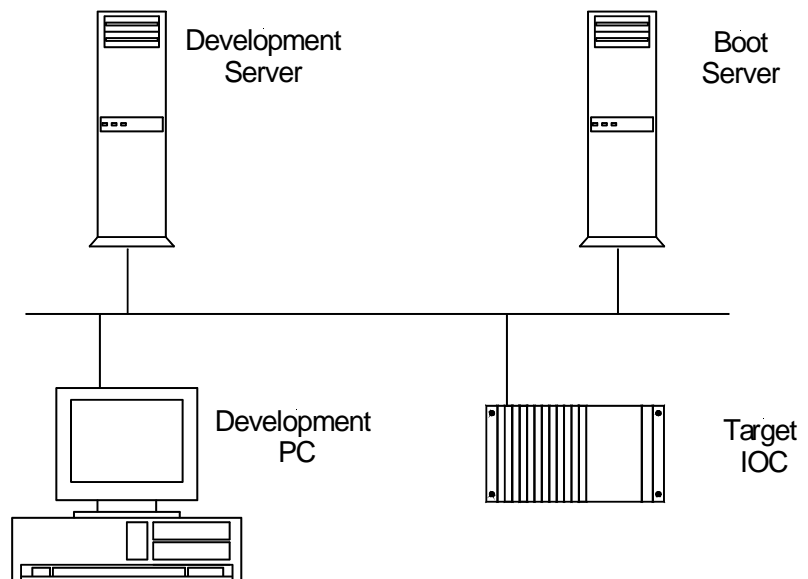
### 6.4.5.1 Distributed Development

Each developer will work on either a Linux PC or a Windows PC. These will be networked to a development file server providing read-access to all the necessary development tools and applications (VxWorks, RTEMS, Matlab, XAL EPICS base and extensions, configuration and database files, etc.), see Figure 6.4.4.

Modifications will only be made to local copies of applications, which will then be checked in to a branch of the CVS repository to enable any changes to be backtracked. When the application has been fully tested and is stable, this branch will become the main development branch for the control system.

A central boot server will be used to provide all the necessary files required by the local IOCs for booting. These files will be generated from the CVS repository. This will ensure that all IOCs are running a consistent and stable version of the control system. The contents of the central boot server will be mirrored on boot servers located in the control room, which will provide local booting of the IOCs.

**Figure 6.4.4** Distributed development structure.



## File Management with CVS

CVS [6.5] is a version control system for keeping track of all modifications to project source code files. CVS is widely used in both open source and proprietary software development projects, and is generally

considered to be the best freely available, full-featured version control tool. Two features make CVS particularly suited to collaborative development across any network, including the Internet:

- Multiple developers can edit their own working copies of files simultaneously. CVS then deals with combining all the changes and notifying developers when there are conflicts.
- Developers have remote access to source code file repositories. Project members can obtain and modify project files from virtually anywhere.

CVS is a client-server system. The CVS repository is maintained on a server; clients run on users' machines and connect to the server via the network (or Internet). Clients are available for nearly all platforms, including Unix, Windows, Macintosh, and any Java-based platform. CVS allows project members to:

- Check out source files and directories
- View differences between versions of files
- View change log history and comments
- Commit changes made in their local copies of the source files to the main source code repository
- Update their local project files when they want to remain in sync with changes committed by other project members

CVS has proven very beneficial to many other accelerator projects in the world, and there is a very large CVS knowledge base within the EPICS community.

#### 6.4.5.2 Application Development

Most application requirements can be met through the standard tools discussed in this section. Where more intelligence is required at the application level, there are EPICS interfaces to all the popular programming languages. The preferred solution will be to use C/C++, Java, or scripting languages to minimize the number of supported languages.

**C/C++.** C, and C++ are high-level programming languages that have become the de facto standard for portable open systems solutions on Unix/Linux platforms, with C++ usage increasing due to the popularity of Object-Oriented design and programming. Both languages have been widely used both for the EPICS baseline product and for driver software and other applications built on top of the baseline. For the NSLS-II Control System, the emphasis will be on re-use of existing software. Improvements are expected to meet NSLS-II requirements.

**Tcl/Tk, Python/Jython.** Tcl and Python are widely-used open-source scripting languages. They have simple and programmable syntax and can be either used as a standalone application or embedded in application programs. Tk and Python are Graphical User Interface toolkits that can be used for rapid development of powerful GUIs. Tcl/Tk and Python are highly portable, running on essentially all flavors of Unix (Linux Solaris, IRIX, AIX, \*BSD\*, etc.), Windows, Macintosh, and more. Tcl/Tk and Python are well supported and extensively used on many EPICS-based projects, particularly for GUI development.

**Java.** Java is an object-oriented interpretative programming language with a built-in Application Programming Interface that can handle graphics and user interfaces. Java can be used to create standalone applications. However, a more important use is in the development of applets, programs that can be embedded in a Web page. The growth of the Internet, together with Java's hardware independence, has made the language essential for web-based developments.

Currently, Java performance issues mean its usage will only be considered for applications where response time is unimportant. Generally, though, Java solutions providers are seeking to improve performance with developments such as just-in-time compilers and Java processors. If these developments yield effective

performance improvements during the development phase of the NSLS-II project, then Java's importance to the project will increase.

### 6.4.5.3 Server Development

Development of EPICS at the server level is required potentially in three places, namely record and device support, database, and state notation language.

### 6.4.5.4 Record and Device Support

While there is extensive record and device support available for EPICS, addition of unsupported hardware will necessitate the development of Device and possibly Record Support layers. The EPICS toolkit provides well-defined interfaces to each of these layers and examples to aid development. Device development is carried out in C within the standard EPICS development environment.

Building and developing EPICS requires either the VxWorks [6.6] or RTEMS development environment. VxWorks is currently only available for Windows or Solaris. However, given that the development environment is based on the GNU tool chain, it should be possible to run the RTEMS tools on Linux. The preference will be to standardize on one operating system for development, preferably Linux.

## Database Configuration Tools

There are several Database Configuration Tools available. These DCTs allow designers to create EPICS databases by implementing them visually with a "block diagram and link wire" approach, similar to that used in electronic schematic design packages.

NSLS-II will use VisualDCT [6.7] as its database configuration tool. VisualDCT is an EPICS database configuration tool written in Java. It can therefore run under any operating system that supports a Java Runtime Environment. It was developed to provide features missing in existing configuration tools and to make databases easier to understand and implement.

The database development cycle will involve importing the EPICS runtime database into the central relational database to have a single repository of all control system information. VisualDCT has a powerful database parser, which allows existing DB and DBD files to be imported with ease. The parser detects syntax errors in databases, as well as defective visual composition data or its absence. Faults in DB files are safely handled and do not raise any critical errors. VisualDCT automatically lays out all objects that have no visual composition data and saves all visual data as comments to maintain backward compatibility. The output from VisualDCT is also a DB file, with all comments and record order preserved.

Visual DCT has been written within the EPICS community specifically to support EPICS, and is available free to EPICS database developers. However, some development of VisualDCT required to add some missing functionality will need to be undertaken.

## State Notation Language / Sequencer Tools

The sequencer is a tool within EPICS that allows the implementation and control of one or more state machines on the IOC. The state machines are created using EPICS SNL. SNL has a C-like syntax, with constructs for building state machines. Once the SNL source code has been written, a SNC pre-processes it into "C" code and then compiles it to create an object file which the sequencer runs in the IOC.

#### 6.4.5.5 Client Tools and Middleware Data Servers

Client tools are available at level 2 of the control system architecture. Clients at this level can directly access all channels in the control system through the Channel Access protocol. These data are time stamped by the Event System for reconstruction of accurate time sequences or correlation of events. At this level, client tools can use data from the IOCs directly, use control system data along with accelerator equipment information for model-based physics applications, or provide computed or correlated data to other clients.

#### 6.4.5.6 Console Applications

The EPICS software package offers comprehensive operator display applications, which include:

- Extensible Display Manager
- Channel Archiver and Archive Viewing Tools
- Strip Chart Tool (StripTool)
- Array Display Tool (ADT)
- Parameter Display Page (DP)
- Alarm Handler
- Knob Manager (KM)
- Operator Electronic Log (CMLOG)

These applications will be used to supply operator display facilities, which will include the following functions.

#### Operator Menu Bar

This will provide rapid single-click access to all key operator facilities.

#### Plant Synoptics

These full-screen plant schematic diagrams will provide operators with an at-a-glance indication of plant conditions. Each process value displayed on a synoptic will constitute a “hotspot”; clicking on a hotspot will produce a pull-down menu providing access to further information and control actions relevant to that process value. Typically, a text description of the signal, the units of measurement, alarm limits, maximum and minimum, trend, alarm history, wiring information, operator comment and web access to online help might be provided. By this means, plant synoptics will act as the launch platforms which allow operators to access a wide variety of data in a seamless manner.

Ease of navigation will be considered during the detailed design stage for plant synoptics. An overall Synoptic Menu will be provided, which lists all synoptics grouped by functional area, presenting a clear hierarchy. In addition, where appropriate, plant synoptics will contain links to other associated synoptics. The design aim will be that operators should be able to navigate around the hierarchy without the constant need to return to the Synoptic Menu. Plant synoptics will be designed to have a simple, uncluttered appearance so as not to present more information to the operator than can reasonably be taken in.

#### Control Panels

Usually sized smaller than full-screen, control panels will be available with a wide variety of control widgets (radio buttons, slider bars, data entry fields with data validity checking, etc.) to allow users to apply control actions to the plant.

Control panels can be configured such that a single slider bar is used to control simultaneously a number of control outputs. Mathematical functions are available to define how these combined control outputs operate in relation to one other.

### **User-Configurable Tabular Displays**

Operators will be able to configure their own sets of tabular displays showing closely-related accelerator parameters. Facilities will be provided to save these user-configured displays with a user-chosen name, and to recall the display from a list presented in a pull-down menu.

### **System Status Indicators**

These schematics will show the status of IOCs, operator monitors, printers, etc. They will also display the health of key applications—so that, for example, operators are made aware quickly if alarm processing stops due to an alarm server program crash.

### **Operator Comments Facility**

This will allow operators to enter lines of text comment for any plant input—to record, for example, when an input is not reading correctly due to a known fault. The presence of an operator comment for a process variable will be clearly indicated on any synoptic which displays that process variable. Individual comments will be easily readable via a suitable control panel, and it will also be possible to collate lists of comments (e.g., all operator comments entered during a shift).

### **Signal Information Panel**

Only a subset of the process variables will be displayed on plant synoptics. However, operators require rapid access to information about any process variable and the Signal Information Panel satisfies this requirement. The panel will provide a Search section and a Display section. The Search section will enable the user to carry out a name search on the relational database, using a name mask to search for either an EPICS database record name or an EPICS record descriptor. Clicking on one of the returned search results will enable the user to request further information (e.g., trend, alarm history, operator comment, etc.).

### **Message Logging**

The CMLOG package available with EPICS will be used to provide a distributed message logging system. This package can be used by any application or system that needs to log messages to centralized log files and display distributed messages to users. The CMLOG package supports C++, C, and CDEV application interfaces for logging messages and has C++ application interfaces for searching/retrieving messages from a dedicated logging server. Applications may send a selection rule to the server to select a subset of log messages for viewing; these rules can be in a form similar to C logic syntax or in a form similar to SQL.

A sample Message Log Browser (an X-Windows Motif application) is included with the CMLOG package. An additional browser will be developed using the supplied application interfaces once detailed requirements are established during the detailed design phase of the project.

### 6.4.5.7 Alarm Handling

The EPICS Alarm Handler package will be used to provide the following facilities:

An alarm list allows the users to view and manipulate current plant alarms. The alarm list will incorporate the following facilities:

- Indication of alarm acknowledgement state.
- Alarm message which includes EPICS record name, descriptive text, alarm value and date/time of alarm generation.
- Removal of acknowledged alarms from the Alarm List when they are no longer in the alarm state.
- Access to a menu-based set of facilities from each alarm in the Alarm list. The menu would give access to further information about the alarmed signal, including:
  - Trend
  - Alarm history
  - Access to a synoptic which includes the alarmed signal.
    - Web access (e.g., a link to a text page with more details about the alarm condition and possible corrective action)
    - Operator-selectable alarm inhibition to prevent use of the Alarm List from being disrupted by non-genuine alarms (e.g. “flickering” alarms being generated by a faulty switch). The names and descriptions of inhibited signals will be viewable on a separate list, from where it will be possible to de-inhibit each signal.
    - Association of each alarm with a plant area, along with the ability to display only alarms for a particular plant area.
    - Color indication of alarm severity.

All alarm messages will be logged to a text file for interrogation and archiving purposes. An alarm log viewer will be available, with various filtering options such as date/time, alarm severity, input name, etc. Provision will be made for audible alarm tones, driven from software using wav files. A separate alarm tone will be available for each alarm severity. An alarm banner window will be available to display a configurable number of recent alarms in a dedicated window at the top or bottom of the screen. Alarms can be acknowledged via the banner without having to call up the main Alarm List.

### 6.4.5.8 Archiving

The EPICS software toolkit offers comprehensive short, medium, and long-term data collection, archiving and retrieval through the EPICS Channel Archiver package. This package will be used to provide the following facilities. For long-term archiving, the archiver provides support for:

- Data retrievable in tabular and trend form
- A data quality indicator associated with each item of data
- Data compression to minimize the size of archive files
- Dumping of data to removable storage media, for long-term storage
- Loading of archive data from removable storage media for data analysis
- Timely warning to operators when archive data collection is compromised by a “disk full” condition on the archive server
- Variable data collection intervals for archiving
- A mechanism for easily configuring large numbers of process variables for archiving (e.g., by use of name masks)
- Facilities for collecting data in user-definable data sets, where data sets can include files as well as process variable data



The Historical Data Collection provides for short- to medium-term data collection offering the following features:

- Data retrievable in tabular form and trend form
- Data quality indicator associated with all data
- Variable data collection intervals
- Mathematical functions (e.g., averaging, MIN-MAX, etc.) applicable to historical data

A wide variety of data retrieval and data management tools are available with the standard Channel Archiver package, including:

- Retrieval via scripting tools, provided by the Channel Archiver Scripting Interface. Tcl, Python or Perl can be used to develop automation of archive handling.
- Retrieval via native tools, with Xarr/Striptool for UNIX-based systems and WinBrowser for Win32 systems. WinBrowser also provides data export in spreadsheet format or in a format suitable for the Matlab data analysis and modeling package.
- Retrieval via a web server plug-in, offered by the CGIExport client, which allows users to browse the archive via any web browser. File download in spreadsheet or Matlab format is supported by this plug-in.
- Command-line tools provided by the ArchiveExport/ArchiveManager component, providing commands to manage archives and to export data to a spreadsheet, to Matlab or to the GnuPlot plotting utility program.
- The Archive Engine component of the Channel Archiver package includes a built-in Web server. By using this feature, current operational parameters can be viewed and interactive configuration can be carried out via any Web browser.

#### 6.4.5.9 Plotting

The StripTool program will be used for displaying trends of current and archived data. The key features of the StripTool program are:

- A StripTool chart displaying recent live data can be scrolled back to view archive data.
- Data acquisition via both Channel Access and CDEV, thereby allowing trending of both EPICS and non-EPICS data on the same axes.
- Ability to drag signals from synoptic diagram (drawn using MEDM) into a graph window.
- Flexible configuration options, including logarithmic and linear transformations, sampling rate, graph refresh rate, plot colors, grid lines, graph legend coloring, and plot line width. The trend can also be easily reconfigured to make one or more plot curves invisible without removing the plot configuration information for that curve.
- Trends can be printed and trend data saved to file.
- Trends are customizable via X resources, giving access to a wider set of configuration options than those offered by the standard StripTool configuration facilities.

#### 6.4.5.10 Automatic Sequencing

For increased operational efficiency, and in support of a demanding accelerator availability requirement, the control system will include the capability of automatic sequencing, including decision making. These sequences could include automatic run-up procedures, automatic fault-recovery sequences, and automatic data-taking routines. The system will provide simple tools for defining sequences as experience is gained and will be capable of monitoring the status of automatic sequences, annunciating problems encountered in sequences, and intervening or overriding sequences if necessary.

### 6.4.5.11 Data Server

Computed data and aggregate data are to be done with consideration to overall performance metrics. Where it is reasonable, these data are to be created once in a server and provided to other clients in the control system. Examples of this are first turn data, ring current, and emittance measurements.

## 6.5 Physics Applications Rapid Prototyping

Rapid prototyping of physics applications is supported through a number of programming language interfaces to the Channel Access protocol. These include: analysis packages such as Matlab, Labview and Mathematica; scripting languages such as Jython, Pearl, Tcl/Tk, and SWIG; and programming language interfaces such as: Java, C, and C++. Applications that are prototyped in this environment can be migrated into the standard EPICS front end controllers and the XAL environment for operations. (Figure 6.5.1).

### 6.5.1 Model-Based Physics Applications

Model-Based Physics applications must be available for all phases of commissioning. The system should be capable of operating in online and predictive modes. A RDB must contain the model parameters needed for the model based control (Figure 6.5.1). A physics modeling system will be needed to provide an interface between the control system and standard codes such as Tracy2, Elegant, or RING. These codes can mathematically model the behavior of various accelerator systems. They can be used to aid understanding of the machine, as well as being a vital tool for optimizing and operating a complex accelerator.

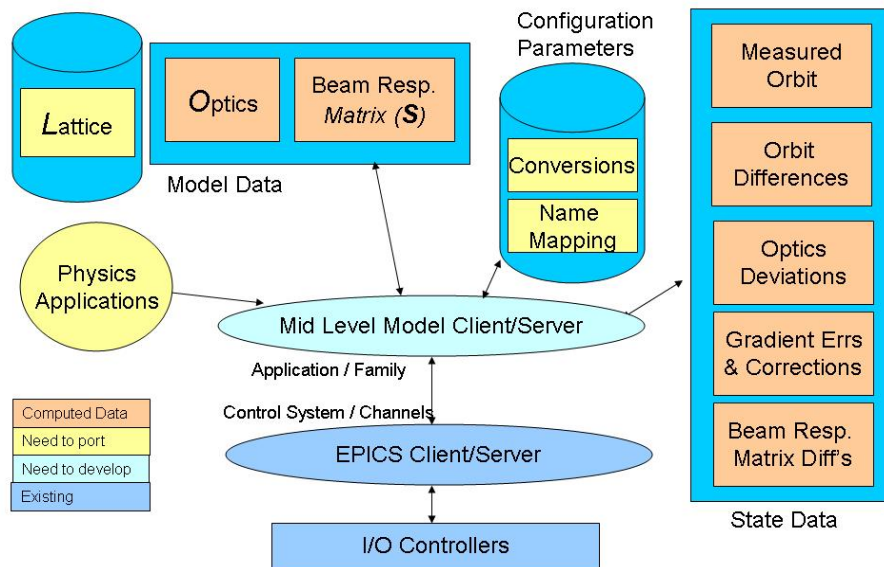


Figure 6.5.1 High-level application architecture.

### Matlab Middle Layer Toolkit

Initial model based control is to be implemented using the Matlab Middle Layer Toolkit in conjunction with an accelerator simulation running through the EPICS process database. This provides an environment to develop commissioning tools that can be tested well in advance of the presence of any equipment.

## Online Mode

Real-time magnet and RF data will be passed to the modeling system. Computed values of Twiss parameters, Q values, chromaticity, momentum compaction factor, etc. will be made available to the rest of the control system or to Accelerator Physics applications.

## Predictive Mode

In this mode, offline magnet and RF values are supplied to the modeling system rather than real-time data. This will allow predictive and “look-and-see” experiments to be performed using the machine model to predict the behavior of the accelerator.

## Middleware Data Servers

Middleware data servers will be provided to separate the data collection from the visualization layers. All client applications that collect data from the control system that result in the production of new data will be served to multiple, distributed clients. The distribution of this data is done over a standard protocol such as DDS or Croba. Alarm information, orbit, archive data, and emittance are some examples of data that may be produced by clients and served to other clients. The goal is to define a narrow interface that supports the reuse of clients of the API.

## XAL – the Model-Based Control Framework

NSLS-II will use the new Middleware Data Servers to create applications for commissioning and operation. Operational tools are to be derived from commissioning tools. They will be modified for ease of use and clarity, maintainability, and revision control. Many of these tools are expected to be from the XAL toolkit in use at the SNS.

### 6.5.2 High Level Application Tools

High level tools include: system queries by physics devices or computed values, correlation plots, beam trip displays, machine protection first fault displays, and others as identified by the commissioning and operations teams.

## 6.6 Relational Database

MySQL will be used as the main data store for all beamline component information that is needed for model-based control. The IRMIS Entity Relationship Diagram will be used to describe all component and wiring data. It will be extended to support the Lattice information early in the project. Tools will be provided to enter this data, produce reports, and create files needed for all aspects of the project. These tools are to be developed early in cooperation with the users.

## 6.7 I/O Controllers / Equipment Interfaces

The I/O controllers and equipment interfaces must support the wide range of applications that are encountered in an accelerator control system. To minimize integration, training, and maintenance costs, this hardware should be limited to a solution that can meet each class of hardware integration needed. The front-end computers will run a Real-Time Operating System. The RTOS candidates are vxWorks and RTEMS. Although vxWorks runs on a wide variety of CPUs and provides much functionality, it does not provide

source code without a prohibitive investment. RTEMS is an open-source RTOS that requires more manpower to wield. Several EPICS sites now support RTEMS. Control at this level of the architecture can be done at the rate of 1 kHz with latencies of 33  $\mu$ sec. Dedicated data and timing buses are required to achieve this level of performance over distributed controllers.

### 6.6.1 High-Speed Signals

High-speed signals such as RF, image diagnostics, and beam position signals may be processed with an FPGA to produce results that are used by the control system at a slower rate. These devices may operate on data into the MHz range and be used to analyze high-speed signals from LLRF, Beam Position Monitors, and Power Supply Controllers. These may be implanted as single device controllers that are equipped with dedicated processors to run EPICS and provide the interface to the control system, an FPGA to process the signal, a high-speed interface between the FPGA and the control system, and an interface to the timing system. These device controllers may control a single device or a set of devices. A standard architecture that includes a Power PC with a PCI or PCI interface in the Coldfire format is a candidate for this application.

### 6.6.2 Low Latency Response I/O

I/O that requires the control system to respond in the minimum time (known as high-density I/O) requires an instrumentation bus that provides interrupts on an external trigger and reasonable data transfer times between I/O boards. This can be implemented using either VME or PCI.

### 6.6.3 High-Reliability IO

Applications such as vacuum interlocks, flow switch interlocks, and cryogenic control require high reliability control of simple processes. A Programmable Logic Controller will be provided for these applications. All data from the PLC shall be available through the control system. The Control Logix PLC in conjunction with the Flex-I/O line could provide this function at a reasonable price. In any case, one PLC family will be chosen as the NSLS-II standard. These PLCs will be integrated into the control system through an IOC.

## 6.7 Global Control System

The control system must provide some global communication that requires higher performance than is available in a commercial network. NSLS-II requires: an Event System for synchronizing data acquisition and control; a high-speed data network for providing beam-steering data to all ring power supplies for orbit correction; and a Machine Protection System that is a fast-response bus provided for mitigation against failures that greatly impact the operation of the facility by either producing excessive radiation or causing equipment damage. We will evaluate the systems available from other laboratories. We are also considering the development of an open-source set of functionality that provides the timing, event, and data communication needed for high speed, distributed applications such as Fast Orbit Feedback and Machine Protection.

### 6.7.1 Event System

The Event System, also referred to as a timing system, provides all beam and RF synchronization for all control and data acquisition. The event system provides a master pattern of events that reflect the operation mode of the machine. It provides the synchronization needed to control the beam injection into the ring for initial fill and top-off. The event system may also communicate data that are required for operation and data

correlation, as well as data communicated to the subsystems that change with the mode of the machine. Examples include time stamp/pulse ID, machine mode, and global machine status.

The timing system is required to provide control of the beam transfer from the electron source to the storage ring and provide diagnostic equipment and beamline equipment with synchronization signals. The most recent light sources [8] have made use of commercial equipment and built on equipment designed by other light sources, often in collaboration with industry; it is envisaged that the same approach will be adopted for NSLS-II.

### 6.7.1.1 Fast Timing

The task of a timing system is to synchronize all the relevant components in an accelerator complex. One part of this task is to control the injection by triggering the particle source and firing the transfer line components, such as injection- and extraction-pulsed magnets, at the correct times. Also, beam diagnostic components such as beam position monitors and current transformers must be synchronized to the passage of the beam. This has to happen with fine time resolution, to RF frequency, clock precision, and low jitter, and is termed Fast Timing.

### 6.7.1.2 Event System Signals

Other tasks for the timing system are related to synchronizing components where the resolution is more relaxed. Examples include triggering the magnets for an acceleration ramp, triggering operational sequences such as the filling of the storage ring, BPM acquisition, feedback timing, insertion device control, and supplying the distributed control system with time synchronization for control and correlation of data. The time resolution for these tasks is less demanding; these tasks are often termed Events. Event Signals will be produced with a precision set by the storage ring revolution period and with predictable jitter.

### 6.7.1.3 Timing System Components

In designing the accelerator timing system, it is important to consider what has been used at other recently constructed sources and the integration into the EPICS control system. The time-stamp system already exists within the EPICS infrastructure and can be used in conjunction with the Event System, which was developed at APS [6.9] and enhanced by SLS and, more recently, DIAMOND (Table 6.7.1). The APS/SLS Event System can be used to meet all slow timing requirements. The Event System is fully EPICS compatible and the required VME modules are available.

**Table 6.7.1 Diamond Version of the SLS Version of the APS Event System Specification.**

Events	8-bit code – 255 events
Resolution	8 ns
Event TX trigger	Hardware input, software, Event Ram Clock.
Event RX output	Hardware output, software (EPICS record process)
Transmission medium	Gigabit Ethernet

The requirements for fast timing are more specific to a particular accelerator dimensions and operation. Two options (Table 6.7.2) are available for the hardware for fast timing, the KEK TD4V as a VME module delay generator and the Stanford Research DG535 as a self-contained instrument. Each is available with EPICS drivers to provide the controlled delays.

**Table 6.7.2 Fast Timing Hardware Options.**

	KEK TD4V	Stanford Research DG535
Form	VME 6U	Bench / Rack mounting
Delay	16 Bit / RF clock	0 to 1000 s – 5 ps steps
EPICS Support	Yes	Yes, via GPIB
Channels	1	4
Jitter	4.5 ps at 508 MHz	<60 ps

### 6.7.1.4 System Structure

Figure 6.7.1 gives an overview of the Event System and Fast Timing control. The Event Generator receives a start signal from the RF clock gated with a line frequency component. Events are then sent to all IOC Event Receivers for timestamp synchronization and to output relevant event signals or process EPICS records. The fast-timing IOCs will require a fast clock and trigger derived from the RF source, but fast sequences can also be initiated upon receipt of an event.

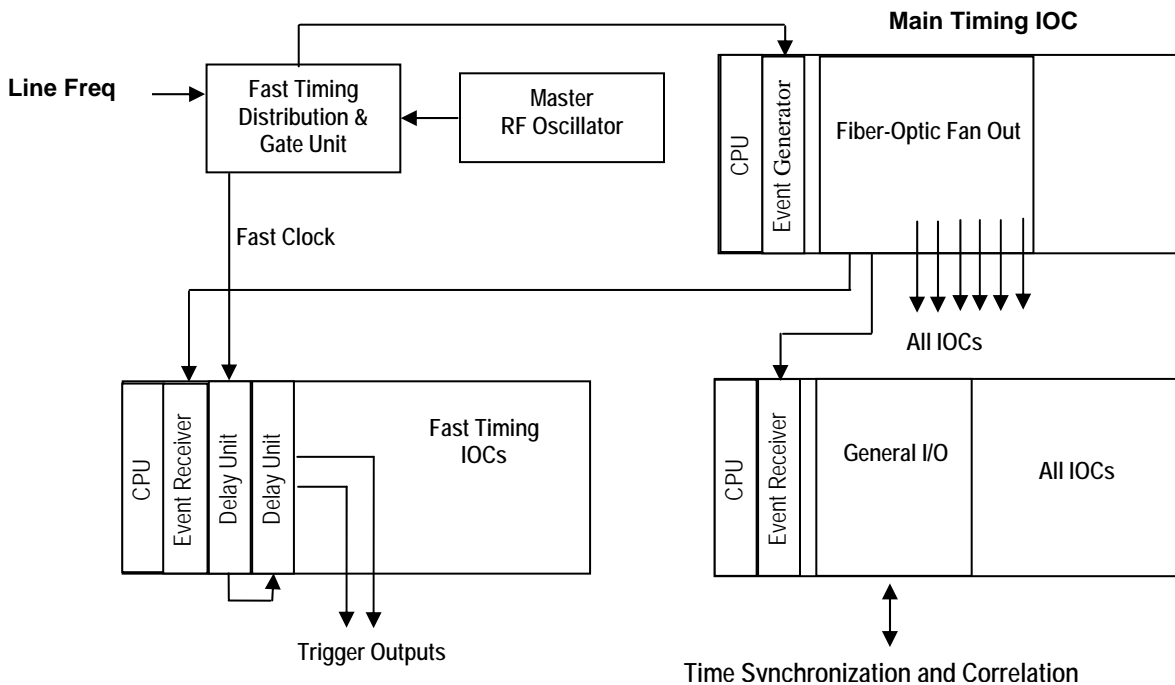


**Figure 6.7.1** Block diagram of the Event system and Fast Timing system.

### 6.7.1.4 Signal Distribution

The Fast Timing and Event signals will be distributed over fiber-optic cable for reasons of noise immunity and distance capabilities. Further investigation is needed into the delay drifts that could be introduced by the fiber installation from temperature differentials and the standardization of length-induced delays in a facility the size of NSLS-II.

## 6.7.2 Fast Feedback

A beam position stabilizing system is required to maintain orbit stability to within 10% of beam dimension and to provide dynamic correction of low-frequency orbit disturbances. The proposals presented here are very much based on the work on Diamond, APS [6.10], ALS [6.11], and SLS [6.12].

### 6.7.2.1 Global Feedback

The feedback system will use measurements of the position of the electron beam in the storage ring and the photon beams in the beamline front-ends. This information will be compared against a reference orbit and the error used to calculate desired corrections to be applied to corrector magnets in the storage ring.

The response matrix relates the effect of small changes in corrector magnet fields to the resulting changes in the particle beam orbit as measured at chosen BPMs. By inverting the response matrix the relationship that maps orbit perturbations to changes in corrector magnet fields is obtained. For small orbit errors, this relationship is assumed to be linear and time-invariant. Different objectives, such as correcting the orbit in an rms sense or correcting specific locations, can be achieved by choice of BPM and corrector locations and by applying different weights to correctors or BPMs when computing the inverse response matrix.

### 6.7.2.2 Performance

Two global feedback systems, operating in parallel, are proposed to correct orbit errors on NSLS-II, namely a Slow system, correcting DC drift, and a Fast system, correcting beam disturbances to 5 KHz (Table 6.7.3). These systems will use data from both the electron and photon BPMs and operate on either or both of the steering magnet or fast correctors. For both systems, the BPMs need to be sampled synchronously, which will be achieved using Events distributed to the IOCs. In addition, this architecture must support the capture of beam dump failures.

**Table 6.7.3 Feedback System Comparisons.**

	Correcting Feedback	Update Rate Feedback
Slow	DC drift	0.1 Hz
Fast	0.2 mHz – 100 Hz	5 KHz

#### 6.7.2.2.1 Slow Correction

The Slow correction will correct the orbit at 10 second intervals, using the desired correctors and BPMs to compensate for slow changes in the orbit. This will maintain the user-steered orbit applied at the beginning of each fill. Communication to the BPM and Steering IOCs will use the EPICS CA communication mechanism. The slow correction will be realized as a dedicated application running on either a console or a computer server.

#### 6.7.2.2.2 Fast Correction

Fast correction is not possible through EPICS CA mechanisms because of insufficient bandwidth. It will be realized at the IOC level on separate feedback processor boards dedicated to this function. This involves partitioning the correction calculation across the 30 Steering IOCs to calculate the correction values for the steering elements local to that IOC. Each steering IOC requires access to all the BPM values, to give flexibility in the correction algorithm. This requires a high speed connection to share data between the all BPM devices and 90 Steering IOCs. Two potential solutions for this are to use either reflective memory or network broadcasts.

EPICS process variables will be used to control the feedback process, by downloading algorithms to the feedback processors and setting coefficients and update rates.

### 6.7.2.3 Reflective Memory

Reflective memory is an off-the-shelf solution to distribute information across multiple computer systems without requiring processor time. It enables BPM data to be written to the reflective memory module in each of the BPM IOCs and appear in memory in all the Steering IOCs. In the system shown in Figure 6.7.2, an event received by all BPM devices would cause the photon and electron BPM values to be read by the feedback processor and written to the reflective memory board for each of the processors. The data would propagate to all the steering IOCs and when all values are received, the feedback calculation would be carried out on the Steering IOC to produce the new steering settings. These values would then be written to the steering elements in conjunction with the slow system values received through EPICS process variables.

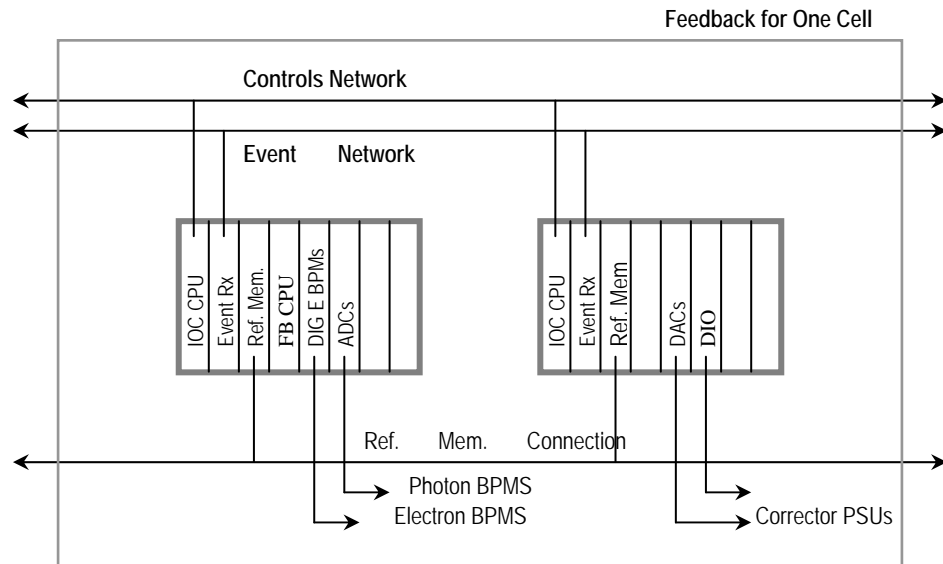


**Figure 6.7.2** Reflective memory structure for one cell.

Commercially available reflective memory sizes and update rates provide for moving multi-megabytes per second across tens of boards, and so should easily meet the requirements of this application.

As the BPMs and Motor Controllers may be implemented using special FPGA boards, a second level of communication may be required to meet specifications. The architecture under consideration is shown below (Figure 6.7.3).



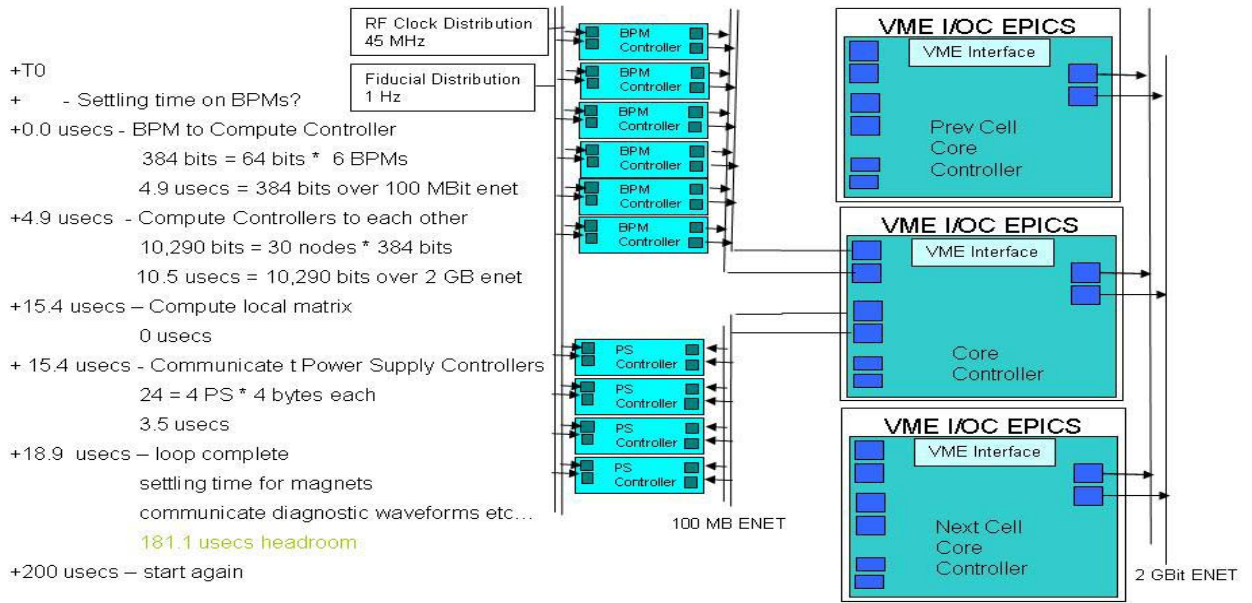


Figure 6.7.3 Architecture for the BMPs and motor controllers.

#### 6.7.2.4 Network Broadcast

In the Network Broadcast system each of 60 feedback processors in the BPM and Steering IOCs is connected to a private network with a central switch in a star configuration. The feedback processor in each of the BPM IOCs reads the BPM values and broadcasts them over the network to be received by each steering IOC. The broadcasts take place simultaneously but do not collide, because the switch buffers each packet as it receives it. The switch then forwards the packets to all the Steering IOCs.

In the system shown in Figure 6.7.4, an event received by all BPM IOCs would cause the photon and electron BPM values to be read by the feedback processor and broadcast over the private network. When each of the 30 broadcasts has been received by all of the Steering IOCs, the calculation would be carried out on each Steering IOC to produce the new steering settings. These values are then written to the steering elements in conjunction with the slow system values received through EPICS process variables.

This option is cheaper in terms of hardware because it alleviates the need for the reflective memory boards, but incurs a development overhead to produce software for the broadcasting. The performance achievable using broadcasts also needs to be determined, to establish whether it would meet the requirements of this application.

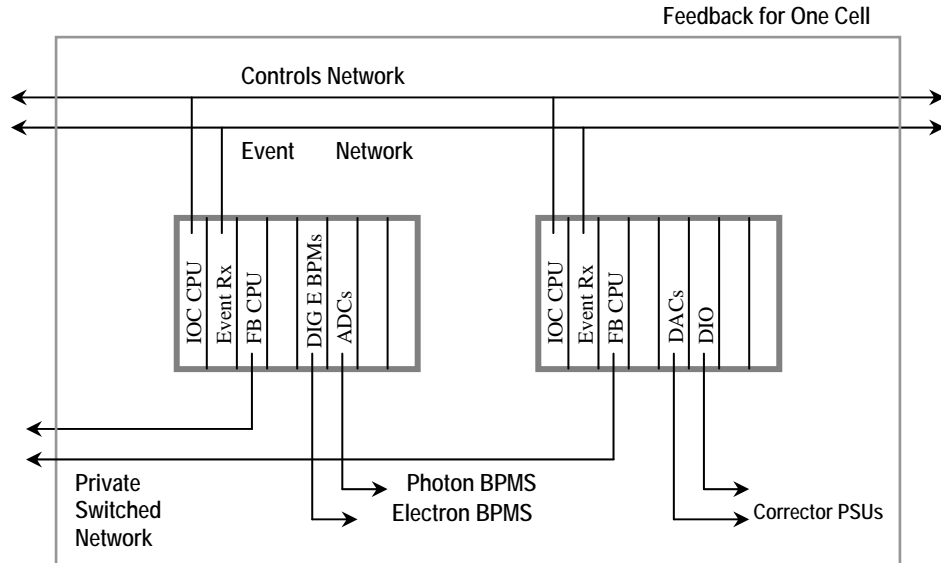


Figure 6.7.4 Network broadcast structure for one cell.

### 6.7.2.5 Feedback Processor

On the Steering IOC, the calculation to produce the new steering values from BPM values and the inverse response matrix needs to be carried out. The time available to carry out this calculation is dependent on the desired update rate, the time to acquire and distribute the data, and the time for the correction to propagate through the steering power supply, magnet and vessel to the beam. While the current generation of PPC processors offers similar performance as DSP processors, in terms of operations per second, they do not have the architectural feature of DSP processors for signal processing intensive calculations. However, the performance available from current PPC makes them suitable to carry out the feedback calculations at a price advantage over DSP processors.

### 6.7.3 Machine Protection

The control system must monitor beam envelope and other operational parameters that determine if the beam is threatening to damage equipment. Detection and reaction to dangerous conditions must be completed within 20 msec. A node on the fast feedback bus is to be used to determine if the beam is in a safe orbit.

## 6.8 Subsystem Control

The major subsystems being controlled are: diagnostics, power supply control, low level RF, vacuum, personnel protection, equipment protection, undulator, experimental beamlines, and conventional facilities. They fall into two distinct categories: those requiring high speed, low latency performance such as the LLRF, Diagnostics, Undulator Control, Beam Envelope Equipment Protection, and Fast Correctors, and those that do not require this such as: Slow power supply control, vacuum, personnel protection, slow equipment protection, and conventional facilities. Beamline control is a special case, in that the beam lines are a special cast in that they are run by groups outside of the NSLS II machine group.

### 6.8.1 High-Speed, Low-Latency Applications

High-speed, low-latency applications are integrated into the global control system through the EPICS Channel Access protocol, over Ethernet (Figure 6.8.1). This provides integration with modeling, archiving, and other operations tools. It is not adequate for response times required for FOFB at 5 KHz or machine turn-off in under 20 msec. To meet these needs requires the event system, in conjunction with a fast, reliable, low-latency communication network. Intelligent device controllers in the front end process the signals at the 500 MHz rate and deliver data to the other device controllers over dedicated networks at the 20 KHz rate to support global feedback at 5 KHz. The intelligent device controllers also support turn-by-turn data collection, where a trip is detected and distributed over the event system.

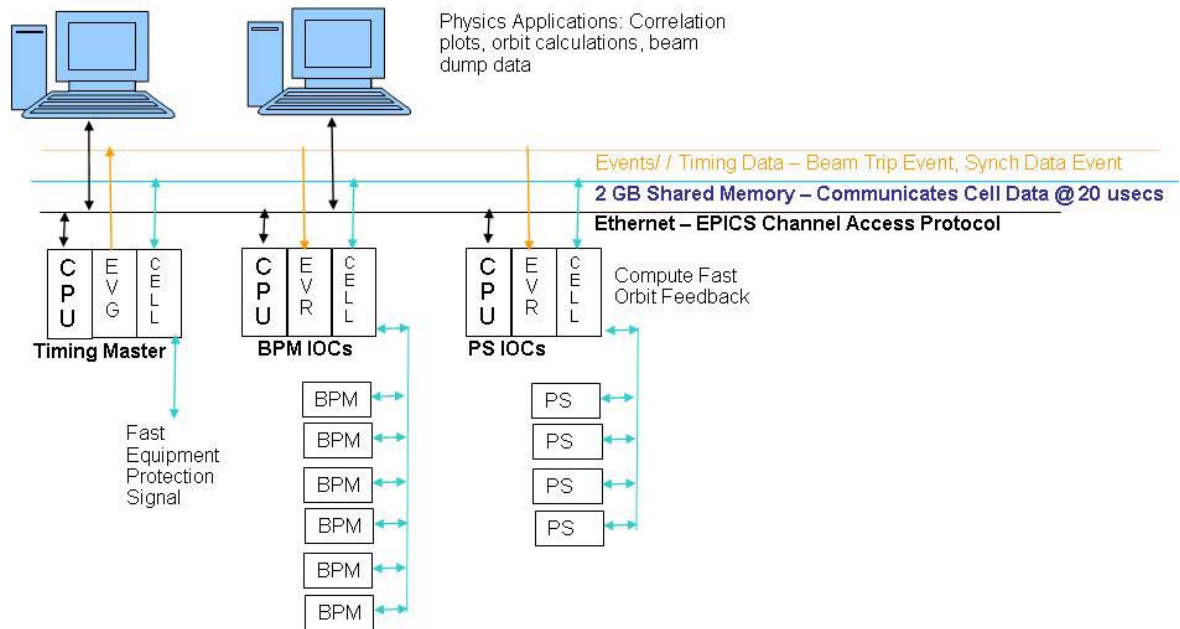


Figure 6.8.1 Control system for high-speed, low-latency applications.

### 6.8.2 Diagnostics Control

The slow applications, which require control and synchronization to the machine in the 60 Hz to .5 Hz range, have no need of specialized data communication buses. The event system may be used to provide triggers for synchronous data collection and time stamps for correlating events. All data communication is accomplished through the EPICS Channel Access Protocol (Figure 6.8.2). The I/O may be distributed over Ethernet or serial communication to slow, remote, controllers such as PLCs or off-the-shelve gauge controllers. This distribution of I/O reduces cable and maintenance costs. These distributed I/O are used when the data being correlated only needs to be within 500 msec. I/O requiring tighter correlation, such as slow magnets or motion controllers, are placed directly in the EPICS I/O Controller typically in a VME crate.

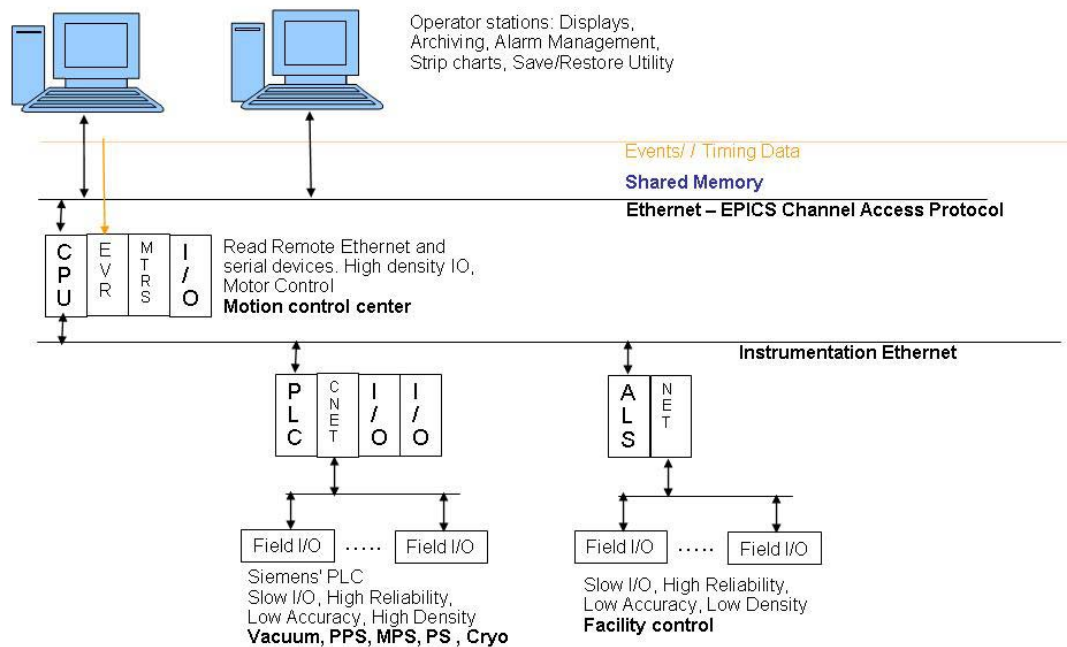


Figure 6.8.2 Control system for slow applications (within 500 msec).

### 6.8.3 Beamline Control

The NSLS-II accelerator control system will be in an isolated network by itself and each beamline is expected to have its own network to connect its computers and its hardware. Connections between these systems will be designed to provide the integrated flow of information between the accelerator and end stations that is needed to meet the requirements for beam monitoring and stability.

All insertion device beamlines require control of the insertion devices [6.13] which are located in the controls network. In addition beam position information, as well as numerous other signals, is needed from the accelerator control system. Similarly, beamline information, along with intensity and beam position from the beamlines, will be needed in the accelerator control system to provide continuous control of the beam.

The infrastructure needed for the exchange of information between the beamlines and the accelerator will be built into the facility. It is anticipated that single-mode fiber will be employed to connect the beamline EPICS hardware and accelerator EPICS hardware. Every beamline will be provided with a dedicated single-mode fiber bundle from the beamline to the accelerator control system racks located on top of the storage ring. In addition, there will dedicated single-mode fibers to the main control room, where some of the timing hardware is expected to be located. These single-mode fibers will be used to provide high-precision timing signals to synchronize the beamline experiments with the arrival of the x-ray beam.

Data exchange between the beamline and the accelerator EPICS systems, which do not require a very fast data rate, will be provided through an EPICS channel access process variable gateway system. This system will reside in the accelerator control system and will have an additional network connection to each of the beamline networks. This way the control, as well as data readbacks, can be accomplished with a high level of security without jeopardizing the integrity of the accelerator or beamline control systems. Such schemes have been used successfully at other facilities, such as APS and BESSY.

The development of the EPICS software for the beamline will be conducted in parallel with the accelerator to ensure that they are consistent and the exchanges of data between the two are seamless.

The beamlines will have their own computers and servers for data acquisition and control. There will be large storage capacity at the beamlines, and a central storage and backup service, with large disk farms, will be available as well. There will be 10 gigabit redundant network structure built into the facility. Each beamline network will be redundantly connected to a central computing facility, which will have a firewall to provide secure access to the outside world.

The offices in the LOBs will also have computing capability. Each LOB will be on a different network and will be serviced by a central computing facility. The LOBs will also be serviced by 10-gigabit network infrastructures. The centralization of data collected from the beamline will allow a user to retrieve data from multiple beamlines for analysis. Data reduction and analysis software will be developed by, and available from, the central computing services.

The variety of information exchange between the various control systems related to the needs of the experimental facilities is schematically indicated in Figure 6.8.3. Patterned after the system at APS [6.14], this system will be based on EPICS process variables, as discussed above.

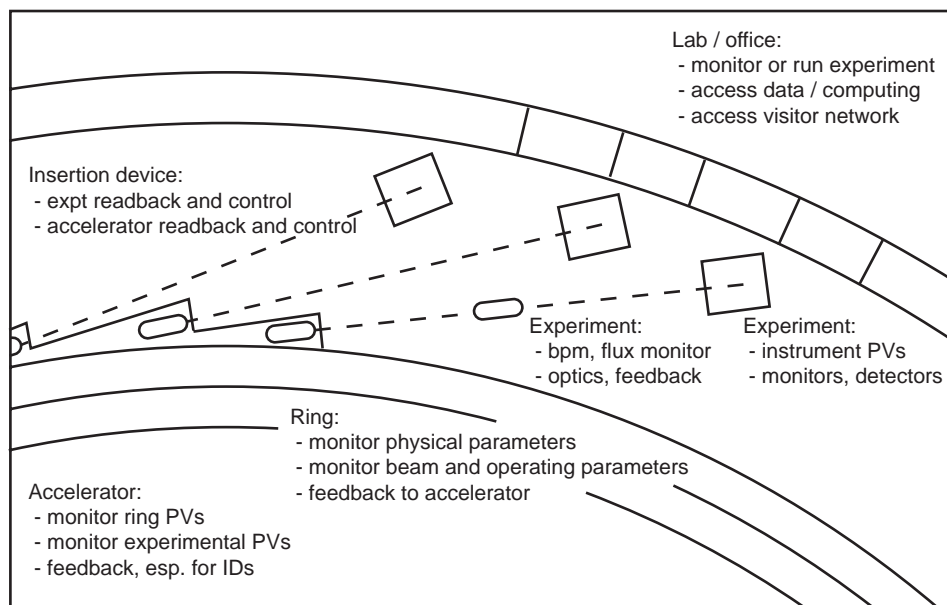


**Figure 6.8.3** Activities requiring information distribution in experiment hall.

### 6.8.3.1 Design Concepts

From the point of view of the beamline and end station, the requirement is that every beamline have at least one dedicated EPICS IOC controlling its insertion devices and intercepting other information from the facility. For many of the hard and soft x-ray facility beamlines, EPICS will be used as a standard to control optics and beamline motors also. Specialized equipment may have different control systems, which may exist as additional EPICS clients or may in some cases be independent. It will be beneficial for the EPICS IOCs to be of a standardized hardware type. VME is a current favorite, due to its reliability, but the availability of drivers in the future and the improvements in PC-based hardware may cause the latter to be more favorable some years from now. The standardization of beamline server hardware will be assessed during the years preceding beamline commissioning and a standard will be chosen. The same requirements we have today must be satisfied. Hardware must be robust and reliable. A large basis set of scalars, motor indexers, analog and digital I/O, multi-channel analyzers, and so on must be in use. Pre-existing EPICS support for the hardware will be a third criterion.

The network as seen from the beamline is illustrated in Figure 6.8.4. As an example, a Linux PC running Medm GUIs may serve as the operator interface, while a VME CPU serves as the IOC for the beamline control system. Beam transport components with PVs that need to be available to the facility are connected to this network. (The insertion devices, on the other side of the shield wall, are networked separately.) A server acting as router, firewall, and PV gateway connects this sector or beamline network to the experimental network, to other beamlines, and to the other facility networks. The PV gateway controls all permissions necessary to establish who has control permission vs. read-only permission of the PVs.

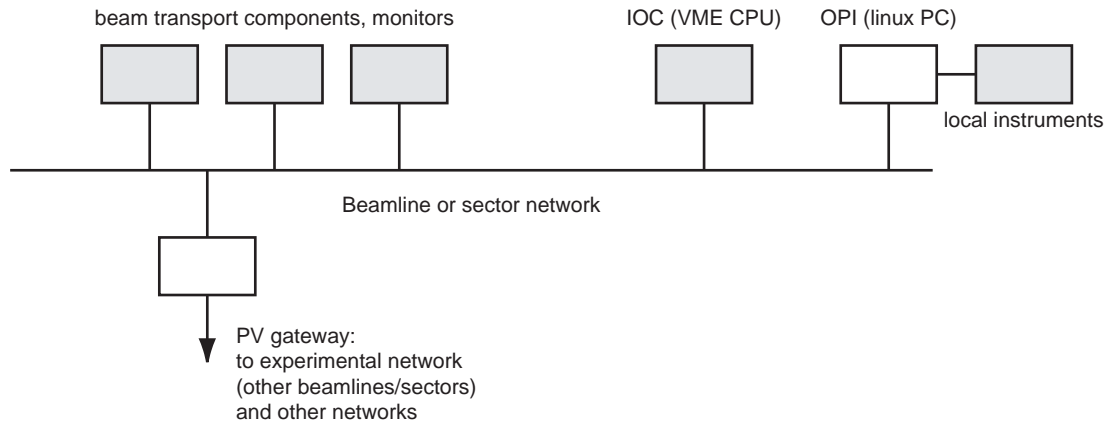


**Figure 6.8.4** Sector networks make important process variables (PVs) available to the entire facility through a PV gateway. IOC=input/output controller, OPI=operator interface (as Medm GUI).

We anticipate that the system will be designed so by default read-access is available for everything, everywhere. This way, there will be no need to make assumptions during the initial configuration as to which machines' PVs and monitor values need to be communicated between the accelerator and the experiment hall. Finally, local instrumentation can be assembled on private networks as desired by the users of the individual beamlines. Specialized detectors and other instrumentation controllers may be interfaced to the beamline controls as applicable, particularly as EPICS clients.

### 6.8.3.2 Considerations for Accelerator–End Station Information Exchange

The accelerator monitoring complex will have far too much information in it to be useful to users as raw PVs. The accelerator group will design simple ways of mapping and colorizing the status of the accelerator with respect to beam excursions, pressure, temperature, and other sensor readouts, and make this digested information available as a monitoring system that the experimenters will be able to use. This will allow the beamline staff and users to gauge where problems may be coming from. It will also provide a unified way for the experimental division to log local beam stability in connection with pertinent information about the ring stability. This information will be provided as part of the general control system information.

The following elements will be expected to provide useful data from the beamlines back to the operations staff:

- position monitors (beams and pipes)
- ambient conditions (pressure, temperature, cooling water flow)
- status of insertion device and recent history (i.e., feedbacks triggered)
- beam figure of merit (quality after optics as defined by the end stations' needs: divergence, angular motions, spatial motions, energy drift).

It will be beneficial to create more generalized “status” readouts for beamlines as well as for the accelerator.

### 6.8.3.3. Design of the Main EPICS Node at Each Beamline

Resident on the experimental network and associated with each beamline, there will be a CPU running an EPICS IOC and a Linux PC configured with control GUIs and administrative scripts for that beamline. These computers will be quite similar across the NSLS-II complex, since many upstream beam components and interfaces to the gateways and other networks will be common. These computers, and the configuration to interface with facility networks and information buses, will be centrally administered. Giving each beamline a similar, centrally managed system benefits operations by allowing a standard set of tools and debugging know-how to be applied everywhere. One important concern is cybersecurity requirements. Even if the experiment network is within a firewall, the laboratory will require certain security scans. Uniformity of the beamline machines on this network will make it easier for staff to provide patches and fixes consistent with both security and smooth operations.

EPICS tools alone are sometimes insufficient for scientific data acquisition. Synchrotron beamlines have diverse needs, such as dedicated detector drivers, reciprocal space calculation, spectroscopic tools, and visualization tools for imaging. The end station equipment will be so varied that a top-down attempt at standardization would be very harmful. Thus, each beamline is expected to instrument itself in an independent way. Still, NSLS-II users and staff will benefit from having as much common support as is reasonable to interface different experimental systems and connect them to the EPICS platforms. Many different data acquisition platforms can be clients of the EPICS system. For example, LabView and Spec are widely used control and data analysis systems.

## References

- [6.1] M.T. Heron, and B.G. Martlew, "A Review of Options for the DIAMOND Control System," Proc. PAC96.
- [6.2] EPICS, <http://www.aps.anl.gov/EPICS>.
- [6.3] TANGO, <http://www.esrf.fr/computing/cs/tango/tango.html>
- [6.4] V System, <http://www.vista-control.com/>
- [6.5] CVS, [www.cvshome.org](http://www.cvshome.org)
- [6.6] <http://www.windriver.com/>
- [6.7] VisualDCT, <http://kgb.ijs.si/VisualDCT>
- [6.8] T. Korhonen, and M. Heiniger, "Timing System of the Swiss Light Source," Proc. ICALEPCS2001.
- [6.9] F. Lenkszus, and R. Laird, "The APS Event System," Proc. ICALEPCS95.
- [6.10] J.A. Carwardine, and F.R. Lenkszus, "Real-Time Orbit Feedback at the APS," Proc. BIW98.
- [6.11] C. Steier, A. Biocca, E. Domning, S. Jacobson, G. Portmann, and Y. Wu, "Design of a Fast Global Orbit Feedback System for the Advanced Light Source," Proc. PAC 2001.
- [6.12] M. Böge, M. Dehler, T. Schilcher, V. Schlott, and R. Ursic, "Global Orbit Feedback System for the SLS Storage Ring," Proc. ICALEPCS 99.
- [6.13] M. Ramanathan, M. Smith, J. Grimmer, and M. Merritt, "Overview of insertion device controls at the Advanced Photon Source," *Rev. Sci. Instrum.*, **73** (2002) 1448.
- [6.14] M. Ramanathan, M. Smith, N. Arnold, F. Lenkszus, R. Laird, K. Evans Jr., J. Anderson, and K. Sidorowicz, "An overview of the information distribution system at the Advanced Photon Source," *Rev. Sci. Instrum.*, **73** (2002) 1445.
- [6.15] <http://hpdrc.cs.fiu.edu/Sem-DDS/documentation.html>







## 7 Equipment Protection System

The beamlines at NSLS-II are expected to handle x-ray beams with very high power and power densities. Therefore, care must be taken to design the beamline with components that can handle these power loads. Any component that has to handle these high levels of power has to be monitored. The beamline Equipment Protection System provides a means of monitoring the components which, when jeopardized, can cause component failure. The EPS has the responsibility to act on alarm conditions by mitigating the situation that has caused the alarms. The system baseline is configured with the infrastructure to support all monitoring of cooling flows and six fully populated front ends. The baseline EPS will support all future expansion in terms of wiring, I/O and control logic. Excluded from the base line is the beamline control and monitor portion of the system, and its cost is captured in the individual beamline budget.

### 7.1 Functionality

Every beamline EPS will monitor and interlock the devices in the front end and the beamline.

All front ends at NSLS-II are expected to have two safety shutters, one photon shutter, and a few masks. In addition, the front end will also have vacuum inline valves to provide vacuum isolation. The front end is also expected to have a fast valve to provide a conductance limitation during a vacuum accident. Most beamlines will also have an x-ray exit window as part of the front end. These x-ray windows will provide a vacuum isolation but will transmit the x-ray beam. Certain beamlines, such as the soft x-ray beamlines, are expected to share the storage ring vacuum with the front end providing the interface. In such cases, the fast valve, along with the rest of the inline vacuum valves, provides the isolation needed in case of accidents.

Due to the large power loads, all components in the front end that intercept the beam will have water cooling. These components are typically the fixed mask, photon shutter, and exit windows. The water flow will be monitored by flow meters and the signals will be fed to the EPS. All vacuum valves will be pneumatically operated. All vacuum valves will be operated by the EPS and have their positions monitored.

Most beamlines are expected to have some beam conditioning optics upstream of their monochromator. The beam conditioning optics will see the large power of the beam and as such will be interlocked by the EPS. Beamlines are also expected to have vacuum valves, which will also be controlled by the EPS.

It is expected that the beamline portion of the EPS system will be customized to suit the condition of the specific beamlines.

### 7.2 Design Specification

The design of the EPS is expected to be robust. The system will be based on programmable logic controllers (PLCs), which provide excellent customization capability and also extensive diagnostics.. The hardware used will be the same as used in the beamline Personnel Protection System and the Accelerator Personnel Protection System (for both topics, see Chapter 8).

Each beamline will have its own EPS system, with the sole function being to provide protection from damage of equipment due to synchrotron radiation. As such, the EPS will consist of only one PLC per beamline. The EPS system will consist of three parts: front-end EPS, beamline-specific EPS, and command/control of PPS components such as shutters and station doors. The front-end portion of the EPS is expected to be similar on most beamlines, while the beamline portion of the EPS will be customized to each beamline. Similarly, for the command/control of PPS components, the front-end shutters will be identical in all beamlines; however, additional shutters on the beamline will be beamline specific.

All front-end components that intercept the synchrotron beam will have water cooling of the components. The water flow of the components will be monitored by the EPS via flow meters. The EPS will be in alarm state if the flow drops below a specified setpoint. Depending on the location of the component it monitors, it will command the photon shutter to close and – for cases where the flow is upstream of the photon shutter – it will request the stored beam to be dumped.

All vacuum valves in the front end will also be controlled by the EPS. Setpoints from vacuum controllers that are provided to the EPS will be used to determine when it is permissible to allow opening of the valves. The EPS will determine when it is necessary to close a valve, and will do so if it senses a vacuum alarm based on the vacuum setpoint to the system.

For specific beamlines, the EPS will be customized based on the user requirements for that beamline. Besides monitoring the water flow and controlling the vacuum valves, the EPS system may be used on beamlines to monitor other variables, such as temperature, position, and so forth.

The EPS will be used to control the actuation of the shutters. It will monitor the status of the PPS for each shutter and, when a permit is available, it will accept requests to open the shutters. The EPS will be responsible for sequencing the shutters in cases that involve a combination of photon shutters and safety shutters. All station doors that are automated will also be operated by the EPS.

### 7.3 Interface

The EPS will have human Interfaces (HMI) located at the main location of the hardware, which is expected to be located directly above the front end on top of the storage ring tunnel. In addition, there will be a minimum of one HMI per beamline at the beamline stations.

The EPS provides the command and control functionality for the beamline PPS. It receives the status information of the PPS and, based on that, can operate the shutters. The PPS, in addition, can request the shutter to close and the EPS will then command the shutter to close. In the event the shutter does not close within a specified time, as determined by the PPS, the PPS will initiate an emergency shutdown (ESD) situation.

The EPS will have an EPICS interface to the control system. The EPICS interface will provide both the main control room and the beamlines a complete overview of the status of each beamline. The data from the EPICS interface will also be logged and archived by the central computing systems.

The EPICS interface to the EPS will be both read and write. The write functionality will be controlled by the EPICS Channel Access Security. This is essential, to isolate the possibility of accidental control of the wrong beamline EPS via the control system.

## 8 Personnel Protection System

### 8.1 Beamline Area PPS

NSLS-II will produce intense light from IR, UV, and hard x-rays. Beamlines are designed to use either the bending magnet radiation or the radiation from insertion devices located in the straight sections of the storage ring. Beamlines may have more than one station along the beamline for every port. These stations are expected to work in parallel or sequentially.

The Personnel Protection System (PPS) is an engineered system that provides a means to ensure that personnel are not exposed to the radiation in the beamline. At NSLS-II, the role of the PPS is specifically to protect personnel from prompt radiation that is present only when there are stored electrons in the storage ring. The PPS is an engineered interlock system and is expected to monitor the various devices installed in the beamline for personnel safety and to provide emergency shutdown in case of breach of the interlock.

The PPS system, along with the required shielding in the beamlines, is expected to provide personnel safety during routine operation of the facility.

#### 8.1.1 Functionality

Beamlines will consist of stations where synchrotron radiation is expected to be admitted. The beamline stations are expected to be made of lead-lined walls and roof, as appropriate for the particular radiation characteristics. These stations will house beamline optical components or beamline experimental equipment. The stations are expected to be large enough for personnel to work with the equipment inside.

The beamlines will have one or more shutters based on the particular layout, which is expected to vary from beamline to beamline. However, the functionality of the shutters, from the Personnel Protection System perspective, is expected to be the same and they will be monitored by the PPS. All x-ray beamlines will have shutters in the front-end area inside the storage ring shield wall (see Section 7.4). The bremsstrahlung radiation emitted by the synchrotron can only be stopped by heavy metal elements such as tungsten or lead. The heavy metal device that stops the bremsstrahlung radiation is referred to as the safety shutter. For the sake of safety, the shutter is expected to be redundant. The synchrotron beam, consisting of very high total power and power density, will be stopped by a device that is water cooled, made of copper or alloys of copper, and referred to as the photon shutter. These three devices, the two safety shutters and the photon shutter, will form a shutter cluster and their positions are monitored by the PPS.

Along the beamline are beamline optical elements that will condition the beam, including, for example, monochromators and mirrors. These devices change the characteristics of the synchrotron radiation. The radiation passing through the monochromator will, in most cases, be displaced in either the vertical plane or the horizontal plane from the incident radiation and only a small fraction of the incident radiation with a band pass (of about 0.1% or less) will be passed, with little or no power. In such cases the shutters, located downstream of the monochromator, will be called monochromatic shutters. They will be made of heavy metal and will be much shorter than the safety shutters. Once again, these monochromatic shutters are expected to be redundant for safety and will be monitored by the PPS.

A major role for the PPS will be to provide a means of ensuring that no personnel are inside beamline stations when the station is opened to synchrotron radiation. Prior to admitting the synchrotron radiation inside these stations, a search of the area has to be performed by a human. It is expected that the station search will be performed by one person only. There will be PPS devices called “search boxes” inside the station which must be visited as part of the search. Search boxes are strategically placed to ensure that during the

search all parts of the station are either visible or visited by the search personnel and no person is left behind inside the station. The search is completed when the station door is closed. The PPS will then lock the door.

Once the search process is started the PPS will start a beacon and audio signal inside the station, warning all personnel to exit. This signal is expected to last for some time, on the order about 20 to 30 seconds after the station door is closed. The function of the beacon and audio signal is to warn any personnel overlooked by the search person of impending danger. There will be very distinct emergency shutdown buttons placed inside the station which, when pressed, will instantly remove the presence of the prompt synchrotron radiation hazard. In addition, there will be also emergency egress buttons inside the station to unlock and open the door.

### 8.1.2 Design Specifications

The PPS will be designed to be robust and provide the emergency shutdown functionality to provide personnel safety from prompt radiation. Like the EPS, the PPS is expected to be based on programmable logic controllers. PLCs have numerous advantages over the relay logic scheme of interlocks. They can be reprogrammed to reflect changes in configurations and also have numerous diagnostics. The use of PLCs in safety system is very common now.

All devices attached to the PPS are expected to be designed to be fail-safe—that is, in case of failure the device will fail in such a manner as to either remove the hazard or remove the permit to generate or maintain the hazard.

Every beamline PPS will be designed under the same guidelines. The PPS will consist of two PLCs, referred to as chains A and B. The two PLCs will provide redundancy and will independently monitor all the devices.

All shutters will have two switches, one for chain A and one for chain B. There will be switches to monitor the closed and open positions. Similarly, all station doors will be monitored with two switches, one each for chains A and B.

At beamlines, there will be circumstances when a device such as a mask or photon beam stop is provided to absorb the power of the beam, while the radiation safety is provided by lead shielding as collimators or radiation stops. In such cases, the integrity of the masks and beam stops cannot be compromised, as they, in turn, protect the lead shielding which provides the personnel safety. In these cases, the mask or beam stop will be monitored by the PPS to ensure that it is not compromised. In most cases, the water flow to these components will be monitored independently by chains A and B of the PPS.

All PPS equipment will be clearly identified, and secured in locked cabinets. Cabling for the PPS equipment to field devices will be on separate closed raceways, which will be used exclusively for the PPS. All power to the PPS will be provided by uninterruptible power supplies, which will be backed up by generators.

### 8.1.3 Interface

The PPS must interface with numerous systems. The primary functionality of the PPS is to monitor and provide emergency shutdown.

To provide emergency shutdown, the PPS interfaces to the Accelerator Personnel Protection System. The PPS will remove a permit to the APPS to operate the storage ring. In the event of the removal of the permit by the PPS, it is the responsibility of the APPS to remove the hazard by dropping the dipole power supply and the RF to the storage ring systems.

The APPS will monitor the positions of the front-end shutters located inside the storage ring shield wall. The APPS will fan-out the status of the shutters to the PPS. There will be a provision in the APPS to remove

the PPS interactions for a specific beamline. This is expected to be in the form of a Kirk Key in an interface box between the PPS and APPS for each beamline. The APPS will monitor the closed positions of the front end shutters when the PPS is not available and will remove the storage ring permit if it experiences any “not closed” activity. When the PPS is available, the APPS will ignore the status of the shutters. This scheme will allow installation, maintenance, and validation of the PPS to take place while the machine is in operation.

All PPS functions will be monitored and data archived using the control system at NSLS-II. It is expected that EPICS will interface to the PPS PLCs to monitor their functionality. The EPICS interface will be read-only; there will be no writing to PLCs from the EPICS interface. Changes to the PLC operating codes will be possible from the field devices or when the PLC software is downloaded to the PLCs during routine validation of the system.

All command and control functionality for the PPS will reside with the EPS for the beamlines and front ends. The EPS will interface to the PPS and will receive signals from the PPS prior to operation of the shutter. In the event the EPS malfunctions, the ESD procedure of the PPS will activate and will remove the permit for the machine to operate. The PPS will only provide the ESD functionality and hence it is expected to be simple and easy to maintain and validate.

## **8.2 Accelerator Personnel Protection System**

As it relates to personnel protection, the NSLS-II facility consists of an electron gun and linac enclosed in a shielded area, and a main storage ring and booster enclosed in a heavily shielded tunnel. There are also numerous beamline experimental stations located on the perimeter of the accelerator tunnel. Protection from beamline radiation will be provided by the Personnel Protection System (discussed in the previous section), from linac radiation by the Linac Personnel Protection System (discussed in this section), and from radiation from the main ring and booster by the Accelerator Personnel Protection System (also discussed in this section).

### **8.2.1 Linac/Gun Personnel Protection System**

The Gun/Linac area will contain linac accelerating sections where electrons emitted from the gun will be accelerated to an energy level for injection into the booster. The radiation hazards present during linac operation are two-fold, resulting from: 1) a high level of RF present in the linac sections that can accelerate free electrons and produce ionizing radiation fields, and 2) the acceleration of electrons to the full linac energy. RF power is supplied through klystron amplifiers powered by pulse modulators. Turning off the RF power will stop the production of radiation.

The Linac Personnel Protection System is specifically designed to protect personnel from radiation which is present only during linac operations. The LPPS is an engineered interlock system and is expected to monitor the various devices installed in the linac for personnel safety and provide emergency shutdown in case of breach of the interlock.

#### **8.2.1.1 LPPS Functionality**

A major role for the LPPS is to provide a means of ensuring that no personnel are inside the linac when the gun is on or the klystrons are pulsing. Prior to Linac operation, a search of the area has to be performed by a human. It is expected that the linac search will be performed by one person only. There will be LPPS devices called “search boxes” inside the linac, which must be visited as part of the search. The search boxes are strategically placed to ensure that during the search all parts of the linac are either visible or visited by the search personnel and no person is left behind inside the linac area. The search is completed with the closing of

the linac door. The person searching will lock the door when the search is completed and use a Kirk Key system to complete the search process.

Once the search process is completed, the LPPS system will start a beacon and audio signal inside the linac, warning all personnel to exit. This signal is expected to last on the order of about 60 to 120 seconds after the linac door is closed. The function of the beacon and audio signal is to alert any personnel who have been overlooked by the search person and trapped inside.

Emergency shutdown buttons which are very distinct will be placed inside the linac; when pressed, a shutdown button will instantly remove the radiation hazard.

### **8.2.1.2 LPPS Design Specifications**

The LPPS will be designed to be robust and provide the emergency shutdown functionality for providing radiation safety to personnel in the linac area. The LPPS is expected to be based on programmable logic controllers. PLCs have numerous advantages over the relay logic scheme of interlocks. A PLC can be reprogrammed to reflect changes in configurations and also has numerous diagnostics. The use of PLCs in safety systems is very common and is an accepted practice at accelerator facilities across the United States.

All devices attached to the LPPS are expected to be designed to be fail-safe—in case of failure the device will fail in such a manner to either remove the hazard or remove the permit to generate/maintain the hazard.

The LPPS system will consist of two PLCs, referred to as chains A and B. The two PLCs will provide redundancy and independently monitor all the devices. To immediately stop the production of radiation, power to the modulator power supplies will be removed redundantly. This will be accomplished through the use of AC contactors, one for chain A and one for chain B.

Two critical devices will prevent radiation from entering the main ring from the linac: 1) the linac-to-main-ring stop, and 2) the bending magnet located upstream. The linac-to-main-ring stop will have two switches to monitor the closed and open positions, one switch each for chains A and B. The bending magnet upstream of the stop will be redundantly monitored for current and voltage by both chains. When the magnet is not powered it will prevent electrons from entering the accelerator tunnel area. All linac doors also will be monitored with two switches, one tied into each chain.

All LPPS equipment will be clearly identified and secured in locked cabinets. Cabling for the LPPS equipment to field devices will be separated in raceways. All power to the LPPS will be provided from an uninterruptible power source, backed by generators.

### **8.2.1.3 LPPS Interface**

All LPPS functions will be monitored and data will be archived using the NSLS-II control system. It is expected that EPICS will interface to the LPPS PLCs to monitor their functionality. The EPICS interface will be only read-only; there will be no writing to the PLCs from the EPICS interface. Changes to the PLC operating codes will only be possible locally.

## **8.2.2 Storage Ring and Booster Personnel Protection System (APPS)**

The storage ring and booster will coexist inside the same tunnel. The Accelerator Personnel Protection System interlock will be required to serve both the storage ring and booster. Radiation hazards during normal operations and conditioning are produced from multiple sources under different operational conditions. Operation of the RF accelerating cavities, both booster and main ring, can produce high radiation fields from secondary emissions that are accelerated by high RF fields. This radiation can be produced without electrons injected or stored in either ring.

The electron beam injected from the linac is another hazard, and, finally, stored beam in either the booster or main storage ring will produce synchrotron and bremsstrahlung radiation. The APPS must protect personnel from all conditions.

### 8.2.2.1 APPS Functionality

The APPS protects personnel from radiation hazards by 1) ensuring that no one is left inside the ring enclosure before operations that will produce radiation and 2) by providing a means of emergency shutdown of components, enabling personnel to stop the production of radiation in an emergency.

The ring enclosure is physically very large and will be divided into six searchable sections. Each section will be separated by a physical barrier in the form of a gate. Before operations begin, each section will be physically searched by a human. Once the search process is completed, the APPS system will start a beacon and audio signal inside the section being secured, as a warning to any overlooked personnel to exit. This signal is expected to last on the order of 60 to 240 seconds after the section gate is closed.

Emergency shutdown buttons, which have a very distinct appearance, will be placed inside the tunnel. When pressed, a shutdown button will instantly remove the radiation hazard.

The gates, along with Kirk keys, will be part of a system to allow controlled access to parts of the ring under defined conditions while other sections remain secured. With the APPS, beam will be dumped to allow authorized personnel controlled access to the ring sections while ensuring that no electron beam can be injected. Access will be monitored via a remote TV camera hookup to the control room. Each person entering the ring must remove a Kirk key; this inhibits the radiation source. A physical search of the section will be required before operations and radiation production can be resumed.

The first application of this concept defines an area around the RF accelerating cavities. The booster and storage ring cavities will need to be powered with RF for conditioning but without injected electron beam. The APPS will ensure no personnel are in the vicinity of the RF cavities during conditioning, while inhibiting electron beam from being injected into the ring. If the area is breached, the RF power source will be immediately shut off, redundantly.

During injection, while the linac-to-main-ring stop is open, if the storage ring area is breached the APPS interlock must dump stored beam and reach back to the LPPS to shut down the linac modulators.

The APPS may also be required to monitor conditions required for top-off operation of the injector. These conditions have not been determined but could include requiring a minimum stored current before top-off mode is enabled and requiring the dipole current to be at the proper energy level.

The APPS will also monitor the status of the front-end ports and will dump the beam if a port is open and the PPS detects a breach of an experimental station.

All APPS conditions and access modes are displayed and controlled from a dedicated rack in the control room.

### 8.2.2.2 APPS Design Specifications

The APPS will be designed to be robust and provide the emergency shutdown functionality to ensure personnel safety for the storage ring/booster area. The APPS is expected to be based on programmable logic controllers. PLCs have numerous advantages over the relay logic scheme of interlocks. A PLC can be reprogrammed to reflect changes in configurations and also has numerous diagnostics. The use of PLCs in safety systems is very common and is an accepted practice at accelerator facilities across the United States.

All devices attached to the APPS are expected to be designed to be fail-safe—in case of failure the device will fail in such a manner to either remove the hazard or remove the permit to generate/maintain the hazard.

The APPS system will consist of two PLCs, referred to as chains A and B. The two PLCs will provide redundancy and will independently monitor all the devices. To immediately stop the production of radiation, power to the RF plate power supplies and low level RF will be removed redundantly both for storage ring RF and booster RF. This will be accomplished through the use of AC contactors, one for chain A and an RF switch for chain B. The redundant means for dumping beam will also shut off the main dipole power supply through the AC contactor with both chains A and B.

The storage ring tunnel circumference is large; to avoid ground loops and EMC effects on APPS signals, fiber optic transmission of bus signals (one for each chain) will connect field I/O blocks around the ring to the main PLCs located in the control room. The control room PLCs will also connect to the RF and dipole power supply via a fiber optic I/O bus to avoid interference and corruption of signals.

The system will be designed for testability and will have built-in test features. The concept of diversity will be applied where possible.

The APPS main ring doors, emergency stops, and section gates have two switches, one each for chains A and B. All APPS equipment will be clearly identified and secured in locked cabinets. Cabling for the APPS equipment to field devices will be separated in raceways. All power to the APPS will be provided from an uninterruptible power source, backed by generators.

### **8.2.2.3 APPS Interface**

The PLC program will incorporate a circular buffer of each scan that is triggered by an interlock breach. The buffer will be retrieved via EPICS to troubleshoot problems. All APPS functions will be monitored and data will be archived using the NSLS-II control system. It is expected that EPICS will interface to the APPS PLCs to monitor their functionality. EPICS will read data from a dedicated group of registers that reflect conditions and I/O points in the PLCs. The EPICS interface will be separate from the I/O bus. The EPICS interface will be only read-only; there will be no writing to the PLC from the EPICS interface. Changes to the PLC operating codes will only be possible locally.



## 9 GLOBAL SUPPORT SYSTEMS

### 9.1 Survey and Alignment

#### 9.1.1 Scope

This section outlines the survey and alignment requirements and the technology and tools for achieving the NSLS-II equipment positioning goals. The required alignment tolerances are defined primarily by the physics requirements of the accelerator. At this stage of preliminary design, these tolerances are not known with high precision; however, similar parameters are available for other light sources of equivalent dimension. Our preliminary design of the survey and alignment system is based on the assumption that the tolerance requirements for NSLS-II will be similar to those of the APS, for example. An assessment will be performed, however, during the preliminary engineering design phase to identify any extraordinary position requirements of the accelerator systems, and the survey and alignment system will be modified as necessary to meet them. State-of-the art equipment and methods will be employed, but no new technology will need to be developed to meet the NSLS-II alignment requirements.

Survey and alignment provides the foundation for positioning the beam-guiding magnet structures in all 6 degrees of freedom within the required tolerances. Although the tools and instrumentation available for this task have changed over the years and faster and more accurate measurements are possible, only limited control of the environmental conditions is possible. This ultimately sets an upper limit for the achievable measurement and subsequent control network accuracy.

The scope of the survey and alignment work for NSLS-II includes the following:

- Provision of engineering staff to review the design of components having stringent alignment requirements. Engineering staff trained in state-of-the-art methods, software, and systems will be required to ensure that component designs are consistent with the survey and alignment systems that will be used to obtain the anticipated tight tolerances needed to achieve the desired emittance levels.
- Specification of alignment tolerances for each piece of equipment, and a determination of how to achieve them within the limitations of available equipment and hardware. Procedures, methods, and equipment will be specified.
- Procurement of alignment equipment, measurement equipment and instruments, targets, monuments, and hardware.
- Technical staff to achieve the precise alignment requirements during fabrication, assembly, and field installation. Technical staff trained in the use and calibration of state-of-the-art instruments and systems will be required.
- Provision of calibration equipment and facilities to maintain survey equipment within calibration tolerances.

#### 9.1.2 Tolerances

The required positioning tolerances are an essential part of the survey and alignment design. Those tolerances dictate the instruments and methods necessary to obtain the positioning goals. Table 9.1.1 provides the required global tolerances, while Table 9.1.2 outlines the relative tolerances for the NSLS-II girder-to-girder positioning. These tolerances represent the most stringent requirements for the storage ring.

**Table 9.1.1 NSLS-II Required Global Tolerances.**

Global tolerances	$\pm 3$ mm
Horizontal positioning	$\pm 3$ mm
Vertical positioning	$\pm 3$ mm

**Table 9.1.2 NSLS-II Girder-to-Girder Positioning Tolerances.**

Relative tolerances	Girder to Girder
Horizontal positioning	$\pm 0.15$ mm
Vertical positioning	$\pm 0.15$ mm
Longitudinal	$\pm 0.50$ mm
Roll angle	$\pm 0.5$ mrad

### 9.1.3 Design Philosophy

#### 9.1.3.1 Control Network Design

Depending on the size of the system to be constructed, a primary and secondary control network may be required to achieve these tolerances. NSLS-II covers an area of about one-eighth of a square kilometer with a radius of  $\sim 124$  m and a circumference of  $\sim 780$  m. The NSLS II construction methodology demands that separate tunnel segments be successively available and ready for installation purposes. This requires that each segment be fitted with an independent preliminary control network terminated by a primary monument at each end suitable for less demanding layout work such as the blue-line survey of the major beamline components, girder supports, and photon beamline layout in the front-end sections [9.1.1]. Only after all segments have been measured, processed by least squares, and analyzed will the final control network be ready for the positioning of the girders. Prior to construction, a calculation of the anticipated error propagation of the primary and secondary control network geometry will be needed.

##### 9.1.3.1.1 Primary Control Network

The primary control network spans the entire accelerator facility and ties the accelerator enclosures into one reference system. It consists of a monument, M0, located at the center of the storage ring, a second similar one, M1, located at a convenient location in the infield close to the storage ring enclosure (Figure 9.1.1, left). Other monuments are distributed throughout the storage ring—for instance, at the beginning and end of each separate tunnel segment. The two monuments located in the infield should be very stable. Therefore, they require a deep foundation and a secondary outer shell for temperature stability [9.1.2], as shown in Figure 9.1.1(right). In this case a Kern centering plate is shown that will be changed for a tribrach adaptor system currently widely in use. These monuments can also be used by the construction companies for layout and construction surveys.

The central monument usually defines the origin of the local right-handed coordinate system, while the second infield monument provides the orientation of the control network. The storage ring monuments are accessible through penetrations in the roof wall shielding. One of these should be located near the linac so no additional penetrations for the linac are necessary. Depending on the instrumentation used, all of the primary control points should be inter-visible. The spacing between storage ring penetrations is normally guided by the law of error propagation and should not exceed approximately 250 m.

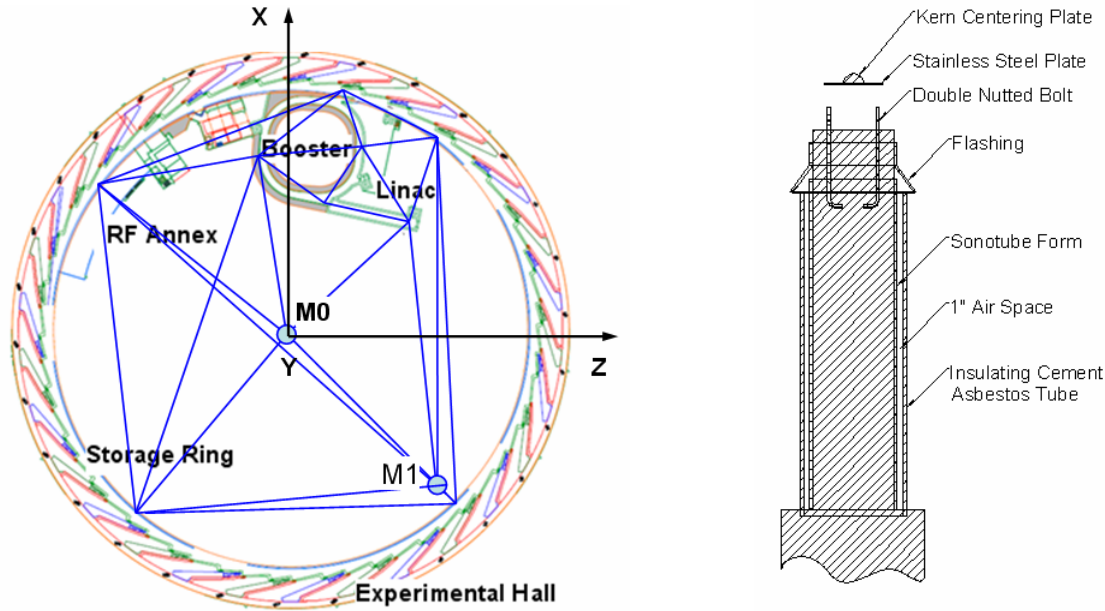


**Figure 9.1.1** (Left) primary control network and global coordinate system; (Right) design of the stable monuments.

The primary control network can be measured as a trilateration network only. Current instruments are able to resolve distances to  $\pm(0.1 + 0.1D [Km])$  [mm], where  $D$  is the length of the measured distance in units of kilometer. This level of accuracy is not attainable with triangulation networks. By using a trilateration network, it should be possible to obtain a control network point accuracy of  $\pm 0.3$  mm, similar to what has been achieved at the APS [9.1.3].

An alternative approach to determine the primary control network utilizes GPS observations for all primary control points. If public reference stations are not conveniently available, a local GPS reference station needs to be established at the storage ring center monument [9.1.4]. This base station supports differential GPS and would also be beneficial for the construction survey, as many survey companies have access to GPS and Real Time Kinematic (RTK) positioning technology. It is expected that utilizing DGPS, millimeter accuracies can be obtained. This approach needs to be further evaluated during the preliminary design phase to determine if it meets the requirements.

Both methods of measuring the primary network are highly dependent on the construction sequence and method, as lines of sight either between the monuments or the GPS satellites are required. This task has to be scheduled after the storage ring tunnel has been built but before the experiment hall enclosure is constructed.

### 9.1.3.1.2 Secondary Control Network

The design of the secondary control network is determined by the layout of the storage ring. If, as in the case of the APS, ratchet doors for each beamline are available, one can extend the secondary control network into the experiment hall (see Figure 9.1.2), providing a more stable control network design and the means to perform alignment work on beamlines while the machine is operational. The present preliminary design of NSLS-II envisions the installation of similar ratchet doors. Therefore, the secondary control network in the storage ring enclosure will be extended to the experiment hall.

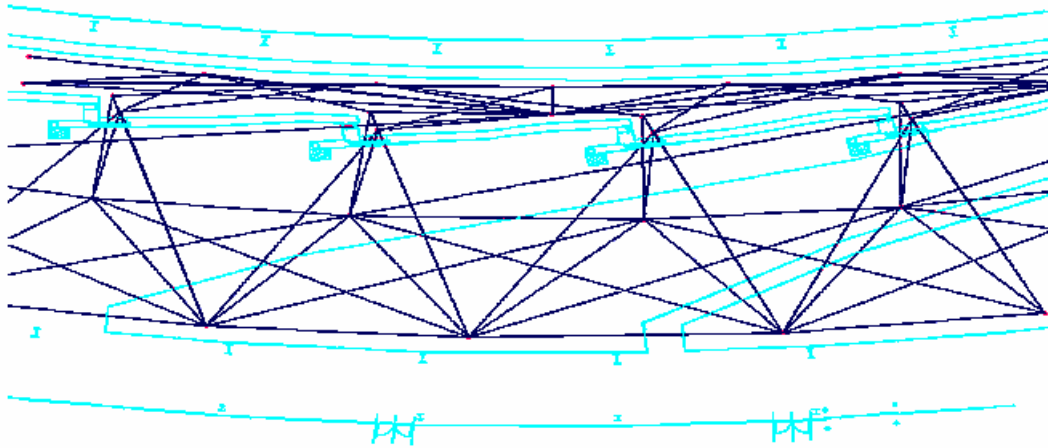


**Figure 9.1.2** A secondary control network

Extending the secondary network to the experiment hall floor will benefit the layout work for the individual beamlines while the accelerator is in the commissioning phase. Each BM and ID beamline should receive two control points strategically located at an offset from the ideal beamlines and visible from the storage ring through the ratchet wall openings. Prior to the installation of the ratchet wall collimators the tie between the beamline layout in the front end and the experiment hall has to be established using optical tooling instruments. The marking of the front ends needs to be done while no girders have been placed in the tunnel and is best performed while the quadrupole and girder support locations are being laid out. Otherwise, line-of-sight to these areas will be very restricted and the markings may no longer be possible. The layout of the front-end locations is very important, as it provides the only means to extend the alignment control through the beam ports to the experiment floor.

Laser tracker instruments will be used for measuring the secondary control network, followed by a least squares analysis of the data to produce the final control points prior to setting out the machine components.

Current laser tracker systems obtain point accuracy on the order of  $\pm 0.05$  mm in a spherical volume with a radius of 10 m around the instrument measurement head. For measuring the secondary control network with laser trackers, the primary control points are included in the measurement process and are part of the data analysis. This constrains the error propagation of the secondary control network to the level achieved by the primary reference network. The primary and segments of the secondary networks must be established, measured, and analyzed before accelerator equipment can be installed. However, sufficient time has to elapse for the concrete to cure before the control network monuments can be considered stable. Installing the floor monuments of the storage ring will necessitate core drilling to recess the target fixtures. The wall-mounted targets will be attached to concrete anchors with threaded inserts.

The secondary storage ring tunnel network should consist of at least four survey monuments located in cross sections of the storage ring spaced 10 m apart, as shown in Figure 9.1.3. An *a priori* error analysis needs to be performed to estimate the optimum locations for these targets and the expected point accuracy. The envisioned tunnel network creates a compact box structure to obtain a stable network geometry. Control points on the infield side of the tunnel are usually always accessible. The control points opposite the aisle should be located such that they will be visible after the girders have been positioned. The floor monuments are measured using common geometric leveling procedures to an accuracy of  $\pm 0.1$  mm or better. This

information, in conjunction with the laser tracker measurements after proper analysis of the redundant data, provides the 3D control network that is used to place the accelerator components. An estimated accuracy of  $\pm 0.3$  mm should be achievable for the secondary control network.

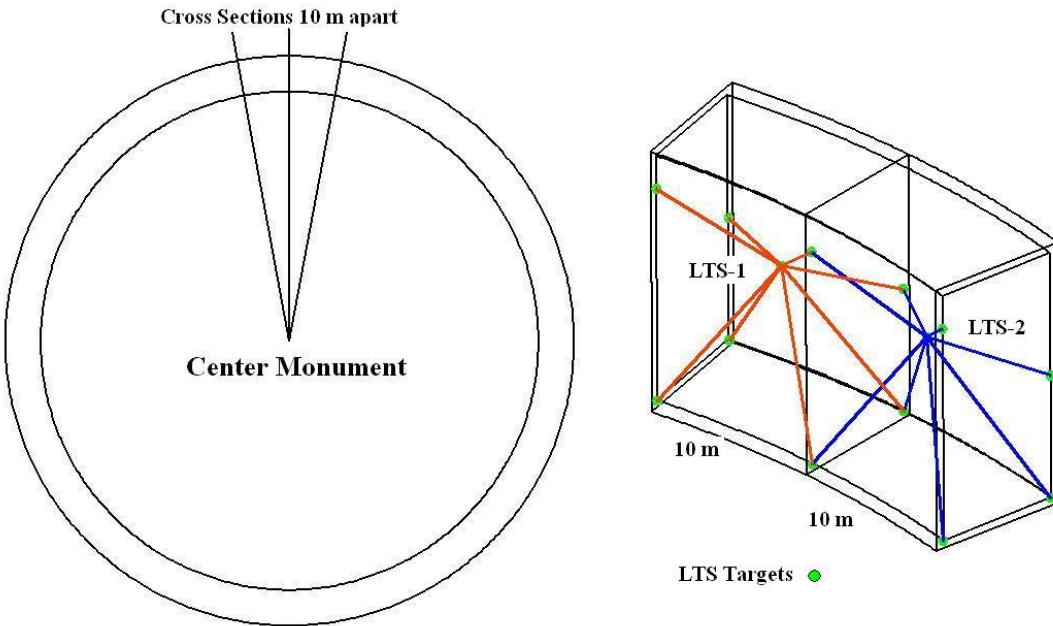


**Figure 9.1.3** Sketch of a possible network design.

A variety of monuments for 1.5 inch Spherical Mounted Retro-reflectors are commercially available and can be mounted at the predetermined locations, as shown in Figure 9.1.4. This type of SMR and its accompanying receptors will be used for all survey and alignment work at NSLS-II, where possible.



**Figure 9.1.4** Laser tracker 1.5 inch sphere mount.

For both the primary and secondary control network, error propagation calculations will be required before the realization of the reference network. This step provides information about the network density, optimal geometry, and minimum required measurement redundancy without diminishing the point accuracy of the control networks.

### 9.1.3.2 Elevation Control Network

Similar to the primary and secondary position control networks described in the previous section, we will establish primary and secondary elevation networks that are measured using common geometric level methods employing digital level instruments of proper accuracy.

Most survey instruments are referenced to local gravity. In particular, the leveling process measures elevation differences between two points with respect to the equipotential surface of the geoid. This leads to differences between a local planar system in which the accelerator is constructed and the curved geodetic reference system.

At the APS, all accelerators are located in a plane tangential to a best-fitting osculating sphere at the latitude of the center monument. The difference between this sphere and the tangential plane is on the order of 2.3 mm at 175 m from the center monument, the location of the storage ring. GEONET, the software used by APS to reduce these measurements to the reference sphere, takes local deviations into account and adjusts accordingly. In the case of NSLS-II, this may not be an issue, as the booster compared to the APS is small in size and located close to the storage ring resulting in negligible small corrections, that if necessary can be taken care of in the transfer line between the booster and storage ring injection region. This issue will be evaluated during the preliminary network analysis.

At the NSLS II components will be placed and rough-aligned first, with the components that are farthest from the tunnel entrances placed first. Care must be taken to maintain line-of-sight. To accomplish this, 3D computer graphic modeling will be used. After the heavier components are placed and aligned roughly, fine alignment will proceed using laser tracker and optical level instruments. Some settling of equipment and facilities is anticipated, and it is expected that the alignment adjustment will require checking several times during set-up, commissioning, and initial operation. Therefore, alignment equipment and expertise will have to be maintained in a constant state of readiness.

In any case, for a project the size of NSLS-II with its required high positioning tolerances, measurements for determining elevations and positions will be two distinct and separate operations. Each step requires specialty equipment designed for that purpose. Even if the existing laser trackers provide 3D point information, it is necessary to supplement the vertical information with elevation measurements derived from optical level instruments for increased accuracy.

### 9.1.3.3 The Lattice

In order to obtain congruence between the survey network and the lattice layout provided by the machine physicists, the datum of both of these systems must be the same. The six parameters (x, y, z, yaw, pitch, and roll) provided by the lattice for each beam component must be transferred to the Survey group and will be stored in a database that is used for all calculations to set the girders and other accelerator components. The database also contains the fiducial information of each component that needs to be placed. GEONET, a software analysis program originally developed at SLAC for this purpose and developed further at ANL and SLAC, performs these calculations and can be used at NSLS-II. However, commercial software that performs similar functions needs to be evaluated prior to starting the project and some software may need to be developed in house.

### 9.1.3.4 Smoothing

The initial positioning using the reference coordinate system can only be as good as the achieved network accuracy. This accuracy represents an upper limit. However, due to inherent target and instrument errors as well as environmental effects, this limit is not achievable and the actual positioning tolerance in the global system will be less than the obtained control network accuracy. Therefore a smoothing step is required.

For this part of the process, the control network is abandoned and only the local relation between adjacent girders is measured and verified. Instruments with sufficient accuracy, such as laser trackers or special offset measurement devices, can be used for this step. In particular, a comparison between the as-built and the ideal location will provide information about the relative girder position. The girder and magnet fiducial markers will be used in this step. As shown in Table 9.1.2, the girder-to-girder tolerances are relaxed in comparison to

the magnet-to-magnet requirements shown in Table 9.1.3. Nevertheless, during the fiducialization process great care has to be taken to obtain the best possible references.

**Table 9.1.3 Magnet-to-Magnet Positioning Tolerances.**

Relative Tolerances	Magnet-to-Magnet
Horizontal positioning	$\pm 0.03$ mm
Vertical positioning	$\pm 0.03$ mm
Roll angle	$\pm 0.2$ mrad

### 9.1.3.5 Fiducialization

During the fiducialization process, reference markers are determined with respect to the magnetic axis of the device. These markers are accessible after the magnet has been assembled on a girder and the vacuum chamber has been inserted. At that time, direct access to the magnetic axis is no longer possible and all positioning is performed with respect to these fiducials. Any positioning error during the fiducialization step can only be uncovered after the machine startup, with beam-based alignment methods. Unlike most of the other steps described here, this step does not provide measurement redundancy unless independent repeat measurements are performed.

For components requiring less accurate positioning, referencing to the mechanical axis may suffice. However, for the NSLS-II, the magnet-to-magnet positioning tolerances, shown in Table 9.1.3, are exceedingly stringent; therefore, a combination of magnetic and dimensional measurements is required.

Usually, rotating coils or stretched wires are used to establish the beam axis. Once the optimum position of the device is found, the information is transferred from the beam axis to the outside reference markers. This is done for each of the magnets prior to the assembly on a girder. The fiducial information is used in the assembly process. The transfer of the position information from the magnetic axis to the reference point can be performed with a 25–50  $\mu\text{m}$  accuracy, depending on the method used. However, in case of NSLS-II, the accumulation of errors in determining the reference targets, the mechanical assembly of the magnets on the girder, the alignment of the magnets on the girder, and so forth may exceed the required tolerance limits. It is therefore envisioned that all multipoles will be assembled and aligned on a girder using the vibrating wire technique [9.1.5]. In this way, the intermediate steps to obtain fiducial information for each magnet separately are circumvented. After this step, the girder will be considered the smallest unit that needs to be placed in the storage ring tunnel.

The girders need to be fitted with permanently mounted SMR receptacles above each of the support feet on both the inboard and outboard side. This is required because the girder will have more than three support feet for reasons of stability and vibration damping. It is envisioned that laser trackers will be used to perform the coordinate transfer from the wire, via a touch-free probe if necessary, to the girder fiducials that are used to position the girder and to check for local deformations while aligning the girder in the storage ring tunnel. It is important that there be a defined stay-clear area around each of the girder fiducials. In particular, above each fiducial no obstructions are allowed; doing otherwise would prohibit the use of level rods on these markers.

R&D is planned to carefully evaluate this approach for the magnet alignment and fiducialization prior to construction of NSLS-II.

### 9.1.4 Implementation

Close coordination between the construction efforts and implementation of the control network must be maintained while NSLS-II is being built. It is also imperative that the survey and alignment team be involved

early in the design of the girder and magnet supports and moving systems, because the positioning resolution and performance are directly linked to these devices.

### 9.1.5 Training

At minimum, operators of survey equipment should have several years of experience in properly handling and operating instruments of that type. Instrument operators will have to work closely with the technicians who will make the required adjustments. In particular, when using laser trackers to provide real-time, online alignment capabilities, Survey and Alignment technicians will apply the required adjustments; these two steps go hand-in-hand. Most laser tracker manufacturers provide onsite training for operating their systems. For the alignment of the front ends and beamlines, optical tooling is required because space is limited. Training in the use of optical tooling instruments is commercially available. All personnel involved with the survey and alignment tasks should have experience and aptitude in the precision alignment of 3D components and hardware.

### 9.1.6 Component Assembly, Testing, and Calibration

Many of the instruments that are employed for survey and alignment must be tested and calibrated on a regular basis. An alignment and calibration room will be provided for this purpose. This room will be environmentally stable and will have sufficient space for secure storage of all calibration equipment (including a Coordinate Measuring Machine and one or more large surface plates), as well as for the survey instruments themselves. The alignment and calibration room will also have enough additional space to align critical assemblies. Because survey instruments are very delicate, in-house calibration is generally preferred over shipping equipment out to a vendor. Calibration procedures and training are therefore required.

The alignment and calibration room will be large enough for calibration as well as for critical assembly work to be completed in a temperature-stable environment, thus allowing alignment processes to be tested accurately before they are used for the accelerator.

### 9.1.7 R&D

Two important R&D tasks have been identified. The first is an error analysis of the network configuration, to determine the network layout. It is also important in that step to incorporate the anticipated construction methodology. The second important R&D task determines the magnet measurement process and its effects on the survey and alignment process. If it can be shown that the vibrating wire method can be used to position the magnets on girders, then the girder will become the smallest unit that the survey team has to contend with. However, close interaction will be required between the magnet measurement and survey groups. In particular, the girder fiducialization process needs to be established, because special equipment for the touchless wire pickup may be required.

## References

- [9.1.1] H. Friedsam, "The Alignment of the Advanced Photon Source at Argonne National Laboratory," International Workshop on Accelerator Alignment, CERN, Switzerland, 1993.
- [9.1.2] R. Ruland, "Synchrotron Radiation Sources A Primer," World Scientific Publishing ISBN 981-02-1856-7.
- [9.1.3] H. Friedsam, M. Penicka, and S. Zhao, "Status Report on the Survey and Alignment Efforts and Results of the Advanced Photon Source," International Workshop on Accelerator Alignment, KEK, Japan 1995.
- [9.1.4] H. Friedsam, R. Ruland, private communication.
- [9.1.5] Z. Wolf, "A Vibrating Wire System for Quadrupole Fiducialization," SLAC, LCLS-TN-05-11.



## 9.2 Process Water Systems

### 9.2.1 Scope

The NSLS-II accelerator and beamline components require a large amount of heat rejection as well as a stringent temperature stability. A number of closed-loop water systems are used that exchange heat with the water from cooling towers and chilled water from the BNL's central plant. The preliminary designs of these closed-loop water systems are described in this section. The description for the cooling tower and chilled water systems can be found in the technical design report for the Conventional Facilities.

### 9.2.2 Thermal Loads

The major sources of heat generation are identified in Table 9.2.1. When all beamlines are built, the total heat rejection is approximately 7.4 MW. This heat is rejected to closed loop water systems at different inlet water temperatures as shown in column 3.

**Table 9.2.1:** Major heat sources in the NSLS-II facility and the nominal inlet water temperature for heat rejection. The total heat rejected adds up to 7,425 kW, not including the air-conditioning load for the building.

Heat Source	Heat Rejected (kW)	Inlet Water Temperature (°C)
Linac	100	24.0 ± 0.5
Booster	400	29.5 ± 0.5
Storage ring magnets	1400	29.5 ± 0.1
Absorber system and front ends	700	29.5 ± 0.1
RF system (klystrons)	1400	29.5 ± 0.5
Cryoplant	300	33
Power supplies and equipment	1100	7.2 ± 1.0
Beamlines (x-ray power)	250	
Beamlines (electrical)	1700	7.2 ± 1.0
Vacuum chambers	75	29.5 ± 0.05

### 9.2.3 Preliminary Designs of the Water Systems

There are three different closed loop water systems: (1) deionized process water systems for the copper components, (2) deionized process water system for the storage ring vacuum chambers, and (3) chilled water system for the heat exchangers of the air-cooled racks of power supplies and electronic. The first two systems are designed to exchange heat mainly with the cooling-tower water, but they can also reject partial heat load to the chilled water system on hot and humid days (wet bulb temperature of > 25 °C).

Each of these three systems are divided into five separate unit in order to keep the pipes, pumps, valves and heat exchangers to reasonable sizes. The reduced system sizes also improve their temperature stability. The pumping stations are housed in 5 mechanical equipment rooms located on the inboard side of the storage

ring (see Figure 9.2.1). Three additional pumping stations for copper systems are provided, 2 in the RF Annex and 1 in the Booster building.

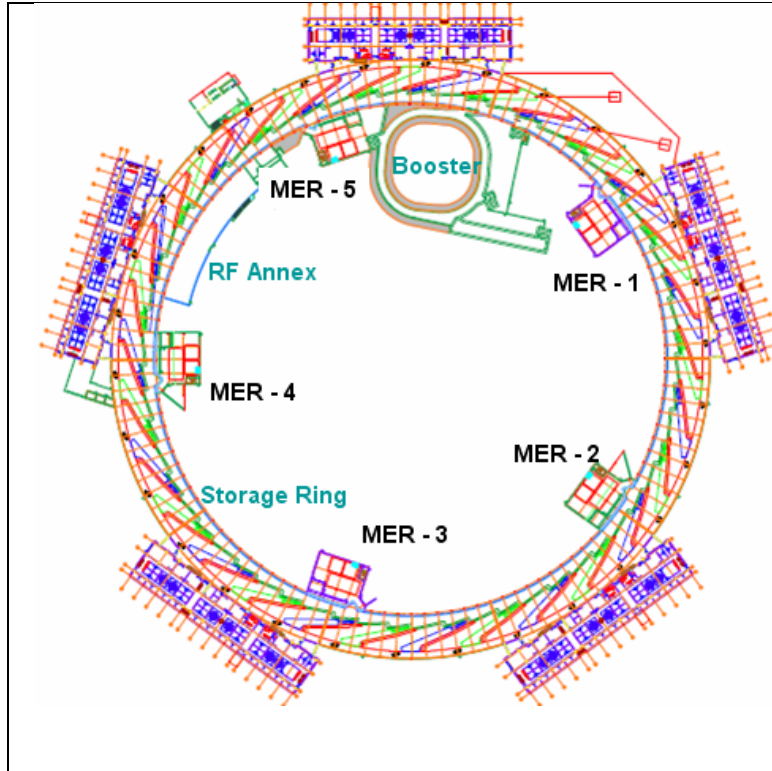


**Figure 9.2.1** Mechanical equipment rooms (MERs) for the pumping stations of the closed-loop water systems. Additional pumping stations are installed in the RF Annex and Booster.

The process & instrumentation diagram (PID) for the copper water system is shown in Figure 9.2.1. The pumping station uses two 75 HP, variable frequency drive (VFD), pumps for redundancy and reliable operation. The VFD pumps, besides being energy-efficient, also provide better control over the supply-side flow, pressure and temperature. A slipstream deionizing skid keeps the resistivity and pH of the water in the specified range to minimize copper corrosion (see below).

A portion of the process water exiting from the pumps exchanges heat with the tower water in order to reject heat from magnets, absorbers, and beamline components. If necessary, heat is also exchanged with chilled water for additional cooling on hot and humid days. Mixing valves are used to regulate the water temperature to  $85 \pm 0.1$  °C before it is supplied to the storage ring. Another chilled water heat exchanger is used, as shown in the figure, to bring down the water temperature for the beamlines to  $75 \pm 0.1$  °C.

Each MER supplies process and chilled water to the equipment and components of six cells. The supply and returns pipes are branched out in the middle to serve 3 cells on each side.

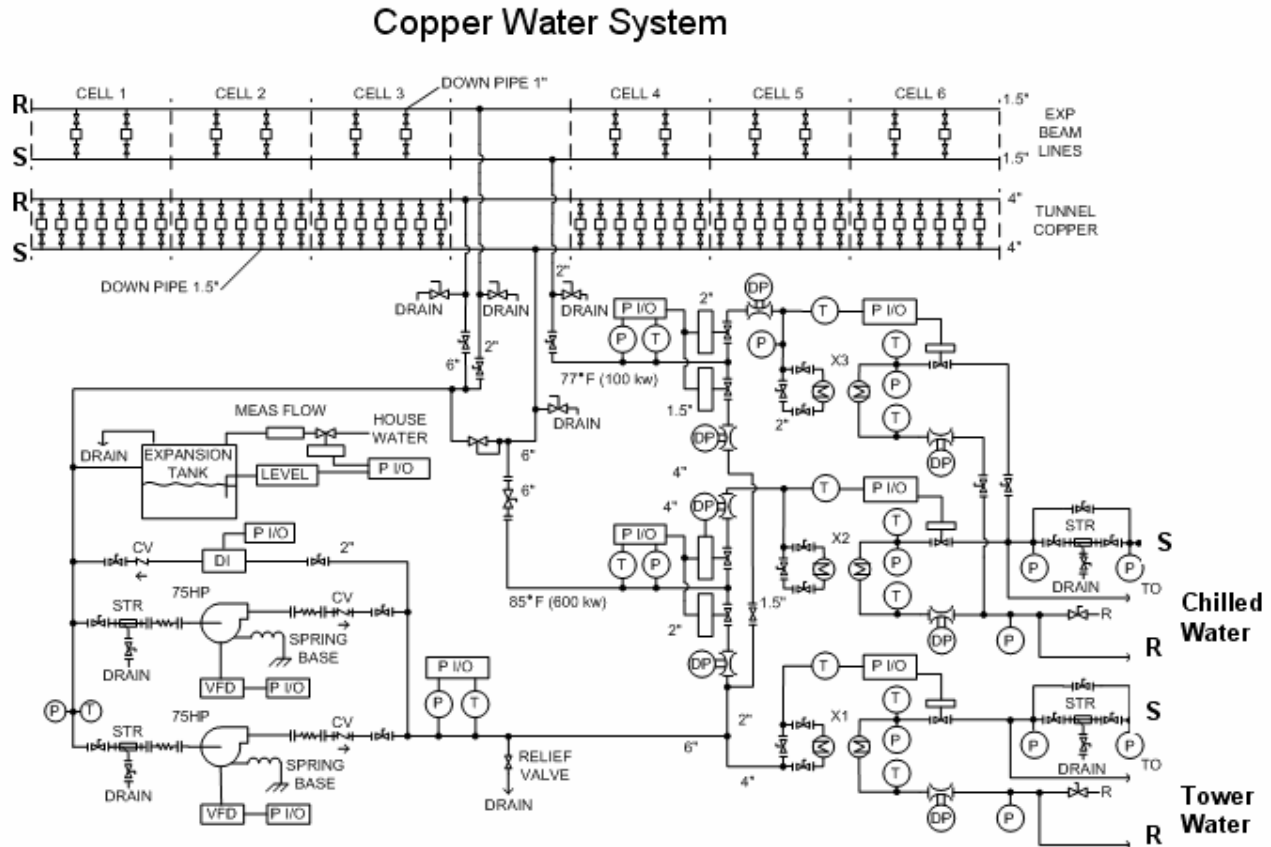


Figure 9.2.2 PID of the pumping station for the copper water system.

A similar but smaller-size pumping station with 10 HP pumps is used for the aluminum water system as shown in Figure 9.2.3. The aluminum water system is also a closed loop system which is completely isolated from the copper components and other water systems to eliminate the possibility of galvanic corrosion. The aluminum chambers of the storage ring do not directly intercept x-rays, but they do intercept x-ray power scattered from the absorbers. Another source of heat is the frictional losses from water flow through the three cooling channels of the chambers. The temperature stability of  $\pm 0.05$  °C is specified for the aluminum water system in order to keep the chamber deformations, which affect the BPM locations, to within acceptable limits.

## Aluminum Water System

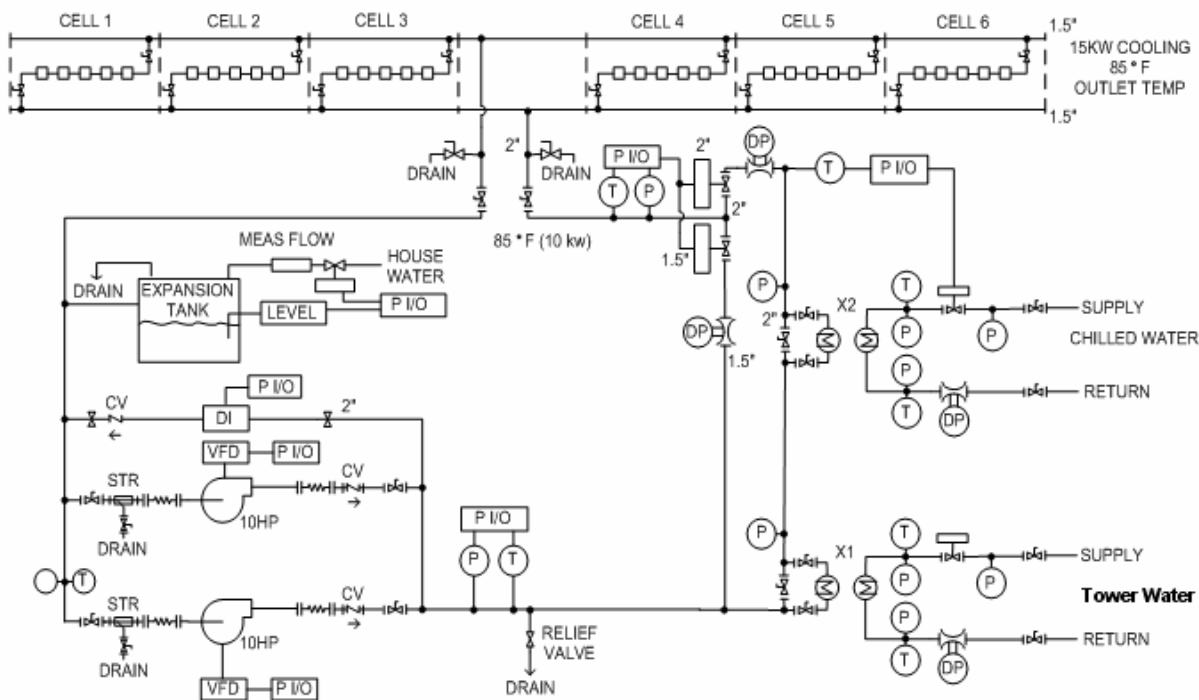


Figure 9.2.3 PID of the pumping station for the aluminum water system.

For the bakeout of aluminum chambers, the present plan is to use NEG strips or kapton heating foils. Bakeout by hot water (as is done at APS) will be considered as a less preferable option because of its complicated design and safety concerns.

The closed-loop chilled water system (not shown) exchanges heat only with the chilled water from central plant. It does not use deionizing skid and requires a moderate temperature stability of only  $\pm 1$  °C.

### 9.2.4 Process Water Quality Control

Copper corrosion in the copper components cooled by deionized water remains a major concern. The main factors that affect the copper corrosion process are: water resistivity, pH, dissolved oxygen and water temperature. An investigation will be made to determine the most appropriate ranges for these parameters. Based on the experience of several accelerator facilities, the following values are selected for the preliminary design:

- Resistivity =  $1 \text{ M}\Omega\text{-cm} \pm 5\%$
- pH =  $7.5 \pm 0.2$
- Oxygen concentration =  $6 \text{ ppb} \pm 1 \text{ ppb}$
- Water temperature <  $40$  °C.